



HAL
open science

Numerical models of volcanic flows for an estimation and delimitation of volcanic hazards, the case of Reventador volcano (Ecuador)

Silvia Ximena Vallejo Vargas

► **To cite this version:**

Silvia Ximena Vallejo Vargas. Numerical models of volcanic flows for an estimation and delimitation of volcanic hazards, the case of Reventador volcano (Ecuador). Earth Sciences. Université Clermont Auvergne [2017-2020], 2017. English. NNT : 2017CLFAC100 . tel-01930269

HAL Id: tel-01930269

<https://theses.hal.science/tel-01930269>

Submitted on 21 Nov 2018

HAL is a multi-disciplinary open access archive for the deposit and dissemination of scientific research documents, whether they are published or not. The documents may come from teaching and research institutions in France or abroad, or from public or private research centers.

L'archive ouverte pluridisciplinaire **HAL**, est destinée au dépôt et à la diffusion de documents scientifiques de niveau recherche, publiés ou non, émanant des établissements d'enseignement et de recherche français ou étrangers, des laboratoires publics ou privés.

UNIVERSITÉ CLERMONT AUVERGNE

UFR Sciences et Technologies

Laboratoire Magmas et Volcans

COLE DOCTORALE DES SCIENCES FONDAMENTALES

THÈSE

présentée pour obtenir le grade de

DOCTEUR D'UNIVERSITÉ

"Mémoire de Recherche"

Par

Uxkl'Zlo gpc'XCNNGLQ'XCTI CU

Vkwr:kt g'f w'O cwtg '4'Tgej gtej g'O ci o cu'gv'Xqrecpu'

**P wo gt kecnò qf gn'qh'xqreple'hny u'ht 'èp'guko c vlap'èpf 'f gko ksc vlap'qh'
xqreple'j c| ct f u 'vj g'ècug'qh'T gxgpvcf qt 'xqrepcq'*Gewef qt +'**

Thèse dirigée par **Mctlo 'Mghqwp'**

Soutenue publiquement le 24/11/2017

.....O go dt gu'f g're'eqo o kulkqp'f øgzco gp<

Karim Kelfoun	LMV, Université Clermont Auvergne, Clermont-Ferrand	Directeur de Thèse
Sonia Calvari	INGV, Istituto Nazionale di Geofisica e Vulcanologia, Catania	Rapporteur
Daniel Andrade	IG, Escuela Politécnica Nacional, Quito	Rapporteur
Andrew Harris	LMV, Université Clermont Auvergne, Clermont-Ferrand	Examineur
Fanny Garel	UM, Université de Montpellier, Montpellier	Examinatrice
Oryaëlle Chevrel	LMV, Université Clermont Auvergne, Clermont-Ferrand	Membre invité

Acknowledgements

The development of this thesis during these three years allowed me to find many interesting, intelligent and humble people, which were always open to share their experience and knowledge.

First of all I would like to thank to the Secretaría de Educación Superior, Ciencia, Tecnología e Innovación (SENESCYT) for having financed this thesis. As well to the Instituto Geofísico of the Escuela Politécnica Nacional for giving me the facilities and permissions for my stay in France. To the Institut de Recherche pour le Développement (IRD) for the support along the development of this research. Likewise, to the Laboratoire Magmas et Volcans for having allowed me to develop my research with them.

Thanks to my colleagues from the Instituto Geofísico for helping me to perform the different field works during these years to El Reventador volcano and for all the fantastic stories that we have built on it. A special thanks to Patricio Ramón for being my boss and my friend, and for having been an inspiration on this fantastic world called volcanology. Likewise, a huge thanks to my IG friends, MaFer, Marco, JC, Daniel A., Lili T. for all the discussions, advices and help.

To my dear thesis advisor, Karim Kelfoun for having trusted on me since the beginning. For his teaching, friendship, patience and guide through these three years. Thank you for your support and for having pushed me up when I needed the most.

Thanks to my friends in Clermont, in whose I have found a truly friendship and more than that a family. For all the special moments that we spent together. A special thanks to Ale, Swetha, Marie Anne, Anne, Patricio, Melo, Federica, Juliette, Cat, Valentin G., Valentin F., Taya, Gio, Diego, Vincent, Corentin, Lola. Thanks for the help, support and encouragement that I have received during those three amazing years. You are simply the best!

To Grace, Priscilla R, Priscilla C, Lorena and Francesca, for all those incredible years of friendship. I appreciate all the advices and good moments that we have shared through time. Thanks for being so present during these years. For listening all my stories about volcanoes and how crazy I can talk about them and their eruptions.

To my geological friends, that life gave to me, Panter, Diego, Jonathan, Fabián. Thank you for the nice moments that we spent together and for teaching me that other interesting things exist outside volcanoes ;-)

The last but the most important, to my family, my parents, sisters, nephews, brother in law, uncles, cousins and dog: Carlos, Paty, Belén, Andrea, Lolito, Camilo, Luán, Stefan, Cenizo. All of this is for you. You always trusted on me and you always pushed me to give and try my best. I wouldn't accomplish this without your love and care even if I was far far away from you. Thanks for have listened my crazy stories and for being passionate about them as well. All the thanks to you as well, for having Cenizo as a part of their family. I'm sure he always will be grateful. As well an especial thanks to my cousins Enriquez-Vargas, Redrobán Vallejo for being part of the path through my volcanological life.

Abstract

Numerical models of volcanic flows for an estimation and delimitation of volcanic hazards, the case of El Reventador volcano (Ecuador)

Lava flows are the most representative volcanic products of effusive eruptions and are formed when the magma is extruded and flows on the surface. When lava flows reach the surface they lose heat and cool. Cooling affects directly the rheology of the lava up to a point where it cannot flow anymore. Rheological parameters that control the dynamics of lava flows are the viscosity and the yield strength which in turn depends on the chemical composition, crystallinity and bubble content. There exist numerous models for the rheology estimation, mostly developed for basaltic lava flows and few for andesitic ones.

Lava flows can highly affect populated areas, infrastructures and environment. A way to forecast the future damages is to developed numerical codes of the lava propagation on real volcanic topography. This challenging method combines the topography, the rheology, the heat loss, and flow dynamics to simulate the emplacement of a particular lava flow. The numerical code VolcFlow which is based on the depth-averaged approach is able to reproduce the main physical characteristics of the deposits like morphology, length and thickness. Here 3 models are proposed for their implementation in VolcFlow with the aim to simulate lava flows. One model is isothermal, the second includes cooling and the associated rheological variations, and the third takes into account the crust formation and its effect on the flow emplacement. To check the validity of the different approaches, the models were tested with four study cases, two with basaltic compositions (molten basalt experiment of the Syracuse lava Project and the August-November, 2015 lava flow from Piton de la Fournaise, France) and two with andesitic compositions (the December 4th-5th lava flow from Tungurahua, Ecuador, and three lava flows from El Reventador, Ecuador). Results of the simulations shows that the isothermal model can reproduce the flows even if it does not consider the cooling and rheology variation. The model that includes rheological laws as function of crystallization induced by cooling down flow can give very good results but is very sensitive to the input data, in particular to the fluid viscosity that is very dependent on chemical composition and temperature. Finally, the model that includes cooling and synthetic sigmoid rheological law shows good coherence for all the cases except at Piton de la Fournaise. The model that aims to simulate the formation of a crust on the lava flow surface, lava flowing underneath and break-out mechanisms leads to the thickening of the crust. Hence, break-out mechanism is not reproduced with VolcFlow.

Keywords: lava flows, numerical simulations, rheology, El Reventador volcano

Résumé

Modèles numériques de coulées de lave pour une estimation et une délimitation du risque volcanique, le cas du volcan El Reventador (Equateur)

Les coulées de laves sont les produits volcaniques les plus représentatifs des éruptions effusives. Elles sont formées quand le magma est extrudé et se répand à la surface de la Terre. Quand la lave arrive en surface, elle perd de la chaleur et refroidit. Le refroidissement affecte directement les propriétés rhéologiques de la lave, jusqu'à arrêter son écoulement. Les paramètres rhéologiques qui contrôlent la dynamique des coulées de laves sont la viscosité et le seuil de plasticité, qui dépendent eux-mêmes de la composition chimique, de la cristallinité et de la teneur en bulles. Il existe de nombreux modèles d'estimation de la rhéologie, la plupart développés pour les coulées de lave basaltiques et quelque uns pour les coulées de lave andésitiques.

Les coulées de laves peuvent grandement affecter les régions peuplées, les infrastructures et l'environnement. Un moyen de prévoir les futurs dégâts est de développer des modèles numériques pour prévoir la propagation des coulées de laves sur des topographies volcaniques réelles. Cette méthode difficile combine la topographie, la rhéologie, la perte de chaleur et la dynamique de l'écoulement pour simuler l'emplacement d'une coulée de lave précise. Le code numérique VolcFlow, qui est basé sur une approche moyennée verticale, est capable de reproduire les caractéristiques principales des dépôts comme la morphologie, la longueur et l'épaisseur. Dans cette étude sont proposés trois modèles implémentés dans VolcFlow et ayant pour but de simuler des coulées de laves. Le premier est isotherme, le deuxième inclut le refroidissement et les variations rhéologiques associées, et le troisième prend en considération la déformation de la croûte à la surface de la coulée et son effet sur l'emplacement de la coulée. Afin de vérifier la validité des différentes approches, les modèles sont testés sur quatre cas d'étude : deux coulées de lave de composition basaltique (expérience de basalte fondu de Syracuse lava Project et la coulée de lave d'août-novembre 2015 du Piton de la Fournaise, France) et deux de compositions andésitique (la coulée de lave du 4-5 décembre 2015 du Tungurahua et trois coulées de lave du Reventador, Equateur). Les résultats des simulations montrent que le modèle isotherme peut reproduire les coulées même s'il ne prend pas en compte les variations de rhéologie et le refroidissement. Le modèle incluant la cristallisation, induite par le refroidissement de la lave au cours de son écoulement, et les variations rhéologiques associées donne de très bons résultats mais est très sensible aux paramètres d'entrée, en particulier à la viscosité, elle-même très dépendante de la composition chimique et de la température. Enfin, le modèle prenant en compte le refroidissement et les variations de rhéologie par une loi synthétique sigmoïde montre une bonne cohérence dans tous les cas simulés, sauf pour le Piton de la Fournaise. Le modèle visant à simuler la formation d'une croûte à la surface de la lave et sa percée par l'écoulement sous-jacent amène uniquement à l'épaississement de la croûte. Le mécanisme de percée n'est pas reproduit avec VolcFlow.

Mots-clés: coulées de lave, simulations numériques, rhéologie, volcan El Reventador

Resumen

Modelos numéricos de flujos volcánicos para una estimación y delimitación de peligro volcánico, el caso del volcán El Reventador (Ecuador)

Los flujos de lava son uno de los más representativos productos volcánicos de erupciones efusivas y se forman cuando el magma es extruido a la superficie. El enfriamiento afecta directamente la reología de la lava hasta el punto en que esta ya no puede fluir más. Los parámetros reológicos que controlan la dinámica de los flujos de lava son la viscosidad y el límite elástico los cuales a su vez dependen de la composición química, cristalinidad y contenido de burbujas. Existen varios modelos para la estimación reológica pero enfocados principalmente en flujos basálticos y muy pocos en flujos andesíticos.

Los flujos de lava pueden afectar grandemente a zonas pobladas, infraestructura y el medio ambiente. Una manera de pronosticar el daño futuro es desarrollar códigos numéricos que simulen la propagación de la lava sobre una topografía real. Este desafiante método combina la topografía, la reología, la pérdida de calor, y la dinámica de flujos para simular el emplazamiento de un flujo en particular. El código numérico VolcFlow está basado en las ecuaciones de profundidad, las cuales pueden reproducir las principales características físicas de los depósitos como la morfología, largo y espesor. En este estudio 3 modelos son propuestos para ser implementados en VolcFlow con el objetivo de simular flujos de lava. El primero es el isothermal, el segundo incluye el enfriamiento y las variaciones reológicas asociadas, y el tercero toma en cuenta la formación de la corteza y sus efectos en el emplazamiento del flujo. Para determinar la validez de los diferentes enfoques, los modelos fueron probados con cuatro casos de estudio, dos con composiciones basálticas (basalto fundido del Syracuse lava Project y el flujo de lava del Piton de la Fournaise, La Réunion-Francia de Agosto-Diciembre 2015) y dos casos con composiciones andesíticas (flujo de lava del Tungurahua, Ecuador del 4 y 5 de Diciembre del 2010 y tres flujos de lava del volcán El Reventador). Resultados de estas simulaciones muestran que el modelo isothermal puede reproducir los flujos a pesar de que el efecto del enfriamiento y la variación reológica no estén considerados. El modelo que incluye las leyes reológicas en función de la cristalización inducida por el enfriamiento del flujo puede dar muy buenos resultados, pero es muy sensible a los datos de entrada, en particular a la viscosidad fluida que es muy dependiente de la composición química y de la temperatura. Finalmente, el modelo que incluye el enfriamiento y la ley reológica empírica sigmoideal muestra una buena coherencia para todos los casos. El modelo que pretendía simular la formación de la corteza en superficie, la lava fluyendo por debajo y mecanismos de rompimiento, generan el engrosamiento de la corteza. De esta manera, el rompimiento no es reproducido por VolcFlow.

Palabras clave: flujos de lava, simulaciones numéricas, reología, volcán El Reventador

"Los ecuatorianos son seres raros y únicos: duermen tranquilos en medio de crujientes volcanes, viven pobres en medio de incomparables riquezas y se alegran con música triste"

Alexander Von Humboldt

Table of Contents

Acknowledgements	
Abstract	
Résumé	
Resumen	
Table of Contents	i
List of Figures.....	vii
List of Tables.....	xxi
Introduction.....	1
Chapter 1: Lava flow description and properties	
1.1 Lava flow characterization	5
1.1.1 Lava flow types	5
1.1.1.1 Pāhoehoe	6
1.1.1.2 ‘A’ā.....	7
1.1.1.3 Block lava.....	8
1.1.2 Size and shape	10
1.1.3 Lava flow distribution systems	11
1.1.4 Inflation.....	12
1.2 Parameters controlling lava flow length.....	13
1.2.1 Effusion rate.....	14
1.2.2 Volume.....	14
1.2.3 Slope surface.....	15
1.2.4 Thermo-rheological properties	16
1.3 Cooling and crystallization of lavas	16
1.3.1 Thermal and rheological structure of a lava interior	17
1.3.2 Heat balance mechanisms	18
1.3.2.1 Heat loss by radiation (q_{rad})	19

1.3.2.2	Heat loss by Convective Force (q_{force}).....	20
1.3.2.3	Heat loss by Rain (q_{rain}).....	21
1.3.2.4	Heat loss by Conduction (q_{cond}).....	21
1.3.2.5	Heat generated by Crystallization (q_{cryst}).....	21
1.3.2.6	Heat generated by Viscosity (q_{visc}).....	22
1.3.3	Cooling Model proposed by FLOWGO	22
1.4	Lava Rheology	24
1.4.1	Viscosity (η)	25
1.4.1.1	Dynamic fluid viscosity (η_f).....	26
1.4.1.2	Relative viscosity (η_r).....	28
1.4.2	Rheological model for lava flows	31
1.4.2.1	Newtonian fluid.....	33
1.4.2.2	Bingham fluid.....	34
1.4.2.3	Pseudo-plastic fluid	34
1.4.2.4	Herschel-Bulkley.....	34
1.4.3	Yield strength (τ_o)	34
1.4.3.1	Yield strength models	35

Chapter 2: Effusive activity from an andesitic volcano, El Reventador (Ecuador)

2.1	Introduction.....	37
2.2	Background	38
2.2.1	El Reventador volcano	38
2.2.2	Regional geology for El Reventador.....	39
2.2.3	Topographic implications.....	40
2.2.4	Historical activity	42
2.2.5	Current activity.....	42
2.2.6	Network monitoring	44
2.3	Tools for the identification of the superficial activity between 2010 - 2014.....	44
2.3.1	Monitoring tools	45
2.3.1.1	Seismicity	45
2.3.1.2	Thermal alerts from MIROVA	46
2.3.1.3	Direct observations	47
2.3.1.3.1	Regular overflights.....	48
2.3.1.3.2	Ground base camera network.....	48
2.4	Field surveys campaigns.....	50
2.4.1.1	Rock sampling.....	52
2.4.1.2	Ground control points (GCPs)	53
2.4.1.3	Photogrammetry	54
2.4.1.4	DEM 2013 10 19	55
2.4.1.5	DEM 2015 04 21	55
2.4.1.5.1	Method	56

2.4.1.5.2	Results.....	56
2.5	Identification and characterization of the superficial activity between 2010 and 2014.....	57
2.5.1	Pyroclastic Cone	57
2.5.2	Lava dome	58
2.5.3	Distribution and characterization of lava flows of El Reventador volcano between 2012 and 2014.....	59
2.5.3.1	Analysis of thermal/visual images	60
2.5.3.1.1	Lava flows from the period 2012-2014.....	60
2.5.3.2	Lava flows mapping.....	66
2.5.3.2.1	Direct mapping using the 2013 and 2015 DEM's.....	66
2.5.3.2.2	Mapping by projecting thermal images over the topography.....	66
2.5.3.3	Lava flows velocity estimation.....	71
2.5.3.4	Error consideration	72
2.5.3.5	Spatial distribution of lava flows	72
2.5.3.6	Lava flows morphology	75
2.5.3.6.1	Lava flow thickness measurements	75
2.5.3.6.2	Lava flow volume estimation	77
2.5.3.6.3	Lava flows emitted between 2002 and 2009	78
2.5.3.6.4	Analysis.....	82
2.5.3.7	Geochemistry	84
2.5.3.8	Petrography	85
2.6	Eruptive phases	86
2.6.1	Phase D: July 2008 – Late 2010.....	86
2.6.2	Phase E: Early 2011 – December 2011.....	86
2.6.3	Phase F: Early 2012 – Late 2014.....	87
2.7	Data as input data of numerical models for lava flow simulations.....	89

Chapter 3: Numerical Codes for Lava Flows Simulation

3.1	Deterministic numerical codes	93
3.1.1	Channeled model: FLOWGO.....	93
3.1.2	Cellular Automata models.....	98
3.1.2.1	SCIARA	98
3.1.2.2	MAGFLOW.....	101
3.1.2.3	MOLASSES	104
3.1.2.4	LavaSIM.....	105
3.1.3	Depth-averaged models.....	107
3.1.3.1	Costa and Macedonio (2005).....	108
3.1.3.2	VOLCFLOW (Kelfoun & Druitt, 2005)	110
3.1.3.3	Code from Bernabeu <i>et al.</i> 2016	110
3.1.4	Generic 3D computational fluid dynamics codes.....	112
3.1.4.1	OpenFOAM.....	112
3.1.4.2	FLOW-3D	112
3.1.4.3	COMSOL	113
3.1.5	Messless and 'bottom-up' methods.....	113

3.1.5.1	GPUSPH	113
3.1.5.2	NB3D	114
3.2	Stochastic or probabilistic numerical codes	114
3.2.1	DOWNFLOW.....	115
3.2.2	Q-LavHA.....	118
3.3	Comparisons between models	120
3.3.1	Benchmark comparison by Cordonnier <i>et al.</i> (2015).....	120
3.3.2	Benchmark comparison by Dietterich <i>et al.</i> (2017).....	122
3.4	Computational cost and time duration simulations	124
3.5	Model to be improved in VolcFlow	125

Chapter 4: Numerical Modelling of Lava Flows: Method

4.1	VolcFlow code, principles.....	127
4.2	Considered rheologies in VolcFlow	129
4.2.1	Model n°1: Isothermal.....	129
4.2.2	Model n°2: Thermorheological variation.....	130
4.2.2.1	Heat budget, cooling and crystallization per unit of time	130
4.2.2.1.1	Cooling from per unit of time:.....	132
4.2.2.1.2	Crystallization per unit of time:.....	133
4.2.2.1.3	VolcFlow improvement with the cooling and crystallization equations.....	133
4.2.2.2	Rheological variation.....	136
4.2.2.2.1	Existing thermo-rheological models	136
4.2.2.2.2	Sigmoid law.....	138
4.2.3	Model n°3: hot interior and crust.....	140
4.3	Summary.....	143

Chapter 5: Numerical modelling of lava flows: Results and Discussion

5.1	Molten basalt benchmark (Syracuse Lava Project).....	146
5.1.1	Description of the lava flow	146
5.1.1.1	Measurements during the advance of the flow	147
5.1.2	Initial conditions	149
5.1.2.1	Numerical topography.....	149
5.1.2.2	Input parameters.....	149
5.1.3	Numerical models.....	150
5.1.4	Simulations	151
5.1.4.1	Model n°1: Isothermal.....	151
5.1.4.2	Model n°2b: thermo-rheological variation with sigmoid model.....	153
5.1.4.2.1	Model n°2b 1: Sigmoidal model considering a constant yield strength and variable viscosity dependent on the temperature	154
5.1.4.2.2	Model n°2b 2: Sigmoidal model considering a constant viscosity and variable yield strength dependent on the temperature	157

5.1.4.3	Model n°3: Crust formation with hot interior.....	160
5.1.5	Discussion.....	163
5.2	Lava flow from Piton de la Fournaise.....	166
5.2.1	Description of the flow: the lava flow from August to November, 2015.....	166
5.2.2	Initial conditions.....	168
5.2.3	Numerical models.....	169
5.2.4	Simulations.....	169
5.2.4.1	Model n°1: Isothermal.....	169
5.2.4.2	Model n°2a: including the effect of the cooling and rheological variation.....	170
5.2.4.3	Model n°3: Crust formation and hot interior.....	173
5.2.5	Discussion.....	175
5.3	Lava flow from the December 5 th , 2010 eruption of Tungurahua volcano (Ecuador).....	177
5.3.1	Description of the flow.....	177
5.3.1.1	Recorded data during the eruption.....	178
5.3.2	Initial conditions.....	180
5.3.3	Numerical models.....	181
5.3.4	Simulations.....	181
5.3.4.1	Model n°1: Isothermal.....	181
5.3.4.2	Model n°2: including the effect of the cooling and rheological variation.....	182
5.3.4.2.1	Model n°2a: Cooling and rheological variation using existing thermo-rheological models.....	183
5.3.4.2.2	Model n°2b: Cooling and rheological sigmoid law.....	187
5.3.5	Discussion.....	190
5.4	Lava flows from El Reventador.....	192
5.4.1	Lava flow from April 2014 (LF25).....	193
5.4.1.1	Initial conditions.....	193
5.4.1.2	Numerical models.....	194
5.4.1.3	Simulations.....	195
5.4.1.3.1	Model n°1: Isothermal.....	195
5.4.1.3.2	Model n°2: including the effect of the cooling and rheological variation.....	195
5.4.2	Lava flow from June – July 2017.....	197
5.4.2.1	Initial conditions.....	198
5.4.2.2	Numerical models.....	199
5.4.2.3	Simulations.....	199
5.4.2.3.1	Model n°1: Isothermal.....	199
5.4.2.3.2	Model n°2: Including the effect of the cooling and rheological variation.....	201
5.4.3	Analogous of lava flow 1 (LF1) from November, 2002.....	205
5.4.3.1	Initial conditions.....	205
5.4.3.2	Numerical models.....	205
5.4.3.3	Simulations.....	206
5.4.3.3.1	Model n°1: Isothermal.....	206
5.4.3.3.2	Model n°2: Including the effect of the cooling and rheological variation.....	206
5.4.3.3.3	Model n°2a: Cooling and rheological variation using existing thermo-rheological models.....	207
5.4.3.3.4	Model n°2b: Cooling and rheological variation using sigmoid law.....	210
5.4.4	Discussion.....	214

Chapter 6: Summary, Conclusions and Perspective

Summary.....217
Conclusions.....218
Perspectives.....222

References225

Appendix

Figures

Chapter 1 – Lava flow description and properties

Figure 1. 1 a) Smooth spheroidal forms, inflation process. b) Surface folds known as ropes. c) New lava flow due to the breakout of the latest unit. d) Tumuli structure. Photos a-d corresponds to lava flow from Pu'u 'O'o volcano. e) Cross-sections of S- and P-type pahoehoe (Wilmoth & Walker 1993).....6

Figure 1. 2 a) Schematic description of an 'A'a lava flow section from Lockwood & Lipman (1980) it shows the layers that compose the flow (surface and basal breccia, solid core) and their surface structures. b) 'A'a lava flow front of Kilauea volcano in 1983. c) Lava flow channel of Etna's eruption in April 2017. d) Spinose clasts of 'a'a lava of Kilauea volcano, 2009.....8

Figure 1. 3 a) San Pietro's silicic flow unit schematic plan, section and detail of their main structures (Harris & Rowland 2015a). b) Flow front from an andesitic lava flow of El Reventador volcano showing polyhedral blocks and some incandescence in their cracks. c) Andesitic lava flows can reach tens of meters of thickness. d) Long duration of the obsidian lava flow of Puyehue-Cordon Caulle (Chile) the lava flowed longer than one year even though the eruption had already finished.9

Figure 1. 4 Classification and characteristic of volcanic rocks which define the approximate range of values for SiO₂ content, eruption temperature, viscosity, density and show a qualitative estimation of the mobility of lava flows depending of their composition (Modified from: Johnson, USGS).10

Figure 1.5 Relationship between thickness and area covered of lava flows of different compositions. Broken lines represent the aspect ratio V/H (Walker, 1973).....11

Figure 1. 6 Lava length versus average effusion rate for lava eruptions of various volcanoes (Walker, 1973).....14

Figure 1. 7 Flow length versus subaerial volume for Hawaiian basaltic flows using Eq. 1.1. Circles are data for Kilauea and triangles are for Mauna Loa. Open symbols indicate cases where the flow entered the ocean, Malin (1980).15

Figure 1. 8 Representation of the rheological threshold temperature versus cooling rate, it shows the cooling rate dependence of the solidification threshold (Kolzenburg *et al.* 2016).....16

Figure 1. 9 Internal thermal layer for a (A) pahoehoe and (B) 'a'a lava flows, shows the variation in depth of each boundary with time. (Harris & Rowland 2015a).....17

Figure 1. 10 Schematic lava flow heat loss and heat gain considering a channelized lava flow (Harris & Rowland 2001).....	19
Figure 1. 11 Viscosity as a function of temperature at 1 bar for natural magmatic melts with compositions from rhyolite to komatiite (From Lesher & Spera 2015).....	26
Figure 1. 12 Comparison between different models for relative viscosity(η_f). Curves represents them as: E: Einstein with B=2.5 (eq. 7), GG: Guth & Gold (1938); ER: Einstein-Roscoe (eq. 8), KD: Krieger & Dougherty with B=2.5 and $\phi_m = 0.67$ (eq. 9) and C: Costa (eq. 10) with B=2.5, $\phi_* = 0.6$, $\alpha = 5$, $\delta = 8$ and $\xi = 10^{-4}$ (Mader <i>et al.</i> 2013).....	29
Figure 1. 13 Shear-stress – strain-rate relationships for Newtonian, Bingham and pseudo-plastic fluids. Viscosity (η) is defined by the slope between shear stress and strain rate (Harris, 2013).	32
Figure 1. 14 Flow regimes that control the lava flow behavior: viscosity dominated, crust yield strength dominated and core yield strength dominated (From Magnall <i>et al.</i> 2017 after Castruccio <i>et al.</i> 2013).	33
 Chapter 2 – Lava flow description and properties	
Figure 2. 1 a) Regional location of El Reventador volcano (from Hall <i>et al.</i> 2008). b) orthogonal view of the volcano showing the current volcanic edifice and the preferential direction of its volcanic products. c) View of the volcano from the south east, showing the main features of the volcano as the volcanic edifice, the caldera rim and the Copete hill (Photo: P. Ramón, IG-EPN).	39
Figure 2. 2 Main topographic features left by the big explosion on the reactivation of the volcano the November, 3 rd 2002. It's recognizing the Eastern, Western summits and the Northern depression. The southern one is hidden by the gas emission column (Photo: P. Ramón, IG-EPN).	41
Figure 2. 3 Photography of the southern part of the volcano taken on October, 19 th 2013. It shows the caldera rim and their steepest caldera wall that influenced the direction of the emplacement of lava flows. The crater at that date showed the eastern and western borders left by the explosion on November 3 rd , 2002. As well it shows the lava flow field generated between 2002 and 2009. (Photo: S. Vallejo Vargas).....	41
Figure 2. 4 Photographs and thermal image of the superficial activity of El Reventador volcano. a) lava flow field of the flows generated between 2002 and 2012. b) explosion and the generation of gas and ash column. c) thermal image of the crater showing an explosion and a lava flow unit. d) a PDC deposit in the southern flank of the volcano. (Photos/thermal image: S. Vallejo Vargas).	43
Figure 2. 5 Deposits of the PDC's (dotted red line) and the lava flow generated during June – July 2017. The lava flow which reached 2.65 km, distance is represented by red color line in the visible image and in white line correspondent thermal image. (M. Almeida, IG-EPN).	43

Figure 2. 6 Network of El Reventador volcano showing the location of the fixed seismic, thermal and visual stations (Source IG-EPN).....	44
Figure 2. 7 Daily count seismic events in CONE short period station for the period 2010 – 2014. It was recognized events like explosions (EXP, red), spasmodic tremor (SP TR, vivid green), harmonic tremor (HR TR, light green), volcano-tectonic (VT, black), hybrid (HB, orange), long period (LP, blue) (Source: IG-EPN).	45
Figure 2. 8 Volcanic Radiative Power (VRP) time series for El Reventador volcano between 2010 and 2014. In that period there were generated 495 thermal anomalies. Each anomaly is represented by a dark red square. (Source: MIROVA).	46
Figure 2. 9 Representative images of the four cameras to make up the visual and thermal network on El Reventador volcano, LAVCAM, REBECA COPTVS and COPTIR (Source:IG-EPN).....	49
Figure 2. 10 a) Photography of El Reventador volcano and the imaging network at Copete hill which is composed by thermal and visual cameras, COPTIR and COPTVS respectively. b) Thermal image from COPTIR camera, it shows thermal anomalies related with the presence of the dome, lava flow and PDC's.	49
Figure 2. 11 Thermal image acquired from COPTIR camera showing the main features recognizable at the volcano and an scale to estimate the distance or height that the flows/columns can reach. (Source: IG-EPN).	50
Figure 2. 12 Activity of El Reventador volcano during fieldwork. a) Typical explosive activity of those days, the ash/gas columns reached less than 2 km high with a dispersion towards the west, b) During the night it was possible to observe glowing on the column after an explosion and incandescent ballistic blocks, c) thermal image of an explosion, there was no thermal evidence of a lava flow, d) deposit of a small PDC occurred on April 19 th . (Photos/thermal image: S. Vallejo Vargas).	51
Figure 2. 13 Location of the collected samples (blue dots) and GPS control points (white dots) for DEM development at El Reventador volcano during.....	52
Figure 2. 14 Ground control points placed over the caldera floor in the south and north part of the volcano. a) REV4 GCP in the south eastern flank of the volcano, an explosion was recognizing during the work. b) REV10 GCP in the northeastern flank beside to the CONE station. c) REV3 and REV8 GCP over the LF5. d) REV9 GCP over the northern levee of LF5 almost at its front. (Photo: K. Kelfoun/S. Vallejo).	54
Figure 2. 15 Orthogonal view of the 2013 DEM.....	55
Figure 2. 16 Orthogonal view of the 2015 DEM.....	57
Figure 2. 17 a) View of the crater and the pyroclastic cone from the north, a weak fumarole activity is recognized. b), explosion and the generation of small PDC's to the south and north of the cone.	58
Figure 2. 18 Pyroclastic cone evolution showed by thermal (left) and visual images (right). White lines show the western and eastern borders of the crater left by the eruption in 2002, notice that	

the highest point of them was given by the western border, blue polygon represents the pyroclastic cone, and the black line is the caldera wall (Images/Photos: IG-EPN).....	58
Figure 2. 19 Lava dome evolution showed by thermal (left) and visual (right) images White lines show the western and eastern borders of the crater left by the eruption in 2002, notice that the highest point of them was given by the western border, blue polygon represents the pyroclastic cone, black polygon is the dome that grew inside the pyroclastic cone and the black line is the caldera wall (Images/Photos: IG-EPN).	59
Figure 2. 20 Aerial thermal images of lava flows identified in 2012: a) LF18, LF19; b) and c) LF20; d) LF21, LF22; e) and f) LF23 (Source: IG-EPN).....	61
Figure 2. 21 Aerial thermal images of lava flows identified in 2013: e) and f) LF23 (Source: IG-EPN).	62
Figure 2. 22 Aerial thermal images of lava flows identified in 2012: g) LF24; h) LF25; i) LF26; j) LF24; k) LF26; l) LF27 (Source: IG-EPN).....	63
Figure 2. 23 Thermal images of lava flows identified in 2014 by thermal images from the fixed camera COPTIR: m) LF28, LF29; n) LF30; p) LF32; q) LF 33; r) LF34. Aerial thermal image: o) LF31 (Source: IG-EPN).....	65
Figure 2. 24 Thermal images of lava flows identified in 2014 by thermal images from the fixed camera COPTIR: s) LF35; t) LFd36; u) LF37. (Source: IG-EPN).....	66
Figure 2. 25 Thermal image from COPTIR of the LF33. Green line represents the contour of the lava flow.....	68
Figure 2. 26 Projection of the thermal image over the 2013 DEM. It is possible to observe the yellow-greenish color as a representation of the lava flow.....	70
Figure 2. 27 Plot of the LF33 X-Y coordinates (yellow dots) obtained from the projection of the thermal image over the 2013 DEM.	70
Figure 2. 28 Advance of the flow 35 on time between the Mars 25 th and April 2 nd of 2014. The green contour shows the border of the crater at that time. MDFC= Maximum distance from the crater.....	71
Figure 2. 29 Time evolution of distance between the lava front LF35 and the source. Analysis done based on the analysis of thermal images from COPTIR.	72
Figure 2. 30 Individual mapping of the 20 flows identified between 2012 and 2014. The greenish color in each map represent the old lava flow deposits.....	73
Figure 2. 31 Map of the lava flows for El Reventador volcano in the period 2012-2014. Twenty lava flows units were identified in this period; those were distributed to the north, north-east, east and south east of the crater.....	74
Figure 2. 32 Scheme to represent the estimation of the LF24 thickness. a) Map of the lava flows emitted between 2002 and 2014 (green polygon) only the LF24 is identifiable respect to the others,	

yellow flow (enmarked in a yellow box). b) Enlargement of the yellow box in which is shown the location of the profiles for this flow, in total five (P1 – P5). c) Profiles of the flow, showing that the thickness of the flow varies between 4m at the front (P1) of the flow and 10m at the top (P5).76

Figure 2. 33 Sketch of the correction of the thickness (h) by the slope topography (θ).....77

Figure 2. 34 Individual and accumulate volume of lava flows LF18 – LF37 emitted between 2012 and 2014 for El Reventador volcano.78

Figure 2. 35 Map of lava flows distribution between 2002 and 2009 (Naranjo *et al.* 2016 after Vallejo 2009).79

Figure 2. 36 Scheme to represent the estimation of the thickness of LF2. a) spatial location of the part of the flow that will be analyzed (white box), b) enlargement of the white box from (a), it shows in detail the portion of LF2, the location of Axis A-B and P1-P10 profiles; c) profile of the Axis A-B; d) cross flow profiles P1-P10 along the Axis A-B; e) photo of the LF2 and LF1; f) thermal image of the LF2 and LF1.....80

Figure 2. 37 Individual and accumulate volume of lava flows LF1 – LF37 emitted between 2002 and 2014 for El Reventador volcano.81

Figure 2. 38 a) Photo of the southeast lava flow field of El Reventador volcano. b) Cartoon of the southeast lava flows field represented in photo (a). It shows the major lava flows features as channels, lava surface ogives and the steep flow front. Lava flow direction is show for each flow with red arrows.83

Figure 2. 39 Variation of the SiO₂ content of the lava flows between 2002 and 2014. Green triangles correspond to data from Samaniego *et al.*, 2008; Naranjo *et al.*, 2016; unpublished data; and blue squares correspond to the analysis of the samples taken during this research.....84

Figure 2. 40 Thin section of LF 2 with amphibol and his oxidized borders, plagioclase as prismatic crystals and dusty surface and inter-growing on clino and orthopyroxene.....85

Figure 2. 41 Thin section of LF 16 with optical zoom of 2.5x. Tabular and euhedral crystals of plagioclase and phenocrystals of orthopyroxene. a)Using white light and b)Polarized light.....85

Figure 2. 42 Scheme of the representation of the eruptive phases for El Reventador volcano between 2002 and 2014 by the combination of seismic signals, MIROVA alerts and lava flows grouping.....88

Chapter 3 – Numerical codes for lava flows simulations

Figure 3. 1 Area of the compound lava-flow fields (north, NW, west and south) of the Piton de la Fournaise December 9th, 2015 eruption (left top). The detail of the west flow field is shown in the right top. Thermal image of the flow field is showed at the bottom (Harris *et al.* 2015).96

Figure 3. 2 Relationships between the core temperature and crystal content with distance, a) and b) respectively. Red squares correspond to the measured data and blue dots are the results of FLOWGO simulation (Harris <i>et al.</i> 2015).	97
Figure 3. 3 Relationships between viscosity and yield strength with distance left and right respectively. Red squares correspond to the measured data and blue dots are the results of FLOWGO simulation (Harris <i>et al.</i> 2015).	97
Figure 3. 4 a) 3D view and b) top view or the schema for cell altitude determination for SCIARA-fv2 numerical model. Altitude values along the diagonals are taken at the intersection between the diagonal line and the circle (From: Rongo <i>et al.</i> 2016).....	99
Figure 3. 5 Lava flow hazard map for Etna volcano as a result of the probability of areas being affected by future eruptions (From: Rongo <i>et al.</i> 2016).....	100
Figure 3. 6 Scheme of a randomized neighborhood in a cellular automata mesh (Vicari <i>et al.</i> 2006).	101
Figure 3. 7 Lava flow simulation thickness for the 23 October 2004 Etna eruption, the result was obtained using the relationship between viscosity and temperature as proposed by Pinkerton and Norton (1995) (from Del Negro <i>et al.</i> 2008).	103
Figure 3. 8 Conceptual principle of LavaSIM	106
Figure 3. 9 Thickness distribution of the flow in time as a result of the simulation carried out by LavaSIM (Hidaka <i>et al.</i> 2005).....	107
Figure 3. 10 Left: Longitudinal profiles of the channel center velocity and temperature, at $t = 2500$ s. Dashed and continuous lines indicate analytical and numerical results, respectively. Right: Longitudinal thickness profiles at $t = 1200$ s (Costa.....	109
Figure 3. 11 Simulated lava thickness of the 3rd and 4th January 1992 Etna lava flow (Costa & Macedonio, 2005).....	109
Figure 3. 12 Simulation of the December, 2010 lava flow from Piton de la Fournaise. The figure presents the comparison between the simulation (colorful deposit) and the real deposit (white line polygon). The scale represents the thickness of the simulated flow (Bernabeu <i>et al.</i> 2016).....	111
Figure 3. 13 Schematic illustration of the algorithm used by DOWNFLOW to trace the steepest descent paths (SDPs) (a) Conceptual scheme of the perturbation of the topography within $\pm\Delta h$. (b) 3D view of a portion of topography with 100 SDPs obtained from a given point. The 3D mesh representing the topography is a TIN (Triangular Irregular Network), and (c) is a zoom showing the TIN triangles and an example of an SDP calculated in vector form over the TIN surface. (After Favalli <i>et al.</i> 2012).....	116
Figure 3. 14 Map of probability of lava-flow inundation by flank eruptions at Etna volcano (From: Tarquini & Favalli 2016).	117
Figure 3. 15 Simulation of the Nyamuragira lava flow showing the result using 50 iterations (left side) and 1500 iterations (right side), (Mossoux <i>et al.</i> 2016).....	119

Figure 3. 16 Representation of the front position versus time for the real flow solution and the tested numerical codes (Cordonnier <i>et al.</i> 2015).	121
Figure 3. 17 Comparison between the different tested numerical codes for CCT1. The different color represents the Boolean operation between the computed (C) and natural lava footprint (F). Green: common invasion areas ($C \cap F$), blue: underestimated are ($F - C$), and red: the union of the calculated and real flow areas ($C \cup F$). The combination between the blue and green polygons, results into the natural lava-flow outline (Cordonnier <i>et al.</i> 2015).....	122
Figure 3. 18 (A) Flow propagation in X and Y with time. (B) Represents the flow thickness downslope of the vent with time when the flow reached the distance of 24.5 mm. (Dietterich <i>et al.</i> 2017).....	123
Figure 3. 19 Left: due to the obstacle incorporated in the slope, numerical codes constrain differently about them. The analysis includes internal angles of 0, 90 and 180. FLOW-3D and VolcFlow results are slightly shifted for the 180° obstacle in order to avoid direct overlap. Right: Normalized temperature profiles from Garel <i>et al.</i> (2012) and the models simulations (Dietterich <i>et al.</i> 2017).....	124
Figure 3. 20 Molten basalt benchmark experiments. (A) Flow advance from the down and cross slope propagation (B) thickness flow front measurements of the flow at 50 cm down in the slope (Dietterich <i>et al.</i> 2017).....	124
Figure 3. 21 Figure that represents the computational costs measured in CPU hours for each code and benchmark (Dietterich <i>et al.</i> 2017).....	125

Chapter 4 – Numerical modelling of lava flows: Methods

Figure 4. 1 Dimensionless front position versus dimensionless time. Note that symbols of FLOW3D are partly hidden by NB3D. The first output depends on each code setting for outputting files, and there is, for example, no data for early times for FLOW3D and NB3D (Cordonnier <i>et al.</i> 2015).	130
Figure 4. 2 Schematic lava flow heat loss and heat gain considering a channelized lava flow. The flow is losing heat by radiation, force convection and conduction, and gaining by crystallization (Modified from Harris & Rowland 2001).....	131
Figure 4. 3 An hemi circular Bingham fluid is released on a slope. The lava spreads out but the temperature remains constant.	134
Figure 4. 4 Sigmoid law model of viscosity (or yield strength) according to temperature	138
Figure 4. 5 Example of a lava flow that cools with time with an associated change of its rheology.	139
Figure 4. 6 Cross-section profiles of the lava flow at t=300s and x=100, 200 and 300m.	140
Figure 4. 7 Scheme of the model formed by a crust, a viscous part and a basal part.....	140

Figure 4. 8 Example of result obtain with the crust model. The crust increases with time (36 mm / hour) and it accumulates to the base at the front and at the edges modifying the topography.142

Figure 4. 9 Chart of the VolcFlow models to simulate lava flows by using different rheologies. Model n° 1 corresponds to the isothermal in which the viscosity and yield strength are constant for the whole simulation. Model n° 2 combines the cooling with the crystal variation and existing rheological laws or the cooling with variable rheology by using a sigmoid law for yield strength or viscosity. Model n° 3 allows the formation of a crust in the flow with a hot lava in the internal flow.145

Chapter 5 – Numerical modelling of lava flows: Results and Discussion

Figure 5. 1 Schema of the experiment setup for the molten basalt at the Syracuse University Lava Project (from Dietterich *et al.* 2017).147

Figure 5. 2 Shows the experimental setup of the Syracuse lava flow project and the advance of the basaltic lava flow since it was poured out onto the metal chute and distributed after onto the inclined plane (a-c). Advance of the front of the flow caught by thermal images are shown in d, e and f figures. (Source: Dietterich H., personal comunicacion).....148

Figure 5. 3 A) Lava flow propagation of the flow since it was poured out from the furnace to the metal chute until it stoped. B) Final shape of the lava flow, emplaced onto the metal chute and the sand inclined plane. C) Schema of the final deposit showing the morphology of the flow. D) Progression of the flow, taking as examples a, b and c from Figure 5.2.148

Figure 5. 4 Numerical topography used for the simulation of the molten basalt.....149

Figure 5. 5 3D view of the flow advance for 10, 40 and 70 seconds as a result of the simulation with VolcFlow using the Model n°1: Isothermal approach.151

Figure 5. 6 Propagation of the flow applying the Model n°1: isothermal for 10, 40 and 70 seconds. It shows the evolution of the flow over the surface (left), the deposit thickness variation (middle) and the advance of the flow in X respect to the time (right) between the results of the simulation (black dots) and the measured data from Dietterich *et al.* 2017 (red dots).....152

Figure 5. 7 Left: Final deposit in 2D of the flow over the inclined plane for 128 s showing a uniform and regular shape. Middle: Comparison of the advance of the flow in X respect the time between the results of the simulation (black dots) and the measured data from Dietterich *et al.* 2017 (red dots). Right: 3D view of the deposit of the flow applying the isothermal model and using a viscosity of 18 Pa s and a yield strength value of 100Pa, both considered as constants.153

Figure 5. 8 3D view of the flow advance for 10, 40 and 70 seconds as a result of the simulation with VolcFlow using the Model n°2b 1: Sigmoidal with a viscosity as a variable and yield strength as a constant.154

Figure 5. 9 Propagation of the flow applying the Model n°2b 1 Sigmoidal for 10, 40 and 70 s with a viscosity as a variable and yield strength as a constant. It shows the evolution of the flow over

the surface (left), the thickness variation of the flow (middle) and the advance of the flow in X respect to the time (right) for 10, 40 and 70 seconds.	155
Figure 5. 10 Left: 2D view of the simulation of the final deposit of the flow for 150s. Right: Comparison of the advance of the flow in X respect the time between the results of the simulation (black dots) and the measured data from Dieterich et al. 2017 (red dots)).	156
Figure 5. 11 3D view of the final deposit of the flow for 150s, it shows the result of the simulation using the Sigmoidal approach for a variable viscosity and constant yield strength. At 120 s, the temperature of the flow varies between 900 and 1130 K. A sigmoidal variation of the viscosity is shown having a value of 480 Pa s in the hottest part of the flow and 900 Pa s in the coldest one.	157
Figure 5. 12 Propagation of the flow with Model n°2b 2 Sigmoidal with yield strength as a variable and viscosity as a constant. It shows the evolution of the flow over the surface (left), the thickness variation of the flow (middle) and the advance of the flow in X respect to the time (right) for 10, 40 and 70 s.....	158
Figure 5. 13 3D view of the flow advance for 10, 40 and 70 seconds as a result of the simulation with VolcFlow using the Model n°2b 2: Sigmoidal with yield strength as a variable and viscosity as a constant.....	159
Figure 5. 14 2D view of the simulation of the final deposit of the flow for 128s using the Sigmoidal approach for a constant value of viscosity and variable yield strength. Right: Comparison of the advance of the flow in X respect the time between the results of the simulation (black dots) and the measured data from Dieterich <i>et al.</i> 2017 (red dots).	159
Figure 5. 15 3D view of the final deposit of the simulation for the flow at 110 s using the Sigmoidal approach which takes into account the cooling of the flow and variable yield strength and a constant viscosity. Temperature of the flow at 110 s varies between 1240 and 1150 K. The figure shows as well features of rheological instability.....	160
Figure 5. 16 Propagation of the flow applying the Model n°3 hot interior and crust. It shows the evolution of the flow over the surface (left), the thickness variation of the flow (middle) and the advance of the flow in X respect to the time (right) for 10, 40 and 70 seconds.	161
Figure 5. 17 3D view of the flow advance for 10, 40 and 70 seconds as a result of the simulation with VolcFlow using the Model n°3: hot interior and crust formation.....	162
Figure 5. 18 Lateral profiles of the advance of the flow in the X axe for 10, 40 and 70 s using the Model n°3: hot interior and crust formation. As it is possible to observe, three layers are represented in the profiles which represent the crust, lava (interior lava) and the base.	162
Figure 5. 19 Left: 2D view of the simulation for 128s using the hot interior and crust formation model. Right: Comparison of the advance of the flow between the results of the simulation (black dots) and the measured data (red dots). Bottom: Profile of the flow in the X axe at the end of the simulation.	163

- Figure 5. 20** 3D view of the final deposit of the flow for 110s using the hot interior and crust formation approach. The deposit of the figure is represented by its thickness.163
- Figure 5. 21** Comparison of the emplaced flow between the real flow deposit (red line) and the four applied models for this case: Model n°1: Isothermal, Model n°2b 1: Thermo-rheological variation – viscosity sigmoid law, Model n°2b 2: Thermo-rheological variation – yield strength sigmoid law and Model n°3: Crust formation with hot interior.....165
- Figure 5. 22** Lava flow advance from the visible camera Piton de Bert for the September 28th, 29th and October 10th, 2015. (Source: M. Gouhier)167
- Figure 5. 23** TADR for the lava flow emitted between August –November 2015. (Courtesy M. Gouhier, LMV).....167
- Figure 5. 24** Preliminary results of the distribution of the August – November lava flow from Piton de la Fournaise based on radar data (Froger *et al.* 2015).....168
- Figure 5. 25** Numerical topography used for the simulations of the August – September 2015 lava flow from Piton de la Fournaise.168
- Figure 5. 26** Progression of the lava flow for 1, 3, 6 and 22 days by using the isothermal model for the simulation.169
- Figure 5. 27** Left: 3D view of the deposit of the flow from August – September, 2010 using the isothermal model. Right: Thickness of the deposit at the end of the simulation, the thicker part is located at the fronts of the flow reaching 10.75 m.170
- Figure 5. 28** Progression of the lava flow for 1, 3, 6 and 22 days, using the model n°2a which takes into account the cooling and the existing rheological laws. The image shows the bifurcations of the flow when it reaches the topography with low slope171
- Figure 5. 29** Representation of the thickness of the flow at 2400 hours (100 days) in which is possible to observe a maximal accumulation of the material at the fronts and at the limit of the numerical domain., in which it reaches about.....172
- Figure 5. 30** 3D view of the deposit of the flow, which shows the accumulation at the fronts and at the border of the numerical domain. The viscosity varies between 0 and 1×10^6 Pa s in a range of temperature of 1114 and 830 °C (1387.15 – 1103.15 K).....172
- Figure 5. 31** 3D evolution of the flow using the model n°3: crust formation with hot interior for 1, 3 and 6 days. The distribution of the flow is not vague in comparison with the results from the previous models. The formation of the crust, which allows the formation of steepest walls could influence in the narrow distribution of the flow.....174
- Figure 5. 32** 3D view of the flow for 13.1 days (314.22 h) in which a rheological instability happened due to the crust formation and brought a thickness of 2730m.175
- Figure 5. 33** Simulations of the August-December 2015 lava flow from Piton de la Fournaise. Left side: 3D view of the simulated flow, right side: 2D view of the simulated flow against the real

deposit (yellow/black line). Isothermal model (a, a'). Cooling and rheological variation using existing thermo-rheological model (b, b'). Crust formation with hot interior model (c, c')176

Figure 5. 34 a) General context of the Tungurahua volcano location. b) Picture of the lava flow deposit from the December 4th and 5th, 2010 (Photo: B. Bernard, IG-EPN).178

Figure 5. 35 Thermal images sequence of the advance of the lava flow over the topography through the northwestern flank of Tungurahua volcano (From: Vallejo Vargas 2012, Source: IG-EPN).179

Figure 5. 36 Scheme that represents the projection of thermal images onto the 4m digital topography with the aim to calculate the position of the front and the extension of the flow through the time (Kelfoun & Vallejo Vargas, 2015).179

Figure 5. 37 a) Time evolution of the distance between the lava front and de source during the generation of the flow between the 4th and 5th December 2010. b) Evolution of the lava flow over the topography. (Vallejo Vargas 2012; Kelfoun & Vallejo Vargas 2015).180

Figure 5. 38 Numerical topographic used for the simulation of the molten basalt.....181

Figure 5. 39 A) Time evolution of the flow between the source and the front. Red dots show the calculated advance of the flow from the analysis of thermal images, black dotted lines the results of the simulations using different values of viscosity and yield strength; black regular line corresponds to the best fit between the simulation and the data (red dots). B) portion of the thermal image projected over the topography showing the advance of the flow over the surface (red dots). C) Deposit of the simulated lava flow with the best fit parameters for viscosity and yield strength (Kelfoun & Vallejo Vargas 2015).182

Figure 5. 40 Progression of the flow with VolcFlow, using the effect of the cooling and existing rheological relationships. The progression is shown for 00:51, 02:37, 8:19 and 26:09 h of generation of the flow. Left side represents the 3D progression of the flow over the topography. Right side shows the comparison of the distance advance of the flow simulation (blue line) with the real data (red dots).185

Figure 5. 41 3D view of the distribution of the flow represented by the temperature variation (417.7 -1038 K). Temperature variation at the black is represented in the T(K) vs t(h) graph which shows that temperature at the black point during the whole simulation varied between 1173.15 and 1029. The hottest point of the flow at 30 h reached 1038 K and presented a viscosity of 1.37×10^{11} Pa s and yield strength of 1.37×10^{-13} Pa.186

Figure 5. 42 Representation of the thickness (a) and temperature (b) distribution of the simulated flow at 30h. a) The thickened part of the flow is located at the front reaching 30.4 m and on the external borders of the flow close to the front. b) The hottest part of the flow is recognized at the inner part of the flow front with 1038 K and the coldest at the borders and source with 417.7 K.186

Figure 5. 43 Cross sections of the flow showing the thickness and the slight thickening at the borders.187

Figure 5. 44 Results of the progression of the flow using the Sigmoid model for a constant viscosity and variable yield strength. The color of the flow shows the cooling process of the flow since its emitted at high temperature (red color, $t=0.85h$) until it has cooled (gray color, $t=26.15h$). Left: 3D progression of the flow over the topography. Right: Comparison of the flow progression between the data (Kelfoun & Vallejo Vargas, 2015) and results of the model.....188

Figure 5. 45 Images of the final thickness (a) and temperature (b) of the Tungurahua's flow at 30h. a) It shows that the flow is thicker at the front (5.54m) than close to the source (0.1 m). The highest temperature is registered in the inner part of the lava front with a value of 756.4 K, the lowest is recorded close to the source with 381.2 K.....189

Figure 5. 46 3D view of the final deposit of the Tungurahua's flow for 30h with the Sigmoid model with a constant viscosity of 4×10^6 Pa s and a variable rheology. After the 30h the flow has reached a maximum temperature of 756.4 K which influenced in yield strength calculation. Since this temperature and lower values yield strength has a value of 4.9×10 Pa s. This maximum temperature has found in the inner part of the front flow. The evolution of the temperature has measured in the point showed in the figure.190

Figure 5. 47 Comparison of the simulations for the December 4th and 5th lava flow from Tungurahua volcano. Results of the Isothermal model (model n°1), 3D (a) and orthogonal (a') views (Kelfoun & Vallejo Vargas 2015). Cooling and rheological variation using existing thermo-rheological model (model n°2a), 3D (b) and orthogonal (b') views. Cooling and rheological sigmoid law model (model n°2b), 3D (c) and orthogonal (c') views.191

Figure 5. 48 Lava flow generated in April 2014. a) thermal image from the COPETE-IR station, the flow is represented in yellow. b) projection of the thermal image over the topography following the method from Kelfoun & Vallejo Vargas (2015), the flow is represented in yellow-green color.194

Figure 5. 49 a) Advance of the flow front by the time (red dots) obtained from the projection of thermal images over the topography (Fig. 4.54b) b) Resulted polygon of the flow over the topography.194

Figure 5. 50 Fit of the resulted flow using the isothermal model for the LF25.....195

Figure 5. 51 (a) Representation of the deposit left by the simulation taking into account the cooling and existing rheological laws. It is possible to see that the thickness of the flow is not regular showing a thickening at the front with about 20m. (b) Deposit of the flow for the sigmoid model.197

Figure 5. 52 Deposit of the lava flow over the north eastern flank of the volcano and the eastern caldera floor taken on August 1st 2017. It is represented with a red outline in the visible image and with a black one in the thermal image. (M. Almeida, IG-EPN).....198

Figure 5. 53 Map of the distribution of the lava flow (yellow) over the flank and caldera floor of El Reventador volcano (M. Almeida, IG-EPN).198

Figure 5. 54 Portion of the 2015 DEM used for the simulation of the June-July 2017 lava flow for El Reventador volcano. It is shown the source of the lava flow (NNW summit border).199

Figure 5. 55 Results of the simulation of the flow at 480h using the isothermal model. Represents the variation of the thickness of the deposit showing an important thickening close to the front of the flow and thinner deposit close to the source of the flow.200

Figure 5. 56 3D view of the flow deposit over the north-east flank and caldera floor of the volcano using the of 25×10^6 Pa s and a yield strength of 6×10^4 Pa s and a yield strength of 6×10^4 Pa.200

Figure 5. 57 2D thickness representation of the simulation showing that the flow is thicker at the low topography reaching ~ 20 m.202

Figure 5. 58 Representation of the temperature at the end of the simulation, the highest measurement was located close to the source and the minimum at the borders with 1250 K and 897 K respectively.202

Figure 5. 59 Cross section along the flow from p1 to p7 showing its thickening when it is emplaced on the caldera floor.203

Figure 5. 60 An important accumulation of the flow is observed close to the front of the flow reaching 28.14 m (reddish color).....204

Figure 5. 61 The maximum temperature (878 K) of the flow was measured in the thicker part of the flow calling the attention that the heat is kept when the flow has an important thickness.204

Figure 5. 62 View of the flow using the sigmoid law. It shows a regular flow and some small branches. The accumulation of material is recognized at the lowest slope of the topography which corresponds to the caldera floor.205

Figure 5. 63 3D view of the deposit left by the isothermal simulation, in which the viscosity and yield strength are constants. The thicker part of the flow is represented with reddish color, reaching ~ 50 m.....206

Figure 5. 64 a) Progression of the flow with 1wt % H₂O, the flow is broadly dispersed over the topography, in which the maximum thickness is found at the border of the domain (~ 50 m). The rest of the flow has thickness thinner than 15 m. b) Progression of the flow with 0wt % H₂O. The dispersion of the flow is shorter than with 1wt % H₂O. The flow reaches maximum thickness of 30m at its fronts. Comparing with old flows from the topography is possible to observe the similarity of the lobes.....208

Figure 5. 65 Left: Viscosity in function of temperature, red line is for the simulation considering 1 wt % H₂O and the black line represents the model with 0 wt% H₂O. Right: relationship of yield strength vs temperature showing a small variation of the yield strength along the simulation.....209

Figure 5. 66 Variation of the yield strength in function of the phenocrystal content. The initial content for this lava flow was 0.4 and the maximum 0.5, the figure shows the small variation.....209

Figure 5. 67 Final deposit of the flow which shows a thickening at the base correspondent to the low topography, the thickness reaches maximum 50 m.....210

Figure 5. 68 Variation of the temperature of the flow thought the time for 1, 3 and 20 days. At the first day the flow still hot with a temperature about 1250 K and for the day 20th the flow had decreased its temperature for about 950 K.211

Figure 5. 69 3D view of the distribution of the temperatures on the flow at 20 days (480h), it shows that the hottest part of the flow is at the base which matches with to the thicker part of the flow.....212

Figure 5. 70 Location of the profiles for the analogous of lava flow 1 using the yield strength sigmoid model.....212

Figure 5. 71 Profiles along the flow shows the thicker part of the flow at its base, which corresponds to the emplacement on the lower topography (profile 3). The thinner part of the flow is located at the flank of the volcano (profile 1).213

Figure 5. 72 Sigmoid curve obtained by the model showing the variation of the yield strength in function of the temperature.....213

Figure 5. 73 Comparison of the simulations for the June-July lava flow from El Reventador volcano and the real deposit (white/yellow contour). a) orthogonal view of the simulation obtained by the Isothermal model (model n°1), b) orthogonal view of the model n°2a which includes the cooling and rheological variation using existing thermo-rheological laws, c) orthogonal view of the model n°2b which takes into account the cooling and rheological sigmoid law.....215

Figure 5. 74 Representation of the LF1 deposit of El Reventador volcano (a) and the simulations of an hypothetical LF1 by using different rheologies (b-d). b) orthogonal view of the simulation obtained by the Isothermal model (model n°1), c) and c') orthogonal views of the models n°2a which includes the cooling and rheological variation using existing thermo-rheological laws with 0%wt. and 1%wt H₂O respectively, (d) orthogonal view of the model n°2b which takes into account the cooling and rheological sigmoid law.216

Chapter 6 – Numerical modelling of lava flows: Results and Discussion

Figure 6. 1 Chart-resume of the input parameters for Models n°1, 2a, 2b and 3.219

Tables

Chapter 2 – Lava flow description and properties

Table 2. 1 Pair coordinates (x-y) of the contour of the flow in the thermal image. For LF33, there were identified 152 pairs.....	68
Table 2. 2 Input parameters for the MATLAB script related with the camera location and its angles.....	69
Table 2. 3 Resume the geometric measurements obtained for lava flows LF18-LF37 of El Reventador. It shows the length, surface, thickness and volume. As well the start day of the flow and their durations are shown up.	77
Table 2. 4 Estimated volumes and lava effusion rates for El Reventador’s last eruptions including the period 2002 – 2009 (Naranjo <i>et al.</i> 2016).	79
Table 2. 5 Estimated lava flow volume for the period 2002 – 2009 from Naranjo <i>et al.</i> (2016) and this current work.	81
Table 2. 6 Number of main lobes generation for lava.	83

Chapter 4 – Numerical modelling of lava flows: Methods

Table 4. 1 Main input parameters to run the.....	129
Table 4. 2 Input parameters to be established previously for the calculation of the cooling and crystallization of the lava.	135
Table 4. 3 Variables calculated during the simulation.	135
Table 4. 4 Input parameters for the viscosity and.....	137
Table 4. 5 Variables to be calculated for the.....	137
Table 4. 6 input parameters for the viscosity/yield strength.....	140
Table 4. 7 Input parameters for the crust and.	142

Chapter 5 – Numerical modelling of lava flows: Results and Discussion

Table 5. 1 Study cases information	146
---	-----

Introduction

Volcanic eruptions pose a major risk to the population depending on how close people are to volcanoes or to volcanic sources. Lava eruptions are generally considered to be less hazardous than explosive eruptions, which generate fast currents that can affect large areas. Nevertheless, lava flows generated during effusive eruptions can highly affect populated areas, infrastructures and environment. Only in the last century, about 19 populated areas were destroyed or damaged by lava flows. Just for six of the most active volcanoes, Vesuvius, Mount Etna, Kilauea, Piton de la Fournaise, Nyiragongo and Mauna Loa; about 2.65 million people are threaten by effusive eruptions (Harris *et al.*, 2016). To better forecast the potential damages, quantitative models of the lava flow propagation on real volcanic topographies are required (Costa & Macedonio 2005).

During the last decade, many scientists brought attention and effort to improve volcanic hazard prediction. One of the ways is to develop numerical codes sufficiently complex to simulate natural flows. This challenging method must take into account the complex interplays between topography, rheology, heat loss, and flow dynamics that lead to the emplacement of a specific lava flow system of given morphology architecture, thickness, length and width (Harris 2013). Lava flow simulation is now a front-edge technique which is more and more accurate and is increasingly used to assess the hazard posed by lava flowing downhill in populated areas.

In the last century, ten volcanoes have had effusive activity in Ecuador, three in the mainland and seven in Galápagos Islands, which suggest the need for developing a tool that can be used for the assessment of hazard and risk posed by lava flows. On the continent, the andesitic volcano El Reventador is characterized by an important eruptive phases that have produced more than sixty flows since 2002, all of them emplaced in the inner part of the caldera. The monitoring carried out for this volcano by the Instituto Geofísico of the Escuela Politécnica Nacional (IG-EPN) (Quito, Ecuador) complemented by our fieldwork campaigns allowed the constitution of a database about lava flow emplacement which includes data on: temperature, velocity, chemical composition, morphologies. The andesitic lava flows of El Reventador volcano and their variations are ideal to check the validity of numerical codes.

General Objective

The main objective of this thesis is to test and modify a numerical code able to reproduce the lava flow emplacement and to check the validity of the different approaches with the data collected in the field. First, we have modified the numerical code VolcFlow by adding energy advection, crust formation and thermo-rheological laws to simulate andesitic lava flows. Then, we have analyzed the quality of the various approaches by comparing the results of the simulations with field data. We have also analyzed the ratio model quality / model complexity to determine what model can be used for hazard assessment and in what conditions they can be used.

Organization of the thesis

The work developed during this thesis is presented and summarized in six chapters as:

Chapter 1 corresponds to a state of the art for lava flows. It synthesizes the existing information on physical characteristics and the properties that govern lava flow rheology. It brings a view on the morphological classification, size and shape, and lava flow distribution systems. A special focus is made on the cooling, the crystallization and the rheology, and to mechanisms and properties that influence lava flow behavior. This chapter seeks to identify and to choose the most complete thermo-rheological models that could be implemented in VolcFlow for the simulation of the various types of lava flows.

Chapter 2 describes the eruptive activity of El Reventador volcano between 2002 and 2014, with a special focus on the period 2009 – 2014. This work is based on our field campaigns and data collected by our colleagues of the IG-EPN of Quito. This chapter also presents the different monitoring data used for the description of the lava emplacement and the methodologies applied for the identification and characterization of the different lava flows emitted during the study period. All those data lead to the first complete mapping of the lava flows and the description of the eruptive activity of El Reventador volcano since its reactivation in 2002.

Chapter 3 lists and discusses the existing approaches and the numerical models developed to simulate lava flows. The models are classified in two main groups: the deterministic and, the stochastic or the probabilistic approaches. A description of the different models and of their capabilities is given. A particular focus is made on the models that use a complete thermo-rheological approach as developed in Chapter 1. This helped to choose the best approach to implement in the numerical code VolcFlow.

Chapter 4 presents the basis of VolcFlow and the improvements that have been done for the simulation of lava flows. Three approaches were developed and tested using four case studies. The three approaches are: (1) an isothermal approach where the temperature and therefore the cooling are not taken into account and the flow is considered to be a Bingham flow, (2) models where the temperature variations induce changes in the rheology of the flow and (3) a model that considers the flow to be formed by two parts, a crust that thickens with time and which is rafted by an internal fluid part.

Chapter 5 shows the description of the different lava flow study cases and their simulations by considering the approaches proposed in Chapter 4. The case studies are (1) a laboratory lava flow (2) a real basaltic flows at La Réunion Island and andesitic lava flows, (3) one of Tungurahua volcano (Ecuador) and (4) three flows of El Reventador volcano. Results and discussions of the simulations are presented for each case study. An analysis of the sensibility of the input data is also presented and discussed.

Chapter 6 corresponds to the summary, conclusion and perspectives of the work done through the thesis and how our results can be used as a tool for hazard management related to lava flow generation during ongoing and future eruptions.

Chapter 1

Lava flow description and properties

1.1 Lava flow characterization

Lava flows are the most representative volcanic products of effusive eruptions and are formed when the magma is extruded effusively on the surface through volcanic vents or fissures. The evolution of lava flows is controlled by many factors including effusion rate, volume, topography and rheology which is in turn dependent on the lava composition as well as degassing and cooling during emplacement (e.g. Cashman *et al.* 1999; Harris & Rowland 2001; Castruccio *et al.* 2014). Lava flows are usually considered as high temperature, multiphase fluids because of the mixture of molten rock (liquid phase), crystals (solid phase) and bubbles (gas phase) (e.g. of recent studies: Cordonnier *et al.* 2012; Harris *et al.* 2015). Kinematically, lava flows can be described as gravity currents, which spread under their own weight, slowed down by their internal viscous resistance or by the topography (Cordonnier *et al.* 2015).

1.1.1 Lava flow types

Lava flow surface morphology acts as an indicator of the cumulative effects of both intrinsic (e.g. composition, temperature, crystallinity, vesicularity) and extrinsic (topography, effusion rate, flow velocity) parameters of emplacement (Soule *et al.* 2004). Three main types of lava flows have been described by Macdonald (1953) based on their surface morphology: pāhoehoe, ‘a’ā and block lava (Fig. 1.1 – 1.3). Recently Harris & Rowland (2015a) proposed many sub-types to better-classify lava flows. The following describes the three main ones.

1.1.1.1 Pāhoehoe

Pāhoehoe flow type is characterized by a smooth surface, with broad billows or hummocks, and local rolls (Fig. 1.1a, b). Sometimes their surface contains folds (“ropes”), hornitos, pressure ridges and tumuli (lava blisters) (Fig. 1.1b, c, d) (Cas & Wright 1987; Harris & Rowland 2015a). Their typical shape is a lobate form and its thickness can vary between 3 and 40 cm. The structure of a pāhoehoe unit is composed by a thin crust that thickens in time and contains a hot core that can still move beneath it (Hon *et al.* 1994). The formation of pāhoehoe is related to very low effusion and advance rates.

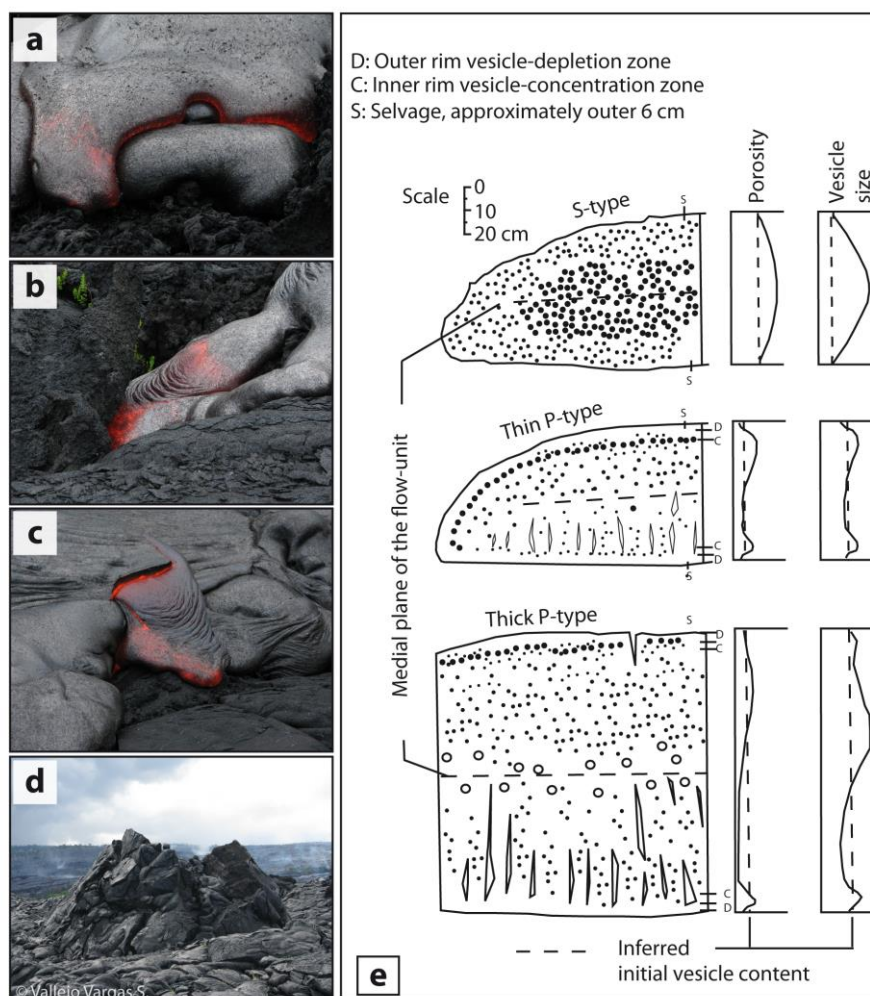


Figure 1.1 a) Smooth spheroidal forms, inflation process. b) Surface folds known as ropes. c) New lava flow due to the breakout of the latest unit. d) Tumuli structure. Photos a-d corresponds to lava flow from Pu’u ‘O’o volcano. e) Cross-sections of S- and P-type pahoehoe (Wilmoth & Walker 1993).

New pāhoehoe units are generated when the crust breaks and the magma is coming out from it (Fig. 1.1c). A pāhoehoe flow field can be composed by hundreds to thousands of units. The pāhoehoe lava flow morphology can vary largely depending on the lava degassing and their

emplacement at lower effusion rates. According to Wilmoth & Walker (1993) pāhoehoe lava flows can be classified by their vesicle content and two types are distinguished. S-Type contains high vesicle contents (>40 vol% of the rock) that are small and approximately spherical and P-Type include vesicles that are larger and not as frequent as in S-type (Fig. 1.1e).

The internal part of a pahoehoe lava flow is characterized by the presence of lava tubes and vesicles with a smooth spheroidal shape. Lava tubes can collapse producing large open channels and depressions on the surface of older flows. The presence of lava tubes is important because they can inhibit radiative heat losses from the surface of a flow and help the flow travel long distances (Cas & Wright 1987).

1.1.1.2 'A'ā

'A'ā lava flow type is characterized by a three-layer system that includes the core (coherent internal layer) and two auto-brecciated external layers (at the base and on the surface) (Fig. 1.2a):

- ❖ **'A'ā breccia layer** is characterized by a rough, jagged and spinose oxidized surface. Scoraceous clasts that compound the auto-breccia are called "clinker" (Fig. 1.2a, b, d). This texture is produced due to the high velocity that the flow can reach. The breccia layer is made up of a mix of clinkers, accretionary lava balls, slabs of pāhoehoe, scoria and occasionally large chunks of cone material that collapse onto the flow (Harris & Rowland 2015a).
- ❖ **'A'ā core** is characterized by having low vesicularity and it is possible to recognize elongate vesicles in the direction that the flow followed. Another characteristic feature is the presence of fractures and flow-parallel shear structures due to the flow undergoing high degrees of shearing as a result of the strong velocity gradients within the flow (Fig. 1.2a).

This type of flow can reach thicknesses between 0.5 and 3 m, and sometimes up to about 20 m (Fig. 1.2b, c). 'A'ā and pāhoehoe are typical of basaltic flows which are erupted from fissures or central vents reaching long distances (>100 km). In detail, basaltic lava flows can be emitted from vents as: coherent flows from small boccas, from the overspill, breaching of a lake ponded in a crater or, as lava fountains that reconstitute around the vent and then flow away (Cas & Wright 1987). The final flow channel morphology of this kind of lava is a function of the underlying

slope and the degree of flow branching, network connectivity and longevity of individual channels (Dietterich *et al.* 2014).

A transition of the surface morphology can occur through the distance, from smooth pāhoehoe to rough ‘a’ā (Wolfe *et al.* 1988, Kilburn & Lopes 1991). According to Peterson & Tilling (1980), this transition (defined as a transition threshold zone) is related to the influence of viscosity and rate of shear strain. Lavas with low viscosity need to experience higher strain rates in order to begin the transition to ‘a’ā while high viscosity lavas need lower strain rates.

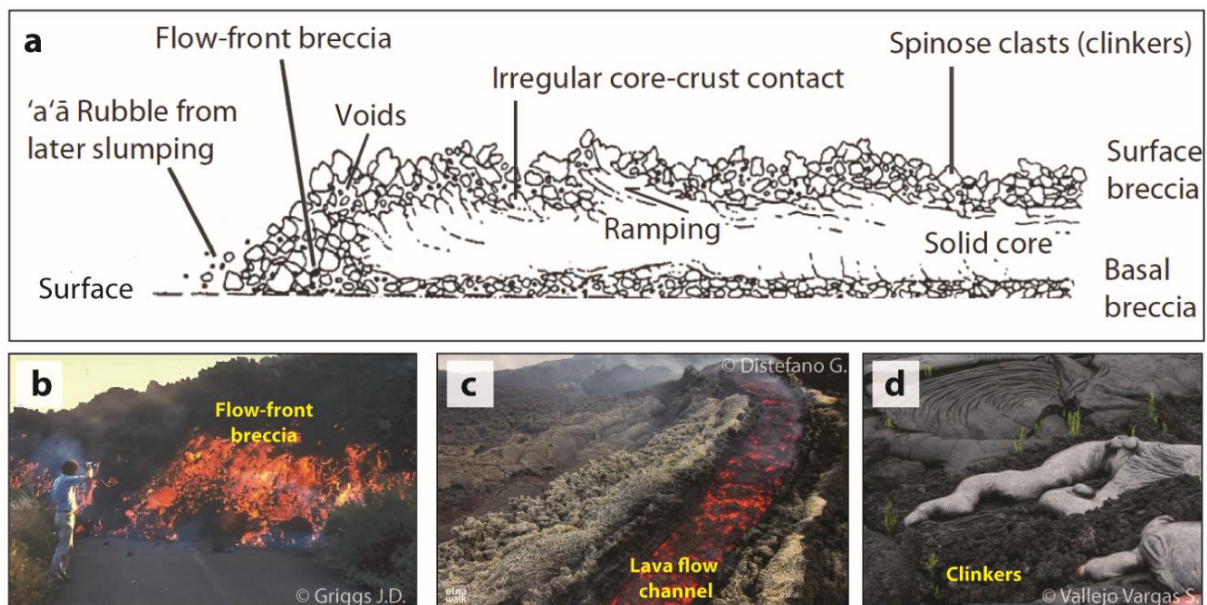


Figure 1.2 a) Schematic description of an ‘A’ā lava flow section from Lockwood & Lipman (1980) it shows the layers that compose the flow (surface and basal breccia, solid core) and their surface structures. b) ‘A’ā lava flow front of Kilauea volcano in 1983. c) Lava flow channel of Etna’s eruption in April 2017. d) Spinose clasts of ‘a’ā lava of Kilauea volcano, 2009.

1.1.1.3 Block lava

Block lava type is more viscous and thicker than ‘a’ā type. This type of flow can vary between tens to hundreds of meters thick. Block lava flows are typically andesitic, dacitic and rhyolitic but basaltic-andesitic compositions may also be found. The internal structure is similar to ‘a’ā type flows, displaying a coherent-dense core between two auto-brecciated layers (Fig. 1.3). The main difference with ‘a’ā type resides in the fragments that are larger, less spinose and are less irregular in form. These fragments are polyhedral blocks with relatively smooth faces bounded by dihedral angles (Macdonald 1953). A famous example is El Chao lava flow in Chile, which has a vesicle free to vesicle poor core and often is crystal-rich (60 vol. %) (de Silva *et al.* 1994). Another example is the San Pietro (SW Sardinia, Italy) silicic lava flow where the surface

morphology and internal structures are well exposed (Harris & Rowland 2015a) (Fig. 1.3a). Surface structures and features are related to shearing, folding and buckling of lava at the margins of the flow while the levees are characterized by being composed of rubbles. The front is mostly characterized for having fold extrusion and secondary fracturing. The lateral section shows a basal and surface rubble with a foliated, folded and fractured obsidian core (Fig. 1.3a). Another kind of structures presents in block lava flows are the columnar joint structures which are formed as a response to thermal stresses accumulated during cooling of a dome or a lava flow when it can flow laterally (Fink & Anderson 1999).

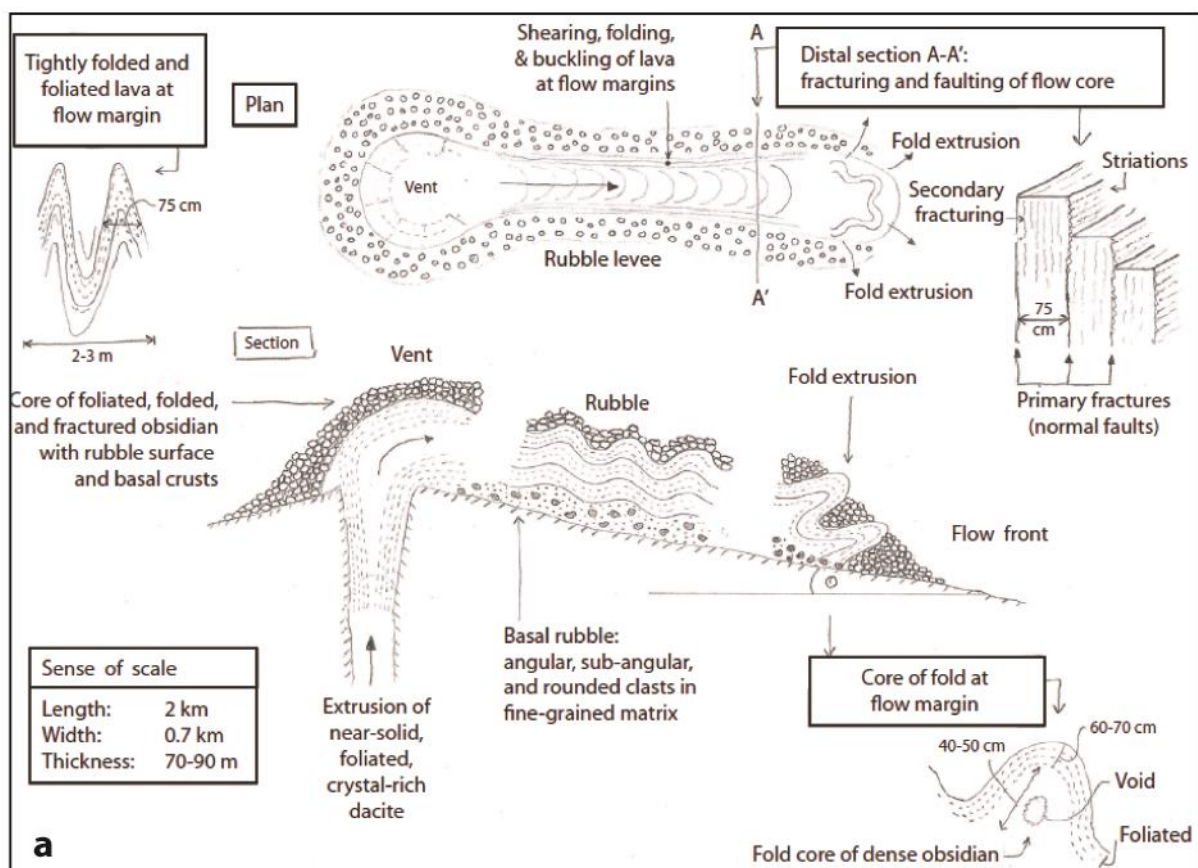


Figure 1.3 a) San Pietro's silicic flow unit schematic plan, section and detail of their main structures (Harris & Rowland 2015a). **b)** Flow front from an andesitic lava flow of El Reventador volcano showing polyhedral blocks and some incandescence in their cracks. **c)** Andesitic lava flows can reach tens of meters of thickness. **d)** Long duration of the obsidian lava flow of Puyehue-Cordon Caulle (Chile) the lava flowed longer than one year even though the eruption had already finished.

Due to their high viscosity, the velocity of their flow fronts are very low to extremely low allowing a long emplacement duration (e.g. 2 - 13 m/day for a dacitic lava flow of Santiaguito volcano, Guatemala (Harris *et al.* 2004).

1.1.2 Size and shape

The size and shape of lava flows can vary by orders of magnitude and strongly depend on lava rheology and the distribution of the flows over the topography. The rheology is dependent on temperature and chemical composition, therefore flows with low SiO₂ content emitted at high temperature are less viscous than flows with high silica content emitted at low temperature (Fig. 1.4). This implies that flows with low viscosity are highly mobile (like pāhoehoe and ‘a’ā flow type) and therefore can extend longer than those with higher viscosity (like block lava flow type).

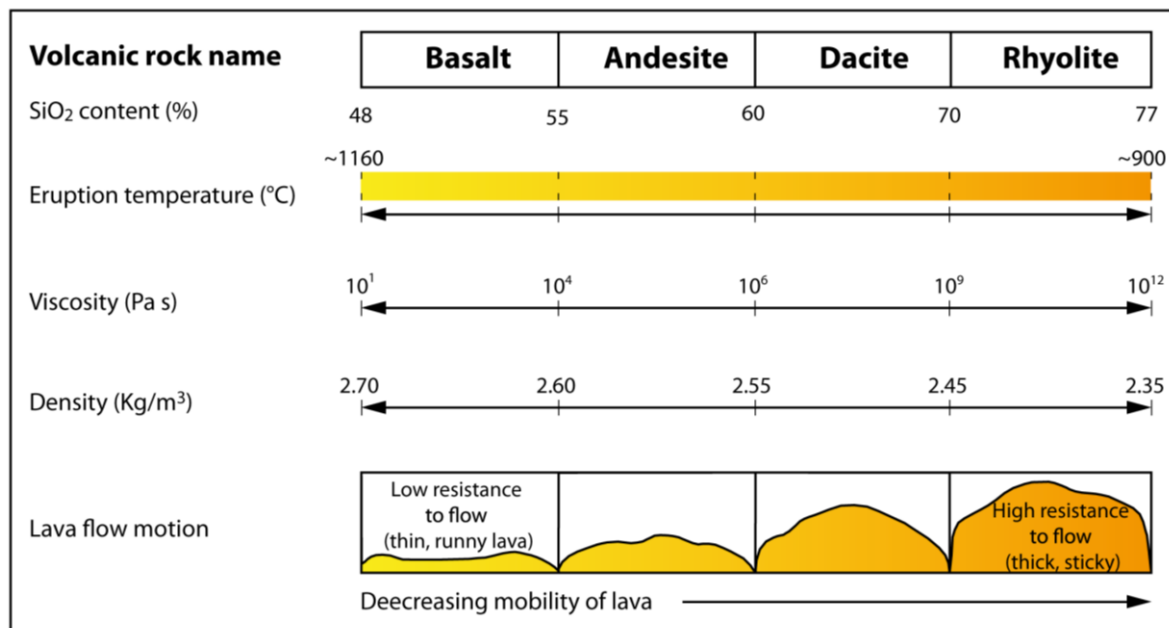


Figure 1. 4 Classification and characteristic of volcanic rocks which define the approximate range of values for SiO₂ content, eruption temperature, viscosity, density and show a qualitative estimation of the mobility of lava flows depending of their composition (Modified from: Johnson, USGS).

A typical and easy way to characterize lava flows is by using the aspect ratio V/H , in which V is the average thickness and H is the horizontal extent (Cas & Wright 1987 after Walker 1973). Thus, a high aspect ratio corresponds to lava flows which are thick in relation to its area (e.g. $V/H = 1/2$), and a low aspect ratio is when the lava is relatively thin (e.g. $V/H = 1/100$), as shown in Fig. 1.5.

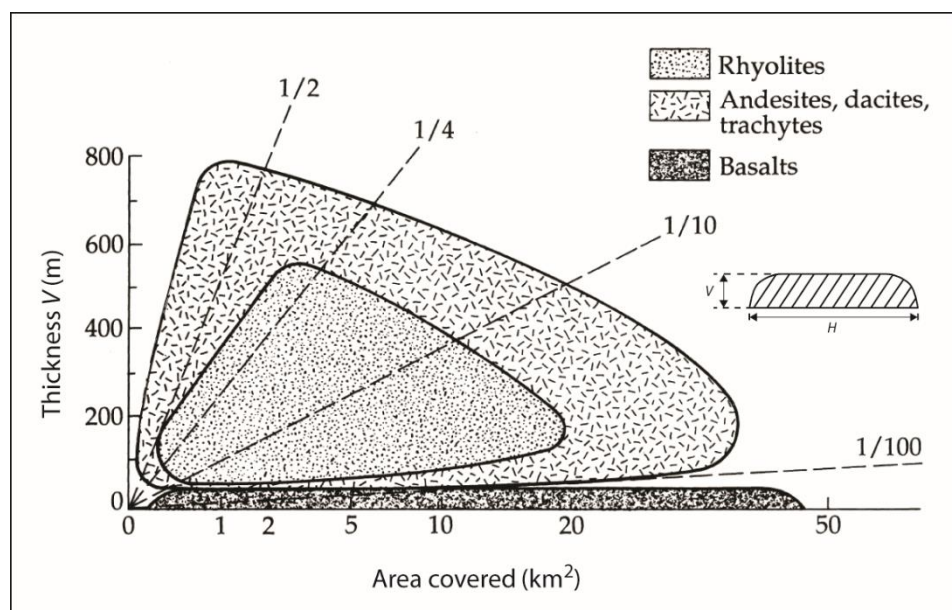


Figure 1.5 Relationship between thickness and area covered of lava flows of different compositions. Broken lines represent the aspect ratio V/H (Walker 1973).

According to the volume of a unit, the two main end members of lava flows are detailed below:

- ❖ *Flood lavas* are the largest volumetrically and they include continental and mid-ocean ridges flood basalts. These flows are typically emitted through large fissures (continuous fractures) and can reach long distances. In the geological record there is evidence of larger lava flows, about 300 km length which corresponds to the Columbia River Plateau (Swanson & Wright 1981). The average flow unit thickness was 17 m according to Walker (1973).
- ❖ Smaller *basaltic lava flows* can be generated from central volcanoes, point-sources vents or small restricted fissures. Compared with flood lavas, these smaller basaltic flows are less voluminous and therefore occupy smaller areas. Opposite to *flood lavas*, more *silicic lavas* are usually small volume and thicker flows, and are not as extensive and thin as basaltic ones. Maximum distances reached by *basaltic lavas* are few kilometers while intermediate lava can exceed 25 kilometers. Silicic lava flows as andesites, dacites and rhyolites can reach thickness up to a few hundred of meters.

1.1.3 Lava flow distribution systems

Depending on their nature, lava flows can form one single unit, several units or thousands to hundreds-of-thousands of units (in the case of flood basalt). According to Walker (1973) they can be divided into flow units, simple lava flow and compound lava flow or lava flow field.

- ❖ **Flow Unit** represents a separate cooling unit, in which its surface is cooled significantly and solidified before another flow-unit is superimposed on it. This description can be applied to a lava flow which presents cooling surfaces.
- ❖ **Simple Lava Flow** is a flow that may not be divisible into different flow-units. Usually they are long and narrow and typical of short duration eruptions.
- ❖ **Compound Lava Flow or Lava Flow Field** is considered as a flow that is divisible into several flow-units. Lava flow units are erupted during the same eruption due to a subsequent generation of simple lava flows and that may be emplaced next to one another; on top of one another, or both. (Harris & Rowland 2015a). Lava flow field emplacement is related to long duration eruptions. Generally, flow fields can be as thick and wide as they are long.

Lava flows can develop and travel along two main structures: lava flows are emitted through the surface from vents or fissures and can flow by open channels or lava tubes.

- ❖ **Channel Systems** are molten lava streams whose surface is exposed to the atmosphere. Based on Sparks *et al.* (1976) levees can be classified as initial, rubble, overflow and accretionary levees. Lipman & Banks (1987) have described the main channel zones of the lava flow of Mauna Loa from 1984 as: flow toe, zone of dispersed flow, transitional channel and stable channel zones.
- ❖ **Tube systems** can be defined as a conduit of solidified lava beneath the surface through which molten lava flows (Greeley 1987). They are formed due to some mechanisms including crustal growth, repeated channel overflow, jamming and lobe advance littoral.

1.1.4 Inflation

Inflation processes can occur in pāhoehoe and ‘a’ā lava flows due to the sustained input of lava during a long-lived eruption. It occurs when fluid lava is continuously injected into a unit with established basal and surface crusts; these crusts are visco-elastic and can resist to pressurization thus allowing the flow surface to expand in all directions (Hon *et al.* 1994; Harris & Rowland 2015a) (Fig. 1.1a). However, at a given point this brittle crust can fracture in order to accommodate the expansion of the inflation process. Pāhoehoe lobes can normally reach a few centimeters thick but with subsequent inflation process they can reach several meters (Calvari & Pinkerton 1998).

Based on the descriptions from Walker (1991), Hon *et al.* (1994), Harris & Rowland (2015a) inflation can create three main features:

- ❖ **Tumuli:** This topographic structure is formed when the inflating fluid mass causes the brittle crust to crack into plates which are then up-tilted. It is common on Hawaiian pahoehoe lava flow fields, particularly on shallower slopes (Fig. 1.1d).
- ❖ **Sheet lobes:** they are formed by coalescence, inflation and thickening of individual pahoehoe units. They can reach various meters thick and kilometers across in flood basalts.
- ❖ **Lava rises:** can be described as very large flat-topped tumuli. These structures have roughly horizontal surfaces. *Lava-rise pits structures* are typical in lava rise features, are characterized for being wider downwards than upwards with concave walls and overhanging rims of the thin pahoehoe slabs (Fig. 1.1d).

1.2 Parameters controlling lava flow length

The physics that govern lava flow behavior are complex. Analogue experiments, direct observations and field measurements have shown that lava's velocity, shape, morphology and emplacement are dominantly governed by viscosity, effusion rate, underlying slope (Dragoni *et al.* 1986; Hallworth *et al.* 1987; Pinkerton 1987; Harris & Rowland 2001; Cashman *et al.* 2013;) but also by its thermorheological control, volume, chemical composition and heat loss (e.g. Macdonald 1953; Cashman *et al.* 1999; Harris & Rowland 2001; Lev *et al.* 2012; Cordonnier *et al.* 2015). Through experimental methods it has been determined that the rheological response of Hawaiian basaltic lavas is affected by cooling and crystallization (Sehlke *et al.* 2014). Heat loss mechanisms and viscosity are described in Section 1.3.2 and 1.4.1 of this Chapter, respectively. The description for the other parameters is shown below.

One of the pioneer studies by Walker (1973) proposed that the length of the flows is primarily controlled by effusion rate. Then after slope, rheology and cooling were included as factor controls (Pinkerton & Wilson 1994). Recently Harris & Rowland (2001) showed that the effect of the heat loss and its relationship with the effusion rate are the main control factor for lava flows length.

1.2.1 Effusion rate

The effusion rate is the volumetric flux of erupted lava that is feeding a flow at any particular point in time (Harris *et al.* 2007). It can directly affect the resulting morphology of the flow i.e. pāhoehoe and ‘a’ā basaltic lava flows are formed when the effusion rate of the flow is low and high respectively (Macdonald 1953; Cashman *et al.* 1999). For example, an effusion rate of $\sim 3 \text{ m}^3/\text{s}$ is slightly below the minimum rates commonly assumed to be necessary for ‘a’ā formation (Walker 1973; Rowland & Walker 1990). Walker (1973) showed that lava flows with high effusion rates can reach long distances (basaltic flows), meanwhile low effusion rates are related with smaller flows (andesitic flows) as shown in Fig. 1.6.

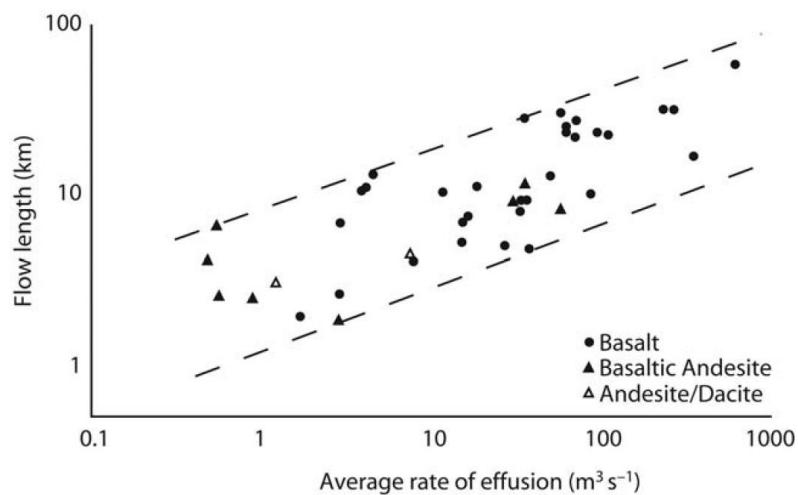


Figure 1.6 Lava length versus average effusion rate for lava eruptions of various volcanoes (Walker 1973).

According to Harris & Rowland (2009) the correlation between eruption rate and length proposed by Walker (1973) should not take in account tube fed lava flows due to the cool, thick, and insulating crust which reduces cooling rates and allow the flow to reach longer distances. They suggest as well that effusion rates from channel-fed, cooling-limited, simple flows should be correlated to the cooling-limited length.

1.2.2 Volume

The volume of emitted magma through the surface has implications for lava flow dimensions. Malin (1980) showed that lava flow length is directly proportional to its volume (Fig. 1.7). Based on statistical approaches, he determines that it is possible to obtain the length of lava flows following the Eq. 1.1:

$$L = 0.60V_T^{0.57}, \quad [1.1]$$

where L is the length of the lava flow and V_T is the total volume of the flow. This is in general true for “volume-limited” flows, which stop because there is no more supply. In general those flows do not reach a “mature” morphology according to the description of Lipman & Banks (1987) and as reported in Rhéty *et al.* (2017). Figure 1.7 shows the result of the relationship between the length of the flow and the volume using the Eq. 1.1 for different Hawaiian basaltic flows.

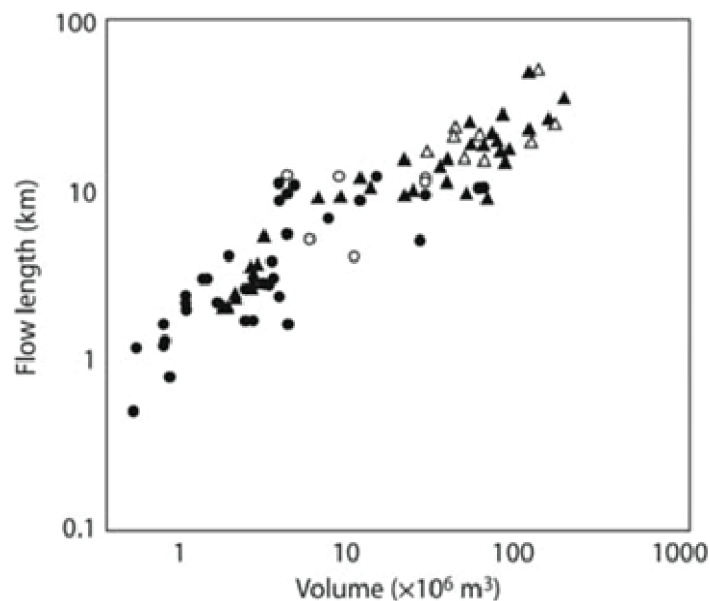


Figure 1. 7 Flow length versus subaerial volume for Hawaiian basaltic flows using Eq. 1.1. Circles are data for Kilauea and triangles are for Mauna Loa. Open symbols indicate cases where the flow entered the ocean, Malin (1980).

1.2.3 Slope surface

Topography has a big influence in the distribution of lava flows (Hon *et al.* 1994). Changes in slope or the lateral redirection of a lava flow imparts a significant fraction of its incident kinetic energy into rotational energy for low viscosity lava flows. It can disrupt the flow surface and have a significant impact on the heat loss and thus the distance the flow can reach (Glaze *et al.* 2009). Together with thickness and viscosity, the slope can affect the velocity of lava flows; e.g. flows can become faster, narrower and thinner on steeper slopes (Lister 1992; Kerr *et al.* 2006).

1.2.4 Thermo-rheological properties

When lava flows are travelling on the surface they lose heat which results in cooling. This cooling will directly affect the rheology of the lava up to a point where the viscosity is such that the lava cannot flow anymore: it is the rheological cut-off and it is attributed to “cooling limited flow” (Rhéty *et al.* 2017). This effect has been described in detail and used by Harris & Rowland (2001) in the FLOWGO model which is presented in Section 4.2, Chapter 4.

Furthermore, the study of Giordano *et al.* (2007) shows that the cooling rate of the flow has a strong influence on the rheological cut-off. In their study Giordano *et al.* (2007) measured the viscosity during dynamic cooling of lava samples from Nyiragongo volcano (Democratic Republic of the Congo). Those measurements showed them to determine that there is a temperature at which the viscosity increases exponentially to the infinite as a result of crystallization, referred to as the ‘cut-off’ temperature and that it is dependent on the cooling rate. Later, Kolzenburg *et al.* (2016) analyzed the thermal characterization of cooling/crystallization of lavas during viscosity measurements in non-isothermal regimes at temperature up to 1160°C and found that the cut-off temperature decays logarithmically as a function of cooling rate (Fig. 1.8).

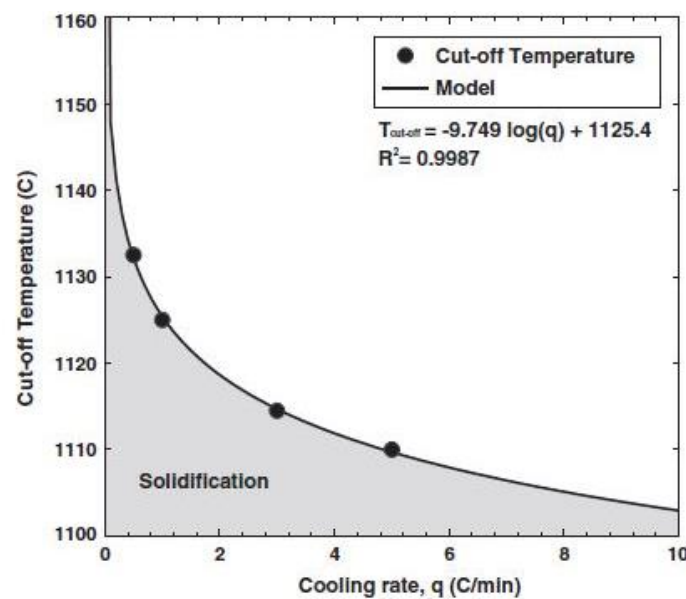


Figure 1. 8 Representation of the rheological threshold temperature versus cooling rate, it shows the cooling rate dependence of the solidification threshold. (Kolzenburg *et al.* 2016).

1.3 Cooling and crystallization of lavas

Temperature is one of the most important parameters that influences lava flow behavior (rheology): when lava flows are travelling they lose heat, crystallizes and therefore their viscosity

increases. It is therefore important to understand the mechanisms of heat exchange (loss and gain) during emplacement (Harris 2013).

1.3.1 Thermal and rheological structure of a lava interior

The thermo-rheological structure of lava flows has yet not been well constrained for all the lava flow types due to the complexity of their internal architecture and permanent evolution during emplacement. Significant advances have been made for basaltic lava flows because they are often observable but andesite and more silicic flows still remain poorly known.

The thermo-rheological structure for pāhoehoe lava flows has been defined by Hon *et al.* (1994) thanks to measurements on active pāhoehoe units at Kilauea, Hawaii. It was reinterpreted by Harris (2013) and later on by Harris & Rowland (2015a) who further redefine the boundaries layers for pāhoehoe lava flows and define them for ‘a’ā flows (Fig. 1.9).

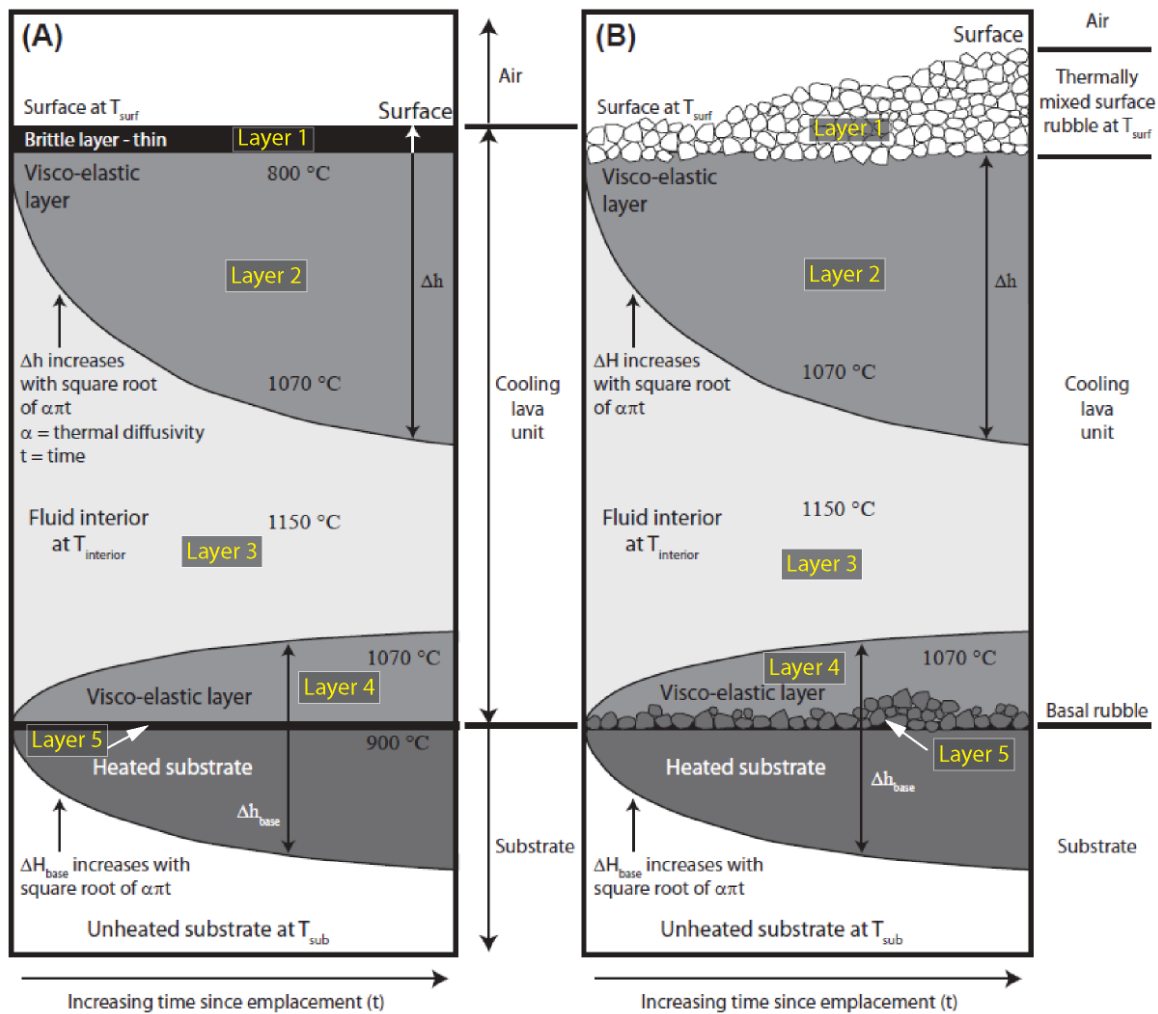


Figure 1. 9 Internal thermal layer for a (A) pahoehoe and (B) ‘a’ā lava flows, shows the variation in depth of each boundary with time. (Harris & Rowland 2015a).

In general, these boundary layers correspond to:

- ❖ **Layer 1: Surface Crust.** Represents the low temperature solid zone of brittle lava. It loses heat fast due to radiation (decreasing temperature by: 50-300°C), then the surface is rapidly air quenched to form a selvage. For a pahoehoe lava flow of Kilauea volcano its temperatures can vary from 1000 to 850 °C compared with its interior temperature of 1150 °C and the isotherm of the base of the surface crust is defined by 800 °C (Hon et al. 1994).
- ❖ **Layer 2: Upper visco-Elastic layer.** Represents a partially molten elastic layer whose top is defined by the 800°C isotherm and whose base is defined by the 1070°C. In this layer it is possible to find crystals and melt in equal proportions.
- ❖ **Layer 3: Core.** It is the layer with the lowest viscosity and highest temperature of the internal structure. The core represents the fluid layer, and is formed by a mixture of melt, crystals and bubbles.
- ❖ **Layer 4: Lower Visco-Elastic layer.** It is the second lower, visco-elastic layer between the flow core and the basal crust.
- ❖ **Layer 5: Basal Crust.** It is the solid glassy layer in pāhoehoe, or zone of clinker in ‘ā between the lower visco-elastic layer and the cold underlying surface.

1.3.2 Heat balance mechanisms

During the last decades a variety of studies were developed to understand and determine the mechanisms that govern the heat transfer between the flow and its surroundings. Depending on whether the flow is channelized or tube fed, heat loss can occur differently. For the first case, if the flow is poorly isolated, heat loss can be high Keszthelyi & Self (1998). For tube fed types, flows can be efficiently isolated and the heat loss can be highly reduced (Keszthelyi 1995). Nevertheless, slow moving channel fed flows can also be efficiently isolated as tube fed due to a crust formation (Harris *et al.* 2002).

As this study is focused on improving thermo-rheological laws in the numerical code VolcFlow, the mechanisms that act between an active channel-fed and its surroundings are taken into account and described below.

In an active channel-fed flow, the lava is in contact with the atmosphere and a crust across the surface is formed over the molten core. In the FLOWGO code (Section 3.1.1, Chapter

3), Harris & Rowland (2001) proposed a heat balance model for a control volume of lava that is confined in a channel of given dimensions, and is moving at a certain velocity over a flat surface with a known slope (Fig. 1.10).

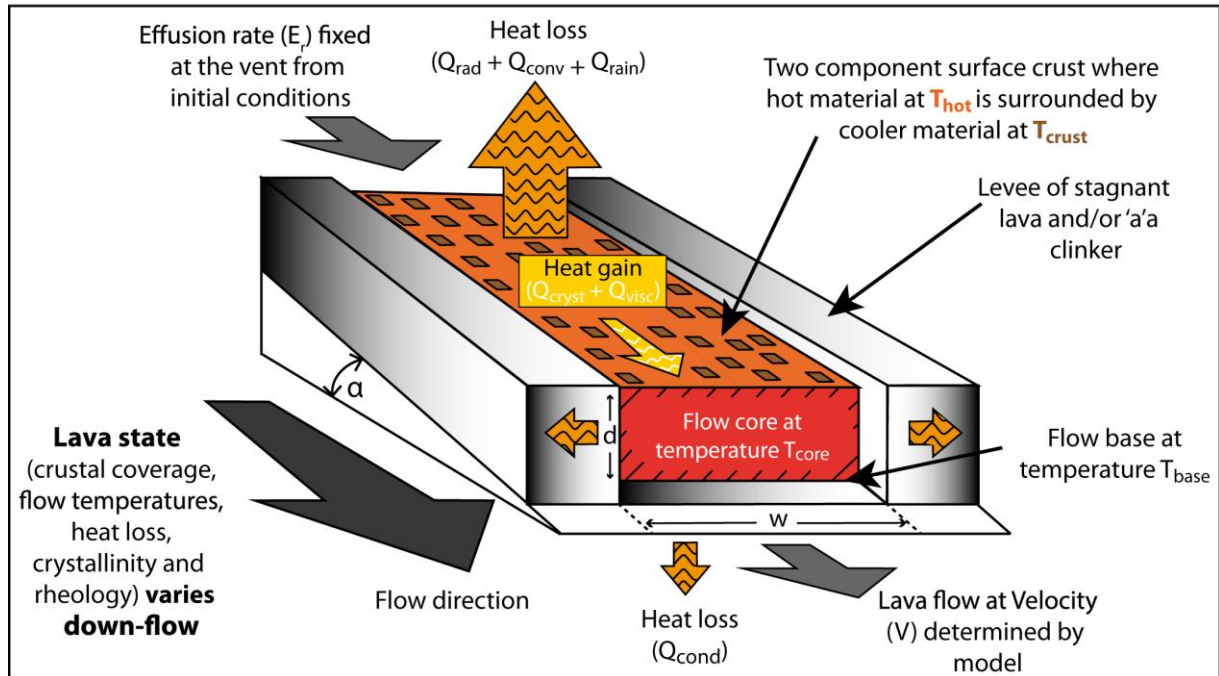


Figure 1. 10 Schematic lava flow heat loss and heat gain considering a channelized lava flow (Harris & Rowland 2001).

Heat loss in channelized lava flows is due to radiation from the upper surface (e.g. Baloga & Pieri 1986; Danes 1972), conduction through the flow levees (e.g. Quareni *et al.* 2004) and through the base (e.g. Fagents & Greely 2001), convection of the atmosphere above the flow surfaces (e.g. Keszthelyi *et al.* 2003), and rain falling on the flow surface. Heat gains in the lava flows can be provided by crystallization (e.g. Crisp & Baloga 1994) and viscous dissipation (Harris & Rowland 2001).

1.3.2.1 Heat loss by radiation (q_{rad})

The lava surface can lose energy to the surrounding by radiation. This heat loss can be assessed using the Stefan-Boltzman law which represents the energy flux radiated directly from the surface of a gray-body (i.e. a body which emissivity is >1):

$$q_{rad} = \sigma \epsilon T_e^4, \quad [1.2]$$

where σ is the Stefan-Boltzman constant, ε is the emissivity of the lava flow ($0 < \varepsilon < 1$) and T_e [K] is the effective radiation temperature of the surface calculated via (Baloga & Pieri 1986; Crisp & Baloga 1990; Pieri *et al.* 1990):

$$T_e = \left[f T_c^4 + (1-f) T_h^4 \right]^{0.25}, \quad [1.3]$$

where, f represents the fraction of the surface which is occupied by a relatively cool crust temperature T_c [K], f can be assumed as a constant value or can be estimated empirically as a function of the velocity (v) [m s^{-1}], where a is an empirically-derived coefficient that relates f to v , Eq. 1.4 (Harris & Rowland 2001). “ $1-f$ ” is the remaining part of the surface which is occupied by molten material with a temperature T_h [K] which is the maximum temperature at the flow surface. T_h can be estimated by the decreasing of the core temperature with time using an established buffer, Eq. 1.5 (Crisp & Baloga 1990):

$$f = \exp(av), \quad [1.4]$$

$$T_h = T_{core} - Buffer, \quad [1.5]$$

where *Buffer* is the temperature difference between the maximum surface temperature and the core temperature.

1.3.2.2 Heat loss by Convective Force (q_{force})

Heat loss by convection from the flow surface involves heat transfer to the atmosphere (Harris 2013). In other words, it represents the cooling effect experienced when cool air blows over a hot surface and it can be described in terms of the convective heat transfer coefficient (h_c) [$\text{W m}^{-2} \text{K}^{-1}$] (Keszthelyi & Denlinger 1996), the convective temperature (T_{conv}) [K] and air temperature (T_{air}) [K] following :

$$q_{force} = h_c (T_{conv} - T_{air}), \quad [1.6]$$

The heat transfer coefficient h_c (Eq. 1.7), can be calculated as a function of density of the air (ρ_{air}), [kg m^{-3}] air specific heat capacity (cp_{air}) [$\text{J kg}^{-1} \text{K}^{-1}$], wind speed (U) [m s^{-1}] and C_H which is given by the relationship $(U^*/U)^2$ where U^* is the frictional wind speed

$$h_c = C_H \rho_{air} c_{p_{air}} U , \quad [1.7]$$

Convective temperature (T_{conv}) is the characteristic surface temperature for convection and can be obtained using (Harris & Rowland 2001):

$$T_{conv} = \left[f T_c^{1.333} + (1-f) T_h^4 \right]^{0.75} , \quad [1.8]$$

1.3.2.3 Heat loss by Rain (q_{rain})

The heat loss caused by the vaporization of rainwater falling over the lava surface can be calculated using:

$$q_{rain} = \frac{\partial R}{\partial t} \rho_{H_2O} L_{H_2O} , \quad [1.9]$$

where $\frac{\partial R}{\partial t}$ [$m s^{-1}$] is the rainfall rate, ρ_{H_2O} [$kg m^{-3}$] is the density of the water and L_{H_2O} [$J Kg^{-1}$] is the latent heat of vaporization of water.

1.3.2.4 Heat loss by Conduction (q_{cond})

Heat loss by conduction occurs across the flow base. It happens when the heat is transferred by molecular contact (Turcotte & Shubert 2002) from the high-temperature core (T_{core}) [K] through a basal boundary layer of thickness (h_{base}) to the cold underlying country rock at base temperature (T_{base}) [K] Eq. 1.10. This heat flux can be calculated using Fourier's Law:

$$q_{cond} = k \left[\frac{T_{core} - T_{base}}{h_{base}} \right] , \quad [1.10]$$

where k [$W m^{-1} K^{-1}$] is the thermal conductivity. Conductive heat flux decreases as a function of time as the basal crust thickens and as the substrate becomes heated (e.g. Kerr 2001).

1.3.2.5 Heat generated by Crystallization (q_{cryst})

The heat generated by the phase change experienced during crystallization, is expressed as:

$$q_{cryst} = \frac{\Delta T}{\Delta x} E_r \rho L \frac{\Delta \phi}{\Delta T}, \quad [1.11]$$

where $\frac{\Delta T}{\Delta x}$ [K m⁻¹] is the cooling experienced by the lava interior per unit distance, E_r [m³ s⁻¹] is the effusion rate, ρ [kg m⁻³] is the density, L [J kg⁻¹] is the latent heat of crystallization and $\frac{\Delta \phi}{\Delta T}$ [K⁻¹] is the fractional crystallization per degree of cooling.

Effusion rate (E_r) can be calculated from the channel cross section with a deep d [m], a width of w and mean velocity of the flow v [m s⁻¹]:

$$E_r = d w v, \quad [1.12]$$

1.3.2.6 Heat generated by Viscosity (q_{visc})

The heat gained produced by viscous dissipation generated by internal friction in a lava channel that is wider than deeper is calculated following Costa & Macedonio (2003) with:

$$q_{visc} = \eta_{bulk} \left(\frac{v}{d} \right)^2, \quad [1.13]$$

where η_{bulk} [Pa s] is the bulk viscosity of the molten lava and v is the mean velocity of the lava.

1.3.3 Cooling Model proposed by FLOWGO

A variety of cooling models have been developed to understand the thermal behavior of channel or tube fed lava flows since they are emitted to the surface until they are cool enough to be stopped. Nevertheless, just one or few mechanisms that govern the heat transfer (Section 1.3.2, this Chapter) were taken in account, e.g. Oppenheimer (1991); Keszthelyi (1995); Keszthelyi & Delinger (1996); Wooster *et al.* (1997); Harris *et al.* (1998); Keszthelyi & Self (1998); Sakimoto & Zuber (1998); Klingelhöfer *et al.* (1999).

For the purpose of this study, the thermo-rheological model FLOWGO proposed by Harris and Rowland (2001) has been chosen. The heat budget and cooling model from FLOWGO (Harris & Rowland 2001; Harris *et al.* 2005, 2015b) is based on the heat budget for a lava control volume as described above (Section 1.3.2). Fluxes of the heat balance mechanism are obtained by multiplying the corresponding mechanism by the channel width and the balance is established via:

$$Q_{in} = Q_{out} \quad [1.14]$$

FLOWGO then considers that the lava flow will gain heat through crystallization and it will lose heat due to radiation, convective force and conduction (Eq. 1.15):

$$Q_{cryst} = Q_{rad} + Q_{force} + Q_{cond} \quad [1.15]$$

FLOWGO's heat budget model allows to determine the cooling and crystallization per unit of distance downflow, $\frac{\Delta T}{\Delta x}$ (K m⁻¹) and $\frac{\Delta \phi}{\Delta x}$ (m⁻¹) respectively, by combining Eq. 1.11 and Eq. 1.15, to obtain:

$$\frac{\Delta T}{\Delta x} E_r \rho L \frac{\Delta \phi}{\Delta T} = Q_{rad} + Q_{force} + Q_{cond} \quad [1.16]$$

Then, the cooling per unit of distance $\left(\frac{\Delta T}{\Delta x}\right)$ is given by:

$$\frac{\Delta T}{\Delta x} = \frac{-Q_{rad} - Q_{force} - Q_{cond}}{E_r \rho L \frac{\Delta \phi}{\Delta T}} \quad [1.17]$$

Note that in Eq. 1.19, terms that represent radiation, convection force and conduction heat mechanisms turned negatives as a result of the loss of heat that occurs during the generation and movement of the flow.

The crystallization per unit distance $\left(\frac{\Delta \phi}{\Delta x}\right)$ is linked to the cooling per unit of distance $\left(\frac{\Delta T}{\Delta x}\right)$

and the crystallization per unit of temperature $\frac{\Delta \phi}{\Delta T}$ via:

$$\frac{\Delta \phi}{\Delta x} = \left(\frac{\Delta T}{\Delta x}\right) \left(\frac{\Delta \phi}{\Delta T}\right) \quad [1.18]$$

Then, by replacing Eq. 1.17 in Eq. 1.18, it is possible to obtain the relationship of the crystallization per unit distance:

$$\frac{\Delta \phi}{\Delta x} = \frac{-Q_{rad} - Q_{force} - Q_{cond}}{E_r \rho L} \quad [1.19]$$

This cooling and crystallization model was created for lava flows of basaltic composition and was tested in specific lava flows of Mauna Loa (Hawaii, USA), Kilauea (Hawaii, USA), Piton de la Fournaise (La Reunion, France) and Etna (Sicily, Italy).

1.4 Lava Rheology

Lava is considered as a three-phase mixture comprising a fluid component (magmatic fluid) with voids (bubbles and/or space opening along shear lines) and solids (crystals, both phenocrysts and microphenocrysts), and its bulk rheology is therefore directly influenced by this mixture (e.g. Pinkerton & Stevenson 1992; Crisp & Baloga 1994, Cashman *et al.* 1999). The transitory nature of rheological properties of a lava flow has been determined by experimental changes in composition, texture and temperature due to gas loss, crystallization and cooling processes (Lev & James 2014; Kolzenburg *et al.* 2017). Rheological properties of lava flows evolve continuously during eruption and emplacement, and their variations can generate strongly heterogeneous flow conditions, morphologies, textures (e.g. Cashman *et al.* 1999; Kolzenburg *et al.* 2017) which evolve in space and time.

Lava temperature, crystallinity, and vesicularity are necessary to calculate the lava rheology (e.g. Crisp & Baloga 1994) or to model lava flow dynamics (e.g. Dragoni 1989; Harris & Rowland 2001). In spite of this, the results are very complex to measure in field conditions or to correctly extrapolate from the lab scale (Lev & James 2014).

Many models have been developed in the last decades and focus mainly in one and two phase magma and/or lava mixtures. One-phase models were developed to obtain fluid viscosity from composition, water content and/or temperature (e.g. Shaw 1969; Giordano *et al.* 2008) meanwhile two-phase models were applied to mixtures of fluid and crystals (e.g. Pinkerton & Stevenson 1992) or fluid and bubbles (Manga *et al.* 1998). Three-phase mixtures have not been deeply explored in context of lava flows due to their complexity. An approach about the study of suspensions and multiphases was developed by Phan-Thien & Pham (1997), which could be applied for the study of three-phase mixture lava rheology.

The next section is directed at reviewing the existing methods to calculate lava bulk viscosity which results from combining dynamic fluid and relative viscosity. As it is shown below, both dynamic fluid and relative viscosity methods have mainly considered in their development one or two phases for the lava mixture.

1.4.1 Viscosity (η)

Following Harris *et al.* (2015b), bulk viscosity of lava flows can be defined as a relationship between the dynamic viscosity of the fluid (η_f) and the effect of particles, called the relative viscosity (η_r):

$$\eta = \eta_f(x, T) * \eta_r(\phi, \beta) \quad [1.20]$$

Dynamic fluid viscosity corresponds to the viscosity of the fluid/melt phase and is dependent of the chemical composition (x) and internal temperature of the melt (T) meanwhile relative viscosity depends on the crystallinity (ϕ) and/or the bubbles content (β) in the magma. Flows with high bulk viscosity can be slower, thicker and wider (Lister 1992; Lyman *et al.* 2005; Kerr *et al.* 2006). Also, bulk viscosity can increase or decrease due to the presence of vesicles and their capillary number (Llewellyn *et al.* 2002; Llewellyn & Manga 2005; Mader *et al.* 2013). For example among many, the presence of 50% bubbles in basaltic lava flows from Hualalai volcano (USA) can increase the bulk viscosity by ~20% (Kauahikaua *et al.* 2002). According to Chevrel *et al.* (2015), the viscosity of andesitic lava is controlled by the crystallization kinetics and the crystal shapes as a result of the cooling path, the undercooling temperature and the deformation history of the liquid.

As the viscosity depends on many parameters, it is complex to integrate all of them in one single model. This is because one single value of viscosity underestimates the physico-chemical processes that affect the rheology of lava (e.g., Shaw 1969; Crisp & Baloga 1994; Cashman *et al.* 1999) and the estimation of the predicted length (Castruccio *et al.* 2013). In the last century many models have been developed with the aim to measure or calculate the dynamic viscosity of the fluid and the relative viscosity of the magma with the main purpose to understand the behavior of lava flows. The applicability of the majority of these models is very restricted due to the specific conditions and chemical compositions at which they were developed. Nevertheless, there are few whose applications are very broad and cover a wide range of compositions and conditions. The existence of these models provides a major key which could be implemented in numerical codes for more realistic lava flow simulations.

The following shows the different models developed to measure or estimate the dynamic fluid and relative viscosities of the lava flows. The ones described are those that were taken into account for this research.

1.4.1.1 Dynamic fluid viscosity (η_f)

Viscosity of natural silicate melts can vary over 10 orders of magnitude depending on the variation in composition and temperature (Leshner & Spera 2015). For example, ultramafic melts are very fluid (10^{-1} - 10^0 Pa s) meanwhile silicic melts are highly viscous (10^7 - 10^8 Pa s) (Fig. 1.11).

Melt viscosity or dynamic fluid viscosity can be largely affected by the content of water, decreasing up to six orders of magnitude for rhyolitic melts and up to 1.5 orders for basaltic melts as water increases (e.g. Dingwell & Mysen 1985; Giordano & Dingwell 2003; Giordano *et al.* 2007; 2008; Richet *et al.* 1996; Whittington *et al.* 2000).

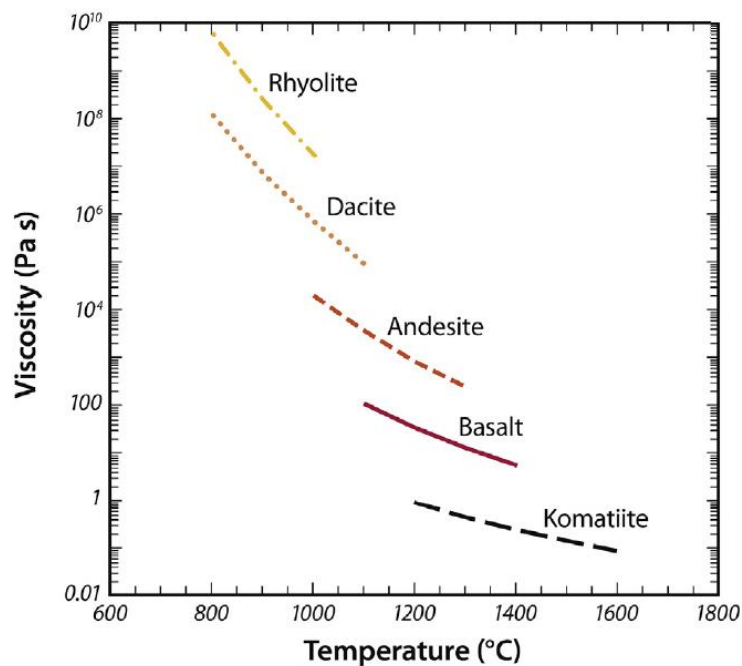


Figure 1.11 Viscosity as a function of temperature at 1 bar for natural magmatic melts with compositions from rhyolite to komatiite (From Leshner & Spera 2015).

A way to determine the dynamic viscosity of the melt is using a simple Arrhenian temperature-viscosity relationship proposed by Shaw (1972). This relationship is dependent on the pressure, temperature, chemical composition of the melt but not on crystallization. For this relationship the fluid or melt is assumed to have a Newtonian behavior (Section 3.3.3.1, this Chapter) which is a good approximation to silicate liquids. The Arrhenius relation that adequately describes this behavior within certain ranges is:

$$\eta(P, T) = \eta_o \exp \left[\frac{E_A + PV_A}{RT} \right] \quad [1.21]$$

where η_o is the asymptotic viscosity as $T \rightarrow \infty$ or the dynamic fluid viscosity at the liquidus temperature T_o [K], E_A is the activation energy for viscous flow, V_A is the activation volume for viscous flow and R is the universal gas constant.

When the temperature of the fluid begins to decrease, the fluid composition changes due to crystallization and the behavior of the fluid reacts as a non-Newtonian fluid. In this way the fluid viscosity (η_f) can be calculated as a function of the temperature according to Dragoni (1989):

$$\eta_f(T) = \eta_o \exp[A(T_o - T_{int})] \quad [1.22]$$

where η_o is the viscosity at liquidus temperature T_o and A is a constant.

Following the approach from Shaw (1972), Bottinga & Weill (1972) include the effect of the water component in the fluid in which the fluid viscosity (η_f) can be calculated as a function of the composition and temperature:

$$\ln(\eta_f) = s(10^4 / T) - sc_T + c_\eta \quad [1.23]$$

where s is the characteristic slope for the viscosity-temperature relationship for a given multicomponent mixture, c_T and c_η are the temperature and viscosity-dependent constants.

Nevertheless, not all the silicate melts can follow the Arrhenian temperature-viscosity relationship. In this case, another method to calculate the dynamic fluid viscosity (η_f) can be applied using the empirical Vogel-Fulcher-Tammann (VFT) relationship (Tammann & Hesse 1926). The VFT model predicts the non-Arrhenian Newtonian viscosity of silicate melts via:

$$\log \eta_f = A + \frac{B}{T - C} \quad [1.24]$$

where η_f is the dynamic fluid viscosity, T [K] is absolute temperature and A , B and C are adjustable parameters depending of chemical composition and representing the pre-exponential factor, the pseudo-activation energy, and the VFT-temperature, respectively.

The most representative model to calculate the fluid viscosity is the one developed by Giordano & Dingwell (2003) and its later improvement by Giordano *et al.* (2006, 2008). This model is based on more than 1770 measurements of viscosity on multicomponent anhydrous and volatile-rich silicate melts and include the effect of the important volatile constituents' H₂O and

F. It is largely used because it is continuous in the composition-and-temperature-space and predicts the viscosity of natural volatile-bearing silicate melts over fifteen log units of viscosity. It also predicts the glass transition temperature, melt fragility and the systematic decrease of this temperature with increasing volatile content.

1.4.1.2 Relative viscosity (η_r)

Relative viscosity is the dimensionless viscosity which considers the effect of crystals and bubbles. The characteristics of these two components are different, bubbles are deformable, have low density, inviscid and compressible meanwhile crystals are rigid with a varied possibility of shapes and are incompressible (Mader *et al.* 2013). Thus their behavior in the lava is different as is the treatment to determine their respective influence in the viscosity of the mixture.

There are some models that can be applied to calculate the relative viscosity or two-phase of the mixture. One of the first attempts to calculate the effect of crystals in the mixture was the Einstein model (Einstein 1906). It considers a flow around an isolated sphere, assuming that the sphere represents a crystal in the flow:

$$\eta_r = 1 + B\phi \quad [1.25]$$

where B is the Einstein coefficient or intrinsic viscosity and ϕ is the particle (crystal) content. For this case the flow is assumed to have a Newtonian behavior. Later, Einstein-Roscoe relationship (Einstein 1906; Roscoe 1952; Ryerson *et al.* 1988; Shaw 1969) was established:

$$\eta_r = \left(1 - \frac{\phi}{\phi_m}\right)^{-2.5} \quad [1.26]$$

in which ϕ is the crystal content and ϕ_m is the maximum crystal content and represent the volume fraction at which the particles can no longer flow ($0 \ll \phi_m \ll 1$).

Krieger & Dougherty (1959) proposed another expression for relative viscosity in which they considered the effect of adding successive particles to a suspension:

$$\eta_r = \left(1 - \frac{\phi}{\phi_m}\right)^{-B\phi_m} \quad [1.27]$$

Another model is the one presented by Costa *et al.* (2009) which is an extension of the model from Krieger & Dougherty (1959), but dependent on the strain rate and applicable to high particle content:

$$\eta_r(\phi_*, \xi, \alpha, \delta) = \frac{1 + \left(\frac{\phi}{\phi_*}\right)^\delta}{\left[1 - F\left(\frac{\phi}{\phi_*}, \xi, \gamma\right)\right]^{B\phi_*}} \quad [1.28]$$

where,

$$F = (1 - \xi) \operatorname{erf} \left[\frac{\sqrt{\pi}}{2(1 - \xi)} \frac{\phi}{\phi_m} \left(1 + \frac{\phi^\alpha}{\phi_*^\alpha}\right) \right] \quad [1.29]$$

where the maximum packing is replaced by the critical particle volume fraction ϕ_* . The rate of growth of viscosity is given by α as $\phi \rightarrow \phi_*$ and by δ as $\phi \rightarrow 1$ in the region $\phi > \phi_*$. The parameter ξ controls the value of the attained viscosity at $\phi = \phi_*$.

Mader *et al.* (2013) made some comparisons between the different models described above for the relative viscosity (Fig. 1.12) assuming a Newtonian behavior for all the cases.

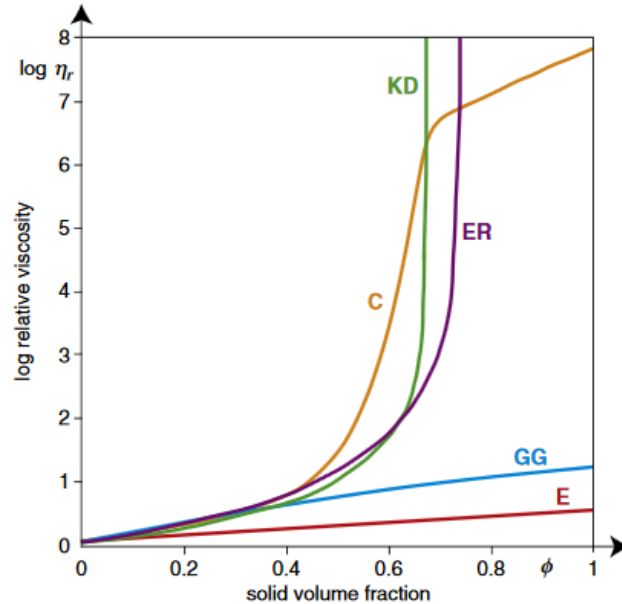


Figure 1.12 Comparison between different models for relative viscosity (η_f). Curves represents them as: **E**: Einstein with $B=2.5$ (eq. 7), **GG**: Guth & Gold (1938); **ER**: Einstein-Roscoe (eq. 8), **KD**: Krieger & Dougherty with $B=2.5$ and $\phi_m = 0.67$ (eq. 9) and **C**: Costa (eq. 10) with $B=2.5$, $\phi_* = 0.6$, $\alpha = 5$, $\delta = 8$ and $\xi = 10^{-4}$ (Mader *et al.* 2013)

Regarding the effect of bubbles, the following relationship was established assuming suspension of spheres in a fluid (Roscoe 1952):

$$\eta_r = \eta_f (1 - 1.35\phi_b)^{-2.5} \quad [1.30]$$

Where ϕ_b is the bubble concentration. Then the increase and decrease of the bulk viscosity depends on the bubble content and shape. For example, if the bubbles remain spherical, the bulk viscosity will increase and deformed bubbles will reduce the viscosity (Manga *et al.* 1998). As the presence of bubbles can increase or decrease the bulk viscosity, Pal (2003) proposed two ways to determine the relative viscosity as a function of the bubble content from eq. 2.29; for mixtures in which the bubbles are spherical and where the bubbles are sheared, Eq. 1.31 and 1.32 respectively.

$$\eta_r = \eta_f \left(1 - \frac{\phi_b}{\phi_{b\max}}\right)^{-\phi_{b\max}} \quad [1.31]$$

$$\eta_r = \eta_f \left(1 - \frac{\phi_b}{\phi_{b\max}}\right)^{-5\phi_{b\max}/3} \quad [1.32]$$

where $\phi_{b\max}$ is the maximum bubble packing concentration, which can be assumed to be 1 (Llewellyn & Manga 2005). Then, Eqs. 1.31 and 1.32 can be simplified as Eqs. 1.33 (Taylor 1932) and 1.34 respectively:

$$\eta_r = \eta_f (1 - \phi_b)^{-1} \quad [1.33]$$

$$\eta_r = \eta_f (1 - \phi_b)^{-5/3} \quad [1.34]$$

Later on, this equation was redefined by Manga & Loewenberg (2001) in which they introduce a constant f that depends on the properties of the suspended bubbles, as given by the capillary number. Corresponding f , to 1 for spherical bubbles and -1.67 for highly sheared bubbles, Eq. 1.35.

$$\eta_r = \eta_f (1 - f\phi_b) \quad [1.35]$$

Finally, the three-phase mixture viscosity (melt, crystals and bubbles) can be represented by the model proposed by Phan-Thien & Pham (1997). It considers a mixture which comprises a

suspension of rigid spheres and bubbles. Harris *et al.* (2008) applied this model in the study of the rheology of basaltic lava flows mixtures concluding that this three-phase treatment can characterize the full range of melt-crystal-bubble mixture viscosities. Nevertheless, the model is very sensitive due to the treatments of the input parameters and the assumptions for choosing the correct equations.

Now, with the information of both the dynamic fluid and relative viscosities it is possible to calculate the bulk viscosity following the Eq. 1.20. The choice of the model needs to consider the availability of the parameters that the different models demand.

One of the important things to keep in mind is that the proposed models for dynamic fluid viscosity and relative viscosity were mainly developed and directed to be applied for lava flows of basaltic composition (e.g. 'a' and pahoehoe). Nevertheless, with correct input parameters it is possible to apply those models to calculate the viscosity of silicic lava flows.

1.4.2 Rheological model for lava flows

With the aim to reproduce lava flows analogically or numerically in an appropriate way, some assumptions have been made in the last decades about how they can behave based on two rheological parameters: viscosity and yield strength. In this way, it has been assumed that lava flows can behave with simple rheologies as Newtonian (Huppert *et al.* 1982; Tallarico & Dragoni 1999) or much more complex likes Bingham, pseudoplastic or Herschel-Bulkley. These rheological models are described by the relationships between shear stress and strain rate (Fig. 1.13), where:

- ❖ **Shear stress (τ)** represents the force per unit area acting on a fluid and depends on the flow thickness (h), density (ρ), gravity (g) and the slope (α) over which the fluid is moving. It is given by the Eq. 1.36:

$$\tau = h \rho g \sin \alpha \quad [1.36]$$

- ❖ **Strain rate ($\dot{\epsilon}$)** is the rate of deformation experienced by a fluid when a load stress is applied with respect to time.

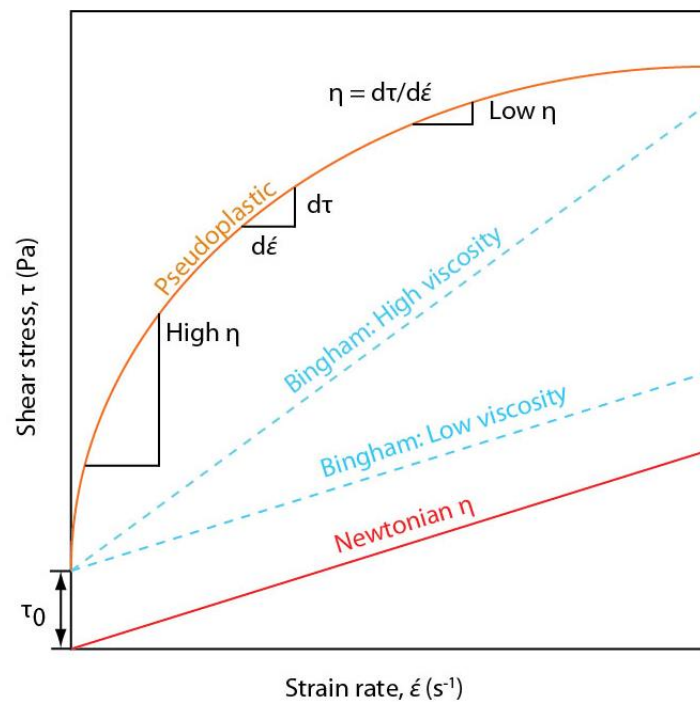


Figure 1.13 Shear-stress – strain-rate relationships for Newtonian, Bingham and pseudo-plastic fluids. Viscosity (η) is defined by the slope between shear stress and strain rate (Harris 2013).

For example, to determine the propagation of silicic lava flows, Castruccio *et al.* (2013) considered three dynamic regimes: a Newtonian viscous regime, a yield strength-dominated and crust-dominant regime. They suggested that for short-lived basaltic eruptions with high effusion rates the flow propagates under a Newtonian viscous regime and for the case of very crystalline blocky lavas the flow is controlled by its core yield strength. Later on, based in Kerr & Lyman (2007) and Castruccio *et al.* (2013), a similar approach was proposed by (Magnall *et al.* 2017) with three regimes: viscosity controlled, crust yield strength controlled and core yield strength controlled (Fig. 1.14).

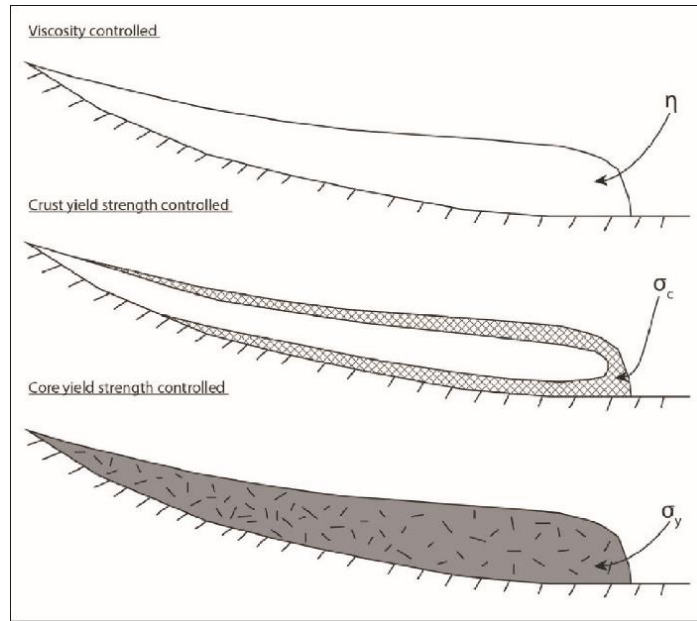


Figure 1.14 Flow regimes that control the lava flow behavior: viscosity dominated, crust yield strength dominated and core yield strength dominated (From Magnall *et al.* 2017 after Castruccio *et al.* 2013).

1.4.2.1 Newtonian fluid

A fluid is called Newtonian when the strain rate or velocity gradient is directly proportional to the applied stress at fixed temperature and pressure, with viscosity being the constant of proportionality between them (Turcotte & Schubert 2002). These kind of fluids will deform when an infinitesimally small force (shear stress) is applied (Fig. 1.13) following the equation 1.37.

$$\tau = \eta \frac{dv}{dy} \quad [1.37]$$

where τ is the shear stress in the fluid, η is the viscosity of the fluid and $\frac{dv}{dy}$ is the derivative of the velocity component.

A Newtonian fluid is a good approximation to silicate liquids when it is above glass transition temperature (Leshner & Spera 2015). Castruccio *et al.* (2013) suggested that short-lived basaltic eruptions with high effusion rate should be treated to have a behavior of Newtonian rheology. Crystal-free fluids can behave as Newtonian but when the crystals began to appear, the rheological behavior changes to pseudoplastic, even at the lowest crystal volume fraction (Sehlke *et al.* 2014).

1.4.2.2 Bingham fluid

A Bingham fluid is the fluid that will only flow once a threshold shear stress has been applied. It will be able to move only if its thickness reaches the critical thickness; otherwise there will be no deformation response and the strain rate will be zero. Bingham fluid is also known as the simple form of non-Newtonian behavior where stress vs strain rate is linear but has a positive intercept on the y-axis that equates to the yield strength (Sehlke *et al.* 2014) (Fig. 1.13) in which the relationship between shear stress and strain rate defines the viscosity of the fluid (Harris 2013). See Section 1.43 and 1.4.3.1 for the description of yield strength and their models respectively.

1.4.2.3 Pseudo-plastic fluid

Pseudoplastic behavior is described by the rate of change in strain rate decreases as shear stress increases (Harris 2013) so that viscosity is decreasing as shear rate increases (Fig. 1.13). Shaw *et al.* (1968) and Pinkerton & Sparks (1978), proposed to characterize a lava flow as a non-Newtonian flow based on field data acquired in active lava flows. Their measurements indicated that lava flow behavior is pseudoplastic and can be approximated by a Bingham fluid. This behavior can be attributed as a rheological response due to the cooling and therefore changes in crystallization of the flow (e.g. Lev *et al.* 2012; Robert *et al.* 2014).

1.4.2.4 Herschel-Bulkley

This rheological model incorporates yield strength and shear-thinning of the lava flow. Some recent experiments have been using Herschel-Bulkley fluids as analog of lava flows (Balmforth & Craster 2000; Balmforth *et al.* 2004; Mueller *et al.* 2010; Castruccio *et al.* 2014; Vera *et al.* 2017). They demonstrate reasonable approximation of rheological measurements from real past eruption cases.

1.4.3 Yield strength (τ_o)

Corresponds to the stress threshold where the Bingham fluids begins to have permanent deformation. Like the viscosity, yield strength depends on temperature, composition, crystal fraction, and vesicularity (Harris & Rowland, 2001, 2015b; Sehlke *et al.* 2014) and it varies with crystallinity in an exponential fashion (Sehlke *et al.* 2014). Yield strength tends to zero when the crystal fraction is lower than the critical crystal fraction content and in turn greater than zero

when the crystal fraction overpassed the value of the critical crystal fraction content in the flow. Yield strength parameter has been incorporated into flow emplaced models to allow the flow to stop even if it is not fully solidified (Cordonnier *et al.* 2012; Kolzenburg *et al.* 2016).

Castruccio *et al.* (2013) have found that the evolution (flow front advance) of mafic eruptions with lower effusion rates or long duration andesitic eruptions is controlled by the yield strength of a growing crust. Meanwhile for the case of very crystalline blocky lavas the flow is controlled by its core yield strength.

1.4.3.1 Yield strength models

There are some models for the estimation of the yield strength parameter for lava flows, the same that can be written in terms of temperature and crystallinity. The next description is based on the review from Chevrel *et al.* (2013) and other models:

- ❖ Gay *et al.* (1969) proposed the following relationship:

$$\tau_o = 1.26\rho g \left(\frac{D_p}{\varphi_m - \varphi} \right) \left(\frac{\varphi_m}{1 - \varphi_m} \right)^2 \left(\frac{1}{\xi^{1.5} - \sigma^2} \right) \quad [1.38]$$

where ρ is the density of the lava; D_p is the mean diameter of particles; φ_m corresponds to the shape factor defined as the ratio of the surface area of a sphere of equivalent volume to the surface area of the particle, σ is the geometric standard deviation that is estimated from a plot of particle diameter versus the cumulative proportion of particles less than a given size.

- ❖ Ryerson *et al.* (1988) proposed to calculate yield strength based on experimental fit obtained from crystallization of picritic lava:

$$\tau_o = 6500\phi^{2.85} \quad [1.39]$$

- ❖ Dragoni *et al.* (1989) offered an equation based on a linear relationship between temperature and crystallization:

$$\tau_o = a \left(\exp^{b(T_l - T)} - 1 \right) \quad [1.40]$$

Where T_l is the liquidus temperature, a and b are fitting parameters.

- ❖ Pinkerton & Stevenson (1992) used a combination of the models from Ryerson *et al.* (1988) and Dragoni *et al.* (1989):

$$\tau_o(T, \phi) = a \left[\exp^{b(\tau_i - T)} - 1 \right] + \left[6500 \phi^{2.85} \right] \quad [1.41]$$

- ❖ Zhou *et al.* (1995) and Saar *et al.* (2001) proposed the following equations:

$$\tau_o = \tau_c \left(\frac{\frac{\phi}{\phi_c} - 1}{1 - \frac{\phi}{\phi_m}} \right)^{1/p} \quad [1.42]$$

where τ_c reflects the total inter-particulate cohesion resistant to hydrodynamic forces and p may reflect the response of the aggregate state to shearing; ϕ_c is the critical minimum particles concentration at which the suspension can sustain some external stress (onset of yield strength).

- ❖ Mueller *et al.* (2010) established the following relationship from analogue experiments:

$$\tau_o = \tau^* \left(\left(1 - \frac{\phi}{\phi_m} \right)^2 - 1 \right) \quad [1.43]$$

where τ^* is a fitting parameter related to the size of the particles. The values used here are similar to Mueller *et al.* 2010 with $\tau^* = 0.234$ for spheres and $= 0.087$ for needles.

- ❖ One of the most recent model was established by Sehlke *et al.* 2014 from laboratory experiments on remelted lava:

$$\tau_o = 1.25 e^{12.93 \phi} \quad [1.44]$$

where being ϕ_c the crystal fraction in the flow.

Chapter 2

Effusive activity from an andesitic volcano, El Reventador (Ecuador)

2.1 Introduction

The identification and characterization of lava flows involve the study and analysis of their inner properties and morphologies. Depending on in which environment they are generated (e.g. subduction, hot-spot), those properties and morphologies can largely vary (e.g. viscosity). Researches about some of those properties have increased in the last decades. Most of them were focused onto try to understand the dynamics that governed the generation and motion of lava flows (e.g. effusion rate, cooling, crystallization, viscosity, etc. See Chapter 1 for more details). Aside to helps to understand their dynamics, this information can become as input data of a specified numerical model for the simulation of lava flows.

Currently there is a vast knowledge of the properties for flows of basaltic composition (e.g. Pinkerton & Sparks 1978; Hon *et al.* 1994; Cashman *et al.* 1999) and just few researches are known for acidic ones (e.g. Castruccio *et al.* 2013, 2014; Chevrel *et al.* 2015). In the same way, most of the numerical models for the simulation of lava flows were developed for flows of basaltic composition. To simulate lava flows, two main things are required: 1) a numerical model and 2) the input data needed for the simulation. Numerical models can be adapted to simulate flows of andesitic composition (Chapter 4) but many parameters of the input data are irreplaceable and non-extrapolable.

In mainland Ecuador there are three andesitic volcanoes that had presented effusive activity in the last 100 years. From south to north they are Sangay, Tungurahua and El Reventador. This last one still in eruption since 2002 and has generated 17 lava flows until 2009 (Hall *et al.* 2004; Samaniego *et al.* 2008; Vallejo 2009; Vallejo & Ramón 2010; Naranjo *et al.* 2016). In early 2012 it was recognized the generation of a new bunch of lava flows, which was continuous until 2014. Even if this volcano has a unique activity in this country, information about its lava flow characterization was very limited and worse yet there was not developed or implemented a numerical model that could be applied for their simulations.

The current research on this volcano has two main aims: 1) to identify, characterize and describe the volcanic activity between 2010 and 2014, and 2) to identify and characterize the lava flows units generated between 2012 and 2014. For the second purpose, the characterization was based on the estimation of their duration, maximum length, area, average thickness, volume, chemical composition, morphology and temperature (maximum and superficial). This chapter describes the different tools that were used for this identification and characterization. The aim of this analysis is to obtain information that could be implemented on numerical models for lava flows simulations of andesitic composition using different approaches (Chapter 4).

2.2 Background

2.2.1 El Reventador volcano

El Reventador, (0.08°S, 77.65°W) located in the northern Ecuador, in the Amazon region (Fig. 2.1), represents one of the most active volcanoes in this country together with Tungurahua and Sangay (Hall *et al.* 2008; Naranjo *et al.* 2016, Arnold *et al.* 2017). This andesitic stratovolcano is hosted at the western side of a ~ 4 km wide horseshoe caldera which is open to the east. The caldera formation is attributed to a debris avalanche generated on 19000 y BP (Aguilera *et al.* 1988). In November 3rd, 2002, El Reventador erupts after 26 years of quiescence generating a subplinian eruption (VEI 4) in which, the upper part of the summit was destroyed leaving thus an open crater orientated north-south and this produced the formation of two summits the western and the oriental ones. This large eruption produced a 17 km eruptive column and copious pyroclastic density currents (PDC) that filled the caldera and travelled to the east about 9km from the crater. Few days later the occurrence of the two lava flows in the south-eastern flank of the volcano was recognized (Hall *et al.* 2004; Samaniego *et al.* 2008). Since its reactivation until those days (March 2018) the eruptive style has been characterized for being strombolian and vulcanian,

producing explosive and eruptive phases along the time. The continuous generation and accumulation of volcanic products, as lava and pyroclastic flows, have contributed with the regrowth of the summit which altitude now reaches 3652 m asl.

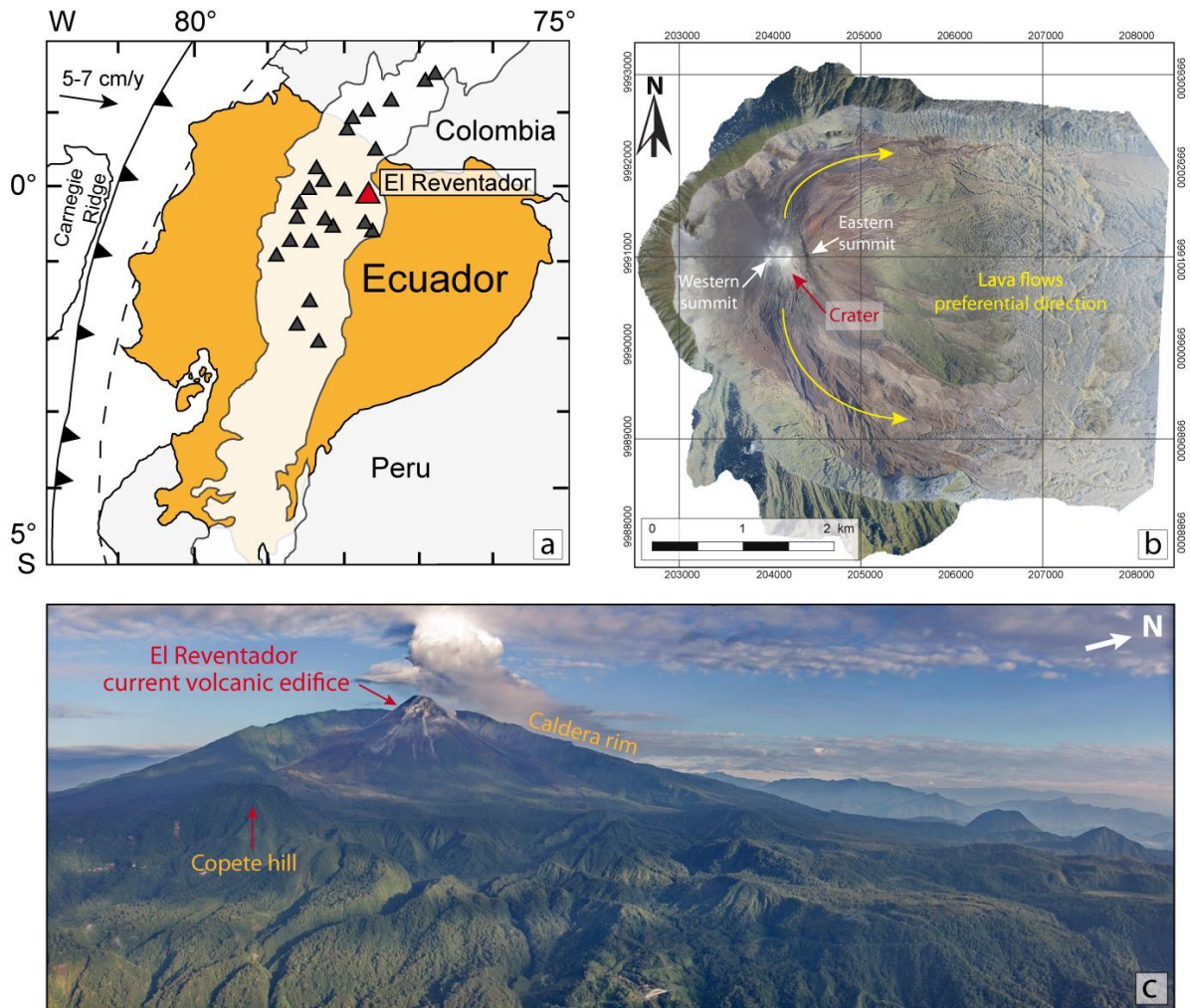


Figure 2. 1 a) Regional location of El Reventador volcano (from Hall *et al.* 2008). b) orthogonal view of the volcano showing the current volcanic edifice and the preferential direction of its volcanic products. c) View of the volcano from the south east, showing the main features of the volcano as the volcanic edifice, the caldera rim and the Copete hill (Photo: P. Ramón, IG-EPN).

2.2.2 Regional geology for El Reventador

The geology of El Reventador volcano (0.08°S, 77.65°W, Fig. 2.1) has been described within a geological survey for the “Hidroelectric Project Coca” by the “Instituto Ecuatoriano de Electrificación” (INECEL) in 1988. They described El Reventador as a volcanic complex which was formed by a ~1000 m succession of effusive and explosive products which lies over the Mesozoic sedimentary Napo Formation. This volcanic complex is divided in three main units separated for sectorial collapses (INECEL, 1988):

- ❖ **Basal volcanic complex (CVB):** It appears to the north and west of the actual eruptive center. It is composed by a succession of ignimbrites, surges, pyroclastic material, lavas and volcanic breccias. In this period the andesitic hill Copete was developed and the domes Lider and Mirador are thought to be formed in a late phase of the CVB. An important debris avalanche of the CVB of $\sim 20 \text{ km}^3$ has been recognized to the east of the young edifice, which has affected the eastern and central part of the old volcano.
- ❖ **Paleoreventador volcano (VPR):** this is formed by a sequence of explosive and effusive products, which are exposed in the western part of the complex and two activity phases can be identified. It seems that the activity of the VPR ended with the generation of some lava flow units. Immediately after those flows there were found deposits of debris avalanche and landslides suggesting that the edifice of the VPR was destroyed for them.
- ❖ **El Reventador volcano or young cone (VER):** is a stratovolcano hosted in a $\sim 4 \text{ km}$ wide within a horse shape caldera open to the east. The caldera formation is attributed to a debris avalanche dated from 19000 y BP (Aguilera *et al.* 1988). This regular cone was developed at the west of the caldera and it has an approximate height of 3462 m a.s.l. This volcano is characterized for had been generated numerous blocky lava flows whose have been accumulated within the depression left for the last debris avalanche.

2.2.3 Topographic implications

Topography plays one of the most important roles for the distribution and emplacement of lava flows over the surface (Hon *et al.* 1994). The current edifice of El Reventador volcano, which is located in the west part of the caldera (Section 2.2.3), is a 1 km high symmetrical cone of $\sim 1 \text{ km}$ diameter with a slope which varies between 35° and 40° . The distribution of lava flows in this volcano is controlled primarily by the morphology of the crater and second by the edifice morphology and third by the shape of the caldera (Section 2.2.4.2).

- a. **Crater shape,** it controls the very first stage of the distribution of lava flow units. The crater depressions (southern and northern) created as a result of the reactivation of the volcano in 2002, influenced on the distribution of the flows to flow directly to the north and to the south of the crater (Fig. 2.2). This tendency of the flows distribution had been maintained in the volcano between 2002 and 2009 (Fig. 2.3). During this period of time, the continuous accumulation of pyroclastic material and lava in the crater in 2002 allowed its progressive re filling. This changing in the morphology of the crater has influenced to

a new complementary distribution of the lava flows to the northeast, east and southeast of the crater since 2012 until the present (Section 2.5.1, this Chapter).

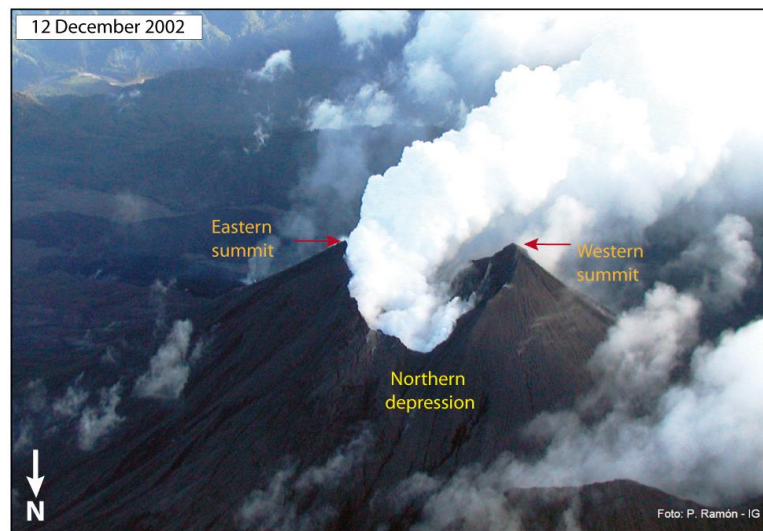


Figure 2. 2 Main topographic features left by the big explosion on the reactivation of the volcano the November, 3rd 2002. It's recognizing the Eastern, Western summits and the Northern depression. The southern one is hidden by the gas emission column (Photo: P. Ramón, IG-EPN).

- b. Caldera walls**, the horseshoe shape opened to the east has an important influence in the distribution of the flows in the inner part of the caldera. Caldera walls represent an important morphology feature whose are characterized for being very steep with a difference of ~1000 m of altitude respect to the caldera floor. The northern and southern ones are considered as structural heights which have been controlled the distribution of some lava flows to the east, following the northern or southern walls (Fig. 2.3).

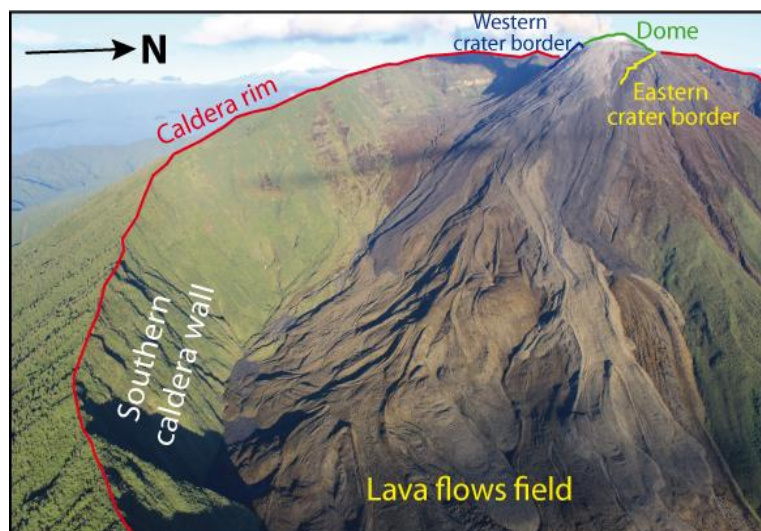


Figure 2. 3 Photography of the southern part of the volcano taken on October, 19th 2013. It shows the caldera rim and their steepest caldera wall that influenced the direction of the emplacement of lava flows. The crater at that date showed the eastern and western borders left by the explosion on November 3rd, 2002. As well it shows the lava flow field generated between 2002 and 2009. (Photo: S. Vallejo Vargas).

2.2.4 Historical activity

The historical activity of El Reventador volcano is related to the eruptions recorded by the Spanish people after their arrival to the territory in AD 1532. As this volcano is located in the Amazon region, the inaccessibility and bad weather conditions have been played an important role to prevent the direct observations of the volcano's activity. El Reventador was officially discovered in 1931 by Paz y Mino (Paz y Mino *et al.* 1931). Based in the historical records Hall (1980) and Simkin & Siebert (1994) considered possible activity in: 1541, 1590, 1691, 1748, 1797, 1802, 1842, 1843, 1944, 1856, 1871, 1894, 1898-1906, 1912, 1926, 1936, 1944, 1955, 1958, 1960, 1972, 1974 and 1976.

Hall (1977) described the occurrence of strombolian/vulcanian activity in April and May of 1976, which was characterized for being moderately explosive. The next eruptive period has begun in 2002 (Hall *et al.* 2004).

2.2.5 Current activity

The reactivation of El Reventador on November 3rd, 2002 generated a subplinian eruption of VEI 4 (Hall *et al.* 2004; Ridolfi *et al.* 2008; Samaniego *et al.* 2008), which corresponds to the strongest one in the last 120 years in Ecuador. Since then, superficial activity in the volcano has been characterized for being strombolian and vulcanian. Effusive and explosive activity has observed, allowing the generation of numerous blocky lava flows, eruptive columns of gases with/without ash content and PDC's. Lava flows of different sizes have been emplaced in the inner part of the caldera (Fig. 2.4a). Eruptive columns of different heights were distributed mainly to the northwest (Fig. 2.4b, c), west and southwest of the volcano; just few were directed to the east reaching populated areas. Current PDC's have different sizes but all of them have been emplaced in the inner part of the caldera (Fig. 2.4d).

An intense explosive activity was registered during June 22nd and 23rd 2017, triggering the generation of PDC's that travelled towards the north-eastern flank and then through the eastern part of the caldera floor. These PDC's represent the largest ones after those generated during the reactivation of the volcano in 2002. After this explosive phase, an effusive phase was recognized and was associated with the generation of a new lava flow emitted from a vent located in the north eastern border of the cone (Fig. 2.5). This lava flow represents the largest one recognized since 2008 at this volcano and has been included in this research as a study case for lava flow simulations (Section 4.2.4, Chapter 4).

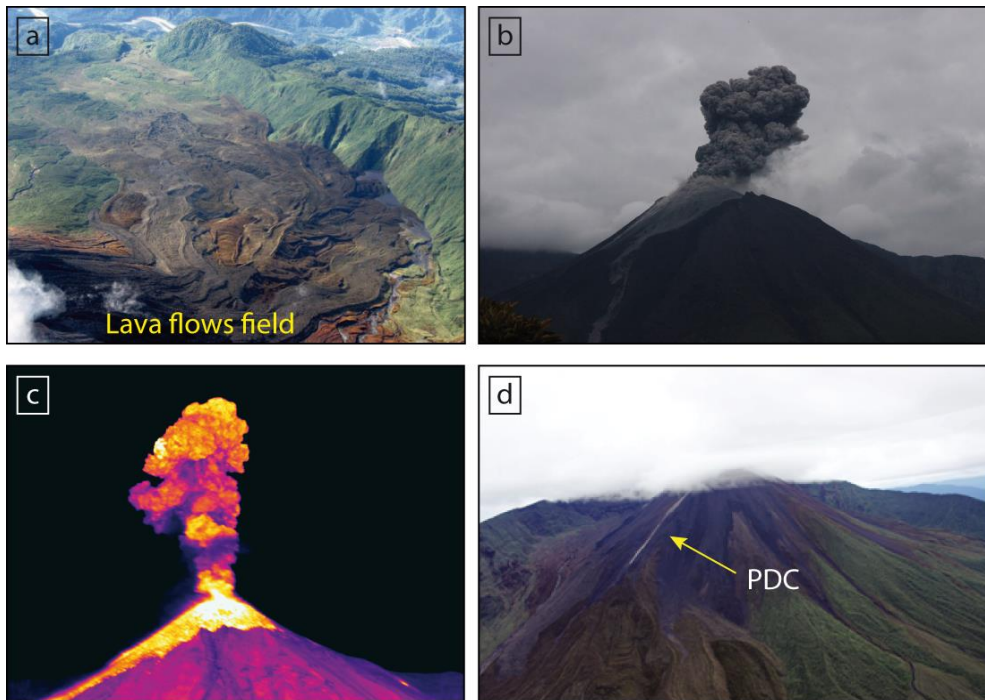


Figure 2. 4 Photographs and thermal image of the superficial activity of El Reventador volcano. a) lava flow field of the flows generated between 2002 and 2012. b) explosion and the generation of gas and ash column. c) thermal image of the crater showing an explosion and a lava flow unit. d) a PDC deposit in the southern flank of the volcano. (Photos/thermal image: S. Vallejo Vargas).



Figure 2. 5 Deposits of the PDC's (dotted red line) and the lava flow generated during June – July 2017. The lava flow which reached 2.65 km, distance is represented by red color line in the visible image and in white line correspondent thermal image. (M. Almeida, IG-EPN).

2.2.6 Network monitoring

El Reventador is monitored by the “Instituto Geofísico” (IG) of the “Escuela Politécnica Nacional” (EPN), which is the official institution in charge of monitoring the seismic and volcanic activity in the Ecuadorian continental and insular territories. Monitoring of El Reventador begun after its reactivation (November, 2002) with aerial visual-thermal monitoring. Later on, it was implemented a seismic and lahar detection networks. At the moment, the monitoring network is comprised by 2 short period seismometers, 2 broad band seismometers, 2 visual cameras and 2 infrared cameras (Fig. 2.6).

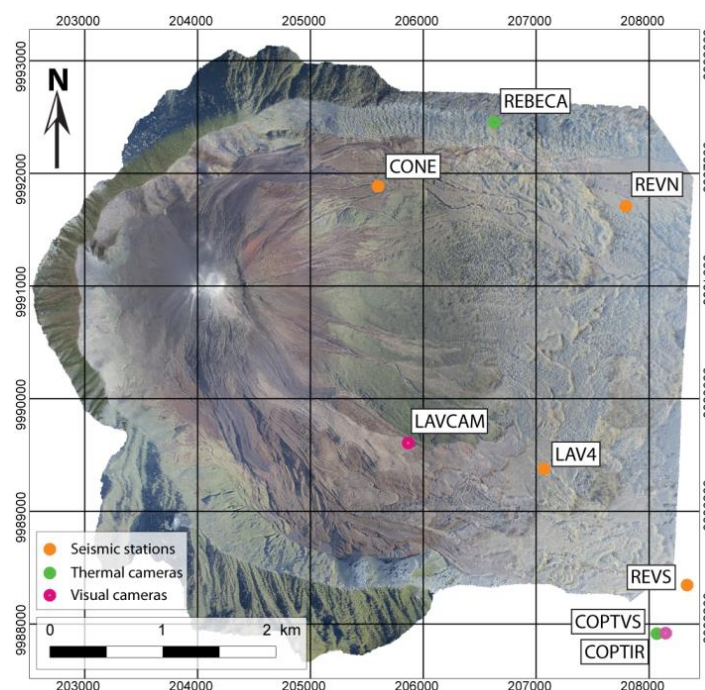


Figure 2. 6 Network of El Reventador volcano showing the location of the fixed seismic, thermal and visual stations (Source IG-EPN).

The information collected by the network is complemented by regular aerial thermal monitoring, sporadic SO₂ measurements; and satellite information. This last one comprises thermal alerts (e.g. MODVOLC, HOT-SPOT, MIROVA), eruptive columns dispersion (e.g. VAAC) and SO₂ dispersion (e.g. TOMS and OMI).

2.3 Tools for the identification of the superficial activity between 2010 - 2014

The identification and characterization was based on the analysis of different monitoring tools as seismicity, thermal alerts, thermal and visual images, and DEM's development.

2.3.1 Monitoring tools

2.3.1.1 Seismicity

During the period 2010 – 2014, only the seismic station CONE was operative almost the whole time. About five months of four years, the station was off (Nov/2011, Aug-Oct/2012). Figure 2.7 shows the daily seismicity count for the period 2010 - 2014. The analysis was based on the daily seismic database generated by the IG-EPN. The seismic activity in this volcano was characterized for showing explosions (EXP), spasmodic (SP TR) and harmonic tremor (HR TR), hybrid, long period (LP) and volcano tectonic (VT) events.

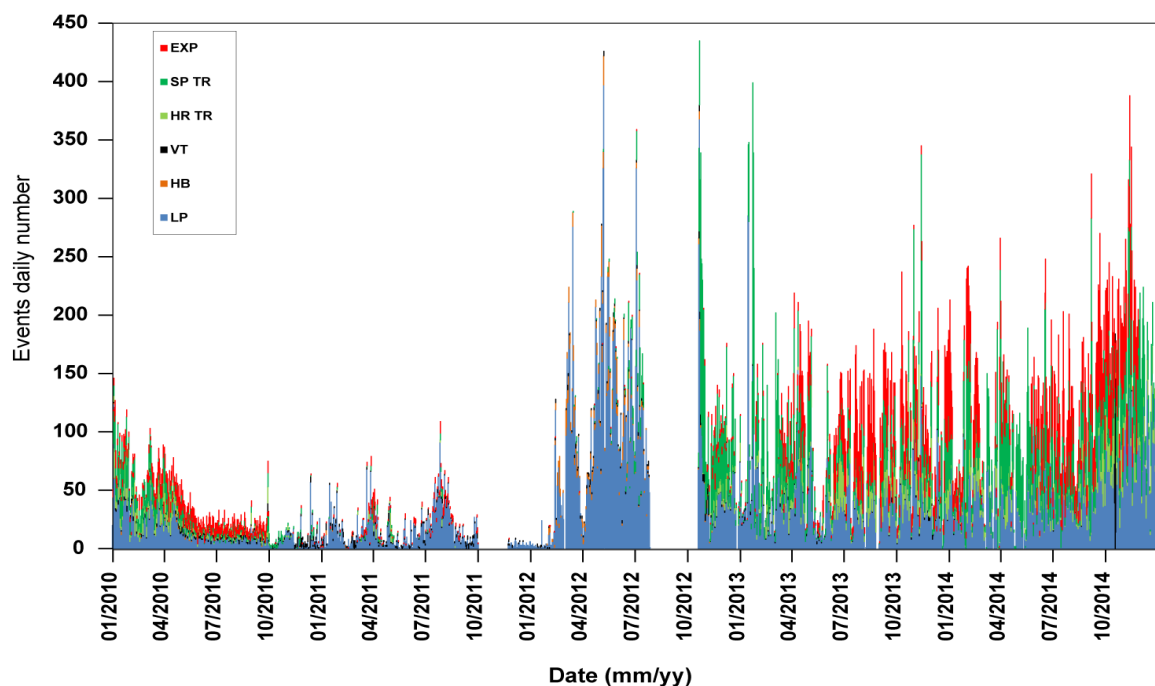


Figure 2. 7 Daily count seismic events in CONE short period station for the period 2010 – 2014. It was recognized events like explosions (EXP, red), spasmodic tremor (SP TR, vivid green), harmonic tremor (HR TR, light green), volcano-tectonic (VT, black), hybrid (HB, orange), long period (LP, blue) (Source: IG-EPN).

Events like spasmodic and harmonic tremor, and long period are related to the movement of fluids at the interior of the volcanic conduit. Volcano tectonic are caused by the fracturing of the rock due to the ascent of fluids. Hybrid events are a combination of both long period and volcano tectonic events. Unfortunately, there were no locations of the seismic events due to the lack of information of other seismic stations.

2.3.1.2 Thermal alerts from MIROVA

The MIROVA (Middle InfraRed Observations of Volcanic Activity) system is a space-based volcanic hot-spot detection system which combines a high sensitivity for the detection of small thermal anomalies with the improved temporal coverage typical of moderate-resolution sensors. The MIROVA system uses the Middle InfraRed Radiation (MIR) in order to detect, locate and measure the heat radiated from volcanic activity, which is called Volcanic Radiative Power (VRP [MW]) (Coppola *et al.* 2015).

This system allows to track short-term and long-term variation in the ongoing volcanic activity. The MIROVA webpage (<http://www.mirovaweb.it/>) provides thermal maps (50 x 50 km) and VRP time-series in a range from 1 to 4 hours per day allowing then to have thermal monitoring of an specific target for about 4 times per day (Coppola *et al.* 2015). The collaboration between IG-EPN and D. Coppola from the University of Turin and Florence (Italy) allowed to have the VRP serial time data between 2002 and 2014.

Only the alerts generated during the night were considered in this research for avoiding the daily solar influence. Between 2010 – 2014 there were registered 495 thermal alerts at El Reventador. They varied between 0.1 and 371 MW (Fig. 2.8). These thermal alerts generally were associated with the generation of lava flows, explosions, PDC's.

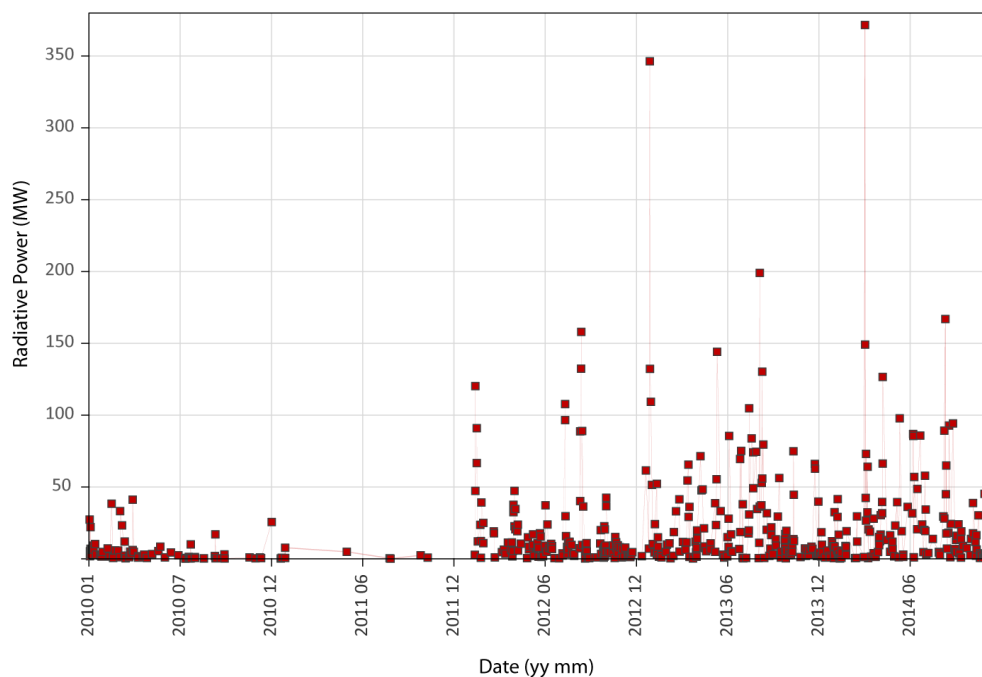


Figure 2. 8 Volcanic Radiative Power (VRP) time series for El Reventador volcano between 2010 and 2014. In that period there were generated 495 thermal anomalies. Each anomaly is represented by a dark red square. (Source: MIROVA).

This information has been very useful to characterize the superficial activity of the volcano and to track the effusive volcanic activity of El Reventador volcano. VRP values and their locations are in Appendix 2.1. It's important to mention that the cloudy weather probably inhibited the generation of more thermal alerts.

2.3.1.3 Direct observations

Direct observations of the superficial activity in active volcanoes represent a fundamental tool for volcano monitoring. It allows to understand the volcanic process during an eruption and helps to quantify the deposits that an eruption can emitted. They can be done through visual and infrared cameras, and as well by using night vision goggles.

Thermal monitoring is a safety and useful tool not only because provides temperature information, but also because it allows to quantify the emission rates of volcanic flows and plumes. For lava flows, it allows to track flow emplacement and to measure different flow parameters such as: length, heat flux and discharge rate (e.g., Calvari *et al.* 2005; Harris *et al.* 2005). Measures of the temperature of volcanic products can help to estimate their superficial thermal evolution on time. Thermal information of the flow is very precious due to it can helps to increase the understanding of the physical process involved during the lava emplacement. Therefore, this information can help to improve existing numerical codes for the numerical simulation of lava flows.

Thermal monitoring can be applied at active volcanoes into three different fields (i) monitoring and analysis of thermal data during non-eruptive states, (ii) searching for thermal anomalies which could represent eruption precursors on resting volcanoes, (iii) monitoring of ongoing eruptions (Spampinato *et al.* 2011). In the case of El Reventador volcano, it was applied to obtain qualitative observations of thermal features (e.g. identification of lava bodies, PDC's deposits) and qualitative results (e.g. temperature variation, spatial distribution of temperature).

Visual recognition of the emplacement of lava flows from El Reventador volcano was made through visual and thermal observations during regular flights over the volcano since November 2002 (Hall *et al.* 2004; Samaniego *et al.* 2008; Vallejo & Ramón 2010; Naranjo *et al.* 2016). Later on, it was complemented by near real-time transmission of images from ground based visual and infrared cameras located in the southeastern part of the volcano to the IG-EPN offices, LAV4 (2360 m.a.s.l.) and Copete (2300 m.a.s.l.) stations (Fig. 2.6). Complementary

information was obtained through ~60 fieldwork campaigns, which allowed the identification of the lava flows spatial distribution, geometric measures of lava flows as length and thickness.

Quality of images (visual or thermal) depended on the weather conditions. At El Reventador they are characterized for being humid, clouded and rainy the most part of the time. This weather behavior affects the record of images in which it could be possible to identify the volcano and its superficial activity.

2.3.1.3.1 Regular overflights

Regular overflights have been carried out continuously since after the reactivation of the volcano (Nov./2002) with visual and infrared handheld cameras. Aerial thermal monitoring has been carried out with a FLIR P650 model between 2002 and 2009 and since then it was replaced by a FLIR SC660 model. The main difference between both cameras is the resolution of the image which is 320x240 pixels for the P650 and 640x480 pixels for the SC660 model. This characteristic can influence the results of the thermal anomalies analysis.

2.3.1.3.2 Ground base camera network

Currently, this network is composed by four cameras, two visual and two infrared (Fig. 2.6). One visual, LAVCAM was installed in 2009 and was located about 3 km to the southeast part of the crater. The second visual, COPTVS, was installed in the Copete hill (Fig. 2.1) together with the first infrared, COPTIR in 2013, about 4.5 to the southeast part of the crater. The second infrared REBECA was installed in December 2015 in the north eastern caldera rim about 3.3 km from the crater. Figure 2.9 shows some examples of the images captured from the network, with them it is possible to observe the superficial activity generated in the volcano and to know which direction the different volcanic products could take.

Images from LAVCAM, COPTVS and COPTIR are collected every 5 minutes and transmitted in near-real time to IG offices by telemetric and microwave via. Images from REBECA are stored in the station and collected periodically by IG technicians. The near real-time transition of the images has helped to improve the volcanic crisis management in different occasions.

The view from Copete Hill (southeastern caldera rim) is perfect because from there it is possible to observe the whole volcano and its superficial activity when the weather conditions are good. Only the northern and western flanks are excluded from this view. The camera network on this

hill (COPTVS and COPTIR) is shown in Fig. 2.10, it shows the view from there (Fig. 2.10b) and the field of view that the infrared camera covers (Fig. 2.10a). The thermal image shows the dome, a lava flow and some PDC's emplaced over the south eastern flank of the volcano.

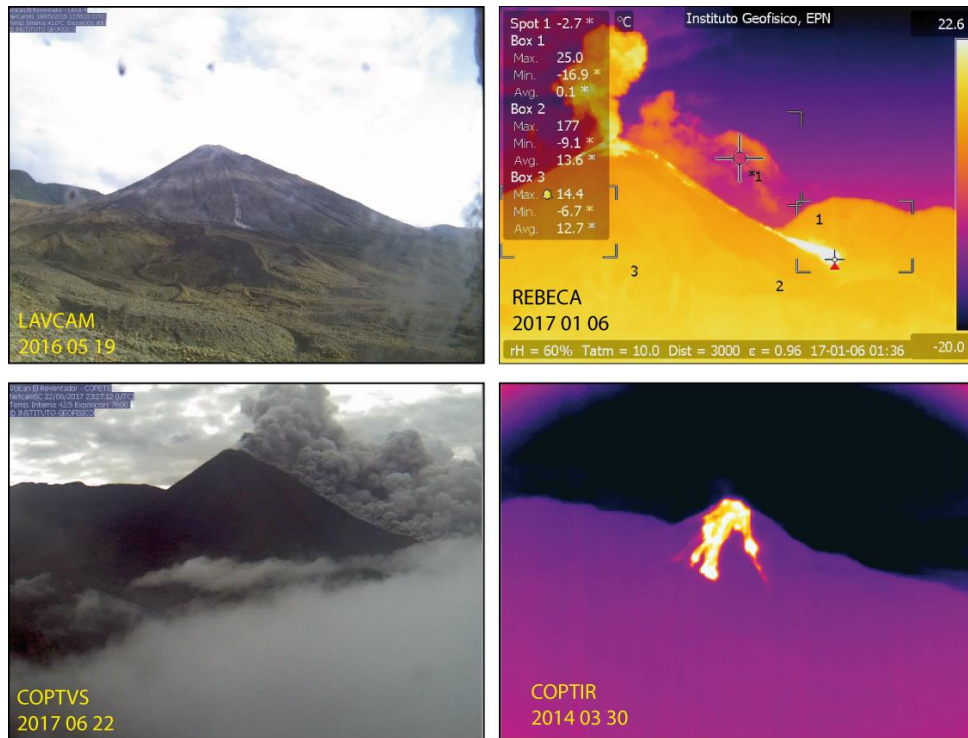


Figure 2. 9 Representative images of the four cameras to make up the visual and thermal network on El Reventador volcano, LAVCAM, REBECA, COPTVS and COPTIR (Source: IG-EPN).

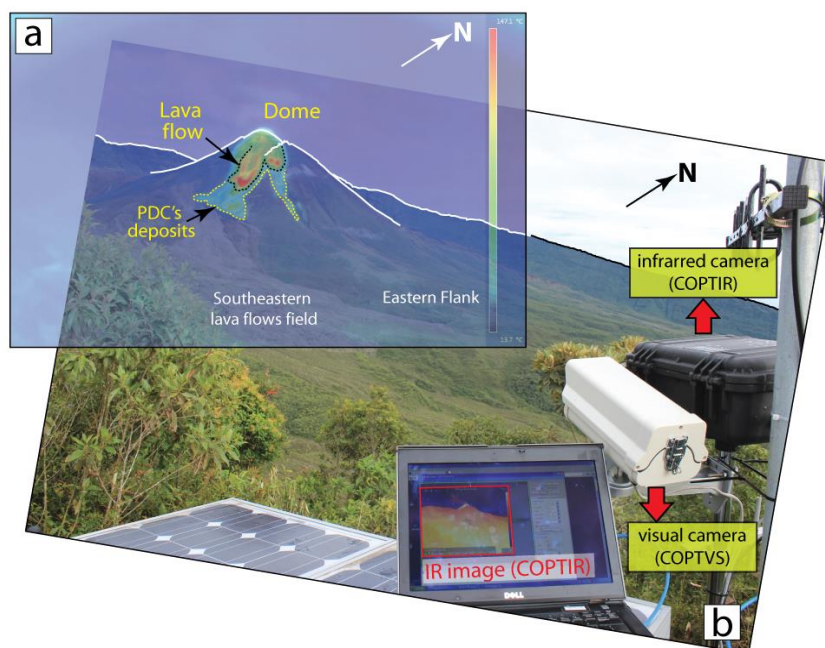


Figure 2. 10 a) Photography of El Reventador volcano and the imaging network at Copete hill which is composed by thermal and visual cameras, COPTIR and COPTVS respectively. **b)** Thermal image from COPTIR camera, it shows thermal anomalies related with the presence of the dome, lava flow and PDC's.

Figure 2.11 shows the schema made for thermal images from COPTIR, which includes the main topographic features of the volcano, iso-lines to estimate the distances and heights that the different volcanic products can reach, and the directions that they could take. This scheme has been used during this research and for the daily monitoring of the volcano in the IG-EPN offices.

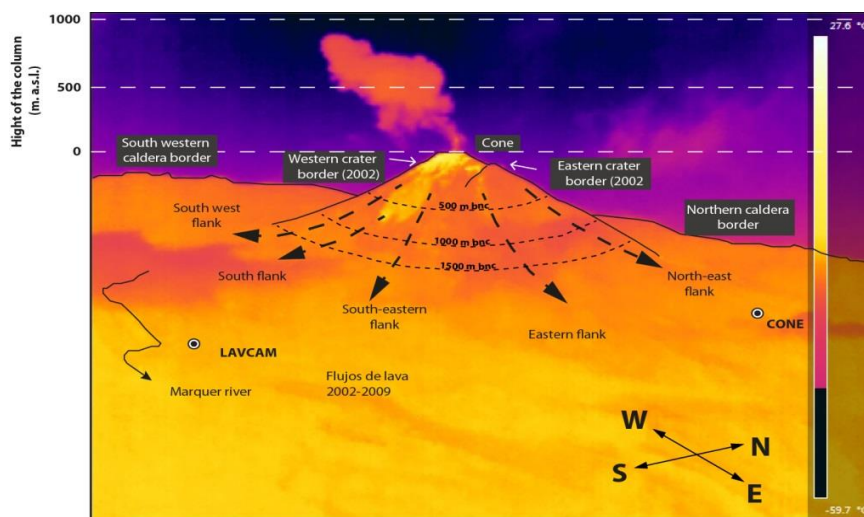


Figure 2. 11 Thermal image acquired from COPTIR camera showing the main features recognizable at the volcano and an scale to estimate the distance or height that the flows/columns can reach. (Source: IG-EPN).

Visual and thermal imaging in near-real time has allowed the IG staff to follow the evolution of currents lava flows, PDC's and gas/ash eruption columns. As well to collect information about the height and direction of gas/ash columns with the purpose to be reported to the VAAC advisory in order to alert the presence of ash in the air.

2.4 Field surveys campaigns

Field campaigns have been carried out to accomplish different objectives as: to have precise topographic measures of the lava flows extension, dispersion and thickness (e.g. Naranjo *et al.* 2016); to sample the different flows (lava and PDC's) (Hall *et al.* 2004, Samaniego *et al.* 2008, Naranjo *et al.* 2016); to obtain ground control points (GCPs) topographic features of the volcano for the development of digital elevation models (DEM's, e.g. this study).

A fieldtrip to El Reventador was carried out during this research between the 16th and the 20th of April 2015 and was supported by the 'Secretaría de Educación Superior, Ciencia, Tecnología e Innovación' (SENESCYT), 'Instituto Geofísico de la Escuela Politécnica Nacional'

(IG-EPN), ‘Institut de Recherche pour le Développement’ (IRD), and ‘Oleoducto de Crudos Pesados Ecuador’ (OCP for helicopter facility). Main objectives of the field survey were:

- ❖ To complete the rock sampling for lavas of the periods 2002 – 2009, 2012 – 2014; and PDC’s generated between 2012 and 2014 for geochemistry and thin sections analysis.
- ❖ To locate ground control points on the volcano for high resolution DEM development.
- ❖ To acquire photographs of the volcano for the development of a high resolution DEM.
- ❖ To acquire thermal images for the identification of new lava flows and PDC’s units.

During the fieldwork the superficial activity of the volcano was characterized for being explosive (Fig. 2.12a), generating ash/gas columns with maximum height of 2 km a. c. (above the crater). Their dispersion was through the west due to the preferential direction of the wind in this region. During the night was observed glowing in the crater and its reflection over the ash/gas emissions (Fig. 2.12b). As a consequence of the explosions, incandescent material was observed rolling down (PDC’s and ballistic blocks rolling down) through the flanks of the volcano (Fig. 2.12c).

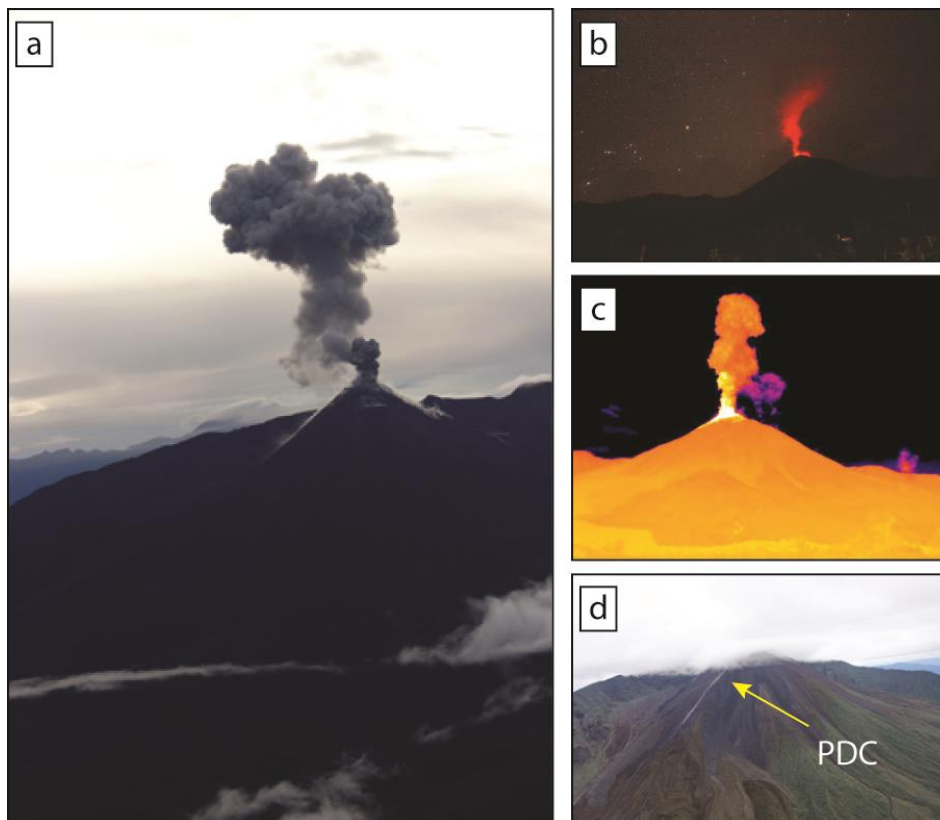


Figure 2. 12 Activity of El Reventador volcano during fieldwork. a) Typical explosive activity of those days, the ash/gas columns reached less than 2 km high with a dispersion towards the west, b) During the night it was possible to observe glowing on the column after an explosion and incandescent ballistic blocks, c) thermal image of an explosion, there was no thermal evidence of a lava flow, d) deposit of a small PDC occurred on April 19th. (Photos/thermal image: S. Vallejo Vargas).

Some of those explosions triggered PDC's whose were travelled through the flanks reaching distances shorter than 2 km from the crater (Fig. 2.12d). No one active lava flow was recognized during this period of time. Weather conditions were mostly rainy and cloudy the most part of the time. The volcano was clear just in few opportunities, so early in the morning (~11:00 UTC) or so late in the afternoon (~22:00 UTC). Fieldwork was done by foot and by helicopter.

2.4.1.1 Rock sampling

It was possible to re-sample four lava flows of the period 2002-2009: LF 5, LF 9, LF 11 and LF 14. For LF 5, seven samples were collected along the northern levee in order to determine if the flow shows variations of the chemical composition and textural characteristics. Lava flows of the period 2012-2014, emplaced in the upper part of the flanks of the volcano were characterized for not having reached long distances (i.e. longest flow: 1.8 km from the crater). During the fieldwork the superficial activity of the volcano was highly explosive (e.g. PDC's generation), this circumstance didn't allow the group to collect the samples needed for the study; only one lava flow (LF 25) from the period 2012-2014 and one PDC's of this period were sampled. In total 14 samples were collected. Coordinates of the samples location is attached in Appendix 2.2. The geographic location of them is shown in Fig. 2.13 (blue marks).

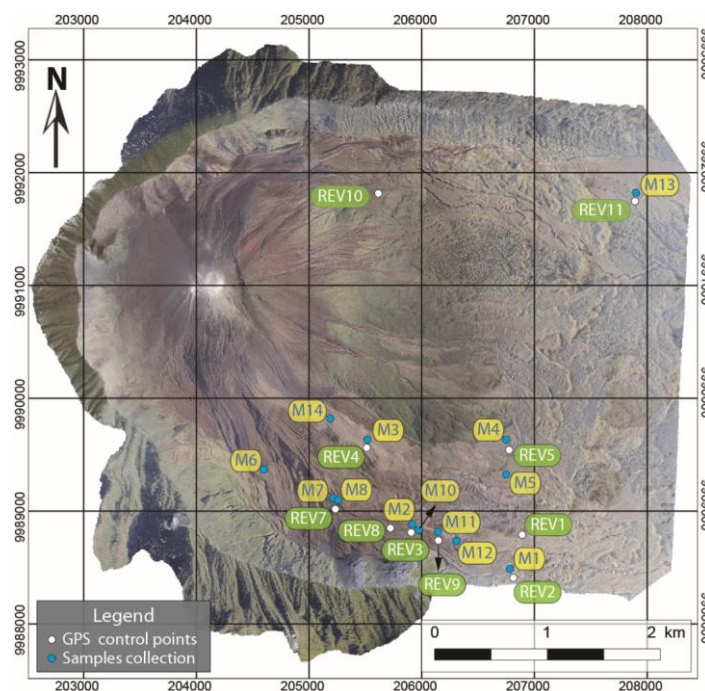


Figure 2. 13 Location of the collected samples (blue dots) and GPS control points (white dots) for DEM development at El Reventador volcano during the fieldwork.

2.4.1.2 Ground control points (GCPs)

The development of DEM by photogrammetry method requires to have measured ground control points in the field. One way to do this, is to place marks on accessible places of the field that can after be visible from the air. The best technique is to place in the area as many marks as possible in order to avoid the error during photo processing. A high resolution GPS measurement of those marks is recommended for build a high resolution DEM.

In the case of El Reventador, there are two main features that may influence the placement of the marks in the area: vegetation and topography. The dense vegetation makes impossible to see the real surface of the topography. Inside the caldera the vegetation is particularly dense in the external and internal walls of the caldera meanwhile in the floor or the caldera the vegetation is mostly small, characterized for the presence of moss, lichen and small trees. This difference can be attributed to the volcanic activity (presence of lava flows, PDC's, acid rain, lahars), which can prevent the regular growth of vegetation.

The second feature is the topography, caldera walls are very step, their slopes varies between 25 and 52°. Caldera floor is more flat having slopes between 15 and 28°.

Looking both conditions it results not optimal to place any mark in the caldera walls but on the caldera floor. GCP points need to be visible and recognizable from the air. For this purpose, a 'yellow square plastic' signs of 1.5x1.5 m were placed in strategic points of the volcano, mostly in the north and south lava flows fields (Fig. 2.6, 2.14).

In total, 11 marks have been placed (Fig. 2.14; Appendix 2.3). For each mark a GPS measure was taken using a Ashtech differential GPS, Movi-Mapper model. Each point was taken for 3 minutes in order to have coherent results.

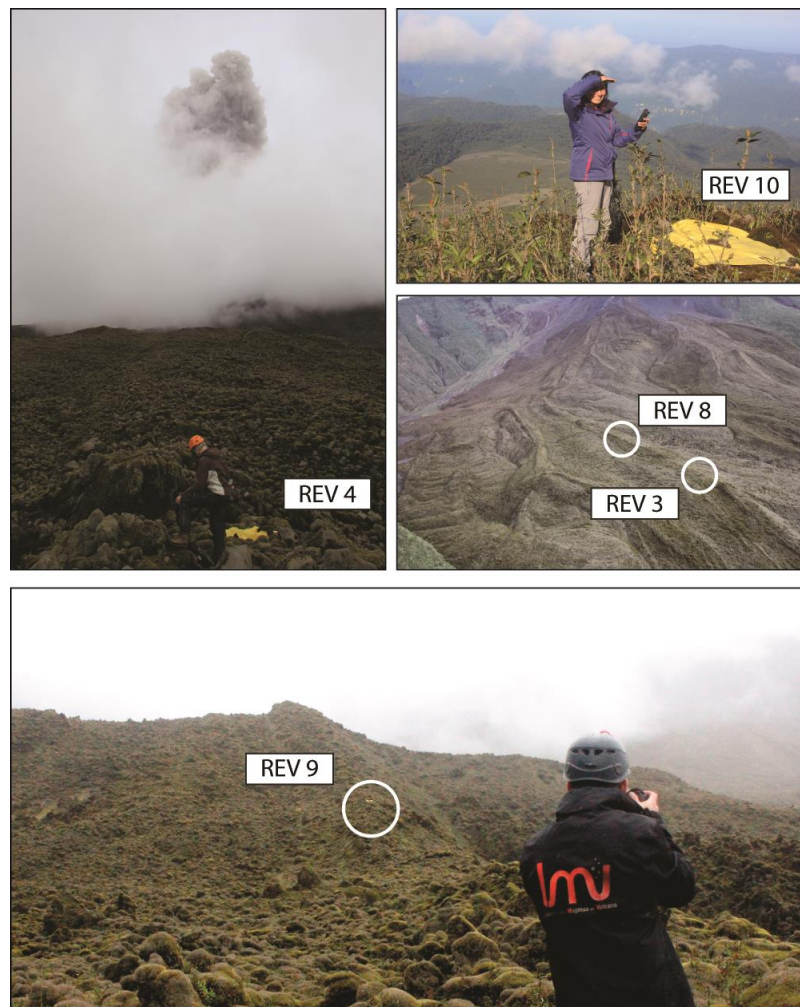


Figure 2. 14 Ground control points placed over the caldera floor in the south and north part of the volcano. **a)** REV4 GCP in the south eastern flank of the volcano, an explosion was recognizing during the work. **b)** REV10 GCP in the northeastern flank beside to the CONE station. **c)** REV3 and REV8 GCP over the LF5. **d)** REV9 GCP over the northern levee of LF5 almost at its front. (Photo: K. Kelfoun/S. Vallejo).

2.4.1.3 Photogrammetry

Morphologic changes of a volcano can be detected by the application of different methods as geodetic levelling, laser scanning, GNSS (Global Navigation Satellite System), InSar (Interferometric synthetic-aperture radar), aerial and terrestrial photogrammetry, and tilmeters and strainmeters. Multiple-image photogrammetry (from ground or UAVs – Unmanned Aerial Vehicle) has been widely used for three-dimensional terrain reconstructions in geosciences. Applications include riverbed morphology, cliff and gully erosion, erosion and glacier monitoring, soil erosion and also active lava flows and domes (James *et al.* 2006; Diefenbach *et al.* 2012; James & Varley 2012; James & Robson 2014, Farquharson *et al.* 2015). One of the advantages to use the

photogrammetry methodology is because it is a lower cost and faster processing technique compared with LiDAR surveys.

The Structure-From-Motion method (SFM) automatically tracks matching features on multiple overlapping offset images, estimates camera position, and generates 3D cloud and mesh (e.g. Verhoeven 2011; James & Robson 2012; Westoby *et al.* 2012; Derrien *et al.* 2015). Then, the obtained model can be georeferenced by implementing Camera Control Points (CCP's) or Ground Control Points (GCPs). Commercial and open-source algorithms are available for implementing image matching, image-distortion correction, point cloud and mesh building, and camera and ground control referencing (e.g. James & Robson 2014; Eltner & Schneider 2015).

Two high resolution digital elevation models (DEM's) of El Reventador volcano were developed using the SFM method in 2013 and 2015 with the aim to analyze the morphological changes in the volcano related to lava flows generation, cone and dome development.

2.4.1.4 DEM 2013 10 19

It has been developed by A. Diefenbach (USGS) with photos took during a survey carried on October 2013. Photographs were obtained from a helicopter at different altitudes. There were no measured control points on the field, then the control was based on structural features of the field as hills, river crossing, lava flows edges, etc. The DEM construction followed the process from Diefenbach *et al.* (2012). The resolution of this DEM is 0.86 m per pixel, Fig. 2.5.

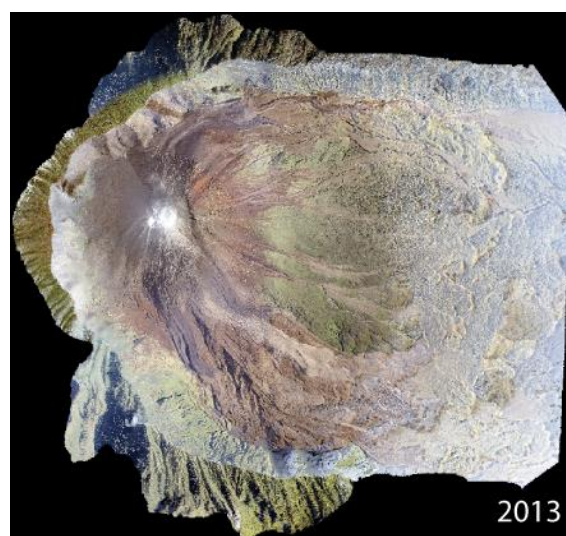


Figure 2. 15 Orthogonal view of the 2013 DEM.

2.4.1.5 DEM 2015 04 21

2.4.1.5.1 Method

To reconstruct the 2015 DEM it was used the commercial software Agisoft Photoscan Pro. The benefit of Photoscan is that it offers an integrated solution, from the detection of matching points and alignment of the images, to the construction of a dense point cloud and triangulated mesh, including a reliable correction of image distortion, and additional calibration of optical lenses at different focal lengths (Agisoft Lens). The dense point cloud is generated from depth information of each aligned image. If GCPs are implemented, a georeferenced DEM can be built from the dense point cloud or from the mesh. The software has been successfully evaluated in terms of GCP residuals and point deviations to the reference measurements (Verhoeven 2011; Koutsoudis *et al.* 2014; Eltner & Schneider 2015).

Field survey at El Reventador volcano was developed in April, 2015. In total, 316 ground photographs were captured from a helicopter at 4150 m a.s.l. using a Canon EOS 60D camera at focal lengths between 18 and 40 mm. The following camera parameters were applied: image size 5184 x 3456 pixels (mean ground resolution ~ 32.1 cm/pix), manual or area autofocus (avoid single-point autofocus), exposure mode set to aperture-priority or manually, 5K white balance, ISO sensitivity 100, no noise reduction, vivid picture control, vignette control (reduces the drop in brightness at the edges of the pictures), and D-lighting (in order to preserve details in highlights and shadows). Masking of the fumaroles at the dome was necessary in order to ensure the homogeneity of the acquired dataset. It was used the tag control. GCPs were previously located in the caldera floor over the northern and southern lava flow fields (see Section 2.3.4, this Chapter) which later were added to the photogrammetry model.

2.4.1.5.2 Results

During the alignment of 316 photographs of El Reventador volcano, 22911 matching points were detected, resulting in a 17,5 x 106 points cloud. The second step was about to introduce directly the coordinates of the CCPs on the triangulated mesh. Planimetric and altimetric errors between measured and estimated coordinates are respectively lower than 4,8 m and 1,68 m respectively. The DEM covered an area of 21.1 km² with a resolution of 1.3 m per pixel, Fig 2.16.

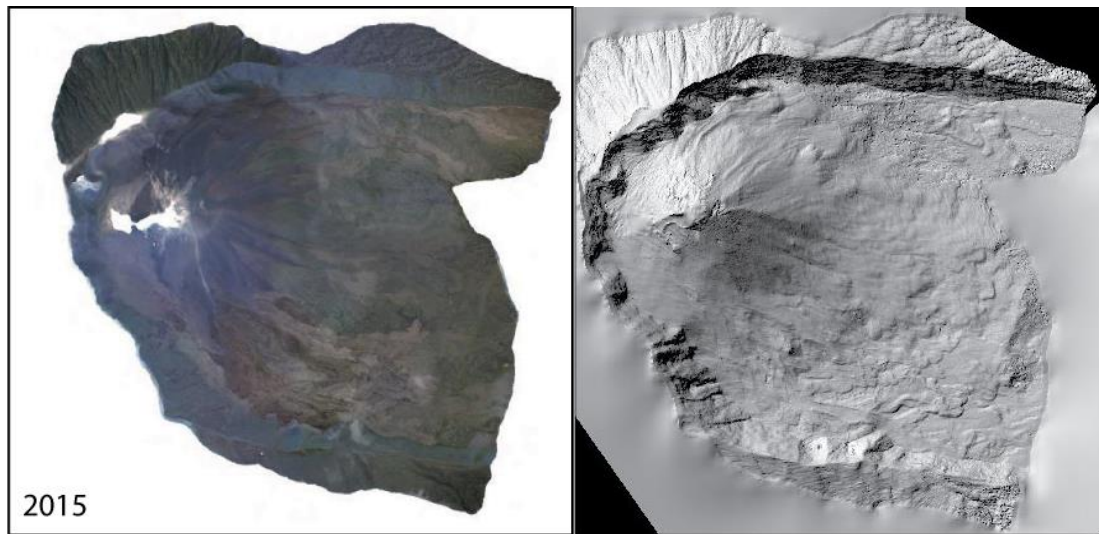


Figure 2. 16 Orthogonal view of the 2015 DEM.

2.5 Identification and characterization of the superficial activity between 2010 and 2014

2.5.1 Pyroclastic Cone

After the generation of the lava flow 17 (October, 2009), an explosive period was recognized (Fig. 2.7, 2.42). It lasted for about 18 months. This explosive activity allowed the formation of a pyroclastic cone over the crater (Fig. 2.17a). This cone was observed for the first time the 31 October, 2009 and then after during the incoming five overflights in 2010. During that period of time it showed an increasing in its size. It was characterized for having a symmetrical truncated cone shape. At the 20 of April, 2010 the cone has a radius and a deep of 150 and 50 m respectively. The white – light gray color that the cone showed is a result of the accumulation of particulate material.

Beside the development of the pyroclastic cone, it was recognized the formation of small PDC's. They reached a maximum distance of 0.5 km from the crater (Fig. 2.17b). This was the first time of PDC's generation after those from 2002. Maximum temperatures of the cone reached the 200 °C and they were located at the base and the internal walls of the cone.

For about one year there was no recognized any feature or signal of effusive activity. The last time that the pyroclastic cone was observed was in October 2010.

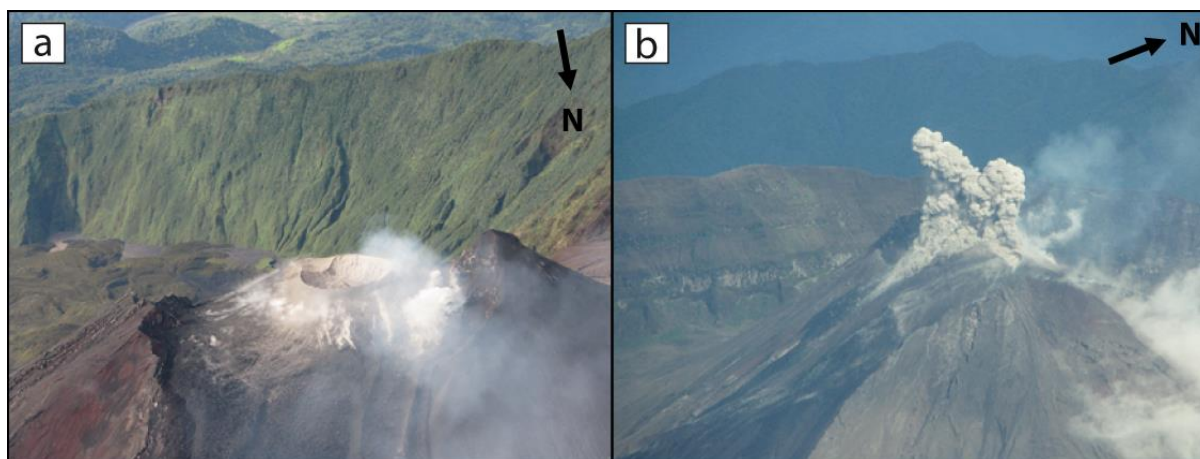


Figure 2. 17 a) View of the crater and the pyroclastic cone from the north, a weak fumarole activity is recognized. b), explosion and the generation of small PDC's to the south and north of the cone.

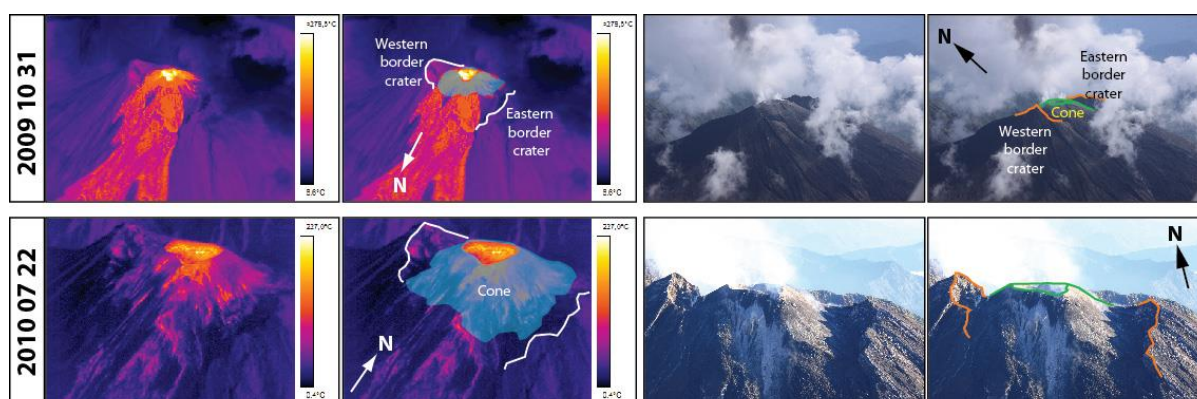


Figure 2. 18 Pyroclastic cone evolution showed by thermal (left) and visual images (right). White lines show the western and eastern borders of the crater left by the eruption in 2002, notice that the highest point of them was given by the western border, blue polygon represents the pyroclastic cone, and the black line is the caldera wall (Images/Photos: IG-EPN).

2.5.2 Lava dome

Subsequently to the explosive activity registered between October 2009 and October 2010, the activity turned effusive but no observations were possible to make until March 2011. During an overflight on March 21st, it was identified the presence the growth of a lava dome inside the cone. The beginning of this extrusion is not well known, but it could had taken some months. No signals of lava flows were identified. The formation of the lava dome lasted for about one year. Seismically it was characterized for presented long period, harmonic and explosion events (Fig. 2.7, 2.42).

The following overflights confirmed the progressive growth of the dome inside the cone. In May 2011, it was observed that the dome overpassed the height of the cone. The dome continued to grow vertically and few side-collapses were recognized. Fig. 2.19 shows the representative

images of the evolution of the dome inside the pyroclastic cone crater through thermal and visual images obtained during the overflights.

The upper part of the dome presented a maximum temperature of 280°C and their walls values lower than 100 °C. These low temperatures on the walls are related to the gravity collapses of the dome. An important degasification was identified during the formation of the dome (Fig. 2.19).

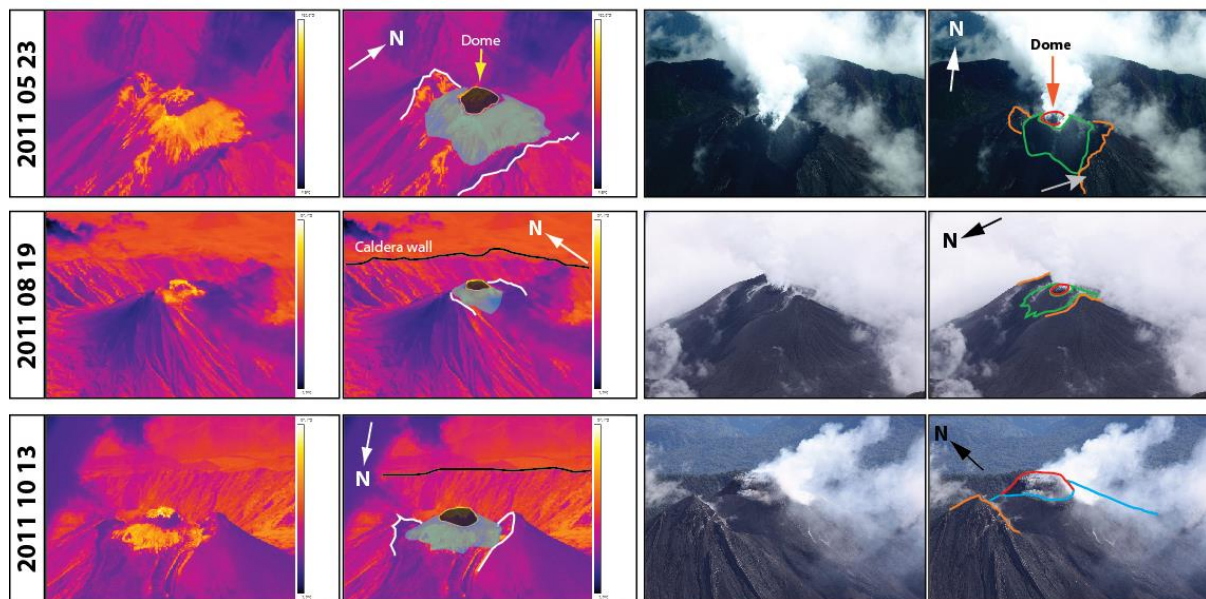


Figure 2. 19 Lava dome evolution showed by thermal (left) and visual (right) images White lines show the western and eastern borders of the crater left by the eruption in 2002, notice that the highest point of them was given by the western border, blue polygon represents the pyroclastic cone, black polygon is the dome that grew inside the pyroclastic cone and the black line is the caldera wall (Images/Photos: IG-EPN).

2.5.3 Distribution and characterization of lava flows of El Reventador volcano between 2012 and 2014

Morphology of lava flows can differ depending on the geodynamical environment they are produced and so, on their chemical composition, effusion rate, etc. Lava flows emitted from El Reventador volcano have basaltic-andesitic to andesitic compositions (53,1 and 59,0 wt.% SiO₂, Samaniego *et al.* 2008; Naranjo *et al.* 2016, this study) and are catalogued as blocky lava flows. This current research was focused into identify the spatial distribution of the blocky lava flows emitted between 2012 and 2014 and their morphology by the estimation of their geometric dimensions as length, surface, thickness and volume.

2.5.3.1 Analysis of thermal/visual images

Previous this current work, 17 lava flows were identified in El Reventador volcano between 2002 and 2009 (Hall *et al.* 2004; Samaniego *et al.* 2008; Vallejo 2009, Vallejo & Ramón 2012; Naranjo *et al.* 2016). From them, 16 were emitted from the main crater and one from a satellite vent located in the southeast flank of the volcano. The last identified unit was the LF17 (lava flow 17) emitted in the latest 2009 through the south eastern flank. During 2010 the activity became explosive allowing the generation of an ash cone over the crater. Later, during 2011 the activity turned again effusive with the development of a lava dome inside the ash cone. During these two years (2010 and 2011) there was no evidence of lava flows generation. Early 2012, during an overflight the June 4th, 2012, two lava flows were identified in the northern flank of the volcano. That day, one flow was active and the other one was already emplaced at its base. Between 2012 and 2014, 20 lava flows units were identified by Vallejo *et al.* 2016 using different monitoring tools described with detail in this current work (Section 2.3, this chapter). By using satellite radar, Arnold *et al.* 2017 mapped 43 lava flows between February 2012 and August 2016.

In this current work the geographical lava flows identification was done based on the analysis of the data obtained from the different monitoring tools (Section 2.3, this chapter) but mostly on the aerial/land thermal/visual images analysis. For the period 2012-2013 it was used thermal images from the hand held infrared camera obtained from the regular overflights meanwhile for 2014 the identification was done using thermal/visual images acquired from COPTVS and COPTIR cameras.

2.5.3.1.1 Lava flows from the period 2012-2014

For the period 2012 – 2014, 20 lava flows units were recognized: LF18 – LF37, all of them emitted through the crater. Followed lines present a summary of the lava flows identified during the flights surveys and as well by analyzing images from the COPTIR camera.

- ❖ **June, 4th 2012 overflight:** was the first flight of that year. Weather conditions were clear at that time. It was observed two lava flows in the northern flank. One lava flow unit, the LF18 was already emplaced at that day, it was emitted from the crater directly to the northeast and then to the east. This last followed path was a consequence of the presence of the caldera wall (Fig. 2.20.a). The second identified flow, the LF19 was active at that day and had travelled over LF18, then LF19 was restricted by the caldera wall as well (Fig.

2.20a). LF19 was branched in the middle of the flow, generating at the end two branches (Fig. 2.20a). There was no evidence of lava flows generation at the southern flank.

❖ **August, 31st 2012 overflight:** weather conditions were good. During this flight a flow was identified in the same zone (northeastern flank), the LF20. At the time of the flight, this lava flow was active and was observed that was being emplaced over LF19 (Fig. 2.20b, c). As the same case of LF19, LF20 presented two branches. There was no evidence of lava flows generation at the southern flank.

❖ **October, 19th 2012 overflight:** weather conditions were good and two lava flow were identified in the southern flank of the volcano, the LF21 and LF22. At the time of the flight the LF21 was already emplaced at that date and the LF22 was active (Fig. 2.20d). LF22 was being emplaced over the LF21.

Then, during 2012, five lava flow units were identified in the volcano; three were emplaced through the northeastern and two through the southern flanks of the volcano and no one reached the caldera floor.

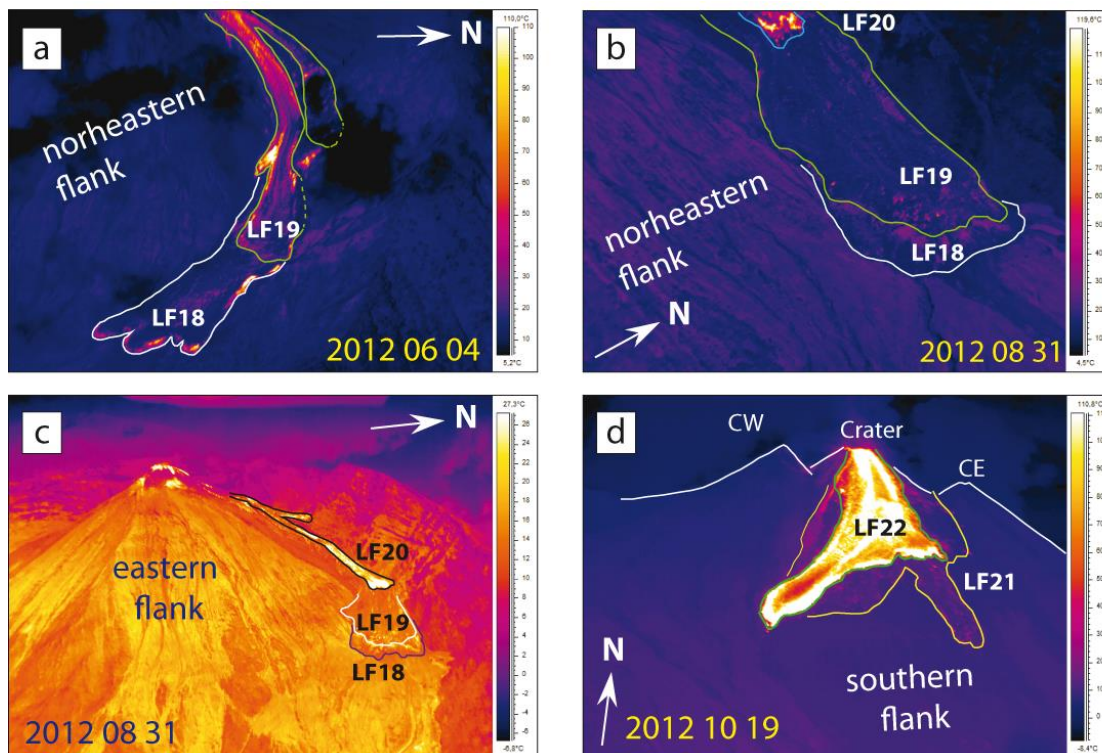


Figure 2. 20 Aerial thermal images of lava flows identified in 2012: a) LF18, LF19; b) and c) LF20; d) LF21, LF22; e) and f) LF23 (Source: IG-EPN).

- ❖ **January, 29th 2013 overflight:** there were good weather conditions. It was identified one active lava flow, the LF23 which was being emplaced in the southeastern flank of the volcano (Fig. 2.21e, f). LF23 followed the same path of one of the branches of the LF17 (August, 2009). Just one branch was identified for this flow and the front at that date almost reached the vent of LF2 (only flow generated by a satellite vent in Nov, 2002).
- ❖ **August, 23rd 2013 overflight:** weather conditions were not good. The upper part of the volcano was clouded at the moment of the flight and just the fronts of two lava flow units were identified in the northern and southern flanks of the volcano, the LF24 and LF25 respectively. It was assumed that at that time both flows were already emplaced due to the lowest temperatures of the flows (Fig. 2.22g, h).
- ❖ **September, 7th 2013 overflight:** weather conditions were good. At first, during this flight it was possible to identify properly the LF24 (Fig. 2.22j). It is probable that the ticker lava deposits left by the flows LF18-LF20 close to the crater did not allow this new unit flowed over them. In that case it was observed that LF24 was emplaced beside them. At the time of the overflight it was identified one active flow in the southeastern flank of the volcano, the LF26. Two active branches were identified, one of them was emplaced over the LF25. An intense explosive activity was recognized at that time with the generation of small PDC's and rolling blocks (Fig. 2.22i, k).
- ❖ **October, 19th 2013 overflight:** during this flight weather conditions were good. At that time, one lava flow was active, the LF27. It was emplaced in the southeastern part of the volcano and was formed by two main branches, one of them emplaced over the eastern branch of the LF26. During this overflight it was taken the photographs for the 2013 DEM development.

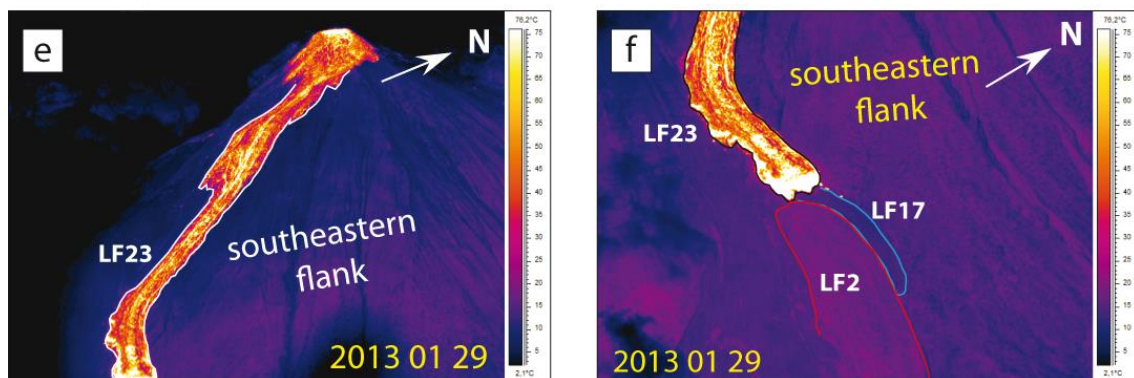


Figure 2. 21 Aerial thermal images of lava flows identified in 2013: e) and f) LF23 (Source: IG-EPN).

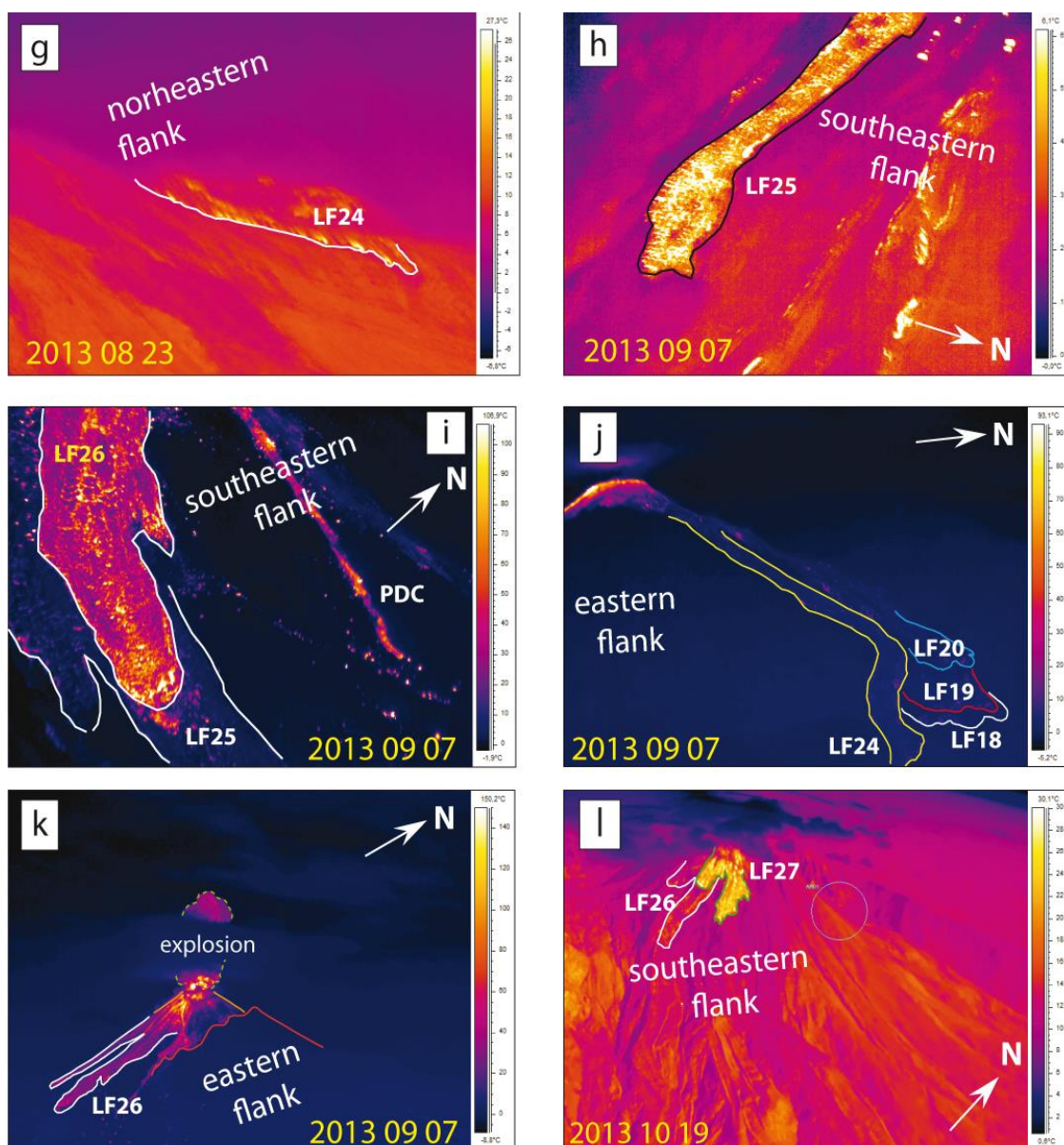


Figure 2. 22 Aerial thermal images of lava flows identified in 2012: g) LF24; h) LF25; i) LF26; j) LF24; k) LF26; l) LF27 (Source: IG-EPN).

The infrared camera COPTIR was installed in October, 2013 together with the visual COPTVS. Both cameras began to transfer images to the IG offices at the end of 2013 in near real time every 5 minutes. Thermal images were collected since February 2014. During this year the COPTIR camera was operative the most part of the time. The analysis of images in near real time allowed to identify the lava flows generation since their first stages.

- ❖ **January, 12th 2014 images:** at that day clear images from COPTIR camera were transmitted and was possible to recognize two lava flows deposits, LF28 and LF29 (Fig. 2.23m); both flows were inactive. LF28 was a tiny flow emitted to the eastern flank. This

flow corresponds then to the first recognized flow emitted to this flank. LF29 was emitted to the northeastern flank. Both flows were small and were emplaced in the upper part of the volcano (Fig. 2.23m, n).

- ❖ **January, 26th 2014 images:** on that day the occurrence of a lava flow through the southern flank was recognized, the LF30. By the analysis of the thermal images it was determined that this lava flow lasted 8 days. Fig. 2.23m shows the thermal image with the flow captured on March, 8th 2014.
- ❖ **March, 6st 2014 overflight:** weather conditions were clouded the most part of the flight. Clouds were present mostly in the upper part of the crater. Two lava flow front were identified in the northeastern flank of the volcano, the already recognized LF29 and a new one LF31. At the moment of the flight both flows were inactive, Fig. 2.23o. LF31 was no identified by COPTIR due to a loss of the signal of the camera during this period.
- ❖ **March, 25th 2014 images:** good weather conditions on that day allowed the recognition of a new lava flow through the southeastern flank of the volcano, the LF32. It lasted 7 days and due to the branching it allowed the formation of 3 branches. One of them was emplaced over the LF28 and the main one over the LF27, Fig. 2.23p.
- ❖ **April, 23th 2014 images:** good weather conditions allowed to identify another lava flow unit emplaced over the southern flank of the volcano, the LF33. This lava flow was formed by a single arm and lasted 5 days. Fig. 2.23q shows the deposit of the flow on the April, 24th. As well, the image shows the deposit of the LF32.
- ❖ **May, 27th 2014 images:** good weather conditions. A new lava flow was recognized descending for the southern flank of the volcano, the LF34. It was observed that this flow followed the same path of the LF33. This flow lasted 5 days. Fig. 2.23r shows the deposit of the flow for May, 28th. The traces of LF33 and LF32 were identified as well.
- ❖ **July, 16th 2014 images:** for a period of xxx days, the transmission from COPTIR was disable. The signal was reestablished on July, 23rd and it was possible to observe a lava flow deposit in the southeastern flank of the volcano, the LF35 (Fig. 2.24s). At that day the flow was inactive. It was composed by a single branch which was emplaced over the main branch of LF32.

- ❖ **September, 2nd 2014 images:** good weather conditions allowed to identify the generation of a lava flow descending through the southeastern flank of the volcano, the LF36 (Fig. 2.24t). LF36 followed the path of LF35 and was emplaced over it. It was formed by four branches and lasted 5 days.

- ❖ **December, 2nd 2014 images:** during that day a lava flow descending through the southeastern flank of the volcano was recognized. It was generated one single arm and lasted 5 days of duration the LF37 (Fig. 2.24u).

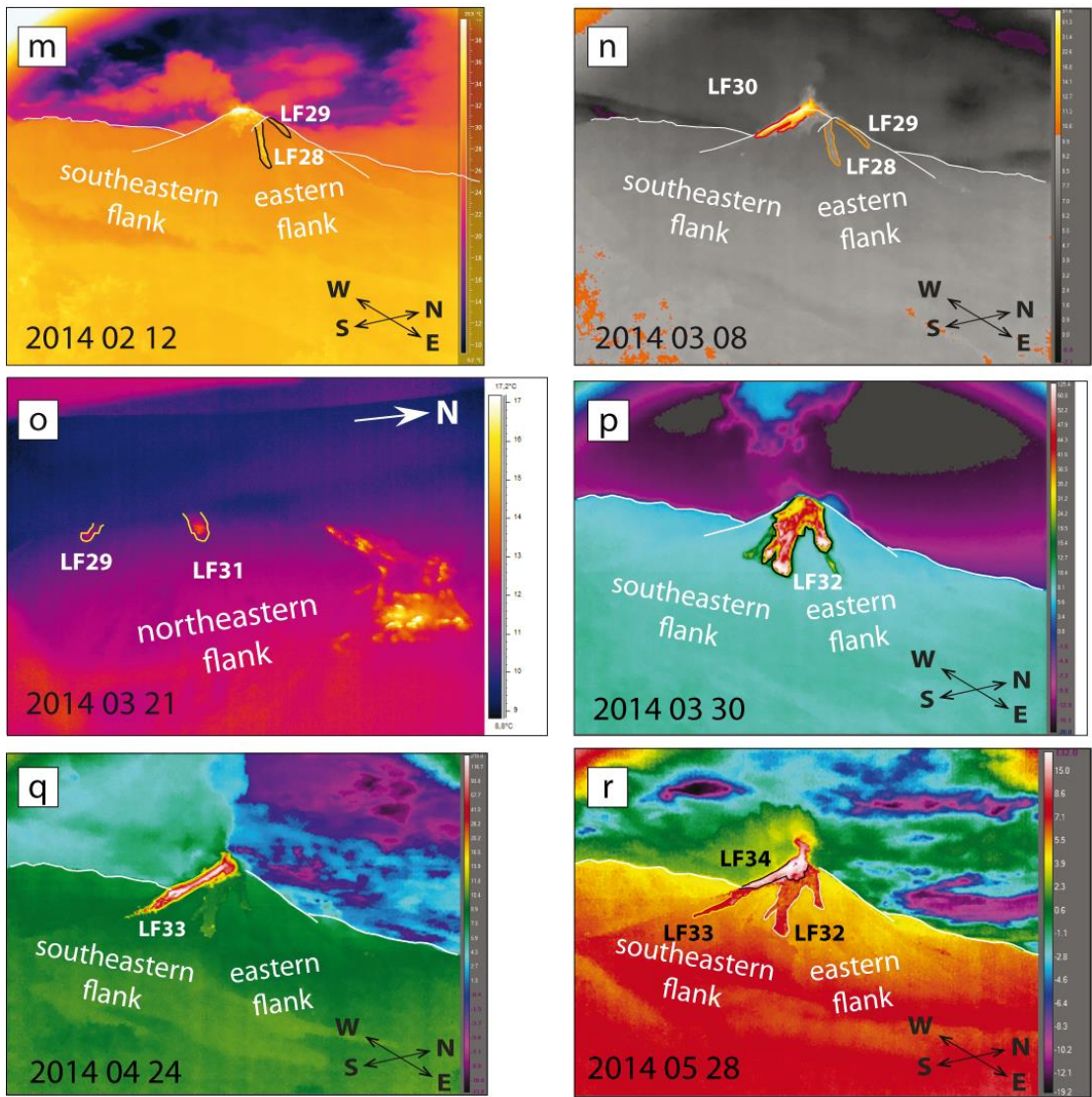


Figure 2. 23 Thermal images of lava flows identified in 2014 by thermal images from the fixed camera COPTIR: m) LF28, LF29; n) LF30; p) LF32; q) LF 33; r) LF34. Aerial thermal image: o) LF31 (Source: IG-EPN).

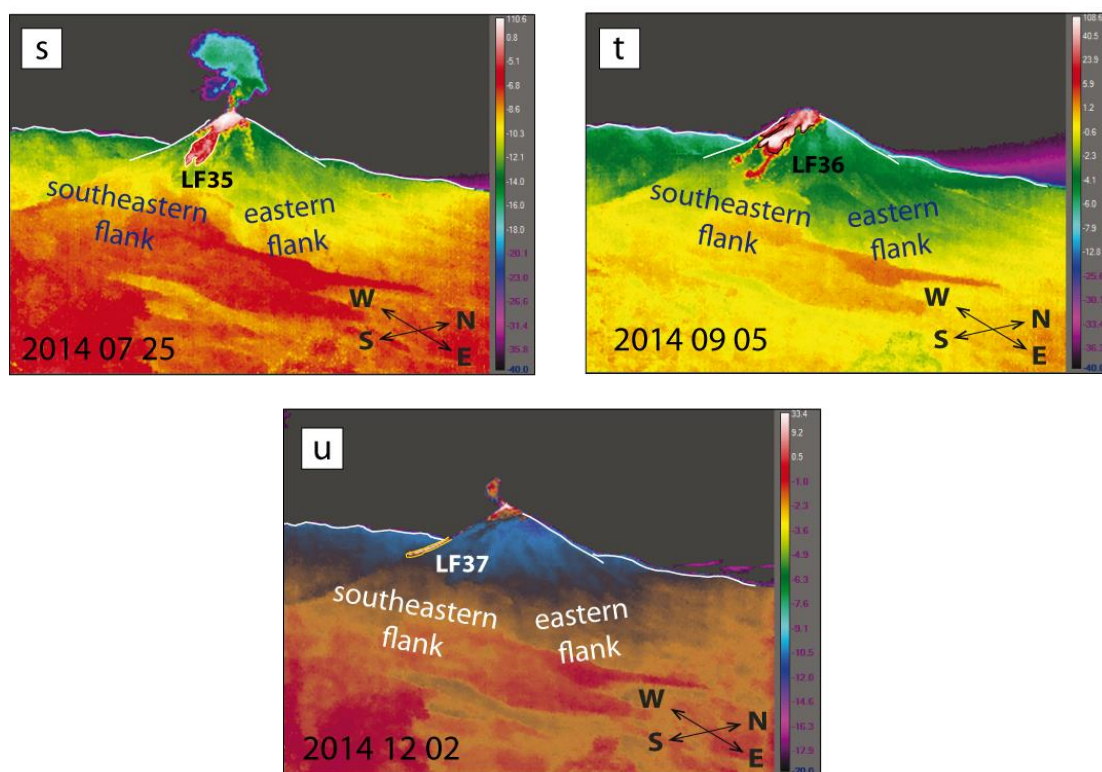


Figure 2. 24 Thermal images of lava flows identified in 2014 by thermal images from the fixed camera COPTIR: s) LF35; t) LFd36; u) LF37. (Source: IG-EPN).

2.5.3.2 Lava flows mapping

2.5.3.2.1 Direct mapping using the 2013 and 2015 DEM's

The high quality of both DEM's from 2013 and 2015 allowed to identify directly important portions of 8 lava flow units. They correspond to LF18, LF19, LF20, LF23, LF24, LF25, LF26 and LF27. Five lava flow units, LF21, LF22, LF28, LF29 and LF31 were mapped based only on thermal images collected from the air.

2.5.3.2.2 Mapping by projecting thermal images over the topography

The analysis of visual and thermal images obtained from digital and infrared cameras respectively help to identify, characterize and map volcanic products by 3D-localization (e.g. Formenti *et al.* 2003; Honda & Nagai 2002; Vallejo Vargas *et al.* 2012; Kelfoun & Vallejo Vargas 2015; Hall *et al.* 2015). 3D-localization or found the spatial location process of volcanic products is more effective by using thermal images of the deposits. The advantage to use this kind of images is given by the highest color contrast present in the image as a result of difference of

temperatures on it. This methodology was applied for 7 lava flow units correspond to LF30, LF32, LF33, LF34, LF35, LF36 and LF37

The aim of this analysis in this study is to obtain:

- ❖ The spatial location of the lava flows units
- ❖ The dimensions of the deposits (length, area).

The 3D- localization of lava flows of El Reventador volcano was done following Vallejo *et al.* (2012) and Kelfoun & Vallejo Vargas (2015), by using thermal images obtained from the ground based infrared camera COPTIR. A MATLAB® script was written for the 3D-localization of lava flows with which was possible to obtain the spatial location of the borders of the flows (Northing-Y, Easting-X and Altitude-Z coordinates).

Some input information is needed to run the script; it corresponds to:

- Spatial location of the infrared camera (northing, easting, altitude)
- Camera orientation: orientation angle of the camera (α), inclination angle of the camera respect to the horizontal measured in a perpendicular plane to the camera (β), and rotation angle of the camera respect to the horizontal measured in a parallel plane of the camera (γ)
- Good quality thermal images
- Field Of View (FOV) angle of the thermal camera
- x, y coordinates of the target in the thermal image
- Previous DEM of the area

For the present work, it was used thermal images obtained from the COPTIR infrared camera. As this camera was fixed since the installation, its location and angles were well known. Thermal images used on this analysis were from 2014 and their good quality depended on the weather conditions. The x-y coordinates of the flow borders of each flow were identified in the different images. It was used the DEM from October 2013.

In simple words the script project the thermal image over the topography (DEM) by using the position and the three angles of the camera (α , β , γ) combined with the FOV angle (Table 2.2). Once the image is projected over the topography and by enter the x, y coordinates of the target,

Enter the data in the script: DEM information, geographic position and angles of the camera, x-y coordinates of the lava flow border.

The DEM used for this process corresponds to the 2013 DEM. The format of the DEM that the script admit can be in .tif, .flt or .mat. Transformation of the DEM to those formats can be done by using a GIS. This DEM a resolution of 0.86 m.

Position angles of the camera (α , β , γ , FOV) are defined in Table 2.2.

The x, y coordinates of the border of the flow were defined in Step 1 (Table 2.1).

Location		Camera angles	
Northing	9987894	orientation angle (α)	6.55
Easting	208018	inclination angle (β)	310.95
Altitude	2323	rotation angle (γ)	5.5
		FOV	15°x11.25°

Table 2. 2 Input parameters for the MATLAB script related with the camera location and its angles.

2. Run the script
3. When the script finished the process, first it brings an image of the thermal image projected over the chosen DEM. Second, it brings a file .txt with the georeferenced coordinates of the border of the flow.

In this example it brought the image from Fig. 2.25 in which is possible to recognize the position of the flow over the volcano (Fig. 2.26).

The .txt file brought by this process shows the northing (Y), easting (X) coordinates and altitude (Z) correspondent to each point of the x-y coordinates correspond to the border of the flow (Appendix 2.4).

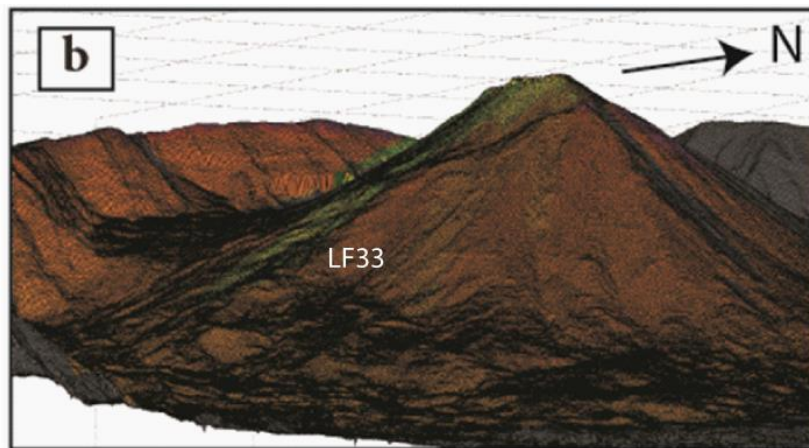


Figure 2. 26 Projection of the thermal image over the 2013 DEM. It is possible to observe the yellow-greenish color as a representation of the lava flow.

Coordinates of the lava flow contour projected over the topography are shown in Appendix 2.4

4. Projection of the coordinates and definition of the lava flow polygon.

Resultant coordinates (Appendix 2.4) can be projected over the same DEM using a GIS.

By matching the coordinates in the GIS, it is possible to define the polygon of the flow, Fig. 2.27.

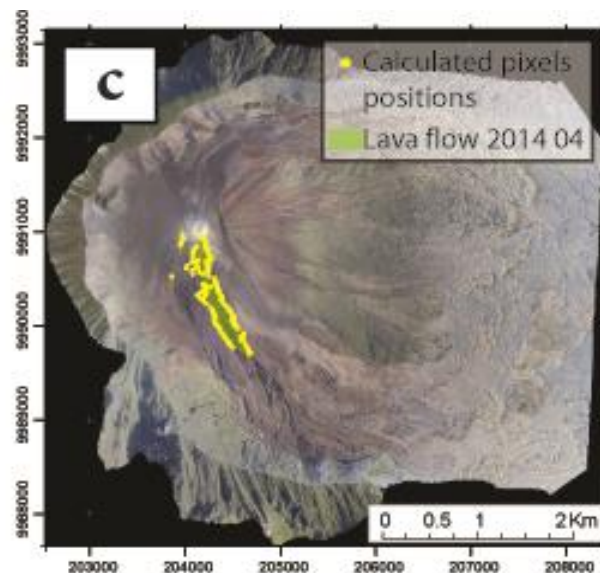


Figure 2. 27 Plot of the LF33 X-Y coordinates (yellow dots) obtained from the projection of the thermal image over the 2013 DEM.

The analysis of the results brought that the flow LF33 reached a distance of 1.45 ± 0.005 km from the crater and occupied a surface of 221 ± 3 m².

This useful method was applied on thermal images from El Reventador volcano for:

1. Mapping seven lava flow units emitted through the south-eastern flank of the volcano,
2. Estimate the front flows velocities of 3 lava units, which can be useful for the calibration of numerical models for the simulation of lava flows using simple rheologies.

2.5.3.3 Lava flows velocity estimation

The velocity of some lava flows was estimated based on the analysis of thermal images from COPTIR. A very clear example was the LF35, which was emitted through the south-eastern flank of the volcano and it took nine days until it was fully emplaced. This flow at the end generated three main lobes (Fig. 2.28 right). The advance of the flow is shown in Fig. 2.28 with images from Mars, 25th and 27th, and April 2nd. Black lines represent the border of the flow. Based on this analysis, LF35 reached a maximum distance from the crater (MDFC) of 1.23 km in 200.1 h.

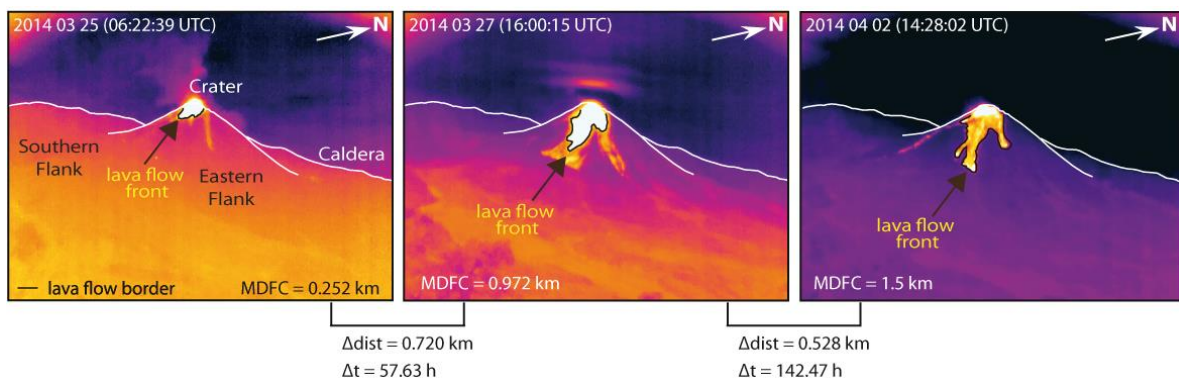


Figure 2. 28 Advance of the flow 35 on time between the Mars 25th and April 2nd of 2014. The green contour shows the border of the crater at that time. MDFC= Maximum distance from the crater.

The estimation of the velocity for LF35 was based on the analysis of the longest lobe's front. It was applied the methodology from Section 2.5.3.2.2 (this Chapter). The analysis was applied for 19 thermal images from COPTIR. The curve of the time evolution of distance between the lava front and the source is shown in Fig. 29. This information turned in important data that can be useful for the calibration of numerical models using a Bingham rheology (e.g. Kelfoun & Vallejo Vargas 2015). This information is used in Chapter 4 for simulation of lava flows from El Reventador volcano.

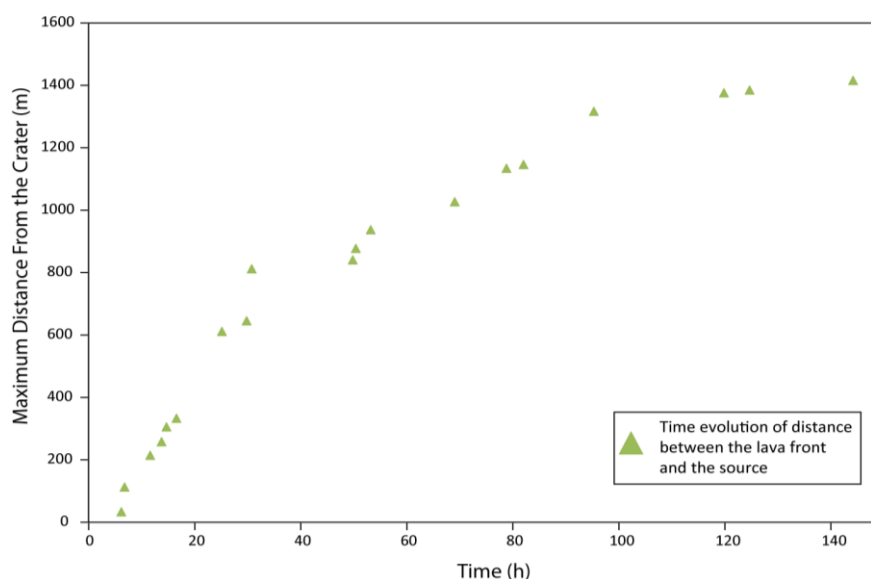


Figure 2. 29 Time evolution of distance between the lava front LF35 and the source. Analysis done based on the analysis of thermal images from COPTIR.

2.5.3.4 Error consideration

To map volcanic flows by applying the methodology of projecting thermal images over the topography can have some errors or problems, they are related to:

- a. Error by DEM precision: Even though the DEM has a high pixel resolution (<1m), it will never represent the real surface of the field.
- b. Error by changes in the surface after the DEM development: As El Reventador is a very active volcano, its topography is changing all the time and mostly at the upper part of the crater. If the DEM that is been used for the analysis is not recently updated, then there is the risk that results won't be super realistic.
- c. Error related to the selection of the pixel at thermal image: This is a human error; it is related to the correct selection of the pixel at the thermal image. When the contour is not very clear it could be chosen erroneous pixels at the sides of the real contour.
- d. Uncertainty due to the slope flank angle: The distance between two consecutives pixel projection is less when the pixel was projected over a steep topography (e.g. 24 m just below the crater). At the opposite, when the topography has a lower slope, the separation between the chosen pixel's increase (e.g. 109 m at the bottom of the flank).

2.5.3.5 Spatial distribution of lava flows

The 20 lava flow units identified (Fig. 2.30, 2.31) were mapped using ArcGis 9.2.

The analysis of these flows with GIS tools allows to measure directly the length, surface and maximum width of the flows, this data is compiled in Table 2.3.

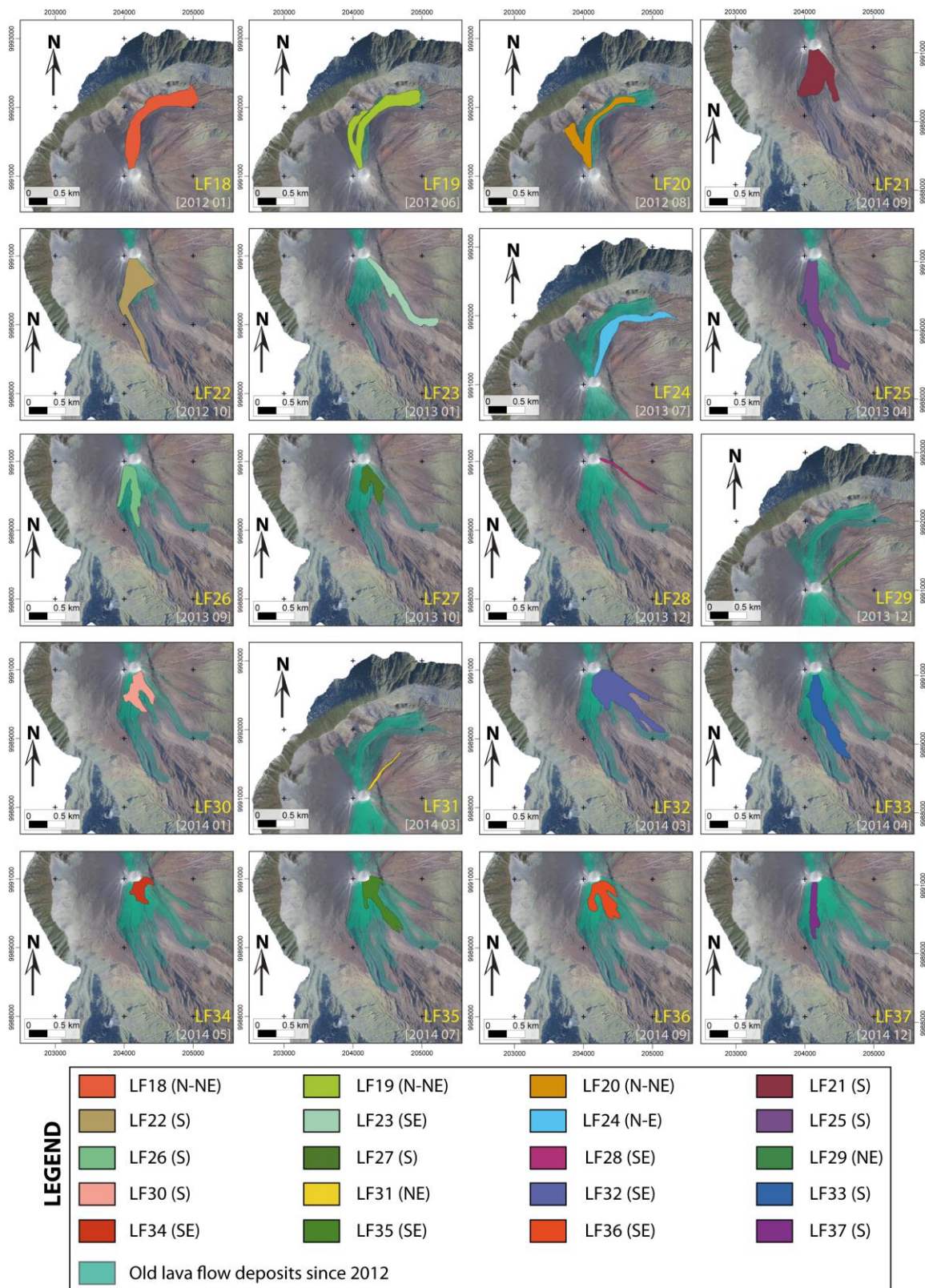


Figure 2. 30 Individual mapping of the 20 flows identified between 2012 and 2014. The greenish color in each map represent the old lava flow deposits

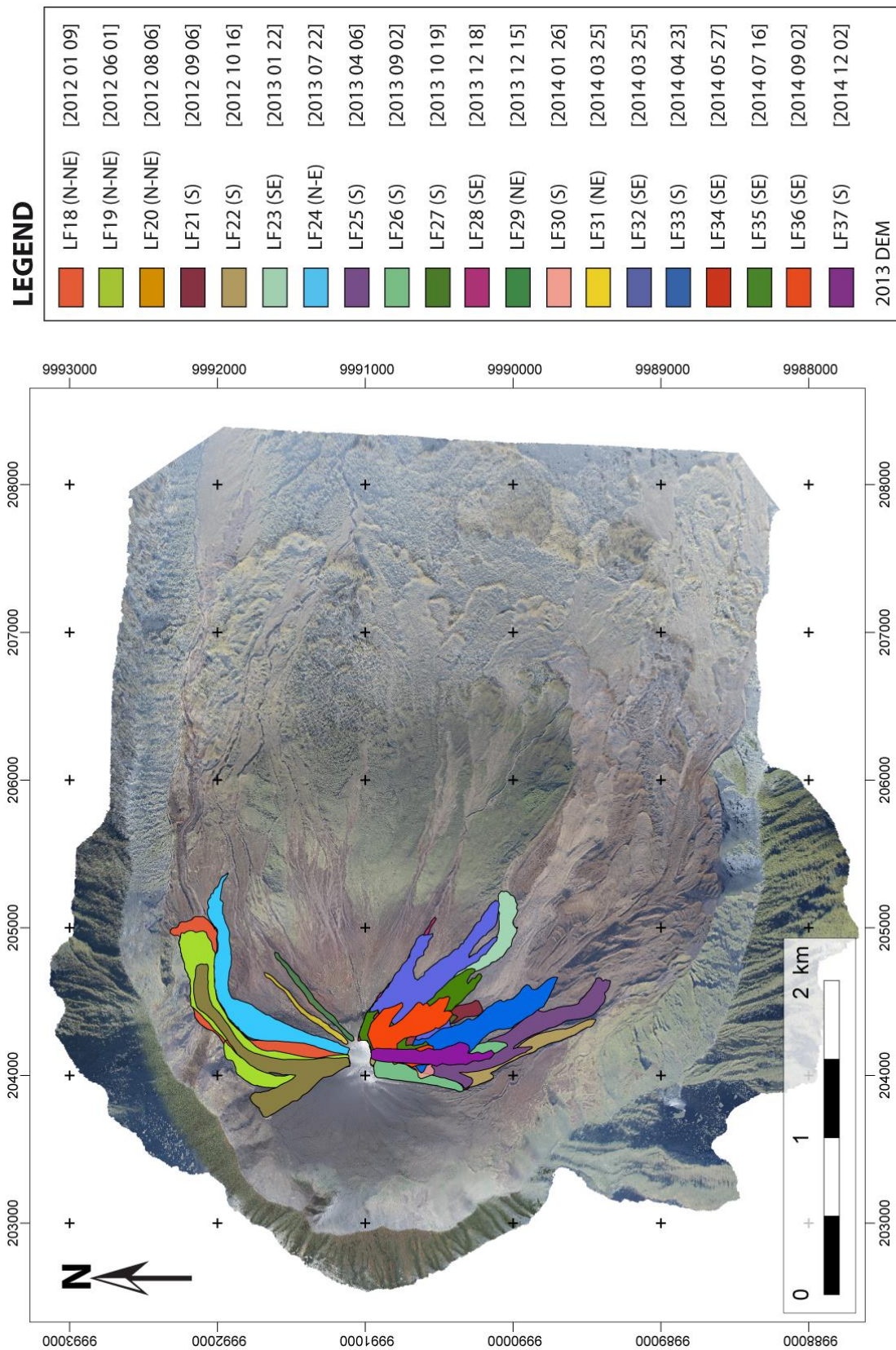


Figure 2. 31 Map of the lava flows for El Reventador volcano in the period 2012-2014. Twenty lava flows units were identified in this period; those were distributed to the north, north-east, east and south east of the crater.

2.5.3.6 Lava flows morphology

2.5.3.6.1 Lava flow thickness measurements

Measures of lava flows thickness have a relevant importance for the estimation of lava flow volumes and effusion rates. Depending on the volcanological and practical considerations, thickness and thus volumes can be estimated by: (1) direct field measurements, (2) topographic satellite radar-based measurements, (3) analysis of the geometry of the flows using a detailed topography (e.g. DEM)

For lava flows emitted between 2012 and 2014 it was not possible to make direct field measurements of the thickness due to the high activity of the volcano during the fieldwork (Section 2.3.4, this Chapter). In the same way, neither an analysis by topographic satellite radar-based measurements has been done due to the inaccessibility to the data. Then, the third methodology was applied, following Jessop *et al.* (2012) in order to estimate the geometrical dimensions of the different flows.

In total 12 lava flows of the 20 were analyzed with this method using both DEM's from 2013 and 2015. For the remaining 8 flows, a thickness of $8.5 \pm 2\text{m}$ was assumed. LF24 was chosen as an example because the whole flow is exposed in the 2013 DEM (Fig. 2.32a, b).

The methodology to estimate the thickness is based on:

1. Define the location of the perpendicular profiles along the main axis of the flow.

For the LF24 it was defined 5 profiles, P1 – P5. Fig. 2.32b shows the beginning and end of the profile, e.g. for P1 the beginning is at A and the end at A'.

The chosen spacing between the profiles depended of the exposed area of the flow.

2. Cross flow profiles using a MATLAB® script.

The five cross flow profiles were obtained using a script. With the use of a topographic base as a DEM, this script allows to define a line which represents the location of the needed profile (e.g. P1, P2, etc.). When the profile is generated (Fig. 2.32c) it is necessary to define the edges of the flow in the profile which in some cases correspond to a lower topography (Fig. 2.32c, profile P1) and others to the contact of other lava flow units (Fig. 2.32c, profile P4).

When those edges are recognized it is possible to estimate the average thickness of the flow in correspondent to the chosen the profile.

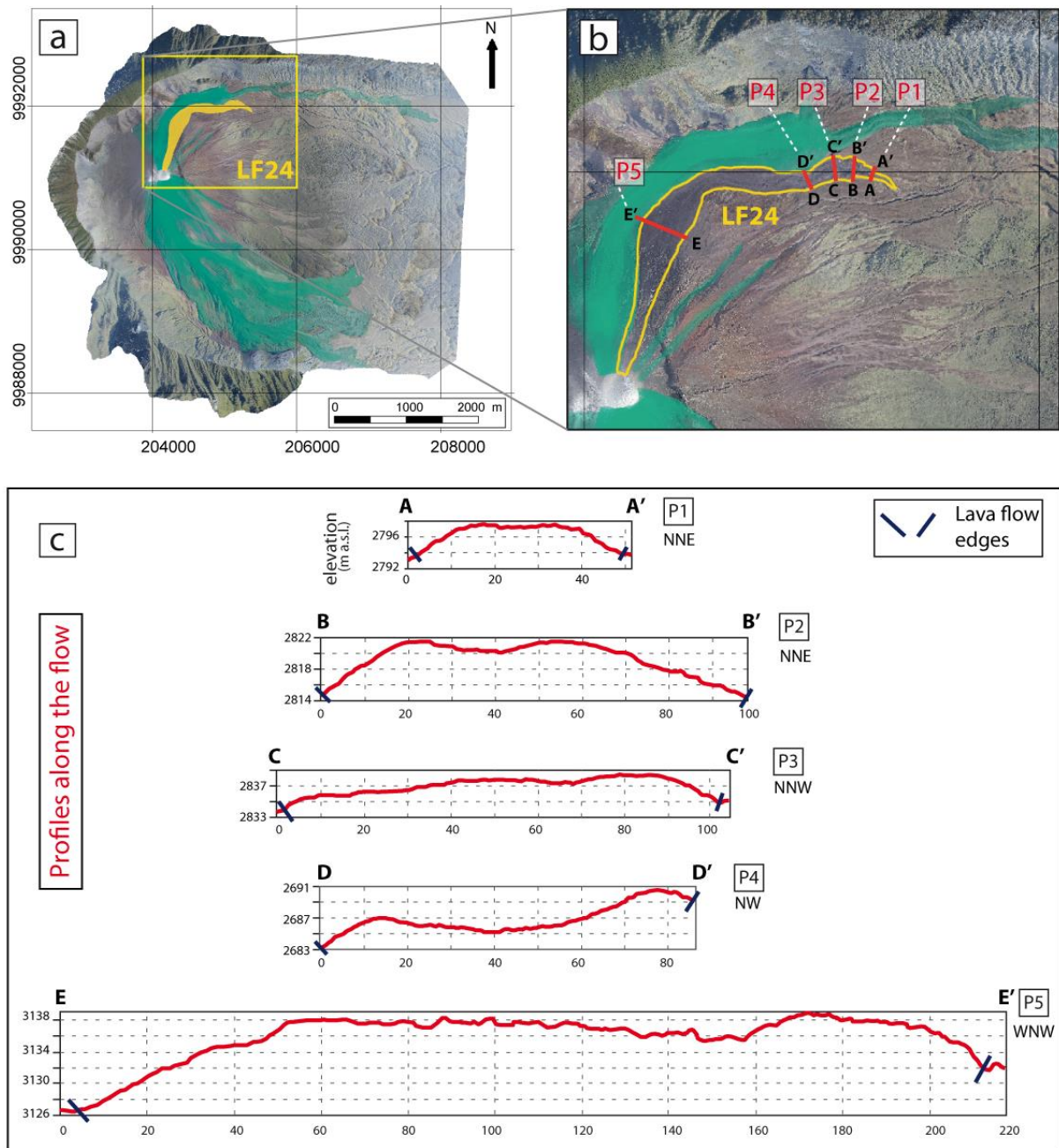


Figure 2. 32 Scheme to represent the estimation of the LF24 thickness. a) Map of the lava flows emitted between 2002 and 2014 (green polygon) only the LF24 is identifiable respect to the others, yellow flow (enmarked in a yellow box). b) Enlargement of the yellow box in which is shown the location of the profiles for this flow, in total five (P1 – P5). c) Profiles of the flow, showing that the thickness of the flow varies between 4m at the front (P1) of the flow and 10m at the top (P5).

Note: It is important to take into account that this averaged thickness value (h') does not always represent the real thickness (h) of the flow and this is due to of the effect of the topography's slope (θ). Is possible to correct the thickness (h') using a simple trigonometric relationship which takes in account the average thickness (h') and the slope (θ) of the topography, (Fig. 2.33).

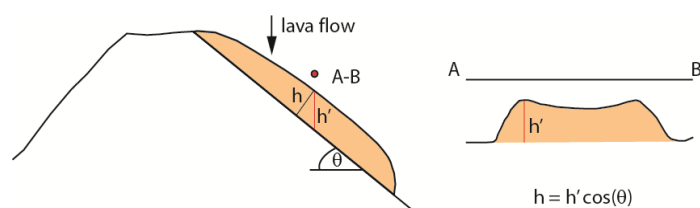


Figure 2.33 Sketch of the correction of the thickness (h) by the slope topography (θ).

2.5.3.6.2 Lava flow volume estimation

The estimation of the volume of lava flows can be determine from various methods:

1. Assume that volume is equal to the relationship between the thickness and surface.
2. Compare DEM's before and after the emplacement of the flow, then the difference between both can bring the value of the volume.

In the current study, the volume was obtained by applying the first methodology. The average thickness and surface estimation is shown in Sections 2.3.2.2 and 2.4.2.1 respectively. Values of both parameters for the 20 lava flows are in Table 2.3. As well this table, includes other parameters of the flows as start day emission, direction, duration, length and maximum width.

Lava flow number	Start day yy.mm.dd	Lava flow direction	Duration (days)	Length $\times 10^3$ (km)	Max width (km)	Surface $\times 10^3$ (m ²)	Thickness (m)	Volume $\times 10^6$ (m ³)
18	2012 01 09	N-NE	4	1,777±0,005	295	311±3	15,0±2,0	4,66±0,62
19	2012 06 01	N-NE	6	1,694±0,005	216	278±3	9,5±3,4	2,65±0,95
20	2012 08 06	N-NE	4	1,480±0,005	248	190±3	6,8±1,8	1,30±0,34
21	2012 09 06	S	5	0,883±0,005	422	249±2	12,5±1,7	3,11±0,42
22	2012 10 16	S	4	1,689±0,005	485	261±3	5,1±1,0	1,36±0,25
23	2013 01 22	SE	4	1,550±0,005	183	168±3	7,7±1,8	1,29±0,30
24	2013 07 22	N-E	6	1,895±0,005	194	180±3	5,5±3,4	0,98±0,61
25	2013 04 06	S	6	1,813±0,005	246	281±4	6,6±2,4	1,85±0,68
26	2013 09 02	S	6	0,967±0,005	222	146±3	8,4±3,9	1,22±0,57
27	2013 10 19	S	5	0,671±0,005	270	100±2	12,6±3,9	1,26±0,77
28	2013 12 18	SE	6	1,066±0,005	37	28±2	8,5±2,0	0,24±0,06
29	2013 12 15	NE	6	0,891±0,005	47	27±1	8,5±2,0	0,23±0,05
30	2014 01 26	S	8	0,686±0,005	281	125±2	8,5±2,0	1,06±0,25
31	2014 03 06	NE	7	0,855±0,005	41	22±1	8,5±2,0	0,19±0,04
32	2014 03 25	SE	7	1,377±0,005	466	336±4	8,1±1,4	2,72±0,48
33	2014 04 23	S	5	1,450±0,005	229	221±3	6,8±2,0	1,51±0,44
34	2014 05 27	SE	5	0,467±0,005	375	68±1	8,5±2,0	0,58±0,14
35	2014 07 16	SE	5	0,973±0,005	337	148±3	5,5±1,9	0,82±0,29
36	2014 09 02	SE	5	0,704±0,005	360	145±2	8,5±2,0	1,23±0,29
37	2014 12 02	S	5	0,912±0,005	150	77±2	8,3±2,0	0,64±0,15

Table 2.3 Resume the geometric measurements obtained for lava flows LF18-LF37 of El Reventador. It shows the length, surface, thickness and volume. As well the start day of the flow and their durations are shown up.

Figure 2.34 show the evolution in time of the individual and accumulated volume for the 20 lava flows. In total, for the period 2012 – 2014 it was emitted a total volume of $4.2 \times 10^7 \text{ m}^3$ of lava.

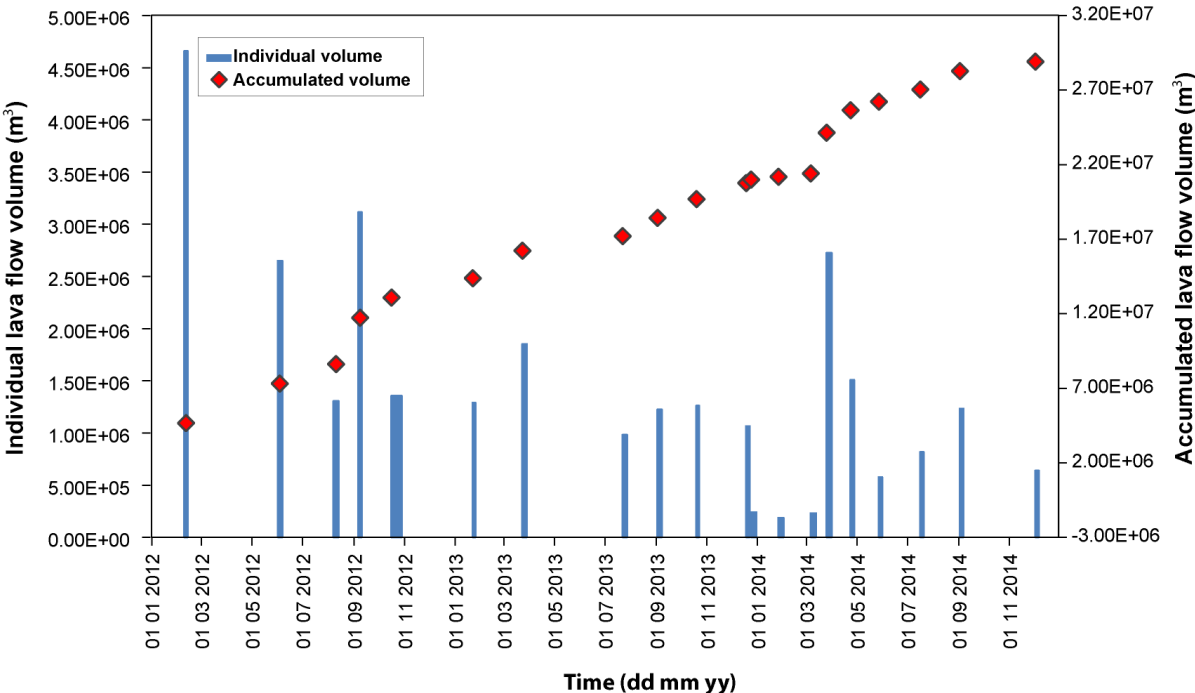


Figure 2. 34 Individual and accumulate volume of lava flows LF18 – LF37 emitted between 2012 and 2014 for El Reventador volcano.

2.5.3.6.3 Lava flows emitted between 2002 and 2009

Between 2002 and 2009 there were generated 17 lava flows at El Reventador volcano (Hall *et al.* 2004; Samaniego *et al.* 2008; Vallejo 2009, Vallejo & Ramón, 2012; Naranjo *et al.* 2016), all of them emplaced in the inner part of the caldera. Naranjo *et al.* 2016 published the article called “Mapping and measuring lava volumes from 2002 to 2009 at El Reventador Volcano, Ecuador, from field measurements and satellite remote sensing” in which I was participated as a co-author (Appendix 2.5), Fig. 2.35. The estimation of the volume of lava flows using field measurements of flow thickness brought a value of $75 \pm 24 \times 10^6 \text{ m}^3$ and a value of $90 \pm 37 \times 10^6 \text{ m}^3$ was obtained from satellite retrieval of flow thickness; corresponding to a time-averaged effusion rates of $9 \pm 4 \text{ m}^3/\text{s}$ and $7 \pm 2 \text{ m}^3/\text{s}$ respectively. Naranjo *et al.* 2016 propose that the activity of the volcano during this period presented four main phases: Phases A – D (Table 2.4).

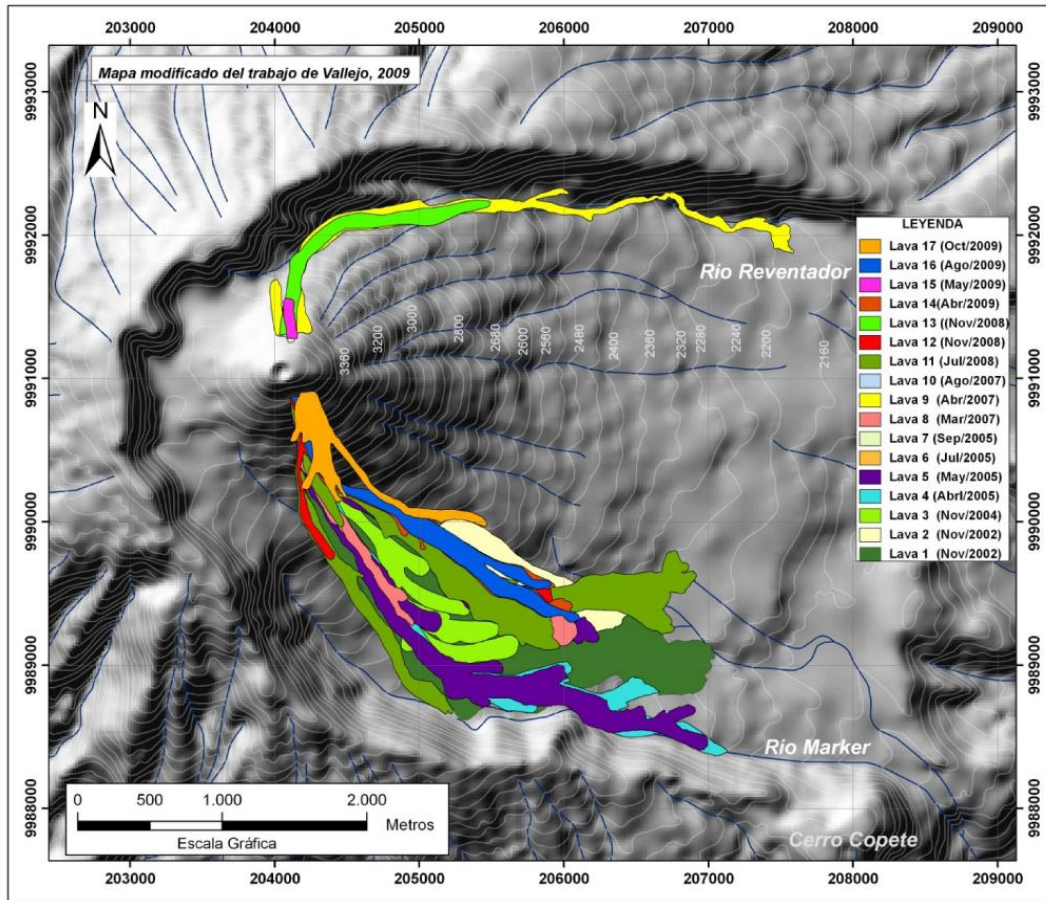


Figure 2. 35 Map of lava flows distribution between 2002 and 2009 (Naranjo *et al.* 2016 after Vallejo 2009).

Eruptive phase	Estimated lava flow volume m ³	average effusion rate x 10 ⁶ m ³ /day
July - September 1972	10.5 × 10 ^{6a}	0.11
Nov 1973 - July 1974	3.8 × 10 ^{6a}	0.02
Jan (April) – May 1976	20.0 × 10 ^{6a}	0.13 (0.33)
Nov 2002 (phase A)	32.8 × 10 ⁶	2.31
Nov 2004 – Sep 2005 (phase B)	20.1 × 10 ⁶	0.53
Mar. – Sep. 2007 (phase C)	8.0 × 10 ⁶	0.29
Apr. – Nov. 2009 (phase D)	26.8 × 10 ⁶	0.76

Table 2. 4 Estimated volumes and lava effusion rates for El Reventador’s last eruptions including the period 2002 – 2009 (Naranjo *et al.* 2016).

The surface, thickness and volume for lava flows emitted between 2002-2009, LF1-LF17 were recalculated based on the methodology described in Section 2.53, this Chapter. Fig. 2.36 shows the thickness estimation for FL2.

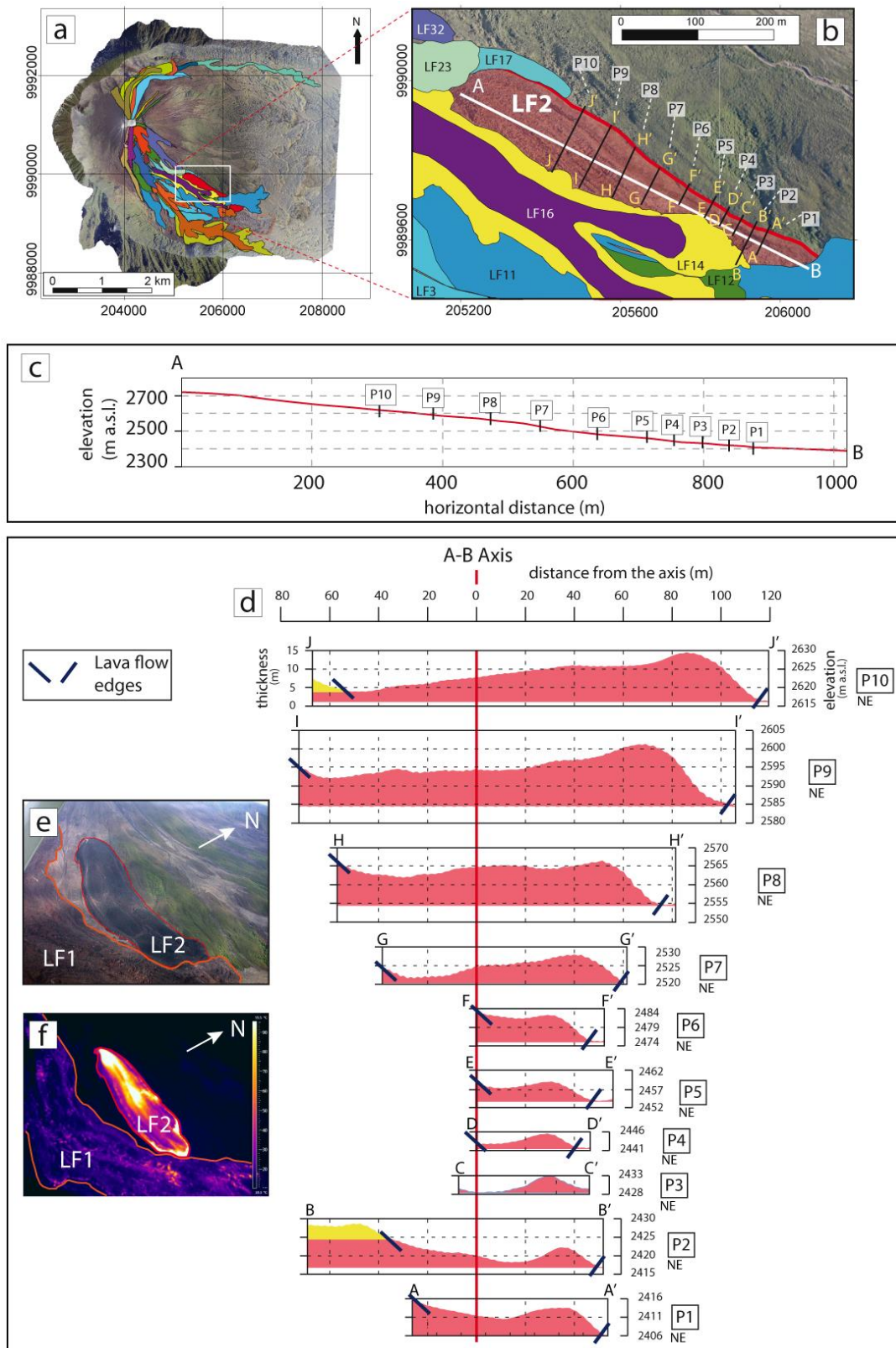


Figure 2.36 Scheme to represent the estimation of the thickness of LF2. a) spatial location of the part of the flow that will be analyzed (white box), b) enlargement of the white box from (a), it shows in detail the portion of LF2, the location of Axis A-B and P1-P10 profiles; c) profile of the Axis A-B; d) cross flow profiles P1-P10 along the Axis A-B; e) photo of the LF2 and LF1; f) thermal image of the LF2 and LF1.

The recalculation of the volumes for Phases A-D shows an increasing in their values in comparison with those estimated by Naranjo *et al.* 2016. The accumulated volume from Naranjo *et al.* (2016) shows a value of $87.7 \times 10^6 \text{ m}^3$ meanwhile this current work through a value of $95 \times 10^6 \text{ m}^3$, showing an increasing of 8.3%. This increasing is a result of the deeper analysis of the thickness and surface of the 17 lava flows done in this current work.

Eruptive phase	Estimated lava flow volume m^3	
	Naranjo et al. 2016	Current work
Nov 2002 (phase A)	32.8×10^6	34×10^6
Nov 2004 - Sep 2005 (phase B)	20.1×10^6	23.6×10^6
Mar - Sep 2007 (phase C)	8.0×10^6	8.4×10^6
Apr Nov 2009 (phase D)	26.8×10^6	29×10^6
Total	87.7×10^6	95×10^6

Table 2. 5 Estimated lava flow volume for the period 2002 – 2009 from Naranjo *et al.* (2016) and this current work.

Fig. 2.37 shows the individual and accumulated volume for lava flows for the period 2002 and 2014. All this values correspond to those obtained in this current work.

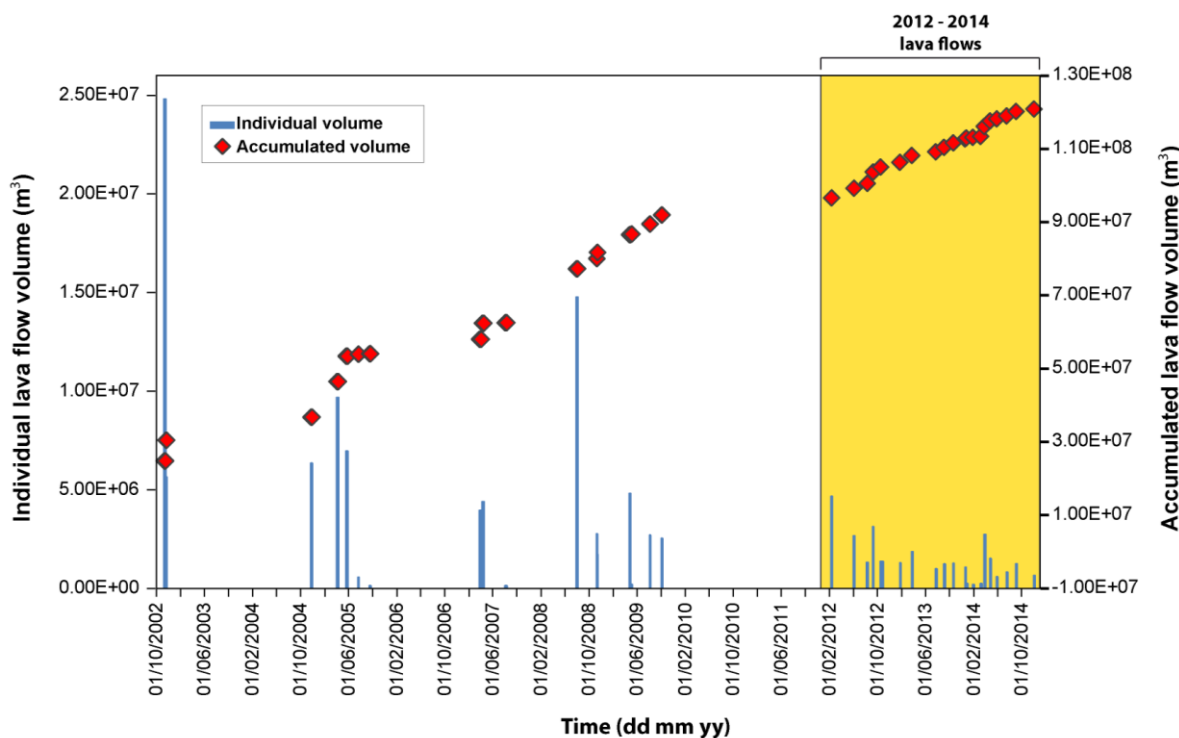


Figure 2. 37 Individual and accumulate volume of lava flows LF1 – LF37 emitted between 2002 and 2014 for El Reventador volcano.

2.5.3.6.4 Analysis

Block lava flows are characterized for having smooth polyhedral blocks bounded by dihedral angles based on the description of Macdonald (1953). These kinds of flows usually tend to advance as single units and they develop channels to feed lava to their fronts. Their fronts collapse continuously producing a snout of debris from the early stages of emplacement (Kiburn 2000). Flow fronts get thicker and thicker during the advance of the flow. For block lava flows they typically can reach about 20 m, extensions of various kilometers and volumes of 1-100 million cubic meters. Those lava flows tend to be emplaced between days and months.

Most of the lava flows from 2012-2014, LF18-LF37 had the same trend as LF1 – LF17, which is travelled to the north/south and then to the east, except for LF23, LF28, LF32, LF34 – LF36 which went directly to the southeast and LF29 and LF31 went to the northeast (see Fig. 2.31 and Fig. 2.35 for the comparison). Lava flows from El Reventador emitted between 2002 and 2014 is possible to differentiated two big groups in terms of their extension and volumes:

- ❖ LF1 - LF17, generated between 2002 and 2009 and
- ❖ LF18 - LF37, generated between 2012 and 2014

The comparison between Fig. 2.31 and 2.35 allows to identify that the extension and occupied surface of the flows is bigger for LF1 – LF17 than for LF18-LF37.

LF1 is the widest, thickest and voluminous flow of the whole period meanwhile the longest corresponds to LF9. LF10 is the shortest and less voluminous meanwhile LF28 is the narrowest and LF22 is thinner one (Table 2.3). The average thickness for LF1 and LF37 varies between 8.3 -16 m, nevertheless in some flows as LF1 and LF4 measures of the fronts reached about 50m. Values correspondent for lava flows of andesitic composition, regularly these lava flows are thicker in their fronts.

Regarding the morphology of the flows is possible to identify that most of them are formed by one single main lobe with some shortest bifurcations at their fronts (e.g. LF11, Fig. 2.31, 2.38). Important bifurcations of the flows were generated by topographic obstacles formed by ancient lava flows, allowing the flows to flow in different directions. Figure 2.38 shows the direction of the flows in which the different flows were bifurcated. Then, sixteen lava flows units are formed for one single lobe, seventeen units by two; two flows by three and one flow by four main lobes (Table 2.5, Figs. 2.31, 2.35, 2.38).

Lobes number	Lava Flows Units								
1	LF1	LF2	LF6	LF7	LF10	LF13	LF15	LF16	LF18
	LF22	LF23	LF24	LF28	LF29	LF33	LF37		
2	LF4	LF5	LF8	LF9	LF11	LF12	LF14	LF17	LF19
	LF20	LF21	LF25	LF26	LF27	LF30	LF34	LF35	
3	LF32	LF36							
4	LF4								

Table 2. 6 Number of main lobes generation for lava flows units for El Reventador.

Most of the flows from El Reventador volcano show an ogive surface (Fig. 2.38). An ogive is described as a corrugation formed in lava flows, their shape is represented by ridges as a response to compression parallel to flow during advance of some silicic lavas (Fink & Anderson 2000).

As well is possible to recognize that clearly examples as LF 4, LF5, LF9, LF16, LF18 etc., formed channels during they movement through the surface. Figure 2.38 shows as an example the scheme of the main morphological features of a part the southeast lava flow field which includes lava flows LF1, LF2, LF3, LF4, LF5, LF8, LF11, LF12, LF16, LF17 and LF18. The ogives surface, channels and direction are represented and as well their steep flow fronts.

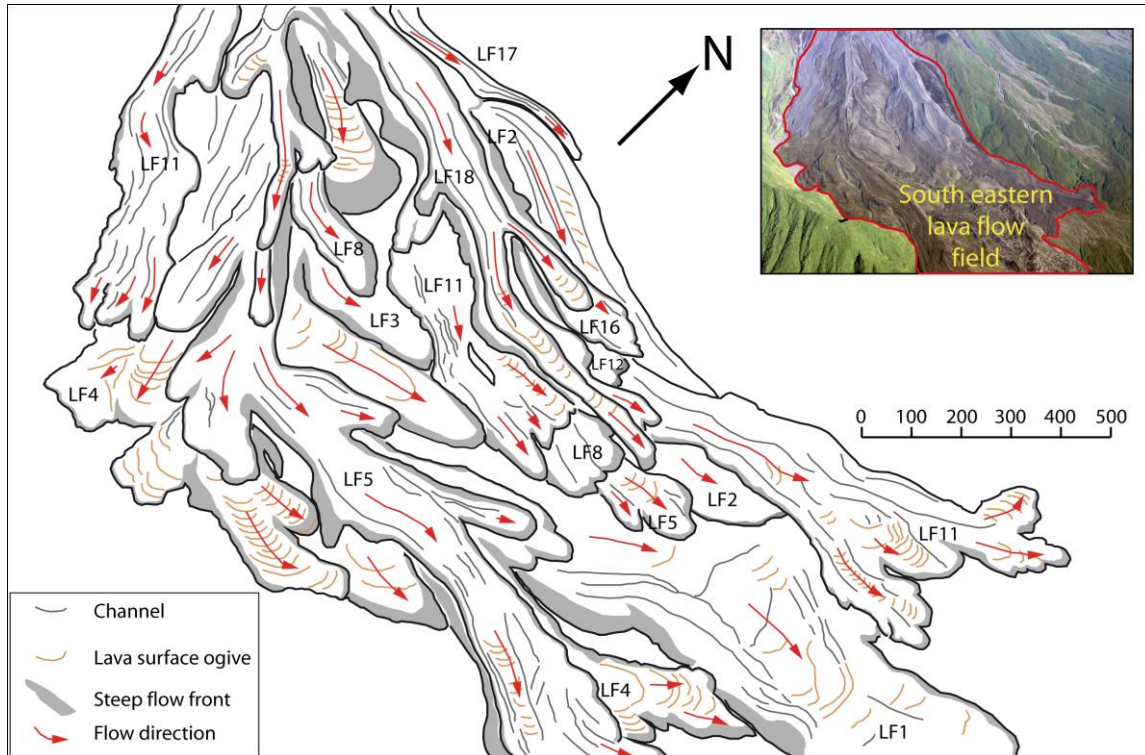


Figure 2. 38 a) Photo of the southeast lava flow field of El Reventador volcano. **b)** Cartoon of the southeast lava flows field represented in photo (a). It shows the major lava flows features as channels, lava surface ogives and the steep flow front. Lava flow direction is show for each flow with red arrows.

2.5.3.7 Geochemistry

The chemical analysis for the samples collected during this study was analyzed at the Laboratoire Magmas et Volcans (LMV). In total 13 samples were analyzed for major and trace elements. Based on the geochemical analysis of lava flows samples from previous and the current studies, lava flows from El Reventador volcanoes varies with SiO_2 content varies between 53,1 and 59,0 wt.% (Fig. 2.39). The highest content of SiO_2 corresponds to samples of the first lava flow emitted (LF1, Nov-2002). After 2002 the range of SiO_2 varies between 52.6 and 56.5 %.

Harker diagrams present a positive correlation with K_2O y Na_2O and some incompatible trace elements, while a negative correlation is observed to Fe_2O_3 , CaO , TiO_2 , MnO , MgO , Al_2O_3 , P_2O_5 and compatible trace elements. The petrological analysis is represented using the models proposed by Samaniego *et al.* (2008) in lava flows from El Reventador volcano during 2002-2005 and the other from Schiano *et al.* (2010) applied for Ecuadorian volcanoes, which models suggest a mixing magma and fractional crystallization, respectively for the magmatic activity on the volcano.

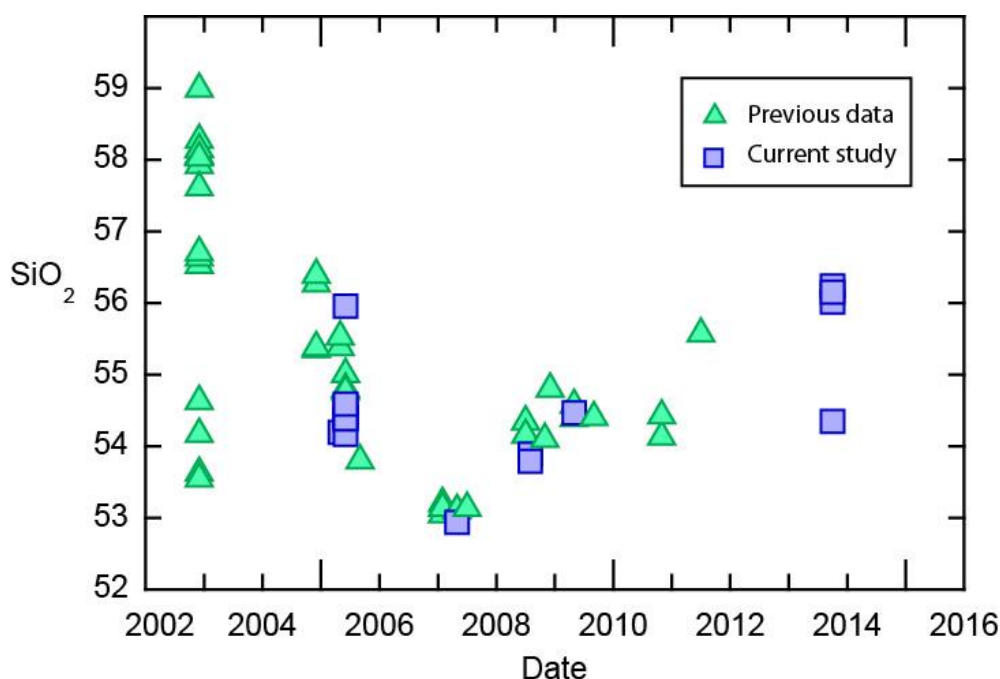


Figure 2. 39 Variation of the SiO_2 content of the lava flows between 2002 and 2014. Green triangles correspond to data from Samaniego *et al.*, 2008; Naranjo *et al.*, 2016; unpublished data; and blue squares correspond to the analysis of the samples taken during this research.

2.5.3.8 Petrography

Reventador's lava flows correspond to andesites and basaltic andesites, whose mineral assemblage is composed by plagioclase (12-35 % vol.), clinopiroxeno (5-15 % vol.), orthopiroxene (5-6 % vol.), amphibol (1-5 % vol.), Fe-Ti oxides inside the matrix and minerals (1 % vol.) and finally a few olivines (< 1 % vol.) (Figs. 2.40, 2.41). After a detailed analysis it has been determined a low level of vesicularity increasing along the time, specially evidenced on the products of explosive dynamic observed at the beginning of the eruption corresponding to the PDCs on November 3, 2002 and block and ash fallout of moderate level of PDC's produced in December, 2013. Lava flows thin section have presented a tendency associated with a decrease in contain of mafic minerals as olivine (since 2002) and apparently there is an increase of plagioclase and minerals with high K. Thin section in mostly of lava flows present porphyritic texture, with relevant textures as hypocristalline, serial and inequigranular from media to fine size grains. The matrix is mainly aphanitic but, occasionally hypocristalline with microstructure fluidal.

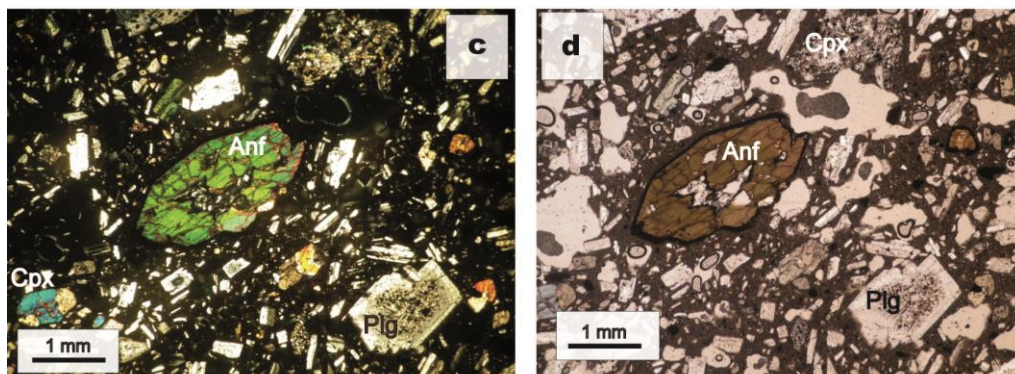


Figure 2. 40 Thin section of LF 2 with amphibol and his oxided borders, plagioclase as prismatic crystals and dusty surface and inter-growing on clino and orthopyroxene.

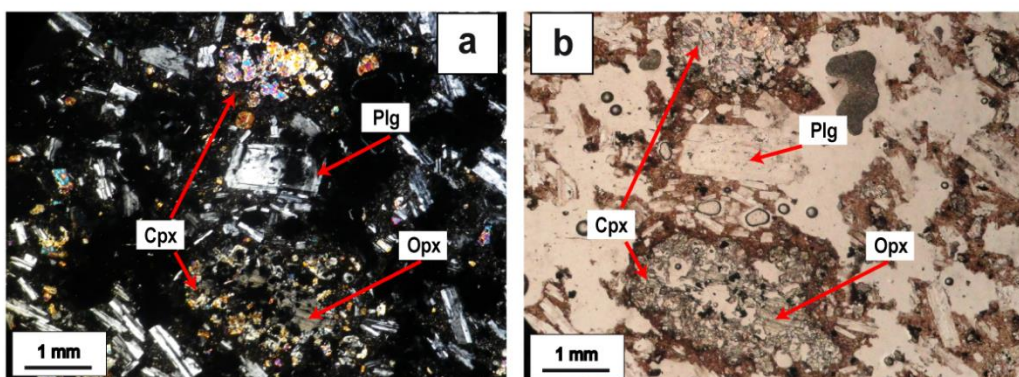


Figure 2. 41 Thin section of LF 16 with optical zoom of 2.5x. Tabular and euhedral crystals of plagioclase and phenocrysts of orthopyroxene. a) Using white light and b) Polarized light.

2.6 Eruptive phases

The classification of eruptive phases has been done based on seismicity, thermal alerts and geomorphological changes in the volcano. Naranjo *et al.* (2016) after Hall *et al.* (2004) and Samaniego *et al.* 2008 identified four phases in the period 2002 - 2009. In the present research I complete this identification until 2014, adding two more phases (Phases E and F) and suggesting some changes in those presented previously. Since the volcano is active, from 2002, there were generated in total 37 distinct lava flows. All of them were emplaced in the inner part of the caldera occupying a surface of 0.57 km² and an average volume of 133.9 m³; it was generated a cinder cone and a lava dome which is growing continuously until this day (March 2018).

After 2002, El Reventador volcano has shown a mixture of effusive and strombolian-vulcanian activity. It was characterized by the generation of explosions, ash columns, lava flows and pyroclastic density currents (PDC's). The characteristic volcanic product were lava flows, PDC's, pyroclastic cone and lava dome.

Description of the phases is showed below:

2.6.1 Phase D: July 2008 – Late 2010

The initial part of phase D, between July 2008 and October 2009 (Naranjo *et al.* 2016) was effusive with a little explosive component. It comprises the period of time between July 2008 and late 2010 (Fig. 2.18, Fig. 2.42). During this phase seven lava flows were generated (LF11 – LF17) through the north and southern part of the volcano. The longest one reached 3.5 km from the crater and corresponds to LF11. Until the generation of the LF17 there was no identified a generation of PDC's. After the last overflow of the volcano on October 2009, an intense explosive activity was recognized. It lasted for about 18 months (October 2009 – Early 2011) and generated an accumulation of pyroclastic material over the crate allowed the formation of a pyroclastic cone (Section 2.5.1, this Chapter). During this explosive phase some small PDC's of 0.5 km length were recognized. The accumulated lava flows volume for this phase (July 2008 – October 2009) is $29.5 \times 10^6 \text{ m}^3$ (modified by Naranjo *et al.* 2016).

2.6.2 Phase E: Early 2011 – December 2011

The phase E was characterized for being mostly effusive with a small explosive component in between. It lasted for about one year, about the whole 2011 (Fig. 2.19, 2.42). The seismic activity was mainly related to long period and tremor events. The effusive activity was

related to the growth of the dome (Section 2.5.2, this Chapter) inside de pyroclastic cone formed in the late part of Phase D (Fig. 2.17) (Section 2.5.1, this Chapter). Since the first records of activity (November 2002) it was the first time that the growth of a lava dome was recognized (Section 2.5.2 this Chapter). This phase was accompanied by an important and continuous degassing phase. This continuous degasification could have allowed the magma to increase the viscosity inhibit the formation of lava flows, but a continue accumulation of lava. During the extrusion of the dome there were generated just few thermal alerts from MIROVA systems. There was no presence of lava flows during this phase. A small explosive phase was recognized but not comparable with the one recognized in Phase E. A volume of the dome was estimated on $6.6 \times 10^6 \text{ m}^3$.

2.6.3 Phase F: Early 2012 - Late 2014

The phase F was characterized for being effusive but as well explosive. It comprises the period of time of early 2012 and the end of 2014 (Figs. 2.42). During this phase 20 lava flows were generated, all of them generated from the upper part of the dome (Phase F) and distributed in the upper parts of the volcano covering the north, north east, south east and south flanks (Section 2.5.3, this Chapter). The longest flow in this period of time reached 1.77 km. The continue accumulation of material in the upper part of the dome helped to build a steep dome. This situation combined to the explosive activity allowed a dramatically increasing of PDC's in this phase having deposits that reached 1.7 km from the vent. The total lava flow volume for this phase was estimated on $4.2 \times 10^6 \text{ m}^3$. The criteria for distinguish between phases E and F was based on the eruptive style, the dome formation and continuous emission of lava flows respectively.

Figure 2.42 present a resume of the eruptive phases based on the MIROVA alerts, seismicity and the lava flow accumulated volume per phase. It is very interesting to see that the accumulated volume from Phase F with 20 lava flow units is in the same volume range of the previous phases, in which few lava flows were generated. This could be as a result of the decreasing of the magma volume in the reservoir.

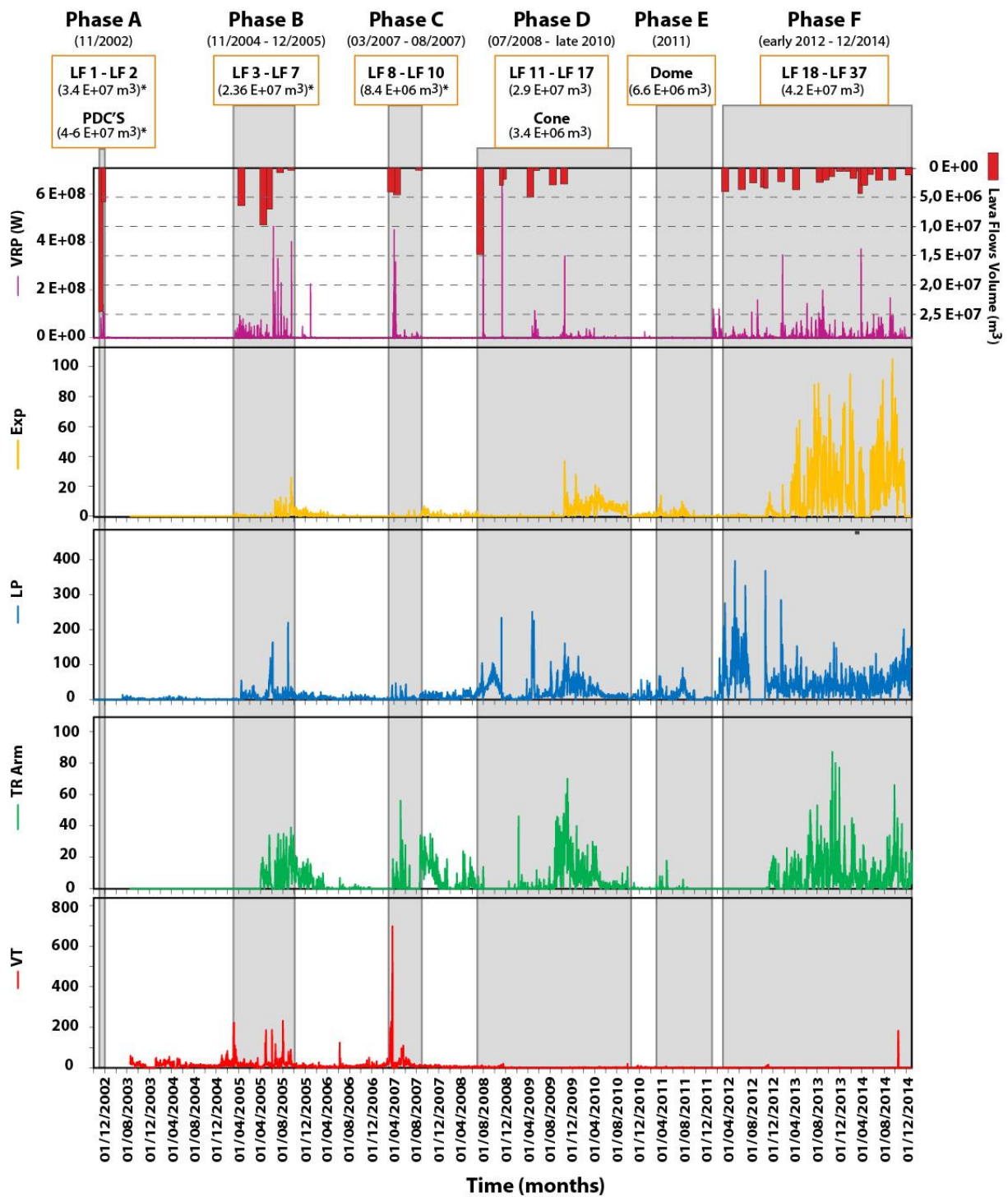


Figure 2. 42 Scheme of the representation of the eruptive phases for El Reventador volcano between 2002 and 2014 by the combination of seismic signals, MIROVA alerts and lava flows grouping.

2.7 Data as input data of numerical models for lava flow simulations

Basically the input data of numerical models are related to known the volume, effusion time, thickness, morphology and their distribution. As well is fundamental to have a good topographic base in which the lava flows can be generated.

The complete analysis done in this current work through many data that can be used as input data for numerical models. This data corresponds to:

- ❖ **Volume:** have been constrained the volume for all the phases can bring a good guide to propose different scenarios for the simulation of lava flows.
- ❖ **Lava flows duration:** this estimation for the majority of the lava flows can help to constrain in a better way the duration of the lava flow simulations.
- ❖ **Thickness:** the deeper analysis of lava flow thickness can help to calibrate and verified the different solutions of the flows simulation.
- ❖ **Velocity estimation:** with this data it is possible to calibrate numerical flows following different rheologies, e.g. Bingham rheology.
- ❖ **Morphology:** the analysis of the lava flow's morphology can bring as well a guide in the solution in order to find similarities between ancient flows and simulations of future probable ones.

All of this data can help in order to have more realistic lava flows that can provide a tool for the hazard management.

Chapter 3

Numerical Codes for Lava Flows Simulations

The development of numerical codes to simulate lava flow emplacement has been increasing during the last decades with the aim to forecast their paths over the topography, to generate a useful tool for hazard management or to reconstruct past flows emplacement.

The main challenge of numerical models is to simulate and link the complex interplays between topography, rheology, heat loss, the free-boundary of the flow, the soil friction, the physics of erosion and flow dynamics that lead to the emplacement of a specific lava flow system of given morphology, architecture, thickness, length and width (Favalli *et al.* 2005, Harris 2013). In that way, it is necessary to make some assumptions about their physical behavior as it represents the link between the forces that act on the flow and its deformation.

As described in Chapter 1, the advance of lava flows is highly dependent on the evolution of their thermo-rheological properties where viscosity and yield strength increase in time due to cooling and crystallization (e.g. Lipman & Banks 1987, Cashman *et al.* 1999). Thusly, it is important to understand how the effusion rate and the thermo-rheological properties of the flow vary with time and space in order to simulate lava flows (Miyamoto & Sasaki 1998). Then, a numerical model that simulates lava flows must take into account the factors that control the behavior and emplacement of a lava flow and consider that their significance during its emplacement may be vary (Cordonnier *et al.* 2015).

Existing lava flow models can differ in physical complexity, dimensionality and simplifying assumptions (Dietterich *et al.* 2017). According to Harris (2013), numerical models for simulating lava flows can be divided in two types:

- ❖ **Type I:** those that have been designed to improve the understanding of the emplacement dynamics and lava flow morphology with the aim to determine the link of the cooling processes and the resulting dynamics, dimensions and morphology of the flow. These models include laboratory based-studies in scaled, tank-based simulations using different materials as an analogous to real lava (e.g. Griffingths & Fink 1993; Griffingths *et al.* 2003; Kerr *et al.* 2006, Castruccio *et al.* 2010; Garel *et al.* 2012; Dietteritch *et al.* 2015; 2017; Vera *et al.* 2017) and theoretical approaches (e.g. Kilburn *et al.* 1995).
- ❖ **Type II:** those that were developed to simulate lava flow emplacement using fluid dynamics and heat transfer principles with the aim to be used for hazard assessment during ongoing eruptions (e.g. Tedesco *et al.* 2007), future eruptions (e.g. Rowland *et al.* 2005; Cappello *et al.* 2016; Rongo *et al.* 2016, Richter *et al.* 2016) and to evaluate and determine the downflow changes in the different properties of the flow.

Numerical models of Type II can be classified based on the methodology that they follow and on the dependence of the approach of the lava flow (e.g. Tarquini & Favalli 2011; Cordonnier *et al.* 2015) as:

1. Deterministic codes are based on transport theory, in which a solution is achieved given a unique set of boundaries and initial conditions.
2. Stochastic codes are based on the maximum slope, in which the solution is achieved from up to thousands sets of simulations using very simple physics.

Validation of a numerical code can be done by the comparison of some morphological characteristics of the real-world flows (e.g. length, area, thickness, structures) against those generated by the simulations (Harris & Rowland 2001; Tarquini & Favalli 2011; Lev *et al.* 2012). These comparisons can help to understand the complex rheology, thermal and dynamic processes involved in lava flow emplacement; to simulate more accurately lava flow emplacement events (Harris 2013); and to test if the given assumptions still allow reproducing the real emplacement of the flow.

One of the objectives of the present study research is to improve the isothermal numerical code VolcFlow (Kelfoun & Druitt 2005) with thermo-rheological laws (laws that relate viscosity and yield strength to the cooling and crystallization) in order to generate more realistic lava flow simulations. As is described below, some numerical codes manage to simulate the emplacement of lava flows using different approaches, nevertheless just few of them take in account the most important factor that control their movement which is the cooling of the lava. Section 1.2.2, Chapter 1 showed that lava flow heat loss depends mainly on radiation, forced convection and conduction, meanwhile heat gain depends on the crystallization. The following description shows that just few of the deterministic and stochastic numerical codes include those components.

Lines below are dedicated to describe the different numerical codes of Type II, their different approaches and purposes in order to determine which model would be chosen to be adapted in VolcFlow.

3.1 Deterministic numerical codes

Simulations obtained from deterministic numerical codes are based on the solution of the equations that govern the physics of lava flow movement. They require the evolution of the mass or volume effusion rate at the eruptive vent, as well as any thermal or rheological model. So far published deterministic codes cannot easily deal with some of the fundamental processes that characterize the emplacement of lava flows such as overflows or the formation of lava tubes. This is because the complexity for the system requires strong computational simplifications (Tarquini & Favalli 2011). Then, some assumptions need to be made about the physics and the input data, generating as a result an abroad approximation of the reality (Cordonnier *et al.* 2015).

These methods require an accurate knowledge of a large number of input parameters, in particular it is fundamental to know with precision the vent location and the topography that is to have a detailed Digital Elevation Model (DEM) of the volcano.

3.1.1 Channeled model: FLOWGO

These kind of models consider that the lava is channeled and flows downslope in a single one direction (Cordonnier *et al.* 2015). This kind of model is focused on the emplacement

physical processes of the flow and also allows the implementation of more complex modelling equations as thermo-rheological laws.

Developed by Harris & Rowland (2001) and later on improved by Harris & Rowland (2015) and Harris *et al.* (2015), FLOWGO is a 1-D model which tracks the control volume of a lava when it is flowing down a channel. This control volume evolution is tracked as a single line of descent centered on the channel axis until it stagnates. Its velocity is calculated using the Jeffreys (1925) equation with its approximation to a Bingham fluid (Moore 1987) which is dependent on the lava viscosity and yield strength (Section 1. 3, Chapter 1) and which in turn are both affected by cooling and crystallization (Section 1. 2, Chapter 1) during the dispersion of the flow over the surface. FLOWGO allows the facility to incorporate to its framework various thermo-rheological models to simulate the down flow heat budget, cooling, crystallinity, viscosity, yield strength, velocity, channel width and maximum length for basaltic lava flows.

Based on mass conservation the width of the channel can be calculated at each down flow step as a relationship between eruption rate, channel depth and mean velocity. Mean velocity is controlled by rheological properties of the lava (Jeffrey's equation) and the effusion rate is estimated at the vent with the initial flow geometry, rheology and velocity. At each step, core cooling and crystallization are calculated allowing the estimation of viscosity and yield strength. After setting input parameters (e.g. starting conditions for control volume, slope, initial rheological starting conditions) the volume is able to move down-channel until cooling and crystallization reduce velocity. The lava flow can be stopped in FLOWGO under three conditions. If one is met during the simulation, then the flow stops otherwise it will continue to flow down the channel. They are related to determine if the velocity is equal to zero, if the temperature is at or below the solidus temperature and if the yield strength at the base of the channel is greater than the downhill stress.

The heat budget model used by FLOWGO for a lava control volume is described in Section 1.2.2, Chapter 1. The heat budget determines the variation of the internal temperature and the increase of crystallinity of the control volume, which are then used to calculate the viscosity and yield strength of the flow. FLOWGO is governed by three main steps, which are related to calculate velocity, rheological parameters and heat budget (Fig. 3.1, Harris *et al.* 2015). These 3 steps are briefly described following the last version of FLOWGO (2015c), it requires thirty-five input parameters to be processed and it calculates systematically twelve variables. The notation and units of all the parameters and variables are detailed in Appendix 2.

1. Mean velocity

FLOWGO bases the movement of the flow in Jeffrey's law equation. Originally this equation was developed considering the fluid to have a Newtonian fluid, however it has been demonstrated that the behavior of a lava flow can vary from Newtonian to Bingham. Moore (1987) modified Jeffrey's equation for a Bingham fluid for a semi-circular channel (Eq. 3.a, Harris & Rowland 2015b) and for a channel that is wider than deeper (Eq. 3.b, Harris & Rowland 2015b), both depending on the radius of the channel, the density of the fluid, gravity, the channel slope, viscosity, yield strength, shear stress. Depending on the characteristics of the channel, one of those two equations can be used in FLOWGO to calculate the mean velocity of the flow.

2. Rheology estimation

This is based on the calculation of lava viscosity and yield strength as a function of the variation of the lava temperature and/or the crystal content (Harris *et al.* 2015). Models and equations are described in Chapter 1, Section 1.3.2 for viscosity and Section 1.3.4 for yield strength as a dependence/relationship with a Bingham fluid.

3. Heat budget, cooling and crystallization rate estimation

The FLOWGO code is based on the heat budget for a lava control volume (See Chapter 1, Section 1.2.2 for a complete description of each of the involved mechanisms for the heat budget.) and viscosity in relationship with eruption rate, density, latent heat and the rate of crystallization. This model allows to estimate the down-flow evolution of the interior temperature of the lava per unit of distance when it is flowing in the channel. FLOWGO as well allows to calculate the mass fraction of crystallization per unit of distance, which is calculated as a function of the cooling experienced by the lava interior per unit distance and the rate of crystallization.

4. Example of study case

FLOWGO has been applied mainly in lava flows of basaltic composition. The study cases correspond to well-studied flows of Mauna Loa and Kilauea from Hawaii, USA (Harris & Rowland 2001, 2015b), Piton de la Fournaise (La Réunion, France) and Etna (Sicily, Italy; Harris & Rowland 2001). FLOWGO is currently used as a tool for hazard assessment in Piton de la Fournaise volcano (La Reunion Island, France).

One of the well-studied cases corresponds to the lava flow of December 9, 2010 of Piton de la Fournaise (Harris *et al.* 2015). This eruption produced mainly an ‘a‘a flow from four fissures and lasted less than 15 h covering an area of 0.269 km^2 and a volume of $0.53 \times 10^6 \text{ m}^3$. In Harris *et al.* (2015) the analyzed flow was the western lava flow unit (Fig. 3.1) which reached a maximum distance of 970 m. Rock samples were collected in the flow every 10-20 m allowing to obtain the chemical; temperature and textural (vesicularity and crystallinity) source data necessary to initialize FLOWGO.

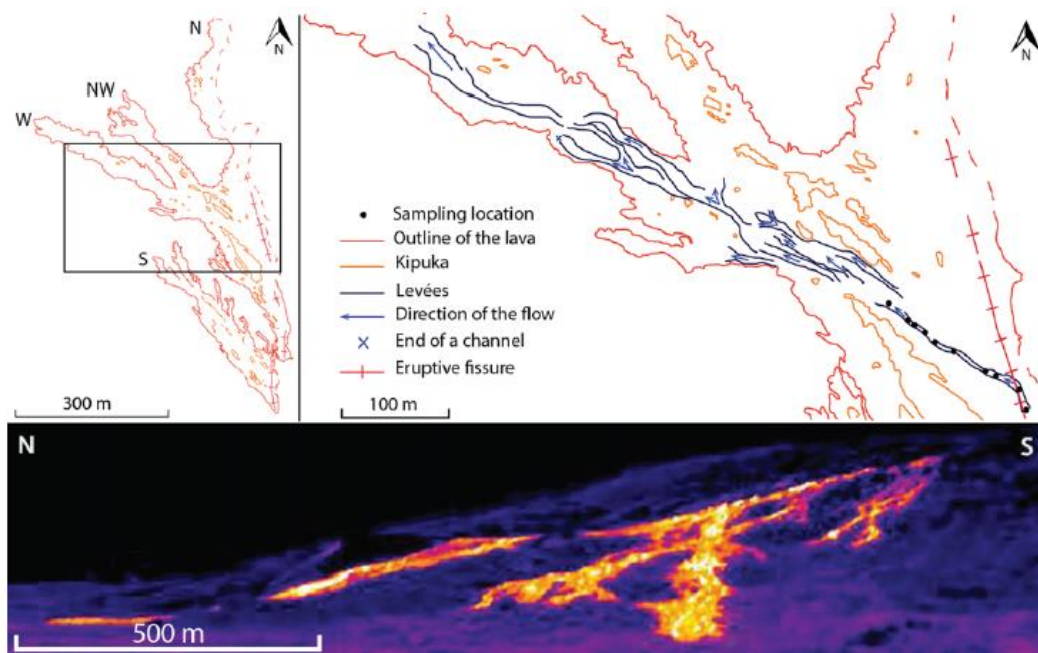


Figure 3. 1 Area of the compound lava-flow fields (north, NW, west and south) of the Piton de la Fournaise December 9th, 2015 eruption (left top). The detail of the west flow field is shown in the right top. Thermal image of the flow field is showed at the bottom (Harris *et al.* 2015).

FLOWGO estimates of the velocity, viscosity, yield strength and the cooling of the flow per unit of distance down flow, were compared with field measurements (Fig. 3.2, 3.3). For this study case, the core temperature, crystal content and viscosity were estimated for the first 150 m of the flow. The FLOWGO simulation showed good agreement with the field data within an acceptance of error for temperature and crystal content. For viscosity the best fit was obtained with a non-Arrhenian relationship (i.e. VFT model, see Section 1.3.2, Chapter 1), however the simulation predicted a run out distance of 3.8 km which is far from of the real length of the flow which was 0.97 km. This mismatch could be explained by the difficulties of simulating perfectly all variables involved and in particular the evolution of viscosity of the lava mixture.

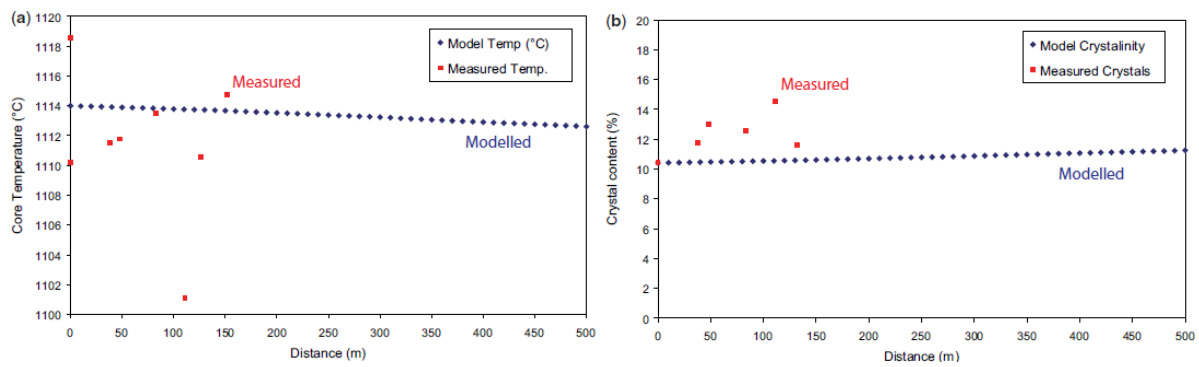


Figure 3. 2 Relationships between the core temperature and crystal content with distance, a) and b) respectively. Red squares correspond to the measured data and blue dots are the results of FLOWGO simulation (Harris *et al.* 2015).

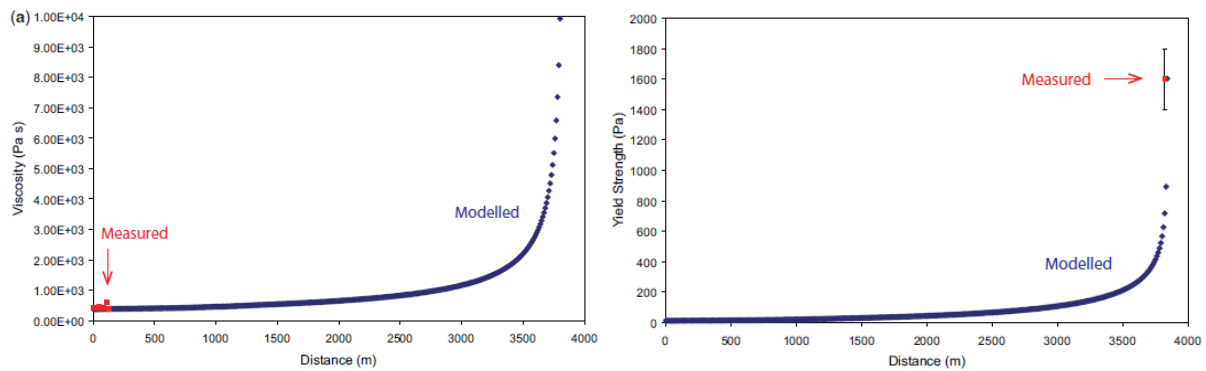


Figure 3. 3 Relationships between viscosity and yield strength with distance left and right respectively. Red squares correspond to the measured data and blue dots are the results of FLOWGO simulation (Harris *et al.* 2015).

5. Numerical coding

FLOWGO was originally written in the programming language IDL (Interactive Data Language) and later on EXCEL, allowing a friendly and broad use of the code by the public. The latest improvement is the PyFLOWGO approach (Chevrel *et al.* 2017) which is an interface written in Python v3 and allows more flexibility to implement models. As FLOWGO does not involve fluid motion calculations are very fast to run. Its validity can be assessed using the best fitting of the various model outputs with all available measurements (e.g. channel shape, temperature etc.). In many cases some values (e.g. crystallization rate) are unique for the study case and sometimes it is not possible to use them. As FLOWGO was developed for basaltic lava flows the applications for silicic lava flows is reduced. Furthermore, FLOWGO cannot determine the inundation area of the lava-flow run out because this code was developed to simulate lava

flows in one dimension, except when combined with stochastic models like DOWNFLOW or Q-Lavaha (see section 3.2.2) (Harris *et al.* 2015; Mossoux *et al.* 2016).

3.1.2 Cellular Automata models

Cellular automata (CA) is a paradigm of parallel computing and represents an alternative to solve differential equations for modelling and simulating some complex systems (Di Gregorio *et al.* 1996). CA is an approach in which the computational domain is represented by a 2D grid of cells. Each cell is characterized by properties such as altitude, lava height and temperature. Lava-flow advance and cooling are described through the evolution of cell properties. The evolution of the cells depends on the state of the neighboring cells with in/out fluxes computed for each cell at each time step. Old versions of CA codes used plastic rheology to stop the flow, nowadays the solidification takes place when the cell temperature gets below a predefined temperature.

In general CA models are fast to run, and each of them has developed specific strategies to transfer mass, energy and momentum between neighboring cells. Nevertheless, 2D models will always lack the detailed vertical structure of the lava flow, which is important in coupling surface and basal heat losses to the bulk rheology evolution.

3.1.2.1 SCIARA

SCIARA which means ‘Smart Cellular Interactive Automata Rheology of Aetnean lava flows’ is a two dimensional CA version model developed by Barca *et al.* (1987, 1993, 1994). It is a simplification of the original three dimensional CA model developed by Crisci *et al.* (1982, 1986) and Barca *et al.* (1987) which was not implemented due to the computation costs and the impossible application for large lava flows. The purpose to develop SCIARA model relies on an accurate analysis of the past behavior of the volcano and is appropriate for land use planning and civil defense applications. It has been improved since 1982 based on the CA approach for modelling spatially extended dynamic systems by proposing improved releases and to apply them to diverse Etnean case studies (Rongo *et al.* 2016). Fields of the application of SCIARA model are:

- ❖ Long term forecasting of the flow direction with different scenarios by locating potential risk areas and allowing to generate detailed risk maps
- ❖ The possibility to follow and predict the progress and its evolution of an event

The SCIARA code was tested with several lava events during the 1986-1987 and 1991-1993 Etna eruptions (Barca *et al.* 1993; Crisci *et al.* 1999, 2004) with the aim to forecast the surface covered by the lava flow. The model was used as well to obtain hazard maps of future events which could be similar to the 1669 eruption event that affected Catania (Sicily, Italy), involving 1km^3 of lava during 130 days.

The input data necessary to run SCIARA model are:

- ❖ Lava discharge rate
- ❖ Topography (DEM) and location vents

The last version of this code is the SCIARA-fv2 which was improved by Spataro *et al.* (2010) and was adopted for the development of lava flow hazard maps. This new version re-introduces a square space instead of the hexagonal cellular space developed in old versions (Crisci *et al.* 2004) with the aim to avoid the anisotropic flow direction problem (Fig. 3.4). It uses a Bingham rheology model considering the concepts of critical height and viscosity (Park & Iversen 1984; Dragoni *et al.* 1986; Ishihara *et al.* 1990). This new version also improves the cooling of the flow by radiation. Lava solidifies when the temperature drops below the temperature of solidification. Lava outflows from the cell towards its neighbors when its thickness is greater than a critical value (critical height) at the time of the basal stress exceeds the yield strength.

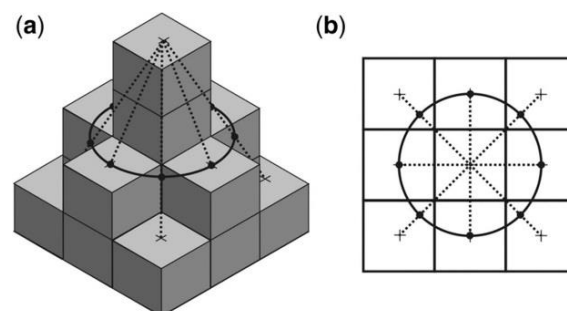


Figure 3. 4 a) 3D view and b) top view or the schema for cell altitude determination for SCIARA-fv2 numerical model. Altitude values along the diagonals are taken at the intersection between the diagonal line and the circle (From: Rongo *et al.* 2016).

Rongo *et al.* (2016) propose the simulation of lava flows for Etna volcano using SCIARA-fv2 using the parallel computing GPGPU (General Purpose computing on Graphics Processing Units) in order to obtain the output of the simulations in short time. SCIARA-fv2 code was tested in two ideal surfaces in order to evaluate the magnitude of anisotropic effects and

calibrated with the 2001 and 2006 lava flows at Etna volcano adopting the real effusion rate of those eruptive episodes. By comparing the overlapped area between the real flow and simulations, results of this calibrated model show that this version is more accurate than the old ones. The combination of the SCIARA-fv2 methodology and a probability density function map allowed to obtain a highly detailed hazard map that can be used to land planning and civil defense, also to quantify in real time the inundation area of an imminent eruption Rongo *et al.* (2016) (Fig. 3.5).

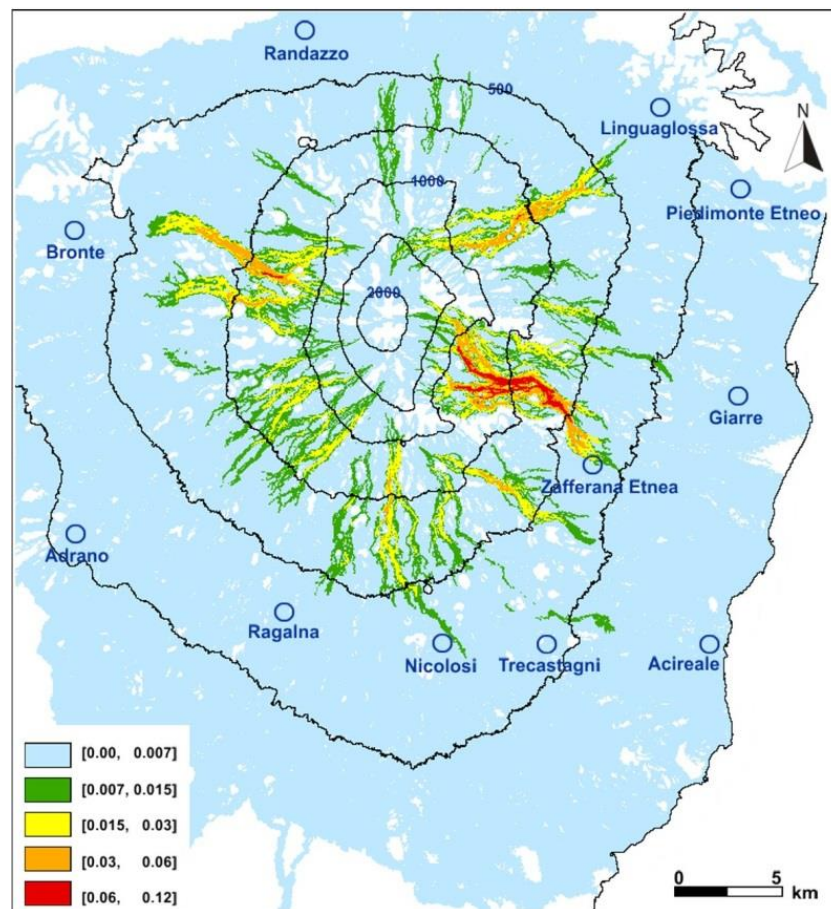


Figure 3. 5 Lava flow hazard map for Etna volcano as a result of the probability of areas being affected by future eruptions (From: Rongo *et al.* 2016).

The SCIARA code considers the radiation as the sole mechanism to cool the flow. As this code uses a Bingham rheology, both yield strength and viscosity parameters are considered as the rheological control parameters. Nevertheless, only the viscosity varies meanwhile the yield strength is fixed as a constant. Viscosity varies as a dependence only on the temperature and not on the chemical composition. On the other hand, crystallization is not considered. Then, this code does not satisfy the need of the present research because it does not consider all the

mechanisms involved in lava cooling and as well the treatment of the viscosity and yield strength is not complete.

3.1.2.2 MAGFLOW

The 2D cellular automata model MAGFLOW has been developed by Del Negro *et al.* (2008) and Vicari *et al.* (2007) at the INGV-Catania (Italy) with the aim to forecast the possible lava flow paths and to predict the evolution of the flow in near real time. The states of the cells are the lava flow thickness and the quantity of heat. Their cells states are synchronously updated according to rules that depend on values of the cell and of its neighbors.

MAGFLOW considers the steady-state of Navier-Stokes equations as an evolution function for CA for a Bingham fluid (yield strength and plastic viscosity) which moves as an incompressible laminar flow suspended on a horizontal plane and its mass conservation is guaranteed locally and globally. An algorithm-based Monte Carlo approach was applied in order to solve the anisotropic flow direction problem (Vicari *et al.* 2007) which is produced by the strong dependence on the cell geometry and position of the flux, with respect to the symmetry axis of the cell. This model considers a cellular automaton which has a randomized neighborhood and defines the neighborhood as all cells that are closer to the central cell than a specified value R , then the model counts the neighbors as those cells whose centers lie inside a circle of radius R , (Fig. 3.6). This method allows to get cell geometry free results and as well to calculate large-scale lava flows with no artificial anisotropy.

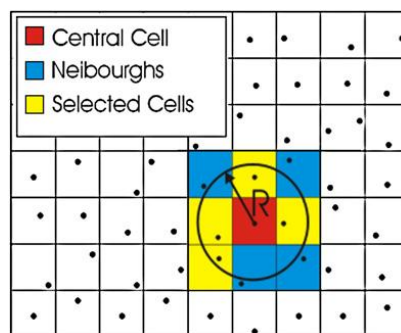


Figure 3. 6 Scheme of a randomized neighborhood in a cellular automata mesh (Vicari *et al.* 2006).

The calculation of the flux on an inclined plane is obtained by the solution of the relationship proposed by Dragoni *et al.* (1986) (Eq. 1 in Vicari *et al.* 2006), of a Bingham fluid using a constant thickness which is moving down the slope due to the gravity. The critical

thickness relationship from Miyamoto & Sasaki (1997) and Mei & Yuhi (2001), (Eq. 2 in Vicari *et al.* 2006) which is dependent of the yield strength and the angle of the slope is incorporated in Dragoni's relationship. Then, the lava flow moves from one cell to another when the thickness reaches the critical value of the cell, i.e. when the basal stress exceeds the yield strength (Rocchi *et al.* 2004). Yield strength and viscosity of the lava flows are dependent of the temperature (Pinkerton & Stevenson 1992; Harris & Rowland 2001). MAGFLOW allows to incorporate different viscosity relationships (e.g. Ishihara *et al.* 1990; Giordano & Dingwell 2003).

MAGFLOW as well allows the calculation of the cooling of the flow at any time and at each cell in accordance with motion of the flow. It considers that the temperature is uniform and that the heat loss is given only by radiation from the surface of the flow. It does not consider the effect of conduction to the ground and convection with the atmosphere. The new temperature then is obtained from the calculated heat loss (Eq. 6 in Vicari *et al.* 2006).

Some input data are necessary to run MAGFLOW:

- ❖ the digital elevation model (DEM)
- ❖ the lava effusion rate at the vent
- ❖ the physical and rheological properties of the lava

In the first initial stage the thickness is set to zero and the flow begins to discharge with a certain rate from one or more cells which correspond to the vent. Then the thickness of the lava at the cells or vent increases with a rate calculated from the volume of lava extruded during each time interval. When the thickness at the vent reaches the critical thickness then the lava spreads over the neighbor cells. This process continues in each cell, meaning that whenever the thickness reaches the critical value at any cell, the lava flows to the surrounding cells.

The MAGFLOW code has been used to predict the inundated areas by lava flows during several eruptions at Etna volcano (Italy). As a first attempt Vicari *et al.* (2006) applied the code with the aim to verify its capability reproducing the lava flow generated during the 2001 Etna eruption. After, it was used to forecast hypothetical scenarios of diverse evolutionary typologies of the vent during the 2004-2005 Etna eruption (Del Negro *et al.* 2008). For the 2006 Etna eruption, it was used to assess the short-term lava flow hazards (Herault *et al.* 2009). Figure 3.7 presents the simulation of the 23 October 2014 flow (Del Negro *et al.* 2008) in which the geometry of the lava flow simulations presented a good match with the real deposit.

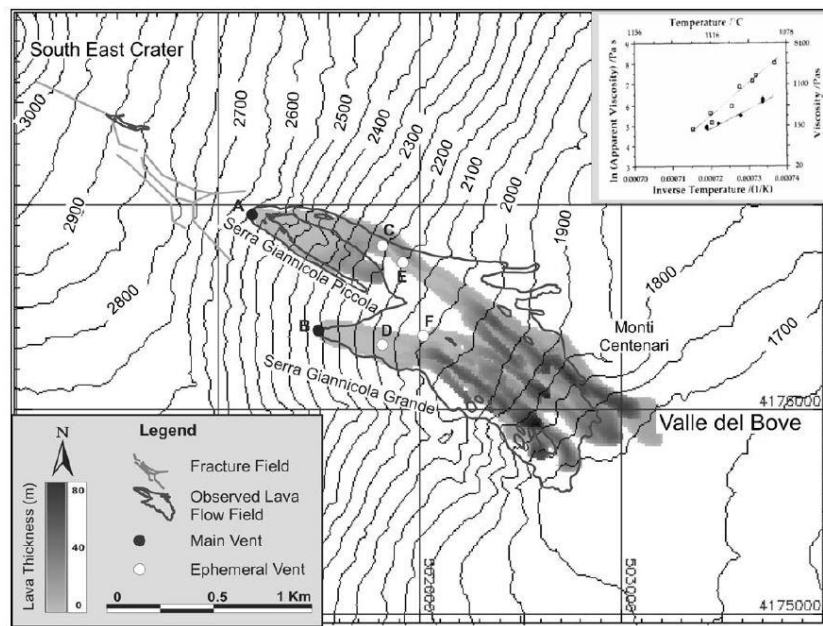


Figure 3. 7 Lava flow simulation thickness for the 23 October 2004 Etna eruption, the result was obtained using the relationship between viscosity and temperature as proposed by Pinkerton and Norton (1995) (from Del Negro *et al.* 2008).

Results show that this model quite accurately reproduces the emplacement of the lava flow and can estimate the potentially inundated area of the flow which presented a good match with the real deposit. In some cases, variations of the shape as a greater length and wider extension in the terminal part of the simulations can be justified by the topographic inaccuracies and imprecision of the input data.

MAGFLOW was also used for long-term lava-hazard assessment and then these results were used to map the susceptibility of areas to lava flow emplacement (Del Negro *et al.* 2013; Cappello *et al.* 2016 Pedrazzi *et al.* 2015)

Lately MAGFLOW was used to discuss its potential to improve the understanding of the dynamics of lava-flow emplacement and in that way the ability to assess lava flow hazards (Cappello *et al.* 2016). Through a sensitive analysis of the input parameters, they determine that water content and solidus temperature are the parameters with which MAGFLOW is most sensitive. By its side, variations of effusion rate influence in the accuracy of lava flow paths. The simulation time can be reduced from days to few minutes due to the implementation of MAGFLOW in graphic processing units.

All the improvements of MAGFLOW through the time suggest that this code can be taken as a part of a monitoring system during an effusive eruption; nevertheless, the reliability of the model

highly depends on the quality of the input parameters related to the rheology and effusion rate. The efficiency of MAGFLOW is correlated with the presence of an efficient monitoring system of the event.

A Bingham behavior is considered by MAGFLOW and it just takes in account the cooling by radiation mechanism. It is adaptable to improve many laws of viscosity and the inundation area highly depends on the topography and as well as on the input data. In MAGFLOW, yield strength and viscosity are dependent on the temperature and not on the chemical composition. No crystallization effect is taken in account.

3.1.2.3 MOLASSES

The MOLASSES (MODular LAva Simulation Software in Earth Science), written in C, is a CA lava flow simulator developed using a modular framework (Richardson 2016) based on the LavaPL algorithm (Connor *et al.* 2012). This code is constructed with nine modules with specific tasks. Lava is advected from source locations over a DEM to more distant grid cells following rules that govern each location spread lava which includes the minimum thickness needed to be spreader to different neighbors. The source code of modules can be modified and then different flow algorithms can be realized affecting in that way the simulated flow behavior. The MOLASSES algorithm has been used to model the 2012–3 Tolbachik lava flows (Kamchatka, Russia) (Kubanek *et al.* 2015) and the long-term hazard of lava flows on infrastructure within the East Snake River Plain (Idaho, USA) (Gallant 2016). Recently it was applied by Dietterich *et al.* (2017) in which a Moore Neighborhood was incorporated, where grid cells interact with 8 adjacent neighbors to avoid mesh-based anisotropy (e.g., Vicari *et al.* 2007). Lava spreading among neighbors is proportional to the relative cell-to-cell slope and it can only spread between cells if flow thickness is above a given critical thickness, this process mimics the behavior of Bingham flows. MOLASSES cannot provide the evolution of the flow inundation but the thickness and the extent of the lava flow.

This specific algorithm has been validated by Richardson (2016) to show that the model is not dependent on slope direction, forms a circle on a horizontal surface, and reproduces a natural lava flow with a fitness >80%.

Other examples of Cellular Automata in 2D models are:

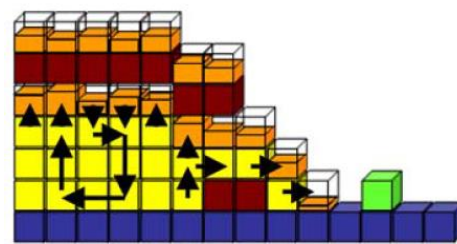
- ❖ Ishihara *et al.* (1988) was one of the first CA approaches to simulate lava flows. It uses the Navier-Stokes equations, Bingham rheology and numerical formulations for discrete space and time intervals to simulate some lava flows in Japan bringing good results. Nonetheless it is not possible to apply this code to multiple flows or those which extrude intermittently.
- ❖ FLOWFRONT from Young & Wadge (1990), and Wadge *et al.* (1994) is a CA code that can simulate lava flows using deterministic method and probabilistic method with deterministic approaches. Even if the results can be obtained relatively fast its use is limited.

3.1.2.4 LavaSIM

LavaSIM is a 3D cellular automata code that has been developed by Hidaka & Ujita, (2001), Hidaka *et al.* (2002, 2005), Fujita & Nagai (2016). LavaSIM is aimed at a real-time hazard assessment system for the purpose of evacuation guidance during eruptions, and for preparing evacuation plans and designing protection structures against lava flows.

LavaSIM calculates the structure of a lava flow in 3D and the displacement using a DEM. It discretizes the space in small cubes (3D-cells) that can be totally or partially filled (Fig. 3.8) in which four kinds of materials are defined: liquid lava, crust, ground and structure. LavaSIM includes the effects of 3D convection; melting and solidification and lava-property dependency on (e.g. temperature, chemical composition). Solidification can occur during lava spreading and consequently the solidified crust can become an obstacle to the flow. In this case, the liquid lava can subsequently surmount the crust. The liquid lava can also flow under the crust after the upper surface of the lava flow is covered by crust.

The code calculates the lava displacement using three-dimensional convection with simultaneous spreading and solidification. The lava flow is modelled as a single-phase flow with solidification and the liquid part is assumed to be a Newtonian fluid. The Navier-Stokes equation is applied for the convection analysis. In the convection analysis, the terms of inertia, viscosity, pressure (pressure derived from lava level, i.e. liquid head), ground elevation and inclination are considered in the momentum equation.



B-B' Longitudinal section

Symbol	Form	Cell attribution
	Liquid lava	Convection cell
	Crust	
	Liquid lava or crust	Free surface cell
	Ground	
	Structure (Protection bank, etc.)	

Figure 3. 8 Conceptual principle of LavaSIM

The code calculates the lava displacement using three-dimensional convection with simultaneous spreading and solidification. The lava flow is modelled as single-phase flow with solidification and the liquid part is assumed to be a Newtonian fluid.

The Navier-Stokes equations are solved in 3D using an equation of mass conservation and three equations of momentum in x , y and z (see Eq. 5-8 of Hidaka *et al.* 2005). Due to the model complexity, some corrections are applied in the numerical scheme to avoid the void formation in the flow. A lot of assumptions are also done to give realistic results: the crust moves vertically to fill the void, cells are filled from their base to assure density conservation. The flow locally stops according to temperature conditions and where its thickness is low compared to the lava yield strength.

The calculation of the lava temperature is done using conductivity transfers from the inner lava to the surface crust and radiative/convective transfer from the surface to the atmosphere. The lava viscosity can be calculated by several viscosity models for example, by the model of Goto *et al.* (1997) which is based on the Williams-Landel-Ferry (WLF) equation (Williams *et al.* 1955); using the equation from Krieger & Dougherty (1950) which includes the effects of crystals and solidifying melt or by the non-Arrhenian relationship (VFT).

LavaSIM has been used to simulate the basaltic lava flow from the 1986 eruption from the Izu-Oshima volcano (Japan) (Fig. 3.9), for the 2001 lava flow from Etna volcano (Italy) and for the lava pancake formation during the Shinmoe-dake Kirishima (Japan) eruption in 2011.

Although the use of parallel computing technology and the improvement of the algorithms in the LavaSIM code version proposed by Fujita & Nagai (2016) made that the code is 3-10 times faster than the previous version by Hidaka *et al.* (2005). Even though, note that this 3D calculation is very time consuming and perhaps not adapted for real-time hazard assessment. Moreover, results presented in the published papers does not prove that the results of LavaSIM are significantly better than the other approach and we cannot state that the ratio quality of results/time of calculation is high enough to prefer this approach to other ones.

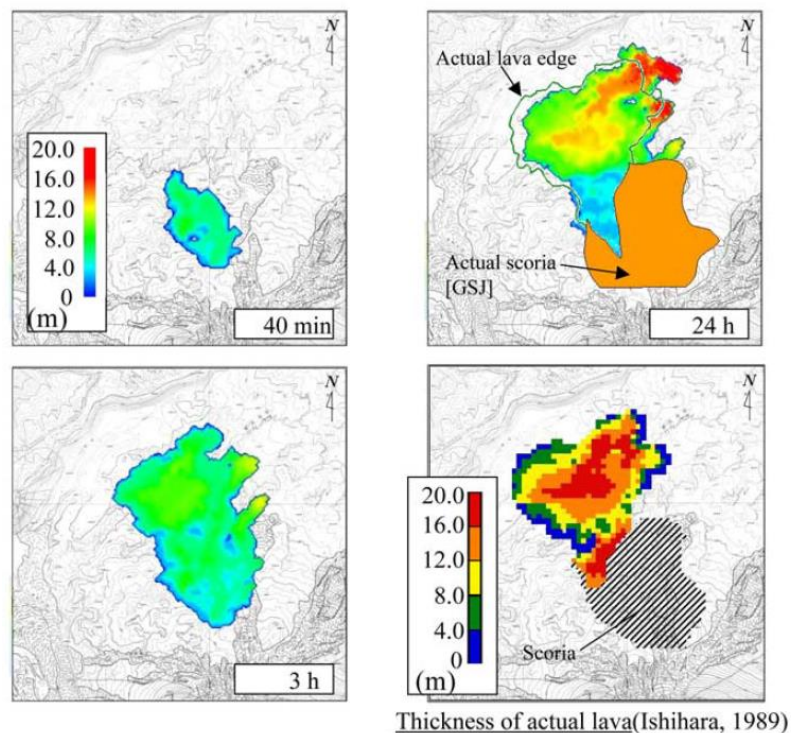


Figure 3.9 Thickness distribution of the flow in time as a result of the simulation carried out by LavaSIM (Hidaka *et al.* 2005).

3.1.3 Depth-averaged models

Depth averaged methods use the shallow water equations (Barré de Saint-Venant 1871) which assumes that the horizontal length scale is much greater than the vertical one and neglects the vertical component (e.g. homogeneous flow properties are assumed throughout the vertical section). They can use a simple rheology as Newtonian but also some more complex ones such as Bingham or Herschel–Buckley.

Since many years shallow water equations have many applications related to hazard assessment as flood simulation (Burguete *et al.* 2002), tsunamis propagation (Heinrich *et al.* 2001), and lava flow simulations (Costa & Macedonio 2005; Kelfoun & Vallejo Vargas 2015, Bernabeu *et al.* 2016).

3.1.3.1 Costa and Macedonio (2005)

The 2D simplified model was developed by Costa & Macedonio (2005). It is based on the depth-averaged equations obtained by integrating mass, momentum and energy equations over the fluid depth, from the bottom to the surface. It considers the lava flow as channelized with a non-continuous roof and the top is a free surface open to the atmosphere. The model is based on some assumptions of the flow like: it has a small vertical scale relative to the horizontal one, it is homogeneous incompressible, it has hydrostatic pressure distribution and has slow vertical variations. These assumptions allow the authors to establish the shallow water equations for a uniform or gradually varied flow (Eq. 1-3, Costa & Macedonio 2005). The depth-average temperature can be calculated with the heuristic equation (Eq. 4, Costa & Macedonio 2005) which includes radiative, convective and conductive exchanges; and viscous heating. As the viscosity is highly dependent on temperature, the authors assume a simple exponential relationship for calculating the viscosity as a function of the temperature (Eq. 5, Costa & Macedonio 2005).

The lava flow modelling over an initially dry downstream region (dry bed problem) was approached following the methods described by Monthe *et al.* (1999). All the source terms in the governing equations were treated using a Godunov splitting method and, since as a simple explicit discretization leads to numerical instabilities all terms were discretized using a semi-implicit scheme.

The model from Costa & Macedonio (2005) was applied for Etna volcano for the second phase of the eruption, which occurred from the 3rd until the 10th January 1992. The model was capable to reproduce semi quantitatively the behavior of the real lava flow and the order of magnitude of thickness, temperature and the time of front propagation of the lava flow (Fig. 3.10, 3.11). Results show that radiative cooling is the main heat loss mechanism, conductive loss is comparable with convection cooling. The effect of viscous heating can be neglected in terms of mean lava temperature.

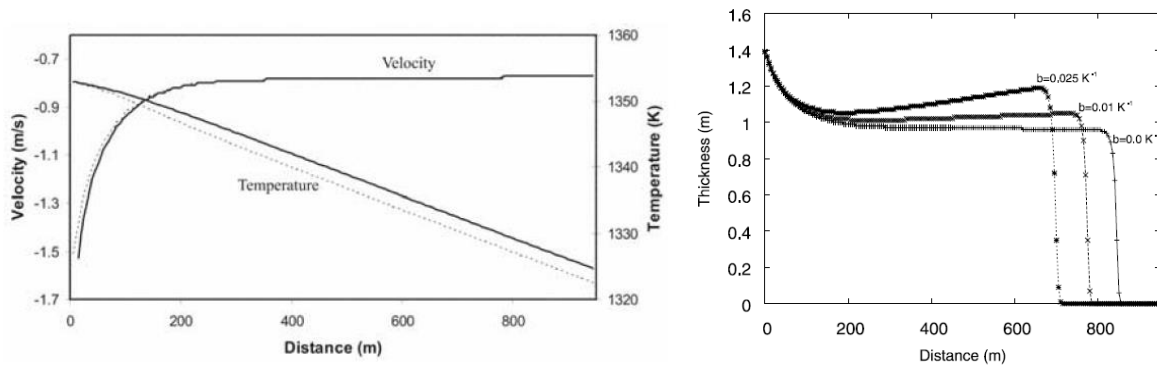


Figure 3. 10 Left: Longitudinal profiles of the channel center velocity and temperature, at $t = 2500 \text{ s}$. Dashed and continuous lines indicate analytical and numerical results, respectively. Right: Longitudinal thickness profiles at $t = 1200 \text{ s}$ (Costa & Macedonio, 2005)

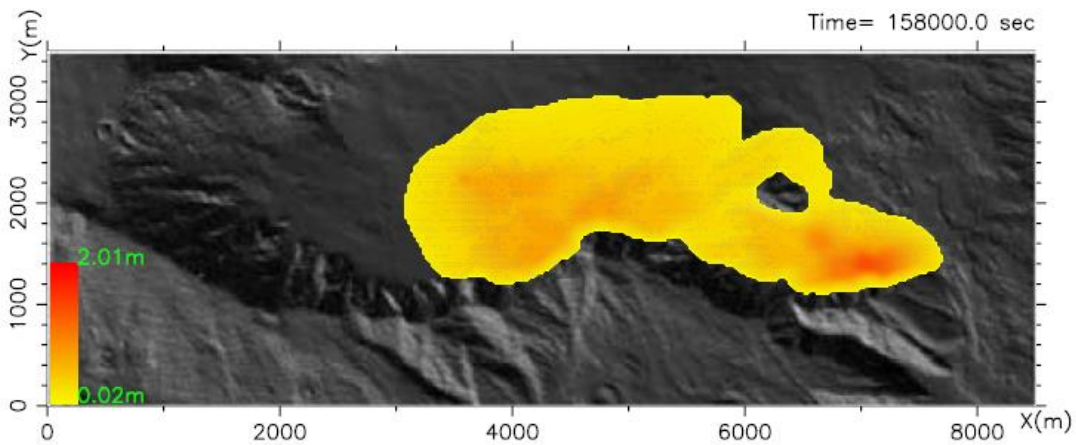


Figure 3. 11 Simulated lava thickness of the 3rd and 4th January 1992 Etna lava flow (Costa & Macedonio, 2005).

This model can reproduce the analytical solutions and is able to simulate real lava flow events (e.g. 1991-93 Etna eruption). Nevertheless, the model does not consider the crystallization and crystallinity-dependence of the viscosity. The main limit during the computing of the model is related to the given numerical treatment used for the source terms arising from topography and viscous friction. Due to the abrupt variations in the topographies, the slope term used in eq. 2 and 3 (Costa & Macedonio 2005) can become infinite generating numerical oscillations, diffusion, smearing and non-physical solutions.

The Costa & Macedonio (2005) approach is one of the most complete deterministic models because it includes the radiation, convection and conduction as heating mechanisms involved in the heat budget. Nevertheless, no formal effect of crystallization of the lava is

included in the model, the authors mentioned that it is implicit in the calculation of the viscosity which depends on the temperature.

3.1.3.2 VOLCFLOW (Kelfoun & Druitt 2005)

This is a finite-difference Eulerian code based on the depth-averaged approach and developed for the simulations of isothermal geophysical flows. This code has been used for the present research and is widely explained in Chapter 4.

3.1.3.3 Code from Bernabeu *et al.* 2016

Developed by Bernabeu *et al.* 2016, this code is an approach used to resolve the shallow-depth approximation for three-dimensional non-isothermal viscoplastic flow on a pre-described topography, while incorporating a temperature-dependent consistency index and yield strength measure. An asymptotic analysis allows a three-dimensional flow scenario to be reduced to a two-dimensional problem using depth-average equations (Bernabeu *et al.* 2016). It is based on the Rheolef C++ finite element library (Saramito 2013), which allows economy of computational time.

This shallow-depth averaged model is based in some assumptions:

- ❖ Flow can be described by viscoplastic Herschel-Bulkley behavior
- ❖ The flow is laminar
- ❖ There is a thin film approximation
- ❖ Temperature can be modelled by a polynomial function in the vertical direction

Heat loss of the flow is based on radiation, convection and conduction. The model considers a flow over a variable topography as erupted from a feeding vent that feeds a flow that then undergoes cooling. The rheology of the flow is assumed to have a Bingham behavior meanwhile fluid viscosity and yield strength follow an Arrhenius law from Dragoni (1989).

This code was tested making simulations with data obtained from an experimental dome carried out by Garel *et al.* (2012) and from the 2010 lava flow from Piton de la Fournaise. For the first case, they use the experiment C14 (Garel *et al.* 2012) which corresponds to a silicone oil dome (Newtonian behavior). By comparing the steady-state surface temperature versus the radius of the simulations and real data they found a good resemblance between those results.

For the December, 9 and 10th 2010 lava flow from Piton de la Fournaise (La Reunion, France) various simulations were carried out by using different values of lava viscosity at the initial temperature of the fluid, lava yield stress at the initial temperature of the fluid, constant viscosity Arrhenius law and constant in yield stress Arrhenius law in order to find the best fit of the simulation with the actual real lava (Fig. 3.12).

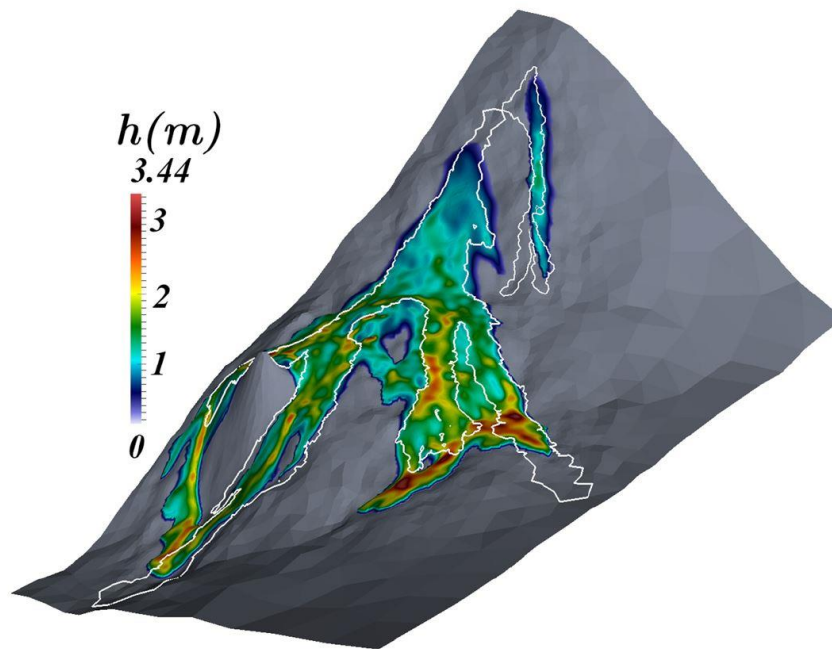


Figure 3. 12 Simulation of the December, 2010 lava flow from Piton de la Fournaise. The figure presents the comparison between the simulation (colorful deposit) and the real deposit (white line polygon). The scale represents the thickness of the simulated flow (From Bernabeu *et al.* 2016).

This model does not take into account solidification, in this case the flow ends even if the flow is still fluid enough to deform, once supply has been cut. The flow stops when yield strength reaches strain rate. Discrepancies between the model and the real deposit are related to the overestimation of the deposit in some places, in some parts the deposit is wider than the real one, and the simulation present some bifurcations. Bernabeu *et al.* (2016) mention that these discrepancies could be a result of the lack of information about the 2010 lava flow such as vent positions and flow rates during the emission period. They found that those parameters were found to slightly influence the final results. The resolution of the DEM could be a cause of the bifurcations of the flow. Another cause can be the absence of the vertical variation of the temperature. This code doesn't consider the crystallization and the thickness variation has no resemblance to the original flow, results of the simulation being higher in the center and shortest at the edges.

3.1.4 Generic 3D computational fluid dynamics codes

Computational Fluid Dynamic codes (CFD) are used in volcanology to predict the flow advance. Nowadays many tools are available to the community, nevertheless it is important to consider that for lava flow simulation, it is possible that those models can require additional capabilities that are not always built-in the code; such as crystallization effects; complex topography, variable effusion rates, complex rheology including both viscous and brittle components, and the strong temperature dependence of physical properties (Cordonnier *et al.* 2015).

3.1.4.1 OpenFOAM

The OpenFOAM code which means ‘Open Field Operation And Manipulation’ is a finite-volume method. It is a C++ open source that can handle complex fluids, chemical reactions, turbulence, heat transfer, solid mechanics and electromagnetics. It can be used as a standard simulation package with their own capabilities, and also users can add new equations, solvers and applications. OpenFOAM is fully parallelized using OpenMPI, it is convenient to simulate moving flows and has interfaces with external meshing that can incorporate a DEM. Dietterich *et al.* (2017) used OpenFOAM with the aim to develop a fully 3D lava flow model. They incorporated viscous flow standard multiphase flow solver in OpenFOAM with the aim to solve the temperature field, thermal interaction with the substrate, and a temperature-dependent viscosity.

3.1.4.2 FLOW-3D

The FLOW-3D code is a commercial software distributed by Flow Science Inc. with emphasis on computational fluid dynamics. It is based on Finite Volume and Volume-of-Fluid algorithms, combined with interface tracking tools. FLOW-3D can simulate all types of heat transfer, as well as porous, two-phase and viscous flows. It is capable as well to model a range of rheologies, including those that depend on temperature and/or strain rate. FLOW-3D can simulate the flow over real topography. The two main downsides for this code are its slow speed and high price.

3.1.4.3 COMSOL

COMSOL® is a commercial multiphysics finite element modeling software which excels in solving problems with several partial differential equations representing different physical fields. Dietterich *et al.* (2017) use the partial differential equations solving module from COMSOL to simulate the idealized viscous flow driven by gravity, for this purpose they use the depth-average approach following Lister (1992). This approach is capable to simplify a 3D problem to 2D reducing in that way the computational requirement. Heat loss of the flow can be obtained only by convection and radiation at the surface. The variation of temperature and viscosity is ignored and the model cannot simulate lava flows that overcome obstacles. The averaged viscosity is derived from the temperature dependent rheology model.

3.1.5 Messless and ‘bottom-up’ methods

3.1.5.1 GPUSPH

The GPUSPH code developed by Bilotta *et al.* (2016) is the latest version of the code previously implemented by Herault *et al.* (2009, 2011). It is a fully three-dimensional model which simulates the thermal and rheological evolution of lava flows. Considering the free surface, the irregular boundaries represented by the topography, the solidification fronts and the non-Newtonian rheology with temperature-dependent parameters. It is based on the Smoothed Particle Hydrodynamics (SPH) numerical method to discretize the 3D Navier-Stokes equations that describe the dynamics of flow evolution. It can assume a Newtonian behavior but as well a non-Newtonian behavior with temperature-dependent rheological parameters, capturing in that way the coupling between the dynamic and thermal features of the flow. It is based in the fundamental equations of fluid dynamics: the continuity equation which represents the conservation of mass (Eq. 1, Bilotta *et al.* 2016), the Navier-Stokes equation that models conservation of momentum (Eq. 2, Bilotta *et al.* 2016), and either the incompressibility condition or an equation of state. The equation that couples the motion and heat is also implemented, which describes conservation of energy (Eq. 3, Bilotta *et al.* 2016). For viscosity, the Herschel-Bulkley rheological model was implemented.

The SPH numerical method is based on a spatial discretization of the fluid with a set of particles each carrying information about the properties (such as mass, density, temperature) of a portion of the modelled fluid. The motion of the particles and the evolution of their properties are

described by a discretization of the equations describing the physics of the continuous problem; which in the case of lava flows are the Navier-Stokes equations and the heat equation.

The SPH discretization of the equations that describe the evolution of lava flows is built in the GPUSPH model builds, those equations are: the mass continuity equation, the heat equation and the momentum equation. Boundary conditions for the interaction of the lava flow with the ground, and for free surface of the flow complement those equations. The heat equation (Eq. 26, Bilotta *et al.* 2016) consists in a conductive part following Cleary & Monaghan (1999) and viscous heating by Cleary & Ha (2003).

The GPUSPH code has been tested using high resolution DEM of Mount Etna volcano (Italy) and the values of physical parameters that represent the typical ones for Etnean lava. Tests were carried out simulating a Newtonian flow with constant viscosity, Bingham and Hershel-Bulkley models (Bilotta *et al.* 2016). Other applications have been carried out by Zago *et al.* (2016) and Ganci *et al.* (2016) for Etna volcano eruptions.

The GPUSPH model is a low cost high performance parallel computing hardware which includes conduction and viscous heating as the mechanisms that control the heat budget in the flow, at the same time it does not consider the crystallization effect.

3.1.5.2 NB3D

The NB3D code developed by Cordonnier (2015) is an SPH algorithm with similar physical grounds to the one described by Herault *et al.* (2011) and explained in the GPUSPH code (Section 3.1.5.1, this Chapter). It has been implemented in MATLAB structure and tested as a benchmark in Cordonnier *et al.* (2015). There are only few examples of this application which are not developed here.

3.2 Stochastic or probabilistic numerical codes

Stochastic or probabilistic numerical codes do not consider the physics of the system at a local scale (e.g. the effect of the crystallization in the cooling process) but at large scale (i.e. the evolution of the system as a whole). The inner dynamics of the flows (i.e. thermal and rheological properties) are not taken into account in these codes. They are developed on the fact that lava flows tend to follow the steepest descent path of the pre-emplacment topography (Tarquini & Favalli 2016).

The progression of real lava flows that stochastic codes proposed is based on the insertion of a perturbation of the steepest descent path. Some models have been proposed in the last years, as from Felpeto *et al.* 2001; Favalli *et al.* 2005; and the main difference between them is the algorithm that they use to perturb this path.

Stochastic codes need only the calibration of a few parameters and they promptly yield results which are often representative of a wide spectrum of possible events. The system's state is not described by unique values but, rather by probability distributions. These models are only determined by the DEM and must account for potential errors between the available DEM's and the real topography.

For the most simplified version, stochastic models are not bound by the criteria to halt the flow advance. They are unable to present a time-evolution or downslope limit of the flow but may be used to generate hazard flow maps and to evaluate the impact of counter-measures to deviate lava flows. Stochastic approach cannot predict the spatial extent of flow through time, nor its thickness nor its final emplacement (Bernabeu *et al.* 2016).

3.2.1 DOWNFLOW

This model was developed by Favalli *et al.* (2005) and then after improved by Tarquini & Favalli (2011, 2016) with the aim to simulate the inundation area of the exposed basaltic lava flows. It considers the fact that lava flow emplacement is mostly controlled by the topography, in the sense that the flow tends to follow the steepest descent path downhill from the vent. In the code, lava flow is treated as a relative slow, gravity-driven mass movement over a surface. The input data that DOWNFLOW requires to run is the DEM of the volcano and the location of the vent. Lava flows simulations are based on:

- ❖ the steepest slope control on the flow
- ❖ a flow spreading, based on a stochastic perturbation of the volcano topography

with the aim to evaluate the maximum slope path on a given terrain. This model computes the possible inundated area by lava flows by deriving a number N , which represents the steepest descent paths (SDP) and each path is calculated over a randomly perturbed topography (Fig. 3.13). The result is a single path which represents the steepest gradient from the source point (i.e. the vent). At each grid point stochastic perturbations are introduced and a “new” path is

evaluated and ranges within the interval $\pm \Delta h$. Then N and Δh are the two basic parameters of the code.

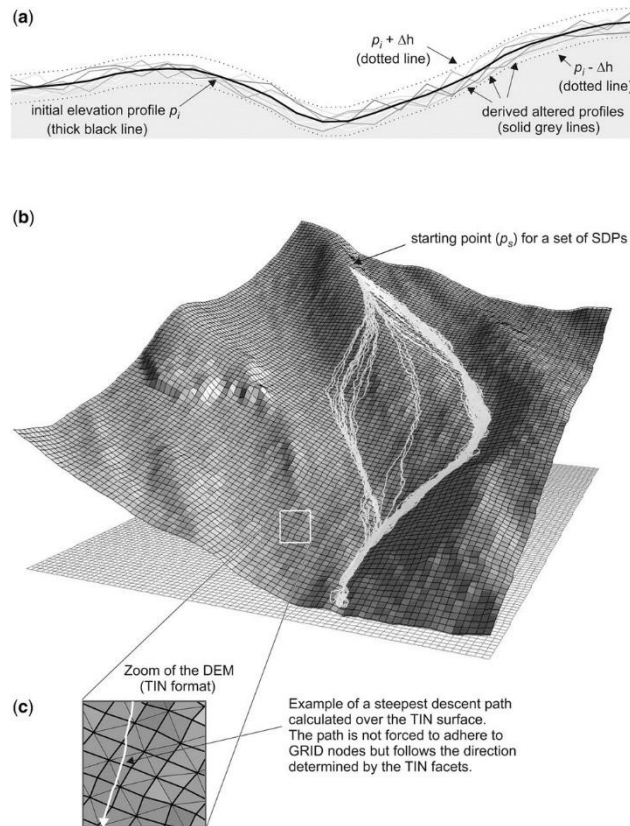


Figure 3. 13 Schematic illustration of the algorithm used by DOWNFLOW to trace the steepest descent paths (SDPs) (a) Conceptual scheme of the perturbation of the topography within $\pm \Delta h$. (b) 3D view of a portion of topography with 100 SDPs obtained from a given point. The 3D mesh representing the topography is a TIN (Triangular Irregular Network), and (c) is a zoom showing the TIN triangles and an example of an SDP calculated in vector form over the TIN surface. (After Favalli *et al.* 2012).

This stochastic code turns out to be simple, fast and undemanding, proving to be ideal for systematic hazard and risk analyses, also results in the prediction to the paths followed by lava flows. The validation of the simulation results is obtained by the comparison between the area covered by the simulation output and the area covered by the corresponding actual lava flow. DOWNFLOW has been used for the analysis of the changing probability of lava flow inundation with time or space as input conditions change.

This code has been broadly tested in Etna volcano (Favalli *et al.* 2005; 2009; Tarquini & Favalli 2011, 2016; Tarquini *et al.* 2013), Nyaragongo (Favalli *et al.* 2005, 2009; Chirico *et al.* 2009) and in Mt Cameroon (Favalli *et al.* 2012). One of this results is the probability map of lava flows by flank eruptions which was developed for Mount Etna by Tarquini & Favalli (2016), Fig. 3.14.

The numerical code DOWNFLOW needs a limited volcanological knowledge at a given volcano to simulate lava flows. As well this code only needs the position of the main vents to provide directly an output which is representative of a rather wide spectrum of possible events without any assumption on TAD; emplacement mechanisms duration and so forth. It is computationally efficient. Each simulation can take few seconds on a general one processor pc or laptop. DOWNFLOW represents an efficient and robust real-time tool for hazard assessment.

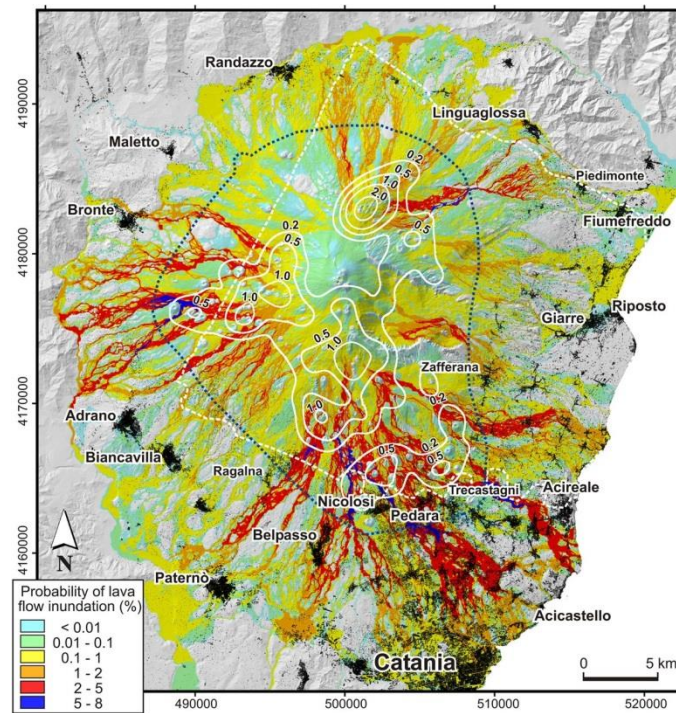


Figure 3. 14 Map of probability of lava-flow inundation by flank eruptions at Etna volcano (From: Tarquini & Favalli 2016).

On the other side the main limit of this code is that it does not provide any information about the velocity of advance. As well it is not possible to forecast the expected runout of an ongoing flow. Nevertheless, it is possible to couple DOWNFLOW with a thermo-rheological model like FLOWGO (Harris *et al.* 2015).

One of the latest application of this code is the probabilistic lava flow hazard at Fogo volcano (Cabo Verde) by Richter *et al.* (2016) for the 2014-2015 eruption. By the comparison between the pre and after DEM's of the zone they calculate the total volume of the flow emitted in that period of time and through the running of thousands of simulations with DOWNFLOW they assess to determine the lava flow hazard before and after the 2014-2015 eruption. They

called the attention that an up-to-date of the topographic information is needed in order to assess lava flow hazards.

3.2.2 Q-LavHA

The code Q-LavHA (Quantum-Lava Hazard Assessment) developed by Mossoux *et al.* (2016), is a free QGIS plugin (<http://we.vub.ac.be/en/q-lavha>) which was created with the aim to simulate channelized ‘a’a lava flow inundation probability from one or regularly distributed eruptive vents on a DEM. The combination of several existing probabilistic (e.g. Felpeto *et al.* 2001) and deterministic models (e.g. Harris & Rowland 2001) in Q-LavHA allows the user to determine the spatial propagation of the flow and its terminal length on a DEM. The eruption sources can be defined by the user as a point, a line or a surface area. The probabilistic model proposed by Felpeto *et al.* (2001) has been chosen to be improved in Q-LavHA. The flow begins to flow from the vent and the code assumes that the flow propagates through the DEM from one source pixel to one of its eight surrounding pixels. The code includes the probability of propagation implying that pixels with higher elevation differences obtain higher probabilities. In that way the flow line is more likely to follow the steepest slope path (Eq. 8, Mossoux *et al.* 2016). The code includes corrective factors that enable the lava to overcome small topographical obstacles or pits.

As to determine the maximum length is important for short-term forecasting, Mossoux proposed three alternatives:

1. Define a maximum length until where the lava can flow (e.g. by studying historical lengths flows).
2. Weight the probability of lava inundation of each pixel along a lava flow line based following Bonne *et al.* 2008 (Eq. 8, Mossoux *et al.* 2016), the flow stops when the weight factor is 0.15%.
3. Define the length based on the FLOWGO cooling-limited model (Harris & Rowland 2001), the flow stops when it reaches one of the three conditions (Section 3.1.1.1, this Chapter).

The result of the simulation is an integration of all the lava flow lines computed from one or multiple eruptive vents in which the number of those flow lines simulated from one vent is defined by the number of iterations defined in Q-LavHA. As a result of the simulation each pixel

is characterized by the probability of being inundated by lava. In this way, a defined threshold can help to keep only those pixels having probabilities higher than a certain value. Probabilities below that threshold are considered as noise and are then neglected. The accuracy of the simulated lava flow can be determined by the calculation of a fitness index. This index compares the simulated lava flow to a real lava flow (Favalli *et al.* 2009).

Q-LavHA was tested in two different lava flows using different resolution DEM's. The first case is the 2001 Mount Etna (Italy) lava flow which was repeatedly modelled by using different approaches, allowing the code to be well parametrized. The second case corresponds to the 2006 Nyamuragira (Democratic Republic of the Congo) lava flow.

The number of sufficient iterations for each simulation is important in order to have coherent results. A few number of iterations produces results not representative of the real lava flow inundation probability and flow spatial propagation meanwhile too many increases computational time. Mossoux *et al.* (2016) mention that in contrast to DOWNFLOW (Section 3.2.1, this Chapter), Q-LavHA does not need a large number of iterations to obtain a good fit between simulations and real flow. They propose that a number of 1500 iterations on average can stabilize a simulation bringing a good estimate of lava flow extension and computation time.

Based on the simulations for Etna and Nyamuragira flows they determine that the highest probabilities are located in the main channel of the real lava flow (Fig. 3.15). They conclude that the DEM's resolution used for the simulations has an important impact on the result. It can impact on the chosen probability threshold, the detail of the morphology and on the final length of the flow.

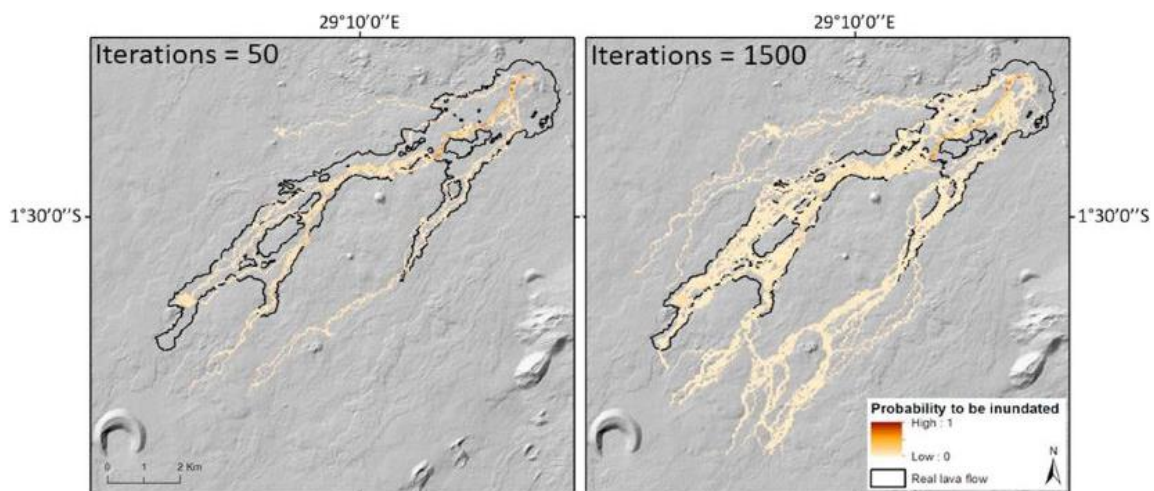


Figure 3. 15 Simulation of the Nyamuragira lava flow showing the result using 50 iterations (left side) and 1500 iterations (right side), (Mossoux *et al.* 2016).

Q-LavHA does not simulate the deposition of specific lava volume or thickness on each cell, thus it is not possible to simulate the temporal evolution of the topography induced by the lava emplacement. Q-LavHA uses simplifications from FLOWGO: heat loss by rain vaporization and heat gain from viscous dissipation are neglected, crystallization is considered as a linear function of the cooling.

3.3 Comparisons between models

One of the aims to test the validity of lava flow numerical codes is to evaluate their suitability for real-time forecasting, risk preparedness and post-eruptive response (Cordonnier *et al.* 2015). As mentioned before, one of the ways to test them is to compare the results of the simulation with a real flow (e.g. inundated area, shape, thickness, etc.). To do that it is important to have a well-studied lava flow, this means to have good record data since the flow is emitted until it is completely emplaced (i.e. thermo-rheological evolution, effusion rate, distribution over the surface).

Through the application of benchmarks, Cordonnier *et al.* (2015) and Dietterich *et al.* (2017) made the comparison between different numerical models. A benchmark couples a numerical code with a specific solution, which may be an analytical solution, an experimental measurement or a natural observation (Cordonnier *et al.* 2015).

3.3.1 Benchmark comparison by Cordonnier *et al.* (2015)

1. **Dam-break flow test (BM1 case):** It refers to an initial reservoir of isoviscous Newtonian ‘lava’ that is released and spreads on a flat surface. In this benchmark the simulation does not consider thermal interactions between the lava and its surroundings. This case was tested with VOLCFLOW, FLOW3D, OPENFOAM and NB3D codes.

Results of the simulations were determined based on the relationship between the front positions versus the time (Fig. 3.16). It shows that all of the codes present an asymptotic behavior at long times characterized by a front advancing with time with a power law of exponent $1/5$. The code VOLCFLOW generates a good match for short and long time periods meanwhile the codes OPENFOAM and NB3D shows divergences for short periods. Respect to the NB3D, results can be a response of the used algorithm and they can be improved by changing the parameters.

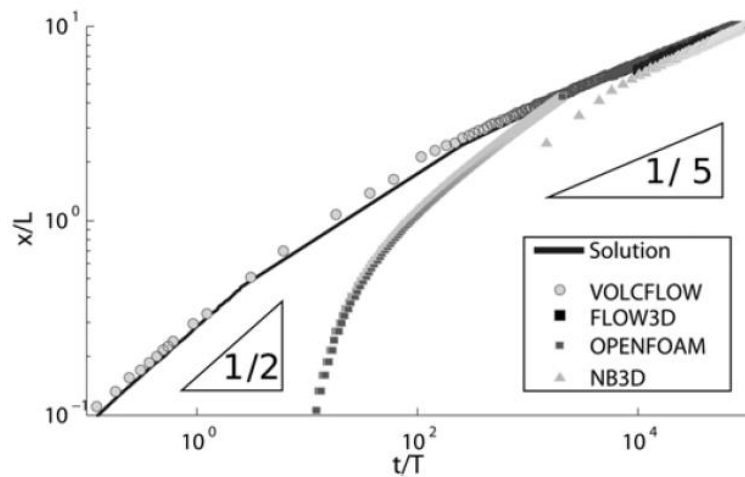


Figure 3. 16 Representation of the front position versus time for the real flow solution and the tested numerical codes (Cordonnier *et al.* 2015).

- 2. Real lava flow from Mount Etna, Italy (CCTC1 case):** This benchmark corresponds to the LSF1 lava flow of the 2001 eruption (Coltelli *et al.* 2007). It has been chosen as a study case because it is a well-studied lava flow. It was tested with DOWNFLOW, FLOWGO, MAGFLOW and VOLCFLOW (isothermal approach, Section 4.1, Chapter 4) codes.

For this benchmark, the comparison was made between the covered area of the real deposit and the simulations, Fig. 3.17. It represents the Boolean combination of the 2001 lava footprint (F) and the computed emplacement (C) based on: the intersection ($C \cap F$) shows the common ground between the calculation and the real flow (Fig. 3.17, green areas). The union ($C \cup F$) represents the total area covered by the calculation and the real flow (Fig. 3.17, red areas). The difference (F-C) represents the simulation (Fig. 3.17, blue areas). It is important to remark that results obtained with the different codes depend on their own objectives. The DOWNFLOW simulations covers the 92% of the real lava footprint and it largely overpasses its length and distribution. Simulations with FLOWGO covers the 98% of the calculated area. Results from MAGFLOW and VOLCFLOW codes show the highest intersection area between the simulations and the real flow even if the fundamentals of the codes have different numerical schemes.

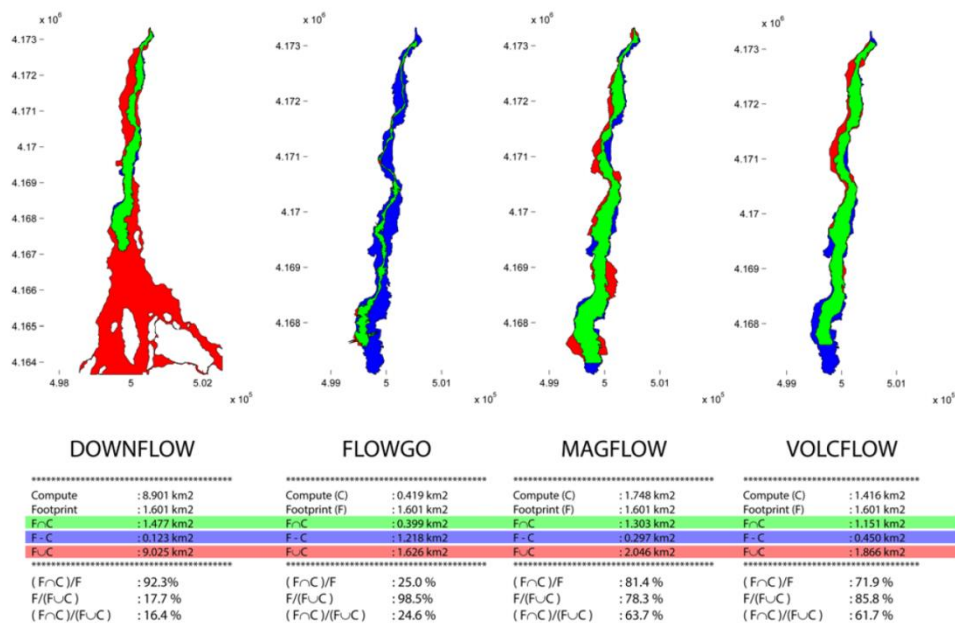


Figure 3.17 Comparison between the different tested numerical codes for CCT1. The different color represents the Boolean operation between the computed (C) and natural lava footprint (F). Green: common invasion areas ($C \cap F$), blue: underestimated are ($F - C$), and red: the union of the calculated and real flow areas ($C \cup F$). The combination between the blue and green polygons, results into the natural lava-flow outline (Cordonnier *et al.* 2015).

3.3.2 Benchmark comparison by Dietterich *et al.* (2017)

The comparison made by Dietterich *et al.* (2017) considers four benchmarks using three fluids as an analogues of lava flows (golden syrup, silicone oil and molten basalt). The proposed benchmarks (detailed below) were simulated with the OpenFOAM, FLOW-3D, VolcFlow, COMSOL and MOLASSES codes. The comparison was made based on numerous time-dependent flow properties as, down slope and cross slope propagation, flow thickness and surface temperature were done. Input parameters information is described in Dietterich *et al.* (2017), Table 1.

1. Isothermal, isoviscous sloping flow: isothermal, isoviscous flow of a Newtonian fluid which erupts from a point source onto a sloping plane with experiments from Lister (1992) and Dietterich *et al.* (2015).

Results show that OpenFOAM present the best approximations between the down and cross slope and flow thickness over long times meanwhile VolcFlow reproduces the early stages of flow evolution (Fig. 3.18).

2. Isothermal, isoviscous sloping flow into obstacles: same rheological characteristics of benchmark one but with an obstacle in its path which is a V-shaped triangle with different internal angles.

OpenFOAM, VolcFlow, COMSOL reproduced the flow but the accumulation before the obstacle is varied. For MOLASSES and FLOW-3D the thickness of the flow is varied depending on the angle of the obstacle (Fig. 3.19A).

3. Cooling, isoviscous axisymmetric flow: a hot Newtonian fluid is extruded from a point source onto a horizontal plane which cooled at ambient air temperature, corresponds to experiments from Garel *et al.* (2012).

For this benchmark all the models reproduce the observed axisymmetric flow spreading and capture the cooling of the flow through time (Fig. 3.19B).

4. Cooling, solidifying, sloping flow: pouring molten basalt at a constant flux onto a sloping plane from the Syracuse University Lava Project (Dietterich *et al.* 2015). See Section 4.1, Chapter 4 for more details about this experiment.

Results show that with OpenFOAM and FLOW-3D the solidification is approximated using a temperature dependent rheology. OpenFOAM captures the lateral spreading of the flow and overestimates the downslope propagation. FLOW-3D, VolcFlow and COMSOL simulate well the downslope propagation but they underestimated the flow width. The flow generated by MOLASSES is shorter and narrower than the experiment. Respect to the thickness of the flow, MOLASSES and FLOW-3D reproduces it well meanwhile for OpenFOAM, VolcFlow and COMSOL it is thinner than the observed (Fig. 3.20).

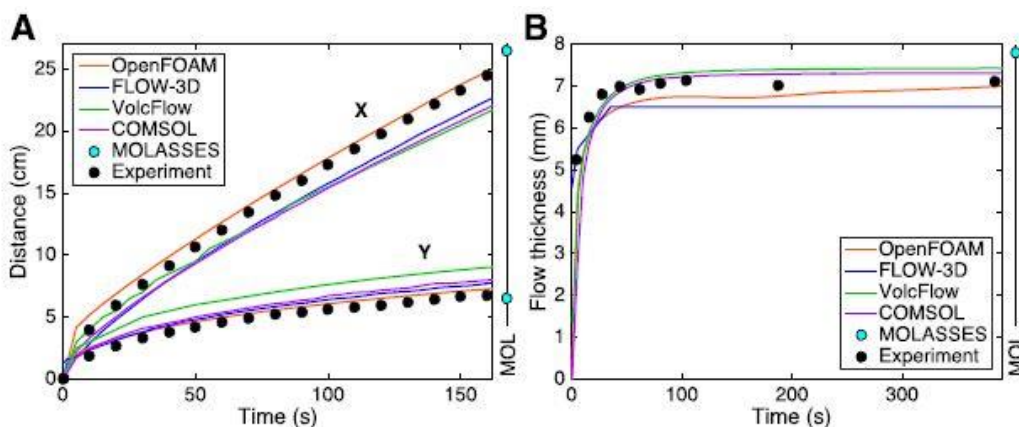


Figure 3. 18 (A) Flow propagation in X and Y with time. (B) Represents the flow thickness downslope of the vent with time when the flow reached the distance of 24.5 mm. (Dietterich *et al.* 2017).

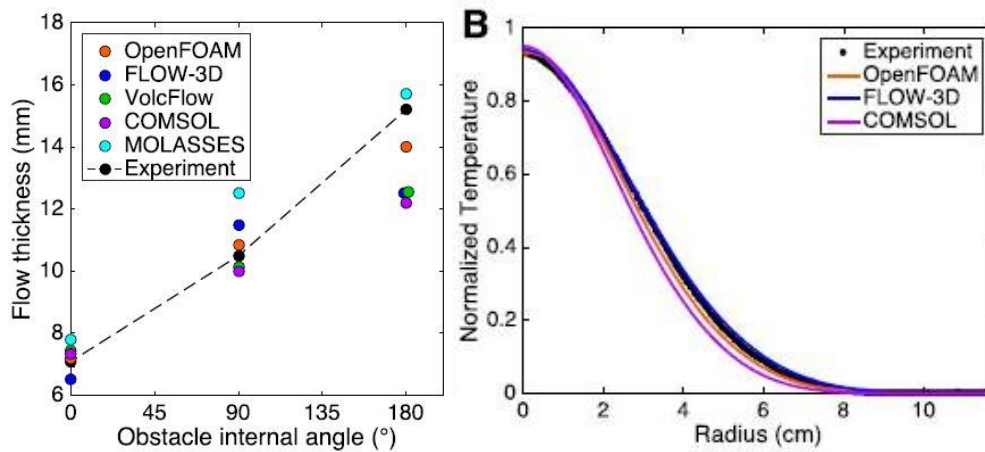


Figure 3. 19 Left: due to the obstacle incorporated in the slope, numerical codes constrain differently about them. The analysis includes internal angles of 0, 90 and 180. FLOW-3D and VolcFlow results are slightly shifted for the 180° obstacle in order to avoid direct overlap. Right: Normalized temperature profiles from Garel *et al.* (2012) and the models simulations (Dietterich *et al.* 2017).

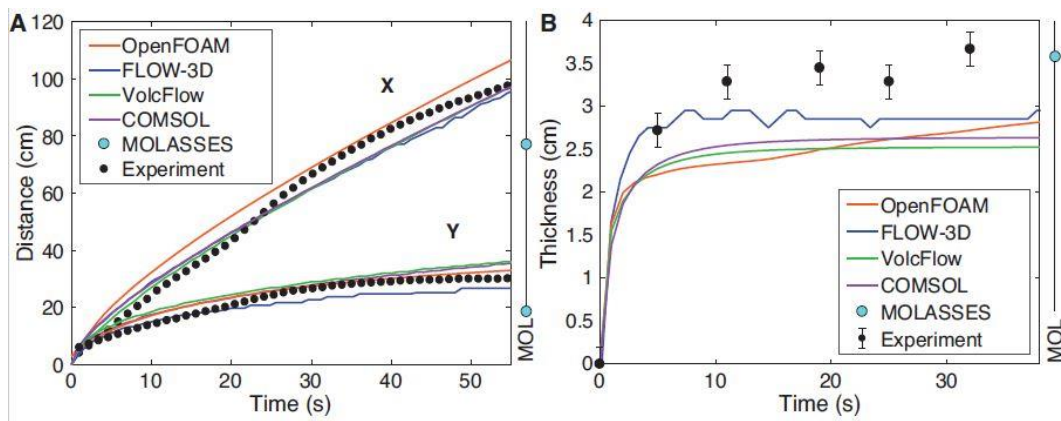


Figure 3. 20 Molten basalt benchmark experiments. (A) Flow advance from the down and cross slope propagation (B) thickness flow front measurements of the flow at 50 cm down in the slope (Dietterich *et al.* 2017).

3.4 Computational cost and time duration simulations

Another way to test the efficacy of a numerical code is to determine which provides accurate results at short duration and cheap computing costs. This fact is mostly important when a simulation is needed for hazard mitigation during an eruptive crisis.

Dietterich *et al.* (2017) has taken this point into account in their study based on the four benchmark comparison using experimental analogues lava flows. Five numerical codes have been used for this purpose (Section 3.3.2, this Chapter) and the effectiveness of their results was measured in computing cost and simulation time duration. This comparison does not consider the common or most known numerical models.

The automata code (MOLASSES) is the less computing consuming time, followed by the depth-average model (VolcFlow). A great computation time was registered by de computational fluid dynamics codes (OpenFOAM, FLOW-3D, COMSOL).

Time consuming can be related to the coding that has to apply to develop the scripts for the codes. VolcFlow, FLOW-3D and COMSOL use interfaces so they do not require time for coding which is not the case for OpenFOAM. MOLASSES does not require coding but just the DEM and the input parameter file. Fig. 3.21 shows the time computational consuming per each benchmark.

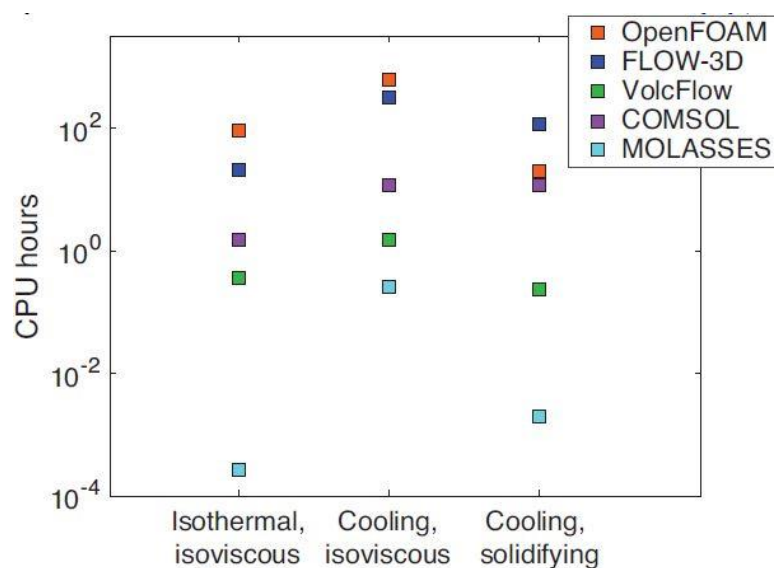


Figure 3. 21 Figure that represents the computational costs measured in CPU hours for each code and benchmark (Dietterich *et al.* 2017).

3.5 Model to be improved in VolcFlow

As it is shown in this review about the main numerical codes to simulate lava flows, it exists a large number of codes with different approaches and objectives to be reached. The interest to link the thermo-rheological effect in the simulations is getting more and more attention by scientists because more realistic simulations can be obtained.

Rheology of lava flows is controlled by the viscosity and yield strength as a result of the cooling and crystallization of the flow when it is spreading over the surface (Section 1.2, Chapter 1). Many models for the calculation of bulk viscosity, dynamic fluid and relative viscosity are available in the literature to be used or adapted according the needs of the applications (Section 1.3.2, Chapter 1). In the same way models for yield strength can be chosen and adapted (Section

1.3.4, Chapter 1). The main heat flux affecting lava flow are radiation, conduction, forced convection, viscous dissipation and crystallization; and even though it is important to consider them to simulate lava flows, their implementation in numerical codes is reduced. It is possible to find those mechanisms in channeled, cellular automata and depth averaged models; and in stochastic ones as an approach after the implementation deterministic models.

The aim of this review was to determine which numerical code has the most complete thermo-rheological laws in their structure in order to incorporate it in the code VolcFlow as a way to generate more realistic simulations of lava flows. The most complete is the deterministic code FLOWGO which includes a thermo-rheological law and all the mechanisms that affect the cooling are involved. In the same way this model allows to adapt viscosity and yield strength laws in the model. On the other side, the depth-average Costa & Macedonio (2005) code includes a thermo-rheological laws nevertheless it is not considering in our study.

Models from cellular automata include just few mechanisms, meanwhile yield strength and viscosity are not always considered as variables. The other models exposed here as generic 3D computational fluid dynamics are not adaptive to solve complex rheologies, or at least not the open source ones. On the other side the messless and bottom-up methods do not consider a complete thermos-rheological law for the simulation of lava flows. However, results of stochastic numerical codes are based on the number of iterations defined by the user and it can be adapted with deterministic codes, nevertheless many assumptions have to be made.

After the analysis of the codes, the advantages and disadvantages, it has been chosen that the thermo-rheological laws from the FLOWGO code are the ones to be adapted in VolcFlow to achieve the purpose of this study (Chapter 4).

Chapter 4

Numerical Modelling of Lava Flows: Methods

Before the work presented in the present manuscript, VolcFlow was not adapted for the simulation of lava flows because it did not take into account the temperature and its effect on the rheology of simulated flows. The aim of this chapter is to present how VolcFlow works, as well to show the modifications brought to adapt it to the lava flows. They are related to include the effect of the cooling in the parameters of the Bingham law. As well the formation of crust at the surface of lava flows has also been invoked to control their dynamics. In total, four approaches are proposed in this study and have been tested with four lava flow study cases (Chapter 5).

4.1 VolcFlow code, principles

VolcFlow is a numerical code developed for the simulation of volcanic flows. The initial version was tested to reproduce the emplacement of the debris avalanche (Kelfoun & Druitt 2005) and dense pyroclastic flows (Kelfoun *et al.* 2009). Then it evolves to take into account two fluids and their interactions: debris avalanche and sea water (simulation of tsunamis), or dense and dilute pyroclastic currents (Kelfoun *et al.* 2010; Kelfoun 2017). Another version models the gas diffusion through a granular medium to explain the high fluidity of pyroclastic flows (Gueugneau *et al.* 2017).

VolcFlow is a finite difference Eulerian code based on a depth-averaged resolution of mass and momentum balance equations (Kelfoun & Druitt 2005). Equation can be solved on a

complex natural topography (DEM, for example). Using a topography-linked co-ordinate system, with x and y parallel to the local ground surface and h perpendicular to it, the general depth-averaged equations of mass (Eq. 4.1) and momentum (Eqs. 4.2, 4.3) conservation are:

$$\frac{\partial h}{\partial t} + \frac{\partial}{\partial x}(hu) + \frac{\partial}{\partial y}(hv) = 0 \quad [4.1]$$

$$\frac{\partial}{\partial t}(hu) + \frac{\partial}{\partial x}(hu^2) + \frac{\partial}{\partial y}(huv) = gh \sin \alpha_x - \frac{1}{2} k_{actpass} \frac{\partial}{\partial x}(gh^2 \cos \alpha) + \frac{R_x}{\rho} \quad [4.2]$$

$$\frac{\partial}{\partial t}(hv) + \frac{\partial}{\partial x}(hvu) + \frac{\partial}{\partial y}(hv^2) = gh \sin \alpha_y - \frac{1}{2} k_{actpass} \frac{\partial}{\partial y}(gh^2 \cos \alpha) + \frac{R_y}{\rho} \quad [4.3]$$

where h is flow thickness, $\mathbf{u} = (u, v)$ is flow velocity, α is ground slope, \mathbf{R} is retarding stress, ρ is the bulk density of the lava flow, $k_{actpass}$ is the earth pressure coefficient (ratio of ground-parallel to ground-normal stress), and the subscripts denote components in the x and y directions.

The variable $\mathbf{R} = (R_x, R_y)$ expresses the basal shear stress, which varies according to the chosen rheology. For lava flows, we will use a Bingham rheology or a Newtonian viscosity and \mathbf{R} is defined by:

$$\mathbf{R} = R_0 + 3\eta \frac{\mathbf{u}}{h} \quad [4.4]$$

where R_0 is the yield strength (null for a Newtonian flow) and η is the dynamic viscosity. The basal shear stress depends on the flow velocity, viscosity and thickness): under the same conditions a thin flow will move more slowly than a thick one. For a Bingham flow ($R_0 > 0$) a plastic term is added to the viscous term. If driving stresses are lower than the yield strength, R_0 , the flow remain at rest. Once it is overcome, the mass begins to flow. Inversely, a flow that spreads out can be thin enough that the driving stress lowers below R_0 , stopping the flow. The value of R_0 influences the final thickness of the lava at rest.

Some main input parameters of the flow are needed to run VolcFlow, Table 4.1. They are related to its volume, time of the generation and emplacement of the flow and its rheological parameters (e.g. viscosity). It calculates two parameters, the velocity and the thickness.

Symbol	Notation	Units
vol	Volume of the flow	m^3
t_{alim}	Time of the effusion of the flow	s
t_{max}	Time of the emplacement of the flow	s
	Parameters related to the chosen rheology (e.g. viscosity, yield strength)	
	Topography (DEM)	

Table 4.1 Main input parameters to run the isothermal model in VolcFlow.

4.2 Considered rheologies in VolcFlow

In order to bring a broader field of applicability of VolcFlow, four approaches which consider different rheological conditions for lava flows are proposed. The number of the input parameters depends on the chosen rheology to be applied.

4.2.1 Model n°1: Isothermal

The isothermal model for simulating lava flows corresponds to the VolcFlow's original model (Section 4.1, this Chapter). As a first approach, it is possible to simulate a lava flow as a Bingham flow where both yield strength and viscosity are constant in time. This simplification, however, does not take into account the effect of the temperature that is known to affect drastically the lava emplacement.

The numerical scheme that solves the viscosity equations in VolcFlow was tested by Cordonnier *et al.* (2015) with other numerical models as FLOW3D, OPENFOAM and NB3D (Section 3.3, Chapter 3). This study shows a very good fit of VolcFlow as illustrated on Fig. 4.1.

As a natural case application using the isothermal model from VolcFlow it is possible to cite the simulation of an andesitic lava flow from the December 4th and 5th, 2010 from Tungurahua volcano (Ecuador) (Kelfoun & Vallejo Vargas 2015). By using the velocity of the front flow it was possible to calibrate the model to simulate an andesitic lava flow with a constant viscosity and yield strength along the motion of the flow. For more details of the flow and simulations check Section 5.3, Chapter 5.

The needed parameters to run the model with an isothermal model are detailed in Table 4.1.

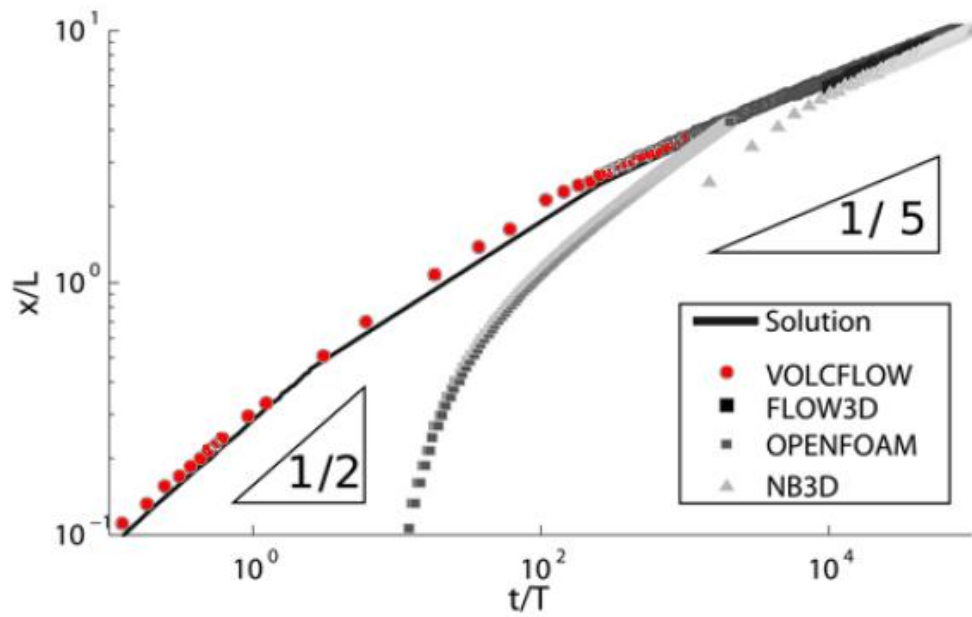


Figure 4. 1 Dimensionless front position versus dimensionless time. Note that symbols of FLOW3D are partly hidden by NB3D. The first output depends on each code setting for outputting files, and there is, for example, no data for early times for FLOW3D and NB3D (Cordonnier *et al.* 2015).

4.2.2 Model n°2: Thermorheological variation

This model takes the basics of VolcFlow which is the general depth-averaged equations of mass and momentum conservation (Section 4.1, this Chapter). Additionally, it incorporates and for the first time the effect of the heat budget, cooling, crystallization rate and a variable rheology along the emplacement of the flow. All of them are given by following FLOWGO model from Harris *et al.* (2015), (Section 2.2.3, Chapter 2).

4.2.2.1 Heat budget, cooling and crystallization per unit of time

The heat budget and cooling model from FLOWGO (Harris & Rowland 2001; Harris *et al.* 2005, 2015b) is based on the heat budget for a lava control volume (Section 1.3.2, Chapter 1; Section 3.3.1, Chapter 3). Gain and loss heat fluxes, (Q_{in} and Q_{out} respectively) of the heat balance mechanism are obtained by multiplying the corresponding mechanism by the channel width. The balance is established via:

$$Q_{in} = Q_{out} \quad [4.5]$$

FLOWGO code assumes that the lava is being feeding with an effusion rate E_r into a channel of a depth h , a width w and a slope α (Fig. 4.2). It considers that the lava gains heat by

crystallization (Q_{cryst} , Eq. 1.11, Chapter 1) and loss heat by radiation (Q_{rad} , Eq. 1.2, Chapter 1), convective force (Q_{force} , Eq. 1.6, Chapter 1) and conduction (Q_{cond} , Eq. 1.10, Chapter 1) as:

$$Q_{cryst} = Q_{rad} + Q_{force} + Q_{cond} \quad [4.6]$$

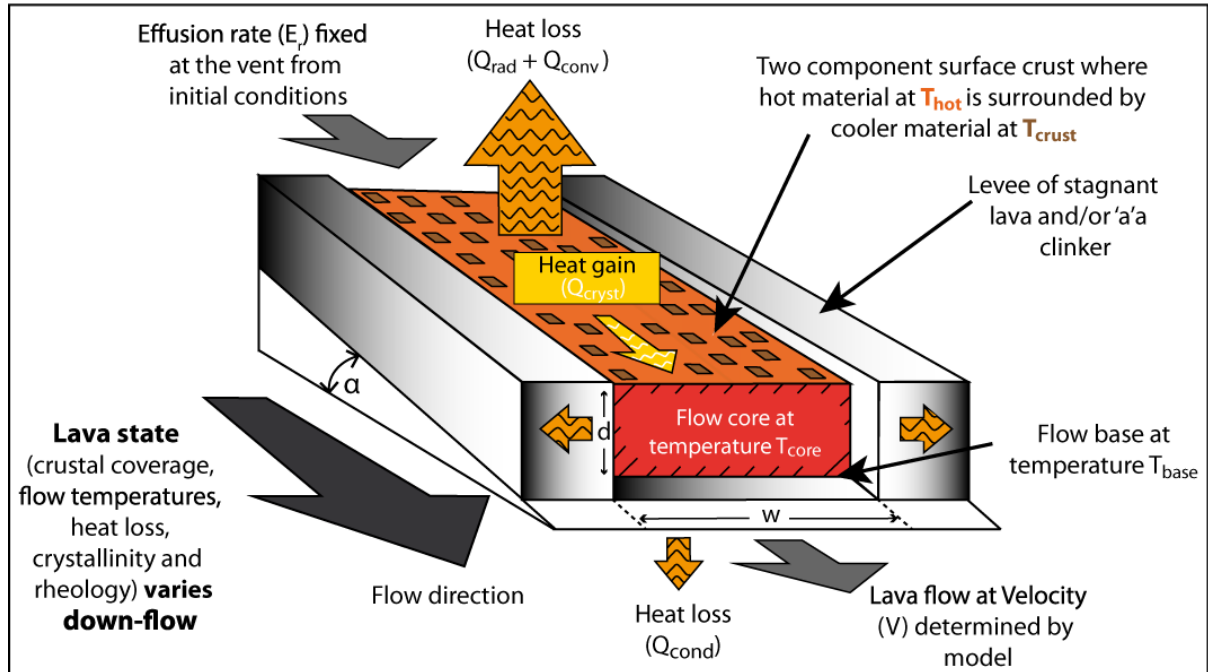


Figure 4. 2 Schematic lava flow heat loss and heat gain considering a channelized lava flow. The flow is losing heat by radiation, force convection and conduction, and gaining by crystallization (Modified from Harris & Rowland 2001).

The cooling ($\frac{dT}{dx}$ [K m⁻¹]) and crystallization ($\frac{d\phi}{dx}$ [m⁻¹]) rates are calculated by replacing Eq. 1.11 (Section 1.3, Chapter 1) in Eq. 4.6, obtaining cooling and crystallization per unit of distance, Equations 4.7 and 4.8 respectively. It is necessary to multiply Q_{rad} , Q_{force} and Q_{cond} by the width of the channel of the flow (w), in order to obtain their fluxes.

$$\frac{dT}{dx} = \frac{(+Q_{rad} + Q_{force} + Q_{cond})w}{E_r \rho L \frac{d\phi}{dT}} \quad [4.7]$$

$$\frac{d\phi}{dx} = \frac{(+Q_{rad} + Q_{force} + Q_{cond})w}{E_r \rho L} \quad [4.8]$$

where E_r is the eruption rate, ρ is the density of the lava, L is the latent heat of crystallization and $\frac{d\phi}{dT}$ is the fractional crystallization per degree of cooling.

Knowing that VolcFlow code is a time-dependent model, it implies that the equations from FLOWGO (Eqs. 4.7 and 4.8) need to be transformed in order to be able to calculate the cooling and crystallization rate per unit of time. The process of the transformation of the equations is shown in the following lines.

4.2.2.1.1 Cooling from per unit of time:

In this section Eq. 4.7 which corresponds to the cooling rate per unit of time, is being modified to calculate the cooling per unit of time. In order to obtain the variation of the temperature through time it is possible to use de chain rule, which means that the variation of the temperature of a fragment of lava can be expressed in terms of the spatial variation of temperature and the mean velocity of the flow as it is expressed in Eq. 4.9:

$$\frac{dT}{dt} = \frac{dT}{dx} \frac{dx}{dt} \quad [4.9]$$

knowing that

$$v = \frac{dx}{dt} \quad [4.10]$$

it is possible to replace Eq. 4.10 in 4.9. This allows to get $\frac{dT}{dx}$ as a relationship between the variation of temperature per unit of time and the inverse of the velocity as:

$$\frac{dT}{dx} = \frac{dT}{dt} \frac{1}{v} \quad [4.11]$$

The effusion rate (E_r , Eq. 4.12) which represents the relationship between the deep (h) and width (w) of the channel and the velocity (v) of the flow is replaced in Eq. 4.7 together with Eq. 4.11.

$$E_r = h w v \quad [4.12]$$

in this step, v and w are completely eliminated from the equation (Eq. 4.13) as

$$\frac{dT}{dt} \frac{1}{v} = \frac{(+Q_{rad} + Q_{force} + Q_{cond}) w}{h w \rho L \frac{d\phi}{dT}} \quad [4.13]$$

With all this simplifications, the cooling of the flow per unit of time is setting as a relationship between radiation, convective force, conduction and the deep of the channel, the density, the latent heat of crystallization and the fractional crystallization per degree of cooling (Eq. 4.14).

$$\frac{dT}{dt} = \frac{+Q_{rad} + Q_{force} + Q_{cond}}{h \rho L \frac{d\phi}{dT}} \quad [4.14]$$

4.2.2.1.2 Crystallization per unit of time:

The crystallization per unit of time can be obtained by using as well the chain rule, in which the variation of the crystal content of a fragment of lava can be expressed in terms of the spatial variation of crystal content and the mean velocity of the flow (Eq. 4.15).

$$\frac{d\phi}{dT} = \frac{d\phi}{dx} \frac{dx}{dt} \quad [4.15]$$

Eq. 4.11 is being replaced in Eq. 4.15 having that the fractional crystallization per unit of distance $\frac{d\phi}{dx}$ is a relationship between the fractional crystallization per degree of cooling and the inverse of the velocity, Eq. 4.16.

$$\frac{d\phi}{dx} = \frac{d\phi}{dT} \frac{1}{v} \quad [4.16]$$

Eruption rate (Eq. 4.12) and Eq. 4.16 are both replaced in Eq. 4.8. With this, v and w are eliminated completely from Eq. 4.17.

$$\frac{d\phi}{dx} \frac{1}{v} = \frac{(+Q_{rad} + Q_{force} + Q_{cond})w}{d w \rho L} \quad [4.17]$$

By following this steps the fractional crystallization per unit of time can be set as a relationship between radiation, convective force, conduction and the deep of the channel, the density of the flow and the latent heat of crystallization (Eq. 4.18).

$$\frac{d\phi}{dt} = \frac{+Q_{rad} + Q_{force} + Q_{cond}}{h \rho L} \quad [4.18]$$

4.2.2.1.3 VolcFlow improvement with the cooling and crystallization equations

With the aim to model the advection of the hot lava in VolcFlow, it is needed to include two additional governing equations.

The first one is for thermal energy transportation:

$$\frac{\partial hT}{dt} + \frac{\partial}{\partial x}(hTu) + \frac{\partial}{\partial y}(hTv) = \frac{+Q_{rad} + Q_{force} + Q_{cond}}{d \rho L \frac{d\phi}{dT}} dx dy \quad [4.19]$$

where T is the temperature (K) of the lava and Q are the thermal fluxes ($J s^{-1}$) by square meter. The other terms are defined in Chapter 1. The thermal energy lost is related to the surface of each cell, $\partial x \times \partial y$.

The second one, rules the advection of the lava crystallinity, which also may influence strongly its rheology (Chapter 1).

$$\frac{\partial hC}{dt} + \frac{\partial}{\partial x}(hCu) + \frac{\partial}{\partial y}(hCv) = \frac{+Q_{rad} + Q_{force} + Q_{cond}}{d \rho L} dx dy \quad [4.20]$$

Figures 4.3 and 4.5 show how the model runs. No cooling is simulated and this test aims to check that the temperature is not affected by the spreading of the flow.

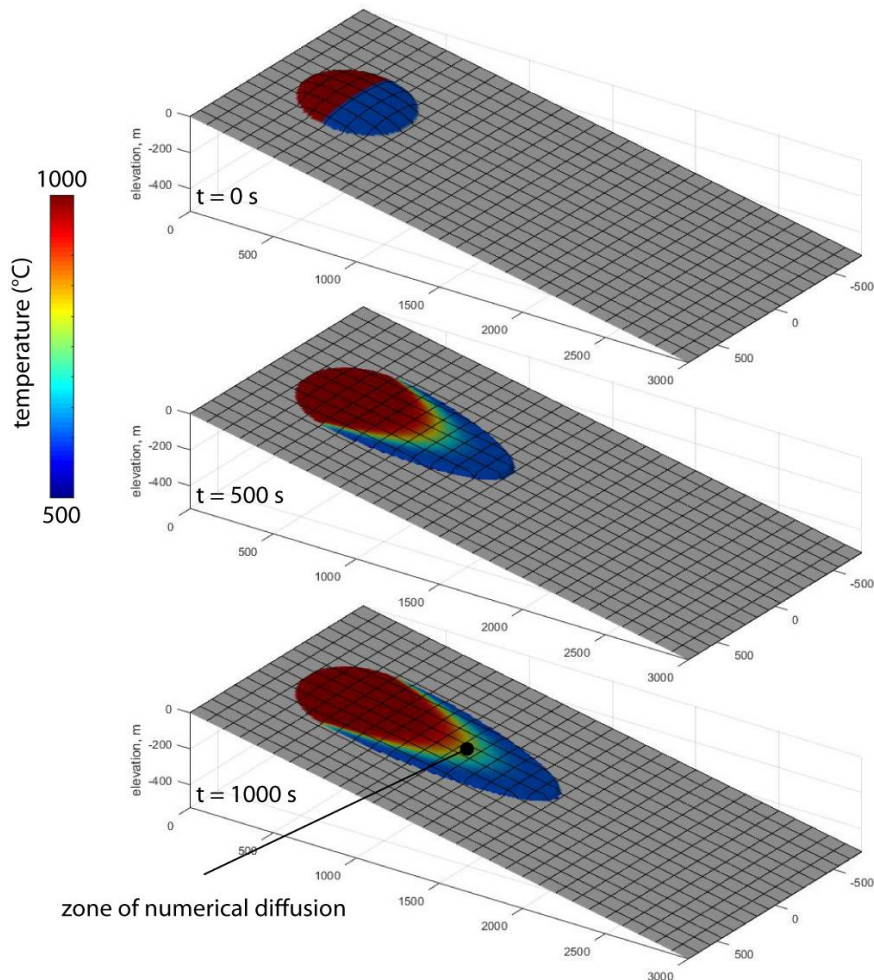


Figure 4. 3 An hemi circular Bingham fluid is released on a slope. The lava spreads out but the temperature remains constant.

For the calculation of the cooling and crystallization of the lava there are needed to know the value of 24 parameters noted in Table 4.2. Description of each of these parameters are shown in Chapter 1.

Symbol	Notation	Units	Symbol	Notation	Units
Cooling			Density and vesicularity		
<u>Radiation parameters</u>			<i>ves</i>	Vesicularity	--
σ	Stefan-Boltzmann	$W m^{-2} K^{-4}$	ρ_{DRE}	DRE density	$kg m^{-3}$
e	Emmissivity	--	<u>Thermal parameters</u>		
<u>Convection parameters</u>			<i>Buff</i>	Buffer (Th=Terupt-Buffer)	--
C_H	CH	--	T_c	Crust temperature	K
cp_{air}	Air specific heat capacity	$J kg^{-1} K^{-1}$	T_{core}	Core temperature	K
T_{air}	Air temperature	K	T_{solid}	Solid temperature	K
U	Wind speed	$m s^{-1}$	T_l	Liquidus temperature	K
ρ_{air}	Air density	$kg m^{-3}$	f	Crust cover	--
<u>Conduction parameters</u>			<u>Crystal parameters</u>		
h_{base}	hbase	m	L	Latent heat of crystallization	$K kg^{-1}$
K	Thermal conductivity	$W m^{-1} K^{-1}$	$\Delta\phi$	Crystals growing during cooling	--
cd	Core to base distance		ΔT	Cooling rate	K
h	Thickness	m	$\Delta\phi/\Delta T$	Rate of crystallization	K^{-1}
T_{base}	Basal temperature	K			

Table 4. 2 Input parameters to be established previously for the calculation of the cooling and crystallization of the lava.

In total there are calculating 7 variables in this model along the simulation of the flow (Table 4.3). They correspond to heat loss by conduction, convective force and radiation, core temperature, cooling and crystallization per unit of time, and crystal content.

Symbol	Notation	Units
Q_{cond}	Heat loss by conduction	$J s^{-1}$
Q_{force}	Heat loss by convective force	$J s^{-1}$
Q_{rad}	Heat loss by radiation	$J s^{-1}$
T_{core}	Core temperature	K
$\frac{\partial T}{\partial t}$	Cooling per unit of time	$K s^{-1}$
$\frac{d\phi}{dt}$	Crystallization per unit of time	K^{-1}
ϕ	Crystal content	--

Table 4. 3 Variables calculated during the simulation for the effect of the cooling.

4.2.2.2 Rheological variation

The model also depends on the thermo-rheological assumptions: how varies the viscosity and the yield strength vary with the temperature and the crystallization of the lava flow. In this study, we have tested 3 models.

4.2.2.2.1 Existing thermo-rheological models

Some existing relationships for calculating viscosity and yield strength are described in Section 1.3, Chapter 1. The calculation of both parameters in this proposed model uses relationships dependent on temperature, composition and crystal content. Bubble content relationship has not been included in the estimation of viscosity in the current research. The next lines show up the models for viscosity and yield strength that had been chosen to be incorporated in VolcFlow.

❖ **Viscosity:** as a relationship between the dynamic fluid and relative viscosity. Dynamic fluid viscosity corresponds to the viscosity of the fluid/melt phase and is dependent of the chemical composition (x) and internal temperature of the melt (T) meanwhile relative viscosity depends on the crystallinity (ϕ) and/or the bubbles content (β) in the magma. (Eq. 4.21).

$$\eta = \eta_f(x, T) * \eta_r(\phi, \beta) \quad [4.21]$$

a. Fluid dynamic viscosity: The VTF relationship with the Giordano & Dingwell (2003) approach (Eq. 4.22).

$$\log \eta_f = A + \frac{B}{T - C} \quad [4.22]$$

where η_f is the dynamic fluid viscosity, T [K] is absolute temperature and A , B and C are adjustable parameters depending of chemical composition and representing the pre-exponential factor, the pseudo-activation energy, and the VFT-temperature, respectively.

b. Relative viscosity: From Einstein (1906) & Roscoe (1952), and from Krieger & Dougherty (1959), (Eq. 4.23)

$$\eta_r = \left(1 - \frac{\phi}{\phi_m}\right)^{-2.5} \quad [4.23]$$

in which ϕ is the crystal content and ϕ_m is the maximum crystal content and represent the volume fraction at which the particles can no longer flow ($0 \ll \phi_m \ll 1$).

❖ **Yield strength:** From Dragoni (1989); Pinkerton & Stevenson (1992) (Eq. 4.24)

$$\tau_o(T, \phi) = a \left[\exp^{b(T_l - T)} - 1 \right] + \left[6500 \phi^{2.85} \right] \quad [4.24]$$

where T_l is the liquidus temperature, a and b are fitting parameters, and ϕ is the crystal content .

The input parameters for the calculation of the dynamic fluid and relative viscosity, and the yield strength are shown in Table 4.5. More details of these parameters in Chapter 1.

Symbol	Notation
<hr/> Dynamic fluid viscosity (Giordano et al. 2008) <hr/>	
VTF_A	Constant independant of composition
VTF_B	Adjustable parameter
VTF_C	Adjustable parameter
<hr/> Relative viscosity (Krieger & Dougherty 1967) <hr/>	
ϕ_{max}	Maximum packing
B	Einstein coeficient
<hr/> Yield strength (Dragoni 1989; Pinkerton & Stevenson 1992) <hr/>	
a	Constant
b	Constant

Table 4. 4 Input parameters for the viscosity and yield strength models

During the simulation of the flow, 4 variables are calculated for the rheological part of the equations (Table 4.6). They are the dynamic fluid viscosity, the relative viscosity, the bulk viscosity and yield strength.

Symbol	Notation	Units
η	Viscosity	Pa s
η_f	Fluid viscosity	Pa s
η_r	Relative viscosity	Pa s
τ	Yield strength	Pa

Table 4. 5 Variables to be calculated for the rheological section

4.2.2.2 Sigmoid law

The parameters of the complete models, however, are relatively difficult to estimate by trials and errors methods, due to their high number (35). Moreover, in some models, the viscosity is not defined for a range of temperature/crystallinity or tends toward infinite values. In order to simplify the estimation of the parameters we have developed a simpler law that mimics the behavior of the previous models and is defined for all the temperature values. For a sake of simplification, the crystallinity is not taken into account and, either the viscosity or the yield strength varies with the temperature, the other parameter being fixed to a constant.

The model is defined by Eq. 4.25 and represented by Fig. 4.4:

$$\eta = \eta_1 + \frac{\eta_2 - \eta_1}{1 + e^{-L(T-T_L)}} \quad [4.25]$$

and is based on 4 parameters:

- 1) The lowest viscosity η_1 (or yield strength) at high temperature;
- 2) The highest viscosity η_2 (or yield strength) at low temperature;
- 3) The transition temperature, T_L ;
- 4) The sharpness of the transition, L .

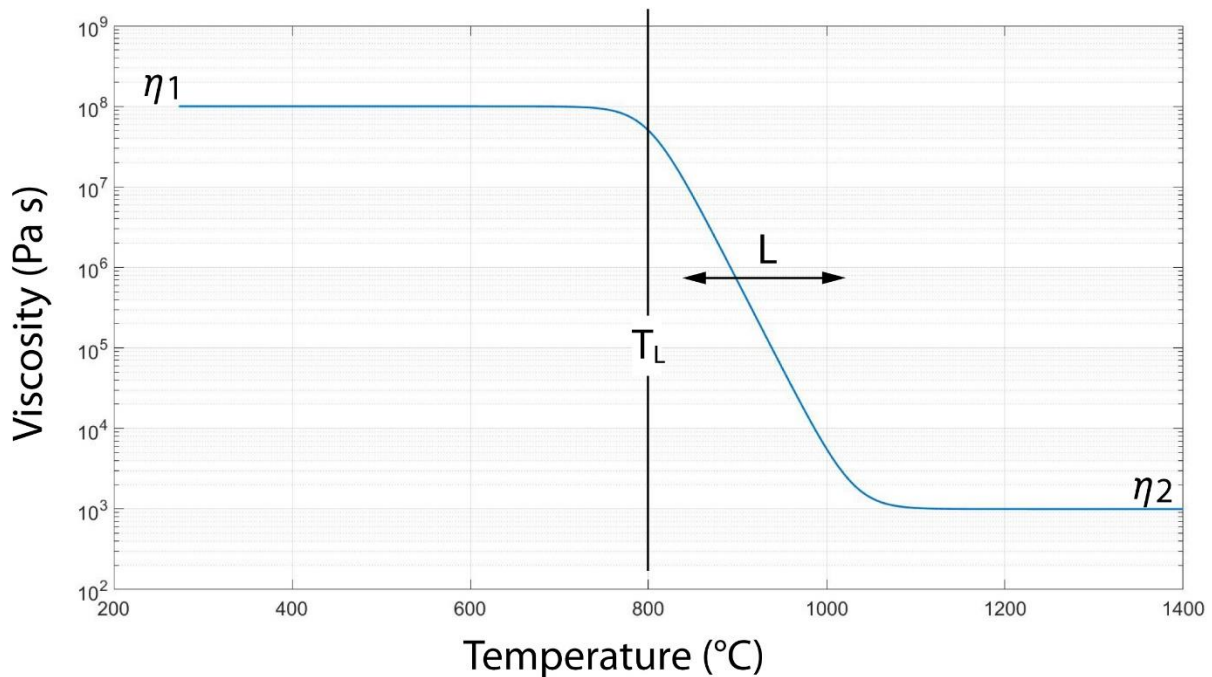


Figure 4. 4 Sigmoid law model of viscosity (or yield strength) according to temperature.

Figure 4.5 shows an example of a lava flow on a 20° slope. At the source, the lava exits with a temperature of 1200 K. It then cools progressively and its rheology changes. For this example, the sigmoid law has been chosen, the cohesion varies with temperature and the viscosity is fixed to 1000 Pa s. The parameters of equation 4.9 are $\eta_1 = 1000$ Pa, $\eta_2 = 10^5$ Pa, $L = 1/50$ and $T_L = 1000$ K.

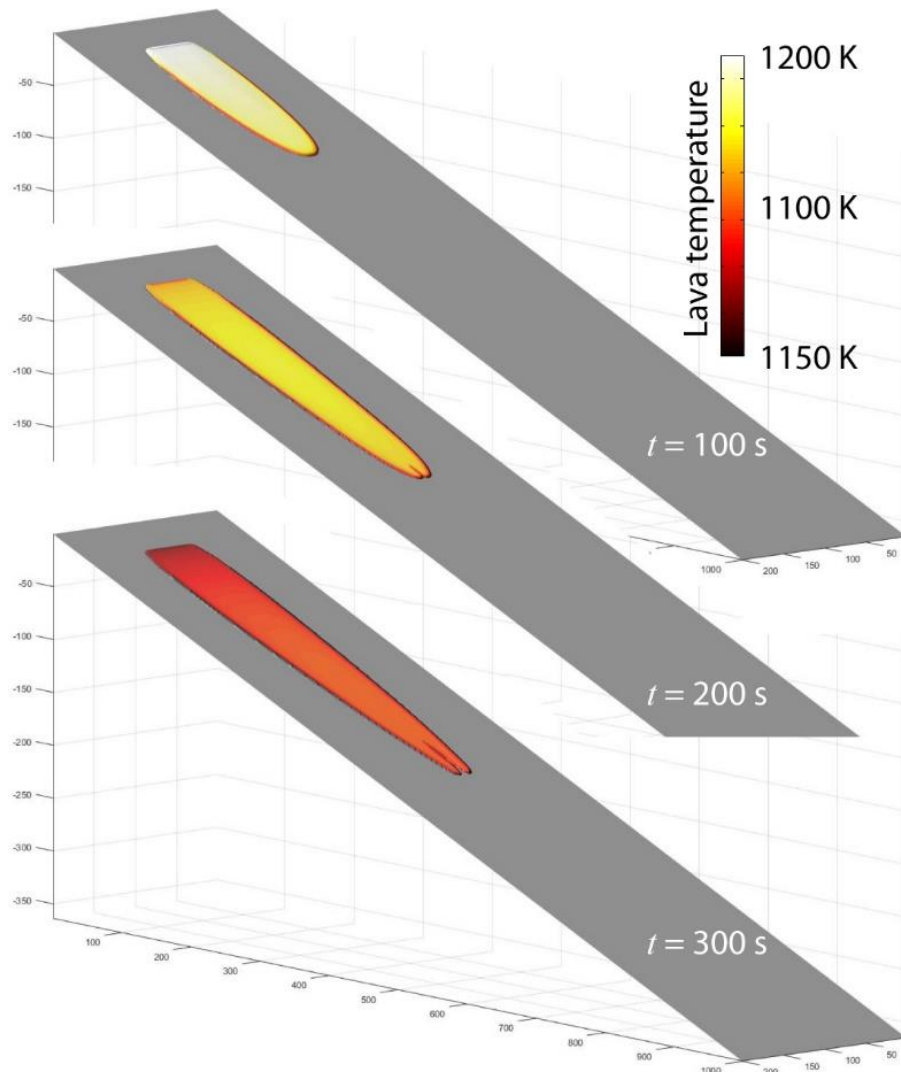


Figure 4. 5 Example of a lava flow that cools with time with an associated change of its rheology.

Initially, at high temperature, the velocity is relatively fast. It cools faster at the edges because they are static and not fed by new hot lava. Due to the cooling, the edges freeze and are more and more static. The hot lava is thus channelized. At the end of the eruption, the hot lava drains down while the edges remain at rest forming a levee-channel morphology (Fig. 4.6).

At the front, lobes can appear. Close to the transition temperature, small temperature difference can create strong rheology variations leading to the formation of a lobate morphology.

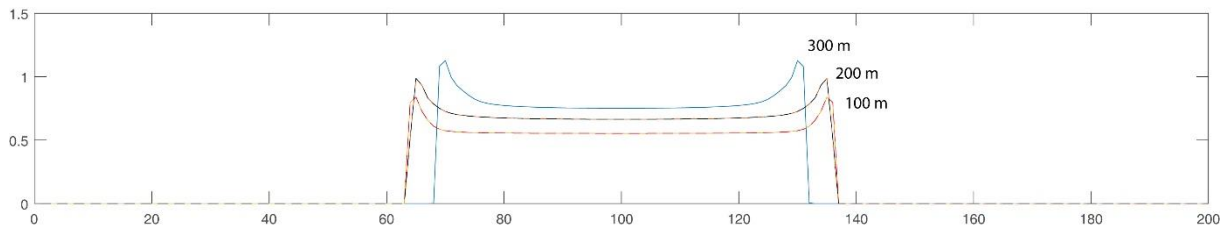


Figure 4. 6 Cross-section profiles of the lava flow at $t = 300$ s and $x = 100, 200$ and 300 m.

For the sigmoid viscosity/yield strength calculation there are needed 4 input parameters (Table 4.7) and two variables are calculated, viscosity and yield strength.

Symbol	Notation	Units
Viscosity (constant) - Yield strength (variable)		
τ_1	Lowest yield strength at high temperature	Pa
τ_2	Highest yield strength at low temperature	Pa
T_L	Transition temperatur	K^{-1}
τ_L	Sharpness of the transition	K

Table 4. 6 input parameters for the viscosity/yield strength by applying the sigmoid law.

4.2.3 Model n°3: hot interior and crust

This model simulates a crust forming on a viscous core (Fig. 4.7). The crust can grow with time and is advected by the lava. A scheme of the model is presented below.

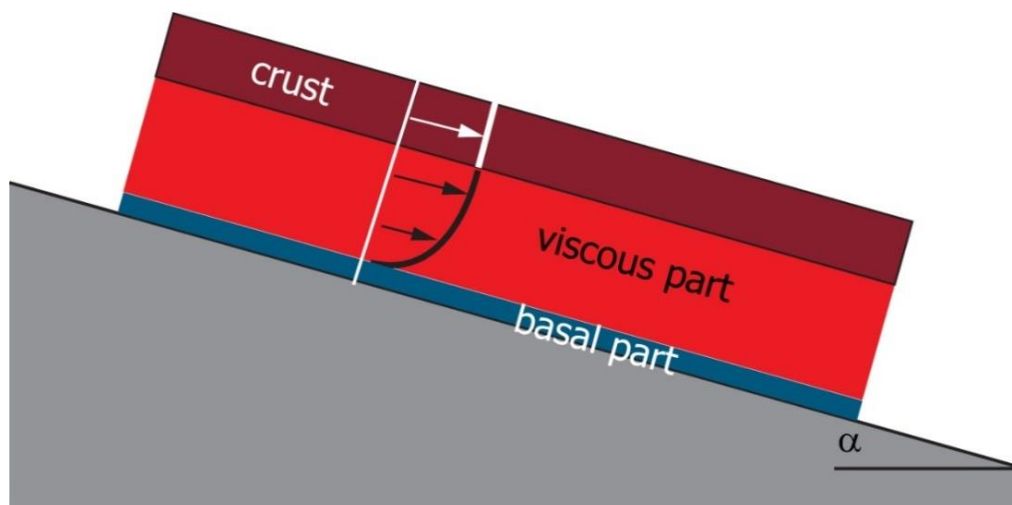


Figure 4. 7 Scheme of the model formed by a crust, a viscous part and a basal part.

The local mean velocity of the flow is demonstrated in Appendix 4.1. It is expressed by Eq. 4.26:

$$u = -\frac{\rho g}{3\eta} \times \sin(\alpha) \times \frac{\left(\frac{1}{3}h_L^3 + h_L^2h_C + h_Lh_C^2\right)}{h_L + h_C} \quad [4.26]$$

where h_c is the crust thickness and h is the thickness of the hot viscous lava $h=h_c+h_L$ is the total thickness of the lava flow.

To transport the crust, another equation of advection has been added in the numerical scheme (Eq. 4.27):

$$\frac{\partial h_c}{\partial t} + \frac{\partial}{\partial x}(h_c u_c) + \frac{\partial}{\partial y}(h_c v_c) = C_g \quad [4.27]$$

The crust thickness can then increase in time according to the rate of growth of the crust, C_g , that can be temperature dependent or be constant (36 mm / hour for Fig. 4.8, for example).

Note that the velocity of the crust is faster than the mean velocity because it is rafted above the faster viscous part. As shown in Appendix 4.1, this velocity is given by (Eq. 4.28):

$$\mathbf{u}_c = \mathbf{u} \times a \quad [4.28]$$

$$\text{with: } a = \frac{\left(\frac{1}{2}h_L^2 + h_Lh_C\right)(h_L + h_C)}{\frac{1}{3}h_L^3 + h_L^2h_C + h_Lh_C^2} \quad [4.29]$$

that gives the crust velocity (Eq. 4.30):

$$u_c = -\frac{\rho g}{3\eta} \times \sin(\alpha) \times \left(\frac{1}{2}h_L^2 + h_Lh_C\right) \quad [4.30]$$

At the edges, where the flow is thin enough and the crust meets the ground, it forms a basal part. Numerically, this is achieved by removing the crust and by adding the corresponding thickness to the topography. The change of topographic elevation and slope is calculated by VolcFlow.

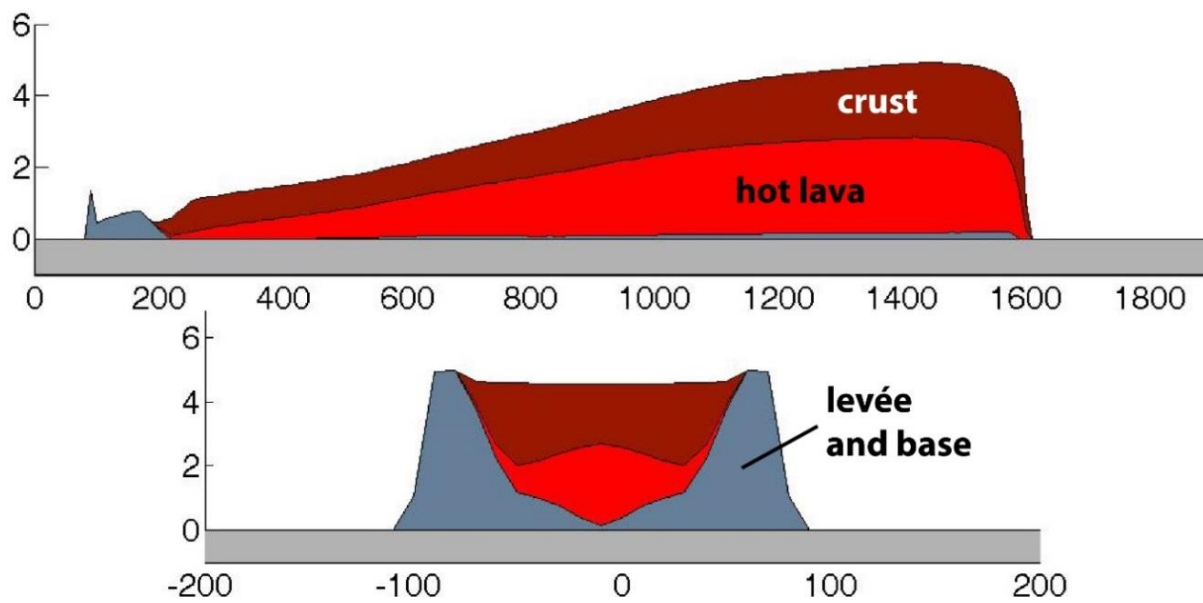


Figure 4. 8 Example of result obtain with the crust model. The crust increases with time (36 mm / hour, here) and it accumulates to the base at the front and at the edges modifying the topography.

The model forms levees that are part of the topography and, then, cannot be reworked. The transformation of the crust in topography, where it meets the ground, allows the lava to continue its flowing.

The additional input parameters for this model are the rate of growth of the crust, viscosity and yield strength (Table 4.7). During the simulation it calculates three variables, the mean velocity of the flow, crust velocity, rate of growth of the crust can be calculated as well.

Symbol	Notation	Units
C_g	Rate of growth of the crust	mm h ⁻¹
η	Viscosity	Pa s
τ	Yield strength	Pa s

Table 4. 7 Input parameters for the crust and hot interior model.

4.3 Summary

In this chapter it was presented the alternatives to simulate lava flows with VolcFlow by using different rheologies. Its schematic representation is shown in Fig. 4.9, which shows the main laws that governed each model, the number of input parameters that are required to run the model and the variables that are calculated along the simulation. Summarizing, they correspond to:

- ❖ **Model n°1:** Isothermal model with viscosity and yield strength constant along the simulation of the flow. It needs 5 input parameters (Table 4.1) and calculate 2 variables during the simulation.
- ❖ **Model n°2:** this model includes the thermo-rheological variation of the flow along the simulation. It is split in two:
 - **Model n°2a:** Combines the cooling, the crystal content and the existing rheological laws for viscosity and yield strength. This model needs in total 39 input parameters (Tables 4.1(except the rheological parameters), 4.2, 4.4) and with them it calculates 12 variables (Tables 4.3, 4.5).
 - **Model n°2b:** combines the cooling and the rheological variation for viscosity and yield strength by applying an empirical sigmoid law. 36 input parameters (Tables 4.1(except the rheological parameters), 4.2, 4.6) are needed to run the model. It calculates instead 8 variables.
- ❖ **Model n°3:** this model allows the formation of a crust in the flow with a hot interior. This model needs 3 input parameters (Table 4.7) and calculates 3 variables during the simulation.

These four proposed models were tested to simulate experimental and natural lava flows cases. Flows of basaltic and andesitic compositions were taken into account for this analysis. Results of those simulations are shown in Chapter 5.

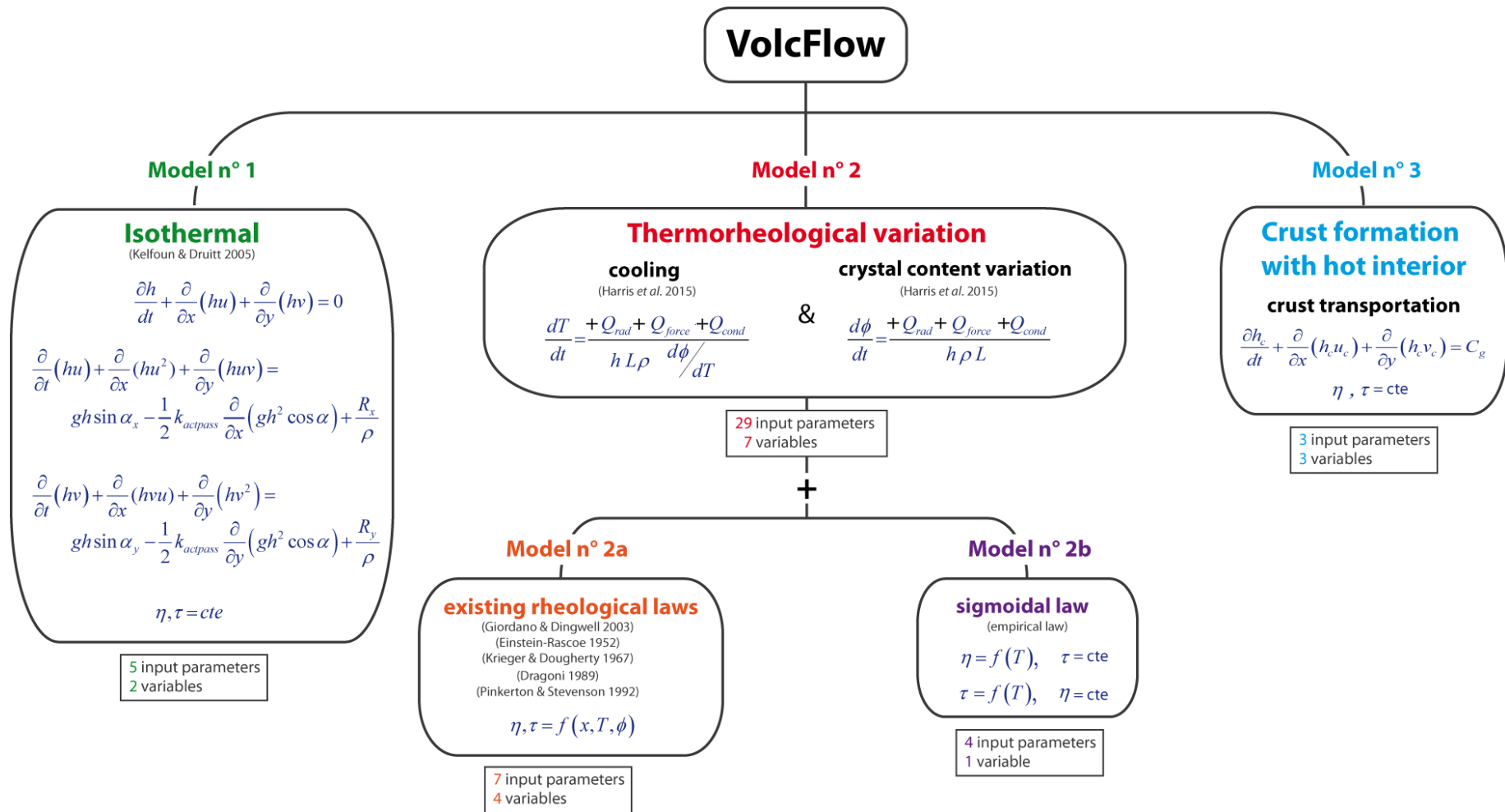


Figure 4. 9 Chart of the VolcFlow models to simulate lava flows by using different rheologies. **Model n° 1** corresponds to the isothermal in which the viscosity and yield strength are constant for the whole simulation. **Model n° 2** combines the cooling with the crystal variation and existing rheological laws or the cooling with variable rheology by using a sigmoid law for yield strength or viscosity. **Model n° 3** allows the formation of a crust in the flow with a hot lava in the internal flow.

Chapter 5

Numerical modelling of lava flows: Results and Discussion

Numerical codes of type I and II are focused on the understanding of the emplacement dynamics and lava flow morphology, and on the simulation of the lava flow emplacement respectively. For the first type, models include laboratory based-studies using different materials as analogs or real lava and theoretical approaches, meanwhile the type II includes models that can be used for hazard assessment during ongoing and future eruptions using different methodologies.

All numerical models should be calibrated and tested before being applied for short-or long-term assessment of lava flows. Based on that, existing numerical codes have been calibrated using analog laboratory and real lava flows cases (See Chapter 4). In the present section, four study cases were chosen to seek two main objectives:

- a) Find the parameters of VolcFlow that reproduce the natural flow emplacement with the approaches proposed in Chapter 4.
- b) Generate numerical simulations of realistic lava flow with the proposed approaches for basaltic and andesitic compositions.

Based on that, four study cases were chosen, one laboratory-scaled basaltic and three real lava flows (one basaltic and two andesitic), Table 5.1.

These four lava flows were simulated with VolcFlow using different approaches from Chapter 4 as it is described below.

Study case		Lava flow	Composition	References
Case 1	Experimental	Chengwatana flows (USA)	Basaltic aggregate	Dietterich <i>et al.</i> 2015 Dietterich, H. personal communication, 2017
Case 2	Natural	Piton de la Fournaise (France) 2015 08-11	Basaltic	Harris <i>et al.</i> , 2015 Gouhier, M. personal communication 2017
Case 3	Natural	Tungurahua (Ecuador) 2010 12 04/05	Andesitic	Hanson, 2013 Kelfoun and Vallejo Vargas, 2015 Chevrel <i>et al.</i> 2015
Case 4	Natural	El Reventador (Ecuador) 1) 2014 04 2) 201706 24 -2017 07 01 3) hypothetical flow similar to LF1(2002 11)	Andesitic	this study, Chapter 2

Table 5. 1 Study cases information.

5.1 Molten basalt benchmark (Syracuse Lava Project)

5.1.1 Description of the lava flow

It is a laboratory-scaled study case and corresponds to an actual basaltic flow produced in laboratory as a part of the Syracuse University Lava Project (<http://lavaproject.syr.edu>). This project was performed with the aim to collect data on the morphology and behavior of flows in a controlled and measureable environment. Lava flows generated by this project are the most complex and approximates closely the behavior of real lava flows (Lev *et al.* 2012; Dietterich *et al.* 2015, 2017). The data described and used for this study case corresponds to the well documented experiment reported in Dietterich *et al.* (2015) which is described below.

The experimental setup corresponds to a large furnace which is capable to melt up to 450 kg of basalt with temperatures over the basalt liquidus. It can mechanically tilt and pour the molten basal over different surfaces, in this case over an inclined sand plane (Fig. 5.1). For this experiment in particular, a basaltic aggregate from the Chengwatana flows in Wisconsin, USA (48 wt.% SiO₂) was melted at 1300 °C and entirely degassed in the furnace. The molten basal was poured onto a metal concave chute of 80 cm length and 29 cm diameter, with a volumetric flux ranging of 220 mL/s. The first part of the trajectory was confined into a concave metal chute which diverted the flow onto an inclined plane (slope: 13.25°) covered by sand (Fig. 5.2 a-c).

The advantage of have melting the rock allowed the research to incorporate the effects of the cooling of the flow with the aim to simulate the real conditions of natural lava flows.

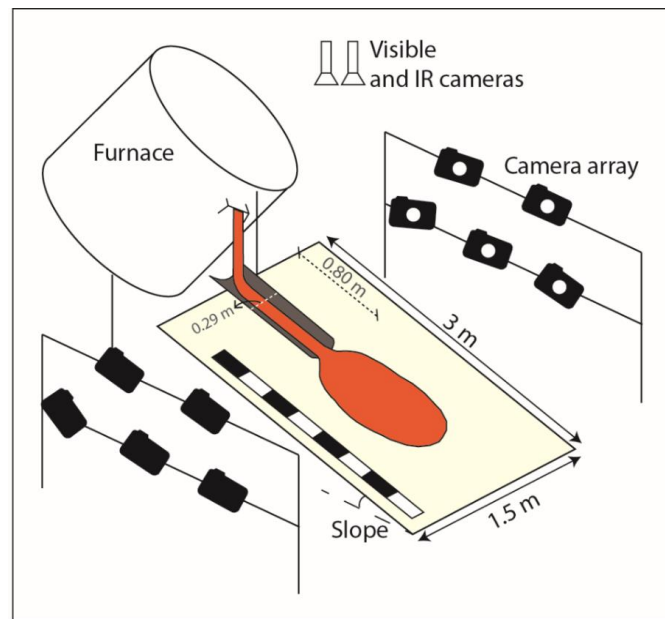


Figure 5. 1 Schema of the experiment setup for the molten basalt at the Syracuse University Lava Project (from Dietterich *et al.* 2017).

5.1.1.1 Measurements during the advance of the flow

The advance of the flow was recorded by visible (JAI B401, e.g. Fig. 5.2 a-c) and infrared (FLIR SC325, e.g. Fig 5.2 d-f) video cameras and from an array of time lapse cameras installed around of the experiment. The surface temperature was obtained only by the FLIR infrared cameras. The scale of the experiments was represented by a steel scale with 10 cm separations (Fig 5.2 a-c, Fig. 5.3D). The advance rate and surface velocities were calculated using Matlab®, Tracker and differential optical flow meanwhile the thickness was measured by a detailed photogrammetric reconstruction of the flow using time-lapse photos obtained from the camera array (Dietterich *et al.* 2015, 2017).

The molten basalt was poured from the furnace into the setup for 60 s and it took 128 s until the flow was fully emplaced over the inclined plane reaching a total length of 196 cm. The total volume of the flow was 0.0132 m^3 .

The progression of the flow is shown in Fig. 5.2, through images taken from the plain view visible camera (a-c) and infrared (d-f) cameras. Once the flow was poured out from the metal chute, it took 18s until it reached and started to divert over the sand inclined plane. During this time (80 cm trajectory) there were no measurements of the flow advance. Once the flow reached the inclined plane, alimentation was kept and the progression was recorded for 60 s (Fig. 5.3A). It finally stopped at 128 s reaching a length of 196 cm (Fig. 5.3A, B, C, D). Morphology

related to shear zones were recognized in the external parts of the flow (Fig. 5.3C). A schematic progression of the flow is represented in Fig. 5.3D based in images showed in Fig. 5.2 (a, b, c).

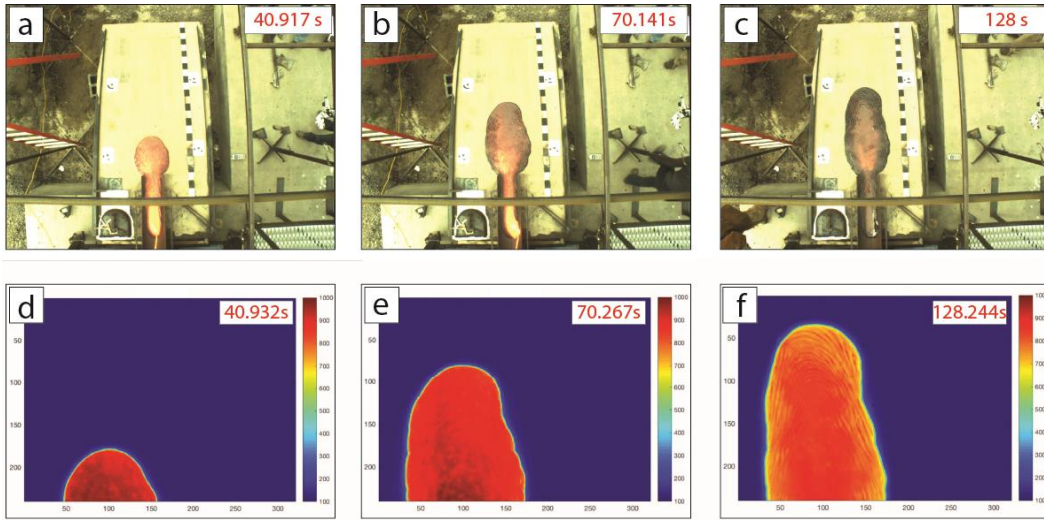


Figure 5. 2 Shows the experimental setup of the Syracuse lava flow project and the advance of the basaltic lava flow since it was poured out onto the metal chute and distributed after onto the inclined plane (a-c). Advance of the front of the flow caught by thermal images are shown in d, e and f figures. (Source: Dieterich H., personal communication).

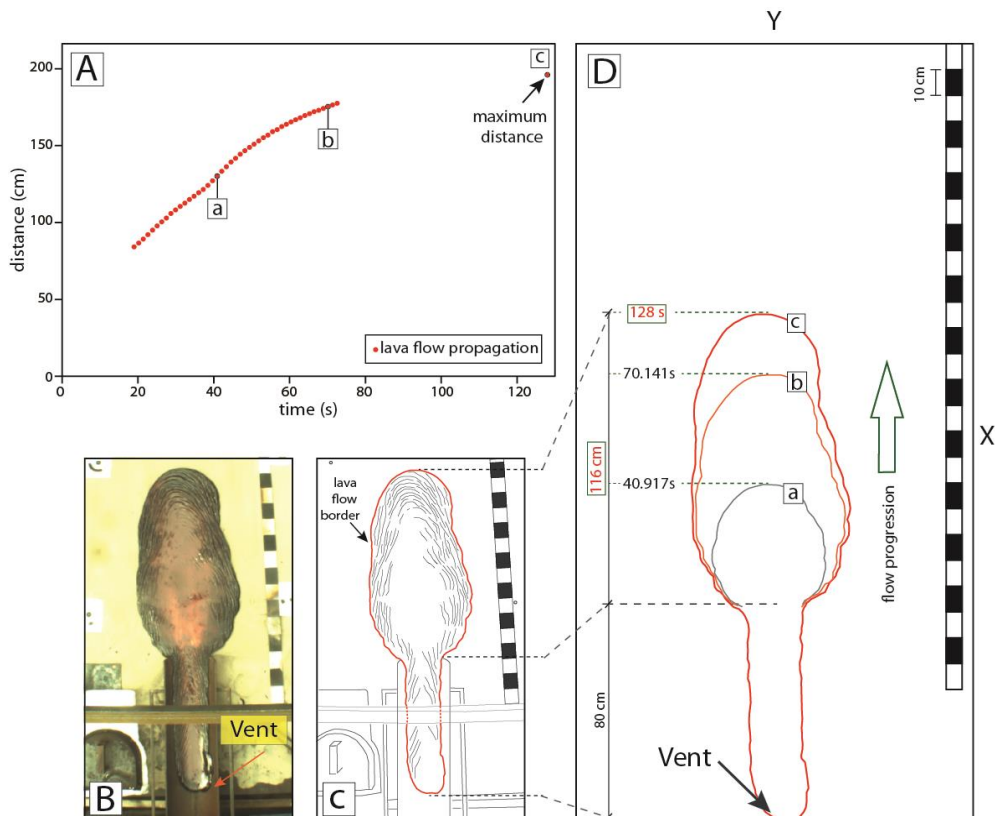


Figure 5. 3 **A)** Lava flow propagation of the flow since it was poured out from the furnace to the metal chute until it stopped. **B)** Final shape of the lava flow, emplaced onto the metal chute and the sand inclined plane. **C)** Schema of the final deposit showing the morphology of the flow. **D)** Progression of the flow, taking as examples a, b and c from Figure 5.2.

The highly detailed records of the input parameters of the flow allowed it to be used as a benchmark for the comparison of the results of different numerical models for simulate lava flows using different approaches (Section 3.3, Chapter 3; Cordonnier *et al.* 2015; Dietterich *et al.* 2017). As well it has been used as a way to understand the behavior of the flow when it faces obstacles in their path (Dietterich *et al.* 2015).

5.1.2 Initial conditions

5.1.2.1 Numerical topography

The calculation domain is 3 m long (X-direction) and 1.5 m large (Y-direction). Each mesh area is 1cm×1cm horizontally (300 m long, 150 m wide). The geometry of the experiment described in Section 5.1.1 (Fig. 5.1) is modeled by an inclination of 13.25° (Fig. 5.4). The shape of the chute where the lava is initially channeled is reproduced by a parabolic surface cut where it exceeds 10 cm: $z_{\text{chute}} = \min(0.1, 4.4y^2)$. The vent location is assumed to be at the concave. This numerical topography mimics the conditions of the original setup in which the flow is emitted through the vent and is channelized in the chute for 80 cm before being dispersed onto the plane, Fig. 5.4.

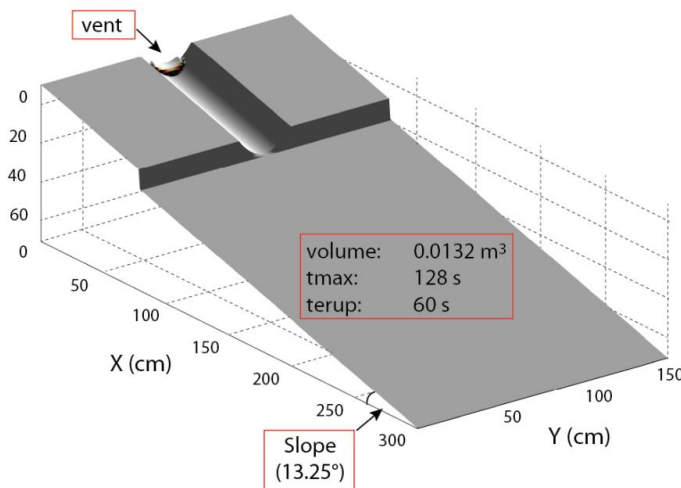


Figure 5. 4 Numerical topography used for the simulation of the molten basalt.

5.1.2.2 Input parameters

The basic input parameters required for the isothermal model are eruption time = 60 s, maximum time=128 s, volume=0.013 m³ and bulk density=2350 kg m³, (Appendix 5.1).

Complementary parameters related to the chosen rheological model are showing respectively in Section 5.1.4.

To simulate the lava rate poured from the furnace, a constant thickness of lava is added on the cells of the chute located at the higher border ($Y = 0$, $-8 \text{ cm} < X < 8 \text{ cm}$) during 60 s (Eq. 5.1):

$$\frac{dh}{dt} = \frac{Q_{lava}}{S} \quad [5.1]$$

where S is the surface of all the cells of the source area and Q_{lava} the volumetric rate ($220 \text{ cm}^3/\text{s}$). The momentum is taken into account for the calculation of the new velocity at the source (previous velocity + new mass added with a null velocity). The temperature of the mass added is constant.

5.1.3 Numerical models

As this lava flow was fully degassed during its generation, there was no crystal formation in the final flow (Dietterich *et al.* personal communication). In that case the thermo-rheological model (Model n°2a, Chapter 4) which takes into account the existing relationships was not used to simulate this flow.

The molten basalt benchmark was simulated using three approaches described in Chapter 4:

1. **Model n°1:** Isothermal
2. **Model n°2b 1:** Thermo-rheological variation – viscosity sigmoid law
3. **Model n°2b 2:** Thermo-rheological variation – yield strength sigmoid law
4. **Model n°3:** Crust formation with hot interior.

Simulations were obtained by using trial and error method. It was based on the comparison of the flow front advance of the simulation vs the measured data given by Dietterich *et al.* 2015 (Fig. 5.3 A). Results are presented and analyzed for 10, 40, 70 and 128 seconds in order to bring criteria for the discussion of the results between the models (Section 5.1.5, this Chapter). The analysis of the results was based on the description of the shape and morphology of the flow left in the plane, the maximum lengths reached for X (X_{max}) and Y (Y_{max}), and the maximum thickness (h_{max}).

5.1.4 Simulations

5.1.4.1 Model n°1: Isothermal

The isothermal model considers that the flow has a Bingham behavior and that the temperature has no effect on the dynamics of the flow. In this case, the rheology of the flow is governed by the viscosity and yield strength, both parameters are constrained as constants during the whole simulation of the flow. They were determined by finding the best fit of the flow front velocity between the simulation and the real data (Fig. 5.3A), using an error-trial method following Kelfoun & Vallejo Vargas (2015). Results shows that the best fit was given with a viscosity=18 Pa s and a yield strength=10 Pa (Appendix 5.1).

Results of the simulations by using the VolcFlow input basic parameters and the best fit values for viscosity and yield strength are shown in Fig. 5.5, 5.6 and 5.7. The evolution of the flow for 10, 40 and 70 seconds are shown for 2D and 3D in Fig. 5.5 and 5.6 respectively. The evolution of the flow in time, their correspondent thickness and the comparison of the advance of the flow between the simulated advance (black dots) and the real data is shown in Fig. 5.5, left, middle and right respectively.

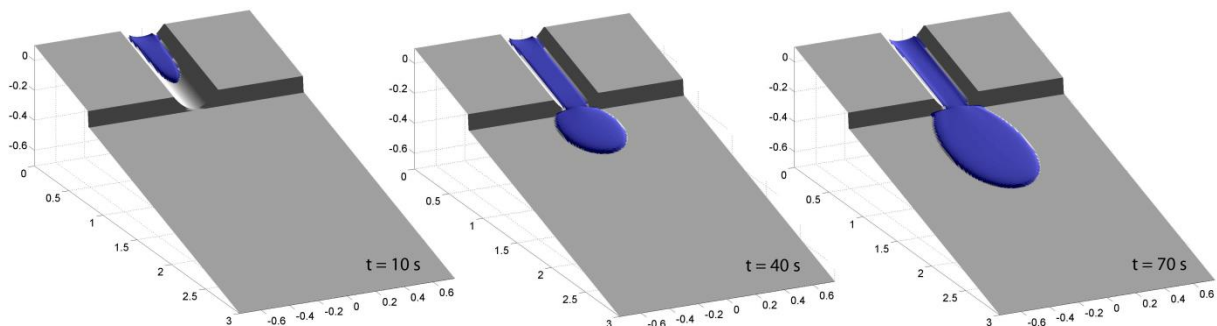


Figure 5.5 3D view of the flow advance for 10, 40 and 70 seconds as a result of the simulation with VolcFlow using the Model n°1: Isothermal approach.

The final deposit of the flow obtained by applying the isothermal model with a viscosity of 18 Pa s and a yield strength of 100 Pa during 128 s is shown in Fig. 5.7. The 2D view of the flow is represented in Fig. 5.7 (left side), in which the flow deposit shows a regular and oval symmetrical shape characterized for $X_{\max}=191$ cm, $Y_{\max}=60$ cm and a $h_{\max}=2.28$ cm. The internal part of the flow is uniformly thicker than the borders. The comparison of the flow advance between the simulation data (black dots) and real data (red dots) is shown Fig. 5.7 (middle side). The 3D view of the deposit is represented in Fig. 5.7 (right side).

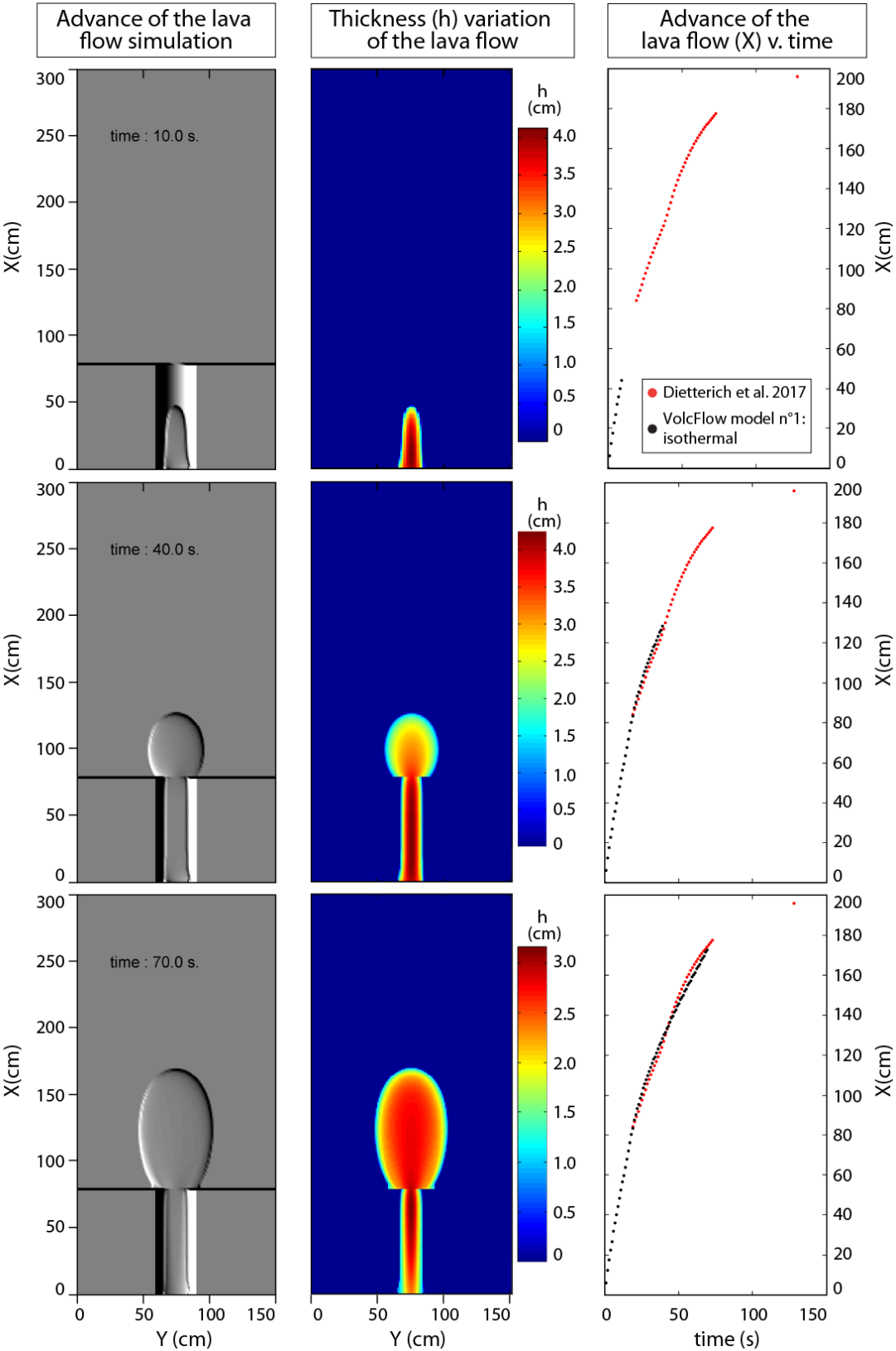


Figure 5. 6 Propagation of the flow applying the Model n°1: isothermal for 10, 40 and 70 seconds. It shows the evolution of the flow over the surface (left), the deposit thickness variation (middle) and the advance of the flow in X respect to the time (right) between the results of the simulation (black dots) and the measured data from Dieterich *et al.* 2017 (red dots).

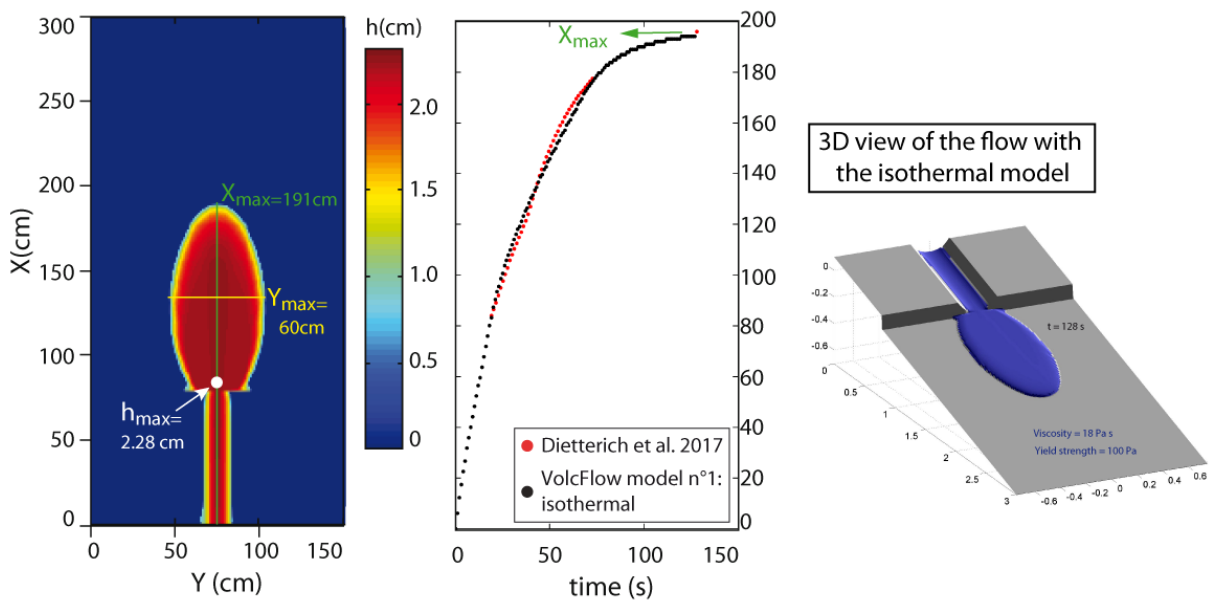


Figure 5.7 **Left:** Final deposit in 2D of the flow over the inclined plane for 128 s showing a uniform and regular shape. **Middle:** Comparison of the advance of the flow in X respect the time between the results of the simulation (black dots) and the measured data from Dieterich *et al.* 2017 (red dots). **Right:** 3D view of the deposit of the flow applying the isothermal model and using a viscosity of 18 Pa s and a yield strength value of 100Pa, both considered as constants.

5.1.4.2 Model n°2b: thermo-rheological variation with sigmoid model

This approach considers the cooling of the flow by using the Eq. 4.19 (Section 4.2.2.1.3, Chapter 4). With it, the cooling per unit of time is estimated, allowing to determine the new temperature with which the rheological parameters (viscosity and yield strength) are calculated. The estimation of the viscosity and yield strength is based on the Eq. 4.25 (Section 4.2.2.2).

This model takes into account the VolcFlow input basic parameters and some others that are needed to estimate the cooling and the rheology as it's explained in Chapter 4. For the cooling it needs radiation, convection and conduction parameters, most of them are described in Dieterich *et al.* 2015. The radiation parameters are the Stefan-Boltzmann = $5.67E-08 \text{ W m}^{-2} \text{ K}^{-4}$ and emissivity = 0.95. The convection estimation includes the $C_H = 0.0036$, the air specific heat capacity = $1500 \text{ J kg}^{-1} \text{ K}^{-1}$, air temperature = 293.15 K, wind speed 0.1 m s^{-1} , air density = 0.4412 kg m^{-3} . Conduction parameters are $h_{\text{base}} = 0.001$, thermal conductivity = $0.2 \text{ W m}^{-1} \text{ K}^{-1}$ and basal temperature = 500 K. The density and vesicularity parameters considers a vesicularity = 0 and a DRE density = 2350 kg m^{-3} . Thermal takes into account the buffer = 0, crust temperature = 973.15 K, core temperature 1323.15 K and a crust cover fraction assumed = 0. The source of these parameters is noted in Appendix 5.1.

Because of there is no crystallization during the experiment (Section 5.1.1.1, this Chapter), only the sigmoidal model has been considered for the rheological estimation, with two cases:

1. Thermo-rheological variation considering a constant yield strength and variable viscosity dependent on the temperature.
2. Thermo-rheological variation considering a constant viscosity and variable yield strength dependent on the temperature.

The simulations for the sigmoidal model took into account the VolcFlow basic input parameters, the cooling and rheological ones and those related with the sigmoidal model (Table 4.6, Chapter 4). All of them are noted in Appendix 5.1. Results of these simulations for both cases are shown below.

5.1.4.2.1 Model n°2b 1: Sigmoidal model considering a constant yield strength and variable viscosity dependent on the temperature

This model assumed a yield strength as a constant with 0 Pa, meanwhile the viscosity depends on the core temperature variation. Viscosity is calculated from Eq. 4.25 (Chapter 4) which considers four variables: the lowest viscosity at high temperature 0 Pa s, the highest viscosity at low temperature=1000 Pa s, transition temperature= $1/60 \text{ K}^{-1}$, sharpness of the transition=1125 K and yield strength=0 Pa (Appendix 5.1). These variables were determined using trial and error methods, by comparing the advance of the flow between the simulation and real data.

Results of this simulation are shown in Figs. 5.8-5.11. The evolution for 10, 40 and 70 seconds in 3D and 2D are shown in Fig. 5.8 and 5.9 respectively. The evolution on time, its thickness and the comparison of the advance of the flow between the simulation (black dots) and real data (red dots) are shown in Fig. 5.9.

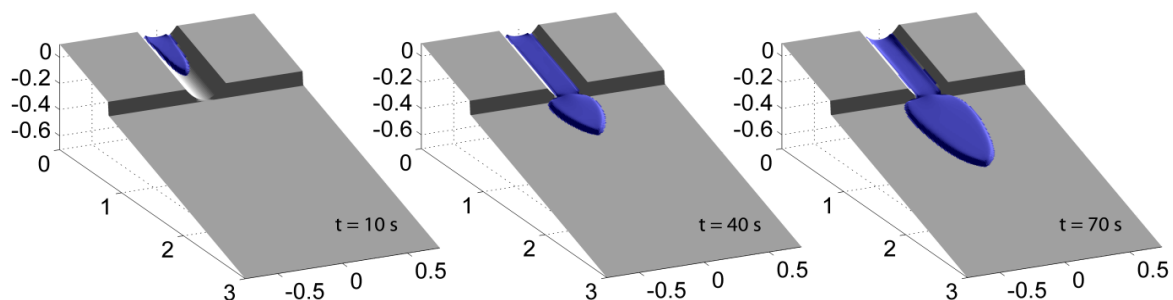


Figure 5. 8 3D view of the flow advance for 10, 40 and 70 seconds as a result of the simulation with VolcFlow using the Model n°2b 1: Sigmoidal with a viscosity as a variable and yield strength as a constant.

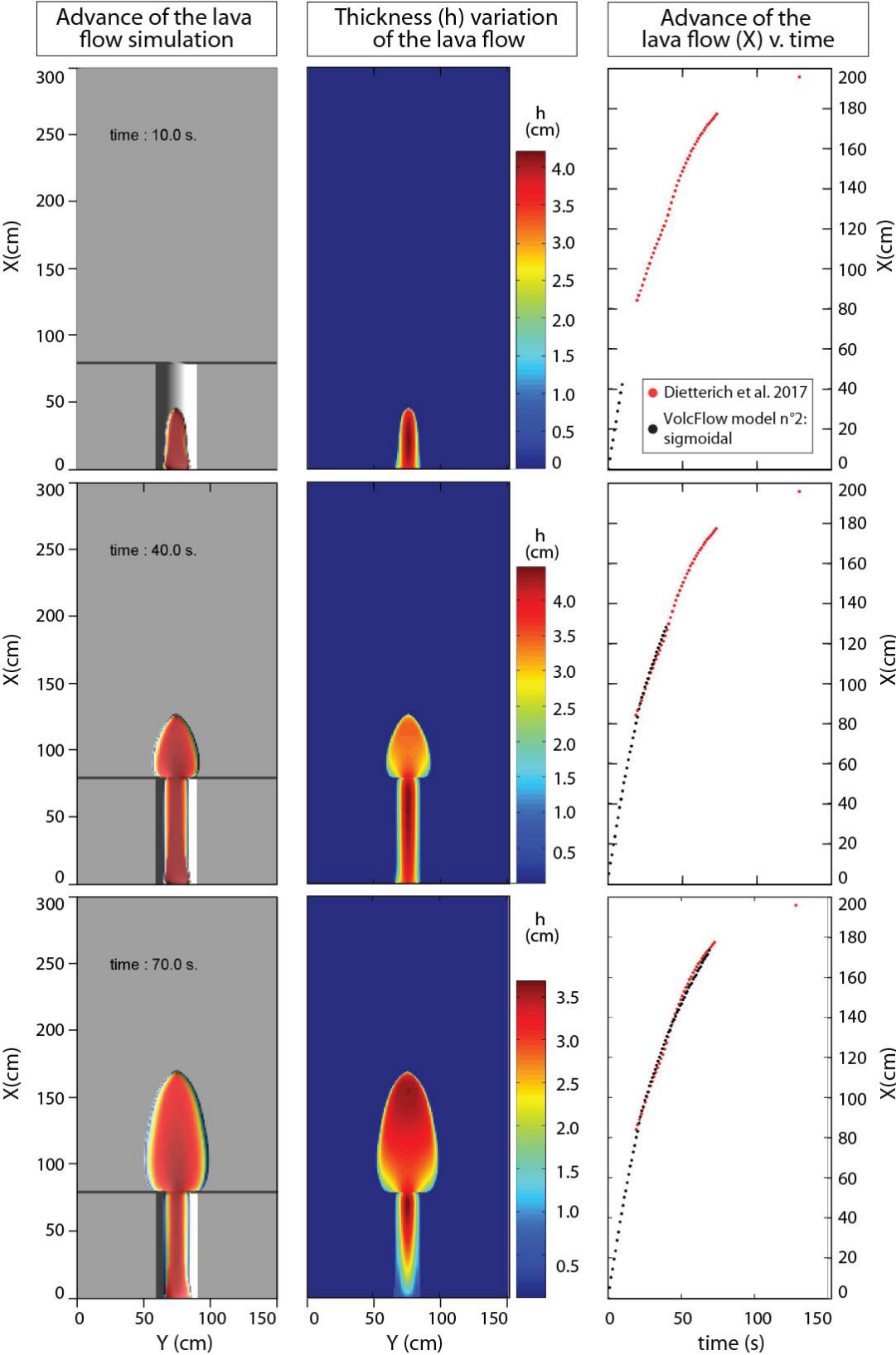


Figure 5. 9 Propagation of the flow applying the Model n°2b 1 Sigmoidal for 10, 40 and 70 s with a viscosity as a variable and yield strength as a constant. It shows the evolution of the flow over the surface (left), the thickness variation of the flow (middle) and the advance of the flow in X respect to the time (right) for 10, 40 and 70 seconds.

The result showing the final deposit of the flow at 128 s. is represented in Fig. 5.10 and 5.11. At that time the flows show a regular and elongated symmetrical shape characterized for $X_{\max}=207$ cm, $Y_{\max}=58$ cm and a $h_{\max}=2.72$ cm. The thickest part of the flow is concentrated in the frontal part of the flow and the thinner at the borders and close to the vent. The comparison of the flow advance between the simulation data (black dots) and real data (red dots) is shown in the right side of the same figure.

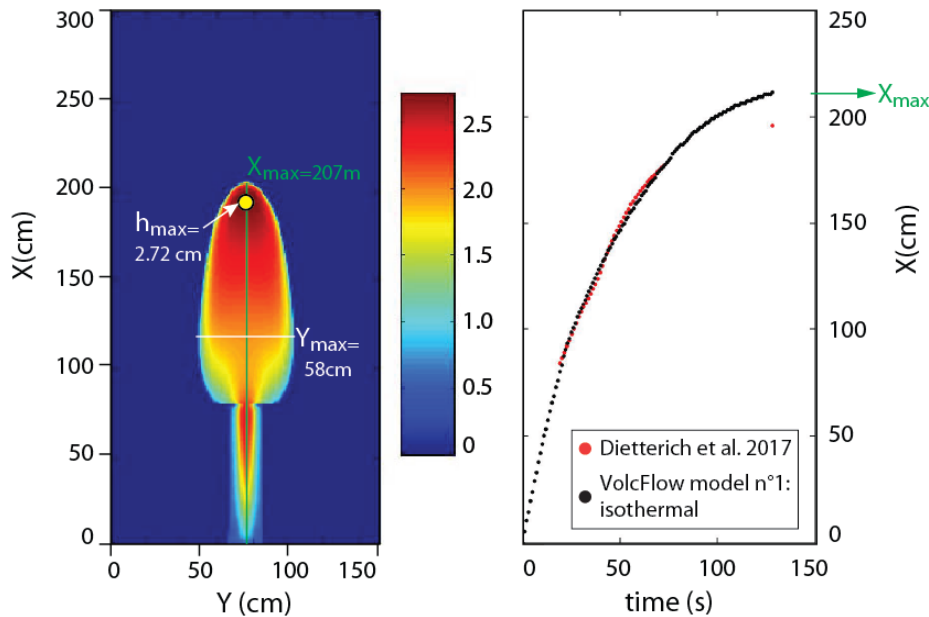


Figure 5.10 **Left:** 2D view of the simulation of the final deposit of the flow for 150s. **Right:** Comparison of the advance of the flow in X respect the time between the results of the simulation (black dots) and the measured data from Dietterich *et al.* 2017 (red dots).

The 3D view of the deposit is represented in Fig. 5.11. It shows at first, the variation of the temperature in the whole deposit at 150 s. Being the coldest (outer part of the flow) and hottest (inner part of the flow) with 900 and 1130 K respectively. Second, the upper-right graph represents the variation of the temperature along the simulation recorded at the white dot located immediately below the concave chute. On it, initially is recognizable the air temperature, then the temperature increases when the flow arrives to that dot and remains high for about 30 seconds, after that it began to decrease linearly. Third, the variation of the viscosity in function of the temperature is represented on the lower-left graph which shows that the viscosity presents the sigmoid variation according to the established law. Fourth, the image shows the highest and lowest viscosity measured in the flow at the end of the simulation. The lowest is located in the hottest part (red color) meanwhile the highest is at the edge of the flow (blue color), with 480 and 9000 Pa s.

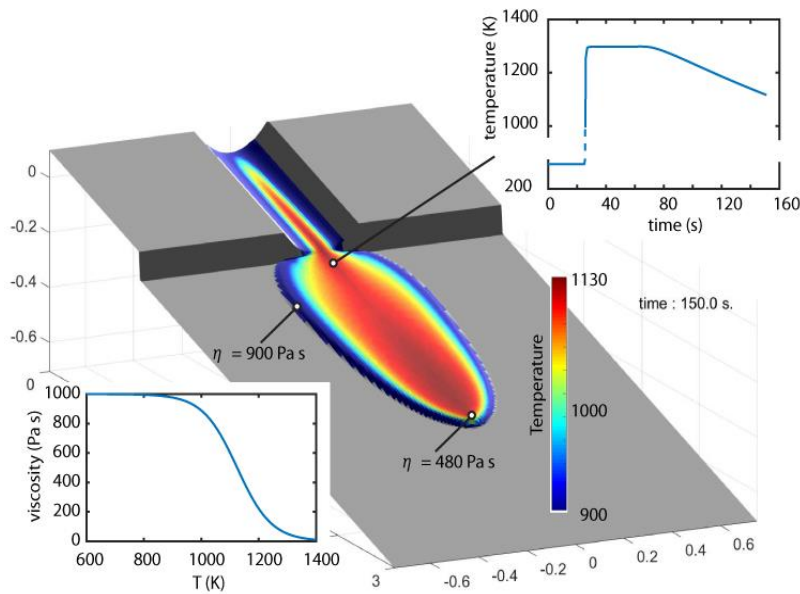


Figure 5.11 3D view of the final deposit of the flow for 150s, it shows the result of the simulation using the Sigmoidal approach for a variable viscosity and constant yield strength. At 120 s, the temperature of the flow varies between 900 and 1130 K. A sigmoidal variation of the viscosity is shown having a value of 480 Pa s in the hottest part of the flow and 900 Pa s in the coldest one.

5.1.4.2.2 Model n°2b 2: Sigmoidal model considering a constant viscosity and variable yield strength dependent on the temperature

This method considers that the viscosity is constant meanwhile yield strength is calculated using the model from Section 4.2.2.2.2 which depends on the core temperature and considers four variables. These variables have been determined using trial and error methods based on the comparison of the advance of the flow between the results of the simulations and the real data. They are the lowest yield strength at high temperature=10 Pa, the highest yield strength at low temperature=900 Pa, the transition temperature=1190 K, the sharpness of the transition= $1/60 \text{ K}^{-1}$, and a viscosity=25 Pa s.

Results of the simulations are shown in Figs. 5.12 – 5.15. The evolution of the flow for 10, 40 and 70 seconds are shown for 2D and 3D in Fig. 5.12 and 5.13 respectively. The evolution of the flow in time, their correspondent thickness and the comparison of the advance of the flow between the simulated advance (black dots) and the real data is shown in Fig. 5.12, left, middle and right respectively. It shows thickening at the borders and some diagonal structures related to rheological instabilities.

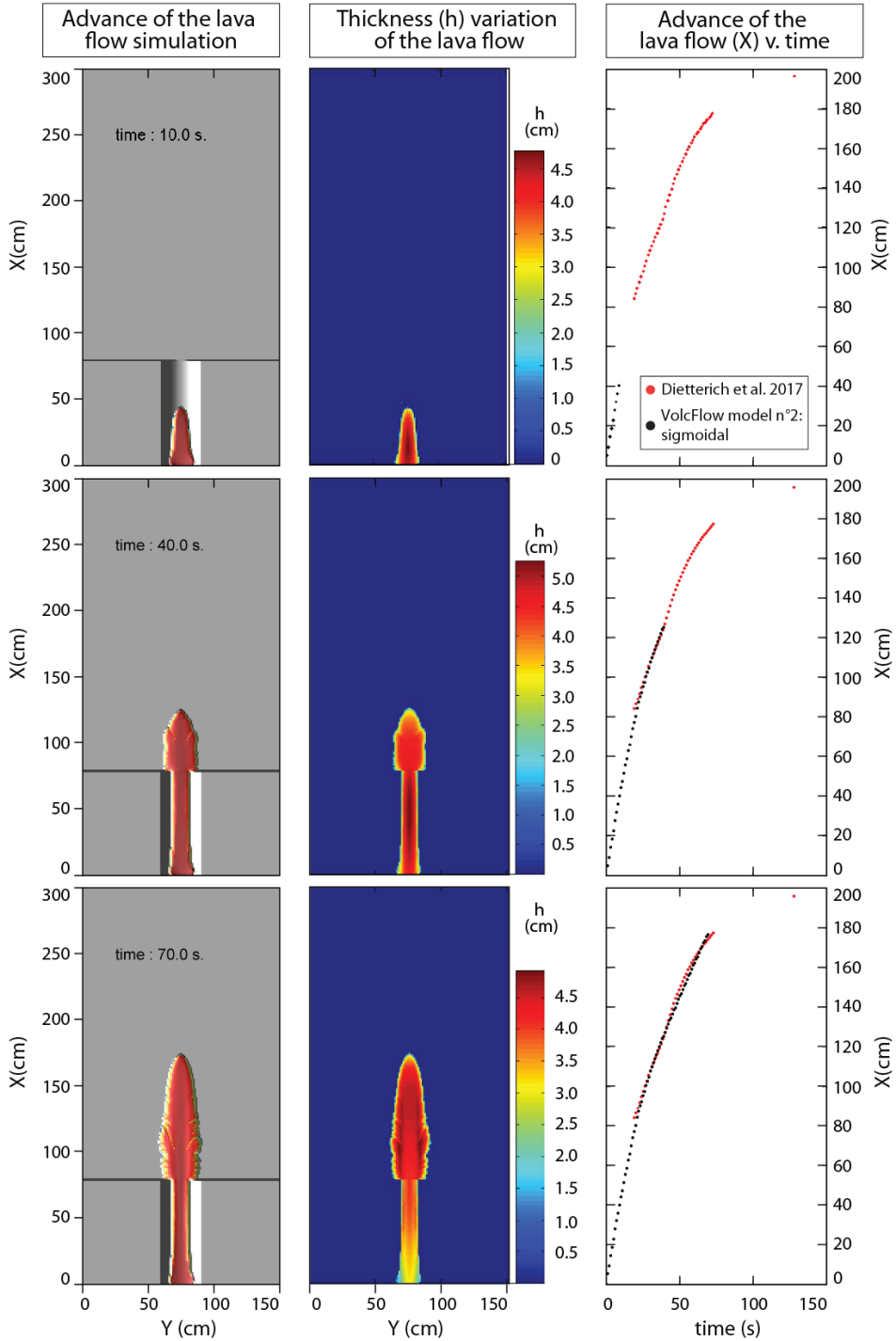


Figure 5. 12 Propagation of the flow with Model n°2b 2 Sigmoidal with yield strength as a variable and viscosity as a constant. It shows the evolution of the flow over the surface (left), the thickness variation of the flow (middle) and the advance of the flow in X respect to the time (right) for 10, 40 and 70 s.

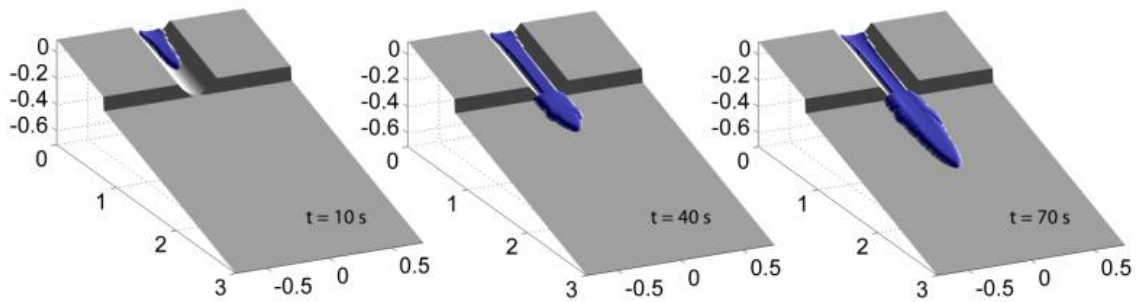


Figure 5.13 3D view of the flow advance for 10, 40 and 70 seconds as a result of the simulation with VolcFlow using the Model n°2b 2: Sigmoidal with yield strength as a variable and viscosity as a constant.

The final deposit for this simulation with a viscosity of 25 Pa s and variable yield strength is shown in Fig. 5.14 and 5.15. The 2D view of the flow shows an elongated shape, wider close to the exit of the chute and narrower at the front. This shape is characterized by $X_{max}=181$ cm, $Y_{max}=36$ cm and a $h_{max}=4.93$ cm (Fig. 5.14, left side). The thickest part of the flow is concentrated at the borders reaching 4.93 cm meanwhile the inner part has values of 3.87 cm, the front reaches 2.7 cm. The right side of Fig. 5.14 shows the comparison of the flow advance between the results of the simulation and the real data.

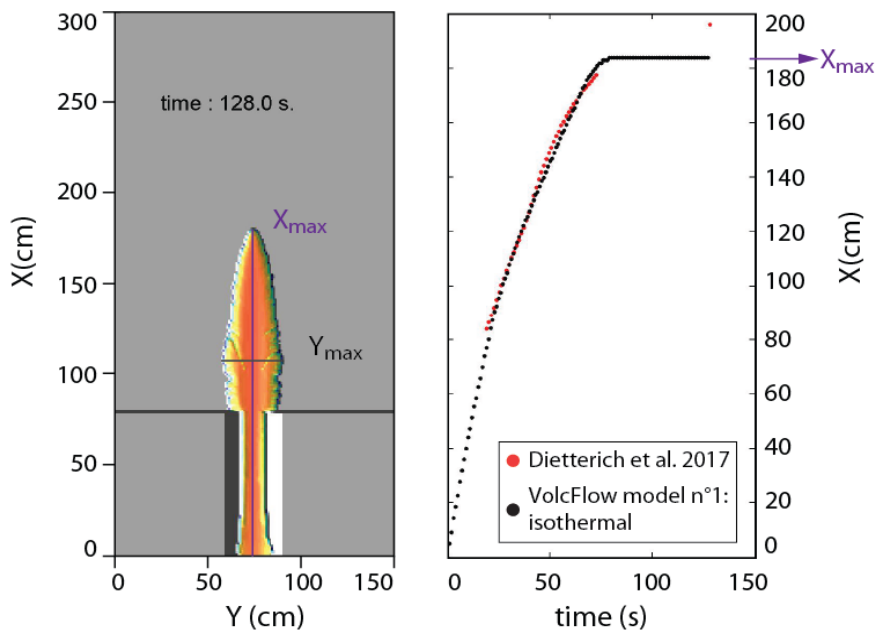


Figure 5.14 2D view of the simulation of the final deposit of the flow for 128s using the Sigmoidal approach for a constant value of viscosity and variable yield strength. **Right:** Comparison of the advance of the flow in X respect the time between the results of the simulation (black dots) and the measured data from Dietterich *et al.* 2017 (red dots).

Figure. 5.15 shows the final deposit in 3D for this model at 110 s. It represents the variation of temperature of the flow at this time being 1150 and 1240 K the lowest (blue colors)

and highest (reddish colors) temperatures. It is possible to observe a progressive cooling of the flow since the inner part of the flow through the borders. External borders of the flow present morphologies related to rheological instabilities. The lower left graph displays the curve of the yield strength variation with temperature obtained from the sigmoid law.

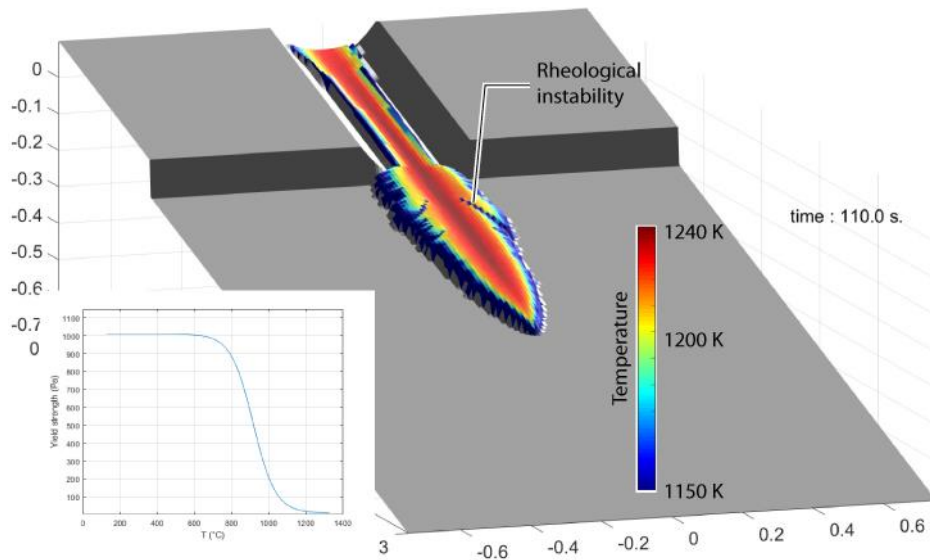


Figure 5.15 3D view of the final deposit of the simulation for the flow at 110 s using the Sigmoidal approach which takes into account the cooling of the flow and variable yield strength and a constant viscosity. Temperature of the flow at 110 s varies between 1240 and 1150 K. The figure shows as well features of rheological instability.

5.1.4.3 Model n°3: Crust formation with hot interior

This model allows the formation of a crust in the flow following the equations from Section 4.2.3 (Chapter 4). This model uses the VolcFlow input parameters and those related to the crust formation, which are the rate of growth of the crust= $6.8 \times 10^{-3} \text{ mm h}^{-1}$, viscosity=12 Pa s and yield strength=0 Pa (Appendix 5.1).

The advance in 2D of this simulation is represented in Figure 5.16 for 10, 40 and 70 s. Left side represents the advance of the flow and shows the progressive formation of levees and crust in the flow. When levees have been developed they become part of the topography, it is for this reason that is not possible to visualize the thickness of the levees in the images (middle side) and just the thickness of the internal hot part is reported, but the thickest part of the flow is has been concentrated at the levees. The right side shows the advance of the simulation (black dots) in comparison to the real data (red dots).

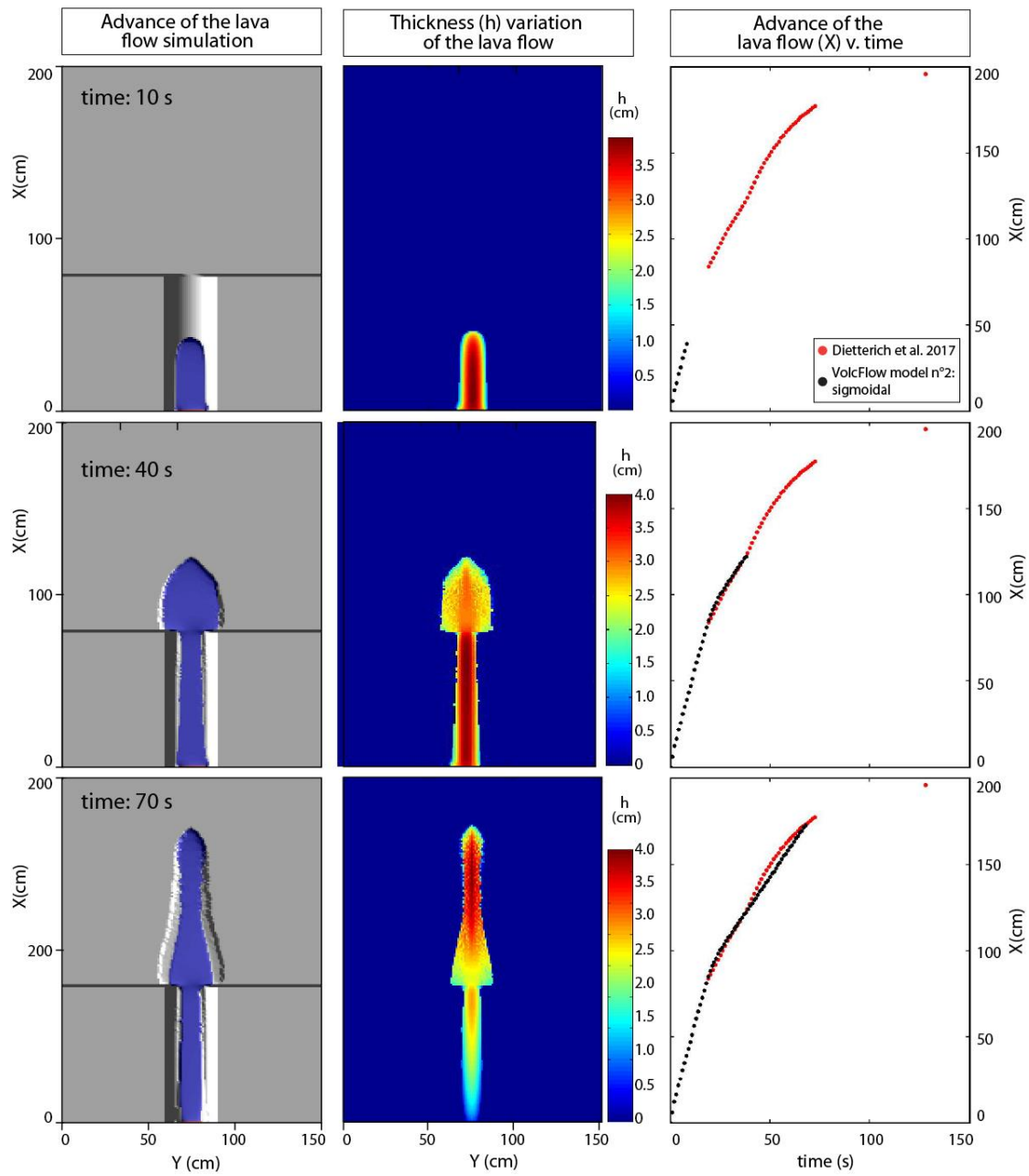


Figure 5. 16 Propagation of the flow applying the Model n°3 hot interior and crust. It shows the evolution of the flow over the surface (left), the thickness variation of the flow (middle) and the advance of the flow in X respect to the time (right) for 10, 40 and 70 seconds.

The representation of the advance of the flow in 3D is shown in Fig. 5.17 for 10, 40 and 70 seconds. For 40 s the image shows a broad dispersion of the flow in the plane and the beginning of the formation of the crust and levees. For 70 s the dispersion changes and it becomes narrower at the front of the flow compared with the previous one, the presence of crust and levees is more obvious.

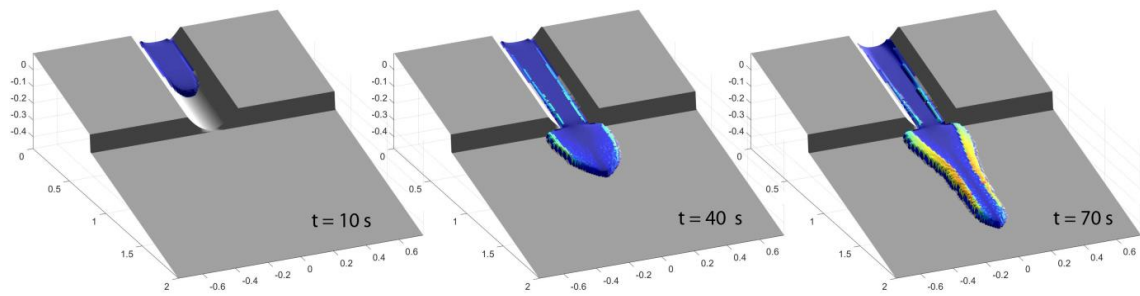


Figure 5. 17 3D view of the flow advance for 10, 40 and 70 seconds as a result of the simulation with VolcFlow using the Model n°3: hot interior and crust formation.

During the simulation the progressive formation of three layers took place: crust (dark red), lava (bright red) and base (gray), Fig. 5.18. This figure represents the advance of the flow in X axe for 10, 40 and 70 seconds. The formation of the crust is visible at the front and top of the flow which increases its thickness by time.

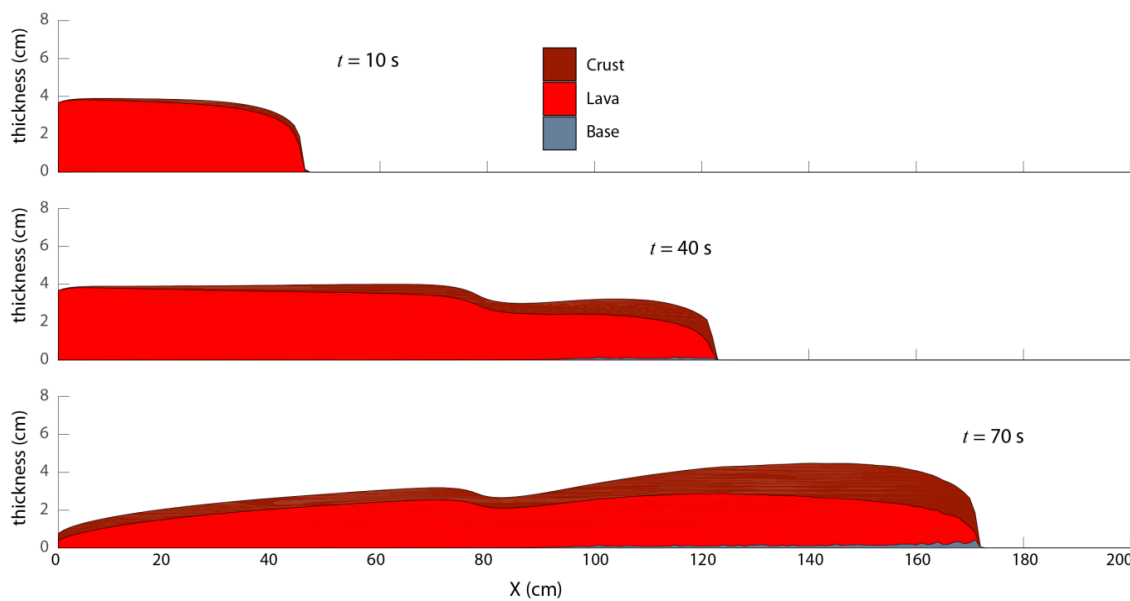


Figure 5. 18 Lateral profiles of the advance of the flow in the X axe for 10, 40 and 70 s using the Model n°3: hot interior and crust formation. As it is possible to observe, three layers are represented in the profiles which represent the crust, lava (interior lava) and the base.

The final deposit using this model for 128 s is shown in Fig. 5.19 and 5.20. Its geometry is characterized by $X_{max}=189$ cm, $Y_{max}=40$ cm and a $h_{max}=6.3$ cm. The first part of the deposit is wide, having a maximum width of 40 cm. A second and frontal part of the flow is narrow with 22 cm width. Due to the formation of the crust and levees, the surface of the flow is irregular. The flow is thicker at the front with 6.3 cm (Fig. 5.19) and at the borders. A comparison of the flow advance between the simulation and real data is shown in Fig 5.19 (right side).

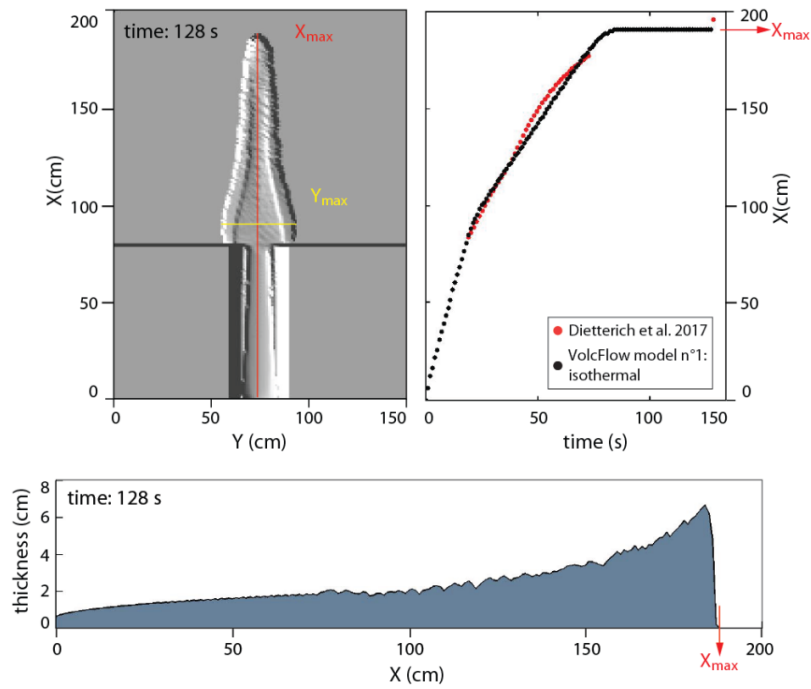


Figure 5. 19 Left: 2D view of the simulation for 128s using the hot interior and crust formation model. **Right:** Comparison of the advance of the flow between the results of the simulation (black dots) and the measured data (red dots). **Bottom:** Profile of the flow in the X axe at the end of the simulation.

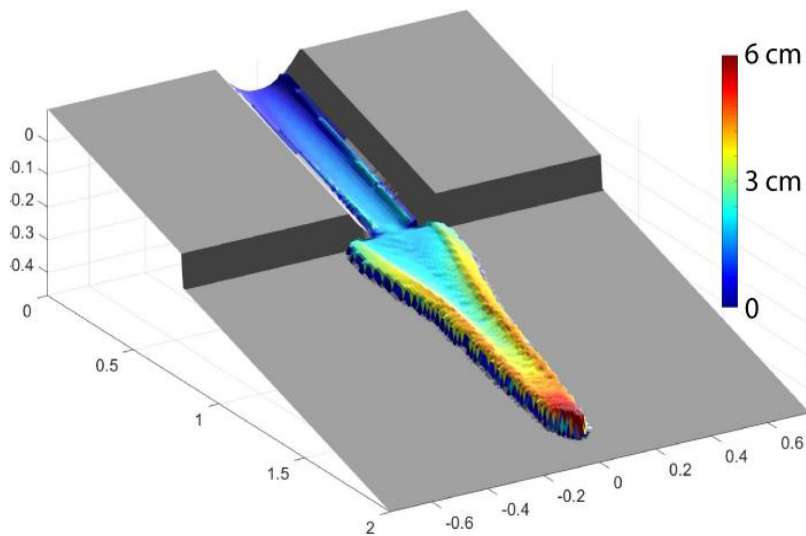


Figure 5. 20 3D view of the final deposit of the flow for 110s using the hot interior and crust formation approach. The deposit of the figure is represented by its thickness.

5.1.5 Discussion

Isothermal simulation (model n°1)

The flow was reproduced quite accurately by comparing with the real deposit (red border in Fig. 5.21). The shape of the simulation displays a rounded lobe with no levee formation. Its

dimensions in comparison with the real deposit are also very similar, having: a maximum length=191 cm, maximum width=60 cm and an average thickness=2.19 cm; against the dimensions of the real deposit: 196 cm, 62 cm and 2.28 respectively. On the other hand, the velocity of the flow front was nearly the same as in the experiment. Note that an exact value of the length could have been obtained by lowering slightly the constant yield strength.

Thermo-rheological variation (viscosity sigmoid law) simulation (model n°2b 1)

The model reproduced the flow very closely to the real deposit (Fig. 5.21). About the velocity, it was nearly the same as in the experiment, except that the front stopped a little bit too far (207 cm). Once again, this could have been improved by changing slightly the sigmoid law parameters. The maximum thickness of the flow was slightly too high: 2.72 cm (vs. 2.28 cm from the experiment). It seems that this model does not allow a regular distribution of material along the flow, but a major accumulation at the front (Fig. 5.10).

Similarities between the simulations from models n°1 and n°2b 1 were found, they are very close even if the physics is different. In model n°1, the final shape was essentially controlled by the yield strength that imposes the thickness of the lava at rest. In model n°2b 1, yield strength is null and the shape was controlled by the effect of the cooling on the lava rheology.

Thermo-rheological variation (yield strength sigmoid law) simulation (model n°2b 2)

This simulation displays a flow shorter than the experimental one (Fig. 5.21). The velocity was pretty similar to the measured one, with the difference that the simulation stops abruptly few centimeters before the real deposit. Furthermore, the shape of the lava at rest was too sharp, the flow became too narrow (36 cm) and too thick (4.93 cm). Some irregularities were observed at the edges, these may be caused by the strong rheological changes themselves as a result of the strong temperature variation in time and space. This strong effect of the cooling at the edges forms a levee and channel morphology, often described in the field, but not observed in the experimental results. Numerous simulations were carried out to try to reduce this effect but no simulation was better than the results presented on Fig. 5.15, 5.21.

Crust formation with hot interior simulation (model n°3)

The simulation was far from the experimental flow (Fig. 5.21). Its velocity was similar for a while but just like in the previous model, the stop was much more brutal than in reality. Levee

and channel morphologies were identified on the simulated flow. The channel became narrower and thicker along the simulation (Fig. 5.19) having a thickness of 6.3 cm at the front. The growth of the crust and the accumulation of hot lava behind the front explain this thickening.

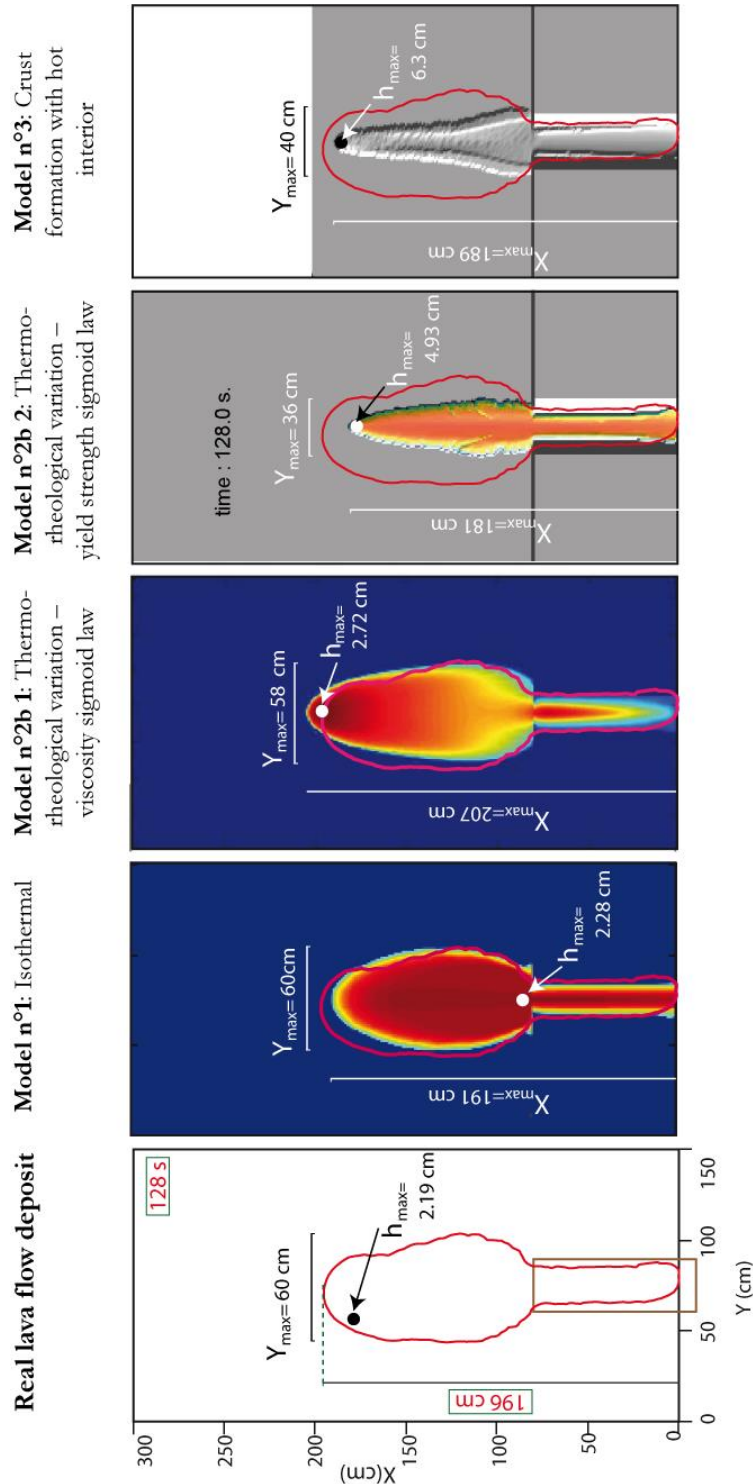


Figure 5. 21 Comparison of the emplaced flow between the real flow deposit (red line) and the four applied models for this case: Model n°1: **Isothermal**, Model n°2b 1: **Thermo-rheological variation – viscosity sigmoid law**, Model n°2b 2: **Thermo-rheological variation – yield strength sigmoid law** and Model n°3: **Crust formation with hot interior**.

Results demonstrate that the two first approaches can be used to reproduce such lava flow generated at the laboratory scale. However, **models n°2b 2** and **n°3**, are not adapted whatever the values of the parameters chosen. This do not mean that they are not adapted for real lava flows, because the size, the emplacement duration and the crystallinity in the field differ strongly from what can be done in laboratory. This is why, they have been confronted with natural lava flows in next sections.

5.2 Lava flow from Piton de la Fournaise

The Piton de la Fournaise volcano, located in the south eastern part of La Réunion Island, is one of the most active volcanoes in the world. This volcano of basaltic composition is characterized for having one eruption every 8 months (average since 1972) (Villeneuve & Bachelery 2006) with an average duration of 20 days (Roult *et al.* 2012).

The present section takes into account two lava flow cases:

1. The December, 9th 2010 lava flow.
2. The August – November 2015 lava flow.

The December, 9th 2010 lava flow case was used as a test case by Harris *et al.* 2015 for being simulated with FLOWGO. They presented the input data (Appendix 5.2) needed for the calculation of the thermo-rheological relationships used in FLOWGO (Harris & Rowland 2001). By its side, the flow emitted between August and November 2015 has the information about the flux of the lava emitted during the eruption (Courtesy M. Gouhier, LMV).

The flow simulated in this section contains information of both flows mentioned above. It was considering the thermo-rheological information from the 2010 flow and the flux emitted in 2015.

The main objective to simulate this lava flow is to observe how the flow behaves with the approaches proposed in Section 4.2 from Chapter 4 and not to reproduce strictly the lava flow deposit.

5.2.1 Description of the flow: the lava flow from August to November, 2015

The case to be simulated corresponds to the lava flow emitted from a fissure located at the south – west part of the Bory crater (western crater, at the border of the Central Cone) between August – November, 2015; combined with the thermo-rheological information from the

December 2010 lava flow. Figure 5.22 shows the images of the flow generation from the fissure and being dispersed through the south flank of the volcano. Based on the time averaged discharge rate (TADR) and visual images from the Piton de Bert (Courtesy M. Gouhier, LMV), M. Gouhier mentioned that the flow began to be emitted on August 23rd and had a duration of 69 days. The TADR information is very useful because of it allows to simulate the discharge of the flow in a realistic way (Fig 5.23). Based on the analysis of radar data, Froger *et al.* (2015) showed the preliminary results of the increasing area of the flow through time between August 29th and November 1st 2015 (Fig. 5.24). Having at November 1st a broad field of lava flows covering the south-south west part of the caldera.



Figure 5. 22 Lava flow advance from the visible camera Piton de Bert for the September 28th, 29th and October 10th, 2015. (Source: M. Gouhier)

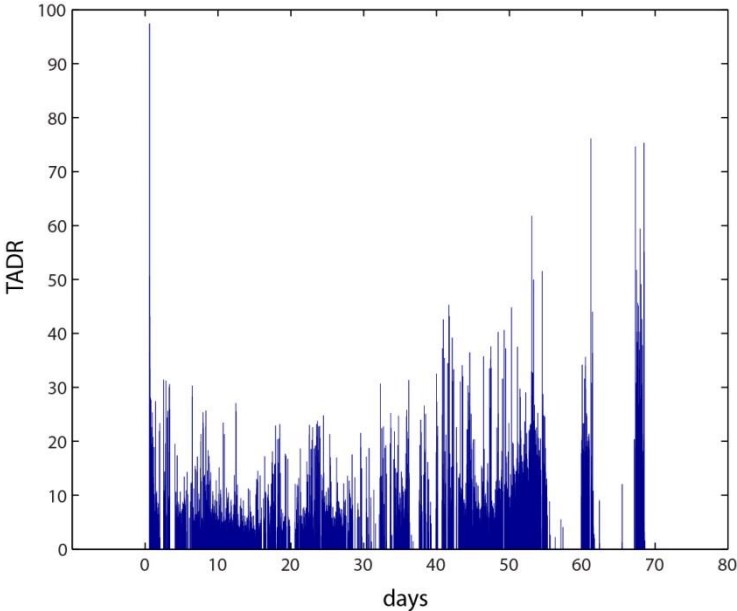
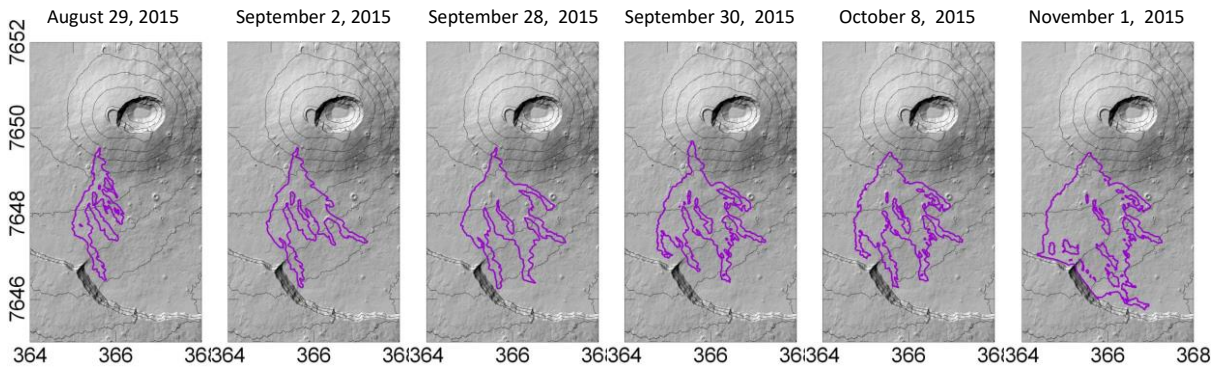


Figure 5. 23 TADR for the lava flow emitted between August –November 2015. (Courtesy M. Gouhier, LMV).

Preliminary results

Mapping of lava flow, exemple of August 2015 lava flow



Workshop ForM@Ter MDIS 7-8-9 October 2015, Autrans

Figure 5. 24 Preliminary results of the distribution of the August – November lava flow from Piton de la Fournaise based on radar data (Froger *et al.* 2015)

5.2.2 Initial conditions

Simulations were carried on using the digital elevation model (DEM) of 5m obtained from a Lidar image (J. L. Froger, LMV). The source of the lava flow generation was located at the external south western border of the Bory crater (Fig. 5.25). For the numerical calculation it was considered that the lava flow was emitted during 57 days (1368 h) and was emplaced in 100 days (2400 h), Appendix 5.2.

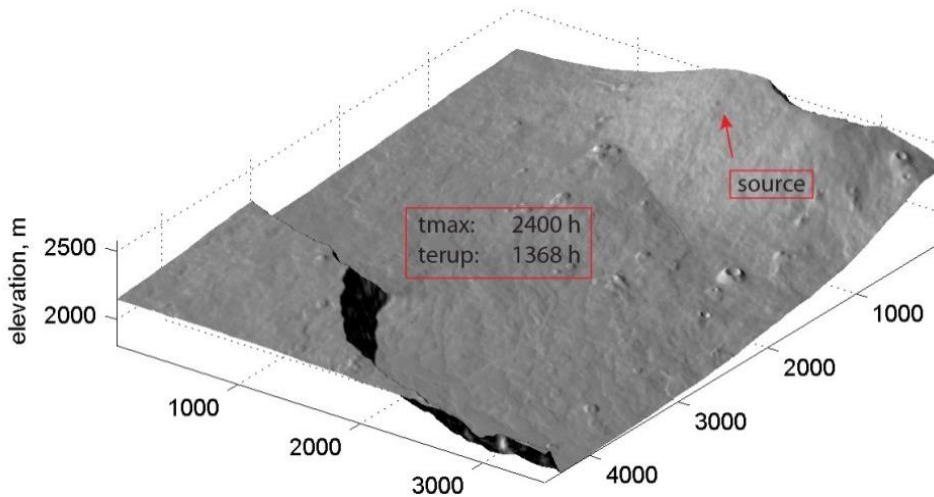


Figure 5. 25 Numerical topography used for the simulations of the August – September 2015 lava flow from Piton de la Fournaise.

The momentum is taken into account for the calculation of the new velocity at the source (previous velocity + new mass added with a null velocity). The temperature of the mass added is constant. The simulations showed below used the VolcFlow basic input parameters which are eruption time=1368 h, maximum time=2400 h, bulk density=1080 kg m³ (Appendix 5.2).

5.2.3 Numerical models

The lava flow from August – November, 2015 was simulated using three approaches:

1. **Model n° 1:** Isothermal.
2. **Model n° 2a:** Cooling and rheological variation using existing thermo-rheological laws.
3. **Model n° 3:** Crust formation with hot interior.

5.2.4 Simulations

5.2.4.1 Model n°1: Isothermal

The isothermal model considers that the flow behaves as a viscous-plastic fluid and is controlled by the viscosity and yield strength, which in this model remain constant during the whole simulation. The simulation uses the VolcFlow input parameters and a viscosity and yield strength of 1×10^5 Pa s and 5×10^3 Pa respectively (Appendix 5.2).

For this case it is possible to see the effect of the topography on the resulted flow. For the first part of its trajectory, in which the topography is steep, the flow travelled as a single unit meanwhile when the flow reaches the low slope it begun to be bifurcated in few fingers (Fig. 5.26, 1 day). As the flow progresses it allows the accumulation in some parts with low slope (Fig. 5.26, reddish color). During the progression, the flow reached thickness of about 5m.

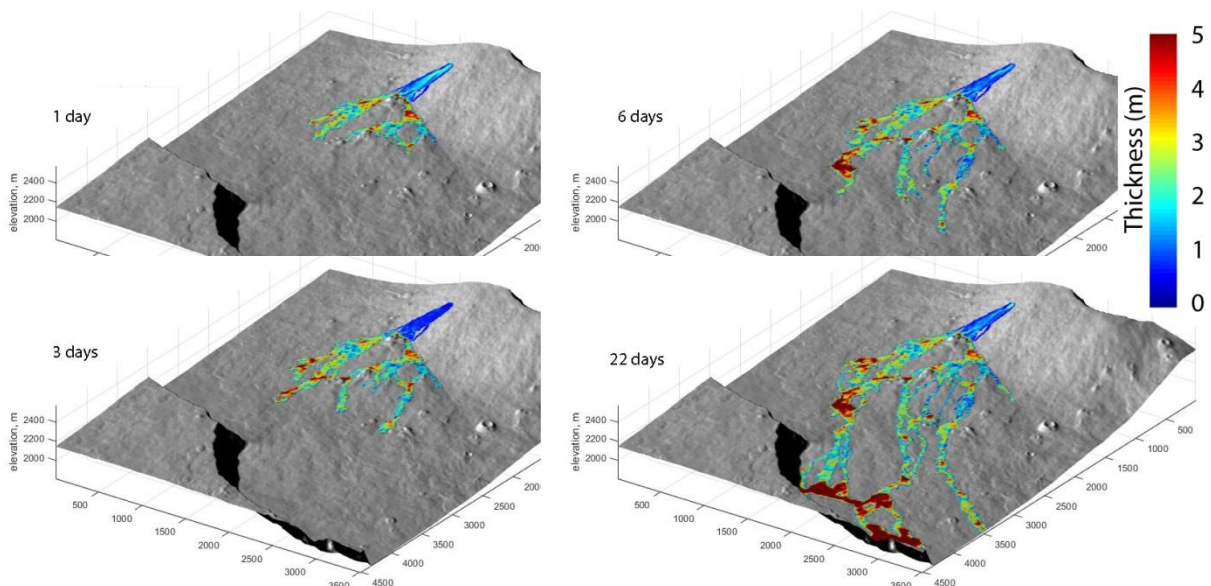


Figure 5. 26 Progression of the lava flow for 1, 3, 6 and 22 days by using the isothermal model for the simulation.

The 3D view of the final deposit after the 30 h of generation is shown in Fig. 5.27, the final deposit shows that the initial flow was bifurcated in many narrow fingers, with thickness $<10\text{m}$. The simulation shows an important accumulation of material in some parts with low slope (Fig. 5.27). The most part of the flow showed thickness between <0 and 4 m (blueish color, Fig. 5.27).

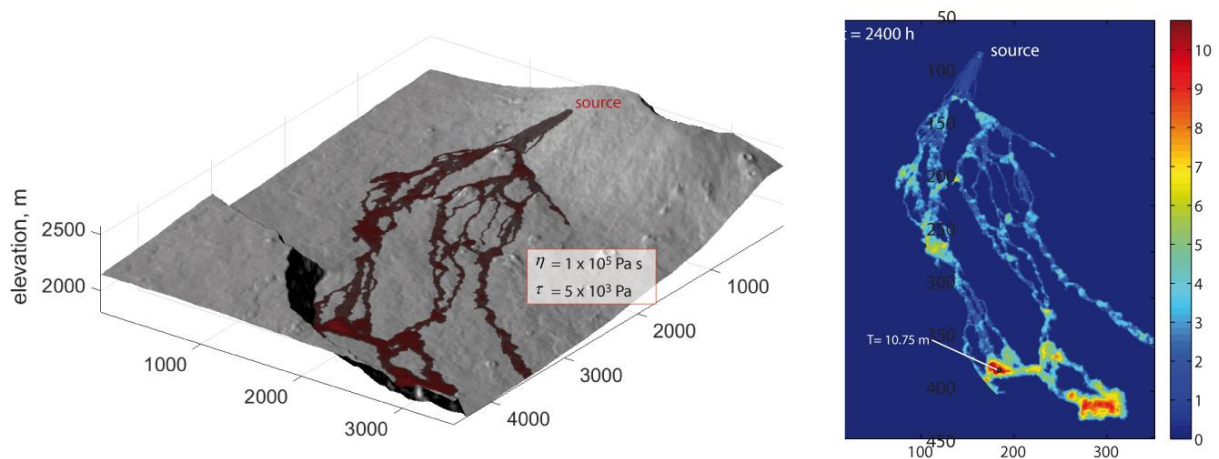


Figure 5. 27 Left: 3D view of the deposit of the flow from August – September, 2010 using the isothermal model. **Right:** Thickness of the deposit at the end of the simulation, the thicker part is located at the fronts of the flow reaching 10.75 m .

5.2.4.2 Model n°2a: including the effect of the cooling and rheological variation

This model uses the VolcFlow basic input parameters and those to estimate the cooling and rheological variation (Appendix 5.2). The cooling for this lava flow was estimated using the Eq. 4.14 (Chapter 4) and considered the radiation, convection and conduction parameters from Harris *et al.* 2015. The radiation parameters are the Stefan-Boltzmann $=5.67\text{E-}08\text{ W m}^{-2}\text{ K}^{-4}$ and emissivity $=0.95$. The convection estimation includes the $C_H=0.0036$, the air specific heat capacity $=1500\text{ J kg}^{-1}\text{ K}^{-1}$, air temperature $=293.15\text{ K}$, wind speed 5 m s^{-1} , air density $=0.4412\text{ kg m}^{-3}$. Conduction parameters are $h_{\text{base}}=0.266\text{ m}$, thermal conductivity $=0.88\text{ W m}^{-1}\text{ K}^{-1}$, core to basal distance $=19\%$, flow thickness $=1.4\text{ m}$, basal temperature $=773.15\text{ K}$. The density and vesicularity parameters considers a vesicularity $=0.64$ and a DRE density $=2970\text{ kg m}^{-3}$. Thermal takes into account the buffer $=140$, crust temperature $=773.15\text{ K}$, core temperature $=1387.15\text{ K}$ and a constant crust cover fraction $=0.6$. The crystal content parameters are the latent heat of crystallization $=3.5 \times 10^5\text{ K kg}^{-1}$, crystals growing during cooling $=0.90$, cooling rate $=150\text{ K}$, rate of crystallization $=0.005973\text{ K}^{-1}$ and the constant $R=1.51$. The source of these parameters is noted in Appendix 5.2.

The rheological variation was estimated by using the following laws:

- ❖ **Dynamic fluid viscosity:** the VTF equation (Eq. 4.22, Chapter 4) from Giordano & Dingwell (2008). This equation requires the knowledge of three parameters: the constant independent of composition (VTF_A), and two adjustable parameters VTF_B and VTF_C. These three are given by Villeneuve *et al.* (2008) and correspond to -4.55, 5558 and 276.711 respectively, Appendix 5.2
- ❖ **Relative viscosity:** from the Einstein 1906 & Roscoe 1952 relationship, Appendix 5.2.
- ❖ **Yield strength:** From Dragoni 1989; Pinkerton & Stevenson 1992. This relationship uses two constants B and C correspondent to 0.01 and 00.8 respectively, Appendix 5.2.

The progression of the lava flow simulation using this model is shown in Fig. 5.28. Once the flow arrives to the caldera floor it begun to branch itself and this process continues along its propagation. At a difference of the previous model, here the fingers are wider (~20-50m). As well with this model the distribution occupied more surface than the previous one.

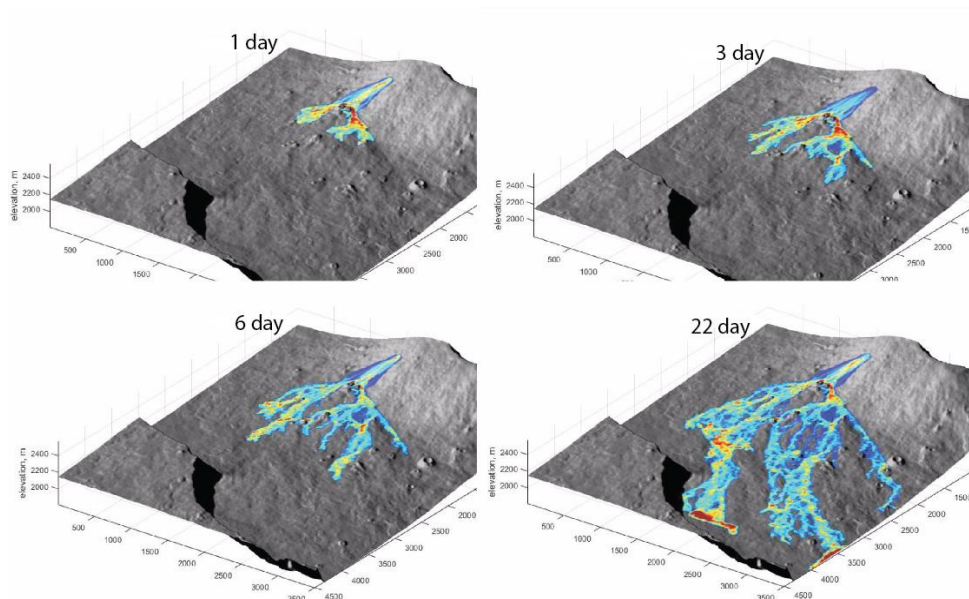


Figure 5. 28 Progression of the lava flow for 1, 3, 6 and 22 days, using the model n°2a which takes into account the cooling and the existing rheological laws. The image shows the bifurcations of the flow when it reaches the topography with low slope

Fig. 5.29 shows the thickness variation along the flow, showing that the most part of the flow had thickness between 0 and 6m. A major accumulation of lava was recognizable at the

fronts and at the border of the numerical domain with ~ 11 m (Fig. 5.29, 5.30). This model allowed a broadly distribution of the flow on the caldera floor (Fig. 5.29, 5.30).

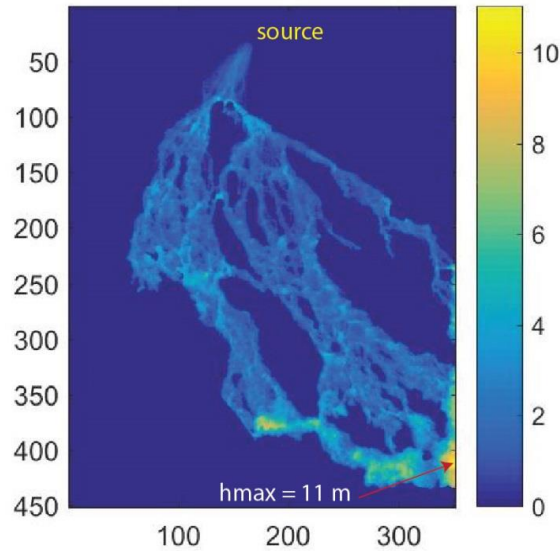


Figure 5. 29 Representation of the thickness of the flow at 2400 hours (100 days) in which is possible to observe a maximal accumulation of the material at the fronts and at the limit of the numerical domain., in which it reaches about 11 m of thickness.

According to the chosen model, viscosity varies between <0 and 1×10^6 Pa s in a temperature range of 830 and 1114 °C (1387.15 K, core temperature).

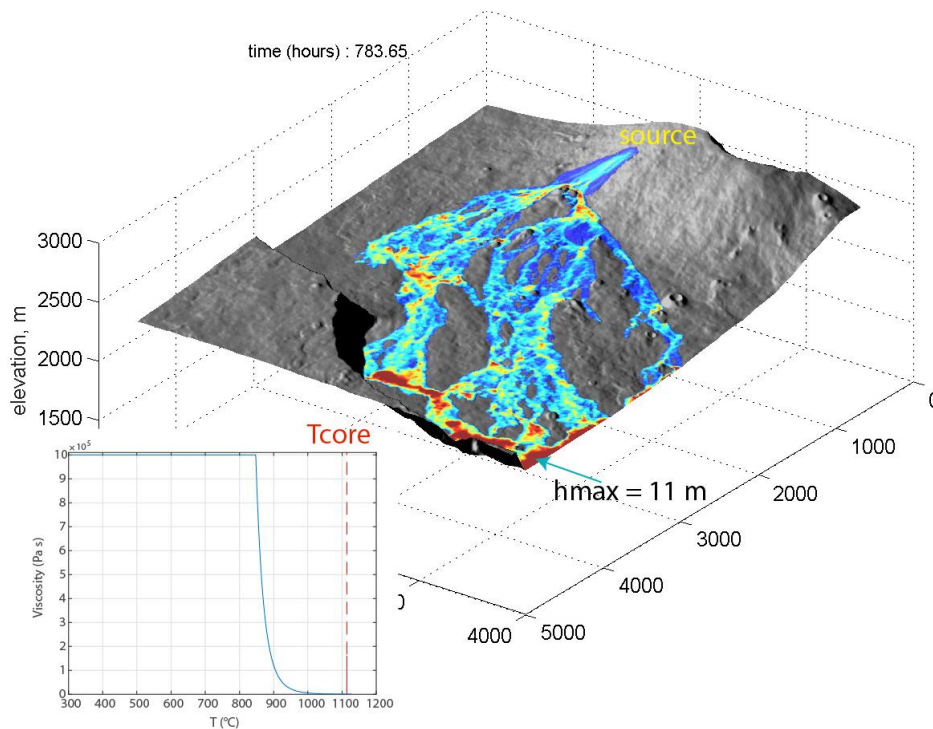


Figure 5. 30 3D view of the deposit of the flow, which shows the accumulation at the fronts and at the border of the numerical domain. The viscosity varies between 0 and 1×10^6 Pa s in a range of temperature of 1114 and 830 °C (1387.15 – 1103.15 K)

This change of viscosity for that range of temperature suggests that the shape of the flow has been controlled mainly for this rheological parameter. About the yield strength, its variation is minimal and suggest that it doesn't have the same influence as the viscosity.

5.2.4.3 Model n°3: Crust formation and hot interior

One of the characteristics of basaltic lava flows it that their external parts can form a crust due to the fast cooling. This viscoelastic layer can isolate the hot flow from the low atmospherical temperature, and can be expanded allowing the hot lava travel beneath it. These characteristics called the attention to simulate this basaltic flow with the crust formation and hot interior model. The aim is to determine if the flow can create crust at the external part of the flow and see if once the flow has formed the crust, another flow can come and travelled over the flows with a developed crust.

The development of the crust is obtained by following the equations from Section 4.2.3 (Chapter 4). This model uses the VolcFlow input parameters those related to the crust formation, which are the rate of growth of the crust= $1 \times 10^{-5} \text{ mm h}^{-1}$, viscosity= $1 \times 10^5 \text{ Pa s}$ and yield strength= $5 \times 10^2 \text{ Pa}$ (Appendix 5.2).

The progression of the flow with this model is shown in Fig. 5.32 for 1, 3 and 6 days. In the steepest part the flow forms a single unit and when it reaches the lowest slope it follows the same tendency. Just small bifurcations are identified in the fronts of the flow, nevertheless it doesn't distribute broadly as in the previous models. The simulation reaches the objective of formed a crust, but when it is formed the lava continue to be accumulated at the front and borders allowing the formation of steepest borders, restricting the formation of new branches. This can explain the vague distribution of the flow over the topography in comparison with the other simulations (isothermal and cooling with variable yield strength).

The thickness during the first six days varies between <0 and 10 m. At 314.22 h (13.1 days) of the propagation of the flow, the calculations generated a rheological instability due to the crust formation. This instability is reflected in an incoherent thickness value of the flow of 2730 m. This instability is located close to the vent and shows an important accumulation of material in their surroundings (reddish colors). Figure 5.33 shows the result of the simulation before the rheological instability came up.

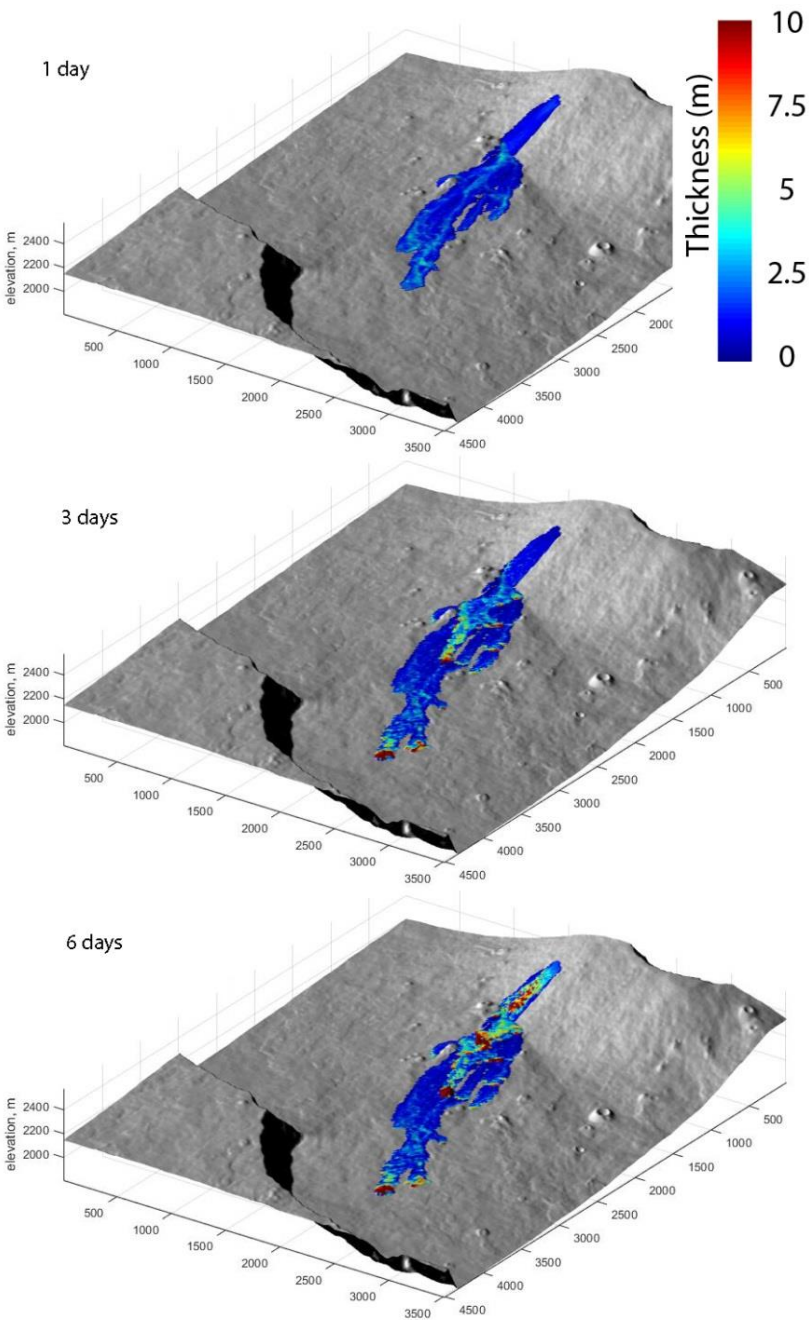


Figure 5. 31 3D evolution of the flow using the model n°3: crust formation with hot interior for 1, 3 and 6 days. The distribution of the flow is not vague in comparison with the results from the previous models. The formation of the crust, which allows the formation of steepest walls could influence in the narrow distribution of the flow.

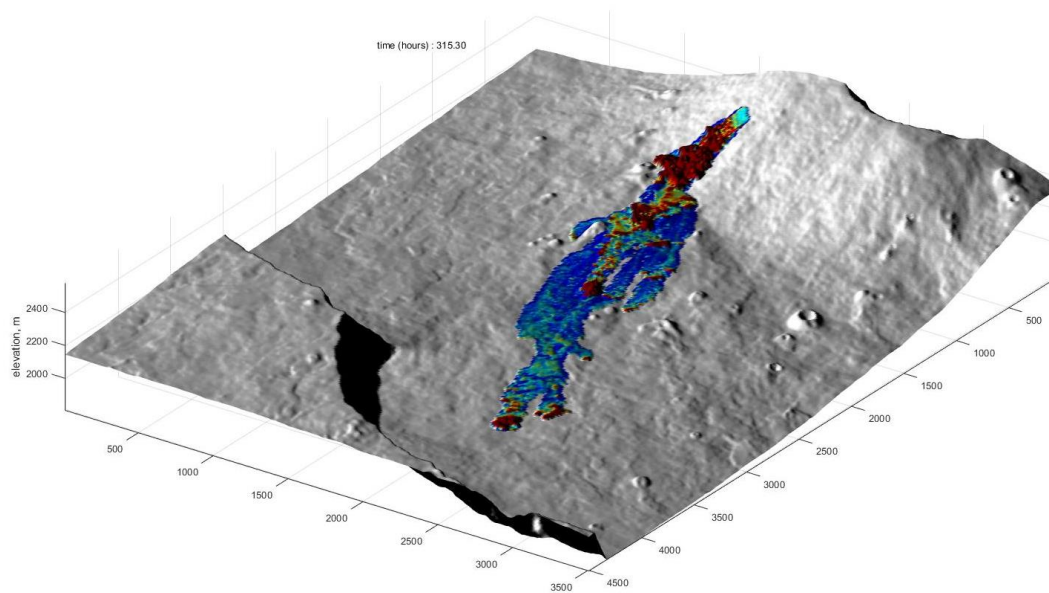


Figure 5.32 3D view of the flow for 13.1 days (314.22 h) in which a rheological instability happened due to the crust formation and brought a thickness of 2730 m.

5.2.5 Discussion

The aim of this simulation was to observe and describe the behavior of the flow with the proposed models. However, Fig. 5.33 shows the deposits of the three simulations carried out here against the deposit of the flow from August-December 2015 (black-yellow contour) as a way to show the final emplacement of the different simulations.

Isothermal simulation (model n°1)

The simulation shows a deposit which is branched in three main narrow units (<10m width each one). A major accumulation of lava was recognized at the fronts (~ 11 m). The rest of the flow had thickness between <0 and 4 m. By comparing the simulation with the real deposit (yellow border, Fig. 5.33 a'), the main part of the simulated flow was emplaced inside the real deposit. Only a small portion of the simulation was emplaced outside of it.

Cooling and rheological variation using existing thermo-rheological laws (model n°2a)

This simulation displays a deposit that covers a broad area, filled up in almost the totality of the real flow (black line, Fig. 5.33 b'). A portion of the simulation was emplaced outside of it. The flow units were wider (~10-20 m) in comparison with those from model n°1. About the

thickness of the flow it presented an accumulation at the fronts of about 11 m and for the rest of the flow the thickness varies between <0 and 6 m.

The variation of yield strength during the simulation is minimal meanwhile the viscosity varies in six orders of magnitude, suggesting that the final shape of the flow is controlled by the viscosity.

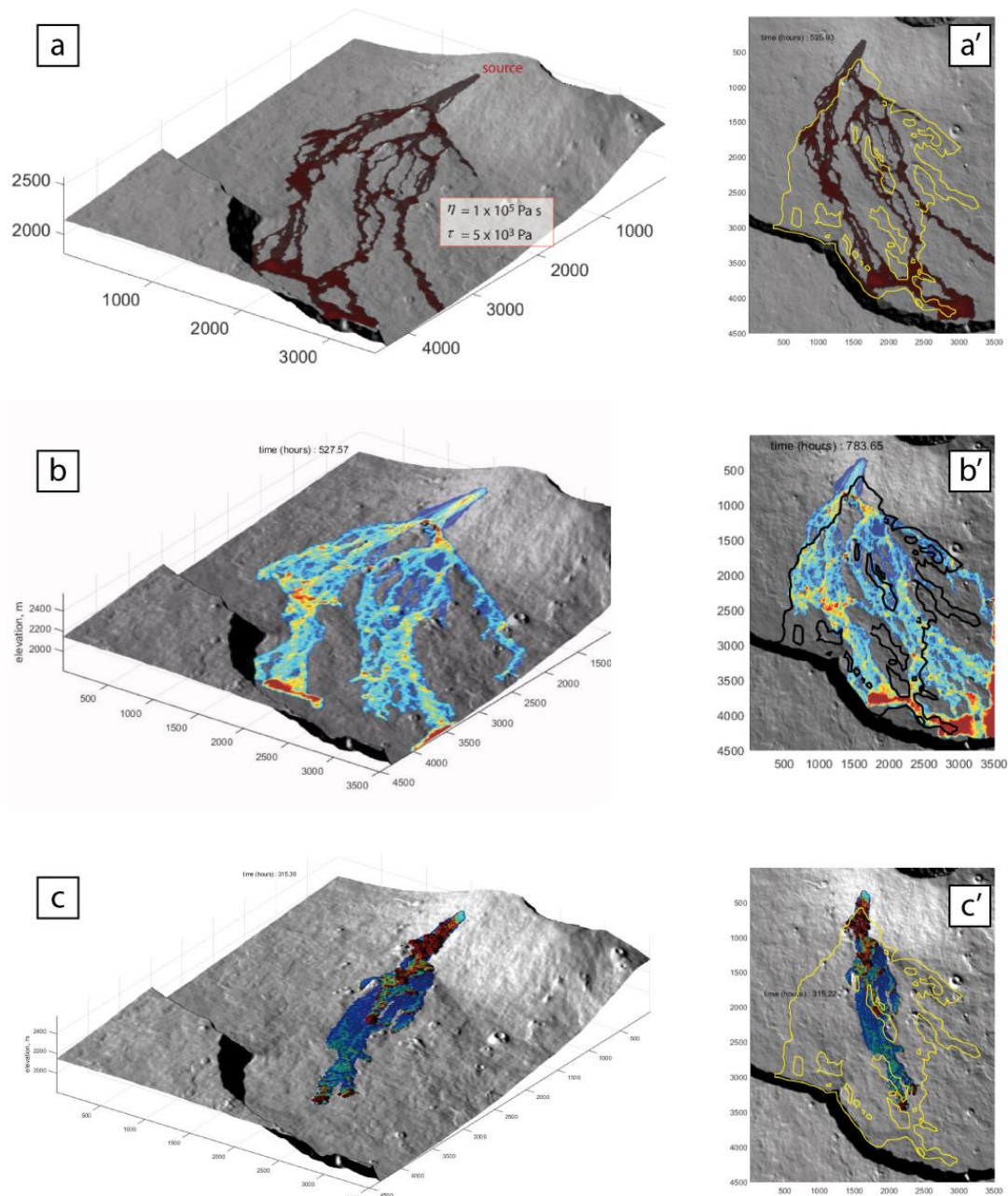


Figure 5. 33 Simulations of the August-December 2015 lava flow from Piton de la Fournaise. Left side: 3D view of the simulated flow, right side: 2D view of the simulated flow against the real deposit (yellow/black line). Isothermal model (a, a'). Cooling and rheological variation using existing thermo-rheological model (b, b'). Crust formation with hot interior model (c, c').

Crust formation with hot interior simulation (model n°3)

It shows a dispersion of the flow totally different to the correspondents of the two previous models. In fact, the distribution of the flow is very limited, this is due to the formation of the crust in the flow. By comparing it with the real flow (yellow line, Fig. 5.33 c') it shows that it was emplaced entirely on its area but it did not show any similarity with the real deposit.

Meanwhile the flow advance over the topography, the crust begun to be developed and as the hot material continue to be fed, the crust continues to grow up. Hence, the formation of the crust does not allow the lava to flow in other directions and therefore not to have a broad dispersion. The rheological instabilities found in during the simulation could be related to crust formation.

Even if the main purpose of these simulations was not to reproduce exactly the flow, model n°2 showed that it is the most likely to reproduce a basaltic lava flow. This based on the distribution and thickness of the flow. As a second option it could be chosen the isothermal one, considering just the extension and thickness but not the emplaced area. In the other hand, the crust model generated a flow that is no larger as the real flow and above all the other parameters, the thickness does not show any similarities with the real one. Then this last model won't be used to simulate the other two cases in this study.

5.3 Lava flow from the December 5th, 2010 eruption of Tungurahua volcano (Ecuador)

This study case corresponds to the first application to simulate lava flows with VolcFlow using an isothermal approach (Section 4.2.1, Chapter 4). Detailed information of the flow generation, data collection and results of this simulation can be found in Vallejo 2012; Kelfoun & Vallejo Vargas 2015 (Appendix 5.3).

5.3.1 Description of the flow

An eruptive phase took place on November-December, 2010 in Tungurahua volcano (Ecuador) after four months of relative calm and it was characterized by an explosive and effusive phases. On December 4th a very strong explosive activity was recognized at 14h38 UTC (Ecuadorian time +5 hours) and was sustained for about 5 hours, generating an eruptive column

of 3-4 km high which produced ash falls to the west of the volcano. Additionally, at least 34 medium size pyroclastic density currents (PDC's) descended the gullies on the northeastern, northwestern, western and southwestern of the volcano. On December 5th at 01h50 UTC, harmonic tremor was detected in the volcano and lasted about 2.5. It was related with the emission of a lava flow which travelled from the crater and halted on the upper part of the NNW flank of the volcano, following the path of the Mandur Gully (Fig. 5.34), (Vallejo Vargas 2012).

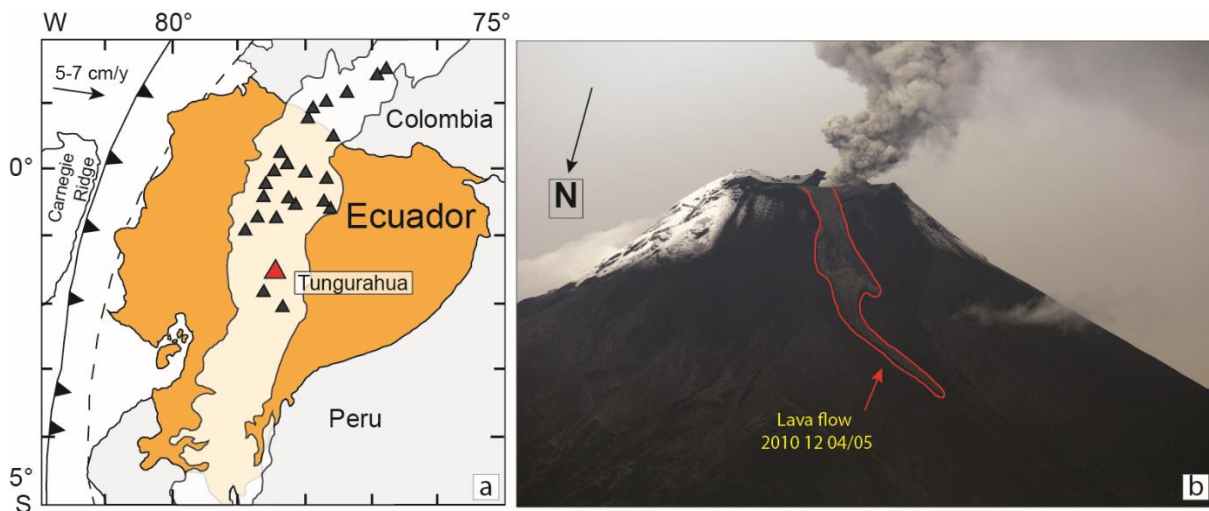


Figure 5. 34 a) General context of the Tungurahua volcano location. **b)** Picture of the lava flow deposit from the December 4th and 5th, 2010 (Photo: B. Bernard, IG-EPN).

5.3.1.1 Recorded data during the eruption

During the generation of this lava flow, 90 thermal images were recorded with an IR FLIR camera in hand-held mode and others by mounting the camera on a tripod. The analysis of the evolution of the flow was done using 10 IR images taken between December 4th and 5th (Fig. 5.35) using a FLIR Systems ThermoCAM PM695 camera (resolution of 320x240 pixels).

The aim to analyze the thermal sequence of the lava flow was to determine the cooling of the flow and to quantify the advance of the flow over the topography. As the sequence was taken from a long distance (13 km) it was not possible to obtain coherent results for the cooling, due to this analysis should be done with images taken at short distances (<5 km). For the second objective a methodology was developed (Vallejo Vargas 2012; Kelfoun & Vallejo Vargas 2015), in which thermal images were projected over a 4 m digital topography by applying a Matlab® script using the position of the camera, angles of the camera (direction (α), inclination (β), rotation(γ)) and its field of view (FOV). Fig. 5.36 shows the schema of thermal images projection over the topography.

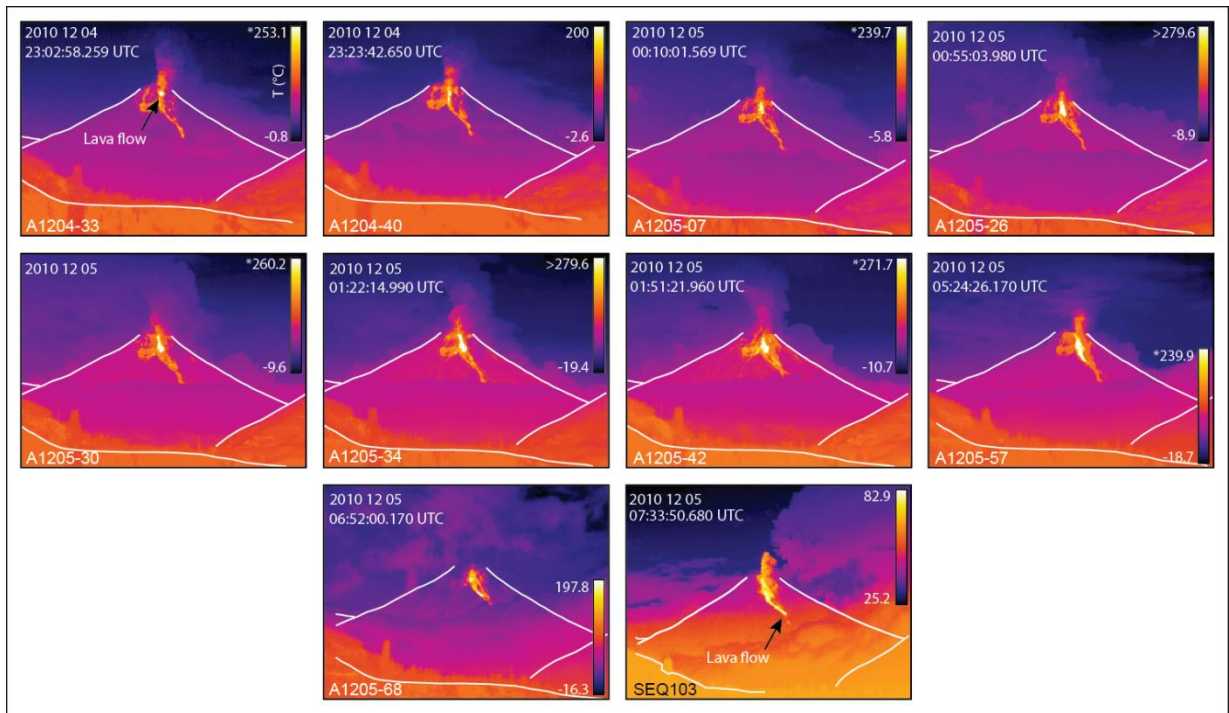


Figure 5. 35 Thermal images sequence of the advance of the lava flow over the topography through the northwestern flank of Tungurahua volcano (From: Vallejo Vargas 2012, Source: IG-EPN).

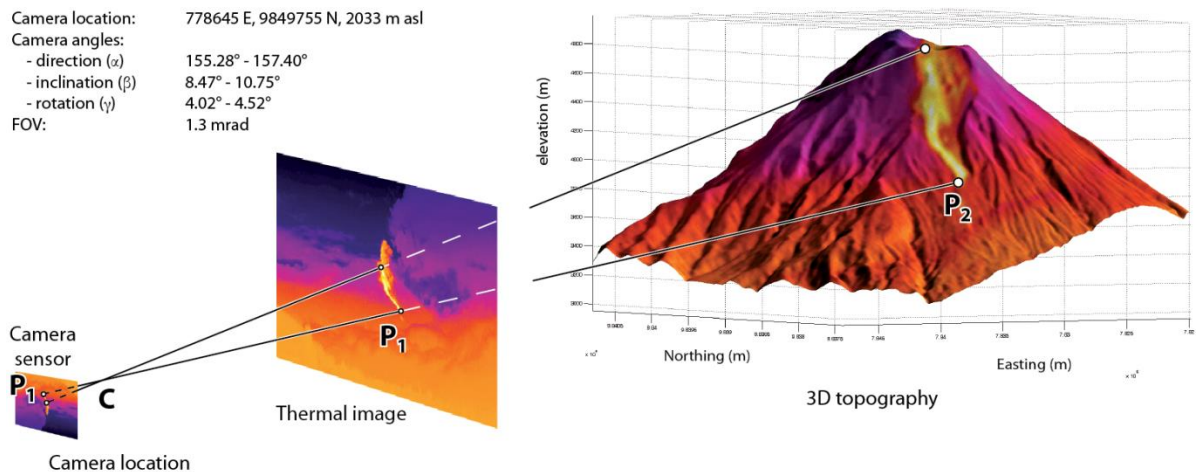


Figure 5. 36 Scheme that represents the projection of thermal images onto the 4m digital topography with the aim to calculate the position of the front and the extension of the flow through the time (Kelfoun & Vallejo Vargas, 2015).

By following this methodology, it was possible to determine the spatial location of the flow contour previously identified in each thermal image. The low resolution of the images constrained to have a precision between 40 and 65 m depending of the topographical slope and

the distance from the camera. The analysis of the ten thermal images helped to determine the advance of the flow front from the crater over the topography (Fig. 5.37).

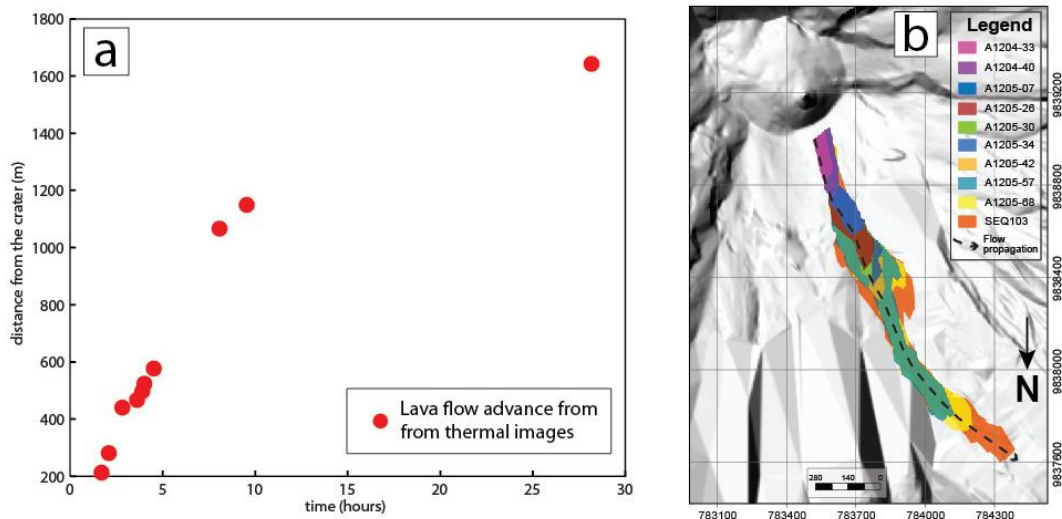


Figure 5.37 a) Time evolution of the distance between the lava front and de source during the generation of the flow between the 4th and 5th December 2010. b) Evolution of the lava flow over the topography. (Vallejo Vargas 2012; Kelfoun & Vallejo Vargas 2015).

The flow stopped 1.64 km from the crater, the thickness was estimated to be about 3 – 5 m (Bernard, B., IG-EPN, personal communication). Its volume was calculated in 10^6 m^3 . There were no rock samples of the flow and therefore no chemical analysis. For the simulations that consider the rheological variation in function of the composition (Section 4.2.2) it was used the chemical composition of the 2006 lava flow in this volcano (Chevrel *et al.* 2015; Appendix 5.4).

5.3.2 Initial conditions

For all the simulations it has been used the digital elevation model (DEM) of 4 m resolution, developed by the SIGTIERRAS project of the Ecuadorian Government in 2011. The 2010 lava flow topography was visible in the 2011 DEM and was removed by extrapolating the topography from it. The source of the flow was assumed to be at the north northwestern border of the crater (Fig. 5.38). The lava flow was simulated with a constant discharge rate (Q_{lava}) of 55.5 m s^{-1} , which is equivalent to generate a volume of 10^6 m^3 in 5h.

The momentum is taken into account for the calculation of the new velocity at the source (previous velocity + new mass added with a null velocity). The temperature of the mass added is constant. The three simulations detailed below used the basic input parameters needed by

VolcFlow, which are detailed in Appendix 5.4 and the source was located at the border of the crater, Fig 5.38.

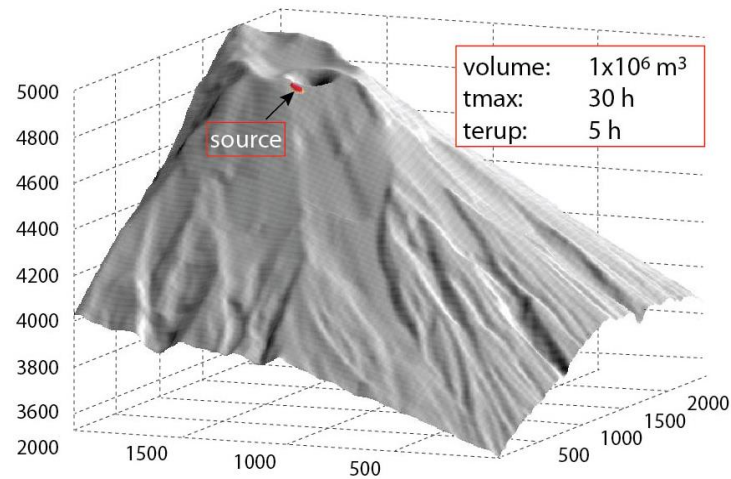


Figure 5. 38 Numerical topographic used for the simulation of the molten basalt.

5.3.3 Numerical models

This lava flow was simulated using three approaches:

1. Model n°1: Isothermal (Kelfoun & Vallejo Vargas 2015).
2. Model n°2a: Cooling and rheological variation using existing thermo-rheological models.
3. Model n°2b: Cooling and rheological sigmoid law.

Best results of the simulations from model n°1 and n°2b were obtained by trial and error method through the comparison of the observed flow advance (this Chapter) and the correspondent simulated ones. These comparisons are shown below for 00:51, 02:37, 8:19 and 26:09 hours.

5.3.4 Simulations

5.3.4.1 Model n°1: Isothermal

The isothermal model considers that the flow is controlled by viscosity and yield strength, which remain constant during the whole simulation. Many pairs of values of these parameters were applied in the model as it is shown in Fig. 5.39. The best fit given from the simulation was obtained with a viscosity of 4×10^6 Pa and yield strength of 6×10^4 Pa (Appendix 5.4). The simulation of the flow using the isothermal approach reproduced a unique flow (Fig. 5.39 B) characterized for a maximum length of 1.65 km and an average thickness of 5 m.

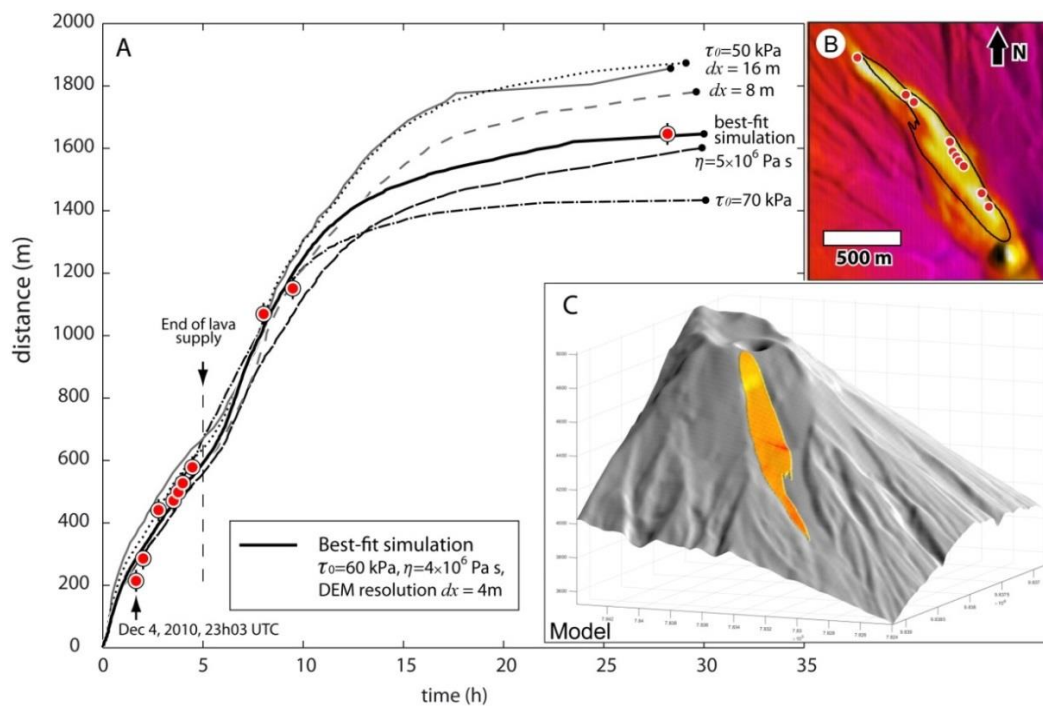


Figure 5.39 **A)** Time evolution of the flow between the source and the front. Red dots show the calculated advance of the flow from the analysis of thermal images, black dotted lines the results of the simulations using different values of viscosity and yield strength; black regular line corresponds to the best fit between the simulation and the data (red dots). **B)** portion of the thermal image projected over the topography showing the advance of the flow over the surface (red dots). **C)** Deposit of the simulated lava flow with the best fit parameters for viscosity and yield strength (Kelfoun & Vallejo Vargas 2015).

5.3.4.2 Model n°2: including the effect of the cooling and rheological variation

Simulations of the Tungurahua's lava flow using the model n°2 were governed by the cooling of the flow and variation of the rheological parameters viscosity and yield strength. The cooling was estimated using the Eq. 4.14 and the rheological variation using models mentioned in Section 4.2.2.2 (Chapter 4). The combination of the cooling with both rheological models allowed to have two approaches for the model n°2, which are:

2. Model n°2a: Cooling and rheological variation using existing thermo-rheological models.
3. Model n°2b: Cooling and rheological sigmoid law.

The radiation parameters are the Stefan-Boltzmann $=5.67E-08 \text{ W m}^{-2} \text{ K}^{-4}$ and emissivity $=0.95$. The convection estimation includes the $C_H=0.0036$, the air specific heat capacity $=1500 \text{ J kg}^{-1} \text{ K}^{-1}$, air temperature $=298.15 \text{ K}$, wind speed $=5 \text{ m s}^{-1}$, air density $=0.4412 \text{ kg m}^{-3}$. Conduction parameters are $h_{\text{base}}=0.266$, thermal conductivity $=0.88 \text{ W m}^{-1} \text{ K}^{-1}$, core to basal distance $=19\%$, flow thickness $=0.95 \text{ m}$, basal temperature $=373.15 \text{ K}$. The density and vesicularity parameters considers a vesicularity $=0.01$ and a DRE density $=2350 \text{ kg m}^{-3}$. Thermal takes into

account the buffer=0, crust temperature=373.15 K, core temperature=1173.15 K and a constant crust cover fraction=1. The crystal content parameters are the latent heat of crystallization= 3.5×10^5 K kg⁻¹, crystals growing during cooling=1, cooling rate=379.35 K, rate of crystallization=0.0026361 K⁻¹ and the constant R=1.51 (Appendix 5.4).

5.3.4.2.1 Model n°2a: Cooling and rheological variation using existing thermo-rheological models

This approach used the VolcFlow basic input parameters and those to estimate the cooling and rheological variation, described above (Appendix 5.4).

Viscosity was estimated by the combination of dynamic and relative and viscosity meanwhile the yield strength was estimated using a single relationship as shown below:

- ❖ **Dynamic fluid viscosity** the VTF equation (Eq. 4.22, Chapter 4) from Giordano & Dingwell (2008). This equation requires the knowledge of three parameters: the constant independent of composition (VTF_A), and two adjustable parameters VTF_B and VTF_C. These three parameters were calculated by using the chemical composition of the Tungurahua's 2006 andesitic lava flow (Chevrel *et al.* 2015) and correspondent to - 4.55, 9740.3 and 417.7 respectively (Appendix 5.4).
- ❖ **Relative viscosity** by applying the Krieger & Dougherty (1959) model assuming that crystals have an aspect ratio=1.7 (Muller *et al.* 2010), having a maximum packing=0.542.
- ❖ **Yield strength:** From Dragoni, 1989; Pinkerton & Stevenson, 1992. This relationship uses two constants B and C correspondent to 0.01 and 00.8 respectively (Appendix 5.4).

The evolution of the flow using the model n°2a is shown in Fig. 5.40 for 00:51, 02:37, 8:19 and 26:09 hours. The 3D evolution (left side) shows the dispersion of the flow over the topography. The comparison of the flow advance between the simulated and the observed flows is shown in the right side of the figure with blue line and red dots respectively.

Figure 5.40 shows that for the first 9 hours approximately, the flow moved with an average velocity of 0.005 m/s and after it decreased substantially to 1.38×10^{-4} m/s. The temperature of the flow at 30 h shows a variation between 417.7 and 1038 K (144 – 765 °C). The highest temperature was found in the inner part of the flow very close to the front with 1038 K

(764.8 °C) and the lowest temperature, close to the source and the borders of the flow with a minimum value of 417 K (144,7 °C) (Fig. 5.41b).

The final deposit of the simulation at 30 h is shown in Fig. 5.41. Firstly, it is representing the spatial distribution of the flow showing that it is composed by a single flow emplaced on the NNW flank of the volcano reaching a distance about 400 m from the crater. Second, it is possible to observe the variation of the temperature during the 30 h of simulation in the graph located in the upper-right side of the figure. It was obtained by a continue measure during the whole simulation of the temperature on the black dot located very close to the lava source. It shows a temperature variation between 1173.15 and 1029 K (900.15 – 756 °C), the highest value corresponds to T_{core} and it lasted 5 hours which is the time the flow has been emitted. After these five hours the temperature starts to decrease because of there is no more lava alimentation.

The thickness of the flow simulation at 30 h is variable showing accumulation of material at its front with 30.4 m meanwhile the thinner deposit is about 0 m close to the source (Fig. 5.42a).

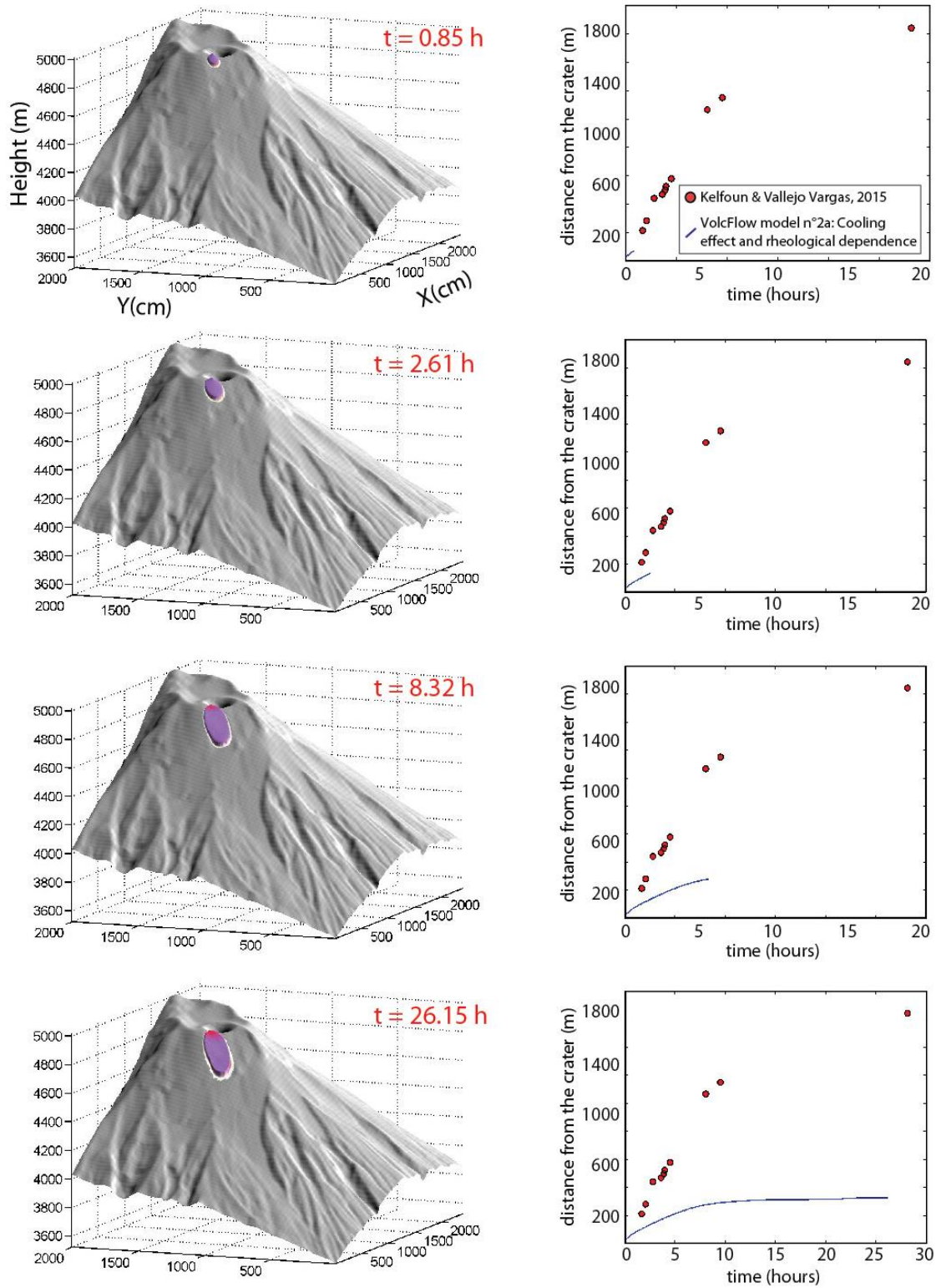


Figure 5. 40 Progression of the flow with VolcFlow, using the effect of the cooling and existing rheological relationships. The progression is shown for 00:51, 02:37, 8:19 and 26:09 h of generation of the flow. Left side represents the 3D progression of the flow over the topography. Right side shows the comparison of the distance advance of the flow simulation (blue line) with the real data (red dots).

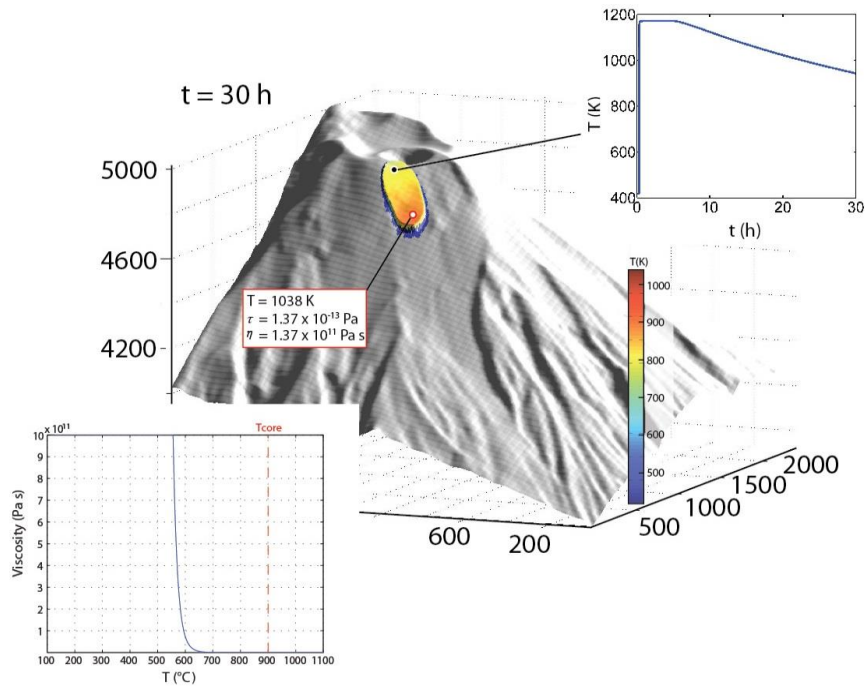


Figure 5. 41 3D view of the distribution of the flow represented by the temperature variation (417.7 - 1038 K). Temperature variation at the black is represented in the T(K) vs t(h) graph which shows that temperature at the black point during the whole simulation varied between 1173.15 and 1029. The hottest point of the flow at 30 h reached 1038 K and presented a viscosity of 1.37×10^{11} Pa s and yield strength of 1.37×10^{-13} Pa.

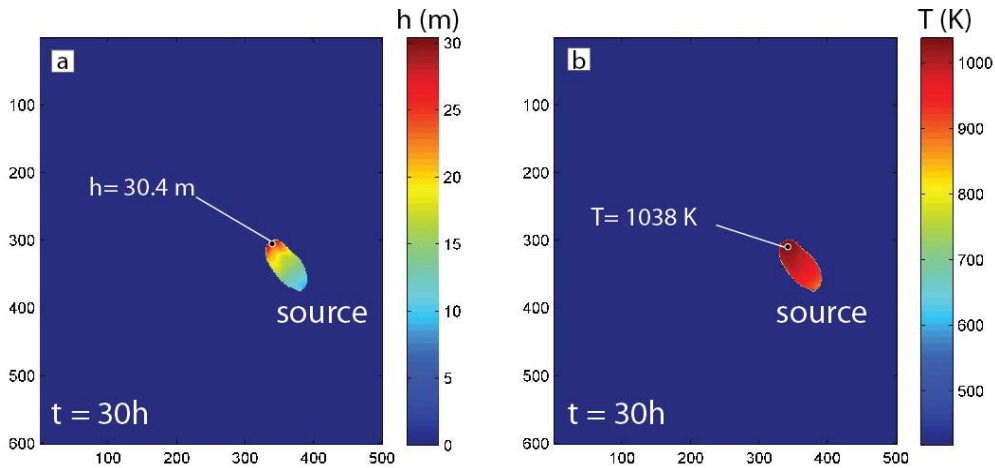


Figure 5. 42 Representation of the thickness (a) and temperature (b) distribution of the simulated flow at 30h. a) The thickened part of the flow is located at the front reaching 30.4 m and on the external borders of the flow close to the front. b) The hottest part of the flow is recognized at the inner part of the flow front with 1038 K and the coldest at the borders and source with 417.7 K.

The morphology of the front and lateral borders at the very initial part of the head of the flow are characterized for having a steep slope in contrast with the thickness measures. A slight thickening was recognized between these borders respect to the inner part or the flow, suggesting the formation of levees structures (Fig. 5.43).

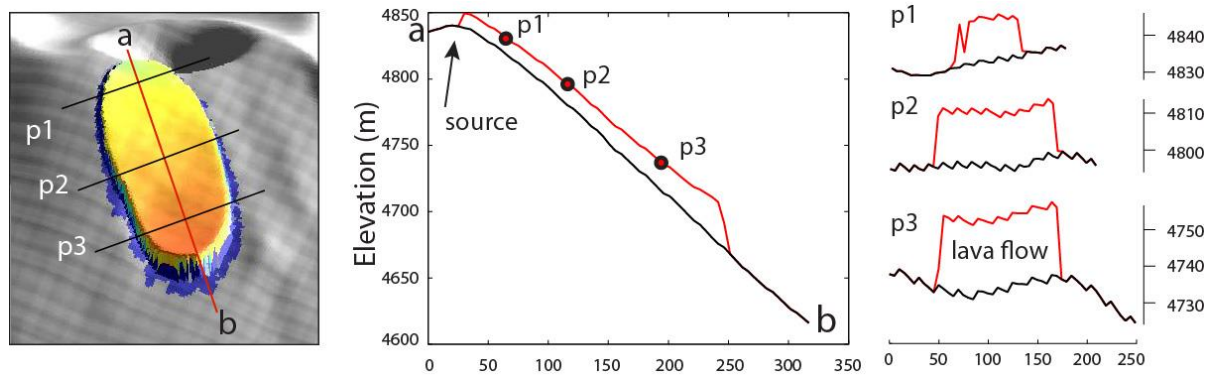


Figure 5.43 Cross sections of the flow showing the thickness and the slight thickening at the borders.

5.3.4.2.2 Model n°2b: Cooling and rheological sigmoid law

This method considers that the viscosity is constant meanwhile yield strength is calculated using the model from Section 4.2.2.2.2 which depends on the core temperature and takes into account four variables. These variables have been determined using trial and error methods based on the comparison of the advance of the flow between the results of the simulations and the real data. They are the lowest yield strength at high temperature = 0 Pa, the highest yield strength at low temperature = 5×10^4 Pa, the transition temperature = 1200 K, the sharpness of the transition = $1/60 \text{ K}^{-1}$, and a viscosity = $4 \times 10^6 \text{ Pa s}$ (Appendix 5.4).

The flow progression over the topography using the model n°2b is shown in Fig. 5.44 for 0.85, 2.61, 8.32 and 26.51 hours. The 3D view of the flow is represented at the left side of the figure and shows the development of one single flow unit with a little outbreak by 26.15h. The variation of the color between red and dark gray represents the effect of the cooling on the flow. Red color represents a hot flow during an ongoing emission (5 h) and the dark gray when the flow has already get cooled. The right side graphs show the velocity of the simulated flow (blue line) in comparison with the measured data (red dots). At 26.15h it is observing that the curve which represents the simulation has a good match with the measured data, showing that the average velocity during the first 8 hours was = 0.045 m/s and after that it decreased to = 0.004 m/s .

The final deposit of the flow presents an elongated shape in which the front is narrower than the middle part of the unit (Fig. 5.44, 5.45). The flow is thicker at the front and at the external borders of the terminal part of the flow. The thickest part of the flow reached 5.54 m meanwhile the thinner part is founded close to the source (Fig. 5.45a). There is no evidence of levees formation. At 30 h the simulated flow presents a maximum temperature of 756.4 K which

was measured at the inner part of the front of the flow (Fig. 5.45b) and the lowest temperature are located in the region close to the source with 381.2 K and at the borders of the flow.

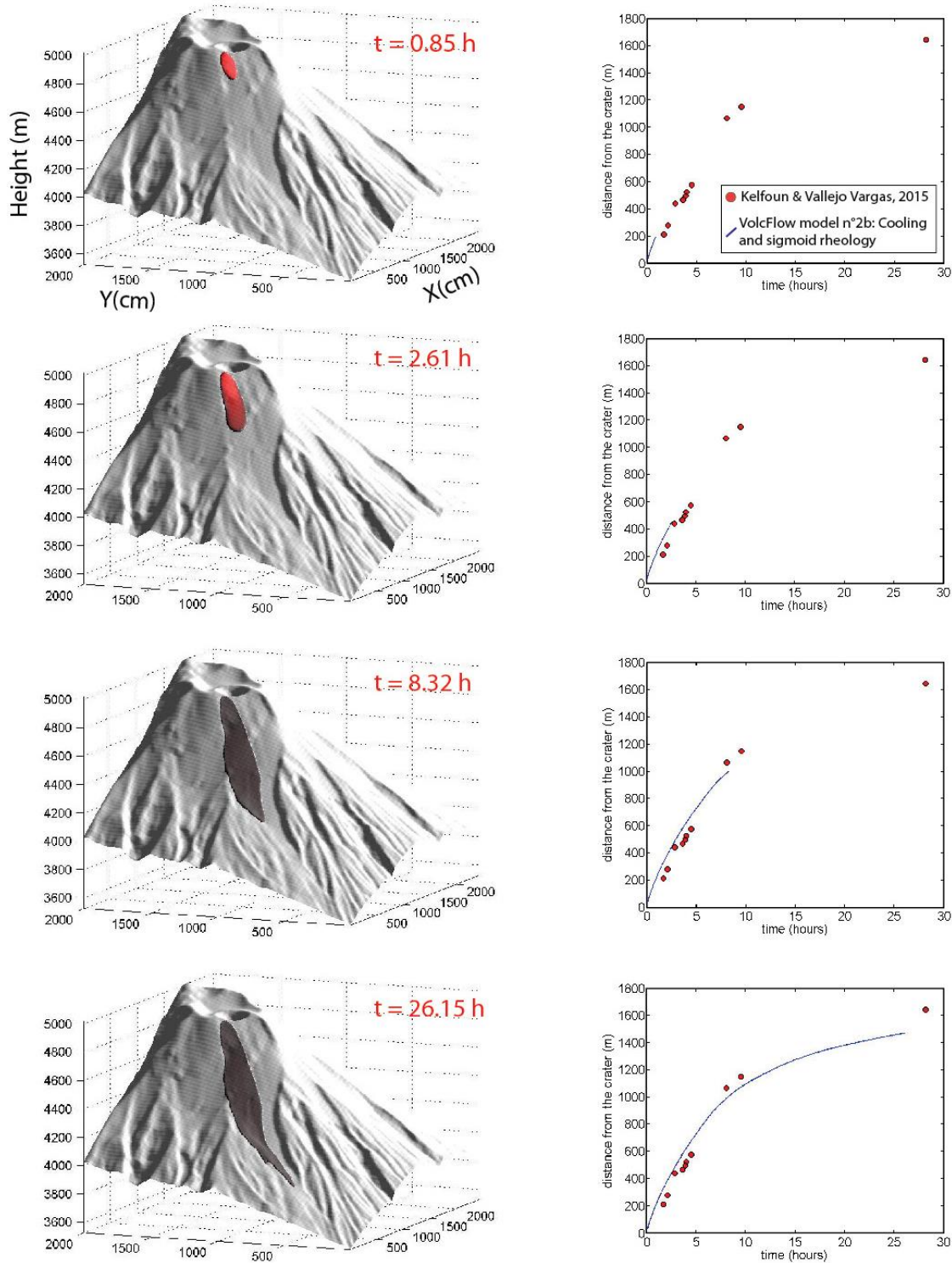


Figure 5. 44 Results of the progression of the flow using the Sigmoid model for a constant viscosity and variable yield strength. The color of the flow shows the cooling process of the flow since its emitted at high temperature (red color, $t=0.85h$) until it has cooled (gray color, $t=26.15h$). Left: 3D progression of the flow over the topography. Right: Comparison of the flow progression between the data (Kelfoun & Vallejo Vargas 2015) and results of the model.

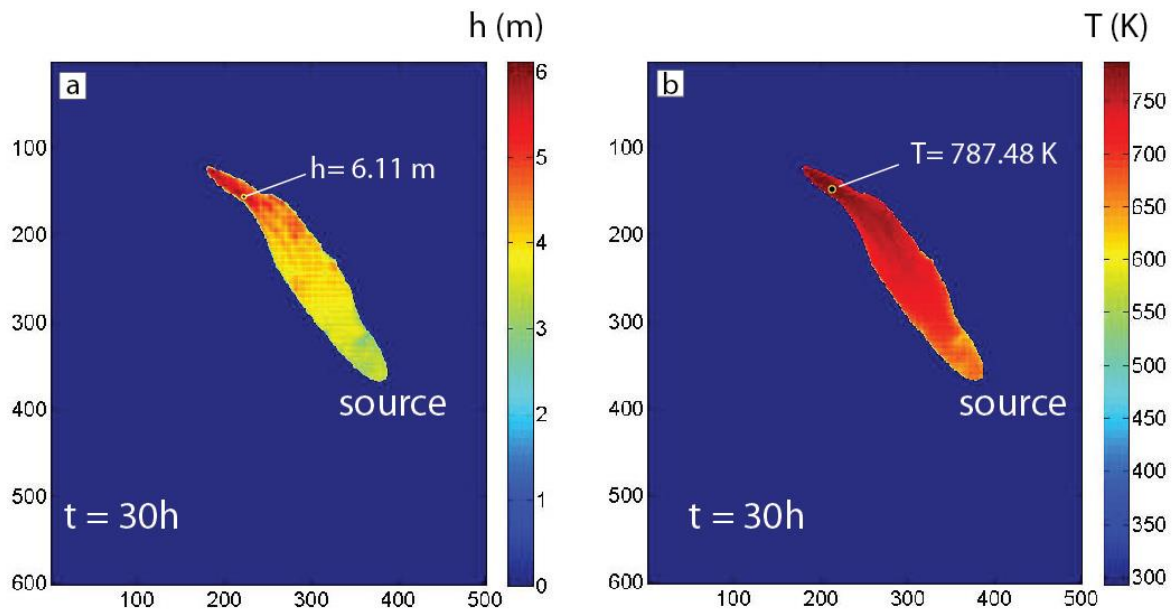


Figure 5.45 Images of the final thickness **(a)** and temperature **(b)** of the Tungurahua's flow at 30h. a) It shows that the flow is thicker at the front (5.54m) than close to the source (0.1 m). The highest temperature is registered in the inner part of the lava front with a value of 756.4 K, the lowest is recorded close to the source with 381.2 K.

The final deposit visualized in 3D for this flow at 30h is represented in Fig. 5.46. Firstly, it shows that the simulation brought one single unit flow on the NNW flank of the volcano reaching a distance of 1.5km from the crater. The highest temperature is located in the inner part of the flow with 787.48 K and its correspondent yield strength is equal to 4.9×10^5 Pa. At the end of the simulation the flow presents a variation of temperature between 381.2 and 755.71 K. Second, the variation of the temperature at the white dot (close to the source) through the 30 h is represented on the upper-right graph, in which the highest temperature corresponds to the core temperature $T_{\text{core}} = 1173.15$ K and remains at this value for the 5 hours of the flow alimentation. After that time the temperature starts to decrease, having 623 K at the end of the 30 h simulation. Third, the variation of yield strength applying the sigmoid law for a temperature range of 600 and 140 K shows a variation between 0 and 10^5 Pa, which is represented in the lower-left graph of the figure.

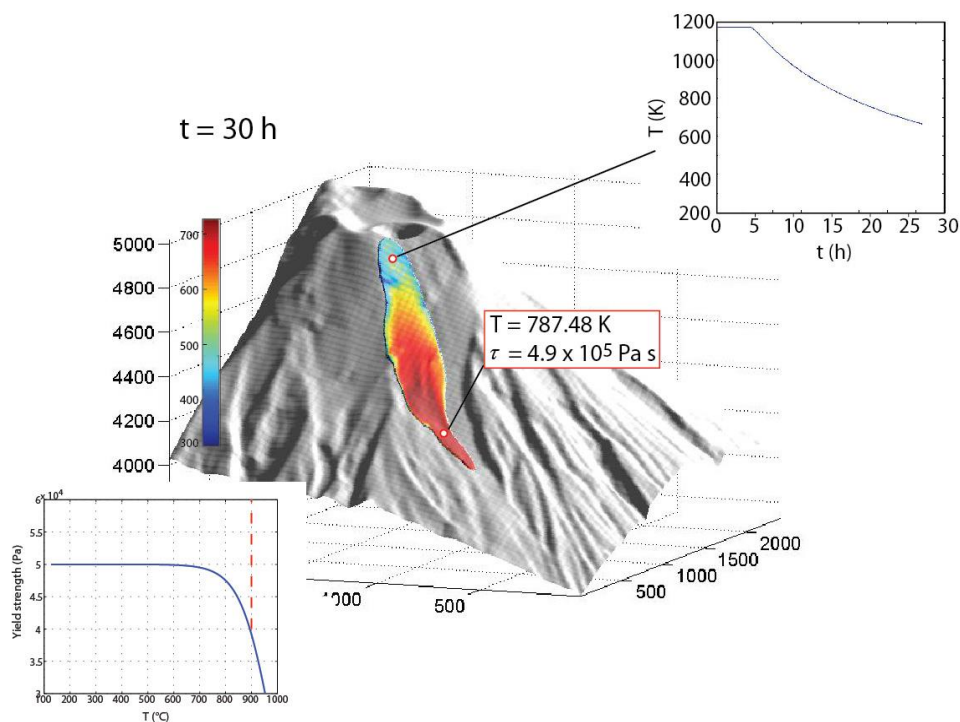


Figure 5.46 3D view of the final deposit of the Tungurahua's flow for 30h with the Sigmoid model with a constant viscosity of 4×10^6 Pa s and a variable rheology. After the 30h the flow has reached a maximum temperature of 756.4 K which influenced in yield strength calculation. Since this temperature and lower values yield strength has a value of 4.9×10^5 Pa s. This maximum temperature has found in the inner part of the front flow. The evolution of the temperature has measured in the point showed in the figure.

5.3.5 Discussion

Isothermal simulation (model n°1)

The simulation (Kelfoun & Vallejo Vargas 2015) shows that the model reproduces accurately the emplacement and the velocity. The simulated flow reached a distance of 1.65 km, pretty close to the measured flow which was about 1.64 km (Fig. 5.47a, a').

Cooling and rheological variation using existing thermo-rheological laws (model n°2a)

The simulation shows some differences with the real flow. It did not follow the velocity of the flow and its final length is 0.32 km, this distance is far below real measure (1.64 km) (Fig. 5.47b, b'). The flow presents an oval shape, in which the lateral and frontal borders present steep slopes. This shape is reflected on the thickening of the flow which can reaches 30.4 m at the front. It is easy to recognize a slight increase of the thickness at the borders close to the front, suggesting the formation of levees. The final shape of the flow was controlled by the viscosity

and therefore by the cooling on the lava rheology. In the other side the variation of yield strength is very short and its influence is minimal in comparison to that from the viscosity.

Other simulations were developed taking in account more basic compositions (e.g. from El Reventador volcano) for the fluid viscosity relationship. Results showed that the flow reached a longer distance (1.2 km) and presents a thickness variation between 0.1 and 21.7 m.

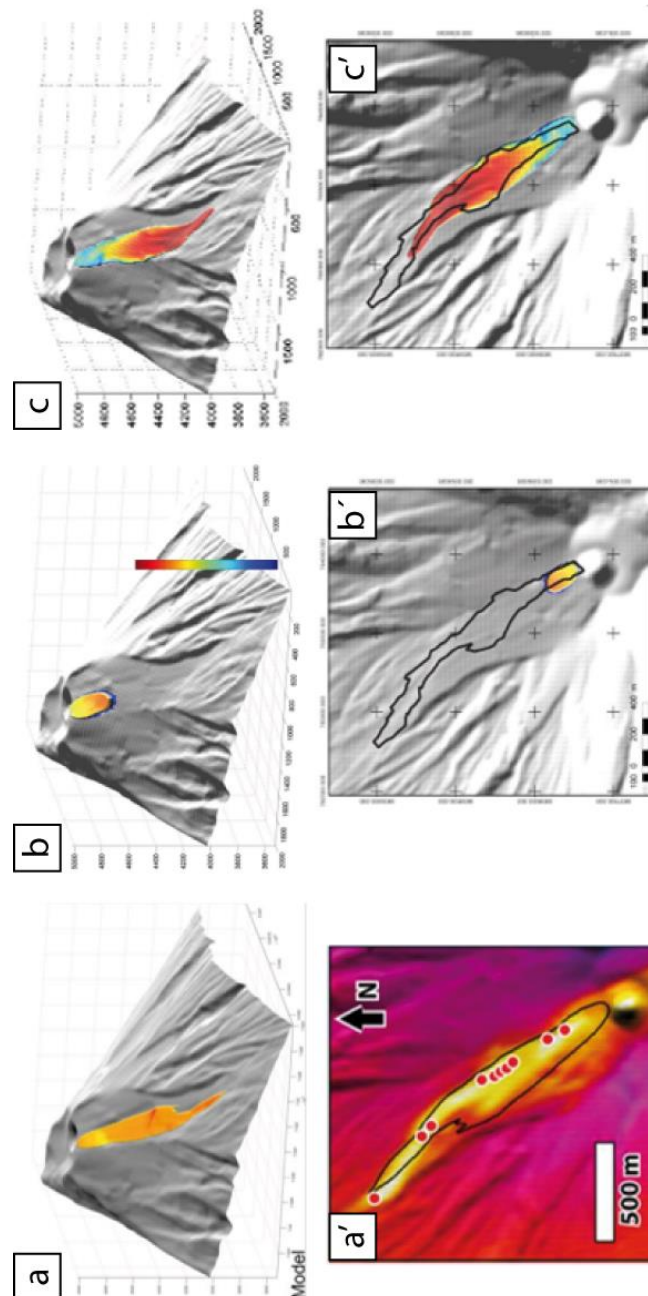


Figure 5. 47 Comparison of the simulations for the December 4th and 5th lava flow from Tungurahua volcano. Results of the Isothermal model (model n°1), 3D (a) and orthogonal (a') views (Kelfoun & Vallejo Vargas 2015). Cooling and rheological variation using existing thermo-rheological model (model n°2a), 3D (b) and orthogonal (b') views. Cooling and rheological sigmoid law model (model n°2b), 3D (c) and orthogonal (c') views.

Thermo-rheological variation (yield strength sigmoid law) simulation (model n°2b)

The simulation shows a velocity which is coherent with the measured. The simulation reached 1.51 length against the 1.64 km from the real flow (Fig. 5.47c, c'). The final shape and the maximum thickness are both as well pretty similar to the real deposit. The thickness is almost regular along the whole flow but it did not present any structures related with levees. In this model the shape and thickness of the flow was controlled by the yield strength with in turn depended on the lava cooling and on the lava rheology.

For this lava case, results show that the models n°1 and n°2b present similarities and this could be that both models are dependent on the yield strength. About the model n°2a, the simulation showed that it is very sensitive to the values of the viscosity and therefore the rheology. Even though that here it was used precise rheological data from a lava flow of Tungurahua, it didn't correspond to the lava flow analyzed here. This could be a reason why the model didn't work at all for this flow.

5.4 Lava flows from El Reventador

In previous sections of this Chapter (5.1 – 5.3) it was shown the simulations of lava flows with different test cases and different rheologies. The three test cases were referred to: (1) the molten basal benchmarck (Syracuse lava flow project), (2) a lava flow from Piton de la Fournaise volcano by combining information of two well-known lava flows, and (3) the December 5th 2010 lava flow from Tungurahua volcano. The first two cases corresponded to basaltic flow and the third one to a flow with an andesitic composition. All of these three study cases were simulated with the approaches proposed in this current work, in Chapter 4, by considering simplex and complex rheologies.

In that way, as another test case to simulate lava flows of andesitic composition, it was proposed flows from El Reventador volcano in Ecuador. Two main reasons support this choice, (1) the almost continuous lava flow generation since its reactivation, around 60 lava flows were emitted between 2002-2016, and (2) the complete and deep knowledge of lava flows from the period 2002-2014 obtained as a part of the research carried out during this current work (Chapter 2).

There are some differences between the lava flows generated between 2002 and 2016. Flows from 2002 and 2009 are more voluminous and longer with mean flow durations up to 60 days meanwhile those from the period 2012 – 2014 are shorter and their emplacement lasted only 5 - 8 days (Chapter 2). Between 2015 and 2016, some small lava flows (length <1 km) were generated in this volcano but they are not considered as a part of this current study. Later on, in June 2017, after a high explosive activity with PDC's generation, a lava flow of ~2.65 km was emitted. This flow corresponded to the longest one since 2008 (LF11, Chapter 2).

This interesting contrast of lava flow behavior and characteristics between the flows emitted in between 2002-2009, 2012-2014 and in 2017 has pushed this PhD research in order to generate appropriated numerical codes that could simulate lava flows of this volcano. In order to reach this purpose, the present section shows the application of three models proposed in Chapter 4 and which were applied to simulate the andesitic flow from Tungurahua volcano:

1. Model n°1: Isothermal.
2. Model n°2a: Cooling and rheological variation using existing thermo-rheological models.
3. Model n°2b: Cooling and rheological sigmoid law.

using the information of three lava flows of El Reventador volcano:

1. Lava flow from April, 2014 (LF25, Chapter 2)
2. Lava flow from June-July, 2017
3. Hypothetical flow with the same characteristics of the lava flow 1 (LF1) emitted in November, 2002.

Results of the simulations for the three test cases are shown in the following subsections.

5.4.1 Lava flow from April 2014 (LF25)

5.4.1.1 Initial conditions

The generation of this lava flow was identified through thermal images from the Copete-IR camera located at the south eastern border of the caldera wall (Fig. 5.48a). It was generated in April, 2014 and emplaced on the southern flank of the volcano for about 6 days. The flow emission was preceded by a short explosive phase accompanied with gas and ash emission columns (Chapter 2). The collection of thermal images (Fig. 5.48a) allowed to follow the same methodology applied for the Tungurahua's lava flow generated in December 4th and 5th (Section 5.3.1, this Chapter), which consist by knowing the IR camera position, project the thermal image over the topography (Fig. 5.48b). With this information it was possible to o:

- ❖ Measure the velocity of the flow (Fig. 5.49a).
- ❖ Map the final deposit of the flow (Fig. 5.49b).
- ❖ Estimate the area and volume of the flow.

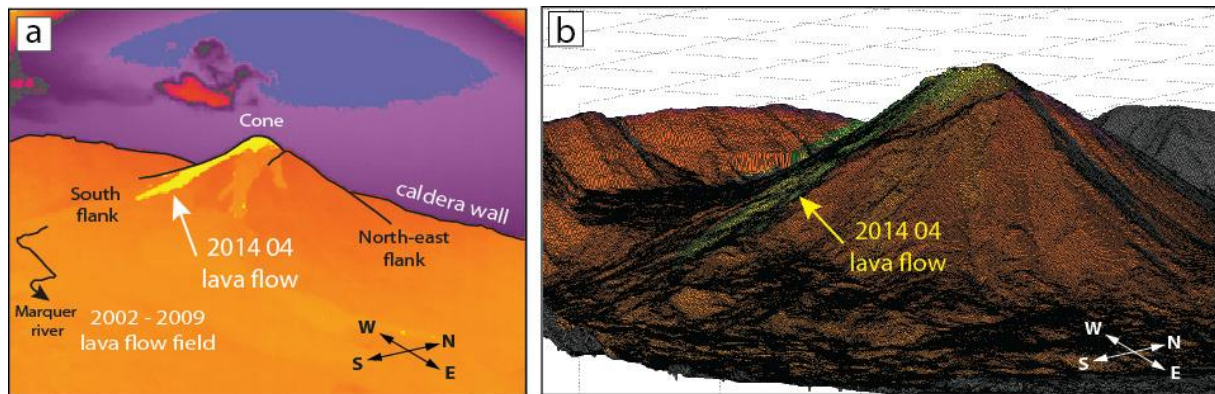


Figure 5.48 Lava flow generated in April 2014. **a)** thermal image from the COPETE-IR station, the flow is represented in yellow. **b)** projection of the thermal image over the topography following the method from Kelfoun & Vallejo Vargas (2015), the flow is represented in yellow-green color.

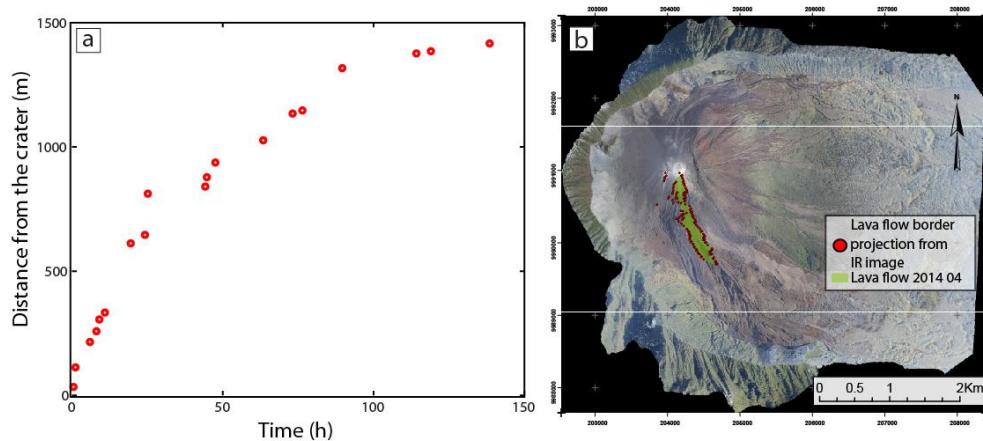


Figure 5.49 a) Advance of the flow front by the time (red dots) obtained from the projection of thermal images over the topography (Fig. 4.54b) **b)** Resulted polygon of the flow over the topography.

5.4.1.2 Numerical models

This lava flow was simulated using three approaches:

1. Model n°1: Isothermal.
2. Model n°2a: Cooling and rheological variation using existing thermo-rheological models.
3. Model n°2b: Cooling and rheological sigmoid law.

5.4.1.3 Simulations

5.4.1.3.1 Model n°1: Isothermal

This study case was previously tested using the isothermal model in which the simulation was calibrated in function of the progression of flow by the analysis of IR images (Vallejo *et al.* 2015) and was carried on following the methodology from Kelfoun & Vallejo Vargas (2015). The isothermal model uses the VolcFlow basic input parameters correspondent to an eruption time=72 h, emplacement flow time=120 h, volume=1,9x10⁶ m³ and bulk viscosity=2350 kg m⁻³. The values of viscosity and yield strength were obtained from trial and error method (e.g. Section 5.1, 5.3), having 25x10⁶ Pa s and 4x10⁴ Pa respectively (Fig. 5.50).

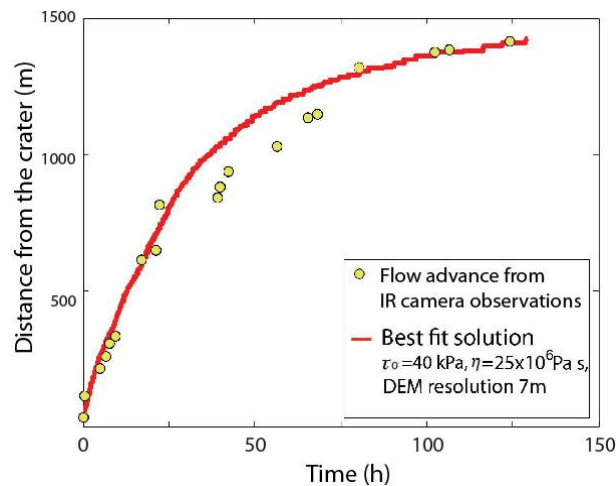


Figure 5. 50 Fit of the resulted flow using the isothermal model for the LF25.

5.4.1.3.2 Model n°2: including the effect of the cooling and rheological variation

Simulations of El Reventador's lava flows using the model n°2 were governed by the cooling of the flow and the variation of the rheological parameters, viscosity and yield strength. The cooling was estimated using the Eq. 4.14 and the rheological variation using models mentioned in Section 4.2.2.2 (Chapter 4). The combination of the cooling with both rheological models allowed to have two approaches for the model n°2, as:

2. Model n°2a: Cooling and rheological variation using existing thermo-rheological models.
3. Model n°2b: Cooling and rheological sigmoid law.

The radiation parameters are the Stefan-Boltzmann constant $=5.67E-08 \text{ W m}^{-2} \text{ K}^{-4}$ and emissivity $=0.95$. The convection estimation includes the $C_H=0.0036$, the air specific heat capacity $=1500 \text{ J kg}^{-1} \text{ K}^{-1}$, air temperature $=298.15 \text{ K}$, wind speed $=5 \text{ m s}^{-1}$, air density $=0.4412 \text{ kg m}^{-3}$. Conduction parameters are $h_{\text{base}}=0.266 \text{ m}$, thermal conductivity $=0.88 \text{ W m}^{-1} \text{ K}^{-1}$, core to basal distance $=19\%$, flow thickness $=2.85 \text{ m}$, basal temperature $=373.15 \text{ K}$. The density and vesicularity parameters considers a vesicularity $=0.24$ and a DRE density $=2350 \text{ kg m}^{-3}$. Thermal parameters take into account a buffer $=0$, crust temperature $=373.15 \text{ K}$, core temperature $=1173.15 \text{ K}$ and a constant crust cover fraction $=1$. The crystal content parameters are the latent heat of crystallization $=3.5 \times 10^5 \text{ K kg}^{-1}$, crystals growing during cooling $=1$, cooling rate $=379.35 \text{ K}$, rate of crystallization $=0.0036 \text{ K}^{-1}$ and the constant $R=1.51$ (Appendix 5.5).

5.4.1.3.2.1 Model n°2a: Cooling and rheological variation using existing thermo-rheological models

This approach used the VolcFlow basic input parameters and those to estimate the cooling and rheological variation, described above (Appendix 5.5).

As well, viscosity was estimated by the combination of dynamic and relative and viscosity meanwhile the yield strength was estimated using a single relationship as shown below:

- ❖ **Dynamic fluid viscosity** the VTF equation (Eq. 4.22, Chapter 4) from Giordano & Dingwell (2008). This equation requires the knowledge of three parameters: the constant independent of composition (VTF_A), and two adjustable parameters VTF_B and VTF_C. These three parameters were calculated by using the chemical of matrix glasses from Samaniego *et al.* (2008), having -4.55 , 10200.978 , $3.75.72$ respectively (Appendix 5.5).
- ❖ **Relative viscosity** applies the Krieger & Dougherty (1959) model assuming that crystals have an aspect ratio $=1.7$ (Muller *et al.* 2010) with a maximum packing $=0.542$.
- ❖ **Yield strength:** From Dragoni 1989; Pinkerton & Stevenson 1992. This relationship uses two constants B and C correspondent to 0.01 and 00.8 respectively (Appendix 5.5).

The simulated flow is shown in Fig. 5.51a. It displays a broadly dispersed flow in the upper part of the flank and three small fingers at the front. The flow was thicker at the fronts with 20 m approximately.

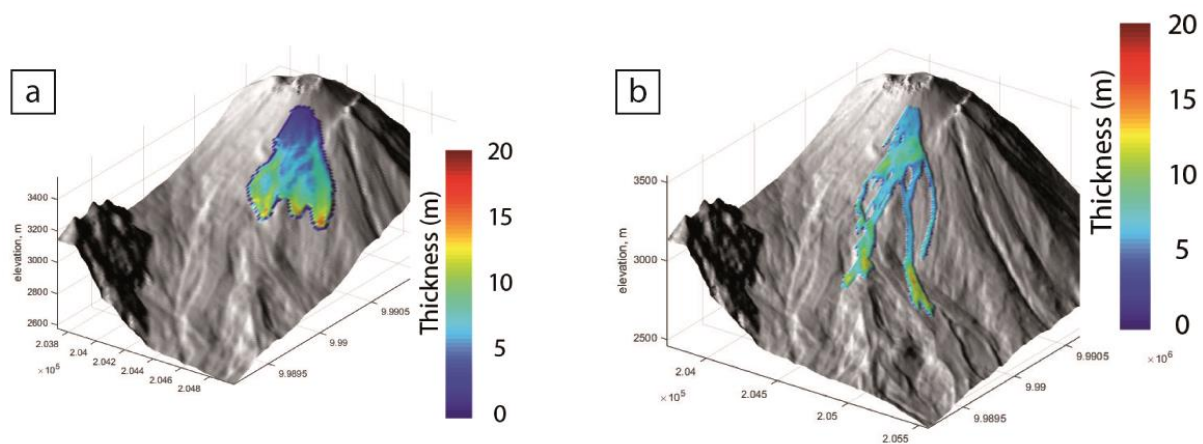


Figure 5. 51 (a) Representation of the deposit left by the simulation taking into account the cooling and existing rheological laws. It is possible to see that the thickness of the flow is not regular showing a thickening at the front with about 20m. **(b)** Deposit of the flow for the sigmoid model.

5.4.1.3.2.2 Model n°2b: Including the effect of the cooling and sigmoid law

This method used the VolcFlow basic input parameters and those to estimate the cooling and rheological variation, described above (Appendix 5.5). It is considering that the viscosity is constant meanwhile yield strength is calculated using the model from Section 4.2.2.2.2 which depends on the core temperature and takes into account four variables. These variables have been determined using trial and error methods based on the comparison of the advance of the flow between the results of the simulations and the real data. They are the lowest yield strength at high temperature=5000 Pa, the highest yield strength at low temperature= 1×10^5 Pa, the transition temperature=1100 K, the sharpness of the transition= 0.02 K^{-1} , and a viscosity= $5 \times 10^6 \text{ Pa s}$ (Appendix 5.5).

The simulation displayed a deposit with narrow fingers with variable thickness between 3 and 13 m (Fig. 5.51b).

5.4.2 Lava flow from June – July 2017

By combining the information obtained by the IG-EPN and SENTINEL images during the emission of the flow it was determined that the flow was active between June 24th and July 1st and reached a distance of 2.6 km from the crater. The deposit was distributed over the north eastern part of the edifice and finally emplaced over the eastern part of the caldera floor occupying a final surface of 0.45 km^2 (Fig. 5.52, 5.53). The average of the thickness measured in

different points of the flow gave a value of 13 m. Based on this information the total volume of the flow was estimated on $4.5 \times 10^6 \text{ m}^3$ (Source: IG-EPN).

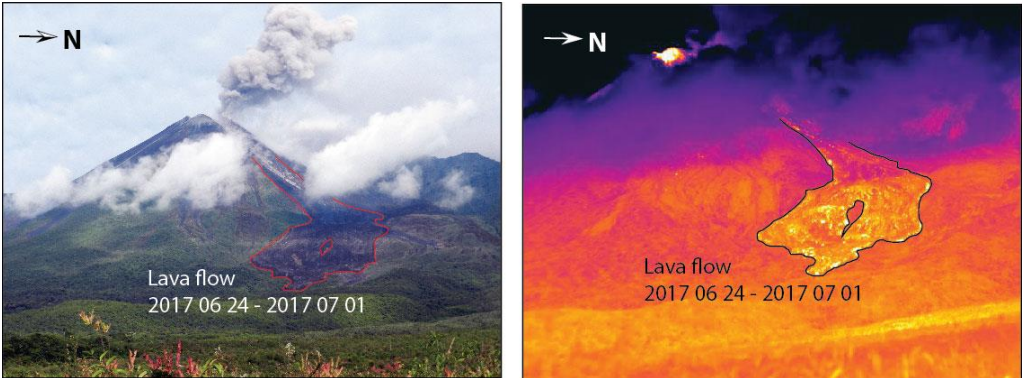


Figure 5.52 Deposit of the lava flow over the north eastern flank of the volcano and the eastern caldera floor taken on August 1st 2017. It is represented with a red outline in the visible image and with a black one in the thermal image. (M. Almeida, IG-EPN).

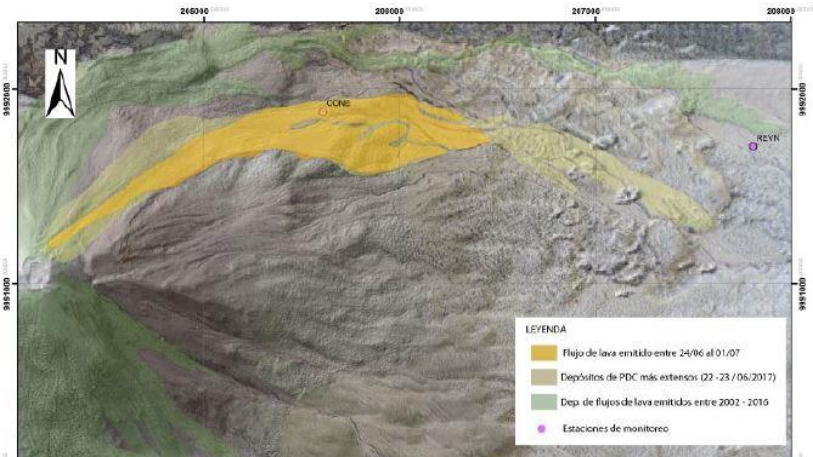


Figure 5.53 Map of the distribution of the lava flow (yellow) over the flank and caldera floor of El Reventador volcano (M. Almeida, IG-EPN).

5.4.2.1 Initial conditions

The source of the lava flow was identified by the analysis of thermal and visible images (Fig. 5.52). All the simulations were done using the 2015 DEM of 1.6 m resolution (Fig. 2.16, Chapter 2, Fig. 5.54), developed by Paris, R., Vallejo Vargas, S. and Kelfoun, K. (LMV) with photos taken during the fieldwork carried out on April, 2015 as a part of this work (Chapter 2).

Simulations of this lava flow considered that the flow was emitted with a constant flux escaping from the source with a volumetric rate of $10.41 \text{ m}^3 \text{ s}^{-1}$, which was equivalent to generate a volume of $6 \times 10^6 \text{ m}^3$ in 168 h. The source of the lava was located on the western part of the summit (Fig.

5.54). The momentum was taken into account for the calculation of the new velocity at the source (previous velocity + new mass added with a null velocity). The temperature of the mass added was constant.

Simulations using the three models presented below used the VolcFlow basic input parameters, which correspond to eruption time=168h, flow emplacement time=480h, volume= $6 \times 10^6 \text{ m}^3$ and bulk density= 2000 kg m^{-3} (Appendix 5.5). Due to the absence of information about the progression of the flow, best results were obtained by the comparison of the final deposit length, width and thickness of the simulation with the real deposit.

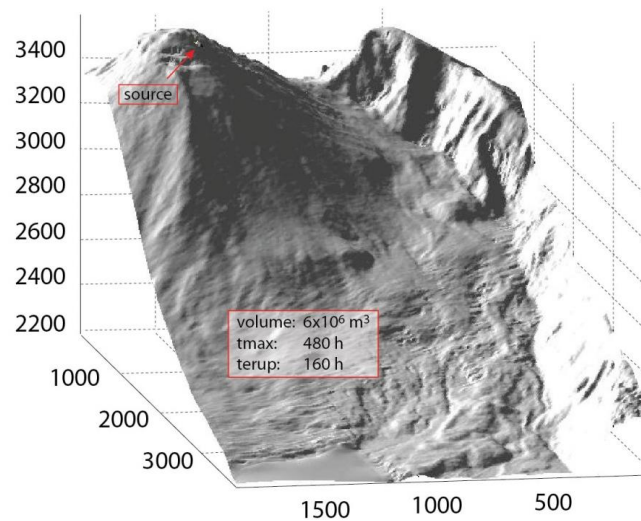


Figure 5. 54 Portion of the 2015 DEM used for the simulation of the June-July 2017 lava flow for El Reventador volcano. It is shown the source of the lava flow (NNW summit border).

5.4.2.2 Numerical models

This lava flow was simulated using three approaches:

1. Model n°1: Isothermal.
2. Model n°2a: Cooling and rheological variation using existing thermo-rheological models.
3. Model n°2b: Cooling and rheological sigmoid law.

5.4.2.3 Simulations

5.4.2.3.1 Model n°1: Isothermal

The isothermal model took in account constant values of viscosity and yield strength during the whole simulation. The best fit of the simulation was obtained by comparing the length

and thickness of the flow with a viscosity= 25×10^6 Pa s and yield strength= 6×10^4 Pa (Appendix 5.5).

Results of the simulations are shown in Fig 5.55 and 5.56. The first image displays the variation of the thickness of the flow at 480h, in which it is recognizable an important accumulation of material at the front of the flow with ~ 21 m. Thinner deposit are located at the steepest part of the volcano, close to the source. With this model, the simulation displays some branches at the final steps of the simulation Fig. 5.55, 5.56.

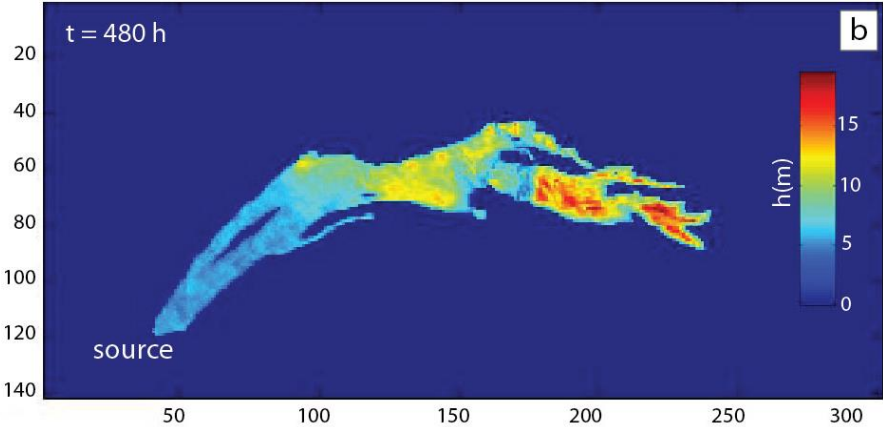


Figure 5. 55 Results of the simulation of the flow at 480h using the isothermal model. Represents the variation of the thickness of the deposit showing an important thickening close to the front of the flow and thinner deposit close to the source of the flow.

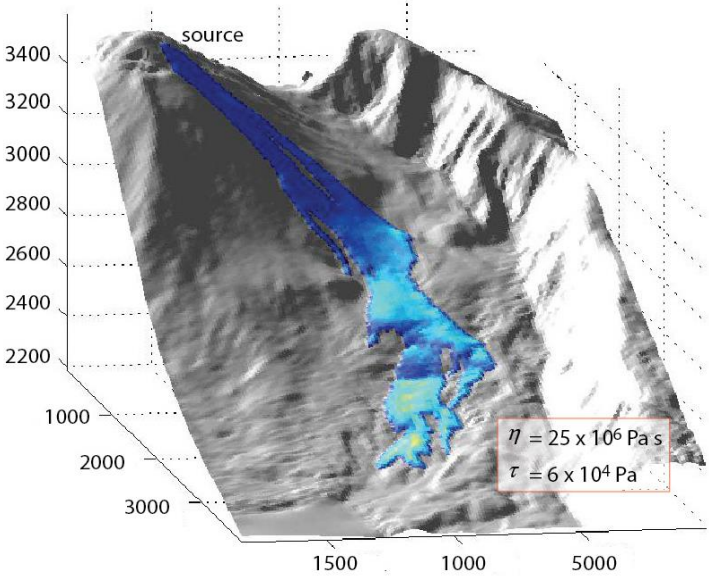


Figure 5. 56 3D view of the flow deposit over the north-east flank and caldera floor of the volcano using the isothermal model with a viscosity of 25×10^6 Pa s and a yield strength of 6×10^4 Pa.

5.4.2.3.2 Model n°2: Including the effect of the cooling and rheological variation

The simulations of this lava flows using the model n°2 were governed by the cooling of the flow and variation of the rheological parameters viscosity and yield strength. The cooling was estimated using the Eq. 4.14 and the rheological variation using models mentioned in Section 4.2.2.2 (Chapter 4). The combination of the cooling with both rheological models allowed to have two approaches for the model n°2, which are:

2. Model n°2a: Cooling and rheological variation using existing thermo-rheological models.
3. Model n°2b: Cooling and rheological sigmoid law.

The radiation parameters are the Stefan-Boltzmann= $5.67E-08 \text{ W m}^{-2} \text{ K}^{-4}$ and emissivity=0.95. The convection estimation includes the $C_H=0.0036$, the air specific heat capacity= $1500 \text{ J kg}^{-1} \text{ K}^{-1}$, air temperature= 298.15 K , wind speed= 5 m s^{-1} , air density= 0.4412 kg m^{-3} . Conduction parameters are $h_{\text{base}}=0.266 \text{ m}$, thermal conductivity= $0.88 \text{ W m}^{-1} \text{ K}^{-1}$, core to basal distance=19%, flow thickness=2.85 m, basal temperature= 373.15 K . The density and vesicularity parameters considers a vesicularity=0.24 and a DRE density= 2350 kg m^{-3} . Thermal takes into account the buffer=0, crust temperature= 373.15 K , core temperature= 1173.15 K and a constant crust cover fraction=1. The crystal content parameters are the latent heat of crystallization= $3.5 \times 10^5 \text{ K kg}^{-1}$, crystals growing during cooling=1, cooling rate= 379.35 K , rate of crystallization= 0.0036 K^{-1} and the constant $R=1.51$ (Appendix 5.5).

5.4.2.3.2.1 Model n°2a: Cooling and rheological variation using existing thermo-rheological models

The resulted simulation displays a regular shape and smooth surface. The flow is thinner at the steepest part of the volcano, close to the source, and it is wider and thicker ($\sim 20\text{m}$) at the front (Fig. 5.57). At the end of the simulation the flow, the highest temperature was measured in the inner part of the flow with 1250 K meanwhile the minimum was 897.4 K and was located at the borders (Fig. 5.58).

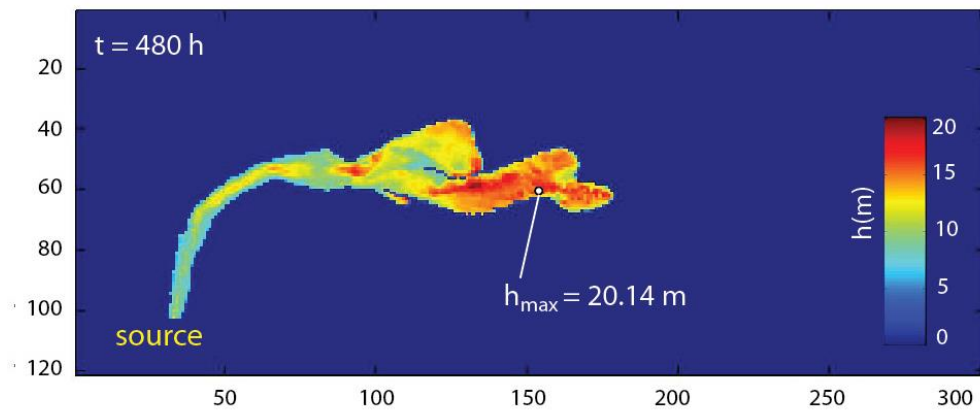


Figure 5. 57 2D thickness representation of the simulation showing that the flow is thicker at the low topography reaching ~ 20 m.

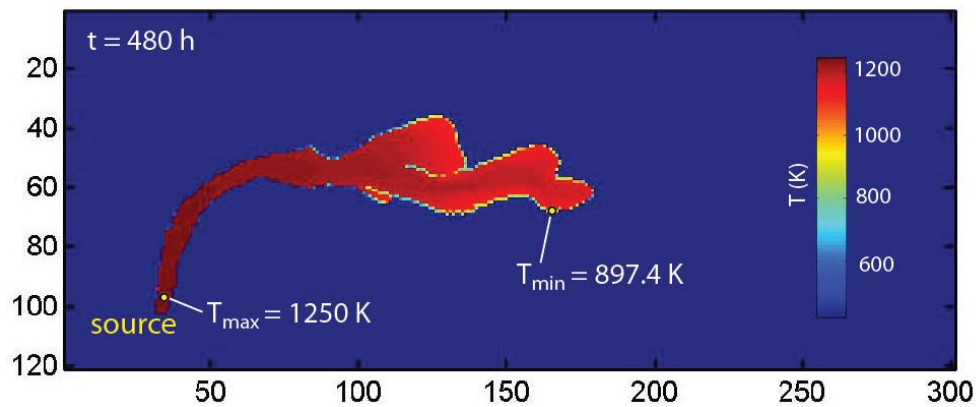


Figure 5. 58 Representation of the temperature at the end of the simulation, the highest measurement was located close to the source and the minimum at the borders with 1250 K and 897 K respectively.

Figure 5.59 displays seven cross-sections along the flow, from p1 (close to the source) to p7 (close to the distal front). They show the thickening of the flow from p1 to p7, reaching values between 15 and 20 m at p7 in comparison to ~ 4 m close to the source. In the other hand, a slight thickening at the borders suggested the formation of levees in the flow (e.g. p4, p5, p7).

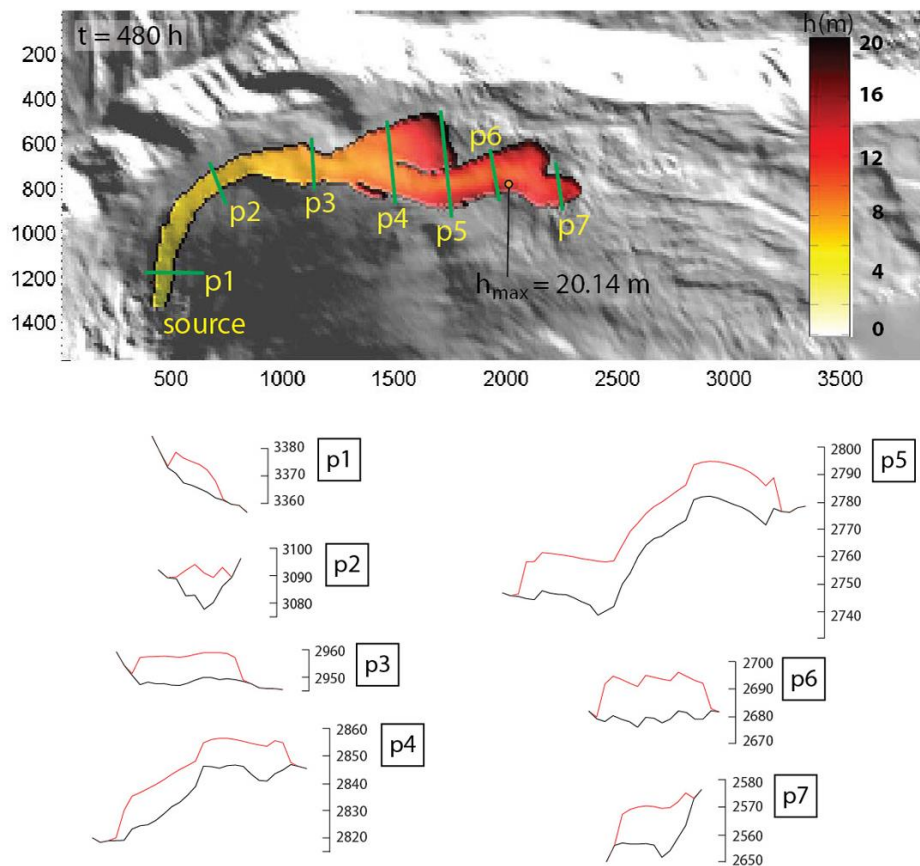


Figure 5. 59 Cross section along the flow from p1 to p7 showing its thickening when it is emplaced on the caldera floor.

5.4.2.3.2.2 Model n°2b: Including the effect of the cooling and sigmoid law

The best result of the simulations of the sigmoid law for this lava flow was obtained with a constant viscosity of 5×10^6 Pa s, a lowest yield strength at high temperature = 5×10^3 Pa, highest yield strength at low temperature = 1×10^5 Pa, transition temperature = 1100 K^{-1} and the sharpness of transition = 0.02 K (Appendix 5.5).

The distribution of the flow is displayed in Fig. 5.60, 5.61 and 5.62. The flow presents some branches, but in general it shows a regular shape. The most important thickening is located close to the front where the topography is almost flat, here the flow reached ~ 28 m. At the upper part of the deposit, close to the source, its thickness varies between 0 and 5 m, showing that during the simulation most of the volume was evacuated and deposited in the caldera floor.

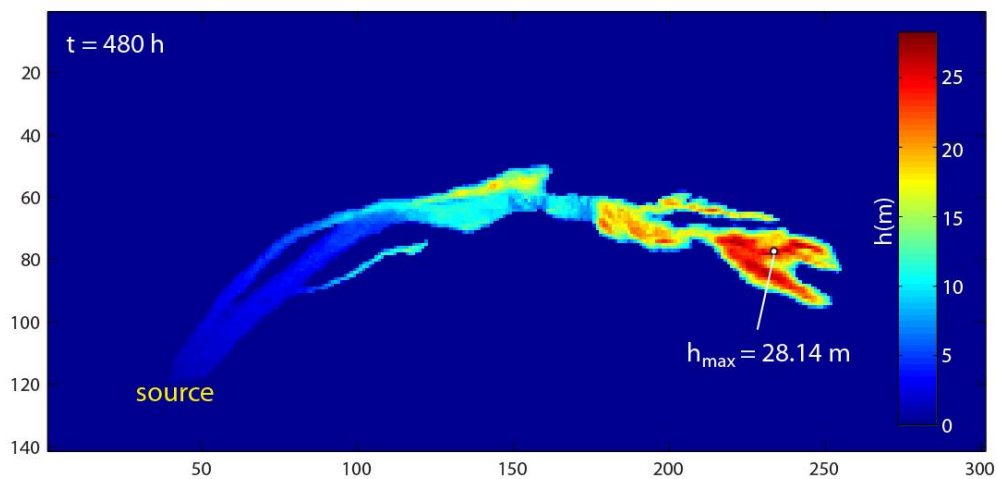


Figure 5. 60 An important accumulation of the flow is observed close to the front of the flow reaching 28.14 m (reddish color).

At the end of the simulation (after 480 h), the maximum temperature was measured in the inner part of the flow with 878 K and the lowest were located close to the source (Fig. 5.61). The fact that the high temperature was measured at the thicker part of the flow suggest that the flow keeps the heat when it is thicker.

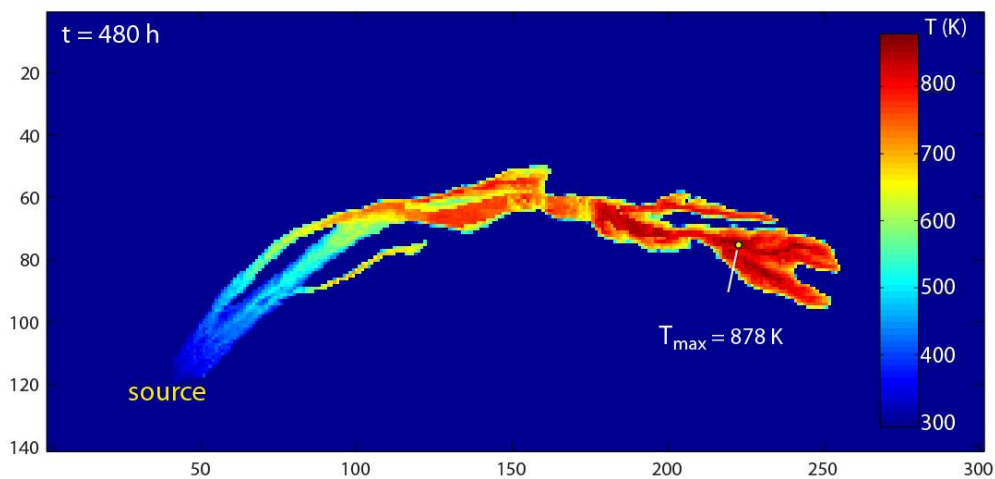


Figure 5. 61 The maximum temperature (878 K) of the flow was measured in the thicker part of the flow calling the attention that the heat is kept when the flow has an important thickness.

The 3D view of the flow is displayed in Fig. 5.62, showing that the distribution of the flow was on the north west flank and the caldera floor. An important thickening (reddish color) is presented at low topography in near the front while the flow is thinner close to the source. The

shape of the flow is given by the variable yield strength which varies between 10^2 and 10^5 Pa in a range of temperature of about 450 K.

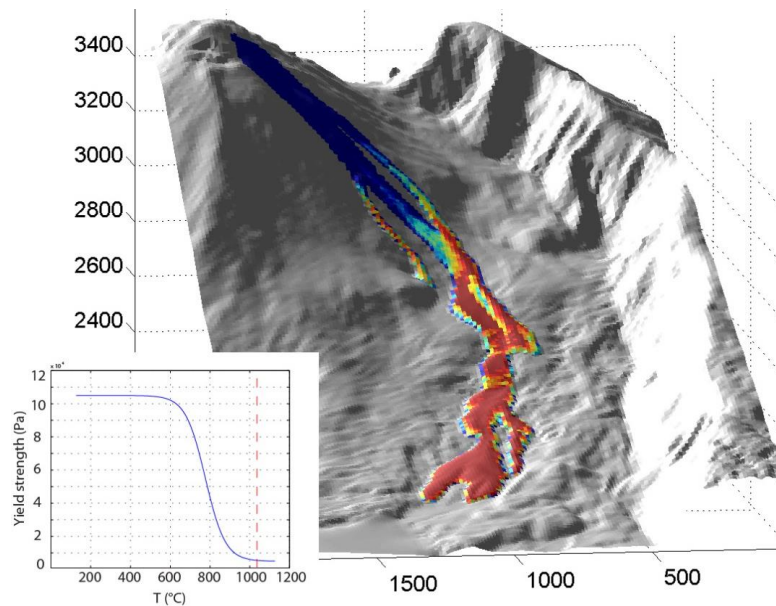


Figure 5. 62 View of the flow using the sigmoid law. It shows a regular flow and some small branches. The accumulation of material is recognized at the lowest slope of the topography which corresponds to the caldera floor.

5.4.3 Analogous of lava flow 1 (LF1) from November, 2002

The aim of this test case is to try to simulate a flow with similar characteristics of the lava flow 1 (LF1) generated on November, 2002.

5.4.3.1 Initial conditions

The input basic parameters for VolcFlow corresponded to an eruption time=168 h, a flow emplacement time=2400 h, a volume of 24.8×10^6 m³ and a bulk density of 2000 kg m⁻³ (Appendix 5.5). The source of the flow was established at the upper part of the southern part of the cone. The flow was simulated by using the topography from the 2013 DEM.

5.4.3.2 Numerical models

This lava flow was simulated using three approaches:

1. Model n°1: Isothermal.
2. Model n°2a: Cooling and rheological variation using existing thermo-rheological models.
3. Model n°2b: Cooling and rheological sigmoid law.

5.4.3.3 Simulations

5.4.3.3.1 Model n°1: Isothermal

The isothermal model for this lava flow used the VolcFlow input parameters and a constant viscosity and yield strength during the whole simulation with 25×10^6 Pa s and 1.5×10^5 Pa respectively (Appendix 5.5). The flow presents some branches but in general the shape of the flow is regular. It was emplaced over the NNE flank and later, on the eastern caldera floor. The thicker part of the flow was located at the front reaching ~ 50 m. The thinner part of the flow (15-8 m) was located at the steepest part, close to the source (Fig. 5.63).

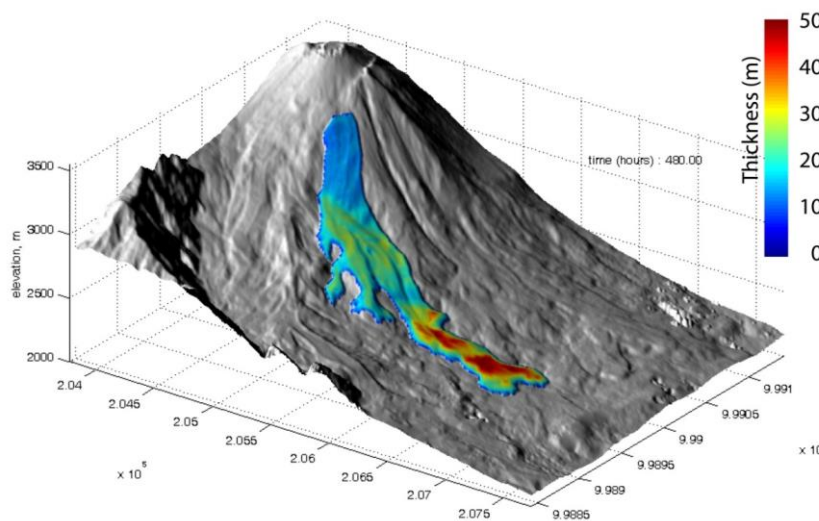


Figure 5. 63 3D view of the deposit left by the isothermal simulation, in which the viscosity and yield strength are constants. The thicker part of the flow is represented with reddish color, reaching ~ 50 m.

5.4.3.3.2 Model n°2: Including the effect of the cooling and rheological variation

The simulations of this lava flows used the model n°2 which is governed by the cooling of the flow and variation of the rheological parameters viscosity and yield strength. The cooling was estimated using the Eq. 4.14 and the rheological variation using models mentioned in Section 4.2.2.2 (Chapter 4). The combination of the cooling with both rheological models allowed to have two approaches for the model n°2, which are:

2. Model n°2a: Cooling and rheological variation using existing thermo-rheological models.
3. Model n°2b: Cooling and rheological sigmoid law.

The radiation parameters are the Stefan-Boltzmann constant $=5.67E-08 \text{ W m}^{-2} \text{ K}^{-4}$ and emissivity $=0.95$. The convection estimation includes the $C_H=0.0036$, the air specific heat capacity $=1500 \text{ J kg}^{-1} \text{ K}^{-1}$, air temperature $=298.15 \text{ K}$, wind speed $=5 \text{ m s}^{-1}$, air density $=0.4412 \text{ kg m}^{-3}$. Conduction parameters are $h_{\text{base}}=0.266$, thermal conductivity $=0.88 \text{ W m}^{-1} \text{ K}^{-1}$, core to basal distance $=19\%$, flow thickness $=2.85 \text{ m}$, basal temperature $=373.15 \text{ K}$. The density and vesicularity parameters consider a vesicularity $=0.24$ and a DRE density $=2350 \text{ kg m}^{-3}$. Thermal takes into account the buffer $=0$, crust temperature $=373.15 \text{ K}$, core temperature $=1173.15 \text{ K}$ and a constant crust cover fraction $=1$. The crystal content parameters are the latent heat of crystallization $=3.5 \times 10^5 \text{ K kg}^{-1}$, crystals growing during cooling $=1$, cooling rate $=379.35 \text{ K}$, rate of crystallization $=0.0036 \text{ K}^{-1}$ and the constant $R=1.51$ (Appendix 5.5).

5.4.3.3.3 Model n°2a: Cooling and rheological variation using existing thermo-rheological models

This approach used the VolcFlow basic input parameters and those to estimate the cooling and rheological variation, described above (Appendix 5.5).

As well, viscosity was estimated by the combination of dynamic and relative and viscosity meanwhile the yield strength was estimated using a single relationship as shown below:

- ❖ **Dynamic fluid viscosity** the VTF equation (Eq. 4.22, Chapter 4) from Giordano & Dingwell (2008). This equation requires the knowledge of three parameters: the constant independent of composition (VTF_A), and two adjustable parameters VTF_B and VTF_C. These three parameters were calculated by using the chemical of matrix glasses from Samaniego *et al.* (2008) (Appendix 5.5).
- ❖ **Relative viscosity** by applying the Krieger & Dougherty (1959) model assuming that crystals have an aspect ratio $=1.7$ (Muller *et al.* 2010), having a maximum packing $=0.542$.
- ❖ **Yield strength:** From Dragoni, 1989; Pinkerton & Stevenson, 1992. This relationship uses two constants B and C correspondent to 0.01 and 0.8 respectively (Appendix 5.5).

Here are presented two simulations with the same chemical composition but different content of water. The first one (Fig. 5.64) has 0 wt.% H₂O and the second (Fig 5.65) consider 1 wt.% H₂O. The dispersion of the flow shows a significant difference by comparing Fig. 5.64 and 5.65 which corresponds to the model with 1 and 0 wt % H₂O respectively. The first one shows a broad dispersion of the flow and its thickness is not regular along the flow. The thicker part is

located at the caldera floor at the limit of the numerical domain. The flow with 1 wt.% H_2O is shorter and its shape has strong similarities with old lava flows of the period 2002-2009. It is easy to compare the shape of this flow and the already emplaced flow showed in the topography. The thickness of this flow is more regular and reaches thickness of about 30 m at the borders.

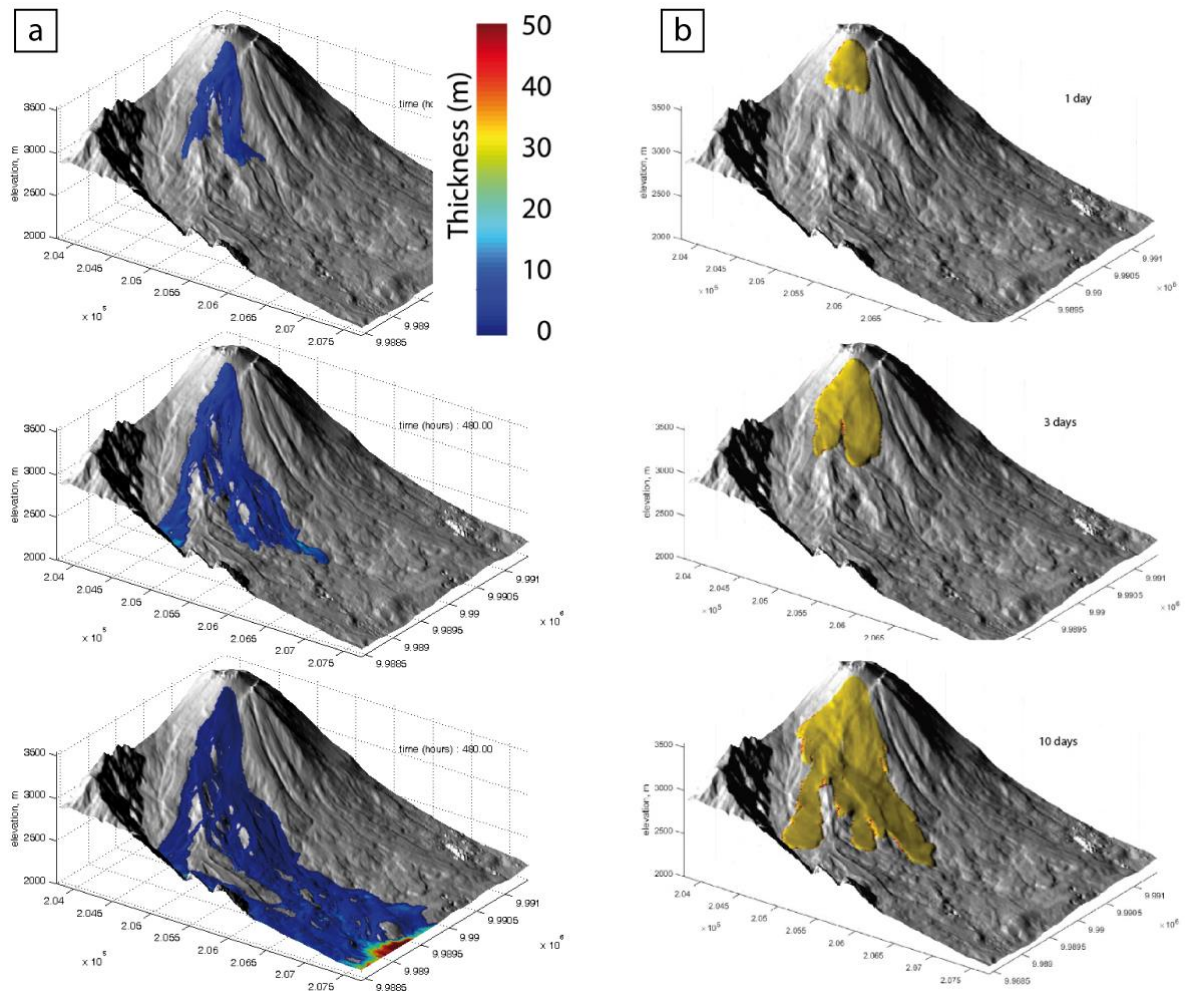


Figure 5.64 a) Progression of the flow with 1wt % H_2O , the flow is broadly dispersed over the topography, in which the maximum thickness is found at the border of the domain ($\sim 50\text{m}$). The rest of the flow has thickness thinner than 15 m. b) Progression of the flow with 0wt % H_2O . The dispersion of the flow is shorter than with 1wt % H_2O . The flow reaches maximum thickness of 30m at its fronts. Comparing with old flows from the topography is possible to observe the similarity of the lobes.

The water content on the composition of the lava flows plays an important role during the estimation of the fluid viscosity. Left side of Fig. 5.65 shows the fluid viscosity in function of temperature for 1 wt.% H_2O (red line) and 0 wt.% H_2O (blue line). The comparison between both results shows that the viscosity for the flow with 1 wt.% H_2O is lower than the viscosity estimated for the flow that have no water content. The difference of the viscosity is faced in about two orders of magnitude for the same temperature. In the other side, the variation of yield

strength during the simulation for both cases is very small, less than 1 Pa in a shorter range of temperature (50° K). These results confirm that water content of water has a direct impact on the initial fluid viscosity.

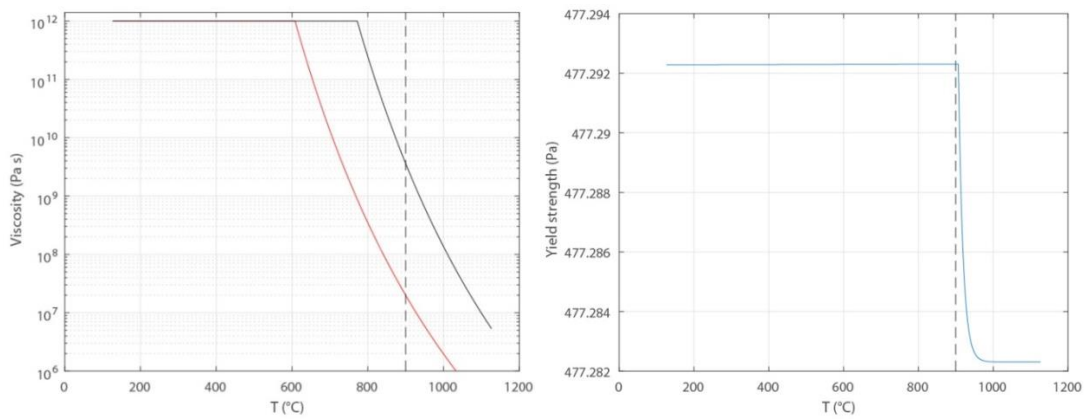


Figure 5. 65 Left: Viscosity in function of temperature, red line is for the simulation considering 1 wt % H₂O and the black line represents the model with 0 wt% H₂O. Right: relationship of yield strength vs temperature showing a small variation of the yield strength along the simulation.

Additionally, for this study case it was taken into account an initial crystal content of 0.4 and a maximum packing of 0.5. Fig. 5.66 shows that the variation of yield strength between this range is very small and therefore it is not the main parameter that governs the rheology in this simulation.

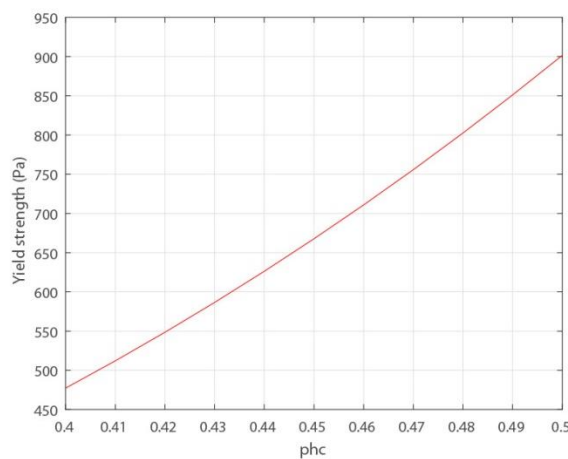


Figure 5. 66 Variation of the yield strength in function of the phenocrystal content. The initial content for this lava flow was 0.4 and the maximum 0.5, the figure shows the small variation

These results shows that the simulations carried on taking into account the cooling model with existing rheological laws is mainly governed by the viscosity.

5.4.3.3.4 Model n°2b: Cooling and rheological variation using sigmoid law

This model uses the VolcFlow basic input parameters and those related to the cooling of the flow (Appendix 5.5). Additionally, the sigmoid law uses a constant viscosity of 5×10^6 Pa s, a lowest yield strength at high temperature = 5×10^3 Pa, highest yield strength at low temperature = 1×10^5 Pa, transition temperature = 1100 K^{-1} and the sharpness of transition = 0.02 K (Appendix 5.5).

The final dispersion of the flow is shown in Fig. 5.67. It is regular and shows little bifurcations at the front. The thicker part of the flow is located at the front, where it reaches a maximum thickness of 50 m. The thinner and narrower part of the flow is located at the steepest part which corresponds to the flank of the volcano with ~ 10 m.

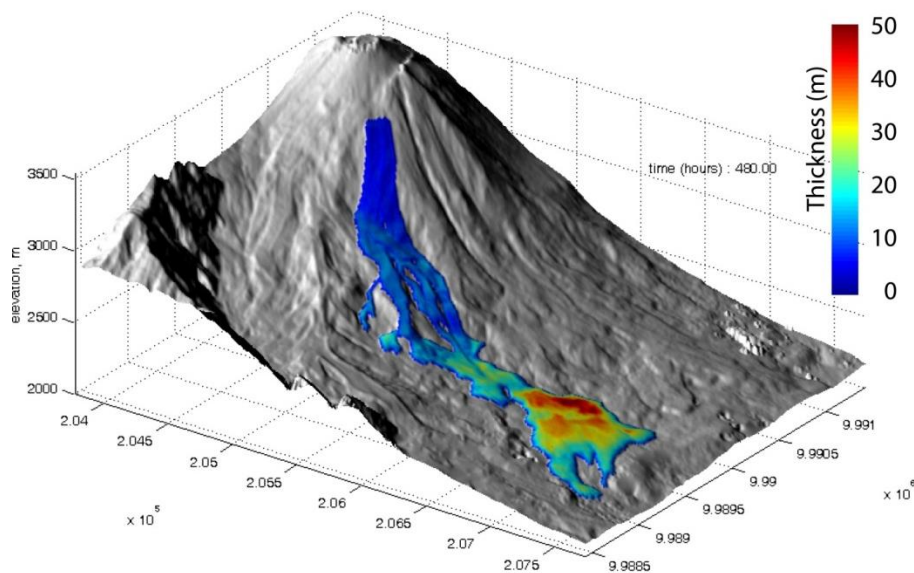


Figure 5. 67 Final deposit of the flow which shows a thickening at the base correspondent to the low topography, the thickness reaches maximum 50 m.

Temperature variation along the simulation is a very important issue for the understanding of the applied rheological models. For this case the variation of temperature is shown as the flow is advancing in time for 1, 3 and 20 days (Fig. 5.68). After the 20 days of simulation the temperature decreases from 1250 K to 950 K.

The detail of the temperature distribution of the flow is shown in Fig. 5.69. The hottest part, which reaches a maximum of 1080 K, is located on the thickest part of the flow. This result was obtained as well in other cases calling the attention that the heat is reaming when the flow is thicker. The coldest part of the flow is located close to the source.

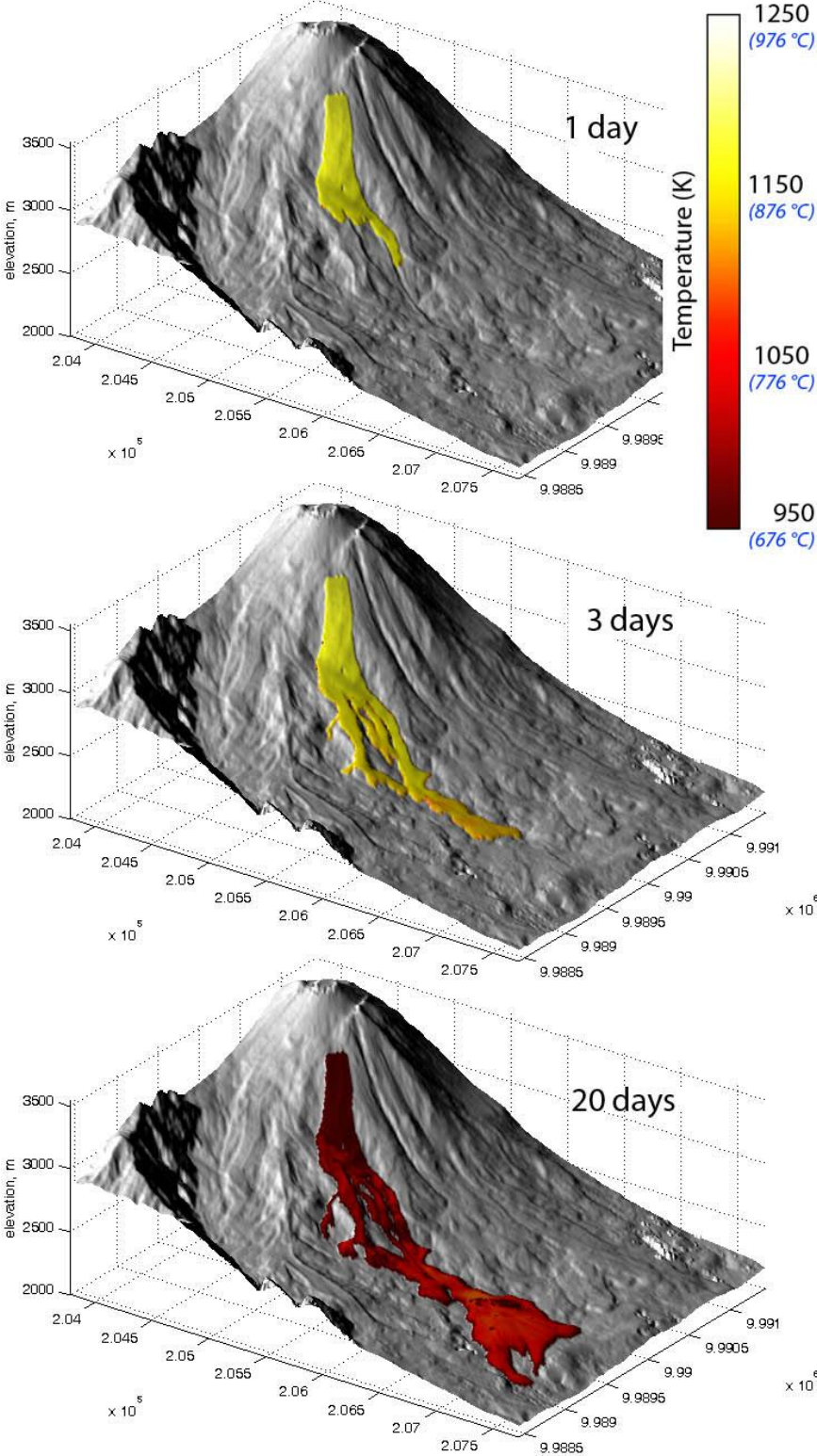


Figure 5. 68 Variation of the temperature of the flow thought the time for 1, 3 and 20 days. At the first day the flow still hot with a temperature about 1250 K and for the day 20th the flow had decreased its temperature for about 950 K.

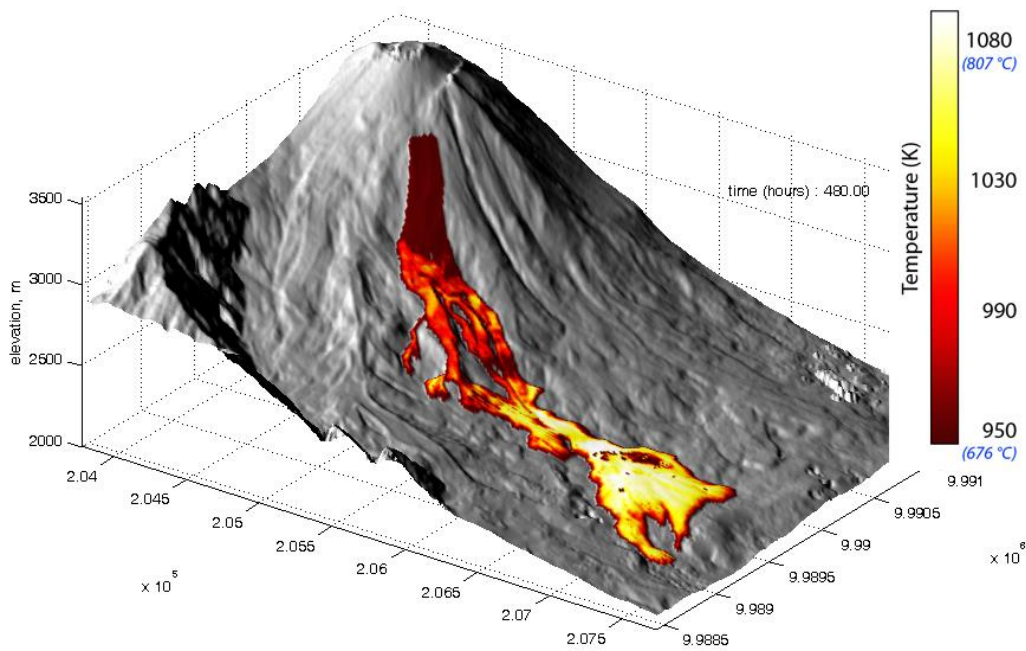


Figure 5. 69 3D view of the distribution of the temperatures on the flow at 20 days (480h), it shows that the hottest part of the flow is at the base which matches with to the thicker part of the flow.

Three cross sections along the flow were done, 1 for the steepest, 2 for the transition between the cone and the caldera floor and 3 for the flow at the caldera floor (Fig. 5.70).

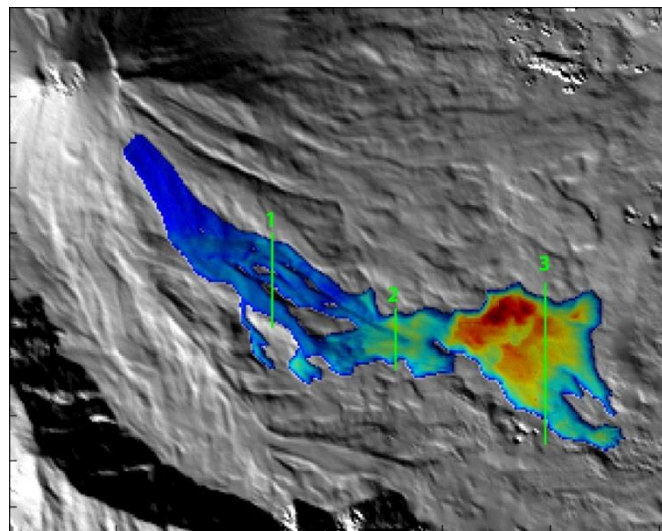


Figure 5. 70 Location of the profiles for the analogous of lava flow 1 using the yield strength sigmoid model.

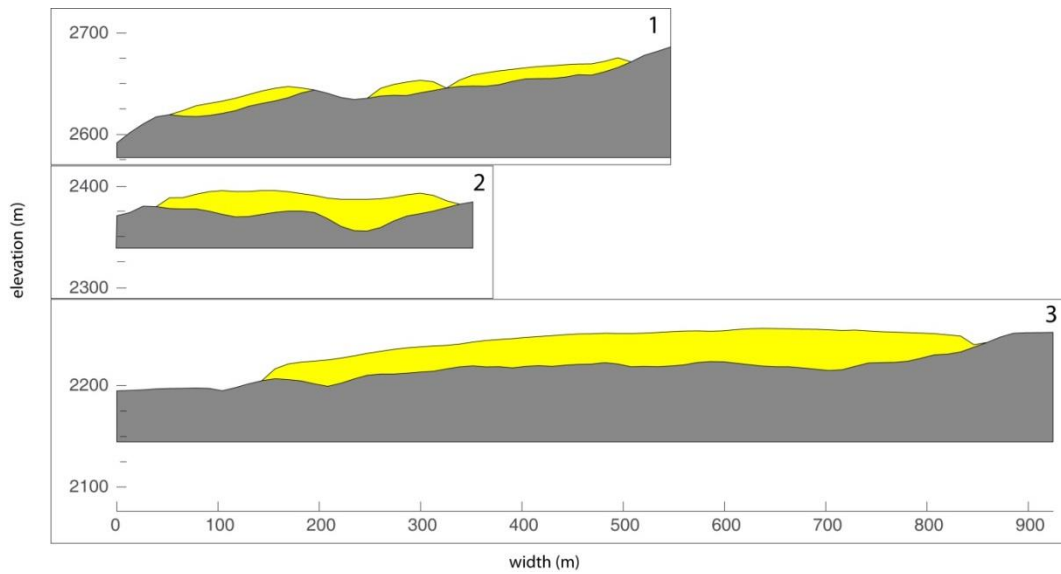


Figure 5. 71 Profiles along the flow shows the thicker part of the flow at its base, which corresponds to the emplacement on the lower topography (profile 3). The thinner part of the flow is located at the flank of the volcano (profile 1).

Fig. 4.80 shows the relationship between the yield strength and temperature obtained from the sigmoid law. It shows the variation of the yield strength which is the parameter that controls the thickness of the flow.

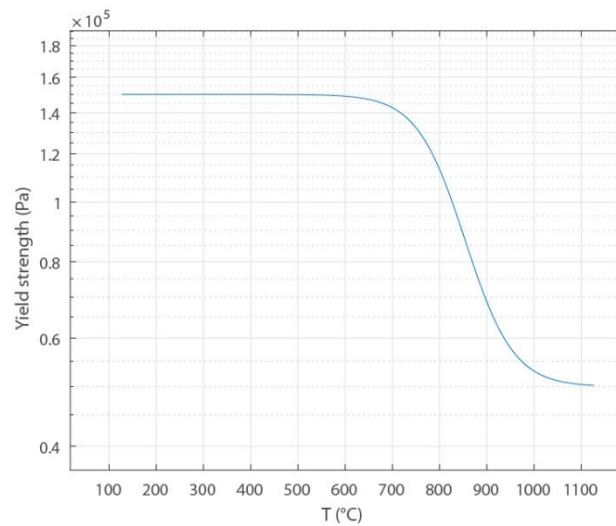


Figure 5. 72 Sigmoid curve obtained by the model showing the variation of the yield strength in function of the temperature.

5.4.4 Discussion

Isothermal simulation (model n°1)

Results of the three flows, showed that this model reproduced well the three cases using a constant viscosity and yield strength. At first, both rheological parameters viscosity and yield strength, were estimated through the calibration of the LF25 simulation by using the measured velocity of the front flow against the velocity of the simulation, as it was done for flows of the Syracuse and Tungurahua's flows (Sections 5.1, 5.3, this Chapter). This methodology helps to constrain in a better way those values that can serve to simulate other flows of the same characteristics.

The best fits for the three cases were obtained with viscosity of 2.5×10^7 Pa s and yield strength of 10^4 and 10^5 Pa. Note that for the simulation generated with a yield strength of 10^4 Pa (April, 2014 and Jun-July, 2017 flows) the thickness of the flow is more realistic than the simulation that used 10^5 Pa (analogous LF1). Even if this model does not take into account the cooling and variation of the rheology, those results seems to be coherent (Fig. 5.73a, 5.74b).

Cooling and rheological variation using existing thermo-rheological laws (model n°2a)

For these simulations it was used the same input parameters for the simulation of the three flows. The dry composition of the interstitial glass matrix of the LF1 from Samaniego *et al.* (2008) was used to estimate the rheology of the three cases. Only for the last case, the hypothetical LF1, it was estimated two different input viscosities: first assuming a dry composition (0 wt. % H₂O, Fig. 5.74c) and the second one with 1 wt. % H₂O (Fig. 5.74c').

For all cases which assumed dry composition (Fig. 5.73b, 5.74c), results displayed flows with regular shape formed by few rounded branches. In general, the thickness was pretty regular along the flows with a slight thickening on the front (similar result as Tungurahua). Also, their shapes are very similar to flows of andesitic composition, and most to previous flows from this volcano. For the hypothetical LF1 with 1 % wt. H₂O, the flow was broadly dispersed with many branches in comparison with the flow that consider a dry composition. This simulation displayed an important accumulation of material at the limit of the numerical domain, assuming that the flow could had been travelled farther (Fig. 5.74c'). The thinner part of this flow was located in the upper part, close to the source. Comparing results of both simulations for the same lava flow, it is graphically evident that the water content has a significant influence on viscosity and therefore on the capability of reproducing reality.

The variation of yield strength during the simulation is minimum in comparison with the variation of the bulk viscosity. These results showed that model n°2a is mainly governed by the viscosity and not too much by the yield strength. Another interesting result of them is that the model n°2a has the capability to develop small levees structures.

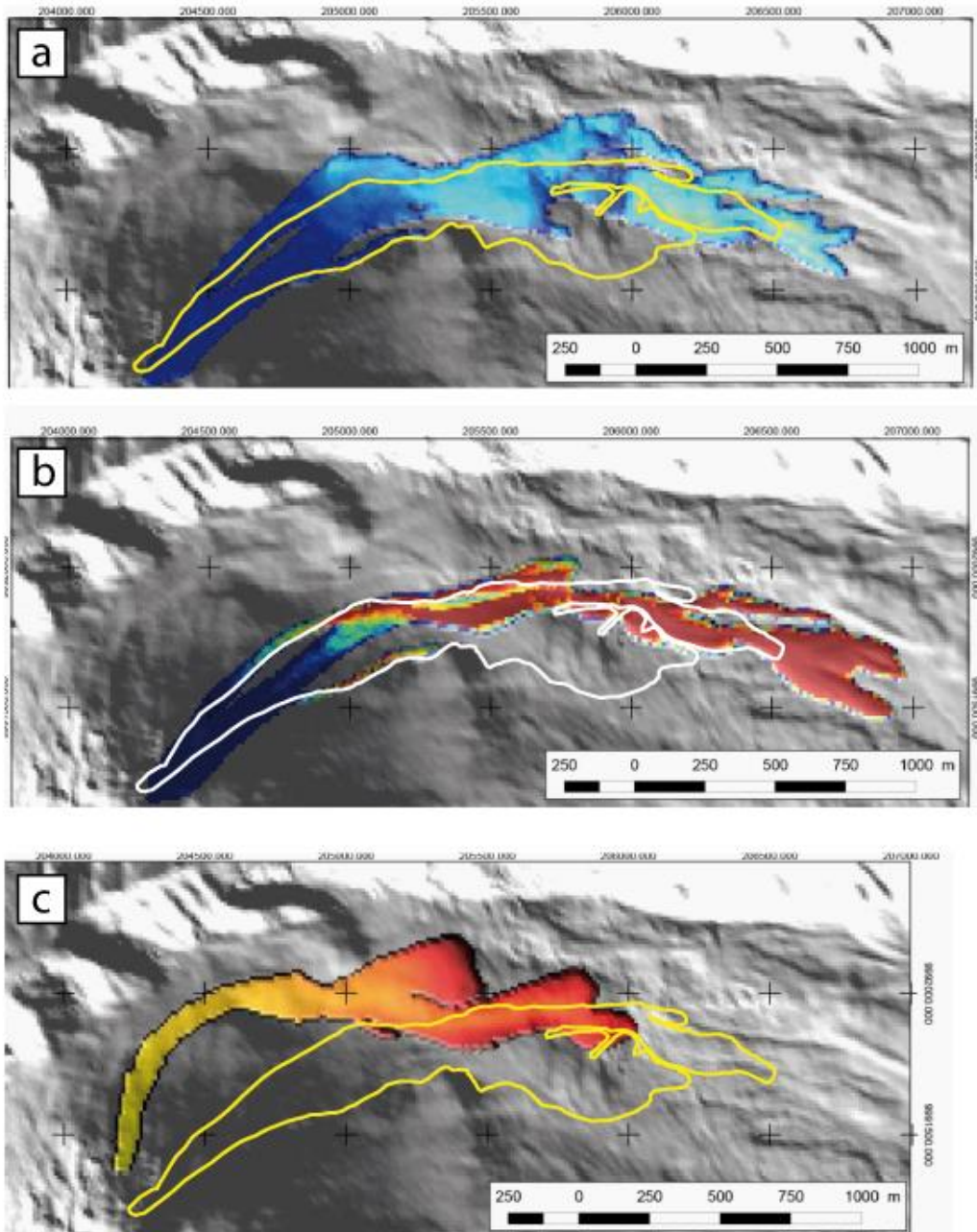


Figure 5.73 Comparison of the simulations for the June-July lava flow from El Reventador volcano and the real deposit (white/yellow contour). **a)** orthogonal view of the simulation obtained by the **Isothermal model (model n°1)**, **b)** orthogonal view of the **model n°2a** which includes the **cooling and rheological variation using existing thermo-rheological laws**, **c)** orthogonal view of the **model n°2b** which takes into account the **cooling and rheological sigmoid law**.

Thermo-rheological variation (yield strength sigmoid law) simulation (model n°2b)

In all cases the simulations showed a good coherence on the results. The shape of the flows was regular and they did not present too many bifurcations at the fronts. The surface of the flows shows a slight increasing of the thickness at the borders suggesting the development of levees. An interesting fact of model n°2, which includes the effect of the cooling and rheological variation, allow the flow to keeps the heat of the flow on the thicker part which is located close to the front of the flow. The coldest and thinner part of the flow is located close to the source.

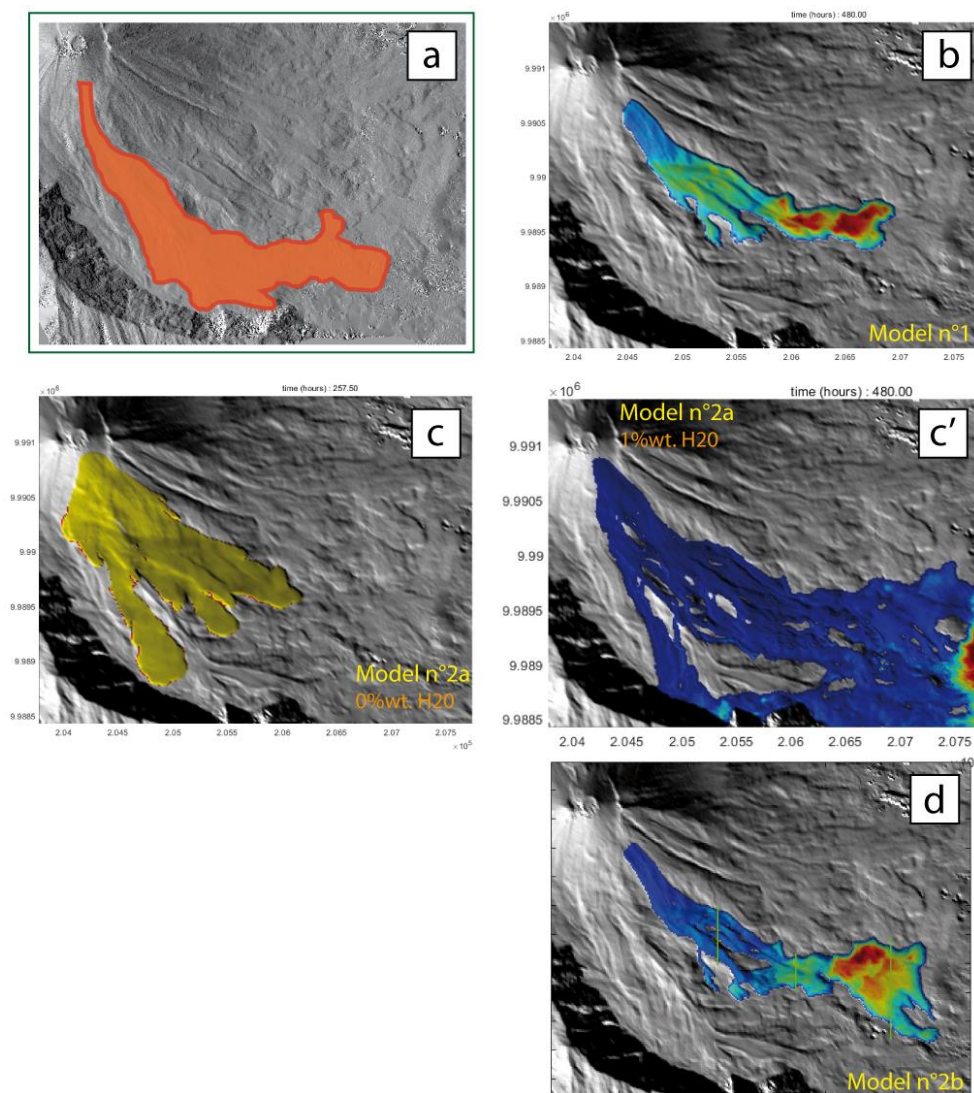


Figure 5.74 o Representation of the LF1 deposit of El Reventador volcano (a) and the simulations of an hypothetical LF1 by using different rheologies (b-d). **b)** orthogonal view of the simulation obtained by the **Isothermal model** (model n°1), **c)** and **c')** orthogonal views of the models n°2a which includes the **cooling and rheological variation using existing thermo-rheological laws** with **0%wt.** and **1%wt H₂O** respectively, **(d)** orthogonal view of the **model n°2b** which takes into account the **cooling and rheological sigmoid law**.

Chapter 6

Summary, Conclusions and Perspectives

Summary

The main objective of this research was to test and modify a numerical code to reproduce the lava flow emplacement and to check the validity of the different approaches with data collected in the field. To accomplish this goal, it was, 1) modified the numerical code VolcFlow by adding energy advection, crust formation and thermo-rheological laws to simulate andesitic lava flows; 2) analyzed the quality of the various approaches by comparing the results of the simulations with the field data; 3) analyzed the ratio model quality/model complexity to determine which model can be used for hazard assessment and in what conditions they can be used.

The development of the present research involved the following topics. The state of art of lava flows (Chapter 1) and the different numerical flows for simulated them (Chapter 3). An analysis of the lava flows from El Reventador volcano between 2012-2014, as it represents the main andesitic target of this project (Chapter 2). It was analyzing in detail the morphology and surface distribution, generating then information that can serve as input data for the simulation of lava flows. VolcFow has been improved with different rheologies to simulate lava flows of different compositions (Chapter 4). Experimental and real basaltic and andesitic flows from the Syracuse lava flow project, Piton de la Fournaise (La Réunion, France), Tungurahua (Ecuador), El Reventador (Ecuador) were simulated by using the different approaches (Chapter 5). All the simulations done here helped to constrain which model is preferable to apply depending on the flow characteristics and the available data.

Conclusions

❖ Effusive activity of El Reventador volcano and field data as input parameters for numerical simulation of lava flows

El Reventador volcano is one of the most active volcanoes in Ecuador mainland since 2002, year of its reactivation. Its eruptions are characterized for being Vulcanian and Strombolian with the generation of gas/ash columns, pyroclastic density currents and lava flows. Since 2002, more than 60 lava flows units were generated, all of them emplaced in the inner part of its caldera floor. It is the only Ecuadorian volcano that has generated that vast number of lavas in such a short period of time. At least six eruptive phases were recognized between 2002 and 2014. Seventeen flows were identified in the period 2002-2009 and twenty between 2012-2014. In contrast to the flows from 2002-2009, the 20 latest flows were shorter, thinner and hence less voluminous.

The lava flows analysis carried out in Chapter 2 helped to compile information of the 37 lava flows generated between 2002 and 2014, which can be used as input parameters for the simulation of lava flows, using different rheologies. Basically, it was related to estimate the volume, effusion time, velocity, thickness, morphology, duration, distribution, chemical composition and superficial temperature measurements. Additionally, the DEM (1.8 m resolution) developed here served as the topographic base to simulate the different flows.

Volume, effusion and emplaced time: A well constrain of the volume, effusion and emplaced time of existent lava flows are basic information that can help to propose different cases scenarios for the simulation of lava flows using different rheologies.

Velocity estimation: It has been demonstrated in this research that the velocity's estimation of a lava flow can plays an important tool at the moment to calibrate a numerical model with any chosen rheology (e.g. isothermal, cooling + sigmoid rheological law).

Chemical composition, temperature (core, surface), crystal content: cooling and rheology interplays during the emplacement of lava flows. A good estimation of the parameters that controls the rheology and the crystal variation are needed to estimate the cooling of the flow.

Morphology (shape, length, thickness), distribution: The analysis of the lava flow's morphology can help to validate a chosen model. The knowledge of the thickness is an advantage at the moment to calibrate and verified the validity of the simulations using the different approaches.

❖ Simulating lava flows with VolcFlow using different rheologies

The numerical code VolcFlow was improved by incorporating rheological laws that can help to simulate realistic lava flows. Three approaches were proposed in this thesis to simulate lava flows by using a modified version of VolcFlow, Fig. 6.1:

- **Model n°1:** Isothermal. Assumes an isothermal lava with a constant Bingham rheology.
- **Model n°2:** Cooling and thermo-rheological variation
 - **Model n°2a:** combines the cooling, the crystal content variation and the existing rheological laws for viscosity and yield strength.
 - **Model n°2b:** combines the cooling and the rheological variation for viscosity or yield strength by applying an empirical sigmoid law.
- **Model n°3:** Crust formation and hot interior. Test the effect of a crust formation on the emplacement.

Chart from Fig. 6.1 shows the input parameters that each model needed to simulate a lava flow by choosing one or another rheology.

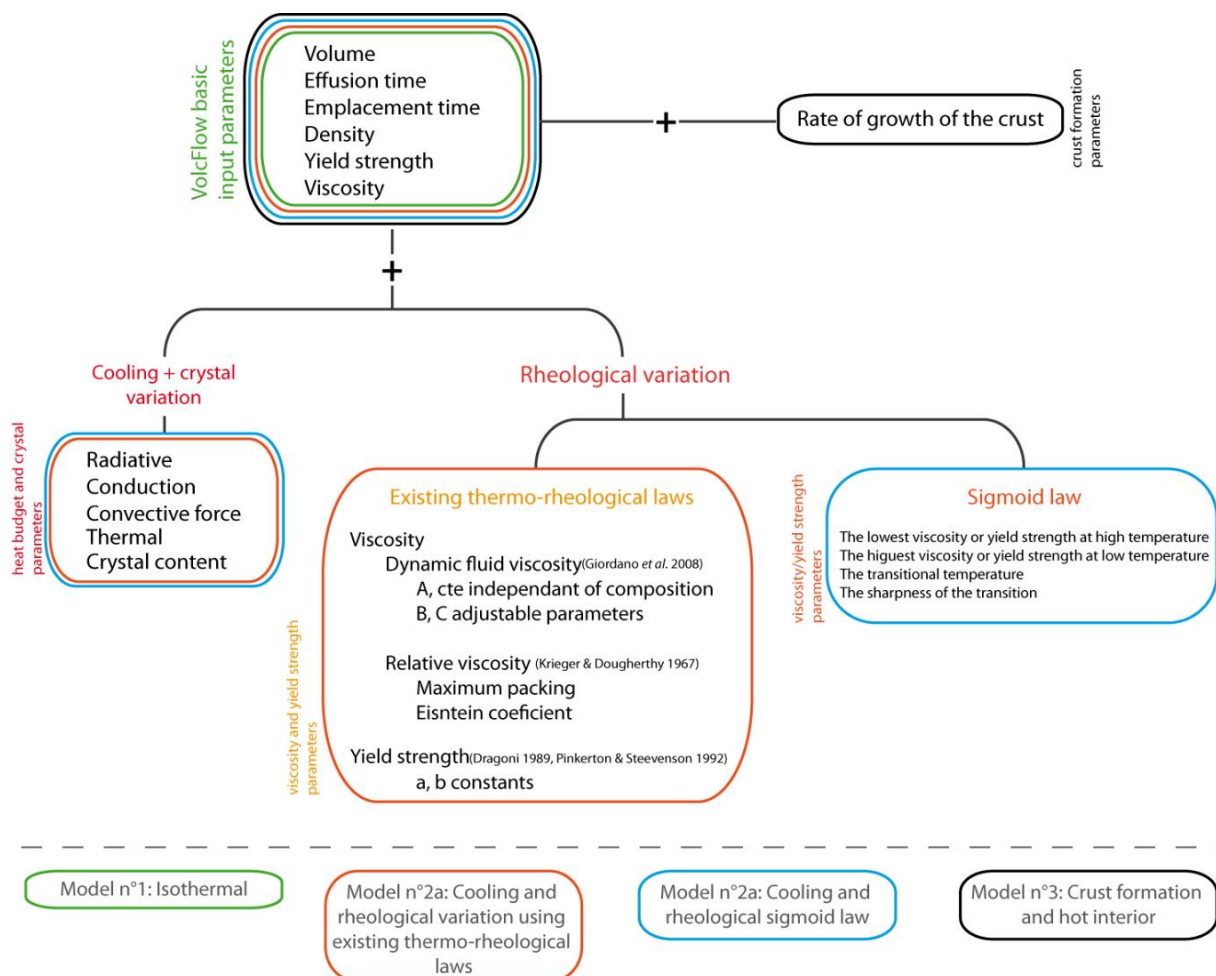


Figure 6. 1 Chart-resume of the input parameters for Models n°1, 2a, 2b and 3.

These models were tested with four study cases:

- **C1:** An experimental flow, the molten basalt flow from the Syracuse lava project;
- **C2:** The August-November 2015 lava flow from Piton de la Fournaise volcano (La Réunion, France);
- **C3:** The December, 4th and 5th 2010 lava flow from Tungurahua volcano (Ecuador);
 - **C4:** Three lava flows from El Reventador volcano (Ecuador) including the flows from April, 2014; June-July, 2017 and a hypothetical flow with the same characteristics of the lava flow 1 (LF1) emitted in November, 2002.

At first, all the test cases proposed here were simulated successfully with the different rheologies. Despite its simplicity, the **isothermal model (n°1)**, that uses a Bingham rheology with a constant viscosity and a constant yield strength, is able to reproduce well the lava flows from the four cases. The choice of the viscosity and of the yield strength depends on the characteristics of each flow, essentially its size and its lava composition. For the first case (**C1**, Syracuse project) which does not take into account the crystallinity; best fits are obtained with a viscosity of 18 Pa s and a yield strength of 100 Pa. For Piton de la Fournaise (**C2**), best fits are obtained with viscosity of 10^5 Pa s and yield strength of 10^3 Pa, while for andesitic composition (**C3** and **C4**) best fits are obtained for a viscosity of 10^6 Pa s and a yield strength of $10^4 - 10^5$ Pa. Using this model, better results can be obtained when it has been previously calibrated with the measured velocity of an ancient flow (e.g. Tungurahua and El Reventador lava flows).

The second model was designed to include **the cooling and the rheological variations** to improve our capability of representing reality. The cooling down flow was estimated via the heat budget from FLOWGO (Harris & Rowland 2001, Harris *et al.* 2015), which was included in VolcFlow. To link the temperature of the flow to its rheology, I have used either existing rheological laws describing the effect of crystallization as used in FLOWGO (Giordano & Dingwell 2003; Einstein 1906; Roscoe 1952; Krieger & Dougherty 1967) or a synthetic empirical viscosity or yield strength sigmoid law. This empirical law only needs 4 parameters and is useful to approximate the first order rheology by a trial and error approach.

Syracuse lava flow (C1)

The simulation fits well with the data in two cases: if the flow viscosity depends on the temperature with the **sigmoid law** and for an **isothermal Bingham flow**. It is interesting to note that a simulation with no yield strength and a variable viscosity (sigmoid law), is nearly identical to

the simulation that uses the Bingham model (constant viscosity and constant high yield strength). The good fits obtained seem to mean that simple approximations are sufficiently good to simulate such small flows where no crystallization occurs.

Piton de la Fournaise lava flow (C2)

For this case, no simulation was able to reproduce the large lateral spreading observed in the field. With an **isothermal Bingham law**, a relatively low yield strength (5×10^3 Pa) is needed to form flow of the thickness observed. Initially, the flow emplacement is correct but, for long eruptions, a large volume is emitted at the source. Because the lava does not cool and the rheology does not change, no lava accumulation can be simulated. This is why, the simulation cannot form the spreading observed but very long lava tongues. A similar problem occurs with the **rheologies that change with cooling** for a different reason. The cooling is stronger at the edges forming levees that channelize the flow. With time, the flow thickness increases up to unrealistic values, increasing the levee height. The flow cannot break the levee to form the large lava field observed. To check if a depth-averaged model can solve the problem of cold lava breaking, we have developed a model of a **crust formation** that can modify the topography where it is in contact with the ground. In theory, this model can break the crust and spread laterally. In practice, the lateral spreading is limited to some tens of meters from the channel and the model forms unrealistic thick deposits as for the rheology dependent models.

4th-5th December, Tungurahua lava flow (C3)

Considering the **complete model of cooling** (existing rheological laws as function of temperature) did not reproduce well the natural flow. Note that, in this model, all parameters are measured and that they have not been modified by trial and error method. Good result could have been found by changing the initial parameters. With the parameter used in these simulations, the emplacement is controlled by the viscosity, the variability of the yield strength with temperature and crystallinity being relatively small. Simulations show that the best results are obtained if the yield strength controls the emplacement: considering an increase of the yield strength with temperature following the **sigmoidal law** or with the **isothermal model**. This probably means that the flow emplacement is ruled by the lava flow thickness to the first order.

El Reventador lava flows (C4)

The **complete model of cooling** can give very good results, for example, for the last lava flow (June-July 2017). If results are good, it is probably because the rheological model, based on measured properties, fits correctly with the flow studied. Indeed, it was noticed that the initial viscosity and therefore the lava chemical composition (in particular water content) had a great impact on the final lava flow shape. For example, flows with dry composition are shorter and thicker than flows having an initial water content. The simulation of lava LF1 that is more fluid and longer than reality, could be explained by an overestimation of its water content. The simulations using the **yield strength sigmoid law** or the **isothermal law** also show a good coherence with the natural deposit. **A sigmoid law on the viscosity** forms high levees that oppose to the flow emplacement and an unrealistically thick flow front.

To conclude, the model which includes rheological laws as function of crystallization induced by cooling down flow can give very good results but is very sensitive to the input data, in particular to the fluid viscosity that is very dependent on chemical composition and temperature. Results as well suggest that the rheology of the flow is governed mainly by the viscosity and little by the yield strength. The model which considers the variation of the yield strength with temperature following the sigmoidal law, shows a good coherence for all the cases except at La Réunion. In view of all the different cases studied, the model seems to be adapted to simulate flows if the eruption duration is shorter than the lava emplacement and if the lava emplaces in a single unit. Otherwise, lava breaking must be taken into account and this cannot be done with VolcFlow.

Perspectives

❖ How can the models presented in this thesis be used for the simulation of basaltic and andesitic flows at other volcanoes with similar compositions?

For basaltic lava flows it was not possible to recreate a correct emplacement because the model neglects the formation of lava tubes structures and cannot simulate the rock breaking. Even if our model of crust is empirical and could be improved by the crust formation model proposed by Fink and Griffiths (1993), it does not seem that this approach can solve the problem.

In terms of risk, the model can probably simulate a short effusive phase of basaltic flow, if a single lava lobe emplaces. For longer durations, the model can be used to have a map of the drainages that can be affected. The isothermal model is relatively simple to use and fast enough for a real-

time estimation of the potentially affected areas. However, it must be kept in mind that the model will overestimate the length of the lava and that the lateral spreading will be strongly underestimated. In order to apply this work for other volcanic area in Ecuador, a good target would be the Galapagos Islands. Indeed, the Galapagos have an eruption almost every 5 years, which threaten local unique biodiversity. It would therefore, be of great interest to explore our ability to simulate those lava flows and to improve the approaches of basaltic flows, for a fast and accurate drawing of hazard maps of future eruptions.

For andesitic lava flows, both the isothermal model and the model considering yield strength increase as function of temperature following a sigmoid law reproduce very well the natural flows. A very good fit can also be obtained with the complete approach but, to do that, we need a rapid measurement of the lava properties. This is probably unrealistic for real time hazard assessment. The good fit is probably explained by the single lobe emplacement of this type of flows. For a long andesitic eruption, if lobes are created, the model will probably fail as for the basaltic lava flows studied.

To go further and to develop and check the future numerical evolutions of the model, we must focus on the characterization of the lava at the source: temperature, volume rate, lava composition and their changes with time. As already mentioned the results of the simulations presented in this work are highly sensitive to the input data. Moreover, we need unambiguous data to prove that a model is adapted or not to simulate a given event. It is then of great importance to have a well study setting in terms of topography but also in terms of lava texture, chemical composition and therefore initial rheological parameters to calibrate the model. For the next years, I want to make an effort to establish a robust database of the lava flows in Ecuador that will allow to check and validate objectively the future numerical approach. This is the only way to develop a tool that will help us to better assess the hazard posed by future lava flows.

References

A

- Aguilera, E., Almeida, E. and Balseca, W. (1988) El Reventador: an active volcano in the sub-Andean zone of Ecuador. *Rendiconti della Società Italiana di Mineralogia e Petrologia*, Vol. 43, p. 853-875.
- Arnold, D.W.D, Biggs, J., Anderson, K., Vallejo Vargas, S., Wadge, G., Ebmeier, S. K., Naranjo, M. F. and Mothes, P. (2017) Decaying lava extrusion rate at El Reventador volcano Ecuador, measured using high-resolution satellite radar. *Journal of Geophysical Research: Solid Earth*, DOI 10.1002/2017jb014580.

B

- Baloga, S. and Pieri, D. (1986) Time-Dependent profiles of lava flows. *Journal of Geophysical Research*. 91(B9), 9543-9552.
- Balmforth, N.J. and Craster, R.V. (2000) Dynamics of cooling domes of viscoplastic fluid. *J. Fluid Mech.* 422, 225–248.
- Balmforth, N.J., Craster, R.V. and Sassi, R. (2004) Dynamics of cooling viscoplastic domes. *J. Fluid Mech.* 499, 149–182.
- Barca, D., Crisci, G.M., Di Gregorio, S. and Nicoletta, F. (1993) Cellular automata methods for modeling lava flows: simulation of the 1986–1987 eruption, Mount Etna, Sicily. In *Active lavas*. UCL Press, UCL Press L (ed) pp 291–309.
- Barca, D., Crisci, G.M., Di Gregorio, S. and Nicoletta, F.P. (1987) Lava flow simulation by cellular automata: Pantelleria's examples. In *Proceedings AMS International Conference Modelling and Simulation Cairo, Egypt*.
- Barca, D., Crisci, G.M., Gregorio, S. Di and Nicoletta, F. (1994) Cellular automata for simulating lava flows: A method and examples of the Etnean eruptions. *Transport Theory and Statistical*

Physics, 23, 195–232.

- Barré de Saint-Venant (1887) Mémoire sur le choc longitudinal de deux barres élastiques, etc. J.M. Journal de Mathématiques Pures et Appliquées. Paris, 12, 237-376.
Classification: T2a Élasticité des corps solides; équations différentielles du problème de l'élasticité; généralités; Fiche 1256.
- Bernabeu, N., Saramito, P. and Smutek, C. (2016) 'Modelling lava flow advance using a shallow-depth approximation for three-dimensional cooling of viscoplastic flows', Geological Society, London, Special Publications, (2005), pp. 409–423.
- Bilotta, Hérault, Cappello, Ganci and Negro, D. (2016) GPUSPH: A Smoothed Particle Hydrodynamics model for the thermal and rheological evolution of lava flows. Geological Society Special Publication, 426, 387–408.
- Bonne, K., Kervyn, M., Cascone, L., Njome, S., Van Ranst, E., Suh, E., Ayonghe, S., Jacobs, P. and Ernst, G. (2008) A new approach to assess long-term lava flow hazard and risk using GIS and low-cost remote sensing: the case of Mount Cameroon, West Africa. *Int. J. Remote Sens.* 29, 6539–6564.
- Bottinga, Y. and Weill, D. (1972) The Viscosity of Magmatic Silicate Liquids: A Model for Calculation. 438–75.
- Burguete, J., Garcia-Navarro, P. and Aliod, R. (2002) Numerical simulation of runoff from extreme rainfall events in a mountain water catchment, *Nat. Hazards Earth Syst. Sci.*, 2, 109– 117.

C

- Calvari, S. and Pinkerton, H. (1998) Formation of Lava Tubes and Extensive Flow Field during the 1991–1993 Eruption of Mount Etna. *Journal of Geophysical Research.* 103: 27,291–27,301.
- Calvari, S., Spampinato, L., Lodato, L., Harris, A.J.L., Patrick, M.R., Dehn, J., Burton, M.R. and Andronico, D. (2005) Chronology and complex volcanic processes during the 2002-2003 flank eruption at Stromboli volcano (Italy) reconstructed from direct observations and surveys with a handheld thermal camera. *Journal of Geophysical Research: Solid Earth*, 110, B2.
- Cappello, A., Ganci, G., Calvari, S., Pérez, N.M., Hernández, P.A., Silva, S. V., Cabral, J. and Del

- Negro, C. (2016) Lava flow hazard modeling during the 2014-2015 Fogo eruption, Cape Verde. *Journal of Geophysical Research: Solid Earth*, 121, 2290–2303.
- Cas, R. A. F. and Wright, J. V. (1987) *Volcanic Successions, Modern and Ancient : A Geological Approach to Processes, Products, and Successions*, 528 pp.
- Cashman, K. V., Thornber, C. and Kauahikaua, J. P. (1999) Cooling and Crystallization of Lava in Open Channels, and the Transition of Pāhoehoe Lava to ‘A’ā.” *Bulletin of Volcanology*, 61, 306–323.
- Cashman, K. V., Soule, S. A., Mackey, B. H., Deligne, N. I., Deardorff, N. D. and Dietterich, H. D. (2013) How Lava Flows: New Insights from Applications of Lidar Technologies to Lava Flow Studies. *Geosphere* 9(6): 1664–80.
- Castruccio, A., Rust, A.C. and Sparks, R.S.J. (2010) Rheology and flow of crystal-bearing lavas: Insights from analogue gravity currents. *Earth and Planetary Science Letters*, 297, 471–480.
- Castruccio, A., Rust, A. C, Sparks and R. S.J. (2013) Evolution of Crust- and Core-Dominated Lava Flows Using Scaling Analysis. *Bulletin of Volcanology* 75(1): 1–15.
- Castruccio, A., Rust, A. C., and Sparks, R. S. J. (2014) Assessing Lava Flow Evolution from Post-Eruption Field Data Using Herschel-Bulkley Rheology. *Journal of Volcanology and Geothermal Research* ,275, 71–84.
- Chevrel, O., Platz, T., Hauber, E., Baratoux, D., Lavallée, Y. and Dingwell, D.B. (2013) Lava Flow Rheology: A Comparison of Morphological and Petrological Methods.” *Earth and Planetary Science Letters* 384: 109–20.
- Chevrel, M. O., Cimarelli, C. and Hanson, J. (2015) Viscosity measurements of Crystallizing Andesite from Tungurahua Volcano (Ecuador). *Geochemistry Geophysics Geosystems*: 1–20.
- Chevrel, O., Labroquère, J., Harris, A. and Rowland, S. (2017) PyFLOWGO: an open-source platform for simulation of channelized lava thermo-rheological properties. *Computers in Geosciences*, underreview.
- Chirico, G.D., Favalli, M., Papale, P., Boschi, E., Pareschi, M.T. and Mamou-Mani, A. (2009) Lava flow hazard at Nyiragongo Volcano, DRC. *Bulletin of Volcanology*, 71, 375–387.
- Cleary, P. W. and Monaghan, J. J. (1999) Conduction modelling using smoothed particle hydrodynamics. *Journal of Computational Physics*, 148(1), 227-264.
- Cleary, P. W. and Ha, J. (2003) Three-dimensional SPH simulation of light metal components.

- Journal of Light Metals, 2, 169–183.
- Coltelli, M., Proietti, C., Branca, S., Marsella, M., Andronico, D. and Lodato, L. (2007) Analysis of the 2001 lava flow eruption of Mt. Etna from three-dimensional mapping. *Journal of Geophysical Research: Earth Surface*, 112, 1–18.
- Connor LJ, Connor CB, Meliksetian K and Savov I. (2012) Probabilistic approach to modeling lava flow inundation: a lava flow hazard assessment for a nuclear facility in Armenia. *J Appl Volcanol.* 2012;1:1–19.
- Costa, A. and Macedonio, G. (2005) Numerical simulation of lava flows based on depth-averaged equations, *Geophysical Research Letters*, Vol. 32, L05304, doi:10.1029/2004GL021817, 2005.
- Coppola, D., Laiolo, M., Cigolini, C., Delle Donne, D. and Ripepe, M. (2016) Enhanced volcanic hot-spot detection using MODIS IR data: results from the MIROVA system, *Detecting, Modelling and Responding to Effusive Eruptions*, A. J. L. Harris, T. De Groeve, F. Garel, S. A. Carn.
- Cordonnier, B., Caricchi, L., Pistone, M., Castro, J., Hess, K.U., Gottschaller, S., Manga, M., Dingwell, D. B. and Burlini, L. (2012) The Viscous-Brittle Transition of Crystal-Bearing Silicic Melt: Direct Observation of Magma Rupture and Healing. *Geology*, 40(7), 611–14.
- Cordonnier, B., Lev, E. and Garel, F. (2015) *Benchmarking Lava-Flow Models*. Geological Society, London, Special Publications, 426, 425–445.
- Costa, A. and Macedonio, G. (2003) Viscous Heating in Fluids with Temperature-Dependent Viscosity: Implications for Magma Flows. *Nonlinear Processes in Geophysics*.
- Costa, A., Caricchi, L. and Bagdassarov, N. (2009) A model for the rheology of particle-bearing suspensions and partially molten rocks. *Geochemistry, Geophysics, Geosystems*, 10(3).
- Crisci, G.M., Di Gregorio, S. and Ranieri, G. (1982) A cellular space model of basaltic lava flow. In *Proc. 11 Int. Conf. Applied Modelling and Simulation '82* pp 65–67. Paris.
- Crisci, G.M., Gregorio, S. Di, Pindaro, O. and Ranier, G. (1986) Lava flow simulation by a discrete cellular model: first implementation. *Int. J. Model. Simul*, **6**, 137–140.
- Crisci, G.M., Di Gregorio, S., Rongo, R., Spataro, W. and Nicoletta, F. (1999) Analysing lava risk for the Etnean area: simulation by cellular automata methods. *Natural Hazards*, **20**, 215–229.
- Crisci, G.M., Rongo, R., Di Gregorio, S. and Spataro, W. (2004) The simulation model SCIARA:

the 1991 and 2001 lava flows at Mount Etna. *Journal of Volcanology and Geothermal Research*, 132, 253–267.

Crisp, J. and Baloga, S. (1990) Influence of crystallization and entrainment of cooler material on the emplacement of basaltic aa lava flows. *Journal of Geophysical Research*, 99, 48–49.

Crisp, J. and Baloga, S. (1994) A Model for Lava Flows with Two Thermal Components. *Journal of Geophysical Research*, v. 98(B2), 1255–1270.

D

Danes, Z. F. (1972) Dynamics of Lava Flows. *Journal of Geophysical Research* 77(1), 1430–1432.

de Silva, S. L., Self, S., Francis, P. W. and Drake, R. E. (1994) Other Young Lavas of the Altiplano-Puna Volcanic Complex. *Geology* 99, 805–825.

Del Negro, C., Fortuna, L., Herault, A. and Vicari, A. (2008) Simulations of the 2004 lava flow at Etna volcano using the magflow cellular automata model. *Bulletin of Volcanology*, 70, 805–812.

Derrien, A., Villeneuve, N., Peltier, A. and Beauducel, F. (2015) Retrieving 65 years of volcano summit deformation from multitemporal structure from motion: The case of Piton de la Fournaise (La Réunion Island). *Geophysical Research Letters*, 42, 6959–6966.

Di Gregorio, S., Serra, R. and Villani, M. (1996) Combining cellular automata and genetic search in complex environmental modelling. *Proc. 3rd Systems Science European Congr.*, 1127–1131.

Diefenbach, A.K., Crider, J.G., Schilling, S.P. and Dzurisin, D. (2012) Rapid, low-cost photogrammetry to monitor volcanic eruptions: an example from Mount St. Helens, Washington, USA. *Bulletin of Volcanology*, 74, 579–587.

Dietterich, H. R. and Cashman, K. V. (2014) *Journal of Geophysical Research : Earth Surface*, 1704–1724.

Dietterich, H.R., Cashman, K. V., Rust, A.C. and Lev, E. (2015) Diverting lava flows in the lab. *Nature Geoscience*, 8, 494–496.

Dietterich, H.R., Lev, E., Chen, J., Richardson, J.A. and Cashman, K. V. (2017) Benchmarking computational fluid dynamics models of lava flow simulation for hazard assessment,

forecasting, and risk management. *Journal of Applied Volcanology*, 6, 9.

Dragoni, M., Bonafede, M. and Boschi, E. (1986) Downslope Flow Models of a Bingham Liquid: Implications for Lava Flows. *Journal of Volcanology and Geothermal Research*, 30, 305–325.

Dragoni, M. (1989) A Dynamical Model of Lava Flows Cooling by Radiation. *Bulletin of Volcanology* 51(2): 88–95.

Dingwell, D. B. and Mysen, B. O. (1985) Effects of Water and Fluorine on the Viscosity of Albite Melt at High Pressure: A Preliminary Investigation. *Earth and Planetary Science Letters* 74(2–3): 266–74.

E

Einstein, A. (1906) Eine neue bestimmung der moleküldimensionen. *Annalen Der Physik*, 324(2), 289–306.

Eltner, A. and Schneider, D. (2015) Analysis of Different Methods for 3D Reconstruction of Natural Surfaces from Parallel-Axes UAV Images. *The Photogrammetric Record*, 30, 279–299.

F

Fagents, S. A. and Greeley, R. (2001) Factors influencing lava-substrate heat transfer and implications for thermomechanical erosion. *Bulletin of Volcanology*, 62, 519–532.

Farquharson, J.I., James, M.R. and Tuffen, H. (2015) Examining rhyolite lava flow dynamics through photo-based 3D reconstructions of the 2011–2012 lava flowfield at Cordón-Caulle, Chile. *Journal of Volcanology and Geothermal Research*, 304, 336–348.

Favalli, M., Pareschi, M.T., Neri, A. and Isola, I. (2005) Forecasting lava flow paths by a stochastic approach. *Geophysical Research Letters*, 32, 1–4.

Favalli, M., Chirico, G.D., Papale, P., Pareschi, M.T. and Boschi, E. (2009) Lava flow hazard at Nyiragongo volcano, D.R.C. 1. Model calibration and hazard mapping. *Bulletin of Volcanology*, 71, 363–374.

- Felpeto, A., Araña, V., Ortiz, R., Astiz, M. and García, A. (2001) Assessment and Modelling of Lava Flow Hazard on Lanzarote (Canary Islands). *Natural Hazards*, 23, 247–257.
- Fink, J. H. and Anderson, S. W. (1999) In *The Encyclopedia of Volcanoes: Lava Domes and Coulees*, eds. eds. Sigurdsson, H., Houghton, B., McNutt, S., Rymer, H., Stix, J., Academic Press of Elsevier, 307.
- Formenti, Y., Druitt, T. H. and Kelfoun, K. (2003) Characterisation of the 1997 vulcanian explosions of Soufrière Hills Volcano, Montserrat, by video analysis. *Bulletin of Volcanology*, 65, 587–605.
- Gruen, A. (2012) Development and Status of Image Matching in Photogrammetry. *The Photogrammetric Record*, 27, 36–57.
- Froger, J.L., Cayol, V., Grandin, R., Villeneuve, N., Peltier, A., Rivet, S., Ordoqui, P., and Mora, O. (2015) Last eruption of Piton de la Fournaise imaged with new generation radar data, Workshop MDIS 7-9 October, 2015
- Fujita, E. and Nagai, M. (2016) *LavaSIM: its physical basis and applicability*. Geological Society, London, Special Publications, 426, 375–386.

G

- Gay, E.C., Nelson, P.A. and Armstrong, W.P. (1969) Flow properties of suspensions with high solid concentrations. *AIChE J.* 15, 815–822.
- Gallant E. A. (2016) *Lava Flow Hazard Assessment for the Idaho National Laboratory, Idaho Falls, and Pocatello, Idaho, U.S.A.* Masters Thesis, University of South Florida.
- Ganci, G., Zago, V., Bilotta, G., Cappello, A., Herault, A. and Del Negro, C. (2016) Lava cooling modelled with GPUSPH, EGU General Assembly 2016, Vol. 18, EGU2016-821.
- Garel, F., Kaminski, E., Tait, S. and Limare, A. (2012) An experimental study of the surface thermal signature of hot subaerial isoviscous gravity currents: Implications for thermal monitoring of lava flows and domes. *Journal of Geophysical Research: Solid Earth*, 117.
- Giordano, D. and Dingwell, D. (2003) Viscosity of hydrous Etna basalt: implications for Plinian-style basaltic eruptions. *Bulletin of Volcanology*, 65, 8–14.
- Giordano, D., Mangiacapra, A., Potuzak, M., Russell, J. K., Romano, C., Dingwell, D. B., and Di Muro, A. (2006) An expanded non-Arrhenian model for silicate melt viscosity: A treatment

- for metaluminous, peraluminous and peralkaline liquids. *Chemical Geology*, 229(1–3), 42–56.
- Giordano, D., Polacci, M., Longo, A., Papale, P., Dingwell, D. B., Boschi, E. and Kasereka, M. (2007) Thermo-Rheological Magma Control on the Impact of Highly Fluid Lava Flows at Mt. Nyiragongo. *Geophysical Research Letters*, 34(6), 2–5.
- Giordano, D., Russell, J. K. and Dingwell, D. B. (2008) Viscosity of Magmatic Liquids: A Model. *Earth and Planetary Science Letters* 271(1–4): 123–34.
- Giordano, D. and Dingwell D. (2003) Viscosity of hydrous Etna basalt: implications for Plinian style basaltic eruptions. *Bulletin of Volcanology*, 65, 8-14.
- Glaze, L. S., Baloga, S. M., Brent, G. W., Fagents, S. A. and Parcheta, C. (2009) A Hybrid Model for Leveed Lava Flows: Implications for Eruption Styles on Mars. *Journal of Geophysical Research E: Planets*, 114(7), 1–15.
- Goto, A., Maeda, I., Nishida, Y. and Oshima, H. (1997) Viscosity equation for magmatic silicate melts over a wide temperature range. In *Unzen International Workshop: Decade Volcano And Scientific Drilling Univ Tokyo, Shimabara, Japan*.
- Greeley, R. (1987) *The Role of Lava Tubes in Hawaiian Volcanoes*. US Geological Survey Professional Paper 1350.
- Griffiths, R.W. and Fink, J.H. (1993) Effects of surface cooling on the spreading of lava flows and domes. *Journal of Fluid Mechanics*, 252, 667.
- Griffiths, R.W., Kerr, R.C. and Cashman, K. V. (2003) Patterns of solidification in channel flows with surface cooling. *Journal of Fluid Mechanics*, 496, 33–62.
- V. Gueugneau, V., Kelfoun, K., Roche, O. and Chupin, L. (2017) Effects of pore pressure in pyroclastic flows: Numerical simulation and experimental validation, *Geophysical Research Letters*.

H

- Hall, M. (1977) *El volcanismo en el Ecuador*. Biblioteca Ecuador, 120.
- Hall, M., Ramón, P., Mothes, P., LePennec, J.L., García, A., Samaniego, P. and Yepes, H. (2004) Volcanic eruptions with little warning: the case of Volcán Reventador's Surprise November 3, 2002 Eruption, Ecuador. *Revista geológica de Chile*, 31, 349–358.

- Hall, M.L. and Mothes, P.A. (2008) Quilotoa volcano - Ecuador: An overview of young dacitic volcanism in a lake-filled caldera. *Journal of Volcanology and Geothermal Research*, 176, 44–55.
- Hall, M. L., Steele, A. L., Bernard, B., Mothes, P. A., Vallejo, S. X., Douillet, G. A., Ramón, P. A., Aguaiza, S. X. and Ruiz, M. C. (2015) Sequential plug formation, disintegration by Vulcanian explosions, and the generation of granular Pyroclastic Density Currents at Tungurahua volcano (2013–2014), Ecuador. *Journal of Volcanology and Geothermal Research*. 306 (2015) 90-103.
- Hallworth, M. A., Huppert, H. and Sparks, S. (1987) A Laboratory Simulation of Basaltic Lava Flows. *Modern Geology* 11: 93–107.
- Harris, A. J. L., Flynn, L. P., Keszthelyi, L., Mougini-Mark, P. J., Rowland, S. K. and Resing, J. A. (1998) Calculation of lava effusion rates from Landstat TM data. *Bulletin of Volcanology*, 60(1), 52–71.
- Harris, A. J.L. and Rowland, S. K. (2001) FLOWGO: A Kinematic Thermo-Rheological Model for Lava Flowing in a Channel. *Bulletin of Volcanology* 63(1): 20–44.
- Harris, A. J. L., Flynn, L. P., Matías, O. and Rose, W. I. (2002) The thermal stealth flows of Santiaguito dome, Guatemala: Implications for the cooling and emplacement of dacitic block-lava flows. *GSA Bulletin*, 114(5), 533–546.
- Harris, A. J.L., Flynn, L. P., Matias, O., Rose, W. and Cornejo, J. (2004) The Evolution of an Active Silicic Lava Flow Field: An ETM+ Perspective. *Journal of Volcanology and Geothermal Research* 135(1–2), 147–168.
- Harris, A., Bailey, J., Calvari, S. and Dehn, J. (2005) Heat loss measured at a lava channel and its implications for down-channel cooling and rheology. *Geological Society of America Special Papers*, 396, 125–146.
- Harris, A. J.L., Dehn, J. and Calvari, S. (2007) Lava Effusion Rate Definition and Measurement: A Review. *Bulletin of Volcanology* 70(1): 1–22.
- Harris, A. J. L. and Allen, J. S., III. (2008) One-, two- and three-phase viscosity treatments for basaltic lava flows. *Journal of Geophysical Research*, 113, B09212.
- Harris, A. J.L. and Rowland, S. K. (2009) Effusion Rate Controls on Lava Flow Length and the Role of Heat Loss: A Review. *Special Publications of IAVCEI* (2): 33–51.

- Harris, A. J. L. (2013) *Lava Flows In Modeling Volcanic Processes : The Physics and Mathematics of Volcanism*, eds. Sarah A. Fagents, Tracy K. P. Gregg, and Rosaly M. C. Lopes. Cambridge University Press, 421.
- Harris, A. J., and Rowland, S. K. (2015a) *Lava Flows and Rheology In The Encyclopedia of Volcanoes*: eds. Sigurdsson, H., Houghton, B., McNutt, S., Rymer, H., Stix, J., Academic Press of Elsevier, 321-342pp.
- Harris, A. J. and Rowland, S. K. (2015b) *FLOWGO 2012, An Updated Framework for Thermorheological Simulations of Channel-Contained Lava*. In *Hawaiian Volcanoes: From Source to Surface*, , 457–81.
- Harris, A.J.L., Rhety, M., Gurioli, L., Villeneuve, N. and Paris, R. (2015) *Simulating the thermorheological evolution of channel-contained lava: FLOWGO and its implementation in EXCEL*. Geological Society, London, Special Publications, 313–336.
- Heinrich, P., A. Piatanesi, and H. Hebert (2001) *Numerical modelling of tsunami generation and propagation from submarine slumps: The 1998 Papua New Guinea event*, *Geophys. J. Int.*, 145, 97–111.
- Herault, A., Vicari, A., Cirauda, A. and Del Negro, C. (2009) *Forecasting lava flow hazards during the 2006 Etna eruption: using the MAGFLOW cellular automata model*. *Computers & Geosciences*, 35, 1050–1060.
- Herault, A., Bilotta, G., Vicari, A., Rustico, E. and Del Negro, C. (2011) *Numerical simulation of lava flow using a GPU SPH model*. In: Del Negro, C. & Gresta, S. (eds) *The Lava Flow Invasion Hazard Map at Mount Etna and Methods for its Dynamic Update*. *Annals of Geophysics*, 54, (5).
- Hidaka, M., Goto, A., Umino, S. and Fujita, E. (2005) *VTFSS project: Development of the lava flow simulation code LavaSIM with a model for three-dimensional convection, spreading, and solidification*. *Geochemistry, Geophysics, Geosystems*, 6.
- Hidaka, M., and H. Ujita (2001) *Verification for flow analysis capability in the model of three-dimensional natural onvection with simultaneous spreading, melting and solidification for the debris coolability analysis module in the severe accident analysis code 'SAMPSON,' (I)*, *J. Nucl. Sci. Technol.*, 38, 745–756.
- Hidaka, M., Sato, N. and Hiroshi, U. (2002) *Verification for flow analysis capability in the model of three-dimensional natural convection with simultaneous spreading, melting and*

solidification for the debris coolability analysis module in the severe accident analysis code ‘SAMPSON,’ (II), *J. Nucl. Sci. Technol.*, 39(5), 520–530.

Hon, K., Kauahikaua, J., Denlinger, R. and Mackay, K. (1994) Emplacement and Inflation of Pahoehoe Sheet Flows: Observations and Measurements of Active Lava Flows on Kilauea Volcano, Hawaii. *Geological Society of America Bulletin* 106(3), 351–370.

Honda and Nagai (2002) Real-time volcano activity mapping using ground-based digital imagery. *Journal of Photogrammetry and Remote sensing*.

Huppert, H. E., Shepherd, J. B., Haraldur Sigurdsson, R. and Sparks, S. J. (1982) On lava dome growth, with application to the 1979 lava extrusion of the soufrière of St. Vincent. *Journal of Volcanology and Geothermal Research*, 14(3–4), 199–222.

I

INECEL (Ministerio de Energía y Minas, Instituto Ecuatoriano de Electrificación) (1988) “Estudio Vulcanológico de El Reventador”. Estudios realizados por INECEL y la Asociación de Firms Consultoras del Proyecto Hidroeléctrico Coca-Codo Sinclair-Electroconsult-Tractionel-rodio-Astec – Ingeconsult – Caminos y Canales. Ambato, Ecuador: Impresión Instituto Geográfico Militar. p. 1–117.

Ishihara, K., Iguchi, M. and Kamo, K. (1988) Reproduction of the 1986 Izu-Oshima lava flows by a numerical calculation. *Bull Volcanol Soc Jpn*, 33, S64–S76.

Ishihara, K., Iguchi, M. and Kamo, K. (1990) Numerical Simulation of Lava Flows on Some Volcanoes in Japan. In *Lava Flows and Domes* pp 174–207. Springer, Berlin, Heidelberg.

J

James, M.R., Robson, S., Pinkerton, H. and Ball, M. (2006) Oblique photogrammetry with visible and thermal images of active lava flows. *Bulletin of Volcanology*, 69, 105–108.

James, M.R. and Varley, N. (2012) Identification of structural controls in an active lava dome with high resolution DEMs: Volcán de Colima, Mexico. *Geophysical Research Letters*, 39.

- James, M.R. and Robson, S. (2012) Straightforward reconstruction of 3D surfaces and topography with a camera: Accuracy and geoscience application. *Journal of Geophysical Research: Earth Surface*, 117.
- James, M.R. and Robson, S. (2014) Mitigating systematic error in topographic models derived from UAV and ground-based image networks. *Earth Surface Processes and Landforms*, 39, 1413–1420.
- Jeffreys, H. (1925) The flow of water in an inclined channel of rectangular section. *Philosophical Magazine*, 49, 793–807.
- Jessop, D. E., Kelfoun, K., Labazuy, P., Mangeney, A., Roche, O., Tillier, L., Trouillet, M. and Thibault, G. (2012) LiDAR derived morphology of the 1993 Lascar pyroclastic flow deposits, and implication for flow dynamics and rheology *Journal of Volcanology and Geothermal Research*, 245–246, 81–97.

K

- Kauahikaua, J., Cashman, K., Clague, D., Champion, D. and Hagstrum, J. (2002) Emplacement of the Most Recent Lava Flows on Hualālai Volcano, Hawai'i. *Bulletin of Volcanology* 64(3–4), 229–253.
- Kelfoun, K. and Druitt, T.H. (2005) Numerical modeling of the emplacement of Socompa rock avalanche, Chile. *Journal of Geophysical Research: Solid Earth*, 110, 1–13.
- Kelfoun, K. Samaniego, P., Palacios, P. and Barba, D. (2009) Testing the suitability of frictional behaviour for pyroclastic flow simulation by comparison with a well-constrained eruption at Tungurahua volcano (Ecuador), *Bull Volcanol* DOI 10.1007/s00445-009-0286-6.
- Kelfoun K., Giachetti T. and Labazuy P. (2010) Landslide-generated tsunamis at Réunion Island. *Journal of Geophysical Research, Earth Surface*, 115, F04012. doi:10.1029/2009JF001381.
- Kelfoun, K. and Vargas, S.V. (2015) VolcFlow capabilities and potential development for the simulation of lava flows. *Geological Society, London, Special Publications*, 426, 337–343.

- Kelfoun, K. (2017) A two-layer depth-averaged model for both the dilute and the concentrated parts of pyroclastic currents, *Journal of Geophysical Research: Solid Earth*, Volume 122, Issue 6.
- Kerr, R. C. (2001) Thermal Erosion by Laminar Lava Flows. *Journal of Geophysical Research B: Solid Earth* 106: 453–65.
- Kerr, R.C. and Lyman, A.W. (2007) Importance of surface crust strength during the flow of the 1988-1990 andesite lava of Lonquimay Volcano, Chile. *Journal of Geophysical Research: Solid Earth*, 112, 1–8.
- Kerr, R. C., Griffiths, R. W. and Cashman, K. V. (2006) Formation of Channelized Lava Flows on an Unconfined Slope. *Journal of Geophysical Research* 111(B10): B10206.
- Keszthelyi, L. (1995) Measurements of the Cooling at the Base of Pahoehoe Flows. *Geophysical Research Letters* 22(16): 2195–2198.
- Keszthelyi, L. and Denlinger R. (1996) The Initial Cooling of Pahoehoe Flow Lobes. *Bulletin of Volcanology* 58(1): 5–18.
- Keszthelyi, L. and Self, S. (1998) Some Physical Requirements for the Emplacement of Long Basaltic Lava Flows. *Journal of Geophysical Research* 103464(10), 447–427.
- Keszthelyi, L., Harris, A. J. L. and Dehn, J. (2003) Observations of the Effect of Wind on the Cooling of Active Lava Flows. *Geophysical Research Letters* 30(19), 1–4.
- Kilburn, C. R. J. and Lopes, R. M. C. (1991) General Patterns of Flow Field Growth: Aa and Blocky Lavas. *Jgr* 96(B12), 19721–19732.
- Kilburn, C. R. J., Pinkerton, H. and Wilson, L. (1995) Forecasting the behaviour of lava flows. *Monitoring active volcanoes: strategies, procedures and techniques*, 346–68.
- Klingelhöfer, F., Hort, M., Kümpel, H. J. and Schmincke, H. U. (1999) Constraints on the Formation of Submarine Lava Flows from Numerical Model Calculations. *Journal of Volcanology and Geothermal Research* 92(3–4), 215–229.
- Kolzenburg, S., Giordano, D., Cimarelli, C. and Dingwell, D. B. (2016) In Situ Thermal Characterization of Cooling/crystallizing Lavas during Rheology Measurements and Implications for Lava Flow Emplacement. *Geochimica et Cosmochimica Acta* 195, 244–258.
- Kolzenburg, S., Giordano, D., Thordarson, T., Höskuldsson and A. Dingwell D.B. (2017) The Rheological Evolution of the 2014/2015 Eruption at Holuhraun, Central Iceland. *Bulletin of*

Volcanology 79(6).

- Koutsoudis, A., Vidmar, B. B., Ioannakis, G. A., Arnaoutoglou, F., Pavlidis, G. and Chamzas, C. (2014) Multi-image 3D reconstruction data evaluation. *Journal of Cultural Heritage* 15(1):73–79 DOI10.1016/j.culher.2012.12.003.
- Krieger, I.M. and Dougherty, T.J. (1959) A mechanism for non-Newtonian flow in suspensions of rigid spheres. *Trans. Soc. Rheol.* 3, 137–152.
- Kubanek, J., Richardson, J.A., Charbonnier, S.J. and Connor, L.J. (2015) Lava flow mapping and volume calculations for the 2012–2013 Tolbachik, Kamchatka, fissure eruption using bistatic TanDEM-X InSAR. *Bulletin of Volcanology*, 77, 106.

L

- Leshner, C. E. and Spera, F. J. (2015) Thermodynamic and Transport Properties of Silicate Melts and Maga, from *The Encyclopedia of Volcanoes, Thermodynamics*, eds. Sigurdsson, H., Houghton, B., McNutt, S., Rymer, H., Stix, J., Academic Press of Elseiver. 113-141 pp.
- Lev, E., Spiegelman, M., Wysocki, R. J. and Karson, J. A. (2012) Investigating Lava Flow Rheology Using Video Analysis and Numerical Flow Models. *Journal of Volcanology and Geothermal Research* 247–248: 62–73.
- Lev, E. and James., M. R. (2014) The Influence of Cross-Sectional Channel Geometry on Rheology and Flux Estimates for Active Lava Flows. *Bulletin of Volcanology* 76(7), 1–15.
- Lipman, P. W. and Banks, N. G. (1987) AA Flow Dynamics, Mauna Loa 1984. US Geol Surv Prof Pap 1350, 1527–1567.
- Lister, J. R. (1992) Viscous Flows down an Inclined Plane from Point and Line Sources. *Journal of Fluid Mechanics* 242(1), 631.
- Llewellyn, E. W., Mader, H. M. and Wilson, S. D. R. (2002) The Constitutive Equation and Flow Dynamics of Bubbly Magmas. *Geophysical research letters*. 29(24): 2170.
- Llewellyn, E. W. and Manga, M. (2005) Bubble Suspension Rheology and Implications for Conduit Flow. *Journal of Volcanology and Geothermal Research* 143(1–3): 205–17.
- Lockwood, J. P. and Lipman, P. W. (1980) Recovery of Datable Charcoal beneath Young Lavas: Lessons from Hawaii. *Bulletin Volcanologique* 43(3), 609–615.
- Lyman, A. W., Kerr, R. C. and Griffiths, R. W. (2005) Effects of Internal Rheology and Surface

Cooling on the Emplacement of Lava Flows. *Journal of Geophysical Research B: Solid Earth* 110(8), 1–16.

M

Macdonald, G. A. (1953) Pahoehoe, Aa, and Block Lava. *American Journal of Science*, 251, 169–191.

Mader, H. M., Llewellyn, E. W. and Mueller, S. P. (2013) The Rheology of Two-Phase Magmas: A Review and Analysis. *Journal of Volcanology and Geothermal Research* 257: 135–58.

Magnall, N., James, M. R., Tuffen, H. and Vye-Brown, V. (2017) Emplacing a Cooling-Limited Rhyolite Lava Flow: Similarities with Basaltic Lava Flows. *Frontiers in Earth Science* 5(June).

Malin, M. C. (1980) Lengths of Hawaiian Lava Flows. *Geology* 8(7): 306–8.

Manga, M., Castro, J., Cashman, K. and Loewenberg, M. (1998) Rheology of Bubble-Bearing Magmas. *Earth and Planetary Science Letters* 87: 15–28.

Manga, M. and Loewenberg, M. (2001) Viscosity of Magmas Containing Highly Deformable Bubbles. *Journal of Volcanology and Geothermal Research* 105(1–2): 19–24.

Mei, C.C. and Yuhi, M. (2001) Slow flow of a Bingham fluid in a shallow channel of finite width. *Journal of Fluid Mechanics*, 431, 135–159.

Miyamoto, H. and Sasaki, S. (1997) Simulating lava flows by an improved cellular automata method. *Computers & Geosciences*, 23, 283–292.

Miyamoto, H. and Sasaki, S. (1998) Numerical simulations of flood basalt lava flows: Roles of parameters on lava flow morphologies. *Journal of Geophysical Research: Solid Earth*, 103, 27489–27502.

Monthe, L., F. Benkhaldoun, and I. Elmahi (1999) Positivity preserving finite volume Roe schemes for transport-diffusion equations, *Comput. Methods Appl. Mech. Eng.*, 178, 215– 232.

Moore, H.J. (1987) Preliminary estimates of the rheological properties of 1984 Mauna Loa lava. *US Geol Surv Prof Pap*, 1350, 1569–1588.

Mossoux, S., Saey, M., Bartolini, S., Poppe, S., Canters, F. and Kervyn, M. (2016) Q-LAVHA: A flexible GIS plugin to simulate lava flows. *Computers and Geosciences*, 97, 98–109.

Mueller, S., Llewellyn, E. W. and Mader, H. M. (2010) The rheology of suspensions of solid particles, *Philos. Trans. R. Soc. A*, 466, 1201–1228.

N

Naranjo M. F., Ebmeier, S. K., Vallejo, S., Ramón, P., Mothes, P., Biggs, J. and Herrera, F. (2016) Mapping and measuring lava volumes from 2002 to 2009 at El Reventador Volcano, Ecuador, from field measurements and satellite remote sensing. *Journal of Applied Volcanology* 5:8 DOI 10.1186/s13617-016-0048-z

O

Oppenheimer, C. (1991) Lava Flow Cooling Estimated from Landsat Thematic Mapper Infrared Data: The Lonquimay Eruption (Chile, 1989). *Journal of Geophysical Research B: Solid Earth* 96(B13), 21,865–21,878.

P

Pal, R. (2003) Rheological Behavior of Bubble-Bearing Magmas. *Earth and Planetary Science Letters* 207(1–4): 165–79.

Park, S. and Iversen, J.D. (1984) Dynamics of lava flow: Thickness growth characteristics of steady two-dimensional flow. *Geophysical Research Letters*, 11, 641–644.

Paz y Mino, L.T., Guerrero and J. and Bonifaz, C. (1931) *La exploración al Reventador*. Ministerio de Educación Pública, Quito.

Pedrazzi, D., Cappello, A., Zanon, V. and Del Negro, C. (2015) Impact of effusive eruptions from the Eguas-Carvão fissure system, São Miguel Island, Azores Archipelago (Portugal). *Journal of Volcanology and Geothermal Research*, 291, 1–13.

Peterson, D. W. and Tilling, R. I. (1980) Transition of Basaltic Lava from Pahoehoe to Aa, Kilauea Volcano, Hawaii: Field Observations and Key Factors. *Journal of Volcanology and*

- Geothermal Research, 7(3–4), 271–293.
- Phan-Thien N. and Pham D.C. (1997) Differential multiphase models for polydispersed suspensions and particulate solids. *J Non Newt Fluid Mech.*;72:305–318.
- Pieri, D. C., Glaze, L. S. and Abrams, M. J. (1990) Thermal radiance observations of an active lava flow during the June 1984 eruption of Mount Etna. *Geology*, 18, 1018-1022.
- Pinkerton, H. and Sparks, R.S.J. (1978) Field measurements of the rheology of lava. *Nature* 276, 383–385.
- Pinkerton, H. (1987) Factors Affecting the Morphology of Lava Flows.” *Endeavour* 11(2): 73–79.
- Pinkerton, H. and Stevenson, R. J. (1992) Methods of Determining the Rheological Properties of Magmas at Sub-Liquidus Temperatures. *Journal of Volcanology and Geothermal Research* 53(1–4), 47–66.
- Pinkerton, H. and Wilson, L. (1994) Factors Controlling the Lengths of Channel-Fed Lava Flows. *Bulletin of Volcanology* 56(2), 108–120.

Q

- Quareni, F., Tallarico, A. and Dragoni, M. (2004) Modeling of the Steady-State Temperature Field in Lava Flow Levées. *Journal of Volcanology and Geothermal Research* 132(2–3), 241–251.

R

- Richet, P., Lejeune, A.-M., Holtz, F. and Roux, J. (1996) Water and the Viscosity of Andesite Melts. *Chemical Geology* 128(1): 185–97.
- Rhéty, M., Harris, A., Villeneuve, N., Gurioli, L., Médard, E., Chevrel, O. and Bachelery, P. (2017) A Comparison of Cooling-Limited and Volume-Limited Flow Systems: Examples from Channels in the Piton de La Fournaise April 2007 Lava-Flow Field. *Geochemistry, Geophysics, Geosystems* 18(9): 3270–3291.
- Ridolfi, F., Puerini, M., Renzulli, A., Menna, M. and Toulkeridis, T. (2008) The magmatic feeding system of El Reventador volcano (Sub-Andean zone, Ecuador) constrained by texture,

- mineralogy and thermobarometry of the 2002 erupted products. *Journal of Volcanology and Geothermal Research*, 176, 94–106.
- Richardson, J.A. (2016) Modeling the Construction and Evolution of Distributed Volcanic Fields on Earth and Mars. Dissertation, University of South Florida.
- Richter, N., Favalli, M., De Zeeuw-Van Dalftsen, E., Fornaciai, A., Da Silva Fernandes, R.M., Pérez, N.M., Levy, J., Victória, S.S. and Walter, T.R. (2016) Lava flow hazard at Fogo Volcano, Cabo Verde, before and after the 2014–2015 eruption. *Natural Hazards and Earth System Sciences*, 16, 1925–1951.
- Robert, B., Harris, A., Gurioli, L., Médard, E., Sehlke, A., and Whittington, A. (2014) Textural and rheological evolution of basalt flowing down a lava channel. *Bulletin of Volcanology*, 76(6), 1–21.
- Rocchi, V., Sammonds, P.R. and Kilburn, C.R.J. (2004) Fracturing of Etnean and Vesuvian rocks at high temperatures and low pressures. *Journal of Volcanology and Geothermal Research*, 132, 137–157.
- Rongo, R., Lupiano, V., Spataro, W., D’ambrosio, D., Iovine, G. and Crisci, G.M. (2016) SCIARA: cellular automata lava flow modelling and applications in hazard prediction and mitigation. Geological Society, London, Special Publications, 426, 345–356.
- Roscoe, R. (1952) The Viscosity of Suspensions of Rigid Spheres. *British Journal of Applied Physics* 3(8): 267–69.
- Roult, G., Peltier, A., Taisne, B., Staudacher, T., Ferrazzini, V., Di Muro, A., The OVPF team. (2012) A new comprehensive classification of the Piton de la Fournaise activity spanning the 1985–2010 period. Search and analysis of short-term precursors from a broad-band seismological station (2012) *Journal of Volcanology and Geothermal Research*, 241–242, 78–104
- Rowland, S. K. and Walker, G. P. L. (1990) Pahoehoe and Aa in Hawaii: Volumetric Flow Rate Controls the Lava Structure. *October*: 615–628.
- Rowland, S.K., Garbeil, H. and Harris, A.J.L. (2005) Lengths and hazards from channel-fed lava flows on Mauna Loa, Hawai‘i, determined from thermal and downslope modeling with FLOWGO. *Bulletin of Volcanology*, 67, 634–647.
- Ryerson, F. J., Weed, H. C. and Piwinski, A. J. (1988) Rheology of Subliquidus Magmas, 1. Picritic Compositions. *Journal of Geophysical Research* v. 93(B5): 3421–36.

S

- Saar, M. O., Manga, M., Cashman, K. V. and Fremou S. (2001) Numerical models of the onset of yield strength in crystal-melt suspensions, *Earth Planet. Sci. Lett.*, 187, 367–379.
- Saramito, P. (2013) Efficient C ++ finite element computing with Rheolef. CNRS and LJ
- Sakimoto, S.E.H. and Zuber, M.T. (1998) Flow and Convective Cooling in Lava Tubes. *Journey of Geophysical research* 103(B11), 465–487.
- Samaniego, P., Eissen, J.P., Le Pennec, J.L., Robin, C., Hall, M.L., Mothes, P., Chavrit, D. and Cotten, J. (2008) Pre-eruptive physical conditions of El Reventador volcano (Ecuador) inferred from the petrology of the 2002 and 2004-05 eruptions. *Journal of Volcanology and Geothermal Research*, 176, 82–93.
- Schiano, P., Monzier, M., Eissen, J.P., Martin, H. and Koga, K.T. (2010) Simple mixing as the major control of the evolution of volcanic suites in the Ecuadorian Andes. *Contributions to Mineralogy and Petrology*, 160, 297–312.
- Shelke, A., Whittington A., Robert, B., Harris, A., Gurioli, L. and Médard, E. (2014) Pahoehoe to 'a'a Transition of Hawaiian Lavas: An Experimental Study.” *Bulletin of Volcanology* 76: 876.
- Shaw, H. R. (1969) Rheology of Basalt in the Melting Range. *Journal of Petrology* 10(3): 510–35.
- Shaw, H. R., Wright, T. L., Peck, D. L. and Okamura, R. (1968) The viscosity of basaltic magma: an analysis of field measurements in Makaopuhi lava lake, Hawaii. *Am. J. Sci.* 266, 255-65.
- Shaw, H. R. (1972) Viscosities of Magmatic Silicate Liquids: An Empirical Method of Prediction. *American Journal of Science* 272(9): 870–93.
- Simkin, T. and Siebert, L. (1994) *Volcanoes of the World*. Geoscience, Tucson, Ariz.
- Soule, S. A., Cashman, K. V. and Kauahikaua, J. P. (2004) Examining Flow Emplacement through the Surface Morphology of Three Rapidly Emplaced, Solidified Lava Flows, Kilauea Volcano, Hawai'i. *Bulletin of Volcanology* 66(1): 1–14.
- Spampinato, L., Calvari, S., Oppenheimer, C. and Boschi, E. (2011) Volcano surveillance using infrared cameras. *Earth-Science Reviews*, 106, 63–91.
- Sparks, R. S. J., Pinkerton, H. and Hulme, G. (1976) Classification and Formation of Lava Levees on Mount Etna, Sicily. *Geology* 4(5), 269–271.

- Spataro, W., Avolio, M. V., Lupiano, V., Trunfio, G.A., Rongo, R. and D'Ambrosio, D. (2010) The latest release of the lava flows simulation model SCIARA: First application to Mt Etna (Italy) and solution of the anisotropic flow direction problem on an ideal surface. *Procedia Computer Science*, 1, 17–26.
- Swanson, D. A. and Wright T. L. (1981) The regional approach to studying the Columbia River Basalt Group. In K. V. Subbarao and R. N. Sukheswala, 58-80.

T

- Tamman, G. and Hesse, W. (1926) Die Abhängigkeit der Viskosität von der Temperatur bei unterkühlten Flüssigkeiten. *Z. Anorg. Allg. Chem.* 156, 245–257.
- Taylor, G. I. (1932) The viscosity of a fluid containing small drops of another fluid.
- Tallarico, A. and Dragoni, M. (1999) Viscous Newtonian laminar flow in a rectangular channel: application to Etna lava flows. *Bull. Volcanol.* 61, 40–47.
- Tarquini, S. and Favalli, M. (2011) Mapping and DOWNFLOW simulation of recent lava flow fields at Mount Etna. *Journal of Volcanology and Geothermal Research*, 204, 27–39.
- Tarquini, S., Favalli, M., Papale, P., Neri, A., Fornaciai, A., Pareschi, M.T. and Mazzarini, F. (2013) Simulating the area covered by lava flows by using the DOWNFLOW code Overview of the presentation : Basics of the DOWNFLOW code (principles and calibrations), Focus on using DOWNFLOW : input data requirements DOWNFLOW vs DEM used.
- Tarquini, S. and Favalli, M. (2016) Simulating the area covered by lava flows using the DOWNFLOW code. *Geological Society, London, Special Publications*, 426, 293–312.
- Tedesco, D, Vaselli, O., Papale, P., Carn, S.A., Voltaggio, M., Sawyer, G. M., Durieux, J. Kasereka, M. and Tassi, F. (2007) January 2002 volcano-tectonic eruption of Nyiragongo volcano, Democratic Republic of Congo *JOURNAL OF GEOPHYSICAL RESEARCH*, VOL. 112, B09202, doi:10.1029/2006JB004762, 2007.
- Turcotte, D. L. and Schubert, G. (2002) *Geodynamics*. Cambridge University Press, Cambridge, Second Edition, 1-13

V

- Vallejo, S. (2009) Identificación de límites de flujos de lava en el Volcán Reventador en base a imágenes térmicas desde el 2002. Quito: IG EPN.
- Vallejo, S. and Ramón, P. (2010) Thermal Images: A useful tool to identify and map recent lava flows, Examples on Reventador Volcano, AGU Meeting of the Americas, Poster, Foz de Iguazu, Brasil.
- Vallejo S. and Ramón P. (2012) Growth And Evolution Of A Scoria Cone And Dome Inside The Reventador Volcano Crater.2010-2011, Cities on Volcanoes 7, Colima, México. Poster.
- Vallejo Vargas, S., Ramón, P., Naranjo, F., Kelfoun, K., Samaniego, P. and Diefenbach, A. (2016) El Reventador volcano (Ecuador): non-stop activity since 2002, Cities on Volcanoes 9, Puerto Varas, Chile, Poster.
- Vera Vidal, C., Castruccio, A., Tamburrino, A. and Roche, O., (2016) The influence of varying effusion rate and front cooling on lava flows: Insights from analogue experiments of plastic flows. Cities on Volcanoes 9, Puerto Varas, Chile, Poster.
- Verhoeven, G. (2011) Taking computer vision aloft - archaeological three-dimensional reconstructions from aerial photographs with photoscan. *Archaeological Prospection*, 18, 67–73.
- Vicari, A., Alexis, H., Del Negro, C., Coltelli, M., Marsella, M. and Proietti, C. (2006) Modeling of the 2001 lava flow at Etna volcano by a Cellular Automata approach. *Environmental Modelling and Software*, 22, 1465–1471.
- Vicari, A., Alexis, H., Del Negro, C., Coltelli, M., Marsella, M. and Proietti, C. (2007) Modeling of the 2001 lava flow at Etna volcano by a Cellular Automata approach. *Environmental Modelling & Software*, **22**, 1465–1471.
- Villeneuve, N., Neuville, D. R., Boivin, P., Bachelery, P. and Richet, P. (2008) Magma crystallization and viscosity: a study of molten basalts from the Piton de la Fournaise volcano (La Re´union island). *Chemical Geology*, 256, 242–251.

W

- Wadge, G., Young, P.A. V. and McKendrick, I.J. (1994) Mapping lava flow hazards using computer simulation. *Journal of Geophysical Research: Solid Earth*, 99, 489–504.
- Walker, G. P. L. (1973) Lengths of Lava Flows. *Philosophical Transactions of the Royal Society of London, Series A. Mathematical and Physical Sciences* v. 274(1238), 107–118.
- Walker, G. P. L. (1991) Structure, and Origin by Injection of Lava under Surface Crust, of Tumuli, 'Lava Rises', 'Lava-Rise Pits', and 'Lava-Inflation Clefts' in Hawaii. *Bulletin of Volcanology* 53(4), 612–634.
- Westoby, M.J., Brasington, J., Glasser, N.F., Hambrey, M.J. and Reynolds, J.M. (2012) 'Structure-from-Motion' photogrammetry: A low-cost, effective tool for geoscience applications. *Geomorphology*, 179, 300–314.
- Williams, M.L., Landel, R.F. and Ferry, J.D. (1955) The Temperature Dependence of Relaxation Mechanisms in Amorphous Polymers and Other Glass-forming Liquids¹. *Journal of the American Chemical Society*, 77, 3701–3707.
- Wilmoth, R. A. and Walker, G. P. L. (1993) P-Type and S-Type Pahoehoe: A Study of Vesicle Distribution Patterns in Hawaiian Lava Flows. *Journal of Volcanology and Geothermal Research* 55(1–2): 129–42.
- Whittington, A., Richet, P. and Holtz, F. (2000) Water and the Viscosity of Depolymerized Aluminosilicate Melts. *Geochimica et Cosmochimica Acta* 64(21): 3725–36.
- Wolfe, E.W., Neal, C., Banks N.G. and Duggan T.J. (1988) Geologic observations and chronology of eruptive events, in *The Pu'u 'O'o Eruption of Kilauea Volcano, Hawai'i: Episodes 1 Through 20, January 3, 1983, Through June 8, 1984*, edited by E.W. Wolfe *Geol. Surv. Prof. Pap.*, 1463 99 pp.
- Wooster, M. J., Wright, R., Blake, S. and Rothery, D.A. (1997) Cooling Mechanisms and an Approximate Thermal Budget for the 1991-1193 Mount Etna Lava Flow. *Geophysical Research Letters* 24(24): 3277–80.

Y

Young, P. and Wadge, G. (1990) FLOWFRONT: Simulation of a lava flow. *Computers & Geosciences*, 16, 1171–1191.

Z

Zago, V., Bilotta, G., Cappello, A., Dalrymple, R., Fortuna, L., Ganci, G., Herault, A. and Del Negro, C. (2016) Recent advances in the GPUSPH model for the thermal and rheological evolution of lava flows, EGU General Assembly 2016, Vol. 18, EGU2016-821,

Zhou, J.Z.Q., Fang, T., Luo, G. and Uhlerr, P.H.T. (1995) Yield stress and maximum packing fraction of concentrated suspensions. *Rheol. Acta* 34, 544–561.

APPENDIX

APPENDIX 2.1

Date	VRP(Watt)	Sat Zen	Sat Azi	Dist(m)	UTM(Lat)	UTM(Lon)
2/1/2010 07:20	27312713.42	58.9486538	-81.5431971	3162.27766	205365.9136	9991423.648
3/1/2010 03:25	1794402.90	28.0867657	81.8008855	1414.21356	203365.9136	9990423.648
3/1/2010 06:25	5253424.86	43.4688364	98.1046807	1414.21356	204365.9136	9991423.648
4/1/2010 04:10	21988288.67	55.5311265	-98.3975737	3000	204365.9136	9990423.648
4/1/2010 07:10	6928131.61	44.8718905	-81.6752139	3000	206365.9136	9991423.648
5/1/2010 03:15	2902339.65	48.2205769	81.876047	2236.06798	203365.9136	9990423.648
6/1/2010 03:55	6363239.06	39.510475	-98.2818837	2236.06798	205365.9136	9990423.648
10/1/2010 03:30	9163747.35	14.8390381	81.6634746	1414.21356	204365.9136	9990423.648
10/1/2010 06:30	6352056.83	33.2868328	98.1360122	1414.21356	203365.9136	9991423.648
13/1/2010 07:00	10276207.39	35.0974833	-81.7369277	2236.06798	205365.9136	9991423.648
15/1/2010 03:50	2931983.59	28.2802283	-98.203282	1414.21356	205365.9136	9991423.648
23/1/2010 03:00	2304788.17	61.2572494	81.8971795	2236.06798	203365.9136	9990423.648
26/1/2010 03:30	1584491.35	15.0214705	81.6553166	1414.21356	204365.9136	9990423.648
28/1/2010 03:20	4680165.91	39.4441931	81.8553318	1000	204365.9136	9991423.648
7/2/2010 06:55	7199385.61	22.9595341	-81.8251969	1414.21356	204365.9136	9991423.648
11/2/2010 03:30	1590557.37	14.7325604	81.672908	1000	204365.9136	9990423.648
15/2/2010 03:10	38337567.86	55.3667674	81.8892296	3162.27766	203365.9136	9991423.648
18/2/2010 03:40	1082930.72	1.19666801	-20.3791579	1000	204365.9136	9991423.648
18/2/2010 06:35	578113.32	20.8667611	98.2022537	0	204365.9136	9991423.648
22/2/2010 03:15	5866448.47	48.1449735	81.8813333	2236.06798	204365.9136	9990423.648
28/2/2010 07:15	5758436.00	52.5747885	-81.6059366	2236.06798	206365.9136	9990423.648
4/3/2010 03:50	1006366.68	28.6527021	-98.2108083	1000	205365.9136	9991423.648
4/3/2010 06:50	33103376.87	8.49567053	-81.7971937	1414.21356	204365.9136	9991423.648
8/3/2010 03:25	23216820.86	27.9320267	81.7868396	1414.21356	203365.9136	9991423.648
13/3/2010 03:45	2090952.17	15.3468228	-98.0405733	1414.21356	204365.9136	9990423.648
13/3/2010 06:45	11954151.26	6.84252841	98.1651136	1000	204365.9136	9991423.648
15/3/2010 03:30	270624.14	14.5126378	81.6588168	1000	204365.9136	9990423.648
22/3/2010 06:35	1008296.16	21.3761877	98.1920399	0	204365.9136	9991423.648
24/3/2010 03:25	4958532.60	27.9576679	81.7901397	1414.21356	203365.9136	9990423.648
25/3/2010 07:05	3512266.42	44.4585982	-81.6941264	1414.21356	204365.9136	9991423.648
29/3/2010 03:45	6125084.20	15.2578678	-98.0402452	1000	204365.9136	9991423.648
29/3/2010 06:45	41124565.54	7.04608466	98.1547293	1414.21356	204365.9136	9991423.648
31/3/2010 03:30	4900592.57	14.6138579	81.6580964	1414.21356	203365.9136	9990423.648
9/4/2010 03:25	1754078.25	28.1063135	81.8006378	1000	203365.9136	9991423.648
9/4/2010 06:25	793944.28	43.8935512	98.0852739	0	204365.9136	9991423.648
18/4/2010 06:20	937469.00	51.9330199	98.0740265	1000	204365.9136	9991423.648
21/4/2010 03:50	2072315.00	28.2566743	-98.1956857	1414.21356	205365.9136	9991423.648
21/4/2010 06:50	2889058.25	8.07273741	-81.8179273	1000	204365.9136	9991423.648
26/4/2010 07:05	587844.56	44.5569488	-81.691437	0	204365.9136	9991423.648
7/5/2010 03:50	3309941.20	28.2857487	-98.1949627	1000	204365.9136	9990423.648
19/5/2010 07:15	5303073.90	52.6283614	-81.62634	2000	204365.9136	9991423.648
23/5/2010 03:50	8356320.55	28.5251471	-98.1988575	1414.21356	203365.9136	9990423.648
1/6/2010 06:40	927523.11	6.49631536	98.1827726	24351.5913	212365.9136	9968423.648
13/6/2010 07:05	4368143.12	44.7783861	-81.6883861	2236.06798	206365.9136	9990423.648
28/6/2010 03:25	2402339.42	27.9515818	81.7906005	1000	204365.9136	9991423.648
12/7/2010 03:40	502677.16	1.19159549	-18.7479694	0	204365.9136	9991423.648
12/7/2010 06:35	113591.91	21.3114505	98.1768052	0	204365.9136	9991423.648
19/7/2010 03:45	1314062.68	15.1252597	-98.0202139	1000	204365.9136	9991423.648
19/7/2010 06:40	426676.87	7.11043072	98.1818041	1000	204365.9136	9990423.648
21/7/2010 03:30	298754.96	14.7530433	81.6585569	0	204365.9136	9991423.648

Date	VRP(Watt)	Sat Zen	Sat Azi	Dist(m)	UTM(Lat)	UTM(Lon)
21/7/2010 06:30	181720.40	33.8648768	98.1161884	1000	204365.9136	9990423.648
23/7/2010 03:20	9991750.93	39.3010365	81.8559806	2000	203365.9136	9991423.648
23/7/2010 06:15	257371.19	51.9355468	98.075942	1000	204365.9136	9992423.648
31/7/2010 04:10	1140357.89	55.4475436	-98.388101	1000	204365.9136	9991423.648
31/7/2010 07:05	514163.03	44.344238	-81.6878663	1000	205365.9136	9991423.648
18/8/2010 03:55	239451.64	39.3411974	-98.2682929	0	204365.9136	9991423.648
18/8/2010 06:55	352021.18	22.5033918	-81.8377894	0	204365.9136	9991423.648
9/9/2010 03:20	1933414.20	39.1934544	81.8582506	1414.21356	204365.9136	9990423.648
10/9/2010 04:00	17004313.89	48.4643891	-98.3653859	2236.06798	204365.9136	9990423.648
10/9/2010 07:00	266978.79	34.7280971	-81.7387026	1414.21356	205365.9136	9990423.648
12/9/2010 06:45	357927.54	8.27962366	-81.8116253	0	204365.9136	9991423.648
21/9/2010 03:45	316659.46	15.3542876	-98.0315734	0	204365.9136	9991423.648
28/9/2010 03:50	3018217.68	28.6973797	-98.1962551	1414.21356	204365.9136	9991423.648
28/9/2010 06:45	218281.45	7.95202474	-81.8187093	0	204365.9136	9991423.648
17/11/2010 06:35	970286.74	21.2327137	98.1962189	2000	206365.9136	9991423.648
29/11/2010 07:00	257985.67	34.9134579	-81.7315621	1000	205365.9136	9991423.648
8/12/2010 03:55	875780.22	39.7164256	-98.2961097	1000	205365.9136	9991423.648
10/12/2010 06:40	384425.61	6.46177832	98.1658871	1000	204365.9136	9991423.648
31/12/2010 07:00	25609989.60	34.8911749	-81.7294126	2000	204365.9136	9991423.648
18/1/2011 06:45	127879.50	8.83297678	-81.8260821	0	204365.9136	9991423.648
20/1/2011 06:35	704718.04	20.7484007	98.2104852	0	204365.9136	9991423.648
27/1/2011 03:45	551887.11	14.6398829	-98.0415221	0	204365.9136	9991423.648
27/1/2011 06:40	7701533.27	6.24101661	98.1915148	1414.21356	204365.9136	9991423.648
30/5/2011 03:25	4903407.27	28.2469335	81.7995944	19235.3841	222365.9136	9988423.648
23/8/2011 06:40	341169.21	7.26290414	98.174935	0	204365.9136	9991423.648
25/8/2011 06:30	115784.42	33.9843237	98.1306609	0	204365.9136	9991423.648
24/10/2011 06:50	2371349.60	22.4460579	-81.817666	1000	205365.9136	9991423.648
7/11/2011 04:10	844010.91	55.5786411	-98.4097387	29832.8678	227365.9136	9972423.648
9/2/2012 07:15	2729907.63	58.8412045	-81.5550455	2236.06798	206365.9136	9990423.648
10/2/2012 03:25	120141596.56	28.0779494	81.7947686	2828.42712	204365.9136	9991423.648
10/2/2012 06:20	47249512.18	43.5493673	98.1270299	3000	204365.9136	9991423.648
13/2/2012 03:55	66626062.67	39.6685655	-98.2865837	2236.06798	204365.9136	9991423.648
13/2/2012 06:55	90840501.66	22.8480553	-81.7934366	2236.06798	204365.9136	9991423.648
15/2/2012 03:45	12104899.14	15.3854038	-98.0393496	1414.21356	203365.9136	9991423.648
20/2/2012 04:05	23644327.95	48.6525401	-98.3548582	2236.06798	205365.9136	9991423.648
21/2/2012 03:05	12332508.72	55.21	81.8519194	2236.06798	203365.9136	9991423.648
21/2/2012 06:05	683210.94	63.2913077	98.1512564	1414.21356	205365.9136	9991423.648
22/2/2012 03:50	39217374.74	28.9033294	-98.2096594	1414.21356	203365.9136	9991423.648
26/2/2012 03:25	24931858.09	27.6150949	81.7750316	2000	203365.9136	9990423.648
26/2/2012 06:25	10832269.07	43.4517591	98.2329635	2000	204365.9136	9991423.648
18/3/2012 03:45	19044076.34	15.406905	-98.0459895	1414.21356	204365.9136	9991423.648
18/3/2012 06:40	17741225.65	7.02408114	98.2251805	1414.21356	204365.9136	9991423.648
20/3/2012 03:30	934211.99	14.5082769	81.6490093	1000	203365.9136	9991423.648
3/4/2012 03:45	4563833.02	14.738308	-98.0283037	1414.21356	204365.9136	9991423.648
7/4/2012 06:15	6364715.77	51.5049935	98.1154237	2000	204365.9136	9991423.648
10/4/2012 06:45	3537035.87	8.8719833	-81.7660251	1000	204365.9136	9991423.648
15/4/2012 04:10	11210770.90	55.4774093	-98.3962867	2000	203365.9136	9990423.648
21/4/2012 06:30	6026163.93	33.3247102	98.148975	1000	204365.9136	9991423.648
23/4/2012 03:20	11321582.65	39.1920179	81.8483782	1414.21356	203365.9136	9991423.648
24/4/2012 04:05	1692232.87	48.4922414	-98.3451355	1414.21356	204365.9136	9992423.648
25/4/2012 06:05	5370140.57	63.3114286	98.1404935	2828.42712	205365.9136	9992423.648
26/4/2012 03:50	32412880.64	28.5906578	-98.208442	1414.21356	204365.9136	9991423.648
26/4/2012 06:45	37599912.02	8.64669647	-81.6616093	1414.21356	204365.9136	9991423.648
28/4/2012 03:40	47250183.07	1.20705835	-22.641831	1414.21356	204365.9136	9991423.648
28/4/2012 06:35	22613789.99	20.997619	98.2066667	1414.21356	204365.9136	9991423.648

Date	VRP(Watt)	Sat Zen	Sat Azi	Dist(m)	UTM(Lat)	UTM(Lon)
30/4/2012 03:25	34676335.49	27.951236	81.790519	1414.21356	204365.9136	9991423.648
30/4/2012 06:25	20485774.53	43.598241	98.1106596	1414.21356	204365.9136	9991423.648
4/5/2012 03:00	19174644.57	61.0593151	81.895	2236.06798	204365.9136	9991423.648
5/5/2012 03:45	23668956.75	15.3296422	-98.0442103	1414.21356	204365.9136	9991423.648
5/5/2012 06:40	5745415.32	6.72748782	98.1931534	1414.21356	204365.9136	9991423.648
11/5/2012 03:10	10436703.26	55.2842048	81.7839434	2000	204365.9136	9991423.648
23/5/2012 06:30	401155.21	33.8034828	98.1260197	0	204365.9136	9991423.648
25/5/2012 03:20	14956688.84	39.373687	81.8516253	2236.06798	203365.9136	9990423.648
27/5/2012 03:05	6606633.37	55.4849924	81.8795008	2236.06798	203365.9136	9990423.648
27/5/2012 06:05	8380049.62	63.4835263	98.1223421	2236.06798	204365.9136	9991423.648
4/6/2012 03:55	9659553.80	39.1313408	-98.2700399	2236.06798	204365.9136	9991423.648
4/6/2012 06:55	16935833.76	22.504266	-81.817734	1414.21356	204365.9136	9991423.648
6/6/2012 06:40	2011477.01	6.88287688	98.1934579	0	204365.9136	9991423.648
13/6/2012 03:50	7738972.17	28.0766893	-98.1842712	1000	204365.9136	9991423.648
13/6/2012 06:45	10879510.59	8.21543388	-81.8029959	1000	204365.9136	9991423.648
15/6/2012 03:40	7686895.27	1.17564392	0.16163101	1414.21356	203365.9136	9990423.648
15/6/2012 06:35	1353516.32	21.367817	98.1916033	1000	204365.9136	9991423.648
18/6/2012 07:05	17749565.79	44.4691724	-81.6789163	2236.06798	205365.9136	9991423.648
19/6/2012 03:15	15334035.73	48.3519243	81.880627	2236.06798	204365.9136	9991423.648
21/6/2012 03:00	1243557.96	61.1994023	81.8951494	2236.06798	204365.9136	9991423.648
23/6/2012 07:25	2318866.17	63.8041139	-81.5261709	2236.06798	206365.9136	9991423.648
24/6/2012 03:30	1815568.26	14.8602676	81.6609006	1000	203365.9136	9991423.648
28/6/2012 03:05	9022071.90	55.4001205	81.8819127	2000	204365.9136	9991423.648
29/6/2012 06:45	37148705.14	8.2942314	-81.8070909	1414.21356	204365.9136	9991423.648
1/7/2012 03:40	4843468.25	1.18043215	-15.9647577	1414.21356	204365.9136	9991423.648
3/7/2012 03:25	23794135.65	28.0714595	81.7921459	1000	204365.9136	9991423.648
6/7/2012 03:55	7569965.93	39.5765789	-98.2825082	1414.21356	204365.9136	9991423.648
10/7/2012 03:30	7110500.71	14.6300169	81.6480567	1414.21356	204365.9136	9991423.648
10/7/2012 06:30	10327312.77	33.4271944	98.1246577	1414.21356	204365.9136	9991423.648
12/7/2012 03:20	8762750.31	39.1876986	81.8495471	1414.21356	205365.9136	9991423.648
12/7/2012 06:15	6811674.62	51.6307843	98.085085	2828.42712	204365.9136	9993423.648
17/7/2012 06:35	384771.39	20.9548197	98.1928765	0	204365.9136	9991423.648
26/7/2012 06:30	254301.73	33.4930477	98.125049	0	204365.9136	9991423.648
2/8/2012 03:40	3696888.48	1.17232877	-9.19309025	1414.21356	203365.9136	9990423.648
2/8/2012 06:35	2245556.35	21.231014	98.1933137	1414.21356	204365.9136	9991423.648
7/8/2012 03:55	96522768.32	39.344544	-98.2671994	2236.06798	204365.9136	9991423.648
7/8/2012 06:55	107626115.73	22.3673527	-81.8231084	1414.21356	204365.9136	9991423.648
8/8/2012 03:00	29579885.53	61.2388811	81.8991375	5000	202365.9136	9991423.648
9/8/2012 03:45	15793521.66	14.7875856	-98.0274252	1000	204365.9136	9991423.648
11/8/2012 03:30	8304674.48	15.0264768	81.6591203	1414.21356	204365.9136	9991423.648
12/8/2012 07:10	3410360.10	52.3506938	-81.6151584	2236.06798	204365.9136	9992423.648
13/8/2012 03:20	10947982.22	39.4270211	81.8588084	2236.06798	203365.9136	9991423.648
13/8/2012 06:15	6667151.23	51.8733818	98.0861559	1414.21356	203365.9136	9991423.648
16/8/2012 03:50	11874044.43	28.3426479	-98.1970419	1414.21356	203365.9136	9991423.648
20/8/2012 03:25	9620790.72	28.1418491	81.7998005	1000	203365.9136	9991423.648
21/8/2012 07:05	3530911.77	44.5684304	-81.6753208	1000	204365.9136	9991423.648
25/8/2012 03:45	2022116.31	15.2284391	-98.0288783	0	204365.9136	9991423.648
25/8/2012 06:40	3210631.42	6.85362013	98.1742045	1414.21356	204365.9136	9991423.648
5/9/2012 06:20	7244371.57	43.7833511	98.1073582	1414.21356	203365.9136	9991423.648
6/9/2012 04:10	88622951.69	55.6646842	-98.3897719	3000	204365.9136	9990423.648
6/9/2012 07:05	40096779.54	44.5100883	-81.6725515	2236.06798	205365.9136	9991423.648
8/9/2012 03:55	132268343.69	39.7362272	-98.2810779	2236.06798	205365.9136	9991423.648
8/9/2012 06:55	157931058.04	22.351212	-81.820846	2236.06798	204365.9136	9991423.648
10/9/2012 03:45	9592782.16	15.4039719	-98.0233801	1414.21356	204365.9136	9990423.648
10/9/2012 06:40	88870187.88	7.16755492	98.1942148	2236.06798	204365.9136	9991423.648

Date	VRP(Watt)	Sat Zen	Sat Azi	Dist(m)	UTM(Lat)	UTM(Lon)
12/9/2012 03:30	36405564.54	14.4728807	81.6516751	2236.06798	204365.9136	9990423.648
16/9/2012 03:05	1855697.65	55.2938438	81.8858108	2000	204365.9136	9991423.648
16/9/2012 06:05	187434.40	63.5694415	98.1313032	1000	205365.9136	9991423.648
17/9/2012 03:50	8548118.75	28.6494942	-98.1957616	1414.21356	204365.9136	9990423.648
17/9/2012 06:45	9687800.36	7.80398186	-81.7975227	1414.21356	204365.9136	9991423.648
19/9/2012 03:40	10858897.03	1.20999196	-23.3498272	1414.21356	204365.9136	9990423.648
19/9/2012 06:35	5085871.90	21.6903279	98.2019353	1414.21356	204365.9136	9991423.648
21/9/2012 06:20	886072.29	44.0335542	98.1066965	1000	204365.9136	9990423.648
24/9/2012 06:55	463906.02	22.0842777	-81.8887879	0	204365.9136	9991423.648
5/10/2012 03:40	977595.04	1.17229343	-4.01873438	0	204365.9136	9991423.648
10/10/2012 06:55	957327.14	22.5528946	-81.8134478	0	204365.9136	9991423.648
16/10/2012 03:20	10646127.06	39.4632753	81.8387368	2236.06798	203365.9136	9990423.648
17/10/2012 07:00	19926117.38	34.8273529	-81.728008	2236.06798	205365.9136	9991423.648
18/10/2012 03:05	3394630.47	55.5049088	81.8662918	2828.42712	203365.9136	9990423.648
22/10/2012 07:15	6280565.71	58.7968246	-81.5396919	4000	207365.9136	9991423.648
23/10/2012 06:20	804390.64	43.7022085	98.1083922	0	204365.9136	9991423.648
24/10/2012 04:10	8050769.67	55.4367071	-98.4092894	2236.06798	204365.9136	9989423.648
24/10/2012 07:05	22671205.86	44.6082115	-81.6646344	3162.27766	206365.9136	9990423.648
25/10/2012 03:15	1575637.33	48.3480562	81.8658963	2236.06798	204365.9136	9990423.648
25/10/2012 06:10	20359308.19	58.2172088	98.0937349	2828.42712	204365.9136	9991423.648
26/10/2012 03:55	3556419.69	39.3708381	-98.2932384	2236.06798	204365.9136	9990423.648
26/10/2012 06:55	9184416.64	22.4800714	-81.8202807	2000	205365.9136	9990423.648
27/10/2012 03:00	4841623.81	61.2238515	81.8805104	2828.42712	202365.9136	9990423.648
28/10/2012 03:45	42427220.06	14.8615689	-98.0480704	2236.06798	204365.9136	9990423.648
28/10/2012 06:40	36587077.77	7.04505481	98.206147	2000	204365.9136	9990423.648
1/11/2012 03:20	5046812.82	39.5088075	81.8440151	2236.06798	204365.9136	9990423.648
4/11/2012 03:50	4565504.31	28.1008701	-98.2029322	1414.21356	204365.9136	9990423.648
10/11/2012 03:15	3688298.75	48.5027113	81.8724479	1414.21356	203365.9136	9991423.648
11/11/2012 06:50	9287818.90	21.7870755	-81.8043491	1414.21356	205365.9136	9991423.648
14/11/2012 07:25	607929.28	63.6873885	-81.5075478	1000	204365.9136	9991423.648
15/11/2012 06:30	15138403.38	34.0725263	98.1457833	1000	204365.9136	9991423.648
17/11/2012 03:20	11426285.29	39.446566	81.8431321	2000	203365.9136	9991423.648
17/11/2012 06:15	7403406.63	51.9997745	98.101817	2236.06798	203365.9136	9992423.648
20/11/2012 03:50	4236929.42	28.2883219	-98.2069806	1000	204365.9136	9991423.648
20/11/2012 06:45	9406180.19	7.93252883	-81.8102471	1000	204365.9136	9991423.648
24/11/2012 03:25	8092501.72	28.2382331	81.7897778	2236.06798	204365.9136	9990423.648
28/11/2012 03:00	937508.16	61.1762243	81.8848513	1414.21356	204365.9136	9990423.648
29/11/2012 03:45	7805995.89	15.0043584	-98.0554197	1414.21356	204365.9136	9990423.648
29/11/2012 06:40	6567623.21	7.13378103	98.2032723	1414.21356	204365.9136	9991423.648
3/12/2012 03:20	1427238.79	39.3519503	81.8408283	1000	204365.9136	9991423.648
5/12/2012 03:05	7830971.09	55.4454504	81.8725649	3162.27766	202365.9136	9990423.648
10/12/2012 03:25	2453613.03	28.2779554	81.7936596	1414.21356	204365.9136	9990423.648
12/12/2012 03:15	1480076.74	48.3265476	81.8734957	2236.06798	204365.9136	9990423.648
15/12/2012 03:45	1187805.67	14.8779878	-98.0543764	1414.21356	204365.9136	9990423.648
15/12/2012 06:40	2272852.74	6.23433306	98.2070008	1000	204365.9136	9991423.648
17/12/2012 03:30	2882689.39	15.0178462	81.6591334	1000	204365.9136	9990423.648
17/12/2012 06:30	4628156.95	33.1191201	98.148932	1000	204365.9136	9991423.648
19/12/2012 03:20	4628156.95	39.4935758	81.8525985	1414.21356	203365.9136	9990423.648
7/1/2013 03:50	1775881.56	28.5402653	-98.2126125	1000	204365.9136	9991423.648
15/1/2013 03:00	61454648.11	61.078945	81.8986239	4000	201365.9136	9991423.648
21/1/2013 04:05	7060504.51	48.4771618	-98.3568841	2000	206365.9136	9991423.648
23/1/2013 03:50	346342880.57	28.5428316	-98.211955	2236.06798	204365.9136	9990423.648
23/1/2013 06:45	132154075.15	8.52924762	-81.7872592	2236.06798	204365.9136	9990423.648
25/1/2013 06:35	109311936.47	21.1570899	98.2174605	2236.06798	204365.9136	9990423.648
27/1/2013 03:25	51445102.97	28.0827733	81.8002262	2236.06798	204365.9136	9990423.648

Date	VRP(Watt)	Sat Zen	Sat Azi	Dist(m)	UTM(Lat)	UTM(Lon)
29/1/2013 03:15	10239791.76	48.2183581	81.8780614	2236.06798	203365.9136	9990423.648
1/2/2013 06:40	4341178.83	6.87515225	98.2022087	1414.21356	205365.9136	9990423.648
2/2/2013 07:25	24103786.67	63.8614839	-81.4971935	6324.55532	208365.9136	9990423.648
6/2/2013 04:05	52130870.49	48.3392651	-98.3547229	3162.27766	205365.9136	9991423.648
6/2/2013 07:00	2705636.16	34.6185837	-81.7140503	1414.21356	205365.9136	9991423.648
7/2/2013 06:05	4506332.64	63.470544	98.1517876	2000	204365.9136	9991423.648
8/2/2013 03:50	14926749.82	28.2899201	-98.2001084	1414.21356	204365.9136	9990423.648
8/2/2013 06:45	8396559.49	8.11215613	-81.7874308	1000	204365.9136	9991423.648
10/2/2013 06:35	1422983.08	21.4657357	98.2140509	1000	204365.9136	9991423.648
15/2/2013 03:55	2700036.06	39.3354927	-98.2802423	1000	205365.9136	9991423.648
15/2/2013 06:55	911591.39	22.1580757	-81.7889078	0	204365.9136	9991423.648
24/2/2013 06:45	4695788.98	8.20630884	-81.7850537	1000	204365.9136	9991423.648
26/2/2013 03:40	9900603.13	1.18303593	-16.8512475	1414.21356	204365.9136	9991423.648
3/3/2013 03:55	10785306.91	39.6704856	-98.2926831	2236.06798	205365.9136	9991423.648
5/3/2013 06:40	353705.19	6.79812576	98.1904909	0	204365.9136	9991423.648
11/3/2013 03:10	2050202.85	55.1986826	81.8759431	1414.21356	204365.9136	9990423.648
12/3/2013 03:50	18575285.14	28.8401227	-98.2174942	1414.21356	204365.9136	9991423.648
16/3/2013 03:25	33070788.06	27.6702054	81.7832543	2236.06798	204365.9136	9990423.648
23/3/2013 03:30	41399017.38	14.1733361	81.6617883	2236.06798	204365.9136	9990423.648
23/3/2013 06:30	5029405.09	33.4557282	98.1504083	1414.21356	204365.9136	9991423.648
30/3/2013 03:40	11745586.45	1.35701655	-43.645438	1000	204365.9136	9991423.648
4/4/2013 06:55	6168284.60	23.2376536	-81.7926296	1414.21356	205365.9136	9991423.648
6/4/2013 03:45	11411725.41	15.863285	-98.0653228	1414.21356	204365.9136	9991423.648
8/4/2013 03:35	54448107.18	13.8822653	81.5616867	1414.21356	204365.9136	9991423.648
10/4/2013 03:20	65479749.57	38.7361799	81.8391151	3000	203365.9136	9991423.648
10/4/2013 06:15	29167211.93	51.3340774	98.1099226	2236.06798	204365.9136	9991423.648
12/4/2013 03:10	1329754.97	55.0578689	81.8838152	2000	203365.9136	9991423.648
12/4/2013 06:05	36097620.94	63.1410914	98.1459898	3000	204365.9136	9991423.648
19/4/2013 03:15	132364.61	47.8588797	81.8689212	0	204365.9136	9991423.648
24/4/2013 06:30	11854703.80	32.9380762	98.1362976	1000	204365.9136	9991423.648
25/4/2013 07:10	4645866.77	52.869374	-81.6019542	2236.06798	206365.9136	9991423.648
26/4/2013 03:20	1420121.07	38.9191782	81.8444582	1000	203365.9136	9991423.648
26/4/2013 06:15	7597483.31	51.3273385	98.0990956	1414.21356	204365.9136	9991423.648
27/4/2013 04:05	19616961.70	48.6854172	-98.3644458	2236.06798	204365.9136	9990423.648
27/4/2013 07:00	13964105.17	35.3649899	-81.723025	2000	204365.9136	9991423.648
4/5/2013 04:10	71346677.68	55.6375482	-98.4024518	4000	206365.9136	9991423.648
6/5/2013 06:55	47650358.52	23.0592019	-81.8188606	1414.21356	204365.9136	9990423.648
8/5/2013 06:40	48278891.70	6.37810931	98.1880283	1414.21356	204365.9136	9991423.648
10/5/2013 03:30	7364920.26	14.8045416	81.6736078	1414.21356	204365.9136	9990423.648
11/5/2013 04:15	21204024.11	61.197027	-98.4815405	2828.42712	204365.9136	9991423.648
11/5/2013 07:10	7799018.76	52.539464	-81.6170444	2236.06798	204365.9136	9990423.648
12/5/2013 03:20	8514734.94	39.4012952	81.855866	2000	204365.9136	9990423.648
15/5/2013 06:45	5162393.98	8.09625878	-81.8559653	1000	204365.9136	9990423.648
24/5/2013 03:45	10689385.48	14.9746568	-98.0424674	1414.21356	204365.9136	9990423.648
24/5/2013 06:40	6397548.97	6.73955835	98.1970097	1000	204365.9136	9990423.648
2/6/2013 03:40	38633044.78	1.18997182	-18.5438647	1414.21356	203365.9136	9990423.648
2/6/2013 06:35	4819930.66	21.0781047	98.191065	1414.21356	204365.9136	9990423.648
4/6/2013 03:25	23472689.10	28.0108226	81.7993978	1414.21356	203365.9136	9991423.648
5/6/2013 07:05	55290219.65	44.666413	-81.6789032	3000	204365.9136	9991423.648
6/6/2013 06:10	144030484.36	58.1491502	98.0824506	3162.27766	204365.9136	9991423.648
13/6/2013 06:15	33122667.72	51.811357	98.086087	2828.42712	205365.9136	9990423.648
18/6/2013 06:35	2856486.39	21.4914519	98.1890064	2236.06798	204365.9136	9990423.648
20/6/2013 03:25	781418.00	27.9503757	81.796876	2236.06798	202365.9136	9990423.648
26/6/2013 07:25	1618924.64	63.8344951	-81.5217915	2236.06798	202365.9136	9991423.648
27/6/2013 03:30	15037726.39	14.6319543	81.6611252	1414.21356	203365.9136	9990423.648

Date	VRP(Watt)	Sat Zen	Sat Azi	Dist(m)	UTM(Lat)	UTM(Lon)
29/6/2013 03:20	8247841.32	39.2218053	81.8588484	2000	204365.9136	9991423.648
29/6/2013 06:15	27845976.94	51.8305945	98.0883091	2236.06798	204365.9136	9990423.648
30/6/2013 04:05	85436053.27	48.4453584	-98.3483354	3162.27766	205365.9136	9991423.648
4/7/2013 03:40	17022073.35	1.1788285	-13.5167713	1414.21356	204365.9136	9991423.648
4/7/2013 06:35	5190141.79	21.2554607	98.1925113	1000	204365.9136	9991423.648
6/7/2013 03:25	4788785.66	28.2007301	81.8008924	2236.06798	203365.9136	9990423.648
20/7/2013 06:35	6781009.49	21.3751108	98.1916147	1414.21356	204365.9136	9991423.648
22/7/2013 03:25	69408585.68	28.4820504	81.8086294	2236.06798	203365.9136	9990423.648
22/7/2013 06:25	18551649.77	43.8622487	98.0984832	1414.21356	204365.9136	9991423.648
24/7/2013 03:15	75128353.71	48.4045902	81.886765	3000	203365.9136	9991423.648
27/7/2013 03:45	680311.31	14.8843894	-98.0506867	0	204365.9136	9991423.648
27/7/2013 06:40	37951990.26	7.03866937	98.1599432	1414.21356	204365.9136	9991423.648
28/7/2013 07:25	296789.14	63.8449515	-81.5216505	2828.42712	206365.9136	9989423.648
3/8/2013 03:50	597372.66	28.4329628	-98.2037536	0	204365.9136	9991423.648
8/8/2013 04:10	17603534.53	55.5768174	-98.3964522	4123.10563	207365.9136	9991423.648
8/8/2013 07:05	19616345.85	44.6744115	-81.674817	4000	206365.9136	9991423.648
9/8/2013 03:15	104697939.94	48.1597747	81.8835944	3162.27766	204365.9136	9991423.648
9/8/2013 06:10	30839597.90	58.1359608	98.085451	3162.27766	205365.9136	9992423.648
14/8/2013 03:30	83736750.56	14.5512378	81.6596015	1414.21356	203365.9136	9991423.648
17/8/2013 04:05	74038831.16	48.5389474	-98.354847	3162.27766	206365.9136	9991423.648
17/8/2013 07:00	49098656.64	34.8493053	-81.7366132	2236.06798	204365.9136	9991423.648
23/8/2013 03:25	74417627.15	27.8288771	81.7984034	2000	203365.9136	9990423.648
25/8/2013 03:15	34602260.51	48.030021	81.8798742	2000	203365.9136	9991423.648
28/8/2013 06:40	485310.88	6.91480941	98.1794647	0	204365.9136	9991423.648
29/8/2013 07:25	11135349.90	63.8425	-81.5192105	6000	210365.9136	9991423.648
30/8/2013 03:30	198973431.04	14.326044	81.6602874	2000	204365.9136	9990423.648
30/8/2013 06:30	36320603.89	33.7379103	98.1279779	2236.06798	204365.9136	9991423.648
2/9/2013 07:00	37241535.44	34.4923393	-81.735063	2000	204365.9136	9991423.648
3/9/2013 06:05	52757380.67	63.5231034	98.1306366	3162.27766	204365.9136	9992423.648
4/9/2013 03:50	130171881.03	28.8305487	-98.2122242	2236.06798	203365.9136	9990423.648
4/9/2013 06:45	55846372.38	7.90104046	-81.8209744	2000	204365.9136	9990423.648
6/9/2013 06:35	79425871.41	21.6221516	98.2040218	2000	204365.9136	9991423.648
8/9/2013 03:25	513068.63	27.7469072	81.7945146	1414.21356	203365.9136	9990423.648
13/9/2013 03:45	20110702.45	15.5267555	-98.047131	1414.21356	204365.9136	9991423.648
13/9/2013 06:40	31716894.81	6.95443496	98.2088659	1414.21356	204365.9136	9991423.648
18/9/2013 04:05	1966385.58	48.6191615	-98.3478052	1414.21356	204365.9136	9991423.648
20/9/2013 06:45	6999979.18	8.44092831	-81.7954994	1414.21356	204365.9136	9991423.648
22/9/2013 03:40	21942018.67	1.23538059	-28.1510713	1414.21356	203365.9136	9990423.648
22/9/2013 06:35	16539399.38	21.0587104	98.2029955	1414.21356	204365.9136	9990423.648
25/9/2013 04:10	3144574.73	55.650613	-98.3899825	1414.21356	203365.9136	9991423.648
1/10/2013 03:30	13511128.96	14.6153412	81.6639763	1414.21356	204365.9136	9991423.648
1/10/2013 06:30	9123495.32	33.4313581	98.138173	1414.21356	204365.9136	9991423.648
5/10/2013 03:10	29386695.06	55.3903988	81.8799693	3162.27766	203365.9136	9991423.648
8/10/2013 03:40	56247748.61	1.17393145	-11.1938952	2000	204365.9136	9990423.648
11/10/2013 04:10	805732.79	55.4552496	-98.3928055	2236.06798	203365.9136	9990423.648
12/10/2013 03:15	4809801.37	48.3559184	81.8852954	2000	204365.9136	9990423.648
19/10/2013 03:20	13180392.10	39.6118997	81.8554027	2236.06798	204365.9136	9991423.648
19/10/2013 06:15	7589955.42	51.9649141	98.1010964	1414.21356	204365.9136	9991423.648
20/10/2013 04:00	17254112.69	48.1518505	-98.3481376	2236.06798	205365.9136	9991423.648
20/10/2013 07:00	2898367.87	34.3888309	-81.7261823	1000	204365.9136	9991423.648
21/10/2013 03:05	328538.60	55.6127549	81.8758447	0	204365.9136	9991423.648
22/10/2013 03:50	19435180.09	28.0009545	-98.1947277	1414.21356	204365.9136	9990423.648
22/10/2013 06:45	5643717.92	7.68534788	-81.7957843	1000	204365.9136	9991423.648
28/10/2013 03:15	4708308.43	48.4600217	81.8776522	2000	203365.9136	9991423.648
28/10/2013 06:10	2397385.13	58.2596593	98.0966132	1414.21356	204365.9136	9991423.648

Date	VRP(Watt)	Sat Zen	Sat Azi	Dist(m)	UTM(Lat)	UTM(Lon)
31/10/2013 06:40	3134855.19	6.58521757	98.1795161	1000	204365.9136	9991423.648
2/11/2013 03:30	13048133.34	15.0126941	81.6602588	1414.21356	204365.9136	9991423.648
3/11/2013 04:15	9619855.45	61.1586523	-98.4838275	3162.27766	207365.9136	9992423.648
3/11/2013 07:10	4663467.75	52.7510823	-81.6022256	3162.27766	207365.9136	9990423.648
5/11/2013 04:05	13637836.37	48.3068485	-98.3295152	2236.06798	203365.9136	9991423.648
5/11/2013 07:00	74878814.12	35.3358497	-81.7267908	3000	205365.9136	9991423.648
6/11/2013 03:05	44501803.09	55.4715913	81.8447571	4123.10563	203365.9136	9990423.648
6/11/2013 06:05	12409501.80	63.1245758	98.1417995	3000	204365.9136	9990423.648
19/11/2013 07:10	1150644.43	53.2089704	-81.5994384	2236.06798	206365.9136	9991423.648
28/11/2013 07:05	7183436.21	45.4168288	-81.6633232	2236.06798	205365.9136	9990423.648
30/11/2013 03:55	2029337.09	39.5754568	-98.2909794	1000	204365.9136	9991423.648
2/12/2013 06:40	6125060.62	5.39225375	98.2215322	1000	204365.9136	9991423.648
6/12/2013 03:20	2615996.10	39.2040683	81.8516555	1414.21356	203365.9136	9990423.648
7/12/2013 04:05	6073820.55	48.4596229	-98.3497689	2000	204365.9136	9990423.648
11/12/2013 06:35	8405816.63	20.1280527	98.2114113	1414.21356	204365.9136	9991423.648
13/12/2013 03:25	6897107.23	28.0107953	81.7931112	2236.06798	203365.9136	9990423.648
18/12/2013 03:45	65965562.19	15.4425592	-98.0452805	1414.21356	204365.9136	9990423.648
18/12/2013 06:40	62637806.82	6.18324696	98.2233441	1414.21356	204365.9136	9991423.648
22/12/2013 03:20	1865994.91	38.9512865	81.8468056	1000	204365.9136	9991423.648
25/12/2013 03:50	3081665.20	28.8883948	-98.2103046	1000	203365.9136	9991423.648
25/12/2013 06:45	39729867.35	9.01117427	-81.8056929	1414.21356	204365.9136	9991423.648
27/12/2013 03:40	4231480.46	1.29987097	-37.4442097	1000	204365.9136	9991423.648
30/12/2013 07:05	1661657.62	44.96898	-81.65536	2236.06798	206365.9136	9990423.648
31/12/2013 03:15	18393615.80	47.9122245	81.8743347	2236.06798	203365.9136	9990423.648
1/1/2014 06:55	9737958.13	23.0711632	-81.8018095	1000	204365.9136	9991423.648
2/1/2014 03:00	4499027.40	60.9293409	81.9026136	2236.06798	203365.9136	9990423.648
7/1/2014 06:15	740339.26	51.6251702	98.1121728	0	204365.9136	9991423.648
12/1/2014 06:35	5738772.96	21.2944862	98.2230738	1414.21356	204365.9136	9991423.648
16/1/2014 03:15	1965804.81	48.0372613	81.8793599	1414.21356	203365.9136	9990423.648
17/1/2014 03:55	852068.90	39.7713043	-98.2915886	1000	204365.9136	9991423.648
21/1/2014 03:30	12195539.50	14.5476578	81.6771834	1414.21356	204365.9136	9991423.648
21/1/2014 06:30	10610790.85	33.6708277	98.1535622	1414.21356	204365.9136	9991423.648
24/1/2014 04:05	8799805.51	48.4626002	-98.3433657	1414.21356	204365.9136	9991423.648
25/1/2014 03:10	377446.11	55.3791336	81.814657	1414.21356	203365.9136	9990423.648
25/1/2014 18:25	2870266.54	38.9939372	81.8386413	1414.21356	203365.9136	9990423.648
26/1/2014 03:50	8561928.79	28.4481326	-98.1967493	1414.21356	204365.9136	9990423.648
26/1/2014 06:45	32419550.32	8.34714699	-81.7924525	1414.21356	204365.9136	9991423.648
31/1/2014 07:05	5756790.60	44.6002944	-81.6519921	2236.06798	206365.9136	9991423.648
1/2/2014 03:15	29153803.87	48.3605344	81.8910142	2236.06798	204365.9136	9990423.648
1/2/2014 18:30	41519288.26	27.8170751	81.8111241	1414.21356	204365.9136	9991423.648
2/2/2014 03:55	2280393.46	39.3848413	-98.2726037	2236.06798	205365.9136	9990423.648
3/2/2014 18:20	16778849.66	48.0742827	81.8547644	1000	203365.9136	9991423.648
4/2/2014 03:45	2976579.35	15.0366609	-98.0335866	1414.21356	204365.9136	9990423.648
5/2/2014 07:25	295987.35	63.841877	-81.4968608	2000	202365.9136	9991423.648
6/2/2014 06:30	211201.16	33.7007253	98.1538168	1000	204365.9136	9991423.648
9/2/2014 04:05	699660.40	48.5073006	-98.3466503	2000	206365.9136	9991423.648
9/2/2014 07:00	4315530.81	34.7923215	-81.7144096	2236.06798	206365.9136	9991423.648
17/2/2014 03:15	8890027.56	47.9198013	81.8716423	2236.06798	203365.9136	9990423.648
18/2/2014 03:55	8418886.86	39.9390496	-98.299857	2236.06798	203365.9136	9990423.648
18/2/2014 06:55	2641258.64	22.845978	-81.7925968	2000	205365.9136	9991423.648
19/2/2014 03:00	19212774.50	60.9103881	81.8987215	2236.06798	203365.9136	9991423.648
8/3/2014 06:40	449952.87	7.73831232	98.2127654	0	204365.9136	9991423.648
10/3/2014 03:30	591870.17	14.6501271	81.6490004	1000	204365.9136	9991423.648
12/3/2014 03:20	29532019.96	39.3203069	81.8448578	3162.27766	204365.9136	9991423.648
12/3/2014 06:15	11941667.91	52.0846021	98.1112997	2236.06798	204365.9136	9991423.648

Date	VRP(Watt)	Sat Zen	Sat Azi	Dist(m)	UTM(Lat)	UTM(Lon)
26/3/2014 03:30	1203747.39	14.4250254	81.6516286	1414.21356	203365.9136	9990423.648
28/3/2014 03:20	371596139.71	39.0072933	81.8367593	2236.06798	204365.9136	9990423.648
28/3/2014 06:15	149102932.00	51.715718	98.0918538	3162.27766	205365.9136	9990423.648
29/3/2014 07:00	42291975.11	34.8144184	-81.7395588	2828.42712	205365.9136	9991423.648
30/3/2014 03:10	26494480.93	55.1949625	81.8751724	2828.42712	204365.9136	9989423.648
30/3/2014 06:05	73001359.14	63.3859481	98.1310649	3000	204365.9136	9991423.648
1/4/2014 18:15	32288058.98	55.1863609	81.8832782	2236.06798	203365.9136	9990423.648
2/4/2014 03:40	64035173.52	1.27966519	-34.9907059	2236.06798	203365.9136	9990423.648
3/4/2014 07:20	424127.23	58.8142043	-81.5510926	2000	206365.9136	9991423.648
4/4/2014 03:25	20372940.57	27.6932557	81.7812599	2236.06798	203365.9136	9990423.648
6/4/2014 18:30	18757131.76	27.7113312	81.8442208	1000	203365.9136	9991423.648
9/4/2014 03:45	1483004.57	15.5567236	-98.0628077	1000	205365.9136	9991423.648
14/4/2014 04:05	3840172.72	48.5918103	-98.3647783	2000	205365.9136	9991423.648
14/4/2014 07:00	27870255.85	34.82753	-81.7427696	2000	205365.9136	9991423.648
18/4/2014 06:35	1343293.29	21.157101	98.1890667	0	204365.9136	9991423.648
23/4/2014 03:55	4698203.81	39.4387225	-98.2870789	2000	204365.9136	9990423.648
25/4/2014 03:45	9478537.89	14.8422719	-98.0561642	2236.06798	204365.9136	9989423.648
25/4/2014 06:40	15101193.19	7.03170455	98.1726502	2000	204365.9136	9991423.648
27/4/2014 03:30	12245227.78	14.9443901	81.6582618	2000	204365.9136	9990423.648
28/4/2014 04:15	16870292.99	61.1986792	-98.4854717	2828.42712	204365.9136	9990423.648
28/4/2014 07:10	30306781.63	52.4882556	-81.6183459	4123.10563	206365.9136	9990423.648
1/5/2014 03:10	39573782.64	55.3542097	81.8794833	4000	202365.9136	9991423.648
1/5/2014 06:05	31747616.74	63.3796124	98.1249096	4000	204365.9136	9991423.648
2/5/2014 03:50	66201417.18	28.5613487	-98.2148934	2236.06798	204365.9136	9991423.648
2/5/2014 06:50	126596028.87	8.5580976	-81.8387014	1414.21356	204365.9136	9991423.648
10/5/2014 18:20	13111491.90	47.7534765	81.8760225	2236.06798	203347.3442	9990478.972
17/5/2014 03:10	16349712.04	55.0431148	81.8812966	4123.10563	203347.3442	9991478.972
17/5/2014 06:05	4891381.79	63.2943117	98.1237922	2236.06798	205347.3442	9991478.972
21/5/2014 07:20	7822218.89	58.9155131	-81.548401	2828.42712	206347.3442	9991478.972
21/5/2014 15:05	11872768.02	58.0261155	98.1443028	1414.21356	204347.3442	9990478.972
22/5/2014 03:25	6629500.50	27.36282	81.7702081	1414.21356	203347.3442	9990478.972
25/5/2014 06:55	1694100.28	22.7182713	-81.8226791	1000	204347.3442	9991478.972
27/5/2014 06:40	23075512.54	6.77157531	98.1893301	1414.21356	204347.3442	9991478.972
31/5/2014 06:15	39463792.87	51.7773219	98.087533	3000	205347.3442	9991478.972
3/6/2014 06:45	1079748.84	8.38172243	-81.8310285	1000	205347.3442	9991478.972
5/6/2014 03:40	97737957.44	1.47787268	-53.8105842	2000	204347.3442	9991478.972
9/6/2014 03:15	19154768.53	47.730911	81.8641658	2236.06798	203347.3442	9991478.972
12/6/2014 03:45	2894155.11	15.9637407	-98.0624398	1000	204347.3442	9991478.972
12/6/2014 06:40	1249198.63	6.69393768	98.1785633	0	204347.3442	9991478.972
21/6/2014 03:40	36158358.89	1.34120968	-41.9992218	2236.06798	203347.3442	9990478.972
30/6/2014 03:35	31506753.95	14.4003638	81.6502115	2000	203347.3442	9991478.972
30/6/2014 06:30	31689955.98	33.6738127	98.1310282	1000	204347.3442	9991478.972
2/7/2014 03:20	86814356.78	39.0935055	81.8420959	2828.42712	203347.3442	9990478.972
2/7/2014 06:15	85432046.22	51.7594335	98.0887088	2828.42712	205347.3442	9990478.972
3/7/2014 04:05	987959.73	48.5413447	-98.3523105	1414.21356	205347.3442	9991478.972
3/7/2014 07:00	956976.23	34.7402598	-81.7355097	2000	205347.3442	9991478.972
4/7/2014 06:05	56958940.28	63.3979167	98.1273698	4123.10563	204347.3442	9991478.972
10/7/2014 04:10	20579531.24	55.4885838	-98.4037651	4000	203347.3442	9990478.972
10/7/2014 07:05	48583305.13	44.6402383	-81.6761867	3162.27766	205347.3442	9990478.972
16/7/2014 03:30	85702452.73	15.2640162	81.6537521	2236.06798	204347.3442	9990478.972
20/7/2014 03:10	23795427.82	55.7546759	81.8781327	4000	203347.3442	9991478.972
22/7/2014 15:15	4589100.21	44.5627191	98.1869467	1000	203347.3442	9991478.972
24/7/2014 07:20	20081361.27	58.6704481	-81.5478538	5099.01951	207347.3442	9990478.972
25/7/2014 18:45	57831048.27	1.20813963	-24.4821186	1414.21356	204347.3442	9990478.972
26/7/2014 07:05	19309454.81	44.505998	-81.6748771	3000	206347.3442	9991478.972

Date	VRP(Watt)	Sat Zen	Sat Azi	Dist(m)	UTM(Lat)	UTM(Lon)
27/7/2014 03:15	34249129.20	48.6261179	81.8876641	2000	204347.3442	9991478.972
28/7/2014 06:55	3134689.49	22.4830205	-81.8191282	1000	204347.3442	9991478.972
1/8/2014 06:30	4028168.92	33.5942428	98.1367075	1000	204347.3442	9991478.972
10/8/2014 06:25	13804653.82	43.6317196	98.1061376	2000	204347.3442	9991478.972
22/8/2014 03:50	4768296.23	28.5770006	-98.2072481	1000	204347.3442	9991478.972
22/8/2014 06:45	4379218.02	8.33374172	-81.8073179	1000	204347.3442	9991478.972
24/8/2014 06:35	2793431.04	21.2624231	98.1987523	22135.9436	224347.3442	9984478.972
31/8/2014 03:45	29389175.05	15.3848822	-98.0514267	1414.21356	203347.3442	9991478.972
31/8/2014 06:40	29530334.10	6.85751929	98.2082501	1414.21356	204347.3442	9990478.972
2/9/2014 03:35	27999789.22	14.4574354	81.6493175	1414.21356	203347.3442	9991478.972
2/9/2014 06:30	89140412.41	33.5998406	98.1313611	2000	204347.3442	9990478.972
4/9/2014 03:20	166935378.50	39.0564915	81.8503109	3162.27766	204347.3442	9991478.972
5/9/2014 04:05	44922593.55	48.5755941	-98.3553342	2000	204347.3442	9991478.972
6/9/2014 03:10	64956532.00	55.2608246	81.8822339	4123.10563	203347.3442	9990478.972
6/9/2014 06:05	17627527.12	63.3888251	98.1286423	2236.06798	204347.3442	9992478.972
7/9/2014 06:45	7042794.86	8.4324969	-81.821542	1000	204347.3442	9991478.972
10/9/2014 07:20	18140444.79	58.8234845	-81.5412411	4123.10563	206347.3442	9991478.972
11/9/2014 18:45	92751459.90	1.28863855	-36.5749679	1414.21356	204347.3442	9990478.972
14/9/2014 03:55	1065239.52	39.6808189	-98.2855666	1414.21356	204347.3442	9990478.972
15/9/2014 03:00	24221320.29	61.0639408	81.9021412	2828.42712	204347.3442	9990478.972
19/9/2014 07:10	94255483.92	52.4624811	-81.608593	5000	206347.3442	9991478.972
23/9/2014 19:10	6816756.28	48.7238499	-98.4092251	1000	205347.3442	9991478.972
25/9/2014 06:35	13129537.74	21.0617993	98.2095976	1414.21356	204347.3442	9991478.972
26/9/2014 07:20	4649661.05	58.8446793	-81.5405938	2000	206347.3442	9991478.972
27/9/2014 03:25	16036229.03	28.0989709	81.8021175	1000	203347.3442	9991478.972
30/9/2014 06:55	24000135.49	22.7261663	-81.813695	2236.06798	204347.3442	9990478.972
2/10/2014 03:45	3576145.14	15.3709511	-98.0348386	1414.21356	204347.3442	9990478.972
5/10/2014 04:15	807872.37	61.3658197	-98.4773497	2000	206347.3442	9991478.972
5/10/2014 07:10	13488414.86	52.4838889	-81.6085586	4000	206347.3442	9991478.972
6/10/2014 03:20	19046097.51	39.0227233	81.8498755	2236.06798	203347.3442	9990478.972
9/10/2014 03:50	8928841.18	28.824959	-98.2087646	1414.21356	204347.3442	9990478.972
17/10/2014 03:00	7400975.35	60.9771071	81.9042141	2236.06798	202347.3442	9990478.972
24/10/2014 03:10	2506306.45	55.2516918	81.8910876	2236.06798	203347.3442	9991478.972
25/10/2014 06:45	13775437.81	8.62867769	-81.8112479	1000	204347.3442	9991478.972
29/10/2014 03:25	17699470.15	28.0183539	81.8028472	1414.21356	203347.3442	9990478.972
29/10/2014 06:25	38840896.93	43.4549042	98.115061	2236.06798	204347.3442	9991478.972
3/11/2014 06:40	11843911.47	6.41348479	98.2052901	1414.21356	204347.3442	9991478.972
4/11/2014 07:25	2149418.12	64.0071761	-81.5037542	2236.06798	206347.3442	9991478.972
5/11/2014 03:30	16418128.19	14.978217	81.6608298	1414.21356	204347.3442	9990478.972
5/11/2014 06:30	6464197.33	33.3499453	98.1422932	1414.21356	204347.3442	9991478.972
9/11/2014 06:05	30237149.13	63.3566753	98.1433506	4000	204347.3442	9991478.972
12/11/2014 03:40	626153.01	1.25262882	17.1906723	0	204347.3442	9991478.972
12/11/2014 06:35	3756729.77	21.2450857	98.2070739	1000	204347.3442	9991478.972
13/11/2014 07:20	548699.96	58.7581429	-81.5305	2236.06798	206347.3442	9990478.972
14/11/2014 03:25	2556436.59	28.8848326	81.8136775	1414.21356	203347.3442	9990478.972
18/11/2014 03:00	3630084.40	61.3557611	81.8944262	2236.06798	203347.3442	9990478.972
19/11/2014 06:40	612970.94	6.62327383	98.1913753	0	204347.3442	9991478.972
21/11/2014 03:30	45137354.64	15.2077811	81.6624872	1414.21356	204347.3442	9991478.972
21/11/2014 06:30	3148902.45	33.4668273	98.141629	1000	204347.3442	9991478.972
23/11/2014 06:15	3783407.91	51.6719346	98.1071765	2000	205347.3442	9991478.972
26/11/2014 03:50	13161171.94	28.186863	-98.2006116	1414.21356	204347.3442	9990478.972

APPENDIX 2.2

Code	Date	X	Y	Z	Description
M1	2015 04 15	206782	9988489	2104	LF 4
M2A	2015 04 15	205916	9988884	2423	LF 5
M2B	2015 04 15	205916	9988884	2423	LF 5
M3	2015 04 16	205519	9989635	2572	LF 14
M4	2015 04 16	206749	9989634	2256	LF 11
M5	2015 04 17	206749	9989325	2232	LF 11
M6	2015 04 17	204599	9989370		LF 25
M7	2015 04 17	205212	9989115	2490	LF 5
M8	2015 04 17	205259	9989098	2542	LF 5
M10	2015 04 17	205973	9988835	2420	LF 5
M11	2015 04 17	206145	9988818	2367	LF 5
M12	2015 04 17	206308	9988737	2338	LF 5
M13	2015 04 17	207900	9991821	2150	LF 9
M14	2015 04 19	205187	9989820	2605	PDC

Coordinates of the collected samples in El Reventador volcano during the fieldwork.

APPENDIX 2.3

Code	Date	X	Y	Z
REV1	2015 04 15	206891	9988866	2249
REV2	2015 04 16	206813	9988485	2261
REV3	2015 04 16	205906	9988887	2459
REV4	2015 04 16	205512	9989637	2598
REV5	2015 04 16	206775	9989617	2271
REV6	2015 04 17	205233	9989094	2561
REV7	2015 04 17	205233	9989094	2561
REV8	2015 04 17	205722	9988925	2482
REV9	2015 04 17	206148	9988815	2385
REV10	2015 04 17	205615	9991890	2686
REV11	2015 04 17	207892	9991822	2176

Coordinates of the tag features placed in El Reventador volcano for used as a control points for DEM development.

APPENDIX 2.4

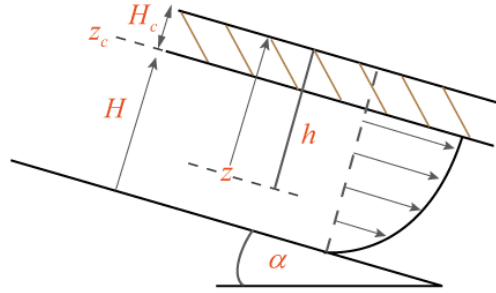
COD_X	COD_Y	X	Y	Z	DISTANCE
78	117	204500	9989772	2825	4020
79	118	204670	9989699	2794	3833
80	118	204676	9989705	2795	3830
81	118	204688	9989711	2796	3823
82	117	204664	9989729	2809	3854
83	117	204664	9989735	2810	3857
84	117	204664	9989747	2813	3863
85	116	204633	9989778	2829	3907
86	116	204633	9989784	2831	3910
87	116	204639	9989796	2832	3910
88	115	204585	9989838	2853	3981
89	115	204609	9989838	2852	3960
90	115	204615	9989844	2853	3958
91	114	204579	9989875	2870	4007
92	114	204591	9989875	2868	3996
93	114	204597	9989881	2869	3994
94	114	204609	9989893	2870	3990
95	114	204615	9989899	2871	3988
96	114	204615	9989905	2873	3991
97	114	204615	9989917	2876	3998
98	113	204554	9989966	2897	4077
99	112	204518	9990002	2917	4129
100	112	204536	9990002	2917	4114
101	111	204493	9990039	2935	4171
102	111	204512	9990039	2934	4156
103	111	204512	9990045	2936	4159
104	110	204493	9990069	2951	4189
105	110	204506	9990075	2952	4182
106	110	204512	9990081	2952	4180
107	110	204512	9990094	2956	4187
108	109	204493	9990118	2971	4218
109	108	204463	9990154	2991	4265
110	108	204475	9990160	2992	4259
111	107	204445	9990191	3011	4303
112	106	204421	9990215	3028	4339
113	105	204396	9990239	3045	4375
114	104	204384	9990264	3063	4401
115	103	204372	9990276	3077	4420
116	103	204378	9990288	3080	4422
117	103	204390	9990294	3079	4415
118	102	204378	9990318	3098	4442
119	101	204360	9990343	3115	4473
120	100	204342	9990367	3134	4504
121	100	204360	9990367	3132	4489
122	99	204342	9990391	3151	4521

COD_X	COD_Y	X	Y	Z	DISTANCE
123	98	204335	9990410	3168	4539
124	97	204323	9990422	3183	4558
125	97	204335	9990428	3181	4552
126	96	204311	9990452	3200	4588
127	96	204323	9990470	3203	4589
128	95	204244	9990531	3235	4693
129	95	204305	9990507	3224	4629
130	94	204232	9990574	3258	4731
131	94	204244	9990580	3258	4725
132	93	204226	9990604	3278	4758
133	93	204232	9990610	3279	4756
134	93	204250	9990616	3277	4745
135	92	204238	9990640	3296	4772
136	91	204220	9990659	3314	4801
137	91	204244	9990659	3312	4781
138	90	204226	9990689	3333	4818
139	90	204238	9990695	3334	4812
140	90	204263	9990695	3330	4792
141	90	204275	9990701	3332	4786
142	89	204263	9990725	3349	4814
143	89	204263	9990732	3352	4818
144	88	204250	9990756	3370	4846
145	87	204238	9990786	3392	4878
146	86	204220	9990811	3412	4911
147	86	204232	9990817	3412	4905
148	85	204214	9990841	3433	4938
149	85	204226	9990847	3432	4932
150	84	204214	9990877	3455	4965
151	83	204202	9990902	3474	4993
152	82	204190	9990926	3495	5022
153	82	204202	9990932	3493	5016
153	81	204165	9990962	3519	5068
144	84	203971	9990962	3502	5214
143	85	204117	9990841	3443	5016
142	85	203983	9990926	3479	5178
141	86	204105	9990823	3429	5011
140	86	203965	9990902	3462	5174
139	87	204086	9990804	3413	5012
138	87	203959	9990877	3444	5161
137	88	204086	9990774	3392	4990
136	88	203953	9990853	3425	5148
135	89	204080	9990750	3374	4977
134	90	204135	9990695	3344	4895
133	90	204080	9990719	3355	4955
132	91	204123	9990677	3330	4892
131	91	204074	9990695	3338	4943
130	92	204123	9990646	3309	4870
129	92	204068	9990671	3321	4930
128	93	204135	9990610	3288	4836

COD_X	COD_Y	X	Y	Z	DISTANCE
127	93	204117	9990610	3289	4851
126	94	204184	9990549	3258	4757
125	94	204147	9990561	3263	4794
124	94	204020	9990634	3292	4943
123	95	204068	9990586	3264	4872
122	95	204013	9990610	3274	4931
121	96	204080	9990549	3242	4837
120	97	204263	9990410	3184	4601
119	97	204214	9990434	3194	4656
118	97	204184	9990440	3197	4685
117	98	204226	9990391	3172	4619
116	98	204214	9990391	3173	4629
115	98	204202	9990385	3172	4636
114	98	204190	9990379	3172	4643
113	99	204226	9990343	3151	4589
112	99	204208	9990343	3151	4604
111	99	204165	9990355	3159	4647
110	100	204208	9990318	3135	4589
109	99	203855	9990525	3219	5005
108	100	204141	9990331	3143	4652
107	100	204123	9990331	3145	4667
106	101	204153	9990294	3122	4619
105	102	204190	9990264	3103	4569
104	103	204220	9990233	3081	4525
103	104	204269	9990191	3058	4458
102	105	204281	9990166	3040	4432
101	106	204299	9990148	3024	4405
100	106	204293	9990142	3024	4407
99	107	204305	9990118	3008	4382
98	107	204299	9990112	3007	4384
97	108	204317	9990094	2990	4356
96	108	204311	9990081	2988	4355
95	108	204305	9990075	2988	4357
94	109	204311	9990057	2974	4341
93	109	204305	9990045	2972	4340
92	110	204329	9990021	2953	4304
91	110	204323	9990009	2952	4303
90	111	204354	9989984	2935	4263
89	111	204354	9989978	2933	4259
88	112	204372	9989948	2916	4227
87	112	204372	9989936	2917	4221
86	113	204396	9989911	2899	4185
85	113	204402	9989899	2894	4174
84	113	204402	9989887	2893	4168
83	114	204427	9989863	2877	4133
82	114	204427	9989851	2875	4127
81	115	204445	9989838	2860	4103
80	116	204469	9989808	2843	4065
79	116	204463	9989802	2843	4068

APPENDIX 4.1

Viscous crust



Velocity of the crust

$$\rho g h \sin(\alpha) = \eta \frac{\partial v}{\partial z}$$

$$v(z) = \int_0^{z_c} \frac{\rho g h \sin(\alpha)}{\eta} \partial z$$

$$h = (H + H_c - z)$$

$$v(z) = \int_0^{z_c} \frac{\rho g (H + H_c - z) \sin(\alpha)}{\eta} \partial z$$

$$v(z) = \left[\frac{\rho g \left(Hz + H_c z - \frac{1}{2} z^2 \right) \sin(\alpha)}{\eta} \right]_0^{z_c}$$

$$v(z) = \frac{\rho g}{\eta} \left(Hz + H_c z - \frac{1}{2} z^2 \right) \sin(\alpha)$$

$$v_{crust} = \frac{\rho g \sin(\alpha)}{\eta} \left(\frac{1}{2} H^2 + H_c H \right)$$

Average velocity of the viscous part

$$v_m = \frac{1}{H} \int_{z=0}^{z_c} \frac{\rho g \sin(\alpha)}{\eta} \left(Hz + H_c z - \frac{1}{2} z^2 \right) \partial z$$

$$v_m = \frac{\rho g \sin(\alpha)}{H \eta} \left[\frac{1}{2} Hz^2 + \frac{1}{2} H_c z^2 - \frac{1}{6} z^3 \right]_0^{z_c}$$

with $z_c = H$

$$v_m = \frac{\rho g \sin(\alpha)}{\eta} \left[\frac{1}{2} H^2 + \frac{1}{2} H_c H - \frac{1}{6} H^2 \right]$$

$$v_m = \frac{\rho g \sin(\alpha)}{\eta} \left[\frac{1}{3} H^2 + \frac{1}{2} H_c H \right]$$

┌──────────┐
influenced by
the crust

Average velocity of the whole body (crust + viscous part)

$$\bar{v} = \frac{\left[H \left(\frac{1}{3} H^2 + \frac{1}{2} H_c H \right) + H_c \left(\frac{1}{2} H^2 + H_c H \right) \right] \rho g \sin(\alpha)}{H + H_c \eta}$$

$$\bar{v} = \frac{\frac{1}{3} H^3 + \frac{1}{2} H_c H^2 + \frac{1}{2} H^2 H_c + H_c^2 H}{H + H_c} \frac{\rho g \sin(\alpha)}{\eta}$$

Appendix 5.1

Study Case 1: Molten basalt benchmark (Syracuse Lava Project)

VolcFlow basic input parameters

Symbol	Notation	Value	Units	Source
terup	Eruption time	60	s	Dietterich <i>et al.</i> 2015
tmax	Maximum time	128	s	Dietterich <i>et al.</i> 2015
vol	Volume	0.0132	m ³	Dietterich <i>et al.</i> 2015
ρ	bulk density	2350	kg m ⁻³	Dietterich <i>et al.</i> 2015

Model n°1: Isothermal

Best fit values for viscosity and yield strength

Symbol	Notation	Value	Units
η	Viscosity	18	Pa s
τ	Yield strength	100	Pa

Model n°2b: thermo-rheological variation with sigmoid model

Cooling and rheological parameters

Symbol	Notation	Value	Units	Source
Cooling				
Radiation parameters				
σ	Stefan-Boltzmann	5.67E-08	W m ⁻² K ⁻⁴	
e	Emmissivity	0.95	--	
Convection parameters				
C_H	CH	0.0036	--	Greeley & Iverson 1987
cp_{air}	Air specific heat capacity	1500	J kg ⁻¹ K ⁻¹	Dietterich <i>et al.</i> 2015
T_{air}	Air temperature	293.15	K	Dietterich <i>et al.</i> 2015
U	Wind speed	0.1	m s ⁻¹	Dietterich <i>et al.</i> 2015
ρ_{air}	Air density	0.4412	kg m ⁻³	Dietterich <i>et al.</i> 2015
Conduction parameters				
h_{base}	hbase	0.001	m	Dietterich <i>et al.</i> 2015
K	Thermal conductivity	0.2	W m ⁻¹ K ⁻¹	Dietterich <i>et al.</i> 2015
T_{base}	Basal temperature	500	K	Dietterich <i>et al.</i> 2015
Density and vesicularity				
ves	Vesicularity	0		Dietterich <i>et al.</i> 2015
ρ_{DRE}	DRE density	2350	kg m ⁻³	Dietterich <i>et al.</i> 2015
Thermal parameters				
$Buff$	Buffer (Th=Terupt-Buffer)	0		Dietterich <i>et al.</i> 2015
T_c	Crust temperature	973.15	K	Dietterich <i>et al.</i> 2015
T_{core}	Core temperature	1323.15	K	Dietterich <i>et al.</i> 2015
f	Crust cover	0	--	Dietterich <i>et al.</i> 2015

Model n°2b 1: Sigmoidal model considering a constant yield strength and variable viscosity dependent on the temperature

Symbol	Notation	Value	Units
η_1	Lowest viscosity at high t_c	0	Pa s
η_2	Highest viscosity at low t_c	1000	Pa s
T_L	Transition temperature	1125	K
L	Sharpness of the transition	1/60	K ⁻¹
τ	Yield strength	0	Pa

Model n°2b 2: Sigmoidal model considering a constant viscosity and variable yield strength dependent on the temperature

Symbol	Notation	Value	Units
τ_1	Lowest yield strength at high t_c	10	Pa
τ_2	Highest yield strength at low t_c	900	Pa
T_L	Transition temperature	1190	K
L	Sharpness of the transition	1/60	K ⁻¹
η	Viscosity	25	Pa s

Model n°3: Crust formation with hot interior

Symbol	Notation	Value	Units
C_g	Rate of growth of the crust	$6,8 \times 10^{-3}$	mm h ⁻¹
η	Viscosity	12	Pa s
τ	Yield strength	0	Pa

Appendix 5.2

Study Case 2: Lava flow from Piton de la Fournaise

VolcFlow basic input parameters

Symbol	Notation	Value	Units	Source
terup	Eruption time	1368	h	M. Gouhier, personal communication
tmax	Maximum time	2400	h	M. Gouhier, personal communication
ρ	bulk density	1080	kg m ⁻³	Harris et al. 2015
vol	Volume	0.013	m ³	Dietterich et al. 2015

Model n°1: Isothermal

Best fit values for viscosity and yield strength

Symbol	Notation	Value	Units
η	Viscosity	1x10 ⁵	Pa s
τ	Yield strength	5x10 ³	Pa

Model n°2: Thermo-rheological variation

Cooling and rheological parameters

Symbol	Notation	Value	Units	Source
Cooling				
Radiation parameters				
σ	Stefan-Boltzmann	57 x 10 ⁸	W m ⁻² K ⁴	
e	Emmissivity	0.95	--	Harris et al. (2015)
Convection parameters				
C_H	CH	0.004	--	Harris & Rowland (2001)
cp_{air}	Air specific heat c _p	1500	J kg ⁻¹ K ⁻¹	Harris & Rowland (2001)
T_{air}	Air temperature	293.2	K	Harris & Rowland (2001)
U	Wind speed	5	m s ⁻¹	Harris & Rowland (2001)
ρ_{air}	Air density	0.441	kg m ⁻³	Harris & Rowland (2001)
Conduction parameters				
h_{base}	hbase	0.266	m	$h_{base} = (cd * h)/100$
K	Thermal conductiv	0.88	W m ⁻¹ K	from Peck (1978) $K = (1,929 - 1,554*ves)^2$
cd	Core to base distat	19 %		Harris & Rowland (2001)
h	Thickness	1.4	m	Harris et al. (2015)
T_{base}	Basal temperature	773.2	K	$T_{base} = T_c$
Density and vesicularity				
ves	Vesicularity	0.64	--	Harris et al. (2015)
ρ_{DRE}	DRE density	2970	kg m ⁻³	Harris et al. (2015)

Thermal parameters

$Buff$	Buffer ($T_h = T_{erup}$)	140	--	Harris et al. (2015)
T_c	Crust temperature	773.2	K	Harris et al. (2015)
T_{core}	Core temperature	1387	K	Harris et al. (2015)
f	Crust cover	0.6	--	Assumed

Crystal parameters

L	Latent heat of crys,	5×10^5	$K \text{ kg}^{-1}$	Harris & Rowland (2001)
$\Delta\phi$	Crystals growing during cooling	0.90	--	Harris et al. (2015)
ΔT	Cooling rate	150.00	K	Harris et al. (2015)
$\Delta\phi/\Delta T$	Rate of crystallizat	0.006	K^{-1}	$= \Delta\phi / \Delta T$
R		1.51		

Rheological parameters - model n°2a

Symbol	Notation	Value	Source
Dynamic viscosity (Giordano & Dingwell 2003)			
vft_a	Constant independc	-4.55	Estimated by Villeneuve et al. (2008)
vft_b	Adjustable parame	5558	following Giordano et al. (2008)
vft_c	Adjustable parame	276.7	

Yield strength (Dragoni 1989; Pinkerton & Stevens)

CB	Constant B	0.01
CC	Constant C	0.08

Model n°3: Crust formation with hot interior

Symbol	Notation	Value	Units
C_g	Rate of growth of	1×10^{-5}	mm h^{-1}
η	Viscosity	1×10^5	Pa s
τ	Yield strength	5×10^2	Pa

APPENDIX 5.3

Article:

**VolcFlow capabilities and potential development for the
simulation of lava flows**

KARIM KELFOUN & SILVIA VALLEJO VARGAS

VolcFlow capabilities and potential development for the simulation of lava flows

KARIM KELFOUN^{1*} & SILVIA VALLEJO VARGAS²

¹*Laboratoire Magmas et Volcans, Université Blaise Pascal–CNRS–IRD, OPGC,
5 rue Kessler, 63038 Clermont-Ferrand, France*

²*Instituto Geofísico, Escuela Politécnica Nacional, Ladrón de
Guevara E11-253 y Andalucía, Apartado 2759, Quito, Ecuador*

*Corresponding author (e-mail: k.kelfoun@opgc.univ-bpclermont.fr)

Abstract: VolcFlow is a finite-difference Eulerian code based on the depth-averaged approach and developed for the simulation of isothermal geophysical flows. Its capability for reproducing lava flows is tested here for the first time. The field example chosen is the 2010 lava flow of Tungurahua volcano (Ecuador), the emplacement of which is tracked by projecting thermal images onto a georeferenced digital topography. Results show that, at least for this case study, the isothermal approach of VolcFlow is able to simulate the velocity of the lava through time, as well as the extent of the solidified lava. However, the good fit between the modelled and the natural flow may be explained by the short emplacement time (*c.* 20 h) of a thick lava (*c.* 5 m), which could limit the influence of cooling on the flow dynamics, thus favouring the use of an isothermal rheology.

Lava flows exhibit complex rheologies that vary in time and space, and control their emplacement. Numerical models simplify their physics, to a greater or lesser extent, in an attempt to predict their evolution and the areas impacted. Some approaches are simply based on trajectory estimation from topographical analysis, adding probabilistic or stochastic variations of the trajectories to calculate a flow width (DOWNFLOW: Favalli *et al.* 2005; VORIS: Felpeto *et al.* 2007). The runout of the lava flow cannot be simulated. Other approaches are in two dimensions (2D), using a thickness below which the lava cannot flow and above which it is distributed to the neighbouring cells. This thickness is dependent on the topographical slope (FLOWFRONT: Wadge *et al.* 1994) or on the lava temperature (SCIARA: Crisci *et al.* 2004) but dynamics are not included in the model. Ishihara *et al.* (1990) and Miyamoto & Sasaki (1998) use fluid dynamics and cooling equations to calculate the lava spreading in 2D (runout and width) on an incline. FLOWGO (Harris & Rowland 2001) estimates the lava trajectory based on similar dynamics and cooling equations on a realistic topography, the lava width being calculated from volume conservation. The equations of mass, momentum and thermal balances have also been solved in 2D (runout and width) using a depth-averaged approach (no variation in the properties vertically or at right angles to the ground) on a realistic topography, the rheology of the lava being related to its cooling (Costa &

Macedonio 2005). LavaSIM (Hidaka *et al.* 2005) uses similar equations to simulate the lava flow but it solves them in 3D. This allows a vertical structure to be calculated with a crust and a fluid core. A more detailed review of existing models can be found in Hidaka *et al.* (2005). The smoothed particle hydrodynamics is a promising approach that is starting to be applied to lava-flow simulation (e.g. Hérault *et al.* 2011).

For hazard assessment, observatories and public authorities need user-friendly tools to predict the emplacement of the lava both sufficiently accurately and relatively rapidly. Some models are not available, others are too simple to be used for hazard assessment, while the more complex models require powerful computing resources and calculation times that are longer than the emplacement times of real flows (e.g. Hidaka *et al.* 2005). The numerical code, VolcFlow, has been created for the simulation of geophysical flows within a few hours using a desktop computer. It has been applied successfully to the simulation of debris avalanches, dense pyroclastic flows and tsunamis generated by landslides (Kelfoun & Druitt 2005; Kelfoun *et al.* 2008, 2009, 2010; Giachetti *et al.* 2011; Charbonnier *et al.* 2013). The aim of this paper is to present the VolcFlow code, which is used in two other chapters of this Special Publication (Cordonnier *et al.*, this volume, in press; Latutrie *et al.*, this volume, in review), and to discuss its limitations and possible evolution for the simulation of lava

flows. We show that the simple isothermal approach of VolcFlow can accurately reproduce – at least for the case studied – the lava-flow emplacement.

Model

VolcFlow uses a topography-linked coordinate system, with x and y parallel to the local ground surface. The flow is simulated by a depth-averaged approach that solves mass (equation 1) and momentum (equations 2 & 3) balance equations:

$$\frac{\partial h}{\partial t} + \frac{\partial}{\partial x}(hu) + \frac{\partial}{\partial y}(hv) = \frac{\partial h_s}{\partial t} \quad (1)$$

$$\begin{aligned} & \frac{\partial}{\partial t}(hu) + \frac{\partial}{\partial x}(hu^2) + \frac{\partial}{\partial y}(huv) \\ & = gh \sin \alpha_x - \frac{1}{2} \frac{\partial}{\partial x}(gh^2 \cos \alpha) + \frac{\tau_x}{\rho} \end{aligned} \quad (2)$$

$$\begin{aligned} & \frac{\partial}{\partial t}(hv) + \frac{\partial}{\partial x}(hvu) + \frac{\partial}{\partial y}(hv^2) \\ & = gh \sin \alpha_y - \frac{1}{2} \frac{\partial}{\partial y}(gh^2 \cos \alpha) + \frac{\tau_y}{\rho}. \end{aligned} \quad (3)$$

The variable h is the flow thickness, perpendicular to the topography, $\mathbf{u} = (u, v)$ is the flow velocity, α is the ground slope, $\boldsymbol{\tau} = (\tau_x, \tau_y)$ is the retarding stress, ρ is the bulk density of the lava flow, and the subscripts denote components in the x and y directions. The approach is similar to the model of Costa & Macedonio (2005), except that VolcFlow does not incorporate an equation of thermal balance, nor is cooling calculated.

Equation (1) means that the thickness, h , of the lava at a given area varies with time depending on the lava flux that enters or leaves the area (second and third terms) or on the lava flux at the vent, $\partial h_s / \partial t$ (this term equals 0 elsewhere). Equations (2) and (3) calculate the momentum variations, and thus the velocity of the lava, related to lava flux (second and third terms) and the stresses exerted (fourth–sixth term). No ‘vent’ term is included in the momentum equations because we have assumed in the following that the lava is emitted with no velocity along x and y . VolcFlow allows the user to define constant or time-dependent effusions rates and several eruptive sources, as well as the locations and the geometries of the sources.

The retarding stress, $\boldsymbol{\tau}$, varies depending on the rheology chosen. The advantage of VolcFlow is that it can solve several types of rheological equations (e.g. frictional, viscous or plastic). It can also solve other more-complex user-defined rheological laws (e.g. Davies *et al.* 2010). A fully molten lava exhibits a Newtonian rheology (Gonnermann & Manga 2007); however, crystallization of lava by cooling and degassing changes this behaviour (e.g.

Pinkerton & Sparks 1978; Cimarelli *et al.* 2011; Lev *et al.* 2012). The lava then requires a minimal shear stress in order to flow. The Bingham law is the simplest approximation of the behaviour of threshold fluids: a Bingham body remains at rest while the applied shear stresses (caused by lava weight, for instance) are less than the yield strength, τ_0 . Once the yield strength is overcome, the body flows with a flow velocity that depends on its viscosity, thickness and yield strength. The latter allows the effect of the resistant crust that stops the flow when it becomes too thin to be simulated. The resisting stress exerted by a Bingham flow is given by:

$$\boldsymbol{\tau} = \tau_0 + \eta \frac{d\mathbf{u}}{dh} \quad (4)$$

where η is the dynamic viscosity (in Pa s). Rewritten in a depth-averaged form compatible with equations (2) and (3), equation (4) becomes:

$$\tau_x = \tau_0 \frac{u_x}{\|\mathbf{u}\|} + 3\eta \frac{u_x}{h} \quad \text{and} \quad \tau_y = \tau_0 \frac{u_y}{\|\mathbf{u}\|} + 3\eta \frac{u_y}{h}. \quad (5)$$

The equations are solved using a shock-capturing numerical method based on a double upwind Eulerian scheme. The method and some tests performed to ensure the quality of VolcFlow using various rheologies are presented in Kelfoun & Druitt (2005). Another test of the capability of VolcFlow to reproduce analytical solutions for viscous rheology is presented in this Special Publication by Cordonnier *et al.* (this volume, in press). VolcFlow runs in the Matlab[®] environment and benefits from its powerful programming capacities for complex scenario definition (e.g. topography, source geometry and rates), the post-treatment of the results and the graphical output. The code and some examples of simulation can be found on the VolcFlow webpage, <http://lmv.univ-bpclermont.fr/volcflow/>.

Application to a lava flow of the Tungurahua volcano

The eruption of 4–5 December 2010

The Tungurahua stratovolcano (5023 m above sea level (asl)) is located in the Eastern Cordillera of Ecuador, and is one of the most active volcanoes in the country (Hall *et al.* 1999; Le Pennec *et al.* 2008). It is andesitic in composition (58–59 wt% SiO₂; Samaniego *et al.* 2011). The present activity, which began in 1999, is characterized by vulcanian, strombolian and subplinian explosions (Steffke *et al.* 2010; Samaniego *et al.* 2011), generating a



Fig. 1. Photographs of the NW flank of the Tungurahua volcano (Ecuador) and of the lava flow studied. This lava flow was emplaced on 4 December 2010 and is contoured with a red line (credit: B. Bernard, IG-EPN). The length of the lava flow is about 1600 m and the slope of the volcano varies from around 40° at the crater to approximately 25° at the front of the lava flow.

variety of volcanic products from the single vent located in the summit crater. In this study we focus on the paroxysm of the November–December phase of 2010, which began on 4 December. The eruption started at 13:50 UTC (=local time +5 h). It initiated a strong explosive phase, which continued for approximately 5 h, with a high eruptive ash column that rose about 4 km asl, accompanied by the generation of around 34 pyroclastic density currents that flowed down gullies to the NE, NW, west and SW of the volcano. At about 22:40 UTC on 4 December a new pulse of activity began, related to a harmonic tremor signal that was recorded for approximately 2.5 h by all of the volcano's seismic stations. Thanks to the favourable weather conditions, scientists at the Tungurahua Volcano Observatory (OVT: 13 km NW of the summit) were able to observe the emission of a lava flow flowing out of the summit crater and descending the upper part of the NW flank of the volcano (www.igepon.edu.ec: *Weekly reports, OVT-IG*) (Fig. 1). The lava-flow emplacement between 4 and 6 December was recorded with a thermal FLIR (Forward Looking InfraRed) camera, model PM 695, from the OVT. Around 90 thermal images of the lava flow were taken. Lava overflowed for a period of 5 h, and travelled for about 1.8 km over 20 h with a velocity that decreased progressively with time from a maximal initial value of about 200 m s^{-1} (Fig. 3). The thickness of the lava was estimated visually and from topography analysis to be about 3–5 m, and its volume about 10^6 m^3 .

Measurement of the lava emplacement

To check the capability of numerical models to reproduce the emplacement of a lava flow, the

extension predicted by a model is often compared with the natural extension once the lava comes to rest. However, the model also needs to be checked dynamically to evaluate the adequacy of the model chosen. To follow the evolution of the lava with time, we have developed an original photogrammetric approach. After having calculated the position and the orientation of the thermal camera, and the characteristics of the lens, we can calculate the equation of the line that passes through the image of a studied object (P_1 in Fig. 2) on the camera sensor and the centre of perspective of the camera (C in Fig. 2). The real position in space of the object (P_2), if it lies on the ground, is located at the intersection between this line and the topography. Each pixel of the lava flow can then be located on the volcano (Fig. 2). The resolution of the thermal camera is relatively low (320×240) and the precision of the lava-front location on the volcano ranges between 40 and 65 m, depending on the topographical slope and the distance from the camera. The error is represented in Figure 3 and is small relative to the 1.8 km extension of the lava.

Simulation of the lava flow

The digital elevation model (DEM) used for the simulation was calculated within the framework of the SIGTIERRAS project of the Ecuadorian government in 2011, some months after the eruption took place. The DEM resolution is 4 m. The 2010 lava is visible on the digital topography and has been removed from the DEM by extrapolating the surrounding topography. The lava is simulated by a constant flux escaping from the lower part of the rim of the summit crater. We assume a constant

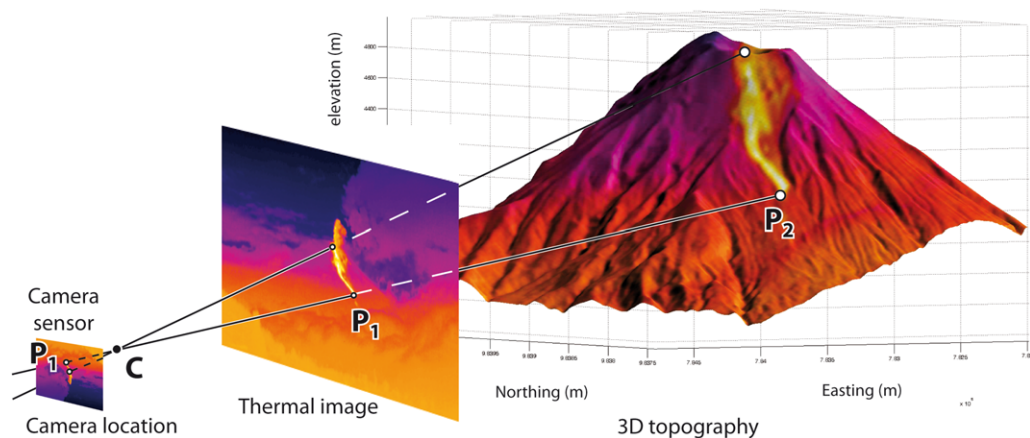


Fig. 2. The calculation of the position of the front and the extension of the lava flow through time is performed by projecting the thermal images onto a 4 m digital topography.

VOLCFLOW: CAPABILITIES AND POTENTIAL DEVELOPMENT

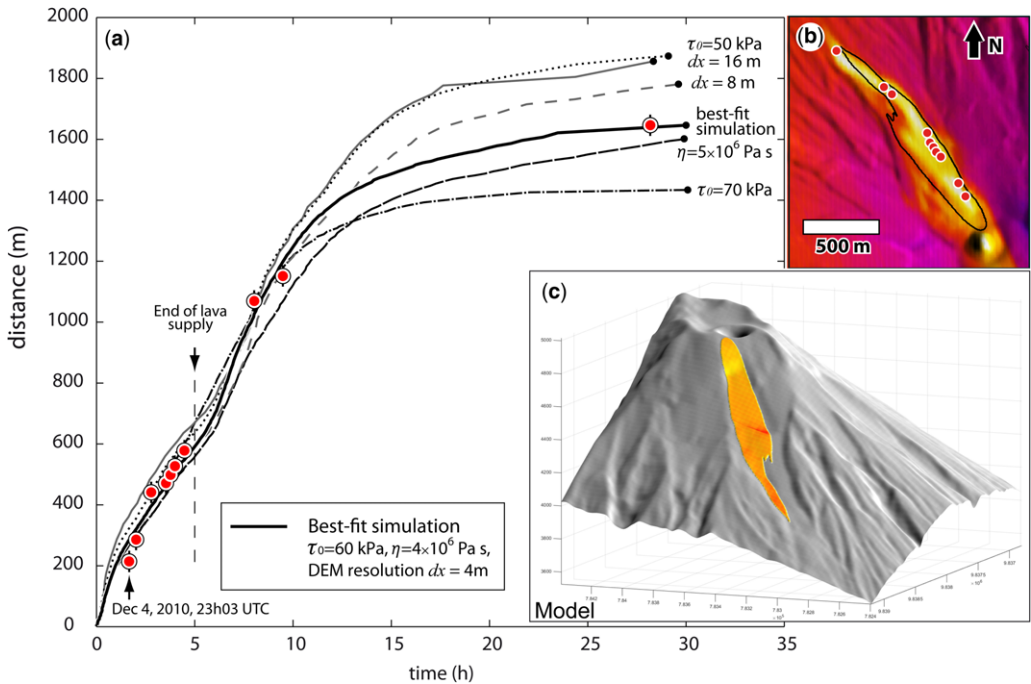


Fig. 3. (a) Time evolution of the distance between the lava front and the source during the eruption of 4 December 2010 at the Tungurahua volcano. The observations are shown by the red dots and the best-fit model by the thick black line. Other lines are simulations performed by varying one parameter of the best-fit simulation: yield strength, τ_0 , viscosity, η , or DEM resolution, dx . Error bars are estimated from the accuracy of the projection technique. Distances are calculated along the slope, following the successive position of the front. (b) The X–Y view of the thermal image projected onto the topography. The red dots are the positions of the lava front with time, as shown on (a). The real lava is in white and yellow. The black line is the simulated lava. (c) 3D view of the simulated lava flow once it is at rest. Colours indicate the lava thickness from 3 m (yellow) to 8 m (red).

rate of lava production of about 55.5 m s^{-1} in order to erupt a volume of 10^6 m^3 in 5 h. The density is fixed at 2200 kg m^{-3} .

Figure 3 shows a comparison between the position of the lava front with time based on the observation (dots) and the model (lines). Ninety thermal images were taken during the eruption but we have used the 10 best images where the lava front can be located unambiguously. The best fit is obtained for a viscosity of $\eta = 4 \times 10^6 \text{ Pa s}$ and a yield strength of $\tau_0 = 60 \text{ kPa}$ (black thick solid line). The position of the lava front with time is reproduced by the model with an error of less than 50 m, apart from the first dot (c. 100 m). The distance reached by the front at rest is simulated accurately (c. 10 m) even if the lava front is located 100 m to the east of the real front (Fig. 3b) owing to small variations in the topography that are not captured by the DEM used. The flow-front velocity, the time lava stopped moving and the thickness of the model are all also compatible with the observations (Fig. 3a, b). The area covered by the simulated lava is generally compatible with reality but

differs by about 100 m close to the lava front and in the middle of the SW edge (Fig. 3b).

To illustrate the sensitivity of the model to the rheological parameters used, Figure 3 also shows curves obtained by varying one of the parameters from the best-fit simulation. The viscosity influences the velocity of the flow (e.g. $\eta = 5 \times 10^6 \text{ Pa s}$), while the value of τ_0 controls the thickness and, consequently, the runout of the lava (e.g. $\tau_0 = 50$ and 70 kPa). A change in τ_0 of 10 kPa changes the runout by approximately 200 m (c. 12.5%).

A critical point for the simulation of some lava flows is the dependence of the results on the DEM resolution. Changing the resolution can slightly change the shape and position of the source. However, the main problem comes from the flow capability of natural lavas and models, which is related to lava thickness: for the same lava, a thick flow can move even on a horizontal surface, while a thin flow can come to a stop even on steep slopes. With a low-resolution DEM, the small-scale topography that can influence lava emplacement is

not reproduced precisely: the simulated flows can spread out more or less than those in reality. If the width changes, then the thickness also changes and, hence, the distance reached by the front. Figure 3 shows results obtained with the parameters of the best-fit model on DEMs with resolutions of 8 and 16 m. The resolution has only a small influence on the emplacement for the initial 1200 m but affects the final position of the front by up to 200 m (Fig. 3). Previous tests have shown that the simulation accuracy increases by improving DEM resolution up to a point where changes no longer have much influence on the flow length. Since we detect a large difference between the simulations carried out at resolutions of 4 and 8 m, we cannot assert that our best-fit model gives the most accurate value of the yield strength, τ_0 , and an error of ± 10 kPa is possible. The strong influence of the resolution change for the lava simulated here is due to its being channelled into a narrow valley downstream: wide, thick flows are less influenced by small variations in topography than thin, narrow flows.

Capabilities of the model and future evolutions

The example of the 4 December 2010 lava flow of Tungurahua shows that a simple isothermal approach can be used for simulating some lava-flow emplacements. VolcFlow, which is freely distributed and runs on a desktop computer, could be a useful tool for hazard assessments related to lava flows. Each simulation needs about 3 h of computation time on one 2.6 GHz processor of a desktop computer for the highest resolution (4 m) and a calculation domain of 601×501 meshes (c. 30 min with an 8 m resolution, <2 min with a 16 m resolution).

However, it should be stressed that the lava studied was emplaced during a relatively short period of time (about 20 h) and was relatively thick (3–5 m). Under these conditions, the effect of the cooling and the subsequent rheological changes is probably small, which explains how an isothermal model can reproduce the lava-flow emplacement. Future studies need to be systematically conducted to explore the limits of this isothermal approach. There is a real need for quantified observations to objectively evaluate the quality of the different models available and the assumptions made.

Cooling and associated rheological changes could also be calculated using VolcFlow (as in the approach of Costa & Macedonio 2005). Indeed, an appealing feature of the code is that it is able to advect any volumetric or surface properties. It can then easily be evolved to take additional balance equations into account, for instance for thermal

energy and crystallinity. The cooling and rheological changes of the flow could thus be calculated, as long as the physics operating in the flow is compatible with the depth-averaged assumptions. This is the principal limitation of VolcFlow: the depth-averaged approach cannot take into account complex 3D phenomena such as crust and tunnel formation, or decoupling between the crust and the hot internal lava.

The calculation time is currently a few hours, but this could easily be reduced to some tens of minutes by simplifying the numerical scheme. At present, VolcFlow uses a time-consuming numerical scheme to solve the momentum advection (equations 2 & 3) that was designed to be stable with fast, thin flows. Because lava flows are relatively slow, momentum equations are simpler to solve. Thus, if VolcFlow were to evolve further towards the simulation of lava flows, it could be simplified to speed up the calculation time.

Two other studies using VolcFlow for lava-flow simulation are presented in this Special Publication: a benchmarking study (Cordonnier *et al.*, this volume, in press), and a damage and evacuation assessment (Latutrie *et al.*, this volume, in review).

We thank the Ecuadorian SENESCYT, the Instituto Geofísico of Quito (IG-EPN) and the Institut pour la Recherche et le Développement (IRD) for their support. This research was also financed by the French Government Laboratory of Excellence initiative number ANR-10-LABX-0006, the Région Auvergne and the European Regional Development Fund. This is Laboratory of Excellence ClerVolc contribution number 135.

References

- CHARBONNIER, S. J., GERMA, A. *ET AL.* 2013. Evaluation of the impact of the 2010 pyroclastic density currents at Merapi volcano from high-resolution satellite imagery, field investigations and numerical simulations. *Journal of Volcanology and Geothermal Research*, **261**, 295–315, <http://doi.org/10.1016/j.jvolgeores.2012.12.021>
- CIMARELLI, C., COSTA, A., MUELLER, S. & MADER, H. 2011. Rheology of magmas with bimodal crystal size and shape distributions: insights from analogue experiments. *Geochemistry, Geophysics, Geosystems*, **12**, Q07024, <http://doi.org/10.1029/2011GC003606>
- CORDONNIER, B., LEV, E. & GAREL, F. In press. Benchmarking volcanic mass flow models. In: HARRIS, A., DE GROEVE, T., GAREL, F. & CARN, S. A. (eds) *Detecting, Modelling and Responding to Effusive Eruptions*. Geological Society, London, Special Publications, **426**, <http://doi.org/10.1144/SP426.7>
- COSTA, A. & MACEDONIO, G. 2005. Numerical simulation of lava flows based on depth-averaged equations. *Geophysical Research Letters*, **32**, L05304, <http://doi.org/10.1029/2004GL021817>

VOLCFLOW: CAPABILITIES AND POTENTIAL DEVELOPMENT

- CRISCI, G. M., RONGO, R., DI GREGORIO, S. & SPATARO, W. 2004. The simulation model SCIARA: the 1991 and 2001 lava flows at Mount Etna. *Journal of Volcanology and Geothermal Research*, **132**, 253–267, [http://doi.org/10.1016/S0377-0273\(03\)00349-4](http://doi.org/10.1016/S0377-0273(03)00349-4)
- DAVIES, T., MCSAVENEY, M. & KELFOUN, K. 2010. Runout of the Socompa volcanic debris avalanche, Chile: a mechanical explanation for low basal shear resistance. *Bulletin of Volcanology*, **72**, 933–944, <http://doi.org/10.1007/s00445-010-0372-9>
- FAVALLI, M., PARESCHI, M. T., NERI, A. & ISOLA, I. 2005. Forecasting lava flow paths by a stochastic approach. *Geophysical Research Letters*, **32**, L03305, <http://doi.org/10.1029/2004GL021718>
- FELPEO, A., MARTÍ, J. & ORTIZ, R. 2007. Automatic GIS-based system for volcanic hazard assessment. *Journal of Volcanology and Geothermal Research*, **166**, 106–116.
- GIACHETTI, T., PARIS, R., KELFOUN, K. & PÉREZ-TORRADO, F. J. 2011. Numerical modelling of the tsunami triggered by the Güimar debris avalanche, Tenerife (Canary Islands): comparison with field-based data. *Marine Geology*, **284**, 189–202, <http://doi.org/10.1016/j.margeo.2011.03.018>
- GONNERMANN, H. & MANGA, M. 2007. The fluid mechanics inside a volcano. *Annual Review of Fluid Mechanics*, **39**, 321–356.
- HALL, M. A., ROBIN, C., BEATE, B., MOTHES, P. & MONZIER, M. 1999. Tungurahua Volcano, Ecuador: structure, eruptive history and hazards. *Journal of Volcanology and Geothermal Research*, **91**, 1–21, [http://doi.org/10.1016/S0377-0273\(99\)00047-5](http://doi.org/10.1016/S0377-0273(99)00047-5)
- HARRIS, A. J. L. & ROWLAND, S. K. 2001. FLOWGO: a kinematic thermo-rheological model for lava flowing in a channel. *Bulletin of Volcanology*, **63**, 20–44.
- HÉRAULT, A., BILOTTA, G., VICARI, A., RUSTICO, E. & DEL NEGRO, C. 2011. Numerical simulation of lava flow using a GPU SPH model. *Annals of Geophysics*, **54**, 5, <http://doi.org/10.4401/ag-5343>
- HIDAKA, M., GOTO, A., UMINO, S. & FUJITA, E. 2005. VTFS project: development of the lava flow simulation code LavaSIM with a model for three-dimensional convection, spreading, and solidification. *Geochemistry, Geophysics, Geosystems*, **6**, Q07008, <http://doi.org/10.1029/2004GC000869>
- ISHIHARA, K., IGUCHI, M. & KAMO, K. 1990. Numerical simulation of lava flows on some volcanoes in Japan. In: FINK, J. (ed.) *Lava Flows and Domes*. IAVCEI Proceedings in Volcanology, **2**. Springer, New York, 174–207.
- KELFOUN, K. & DRUITT, T. H. 2005. Numerical modelling of the emplacement of the 7500 BP Socompa rock avalanche, Chile. *Journal of Geophysical Research*, **110**, B12202, <http://doi.org/10.1029/2005JB003758>
- KELFOUN, K., DRUITT, T. H., VAN WYK DE VRIES, B. & GUILBAUD, M.-N. 2008. Topographic reflection of Socompa debris avalanche, Chile. *Bulletin of Volcanology*, **70**, 1169–1187, <http://doi.org/10.1007/s00445-008-0201-6>
- KELFOUN, K., SAMANIEGO, P., PALACIOS, P. & BARBA, D. 2009. Testing the suitability of frictional behaviour for pyroclastic flow simulation by comparison with a well-constrained eruption at Tungurahua volcano (Ecuador). *Bulletin of Volcanology*, **71**, 1057–1075, <http://doi.org/10.1007/s00445-009-0286-6>
- KELFOUN, K., GIACHETTI, T. & LABAZUY, P. 2010. Landslide-generated tsunamis at Réunion Island. *Journal of Geophysical Research: Earth Surface*, **115**, F04012, <http://doi.org/10.1029/2009JF001381>
- LATUTRIE, B., ANDREDAKIS, I. ET AL. in review. Testing a GIS for damage and evacuation assessment during an effusive crisis. In: HARRIS, A., DE GROEVE, T., GAREL, F. & CARN, S. A. (eds) *Detecting, Modelling and Responding to Effusive Eruptions*. Geological Society, London, Special Publications, **426**.
- LE PENNEC, J.-L., JAYA, D., SAMANIEGO, P., RAMÓN, P., MORENO YÁNEZ, S., EGRE, J. & VAN DER PLICHT, J. 2008. The AD 1300–1700 eruptive periods at Tungurahua volcano, Ecuador, revealed by historical narratives, stratigraphy and radiocarbon dating. *Journal of Volcanology and Geothermal Research*, **176**, 70–81.
- LEV, E., SPIEGELMAN, M., WYSOCKI, R. J. & KARSON, J. A. 2012. Investigating lava flow rheology using video analysis and numerical flow models. *Journal of Volcanology and Geothermal Research*, **247–248**, 62–73.
- MIYAMOTO, H. & SASAKI, S. 1998. Numerical simulations of flood basalt lava flows: roles of parameters on lava flow morphologies. *Journal Geophysical Research*, **103**, 27 489–27 502.
- PINKERTON, H. & SPARKS, R. S. J. 1978. Field measurements of the rheology of lava. *Nature*, **276**, 383–385.
- SAMANIEGO, P., LE PENNECA, J.-L., ROBIN, C. & HIDALGO, S. 2011. Petrological analysis of the pre-eruptive magmatic process prior to the 2006 explosive eruptions at Tungurahua volcano (Ecuador). *Journal of Volcanology and Geothermal Research*, **199**, 69–84.
- STEFFKE, A. M., FEE, D., GARCÉS, M. & HARRIS, A. 2010. Eruption chronologies, plume heights and eruption styles at Tungurahua Volcano: integrating remote sensing techniques and infrasound. *Journal of Volcanology and Geothermal Research*, **193**, 143–160.
- WADGE, G., YOUNG, P. A. V. & MCKENDRICK, I. J. 1994. Mapping lava flow hazard using computer simulation. *Journal Geophysical Research*, **99**, 489–504.

Appendix 5.4

Bulk rock composition of Tungurahua's andesite (Chevrel *et al.* 2015).

Oxide	wt %	Normalized wt %
SiO ₂	56.31	57.49
Al ₂ O ₃	16.41	16.75
Fe ₂ O ₃ T ^a	7.37	7.52
MnO	0.12	0.12
MgO	4.66	4.76
CaO	6.59	6.73
Na ₂ O	3.96	4.04
K ₂ O	1.41	1.44
TiO ₂	0.89	0.91
P ₂ O ₅	0.24	0.25
LOI	-0.20	
Total	97.96	100

^aFe₂O₃T = total iron as Fe₂O₃.

Study Case 3: Lava flow from the December 5th, 2010 eruption of Tungurahua volcano (Ecuador)

VolcFlow basic input parameters

Symbol	Notation	Value	Units	Source
terup	Eruption time	5	h	Kelfoun & Vallejo Vargas (2015)
tmax	Maximum time	30	h	Kelfoun & Vallejo Vargas (2015)
vol	Volume	$1,0 \times 10^6$	m^3	Kelfoun & Vallejo Vargas (2015)
ρ	bulk density	2350	$kg\ m^{-3}$	Chevrel et al. (2015)

Model n°1: Isothermal

Best fit values for viscosity and yield strength

Symbol	Notation	Value	Units
η	Viscosity	$4,0 \times 10^6$	Pa s
τ	Yield strength	$6,0 \times 10^4$	Pa

Model n°2: Thermo-rheological variation

Cooling and rheological parameters

Symbol	Notation	Value	Units	Source
Cooling				
Radiation parameters				
σ	Stefan-Boltzmann	$5,67 \times 10^8$	$W\ m^{-2}\ K^{-4}$	
e	Emmissivity	0.95	--	Assumed
Convection parameters				
C_H	CH	0.0036	--	Harris & Rowland (2001)
cp_{air}	Air specific heat c _p	1500	$J\ kg^{-1}\ K^{-1}$	Harris & Rowland (2001)
T_{air}	Air temperature	298.15	K	Harris & Rowland (2001)
U	Wind speed	5	$m\ s^{-1}$	Harris & Rowland (2001)
ρ_{air}	Air density	0.4412	$kg\ m^{-3}$	Harris & Rowland (2001)
Conduction parameters				
h_{base}	hbase	0.95	m	$h_{base} = (cd * h)/100$
K	Thermal conductiv	3.7	$W\ m^{-1}\ K$	from Peck (1978)
cd	Core to base distar	19 %		$= (1,929 - 1,554*ves)^2$ Harris & Rowland (2001)
h	Thickness	5	m	Kelfoun & Vallejo Vargas (2015)
T_{base}	Basal temperature	373.15	K	$T_{base} = T_c$
Density and vesicularity				
ves	Vesicularity	0.01	--	Chevrel et al. 2015
ρ_{DRE}	DRE density	2350	$kg\ m^{-3}$	Chevrel et al. 2015

Thermal parameters

B_{uff}	Buffer ($T_h = T_{erup}$)	0	--	Assumed
T_c	Crust temperature	373.15	K	IG-EPN, measures
T_{core}	Core temperature	1173.15	K	Chevrel et al. (2015)
T_{solid}	Solid temperature	973.15	K	IG-EPN, measures
T_l	Liquidus temperature	1180	K	Chevrel et al. (2015)
f	Crust cover	1	--	Assumed

Crystal parameters

L	Latent heat of crys	$3,5 \times 10^5$	$K \text{ kg}^{-1}$	Harris & Rowland (2001)
$\Delta\phi$	Crystals growing during cooling	1.00	--	Assumed
ΔT	Cooling rate	379.35	K	Assumed
$\Delta\phi/\Delta T$	Rate of crystallizat	0.00264	K^{-1}	$= \Delta\phi / \Delta T$

Rheological parameters - model n°2a

Symbol	Notation	Value	Source
Dynamic fluid viscosity (Giordano et al., 2008)			
VFT_A	Constant independ	-4.55	Calculated from Giordano et al. (2008)
VFT_B	Adjustable parame	9740.3	with chemical composition from Chevrel et al. (2015)
VFT_C	Adjustable parame	417.7	

Relative viscosity (Krieger and Dougherty, 1967)

ϕ_{max}	Maximum packing	0.542	With an aspect ratio of 1,7 (Muller et al. 2010)
B	Einstein coefficient	3.77	

Yield strength (Dragoni (1989); Pinkerton & Stevens

CB	Constant B	0.01	Composition-dependent constant from
CC	Constant C	0.08	Dragoni (1989), Pinkerton & Stevenson

Rheological parameters - model n°2b

Symbol	Notation	Value	Units
Viscosity (constant) - Yield strength (variable)			
τ_1	Lowest yield stren	5000	Pa
τ_5	Highest yield stren	50000	Pa
T_L	Transition temper	1250	K^{-1}
τ_L	Sharpness of the tr	0.02	K

Appendix 5.5

Study Case 4.2: Lava flow from June-July, 2017

VolcFlow basic input parameters

Symbol	Notation	Value	Units	Source
terup	Eruption time	168	h	This study, Chapter 2
tmax	Maximum time	480	h	This study, Chapter 3
vol	Volume	6×10^6	m^3	This study, Chapter 4
ρ	bulk density	2000	$kg\ m^{-3}$	This study, Chapter 5

Model n°1: Isothermal

Best fit values for viscosity and yield strength

Symbol	Notation	Value	Units
η	Viscosity	$25,0 \times 10^6$	Pa s
τ	Yield strength	$6,0 \times 10^4$	Pa

Model n°2: Thermo-rheological variation

Cooling and rheological parameters

Symbol	Notation	Value	Units	Source
Cooling				
Radiation parameters				
σ	Stefan-Boltzmann	$5,67 \times 10^8$	$W\ m^{-2}\ K^{-4}$	
e	Emmissivity	0.95	--	Assumed
Convection parameters				
C_H	CH	0.0036	--	Harris & Rowland (2001)
$c_{p_{air}}$	Air specific heat c_p	1500	$J\ kg^{-1}\ K^{-1}$	Harris & Rowland (2001)
T_{air}	Air temperature	298.15	K	Harris & Rowland (2001)
U	Wind speed	5	$m\ s^{-1}$	Harris & Rowland (2001)
ρ_{air}	Air density	0.4412	$kg\ m^{-3}$	Harris & Rowland (2001)
Conduction parameters				
h_{base}	hbase	2.85	m	$h_{base} = (cd * h)/100$
K	Thermal conductivity	2.42	$W\ m^{-1}\ K$	from Peck (1978) $K = (1,929 - 1,554 * ves)^2$
cd	Core to base distance	19 %		Harris & Rowland (2001)
h	Thickness	15	m	Kelfoun & Vallejo Vargas (2015)
T_{base}	Basal temperature	373.15	K	$T_{base} = T_c$
Density and vesicularity				
ves	Vesicularity	0.24	--	Naranjo (2013)
ρ_{DRE}	DRE density	2350	$kg\ m^{-3}$	Naranjo (2013)

Thermal parameters

$Buff$	Buffer ($T_h = T_{erup}$)	0	--	Assumed
$T_{c\ off}$	Crust temperature	373.15	K	IG-EPN, measures
T_{core}	Core temperature	1173.15	K	Assumed
T_{solid}	Solid temperature	973.15	K	IG-EPN, measures
T_{liquid}	Liquidus temperature	1180	K	From Samaniego et al. (2008)
f	Crust cover	1	--	Assumed

Crystal parameters

L	Latent heat of crys	$3,5 \times 10^5$	$K\ kg^{-1}$	Harris & Rowland (2001)
$\Delta\phi$	Crystals growing during cooling	0.33	--	Naranjo (2013)
$\frac{\Delta T}{\Delta t}$	Cooling rate	379.35	K	Assumed
$\Delta\phi/\Delta T$	Rate of crystallizat	0.0036	K^{-1}	$= \Delta\phi / \Delta T$

Rheological parameters - model n°2a

Symbol	Notation	Value	Source
Dynamic fluid viscosity (Giordano et al., 2008)			

VFT_A	Constant independ	-4.55	Calculated from Giordano et al. (2008)
VFT_B	Adjustable parame	10201	with chemical composition from
VFT_C	Adjustable parame	375.72	Samaniego et al. (2008) of Matrix

Relative viscosity (Krieger and Dougherty, 1967)

ϕ_{max}	Maximum packing	0.542	With an aspect ratio of 1,7 (Muller et al.
B	Einstein coeficient	3.77	2010)

Yield strength (Dragoni (1989); Pinkerton & Stevens

CB	Constant B	0.01	Composition-dependent constant from
CC	Constant C	0.08	Dragoni (1989), Pinkerton & Stevenson

Rheological parameters - model n°2b

Symbol	Notation	Value	Units
Viscosity (constant) - Yield strength (variable)			
τ_1	Lowest yield stren	5000	Pa
τ_2	Highest yield stren	1000000	Pa
T_L	Transition temper	1050	K^{-1}
τ_L	Sharpness of the tr	0.02	K
η	Viscosity	5×10^6	Pa s

Study Case 4.3: Hypothetical flow with the same characteristics of lava flow 1

VolcFlow basic input parameters

Symbol	Notation	Value	Units	Source
terup	Eruption time	168	h	This study, Chapter 2
tmax	Maximum time	2400	h	This study, Chapter 3
vol	Volume	24.8×10^6	m^3	This study, Chapter 4
ρ	bulk density	2000	$kg\ m^{-3}$	This study, Chapter 5

Model n°1: Isothermal

Best fit values for viscosity and yield strength

Symbol	Notation	Value	Units
η	Viscosity	$25,0 \times 10^6$	Pa s
τ	Yield strength	1.5×10^5	Pa

Model n°2: Thermo-rheological variation

Cooling and rheological parameters

Symbol	Notation	Value	Units	Source
Cooling				
Radiation parameters				
σ	Stefan-Boltzmann	$5,67 \times 10^8$	$W\ m^{-2}\ K^{-4}$	
e	Emmissivity	0.95	--	Assumed
Convection parameters				
C_H	CH	0.0036	--	Harris & Rowland (2001)
$c_{p_{air}}$	Air specific heat c_p	1500	$J\ kg^{-1}\ K^{-1}$	Harris & Rowland (2001)
T_{air}	Air temperature	298.15	K	Harris & Rowland (2001)
U	Wind speed	5	$m\ s^{-1}$	Harris & Rowland (2001)
ρ_{air}	Air density	0.4412	$kg\ m^{-3}$	Harris & Rowland (2001)
Conduction parameters				
h_{base}	hbase	2.85	m	$h_{base} = (cd * h)/100$
K	Thermal conductivity	2.42	$W\ m^{-1}\ K$	from Peck (1978) $K = (1,929 - 1,554 * ves)^2$
cd	Core to base distance	19 %		Harris & Rowland (2001)
h	Thickness	15	m	Chapter 2
T_{base}	Basal temperature	373.15	K	$T_{base} = T_c$
Density and vesicularity				
ves	Vesicularity	0.24	--	Naranjo (2013)
ρ_{DRE}	DRE density	2350	$kg\ m^{-3}$	Naranjo (2013)

Thermal parameters

B_{uff}	Buffer ($T_h = T_{erup}$)	0	--	Assumed
$T_{c_{uff}}$	Crust temperature	373.15	K	IG-EPN, measures
T_{core}	Core temperature	1173.15	K	Assumed
T_{solid}	Solid temperature	973.15	K	IG-EPN, measures
T_{liquid}	Liquidus temperature	1180	K	From Samaniego et al. (2008)
f	Crust cover	1	--	Assumed

Crystal parameters

L	Latent heat of crys	$3,5 \times 10^5$	$K \text{ kg}^{-1}$	Harris & Rowland (2001)
$\Delta\phi$	Crystals growing during cooling	0.33	--	Naranjo (2013)
$\frac{\Delta T}{\Delta t}$	Cooling rate	379.35	K	Assumed
$\Delta\phi/\Delta T$	Rate of crystallizat	0.0036	K^{-1}	$= \Delta\phi / \Delta T$

Rheological parameters - model n°2a

Symbol	Notation	Value	Source
Dynamic fluid viscosity (Giordano et al., 2008)			

VFT_A	Constant independ	-4.55	Calculated from Giordano et al. (2008)
VFT_B	Adjustable parame	10201	with chemical composition from
VFT_C	Adjustable parame	375.72	Samaniego et al. (2008) of Matrix

Relative viscosity (Krieger and Dougherty, 1967)

ϕ_{max}	Maximum packing	0.542	With an aspect ratio of 1,7 (Muller et al.
B	Einstein coeficient	3.77	2010)

Yield strength (Dragoni (1989); Pinkerton & Stevens

CB	Constant B	0.01	Composition-dependent constant from
CC	Constant C	0.08	Dragoni (1989), Pinkerton & Stevenson

Rheological parameters - model n°2b

Symbol	Notation	Value	Units
Viscosity (constant) - Yield strength (variable)			
τ_1	Lowest yield stren	5000	Pa
τ_2	Highest yield stren	1000000	Pa
T_L	Transition temper	1100	K^{-1}
τ_L	Sharpness of the tr	0.02	K
η	Viscosity	5×10^6	Pa s